INTERNAL MICROSTRUCTURAL DESIGN AND CHARACTERIZATION OF METAL SELENIDES ANODE FOR EFFICIENT SODIUM STORAGE

WANG JIAN

FACULTY OF SCIENCE
UNIVERSITI MALAYA
KUALA LUMPUR

2024

INTERNAL MICROSTRUCTURAL DESIGN AND CHARACTERIZATION OF METAL SELENIDES ANODE FOR EFFICIENT SODIUM STORAGE

WANG JIAN

THESIS SUBMITTED IN FULFILMENT OF THE REQUIREMENTS FOR THE DEGREE OF DOCTOR OF PHILOSOPHY

DEPARTMENT OF PHYSICS
FACULTY OF SCIENCE
UNIVERSITI MALAYA
KUALA LUMPUR

2024

UNIVERSITI MALAYA

ORIGINAL LITERARY WORK DECLARATION

Name of candidate: **WANG JIAN**
Matric No: **S2115783**
Name of Degree: **DOTOR OF PHILOSOPHY**
Title of Thesis ("this Work")
INTERNAL MICROSTRUCTURAL DESIGN AND CHARACTERIZATION OF METAL SELENIDES ANODE FOR EFFICIENT SODIUM STORAGE
Field of Study:
PHYSICAL SCIENCE

I do solemnly and sincerely declare that:

(1) I am the sole author/writer of this work;
(2) This Work is original;
(3) Any use of any work in which copyright exists was done by way of fair dealing and for permitted purposes and any excerpt or extract from, or reference to or reproduction of any copyright work has been disclosed expressly and sufficiently and the title of the Work and its authorship have been acknowledged in this Work;
(4) I do not have any actual knowledge nor do I ought reasonably to know that the making of this work constitutes an infringement of any copyright work;
(5) I hereby assign all and every rights in the copyright to this Work to the University of Malaya ("UM"), who henceforth shall be owner of the copyright in this Work and that any reproduction or use in any form or by any means whatsoever is prohibited without the written consent of UM having been first had and obtained;
(6) I am fully aware that if in the course of making this Work I have infringed any copyright whether intentionally or otherwise, I may be subject to legal action or any other action as may be determined by UM.

Candidate's Signature Date: 22 December, 2024

Subscribed and solemnly declared before,

Witness's Signature Date: 22 December, 2024

Name:
Designation:

INTERNAL MICROSTRUCTURAL DESIGN AND CHARACTERIZATION OF METAL SELENIDES ANODE FOR EFFICIENT SODIUM STORAGE

ABSTRACT

The new energy storage system represented by sodium-ion devices has become a promising candidate in large-scale energy storage due to its low cost and fast response kinetics. However, the larger radius of sodium ions relative to lithium ions results in complex reactions and slow transport in the bulk electrode phase, leading to lower energy and power density. Therefore, it is necessary to develop microstructural designs for electrodes to enhance sodium-ion storage capacity and improve transport kinetics. Metal selenides (MSes) can provide higher capacity output through multi-electron reactions, making them promising candidates for efficient sodium ion storage anodes. However, the considerable diffusion energy barriers and narrow active interfaces of MSes are unfavorable for long-range sodium ions transport, making it difficult to achieve both high capacity and fast reaction. Therefore, optimizing the bulk phase microstructural of MSes anodes can help intrinsically improve their electrochemical performance. In this thesis, it is demonstrated that significant enhancement in energy density and power density are achieved through the synthesis of specific MSes and their engineering into heterostructures (analogous cationic heterostructures, analogous anionic heterostructures, and dissimilar heterostructures) and introduction of carbon composite (metal-organic framework (MOF)-derived carbon, monosaccharide-derived carbon (ribose), and polymer-derived carbon (PPy and PAN) carbon coating).

Additionally, this thesis details the electrolyte selection, electrochemical reaction process, and electrode activation behavior applicable to MSes anodes. The main findings are as follows. Firstly, the one-pot method selects Mo and W, which have similar metal properties, to construct bimetallic MOF precursors with different morphologies. Afterward, analogous cationic heterostructure design and homogeneous carbon introduction are achieved through a selenization/carbonization at different temperatures. The final obtained composites have abundant heterogeneous interfaces and homogeneous carbon distribution, exhibiting significant enhancement in electrochemical performance, relative to the unmodified samples. Secondly, analogous anionic heterostructures of similar S and Se are constructed using metal polysulfides (VS_4 and WS_x) precursors. Meanwhile, ribose-derived carbon sphere and polymer-derived carbon coatings (PPy and PAN) are introduced. The obtained composites show expanded lattice spacing and abundant anionic heterogeneous interfaces. Theoretical calculations and physical characterization demonstrate that the constructed anionic heterostructures have improved metal properties and strong adsorption of transformation products, exhibiting excellent cycling lifetimes and electrochemical capabilities relative to unmodified polysulfide electrodes. Thirdly, dissimilar cationic heterostructures with varying crystal structures, based on Mo and Fe bimetallic MOFs as well as Sb and W bimetallic MOFs, were synthesized. On one hand, the significant electronegativity difference between $MoSe_2$ and FeSe, coupled with the flexible valence changes of the Fe atom, creates abundant heterogeneous interfaces and induces distinct crystalline transitions in $MoSe_2$. On the other hand, the Sb_2Se_3 and WSe_2 heterostructures, with their large crystal structure differences, form perfectly parallel

interlayer structures. Exploring these two dissimilar heterostructures suggests that their construction leads to rich heterogeneous interfaces and stimulates more pronounced heterogeneous effects. This generates higher asymmetric built-in electric fields and promotes more efficient storage of Na^+.

Keywords: sodium-ion devices, heterostructure design, carbon introduction, built-in electric fields, bimetallic MOF.

ABSTRAK

Sistem penyimpanan tenaga baru yang diwakili oleh peranti natrium-ion telah menjadi calon yang menjanjikan dalam penyimpanan tenaga berskala besar disebabkan oleh kos yang rendah dan tindak balas kinetik yang pantas. Walau bagaimanapun, jejari ion natrium yang lebih besar berbanding dengan ion litium menyebabkan tindak balas yang kompleks dan pengangkutan yang perlahan dalam fasa elektrod, yang mengakibatkan ketumpatan tenaga dan kuasa yang lebih rendah. Oleh itu, adalah perlu untuk membangunkan reka bentuk mikrostruktur untuk elektrod bagi meningkatkan kapasiti penyimpanan natrium-ion dan kinetik pengangkutan yang pantas. Selenida logam (MSes) boleh memberikan output kapasiti yang lebih tinggi melalui tindak balas multi-elektron, menjanjikan anod yang cekap untuk penyimpanan ion natrium. Walau bagaimanapun, halangan tenaga resapan yang besar dan antara muka aktif yang sempit pada MSes adalah tidak baik untuk pengangkutan ion natrium jarak jauh, menjadikannya sukar untuk mencapai kedua-dua kapasiti tinggi dan tindak balas pantas. Oleh itu, mengoptimumkan struktur mikro fasa pukal pada anod MSes boleh membantu secara intrinsik memperbaiki prestasi elektrokimia mereka. Dalam tesis ini, ditunjukkan bahawa peningkatan ketara dalam ketumpatan tenaga dan ketumpatan kuasa dicapai sintesis MSes tertentu dan kejuruteraannya ke dalam heterostruktur (heterostruktur kationik serupa, heterostruktur anionik serupa, dan heterostruktur tidak serupa) dan pengenalan komposit karbon (karbon daripada rangka organik logam (MOF), karbon daripada monosakarida (ribosa), dan karbon daripada polimer (PPy dan PAN)). Selain itu, tesis ini juga secara terperinci membincangkan pemilihan elektrolit, proses tindak

balas elektrokimia, dan tingkah laku pengaktifan elektrod yang sesuai untuk anod MSes. Penemuan utama adalah seperti berikut. Pertama, kaedah satu-pot memilih Mo dan W, yang mempunyai sifat logam yang serupa, untuk membina prekursor MOF bimetalik dengan morfologi yang berbeza. Selepas itu, reka bentuk heterostruktur kationik serupa dan pengenalan karbon homogen dicapai melalui selenisasi/karbonisasi pada suhu yang berbeza. Komposit akhir yang diperoleh mempunyai antara muka heterogen yang banyak dan taburan karbon yang homogen, menunjukkan peningkatan prestasi elektrokimia yang ketara, berbanding sampel yang tidak diubah suai. Kedua, heterostruktur anionik serupa dengan S dan Se yang serupa dibina melalui prekursor logam polisulfida (VS_4 dan WS_x). Sementara itu, sfera karbon yang diperoleh daripada ribosa dan lapisan karbon daripada polimer (PPy dan PAN) diperkenalkan. Komposit yang diperolehi mempunyai jarak kekisi yang diperluas dan antara muka heterogen anionik yang banyak. Pengiraan teori dan pencirian fizikal menunjukkan bahawa heterostruktur anionik yang dibina mempunyai sifat logam dan penyerapan produk transformasi yang kuat, menunjukkan jangka hayat kitaran yang cemerlang dan keupayaan elektrokimia yang lebih baik berbanding dengan elektrod polisulfida yang tidak diubah suai. Ketiga, heterostruktur kationik tidak serupa struktur kristal yang berbeza, berdasarkan MOF bimetalik Mo dan Fe serta MOF bimetalik Sb dan W, telah disintesis. Di satu pihak, perbezaan keelektronegatifan yang jelas antara $MoSe_2$ dan FeSe, digabungkan dengan perubahan valensi yang fleksibel pada atom Fe, membentuk antara muka heterogen yang banyak sambil mendorong peralihan kristal yang berbeza pada $MoSe_2$. Di pihak lain, heterostruktur tidak serupa pada Sb_2Se_3 dan WSe_2, perbezaan struktur kristal yang besar, membentuk heterostruktur selari yang sempurna.

Penerokaan kedua-dua heterostruktur tidak serupa ini menunjukkan bahawa pembinaannya menghasilkan antara muka heterogen yang kaya dan berpotensi merangsang kesan heterogen yang lebih ketara. Ini menghasilkan medan elektrik terbina dalaman yang lebih asimetrik dan mempromosikan penyimpanan Na^+ yang lebih cekap.

Kata kunci: peranti natrium-ion, reka bentuk heterostruktur, pengenalan karbon, medan elektrik terbina dalaman, MOF bimetalik.

ACKNOWLEDGEMENT

Completing my PhD thesis has been a challenging yet incredibly rewarding journey, and it would not have been possible without the support, guidance, and encouragement of many individuals and institutions. It is with great pleasure and gratitude that I acknowledge and thank everyone who has contributed to my academic and personal growth throughout this process.

First and foremost, I would like to express my deepest gratitude to my supervisors, Assoc. Prof. Woo Haw Jiunn, Prof. Wang Bo, and Prof. Ramesh T. Subramaniam. Your unwavering support, insightful guidance, and constant encouragement have been the backbone of my doctoral journey. Your profound knowledge and enthusiasm for research have been truly inspiring. Thank you for believing in me and for providing me with the freedom to explore my ideas while always steering me in the right direction. Your patience, kindness, and dedication have been invaluable, and I feel incredibly fortunate to have had the opportunity to work under your supervision.

I would also like to extend my heartfelt thanks to my dissertation committee members. Your constructive feedback, insightful comments, and expert advice have greatly enriched my research. I am grateful for the time and effort you have invested in reviewing my work and for your invaluable contributions to this dissertation.

Special thanks go to my colleagues and friends in the Center for Ionics Universiti Malaya and Hebei Key Laboratory of Flexible Functional Materials, Hebei University of Science and Technology. The camaraderie and intellectual exchange we have shared

have made this journey not only bearable but enjoyable. I am grateful for the stimulating discussions, collaborative efforts, and the support we have provided each other. Your friendship and encouragement have been a source of strength during the more challenging times.

I am deeply indebted to the administrative and technical staff of the University of Malaya. Your assistance with the logistics and technical aspects of my research has been indispensable. I appreciate your professionalism and willingness to help with any issues that arose, allowing me to focus on my research.

I would also like to acknowledge the financial support that made this research possible. I am grateful to Fundamental Research Grant Scheme (FRGS) for providing the necessary funding for my studies and research. Your support has been crucial in allowing me to pursue my academic goals without financial constraints.

A very special thank you goes to my family. To my parents, Wang Lijie and He Suling, your unconditional love, sacrifices, and unwavering belief in me have been my greatest source of motivation. Your constant support and encouragement have given me the strength to persevere through the toughest times. To my younger brother, Wang He, thank you for always being there for me and for your continuous encouragement and love.

Finally, to my partner, Feng Xiaoyu, your love, patience, and support have been my anchor throughout this journey. Thank you for standing by my side, for understanding the demands of my work, and for always lifting my spirits. Your belief in me has been a constant source of inspiration, and I am forever grateful for your presence in my life.

This dissertation is as much a product of my efforts as it is a testament to the support

and encouragement of all the wonderful people in my life. To everyone who has been part of this journey, thank you from the bottom of my heart. This accomplishment would not have been possible without you.

TABLE OF CONTENTS

LIST OF FIGURES

LIST OF TABLES

LIST OF SYMBOLS AND ABBREVIATIONS

R_{ct}	:	charge transfer resistance
t	:	current pulse duration
D	:	diffusion parameter of Na+
I	:	discharge current
ΔV	:	discharge potential change
E	:	energy density
V_{min}	:	final discharge potential
V_{max}	:	initial discharge potential
$k_2 v^{1/2}$	:	intercalation current contribution
m_+	:	mass of cathode
m_-	:	mass of anode
M	:	molar mass
V_m	:	molar volume
i	:	peak current value
ΔE_t	:	potential change in constant-current pulse
ΔE_-	:	potential difference of the anode
ΔE_+	:	potential difference of the cathode
P	:	power density
$k_1 v$	:	pseudocapacitance current contribution
τ	:	relaxation time
v	:	scan rate in CV
C	:	specific capacitance
c_-	:	specific capacity of anode

c_+	:	specific capacity of cathode
ΔE_s	:	steady-state potential change
l	:	thickness of the electrode
AC	:	activated carbon
BET	:	brunauer-emmett-teller
COFs	:	covalent organic frameworks
CV	:	cyclic voltammetry
CVD	:	chemical vapor deposition
DEC	:	dimethyl carbonate
DFT	:	density-functional theory
DOS	:	density of states
DME	:	dimethyl ether
DMF	:	dimethylformamide
dQ/dV	:	differential capacity curve
EDS	:	energy dispersive spectroscopy
EC	:	ethylene carbonate
EIS	:	electrochemical impedance spectroscopy
EPR	:	electron paramagnetic resonance
FTIR	:	fourier transform infrared spectroscopy
F127	:	triblock copolymer surfactant pluronic F127
GCD	:	galvanostatic charge-discharge
GGA-PBE	:	generalized gradient approximation of perdew-burke-ernzerhof
GITT	:	galvanostatic intermittent titration technique
GO	:	graphite oxide
HOMO	:	highest occupied molecular orbital

HRTEM	:	high-resolution transmission electron microscopy
ICE	:	initial coulombic efficiency
LIBs	:	lithium-ion batteries
LUMO	:	lowest unoccupied molecular orbital
MOF	:	metal-organic framework
Mo/Fe-MOF	:	Mo and Fe bimetallic metal-organic framework
$MoSe_2$/FeSe	:	$MoSe_2$ and FeSe dissimilar heterostructure
MOs	:	Metal oxides
Mo/W-MOF	:	Mo and W bimetallic metal-organic framework
$MoWSe_2$	:	$MoSe_2$ and WSe_2 analogous cationic heterostructure
$MoWSe_2$/WO_3	:	$MoSe_2$, WSe_2, and WO_3/C with analogous cationic heterostructure
MSes	:	metal selenides
MSs	:	metal sulfides
PAN	:	polyacrylonitrile
PVDF	:	polyvinylidene fluoride
Sb/W-MOF	:	Sb and W bimetallic metal-organic framework
Sb_2Se_3/WSe_2	:	Sb_2Se_3 and WSe_2 dissimilar heterostructure
SEI	:	solid electrolyte interphase
SEM	:	scanning electron microscopy
SIB	:	sodium-ion battery
SIC	:	sodium-ion capacitor
TAA	:	thioacetamide
TEM	:	transmission electron microscopy
TGA	:	thermogravimetric analysis
$Na_xTi_yO_z$	:	sodium titanate

VASP	:	vienna ab-initio simulation package
VSSe	:	$V_{1.11}S_2$ and $V_{1.13}Se_2$ analogous anionic heterostructures
$WSSe_2$	:	S modified WSe_2 analogous anionic heterostructures
XPS	:	X-ray photoelectron spectroscopy
XRD	:	X-ray diffraction
XRF	:	X-ray fluorescence spectrometer
0D	:	zero-dimensional
1D	:	one-dimensional
2D	:	two-dimensional
3D	:	three-dimensional

LIST OF APPENDICES

CHAPTER 1: INTRODUCTION

1.1 Research Background

According to the current energy structure, energy shortage and environmental pollution have become critical challenges with the rapid socioeconomic development. (O'Heir, 2017; Zhenguo Yang et al., 2011) These challenges have accelerated the development of clean and renewable wind and solar energy. (Yayuan Liu et al., 2019) Increasing the proportion of renewable energy systems based on solar, wind, and tidal energy is vital to improving the current situation and controlling CO_2 emissions. (Zuo et al., 2017) However, several inherent shortcomings of renewable energy systems, such as over-reliance on weather/natural conditions and transient nature, make achieving a continuous and stable energy supply impossible. (Yuncai Chen et al., 2019) Therefore, developing stable and efficient energy storage systems is essential for achieving a sustainable energy supply. (B. Wang et al., 2022) Among various energy storage modes, electrochemical energy storage systems represented by secondary batteries and supercapacitors exhibit apparent advantages in terms of energy densities and power densities, respectively. (D. P. Dubal et al., 2015; Y. Sun et al., 2016) Lithium-ion batteries (LIBs) dominate the field of portable energy storage due to their exceptional specific energy. However, LIB systems face challenges in rate and cycling performance due to the slow ion diffusion and high volumetric strains during the charging and discharging process.[1] (F. Yuan, Zhang, et al., 2022) Additionally, lithium resources' uneven distribution and price volatility became the additional factors limiting the

[1] Part of the content in this chapter has been published in Chemical Engineering Journal, 478, 147485.

development of LIBs. The predicted shortage of lithium supply chain beyond 2030 and the high cost of cobalt have restrained the prospects of LIBs. The above shortcomings mean that LIBs cannot be used in large-scale energy storage fields that require power performance and rapid response. Therefore, as the demand for large-scale energy storage continues to grow and the costs of raw materials rise, it is urgent to accelerate the development of alternative and complementary devices for LIBs.

Figure 1.1: Illustration of a sodium-ion battery system. (Hwang et al., 2017)

Sodium-ion energy storage devices represented by sodium-ion batteries and capacitors (SIBs and SICs) have great potential in large-scale energy storage due to their economic advantages. (Kundu et al., 2015; Vaalma et al., 2018) As shown in Figure 1.1, SIBs and SICs mainly comprise anode material, cathode, electrolyte, and diaphragm. The difference is that the cathode of SICs is primarily based on activated carbon, considering the fast charge/discharge capability. However, SIBs employ conventional polyanionic or layered oxide type cathodes similar to LIBs. Since the composition and assembly process of SIBs/SICs is highly identical to that of LIBs, it could simply integrate into the existing infrastructure and product ecosystem of LIBs. SIBs/SICs apply Na^+ as the charge carrier, while LIBs use Li^+ as the charge carrier. Compared to

lithium resources, sodium is available in the ocean and is more environmentally friendly. The supply of sodium is practically infinite. Moreover, SIBs have a similar "rocking chair" energy storage mechanism with LIBs. Remarkably, Na^+ migrates from the cathode and then inserts into the anode during the charging process, respectively. In contrast, Na^+ is released from the anode and inserted into the cathode when discharging occurs (Figure 1.2a). The repeated insertion/de-insertion of Na^+ between the cathode and anode during charging and discharging is pictorially named "rocking chair". Differently, as for the mechanism of SICs, Na^+ and anions in the electrolyte migrate toward the anode and cathode surfaces during the charging process, respectively. Conversely, when the discharge reaction occurs, the ions adsorbed on both electrodes are released and returned to the electrolyte (Figure 1.2b).

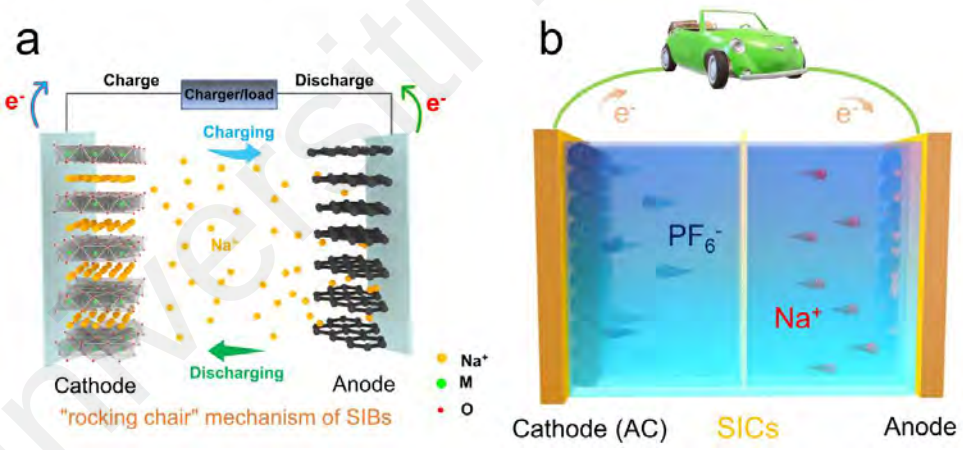

Figure 1.2: The SIBs (a) and SICs (b) energy storage mechanisms.

1.2 Motivations

SIBs/SICs can offer lower raw material costs and better safety, and they are environmentally friendly, which is ideal for large-scale applications. However, the large Na^+ radius (1.02 Å) and molar mass (22.99 g mol^{-1}) make it challenging to utilize electrode materials' performance fully. (Nayak et al., 2018) In SIBs, the anode cost is

about 20−30% of the total equipment cost, and this percentage may increase further in SICs. (Perveen et al., 2020) Therefore, developing electrodes that can accommodate severe structural strains and stimulate fast Na^+ reaction kinetics is crucial for developing SIBs/SICs, especially for anode materials with satisfactory reversible capacity.

Among various anode materials for SIBs, hard carbon is the most widely used commercially. However, the theoretical specific capacity of hard carbon anodes is only 300−400 mA h g^{-1}. The limited specific capacity is the most significant challenge restricting their advancement to high energy density. Additionally, high power density is essential for developing secondary energy storage devices, especially sodium-ion devices, which can be applied to large-scale energy storage. Therefore, it is necessary to work on the development of anode materials with high power density. Metal selenides (MSes) dominated by conversion reactions can provide high specific capacity output through multi-electron reactions. In addition, MSes can stimulate more surface pseudocapacitive reactions through rapid redox capability, which is conducive to achieving fast ion kinetics to meet high power demands. However, most MSes suffer from the challenges of intrinsically low electron/ion mobility and severe volume expansion, which become the main factors hindering their further development. Moreover, during fast electrochemical processes, the specific capacity and fast pseudocapacitive behavior caused by incomplete reactions within the bulk MSes materials are difficult to fully activate. Therefore, it is necessary to design structural modification strategies to enhance the potential of MSes as promising anodes for SIBs/SICs.

1.3 Objectives

Based on the previous description, the objective of this work is to perform structural modification of MSes to accommodate the high power and high energy density requirements for SIBs/SICs anodes. Specifically, this research focuses on addressing the issues of low specific capacity, poor rate performance, and short cycle life caused by the low electronic/ion transport rates and structural degradation of MSes during electrochemical processes through rational structural design. The overall design concept includes both internal microstructure design and introduction of carbon composite. Unlike other work that simply performs nanosizing strategies such as microform design, ion doping, and reducing the particle size of MSes, the optimized design and distribution of the bulk phase structure of the material from the microscopic perspective is expected to improve the electrochemical performance of MSes anodes essentially. Based on that, the internal microstructure design in this research is mainly based on mixed-phase engineering, which in turn facilitates rapid Na^+ transport. From that, the heterostructure engineering can be divided into analogous and dissimilar heterostructure designs. Further, the analogous heterostructure design constructs highly distributed cationic and anionic heterostructures from two similar physical phase structures. On the other hand, the dissimilar heterostructure design is a heterogeneous structure constructed by two different mixed phases. The basic principle of heterostructure involves the cross-distribution of different components within the bulk phase to change the original crystal structure and create a built-in electric field with an uneven electron distribution. The presence of the built-in electric field can improve the intrinsic material

conductivity and accelerate the rapid ion transfer in the bulk phase.

In addition to microstructural modification, carbon is introduced to improve the materials' electrical conductivity and surface ion adsorption capacity. Accordingly, various carbon introduction strategies have been applied to modify the MSes electrode. However, excessive carbon cladding or loading should be avoided, as it may reduce the reactive sites on the material surface and even hinder the deeper insertion of Na^+. Maintaining the homogeneity of carbon distribution and avoiding particle aggregation during carbon introduction are still the key issues requiring attention. Therefore, well-designed carbon introduction strategies are needed to uniformly improve the overall structure's conductivity and stability, thus ensuring the active material's high specific capacity and fast charge/discharge capability. This project focuses on three porous carbon introduction strategies to construct composites: MOF-derived carbon, monosaccharide-derived carbon, and organic polymer-derived carbon, and explores in detail the necessity of each carbon introduction method. Therefore, the specific objectives of the research are:

1. To synthesize analogous cationic heterostructures (abbreviated as $MoWSe_2$/C and $MoWSe_2/WO_3$/C) based on Mo and W bimetallic MOF, Se and MOF-derived carbon.
2. To synthesize analogous anionic heterostructures (abbreviated as $WSSe_2$/C and VSSe/C) based on WS_3 and VS_4 polysulfides, Se, monosaccharide-derived and polymer-derived (PPy and PAN) carbon.
3. To synthesize dissimilar cationic heterostructures (abbreviated as $MoSe_2$/FeSe/C

and $Sb_2Se_3/WSe_2/C$) based on Mo and Fe bimetallic MOF, Sb and W bimetallic MOF, Se, and MOF-derived carbon.

4. To characterize the physical and structural properties (morphology, crystal structure, thermal stability and surface chemical state) of the synthesized composites using advanced analytical techniques and DFT simulations.
5. To investigate the electrochemical performance (CV, GCD, dQ/dV, pseudocapacitance behavior, energy and power density) of the synthesized composites as anode in SIBs and SICs.

1.4 Thesis Outline

This thesis contains 7 chapters: introduction, literature review, experimental methods, results & discussion, and conclusions & suggestion for future works.

Chapter 1 presents the introduction of the thesis, which includes the research background, motivations, objectives, and thesis outline.

Chapter 2 summarizes and discusses the different reactive types of anode materials and scrutinizes various microstructural modification strategies for MSes anodes.

Chapter 3 describes the experimental methods, including materials, equipment, material synthesis and preparation, characterization techniques, and density functional theory calculations.

Chapter 4 synthesized $MoSe_2$ and WSe_2 carbon composite with analogous cationic heterostructure (abbreviated as $MoWSe_2$/C), and $MoSe_2$, WSe_2, and WO_3/C (abbreviated as $MoWSe_2/WO_3$/C) with analogous cationic heterostructure by constructing Mo and W bimetallic MOF (Mo/W-MOF) precursors, respectively. Additionally, the synthesized composites are physically, electrochemically, heterostructurally, and electrolyte-selectively characterized.

Chapter 5 describes the carbon sphere-loaded S modified WSe_2 analogous anionic heterostructures (abbreviated as $WSSe_2$/C) and carbon-coated $V_{1.11}S_2$ and $V_{1.13}Se_2$ analogous anionic heterostructures (abbreviated as VSSe/C), respectively. The excellent properties of the prepared complexes are fully revealed by physical and electrochemical characterization.

Chapter 6 introduces Mo and Fe bimetallic MOF (abbreviated as Mo/Fe-MOF) derived $MoSe_2$ and FeSe dissimilar heterostructure (abbreviated as $MoSe_2$/FeSe/C). Additionally, Sb and W bimetallic MOF (abbreviated as Mo/Fe-MOF) derived Sb_2Se_3 and WSe_2 dissimilar heterostructure (abbreviated as Sb_2Se_3/WSe_2/C) is also synthesized. The above samples are physically structured and electrochemically characterized.

Chapter 7 is the final chapter of the thesis, consisting of conclusions and suggestions for future work.

CHAPTER 2: LITERATURE REVIEWS

2.1 Anode Materials for Sodium-ion Devices

The development of anode materials with high power density is a crucial challenge in advancing SIBs and SICs. The power density of these devices is significantly influenced by the reaction mechanisms occurring both on the surface and within the interior of the anode materials. (B. Wang et al., 2022) Based on these mechanisms, anode materials for Na^+ storage can be classified into four categories: intercalation-type anodes, adsorption/desorption-type anodes, alloying-type anodes, and conversion-type anodes (Figure 2.1). Each type offers unique characteristics regarding reaction mechanisms, specific capacity, cycling performance, stability, and other electrochemical properties.[2]

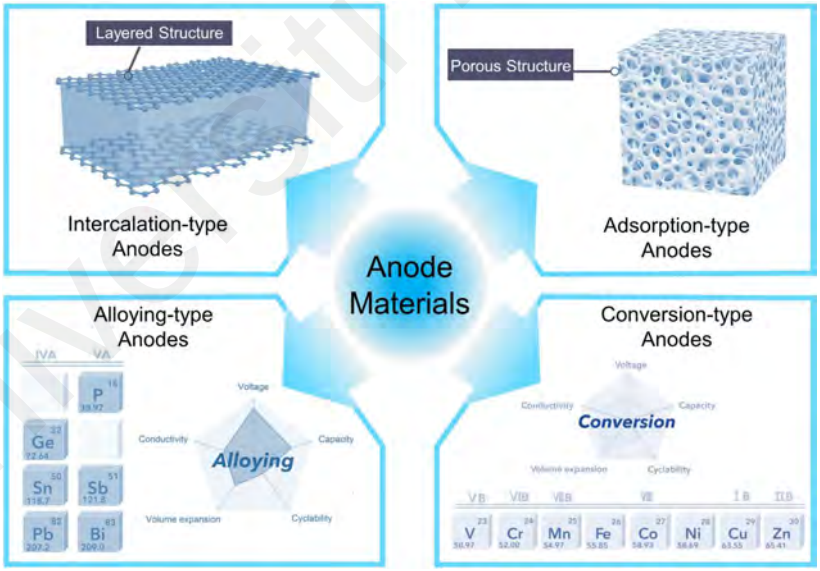

Figure 2.1: Schematic diagram of different anode materials for SIBs/SICs with varying reaction mechanisms.

[2] Part of the content in this chapter has been published in Chemical Engineering Journal, 478, 147485.

2.1.1 Intercalation-Type Anodes

Intercalation-type anodes store energy through the reversible insertion and extraction of Na^+ ions within a layered structure. These materials are generally characterized by small structural changes and good cycling stability but have lower specific capacities. The schematic diagram of the Na^+ intercalation process in intercalation-type anodes is shown in Figure 2.2. Critical examples of intercalation-type anodes include graphite, hard carbon, and sodium titanate ($Na_xTi_yO_z$).

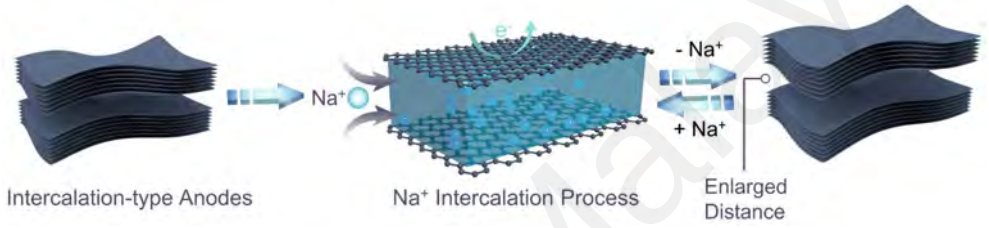

Figure 2.2: Schematic diagram of Na^+ intercalation process in intercalation-type anodes.

2.1.1.1 Graphite

Graphite, a well-known anode material for LIBs, features a long-range ordered layered structure that allows for the insertion of alkali metal ions. However, its application in SIBs is limited due to the larger ionic radius of Na^+ and the thermodynamic instability of binary sodium intercalations, resulting in a low theoretical capacity (~35 mA h g^{-1}) compared to its capacity for LIBs (~372 mA h g^{-1}). Researchers have explored various strategies to improve sodium storage in graphite. By expanding the layer spacing through controllable oxidative reduction, expanded graphite can enhance Na^+ storage while maintaining its ordered structure. As shown in Figure 2.3, Wen et al. successfully prepared expanded graphite with a layer spacing of 4.3 Å, achieving a high reversible specific capacity of 284 mA h g^{-1}. (Wen et al., 2014) Figure

2.3a illustrates that Na^+ ions cannot be electrochemically intercalated into graphite due to its small interlayer spacing. In contrast, Figure 2.3b shows that the increased interlayer distance in graphite oxide (GO), resulting from oxidation, permits the electrochemical intercalation of Na^+. However, this process is hindered by the presence of numerous oxygen-containing groups. Figure 2.3c demonstrates that expanded graphite allows for a significant amount of Na^+ intercalation, thanks to its appropriate interlayer distance and reduced oxygen-containing groups. Reducing the particle size to the nanoscale shortens the diffusion path for sodium ions, improving intercalation kinetics. Dey et al. enhanced Na^+ storage kinetics through surface functionalization and nanostructuring of similar carbon isomers. (Sonjoy Dey et al., 2023)

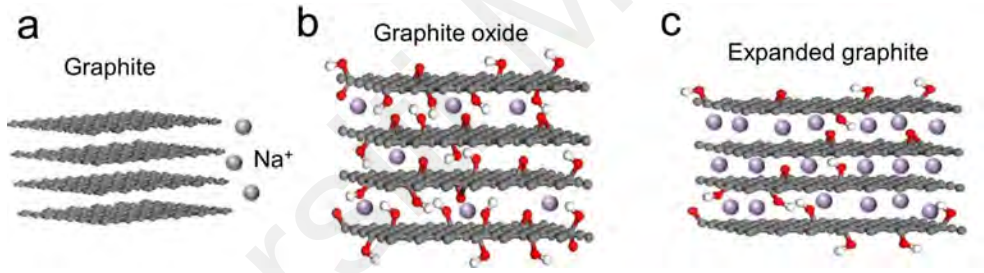

Figure 2.3: Schematic illustration of sodium storage in graphite-based materials. (a) Graphite. (b) Graphite oxide (GO). (c) Expanded graphite. (Wen et al., 2014)

2.1.1.2 Hard Carbon

Hard carbon, an amorphous carbon material with a disordered structure, offers larger interlayer spacing than graphite, facilitating Na^+ intercalation. Unlike graphite, the Na^+ storage mechanism in hard carbon includes quasi-intercalation, adsorption, and microporous filling. Hard carbon is typically prepared by carbonizing biomass or organic polymers that are difficult to graphitize above 2500 °C. The resultant material features a low degree of graphitization, with a microstructure comprising disordered graphite microcrystals and amorphous regions, known as the "house of cards" structure.

(M. Zhang et al., 2021) This disordered structure provides abundant defects and micropores, creating numerous active sites for rapid Na^+ storage. Hard carbon achieves capacities in the range of 250−350 mA h g^{-1}, significantly higher than graphite, making it a promising anode material for SIBs. (X. Fan et al., 2024) One of the main challenges with hard carbon is its low initial coulombic efficiency (ICE), often below 80%. This is primarily due to the formation of a SEI layer and various defects and active sites that consume Na^+ during the first cycle. Moreover, the density of hard carbon is very low, and most of the capacity exertion interval is located at voltages near the sodium plating (0−0.1 V), which further leads to safety issues associated with the formation of Na dendrites at high power densities. Cai et al. prepared hard carbon materials (HCNFs) with short-range graphite layers and large layer spacing (0.37−0.40 nm) to provide efficient insertion storage of Na^+. As shown in Figure 2.4, in-situ XRD and Raman characterization revealed an improved adsorption/insertion-filled Na^+ storage mechanism, verifying that the large layer spacing could provide a smooth channel for rapid Na^+ diffusion. (C. Cai et al., 2022) However, it is important to note that while hard carbon materials offer superior Na^+ storage capacity compared to graphite, their relatively low-capacity utilization poses a drawback in achieving high energy and power density.

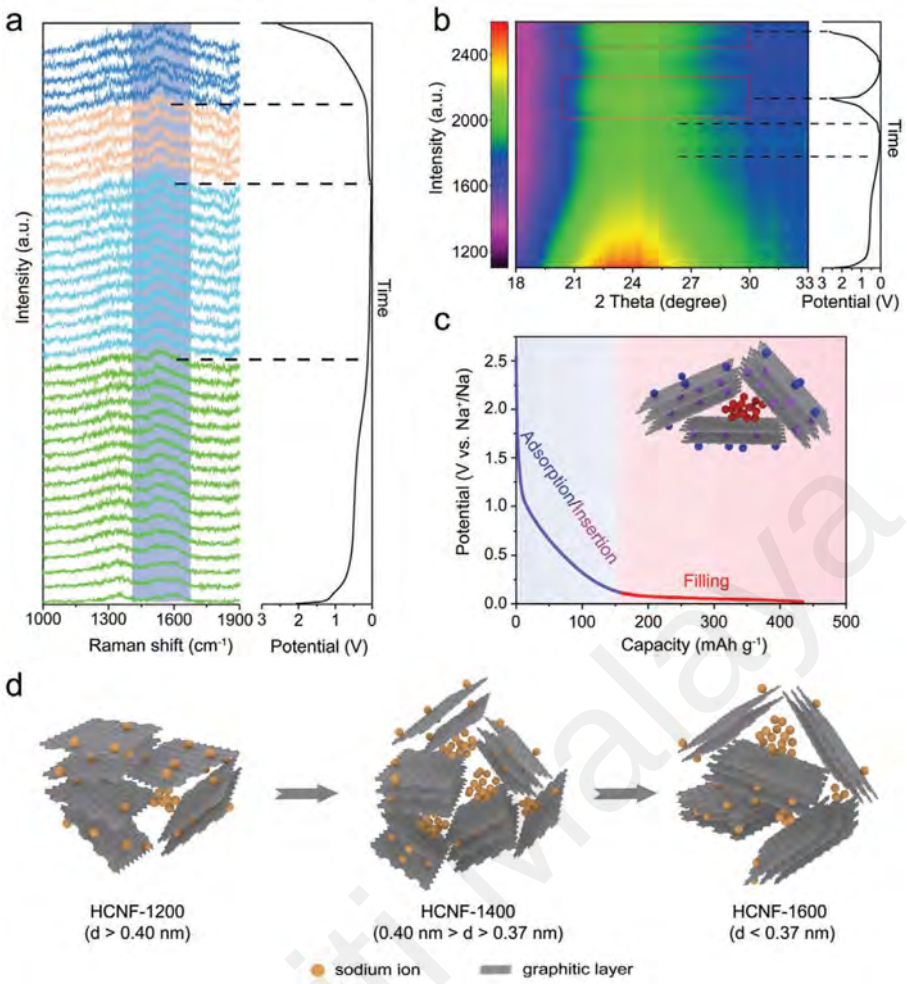

Figure 2.4: In-situ Raman spectra (a) and in-situ XRD patterns (b) of the HCNF-1400. (c) Schematic illustration for sodium storage mechanism in the HCNFs. (d) Schematic illustration for the sodium storage manners of HCNF-1200, HCNF-1400, and HCNF-1600. (C. Cai et al., 2022)

2.1.1.3 Sodium Titanate ($Na_xTi_yO_z$)

$Na_xTi_yO_z$, a layered oxide material, shows promise as an intercalation-type anode for SIBs due to its structural stability and relatively high theoretical capacity. Unlike its lithium counterpart ($Li_xTi_yO_z$), $Na_xTi_yO_z$ is expected to exhibit minimal volume changes during cycling, contributing to excellent cycling stability. However, sodium titanate suffers from a high Na migration barrier (~0.75 eV) and poor electronic conductivity, limiting its cyclable capacity and rate capability. Research efforts focus on ion doping and composite formation to improve performance. For instance, Sarkar et al. achieved a

high specific capacity of 237 mA h g^{-1} and long-term cycling stability of up to 4000 cycles by preparing $Na_2Ti_3O_7$ through a hydrogenated metal doping strategy. Figure 2.5a-c successfully reveal the XRD and crystal structure features of the prepared zirconium-doped hydrogenated $Na_2Ti_3O_7$ (HNTOZr). (Sarkar et al., 2020) Chandel et al. enhanced the conductivity of sodium titanate by partially replacing Ti^{4+} with Mo^{6+} in its crystal structure without compromising the original framework. The Mo^{6+} ions, having an ionic radius comparable to Ti^{4+}, increased the material's conductivity and introduced additional oxygen vacancies, thereby improving the transport efficiency of Na^+ to some extent. However, sodium titanate's intrinsic capacity and structural configuration inherently limit its electrochemical performance in the intercalation mechanism. Despite extensive research efforts to enhance the electrochemical properties of $Na_xTi_yO_z$ electrodes, their poor conductivity and low capacity remain significant challenges, making it difficult for these materials to achieve excellent performance in SIB applications. Chandel et al. first prepared a 15 wt% Mo-doped sodium titanate nanostructured anode (MoNTO-15) by solvothermal method, exhibiting enhanced conductivity and Na^+ transport efficiency. Figures 2.5d-l exhibit the basic morphological structure of the prepared MoNTO-15. Following the analysis, the main reason for the improved electrochemical performance is that Mo doping brings abundant oxygen vacancies and provides multiple diffusion pathways for Na^+ diffusion. (Chandel et al., 2022)

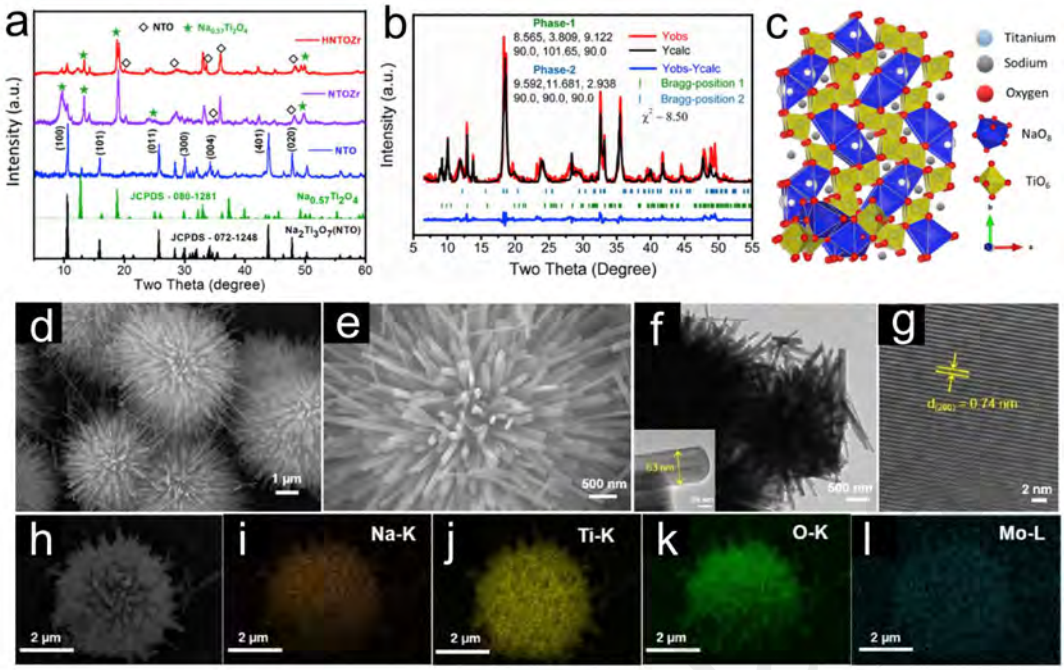

Figure 2.5: (a) Characteristic XRD pattern of as-prepared different $Na_2Ti_3O_7$ showed after zirconium-doped the single-phase NTO converted to the mixed phase of $Na_2Ti_3O_7$ (monoclinic) and $Na_{0.57}Ti_2O_4$ (orthorhombic). (b) The characteristic XRD pattern of mixed-phase HNTOZr was analyzed using commercial FullProf Suite software. (c) typical monoclinic $Na_2Ti_3O_7$ structure with possible sodium intercalation position. (Sarkar et al., 2020) (d) FE-SEM images of MoNTO-15 at low magnification. (e) FE-SEM images of MoNTO-15 at high magnification. (f) FE-TEM images of MoNTO-15. HR-TEM images (g) and representative elemental mapping (h-l) of the MoNTO-15 sample. (Chandel et al., 2022)

In summary, intercalation-type anode materials offer good cycling stability due to minimal structural changes during Na^+ insertion and de-insertion. Among these, hard carbon stands out for its higher capacity and better performance than graphite and sodium titanate. However, challenges such as slow Na^+ insertion/deinsertion, low initial coulombic efficiency, and poor electronic conductivity need to be addressed. Advances in doping, nanostructuring, and composite material development hold promise for improving the performance of intercalation-type anodes, paving the way for more efficient and stable SIBs. Consequently, metal compound materials that utilize transformation and alloying reactions are gaining attention due to their high-capacity

potential.

2.1.2 Adsorption/Desorption-Type Anodes

Adsorption/desorption-type anode materials store energy through the surface adsorption and desorption of Na^+. These materials often exhibit high surface areas and porous structures that facilitate the rapid movement of ions, which can lead to high-rate capabilities and good cycling stability. However, their specific capacities are generally lower compared to alloying or conversion-type materials. The schematic diagram of Na^+ adsorption and desorption process in adsorption/desorption-type anodes is shown in Figure 2.6. Key adsorption/desorption-type anode materials include porous carbon and certain organic compounds.

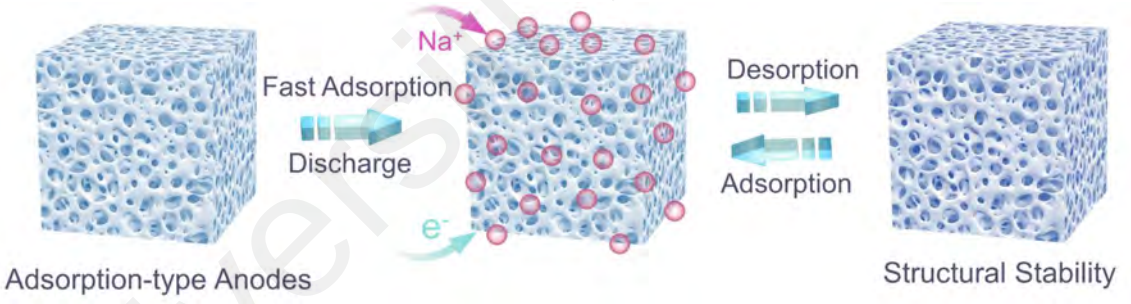

Figure 2.6: Schematic diagram of Na^+ adsorption and desorption process in adsorption/desorption-type anodes.

2.1.2.1 Porous Carbon Materials

Porous carbon materials are widely used for SIB anodes due to their high surface area, good electrical conductivity, and tunable pore structures. These characteristics enable the efficient adsorption and desorption of Na^+. Porous carbon materials have a large specific surface area, which provides numerous active sites for Na^+ adsorption. Moreover, porous carbon materials are generally good conductors, which help reduce

the battery's internal resistance and improve its rate performance. Porous carbon materials have various morphology designs and flexible pore tunability. The pore size and distribution can be engineered to optimize ion transport and storage. Based on the above advantages, porous carbon materials are considered promising anode materials for SIBs and high-quality substrates or frameworks for other electrode materials. Generally, porous carbon materials can be categorized into amorphous carbon, porous graphene/carbon nanotubes (CNTs) materials, heteroatom-functionalized porous carbon, biomass-derived porous carbon, and MOF-derived porous carbon (Figure 2.7).

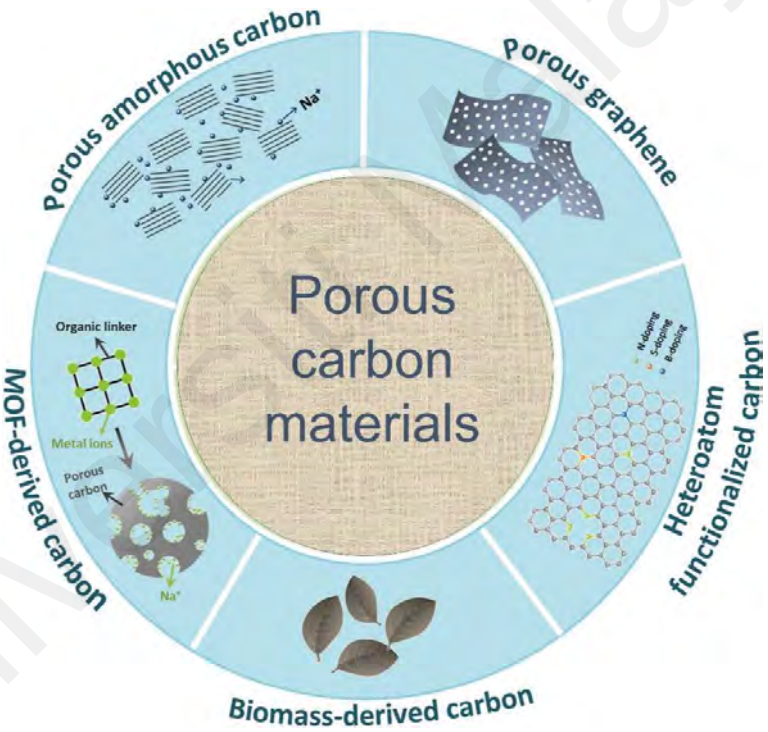

Figure 2.7: Illustration of synthesis strategies and structural design of porous carbon-incorporated anodes for SIBs/SICs.

Activated carbon (AC) is an amorphous carbon material; its abundant pores are produced through physical or chemical activation. The AC anode often offers high surface areas and has been extensively studied in SIBs. (Q. Li et al., 2018) As shown in Figure 2.8a, Kumar et al. first obtained activated carbon by pyrolyzing styrene

acrylonitrile (SAN) plastic and applied it to SIBs anodes, demonstrating excellent rate performance and high-capacity retention. (U. Kumar et al., 2019) Although Na^+ energy storage devices widely study activated carbon anodes due to their rich porous structure. However, limited by the large pore size, it is often applied to the cathode of SICs with bilayer adsorption properties to supply ultrafast adsorption of small amounts of Na^+. When applied to SIBs, activated carbon is often used as a precursor for late-stage pore structure design by constructing a gradient pore structure to accommodate the microporous filling mechanism of Na^+, which in turn ensures more capacity. Tian et al. successfully achieved pore structure tunability of activated carbon materials (XAs) using repeated impregnation and carbonization of liquid bitumen (Figure 2.8b). After the pyrolysis process, the bitumen acted as a gap filler to reduce the specific surface area of the activated carbon. It formed abundant micropores with diameters of less than 1 nm for deep filling of Na^+, significantly improving the initial ICE. (Y. R. Tian et al., 2024) Hard carbon is also a major candidate for amorphous materials whose sodium storage mechanism also involves adsorption behavior. However, hard carbon anodes' low specific capacity and Coulombic efficiency issues are still the main constraints for their further development.

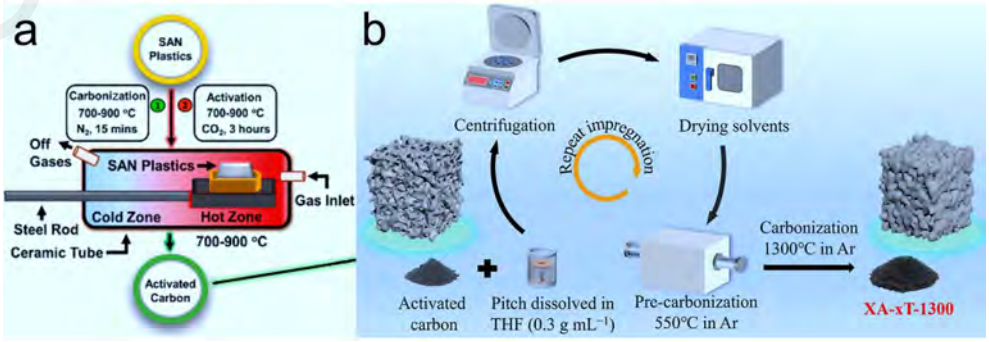

Figure 2.8: (a) The schematic diagram of the preparation of porous carbon by SAN plastics. (U. Kumar et al., 2019) (b) Schematic illustration of the fabrication procedure of XAs. (Y. R. Tian et al., 2024)

Graphene and CNTs have been extensively studied for SIB anodes due to their excellent electrical conductivity and mechanical strength. Graphene is a single layer of carbon atoms arranged in a hexagonal lattice. It has exceptional electrical conductivity, mechanical properties, and a high surface area, making it a promising material for SIBs. However, the two-dimensional nature of graphene makes it intrinsically easy to restack, further reducing the surface area that can be exposed, thus affecting the diffusion behavior of ions during electrochemical processes. Therefore, related works have mostly focused on the preparation of porous graphene using various strategies to reduce the ion diffusion distance. As shown in Figure 2.9a, b, Mace et al. synthesized graphene with a hierarchical pore structure by thermal reduction, exhibiting excellent Na^+ storage properties. (Mace et al., 2020) Similarly, Zhao et al. prepared reduced graphene sheets by a simple H_2O_2 chemical treatment, effectively reducing the problems of small interlayer distances and long ionic transport distances induced by π-π re-stacking, thereby leading to significantly improved capacity and rate performance. (Sheng Huang, Peng Huang, Lei Wang, Junbo Han, Yu Chen, 2024) CNTs are a typical carbon nanomaterial consisting of one-dimensional cavities and graphite walls. When applied to SIB anodes, their unique one-dimensional structure can significantly shorten the transport distance of electrons and ions, which in turn leads to high electrical thermal conductivity and chemical stability. However, CNTs have a narrow layer spacing (about 0.34 nm), which is not conducive to the transfer behavior of large-size Na^+. Hao et al. prepared porous CNTs using the alkali activation method and introduced oxygen-containing functional groups to enlarge the layer spacing while increasing the wettability of the electrode. (J. Hao et al., 2021) In addition, based on the phase

separation theory, Chen et al. obtained porous CNTs by preparing MoO_2@C core-shell nanofibers using electrostatic spinning and removing the internal MoO_2 nanoparticles (Figure 2.9c, d). The porous CNTs with disordered structure and high specific surface area exhibit excellent electrochemical stability. (Z. Chen et al., 2017) Despite the outstanding mechanical properties and electrical conductivity of graphene and CNTs, mass production's high cost and difficulty limit their widespread application. Moreover, porous graphene and CNTs are often accompanied by complex secondary treatment processes, increasing the treatment difficulty and cost. Therefore, considering the good mechanical properties and conductivity of graphene and CNTs, most works employ them as conductive and encapsulating carriers to suppress the large volume strain of high-capacity alloy-type and conversion-type materials during electrochemical processes. (Y. B. Kim et al., 2024; Chencheng Zhou et al., 2021; H. Zhu et al., 2022)

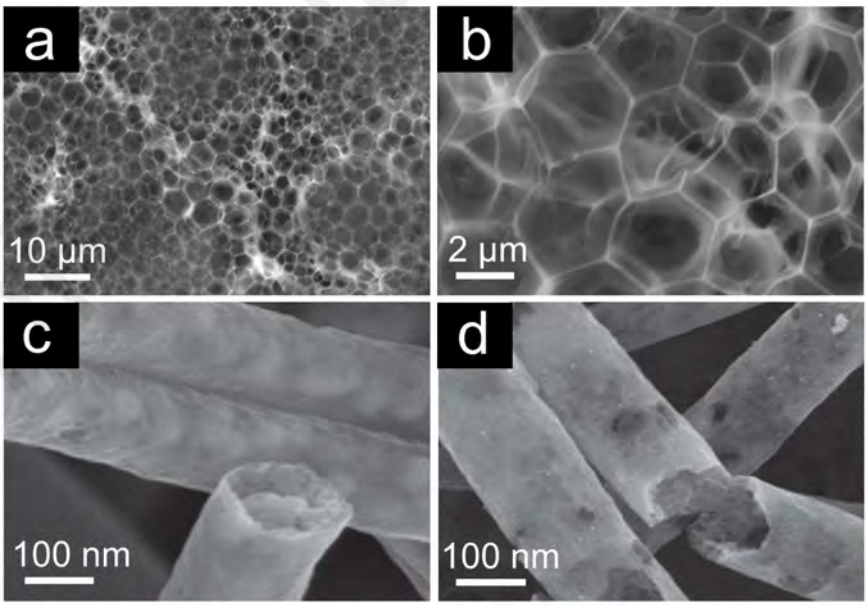

Figure 2.9: (a, b) SEM images of porous GO. (Mace et al., 2020) (c) The SEM image of MoO_2@C core-shell nanofibers annealing at 850 °C. (d) The SEM image of porous CNTs with nitric acid heat treatment. (Z. Chen et al., 2017)

The incorporation of heteroatoms (such as nitrogen, sulfur, phosphorus, and boron)

into the carbon matrix can significantly enhance the electrochemical performance by modifying the electronic structure, creating additional active sites, and improving the overall sodium storage capacity. Heteroatom-functionalized porous carbon can be synthesized through various methods: Chemical Vapor Deposition (CVD), Hydrothermal and Solvothermal Methods, Hydrothermal and Solvothermal Methods, and Chemical Activation. The sodium storage mechanisms in heteroatom-functionalized porous carbon involve several processes. Firstly, Na^+ is adsorbed onto the surface of the carbon material, facilitated by the presence of heteroatoms that provide additional active sites. Secondly, Na^+ can intercalate between the graphene layers in materials with graphitic domains, although this is less common in amorphous structures. Thirdly, the presence of heteroatoms can enhance pseudocapacitive behavior, where charge storage occurs through fast redox reactions at the surface. Heteroatoms in porous carbon can donate electrons to the carbon matrix, improving its electronic conductivity. Moreover, heteroatom doping can introduce defects and active sites in the carbon structure. The introduced defects and active sites can adsorb more Na^+, increasing capacity. Furthermore, introducing heteroatoms can improve the surface wettability of the carbon electrodes, thus enhancing electrolyte infiltration and facilitating ion transport. Additionally, the porous structure and the presence of heteroatoms help accommodate the volume changes during Na^+ insertion and extraction, improving cycling stability. Single-atom doping is one of the most extensively studied modifications. For example, as shown in Figure 2.10a-c, Hu et al. synthesized nitrogen-rich doped porous carbonaceous materials (N content: 17.72 at%) exhibiting a larger electrode/electrolyte contact area. Nitrogen doping brought more defects and active sites, allowing greater

accessibility of Na^+ at the functional interface. (X. Hu et al., 2019) Incorporating multiple heteroatoms can synergistically enhance the electrochemical properties. Zhou et al. used poly(p-phenylenediamine) hydrogel as a precursor to prepare three-dimensional porous carbon (3D-PC) anodes doped with N, O, and P heteroatoms, which provided abundant storage sites for the rapid Na^+ adsorption on the surface (Figure 2.10d). (Chunli Zhou et al., 2020) Heteroatom-functionalized porous carbon materials hold significant promise as anode materials for SIBs due to their enhanced electronic conductivity, increased active sites, improved wettability, and structural stability. However, more straightforward and scaled developing strategies still need to address some challenges related to initial coulombic efficiency, complex synthesis, and limited theoretical capacity.

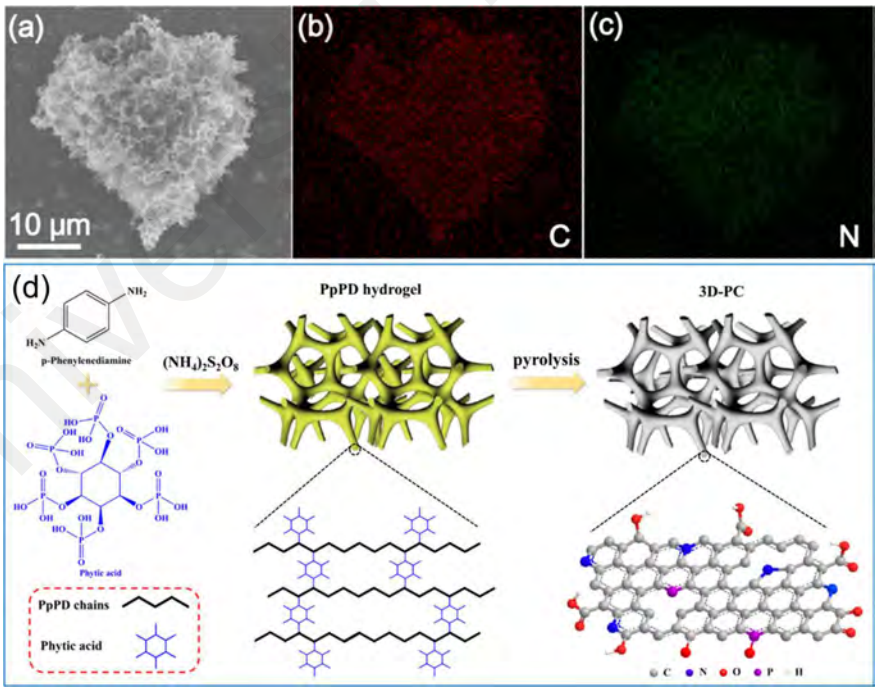

Figure 2.10: (a) SEM image and (b and c) EDS elemental mappings of nitrogen-rich doped porous carbonaceous materials. (X. Hu et al., 2019) (d) Schematic illustration of the preparation of PpPD hydrogel and 3D-PC. (Chunli Zhou et al., 2020)

Biomass-derived porous carbon has emerged as a promising anode material for SIBs due to its environmental friendliness, high surface area, tunable porosity, and potential for low-cost production. Biomass-derived porous carbon is synthesized from renewable biological resources such as agricultural waste, plant residues, and other organic matter. The use of biomass as a precursor not only provides a sustainable and eco-friendly pathway for carbon material production but also leverages the intrinsic hierarchical structure of biomass to create porous carbon with high surface area and unique properties. The synthesis of biomass-derived porous carbon typically involves several steps, including carbonization and activation. During the carbonization process, biomass precursors are heated in an inert atmosphere to decompose the organic components, leaving behind a carbon-rich structure. The temperature and duration of carbonization affect the degree of graphitization and the development of the porous structure. The activation process can be further divided into physical activation and chemical activation. Among them, physical activation involves treating the carbonized biomass at high temperatures with activating gases such as CO_2 or steam, which can create a well-developed porous structure. Otherwise, chemical activation involves impregnating the biomass with chemical agents (e.g., KOH, $ZnCl_2$) before carbonization. This method can produce a highly porous carbon structure with a larger surface area. Biomass-derived porous carbon has several unique advantages over other carbon materials, such as environmental sustainability and cost-effectiveness. This is because biomass is a low-cost and widely available resource, and using biomass as a precursor is environmentally friendly and sustainable. In addition, the synthetic process of biomass-derived porous carbon, especially chemical activation, is cost-effective and scalable. It is worth noting

that the natural components in biomass are accompanied by the release of gases (e.g., CH_4, H_2, and CO) during high-temperature carbonization, which facilitates the formation of high surface area and porosity. In addition, the elemental components of N, P, and S contained in most biomass are favorable for the natural introduction of heteroatom doping, which improves the overall electrical conductivity and the distribution of active adsorption sites. As shown in Figure 2.11a, Ghani et al. constructed biomass-based porous carbon using ultrasound-assisted KOH activation combined with a carbonization strategy. The prepared electrodes exhibited high wettability and cycling stability in the presence of three-dimensional nanopores and abundant functional groups. (Ghani et al., 2022) Besides, to meet the requirements of high-power energy storage applications, Yang et al. constructed N, Fe co-doped carbon micron-tubes using bulk biomass as the precursor, realizing the transition from macroscopic-scale biomass to microscopic-scale carbon tubes (Figure 2.11b). On the one hand, the open structure of the carbon tubes provides the basis for the fast pseudocapacitive process, and on the other hand, the defects brought by heteroatom doping provide more active sites for fast Na^+ storage. (H. Yang et al., 2024) Even though biomass-derived porous carbon displays unique advantages for SIB anode applications, the intrinsic electrochemical shortcomings of carbon materials are still the major issues affecting its development. Firstly, the ICE of biomass-derived porous carbon is relatively low due to the formation of a SEI layer and the presence of numerous defects that irreversibly consume Na^+. Secondly, the natural variability in biomass precursors often leads to heterogeneous carbon structures, which may result in inconsistent electrochemical performance. Lastly, while biomass-derived porous carbon

generally displays good electrical conductivity, it can be inferior to highly graphitized carbon materials. Enhancing conductivity without sacrificing other beneficial properties remains a challenge.

Figure 2.11: (a) Schematic of one-step and two-step activation methods. (Ghani et al., 2022) (b) Schematics of synthesis method for N, Fe co-doped carbon micron-tubes. (H. Yang et al., 2024)

MOF is a crystalline material with a porous structure formed by coordinating metal ions with organic ligands. When used as templates or precursors, MOF can be converted into porous carbon materials with well-defined structures and tunable properties, making them highly suitable for the anode of SIBs. The overall design process for MOF-derived porous carbon materials includes but is not limited to the preparation of MOF precursors, carbonization, and activation. Firstly, the choice of MOF precursor can significantly affect the micromorphology and porosity of the resulting carbon material, which in turn affects the electrochemical performance of the electrode. Subsequently, the MOF precursor is subjected to high-temperature pyrolysis in an inert

atmosphere (e.g., argon or nitrogen). The process involves the carbonization and decomposition of organic ligands at high temperatures, resulting in the formation of a carbon matrix embedded with metal or metal oxide nanoparticles. Finally, the carbonized product employs activation using a chemical reagent (acid or alkali) to remove metal ions from it, thereby further increasing the porosity and surface area of the carbon material. Remarkably, the resulting MOF-derived porous carbon is not limited to adsorption/desorption and pore-filling storage mechanisms but also allows Na^+ storage through defects and edge site interactions. Causally, there is an abundance of defects, edge sites, and heteroatoms within the carbon matrix after metal removal, which creates additional active sites for Na^+ storage.

In addition to high surface area and porosity, the main advantages of MOF-derived porous carbon focus on structural tunability and metal ion retention. Firstly, the properties of the resulting carbon materials can be precisely controlled by selecting appropriate MOF precursors and adjusting synthesis conditions. This tunability allows for the optimization of pore size, surface area, and heteroatom content. For instance, Li et al. synthesized a stable MOF structure containing 1,3,5-triazine-2,4,6-triamine (Figure 2.12). During pyrolysis, the MOF precursor was induced by graphite to reassemble into graphite-like crystals with enlarged layer spacing (4.2 Å), which facilitated reversible insertion/de-insertion of Na^+. (Xianwei Li et al., 2023)

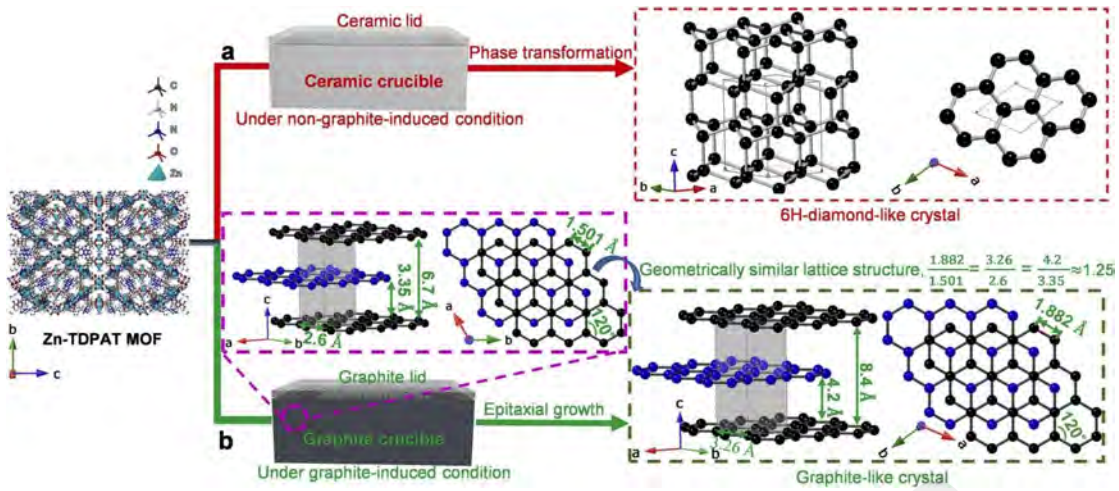

Figure 2.12: Schematic illustration of the preparation process for (a) the crystalline carbon with 6H-diamond-like crystal (Zn-TDPAT-DC) and (b) crystalline carbon with graphite-like crystal (Zn-TDPAT-GC). (Xianwei Li et al., 2023)

Furthermore, the carbonization process of MOF often results in the formation of metal or metal oxide nanoparticles embedded within the carbon matrix. These nanoparticles can enhance electronic conductivity and catalytic activity, improving electrochemical performance. In general, MOF-derived porous carbon is seldom used as a pure carbon material for anodes in SIBs. It often retains embedded metal atoms or serves as a porous carbon matrix to encapsulate alloy-type and conversion-type particles, which typically undergo significant volume expansion. For example, Zhao et al. obtained a porous carbon skeleton by etching MOF and uniformly encapsulated nanoscale Pb particles (Figure 2.13a-c), which effectively mitigated the bulk strain of the alloy-type material and enhanced the Na^+ reaction kinetics during the electrochemical process. (Xiaoying Zhao et al., 2024) Moreover, as shown in Figure 2.13d-f, Yao et al. induced the morphology change from nanosheets to nanocubes by Mo doping Ti-MOF (MIL-125) precursor. As a result, the metal atom doping and carbon hybridization significantly enhance the pseudocapacitive storage behavior and reaction kinetics of $Mo_{0.1}$-TiO_{2-x}@C anode. (T. Yao et al., 2023) MOF-derived porous carbon is a

highly promising anode material for SIBs due to its high surface area, tunable properties, and unique structural features. Combining MOF-derived porous carbon with other volumetric materials (e.g., metal oxides/sulfides/selenides and alloy-type materials) can effectively mitigate volume expansion while increasing the conductivity of the material. In addition, this metal compound/porous carbon composite derived from MOF can realize the uniform distribution of the two compositions due to the alternate assembly of metal atoms and carbon atoms in MOF. The continued development of MOF-derived porous carbon could lead to the realization of more efficient, sustainable, and commercially viable SIBs.

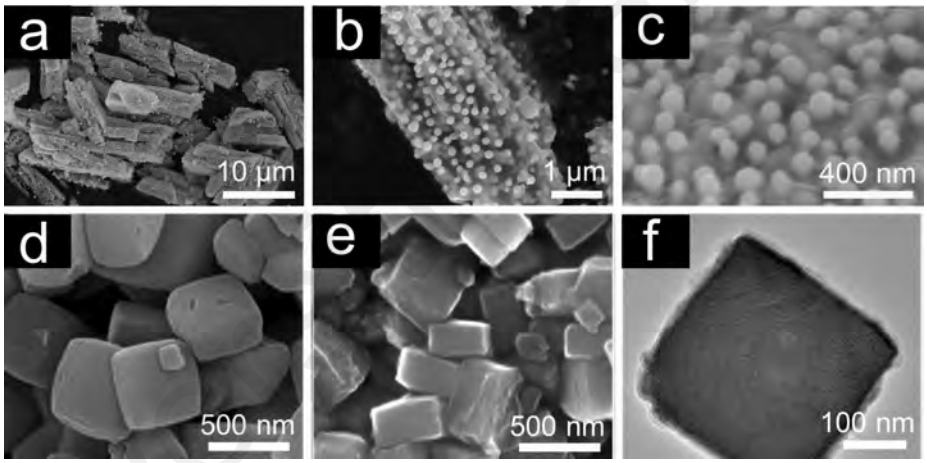

Figure 2.13: (a-c) SEM images at different magnifications. (Xiaoying Zhao et al., 2024) (d) SEM image for $Mo_{0.1}$-MIL-125. (e) SEM, (f) TEM images of $Mo_{0.1}$-TiO_{2-x}@C. (T. Yao et al., 2023)

2.1.2.2 Organic Compounds

Organic compounds as adsorption/desorption-type anode materials offer advantages such as structural diversity, environmental friendliness, and the potential for low-cost production. Key organic compounds include quinones, conductive polymers, and covalent organic frameworks (COFs). Organic compounds can be designed with various functional groups and molecular structures, providing flexibility in tuning their

electrochemical properties. Several organic materials can be derived from renewable resources and are biodegradable, making them environmentally benign. Organic materials can often be synthesized through simple and scalable chemical processes, potentially reducing the overall cost of battery production. Quinones are organic molecules with a conjugated structure that reversibly adsorb and desorb Na^+ through redox reactions. They offer moderate capacities and good cycling stability. However, quinones suffer from shortcomings such as inherent poor conductivity and susceptibility to dissolution in non-proton electrolytes. Zhu et al. employed a salification strategy to improve the structural performance of tetrahydroxyquinone by converting it into its disodium salt form through the substitution of two hydrogen atoms with two sodium atoms. This modification significantly reduced its solubility in ester-based electrolytes, enhancing its electrochemical performance. (L.-M. Zhu et al., 2022) Conductive polymers, such as N-rich conjugated organic polymers and polypyrrole, have been explored as anode materials due to their good conductivity and flexibility. Polymerized carbon nitride as a conductive polymer can facilitate large-size Na^+ high-capacity storage and achieve reliable structural stability by virtue of its layered structure with a two-dimensional π-conjugated structure and an abundance of built-in redox-active groups (e.g., C=N and N=N). Yan et al. applied the strategy of moderate pyrolysis of PCN anode to reduce the band gap and enhance the electronic conductivity. In addition, the structural disorder was increased, and the layer spacing was enlarged by adjusting the microstructure, which facilitates the efficient transport and storage of Na^+. (Yan et al., 2022) Liu et al. employed conductive polypyrrole coated on the surface of hexagonal Bi_2Te_3 nanosheets, which greatly enhanced the conductivity of the composite

while avoiding direct contact with the electrolyte and ensuring the stability of the structure. (X. Liu et al., 2021) COFs are crystalline organic polymers with well-defined porous structures, providing high surface areas and tunable properties for Na^+ storage. The structural design of COFs is based on the fine integration of organic molecules with atomic precision into an ordered structure. Designing organic molecules with specific functional groups and optimizing their molecular weight and structure can improve permanent porosity, specific surface area, and thermal stability. For instance, incorporating electron-withdrawing or donating groups can enhance redox activity. Combining organic compounds with conductive materials (e.g., carbon nanotubes, graphene) can significantly improve their electrical conductivity and overall performance. Hybrid materials leverage the strengths of both components, leading to enhanced capacities and cycle stability. As shown in Figure 2.14, Zhao et al. synthesized COFs based on phthalocyanines enriched with a large π-π system via a coupling reaction (KOH-assisted condensation). On the one hand, the constructed stabilized covalent network structure inhibits the dissolution of the COF structure in the electrolyte and thus enhances the electrochemical cycling stability. On the other hand, the large specific surface area and open mesoporous channels facilitate the adsorption and transfer of active Na^+, which in turn leads to fast redox reaction kinetics. (J. Zhao et al., 2021) In addition to the direct application of COF to electrode materials, the construction of COF-based organic-inorganic hybrid materials holds great promise for high-capacity Na^+ storage and conversion. Xie et al. utilized an in-situ synthesis strategy to anchor ultrafine antimony nanoparticles within COFs uniformly. The introduction of Sb^{3+} acted as a catalyst during COF formation and was subsequently reduced to Sb

nanoparticles confined within the COF pores. This effectively mitigated the high volumetric expansion of Sb during long-term cycling. Charge transfer occurred between the Sb nanoparticles and COF through nitrogen groups and was transmitted outward via the three-dimensional framework. (M. Xie et al., 2022)

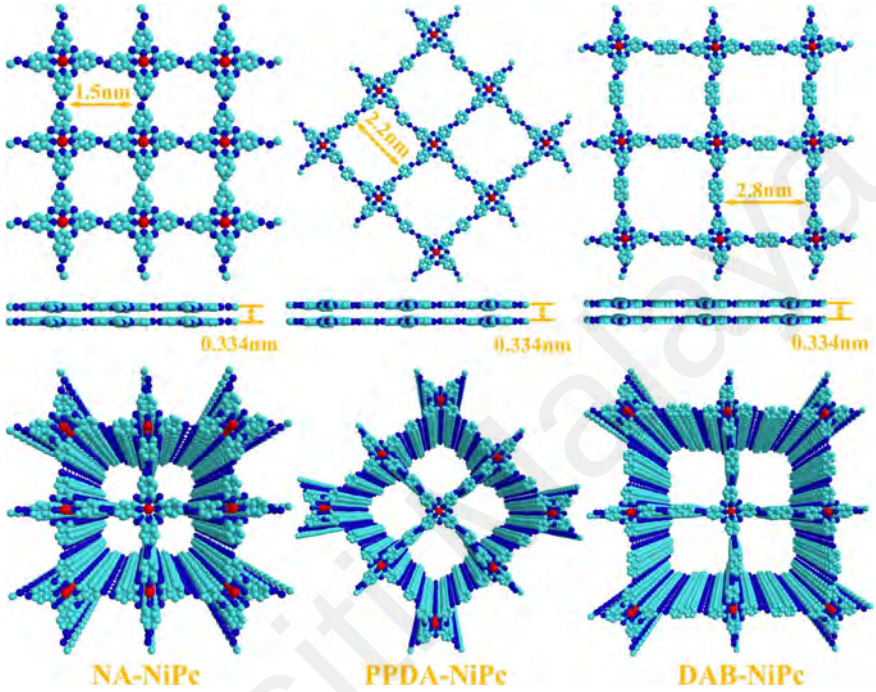

Figure 2.14: Geometry optimization of NA-NiPc, PPDA-NiPc, and DAB-NiPc with HyperChem release 7.5. (J. Zhao et al., 2021)

Organic compounds offer a promising pathway for developing sustainable and high-performance anode materials for SIBs. Their structural diversity, tunability, potential for high capacity, and environmental friendliness make them attractive candidates for future energy storage solutions. However, challenges such as solubility in electrolytes, low electronic conductivity, and structural stability need to be addressed to realize their full potential.

In summary, adsorption/desorption-type anode materials for SIBs are promising due to their high surface areas, good conductivity, and structural flexibility. Porous carbon materials and organic compounds represent the main categories of these materials. While they offer advantages regarding rate capability and cycling stability, challenges such as lower specific capacities need to be addressed. Advances in composite materials, doping, functionalization, and molecular design hold promise for further improving the performance of adsorption/desorption-type anodes, contributing to the development of more efficient and sustainable SIBs.

2.1.3 Alloying-Type Anodes

Alloying-type materials have emerged as promising anodes due to their high theoretical capacities and favorable electrochemical properties. Alloying-type anode materials operate through a mechanism where Na^+ reacts with metals to form alloys during the charge and discharge cycles. This process involves significant volume changes, posing challenges and offering high theoretical capacities. Common alloying-type materials include elements such as tin (Sn), antimony (Sb), and phosphorus (P), which can form sodiated compounds like Na_3Sb and Na_3P. The schematic diagram of the Na^+ alloying process in alloying-type anodes is shown in Figure 2.15. The alloying mechanism involves the following steps: Insertion → Alloying → Dealloying → Deinsertion. Na^+ inserts into the host metal when the discharge process occurs, forming intermediate phases during the insertion process. Continuously, the further insertion of Na^+ leads to the formation of Na-M alloys (e.g., Na_3Sb, Na_3Sn). During the charging process, the alloy phases revert to their original metal forms, releasing Na^+;

Subsequently, deinsertion further releases Na^+ into the electrolyte. Notably, this mechanism is typically accompanied by substantial volume expansion and contraction, which can lead to mechanical degradation of the electrode material.

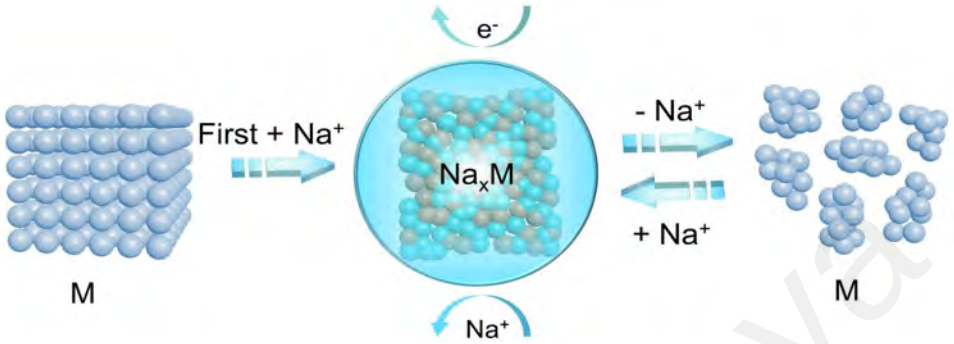

Figure 2.15: Schematic diagram of Na^+ alloying process in alloying-type anodes.

2.1.3.1 Tin-Based Alloys

Tin is a widely studied alloy anode material with a high theoretical specific capacity of 847 mA h g^{-1}. The sodiation and desodiation processes involve multi-step alloying reactions: $Sn + xNa \rightarrow Na_xSn$. This process forms various sodium-tin alloys (e.g., NaSn, Na_3Sn), contributing to its high sodium storage capacity. Despite the high specific capacity, tin-based alloy anodes suffer from significant volume expansion (~420%) during cycling, leading to structural degradation, loss of electrical conductivity, and short cycle life. Aiming to ameliorate the volume expansion problem of Sn anodes, Kim et al. prepared three-dimensional porous coral-like structures connected with a low coordination number by room temperature calcination of nanoscale Sn powder. The unique coral-like structure is conducive to maintaining mechanical stability during volume change and exhibits a self-healing phenomenon during cycling. (C. Kim et al., 2018) Meanwhile, their team has developed a phase change technique for porous tin anodes to accommodate volume changes during the sodiation/desodiation process

efficiently. (C. Kim et al., 2016) Carbon encapsulation is considered to be another effective strategy to address the volume expansion of Sn-based anodes. Liu et al. synthesized ultrasmall Sn nanoparticles (~8 nm) uniformly embedded in a spherical carbon network using aerosol spray pyrolysis. Under the synergistic effect of highly dispersed ultrasmall Sn nanoparticles and conductive carbon network, the prepared electrode can effectively overcome the volume strain and particle aggregation during the prolonged sodiation/desodiation process. (Yongchang Liu et al., 2015) Moreover, Xie et al. synthesized Sn@CNT nanopillar arrays with a core-shell structure using a simple immersion chemical vapor deposition method and applied them as stand-alone electrodes for SIBs. That structure can effectively avoid the problems of Sn anode pulverization and electrical contact loss. (Xiuqiang Xie et al., 2015) However, constructing robust nucleation sites with ultrafine dimensions inside microscopic carbon is crucial for constructing efficient Sn/C composite anodes, but it remains largely unexplored. Xu et al. report a novel design strategy for uniform nucleation and dendrite-free growth of spatially confined atomic tin in hollow carbon spheres. As shown in Figure 2.16a, unlike the conventional space-exposed large-size unalloyed alloying, complete alloy-alloying with high-affinity tin as a persistent nucleation site greatly improves tin utilization and effectively suppresses unfavorable agglomeration and bulk strain. (F. Xu et al., 2022)

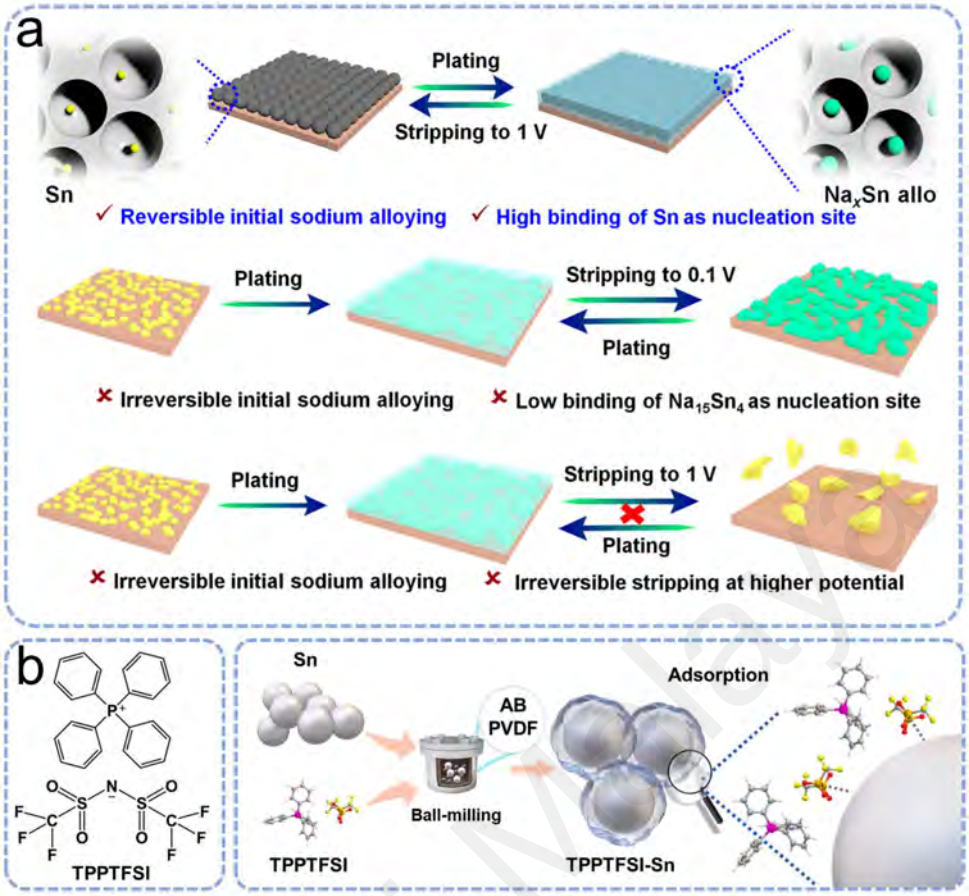

Figure 2.16: (a) Schematic illustration of plating/stripping behaviors for At-Sn@HCN and a large-size Sn system. (F. Xu et al., 2022) (b) The chemical structures of TPPTFSI and the schematic diagram of the preparation of TPPTFSI-Sn electrode. (C. Zheng et al., 2024)

Besides nanostructured electrode design, interface engineering is another important factor limiting the development of Sn anodes in SIBs. The alloying reactions between sodium and tin result in the formation of a solid electrolyte interphase (SEI) layer on the electrode surface, further affecting the battery performance. To reveal the low initial coulombic efficiencies associated with interface problems, Liu et al. suggested that the gas generation at a specific voltage is an important reason for the low coulombic efficiency of tin anode. Therefore. They proposed a strategy of pre-alloying Sn with Na by metallurgical methods to reduce the initial voltage and compensate for the loss of "active" Na. Remarkably, the prepared anodes exhibited a significant increased ICE

(from 24.68% to 75%). (W. Liu et al., 2019) Although various strategies have been proposed for interfacial engineering modification of tin anodes, the relationship between electrode structural stability and SEI during charging and discharging remains controversial and elusive. Daali et al. combined in-situ SEM, X-ray absorption spectroscopy (XRES), and X-ray photoelectron spectroscopy (XPS) to investigate the potential electrochemical-mechanical behaviors of tin anodes during electrochemical processes. Resultantly, abundant voids and pores were formed while tin was pulverized into nanoparticles during the initial charging and discharging. Moreover, by comparing different electrolytes, it was shown that ether-based electrolytes are capable of forming SEI dominated by inorganic substances, which is favorable for improving the specific capacity and cycling stability. (Daali et al., 2023) In addition, Lee et al. investigated the effect of sodium salts in different electrolytes on SEI formation by thermodynamic analysis. From this, compared to the $NaClO_4$-based electrolyte, the $NaPF_6$-based electrolyte produced a thicker and less conductive SEI layer on the surface of the tin anode, which was susceptible to strong thermal decomposition. Furthermore, the findings suggest that the electrochemical decomposition of Fluoroethylene carbonate in the electrolyte contributes to the formation of thermally stable and thin SEI layers. (Y. Lee et al., 2018) Analogously, to further explore the problem of unstable SEI formed on tin anodes during electrochemical processes, Zheng et al. triggered the spontaneous adsorption of Na^+ on the surface of Sn by introducing tetraphenylphosphonium bis(trifluoromethanesulfonyl)imide (TPPTFSI) into the electrodes, which consequently enhanced the specific capacity of the tin anode (Figure 2.16b). The decomposition of the TPP^+ component of TPPTFSI during the initial cycle favors forming the organic

component of the SEI with enhanced flexibility. (C. Zheng et al., 2024)

2.1.3.2 Antimony-Based Alloys

Antimony (Sb) is another promising alloy anode material with a high theoretical specific capacity of 660 mA h g^{-1}. The sodiation and desodiation processes involve the formation of Na_3Sb alloy: $Sb + 3Na \rightarrow Na_3Sb$. Antimony-based alloys also experience significant volume changes (~390%) during cycling, leading to electrode pulverization and capacity decay. Adjusting the morphology and structure at the nanoscale can effectively overcome the volume expansion during alloying. Liu et al. focused on the morphology-modulated synthesis of Sb. They precisely modulated the morphology of nanoporous antimony (NP-Sb) and the size of Sb particles using a top-down chemical dealloying strategy. After electrochemical performance evaluation, the coral-like NP-Sb exhibits a capacity output superior to honeycomb-like NP-Sb and Sb particles. (S. Liu et al., 2016) Zhang et al. prepared hexagonal Sb nanocrystals with a unique crystal morphology, exhibiting excellent electrochemical properties. (N. Zhang et al., 2023) As shown in Figure 2.17, Li et al. controllably prepared zero-dimensional Sb nanoparticles (Sb-NP), two-dimensional Sb nanosheets (Sb-NS), and three-dimensional nanoporous Sb by etching Li-Sb alloys in different solvents, respectively, and explored the morphology evolution mechanism of various Sb nanostructures. (Haomiao Li et al., 2019)

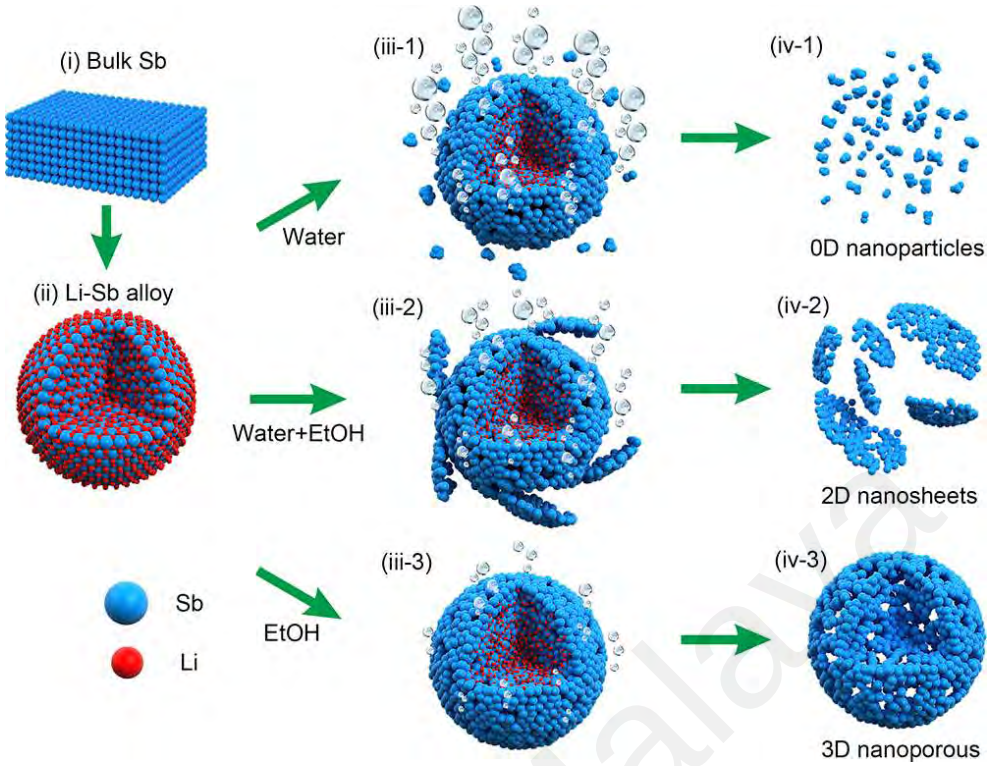

Figure 2.17: Schematic illustration of the synthesis routes of different morphologies of Sb nanomaterials. (Haomiao Li et al., 2019)

Recently, to cope with the high-volume expansion rate of alloy-based anodes, the preparation of composite materials has become a mainstream R&D idea. For example, Wang et al. prepared multiphase zero-valent Sb nanoparticles of Sb, CoSb, and $CoSb_2$ encapsulated in carbon nanotubes using a co-seed-mediated approach. Based on this, nitrogen-doped carbon coating was further performed, and the obtained samples exhibited excellent Na^+ storage durability. (Weixu Wang, Wang, et al., 2023) Liu et al. synthesized unique Sb@C coaxial nanotubes by applying a simple thermally reduced carbon coating strategy. Different degrees of evaporation of Sb at different annealing times can simply regulate the amount of hollow space inside the tubes, thus developing the optimal Sb/C ratio suitable for Na^+ storage. (Z. Liu et al., 2016) Although encapsulating alloy-type particles using a carbon matrix can effectively buffer their volume change during electrochemical processes, the slow Na^+ kinetics in the

conventional carbon layer remains a bottleneck, limiting the composite electrodes to achieve high-rate performance. Accordingly, Liu et al. designed an egg yolk-shelled Sb@Void@graphyne nanobox (Sb@Void@GDY NB) anode, in which the intrinsic faceted inner cavities in the GDY shells provide three-dimensional fast diffusion channels for Na^+ transport. (Yan Liu et al., 2023) As shown in Figure 2.18, in-situ TEM verified that the synthesized Sb@Void@GDY NB exhibited a hollow structure and void space, which significantly buffers the volume change of Sb during cycling and provides effective support for the structural integrity of Sb.

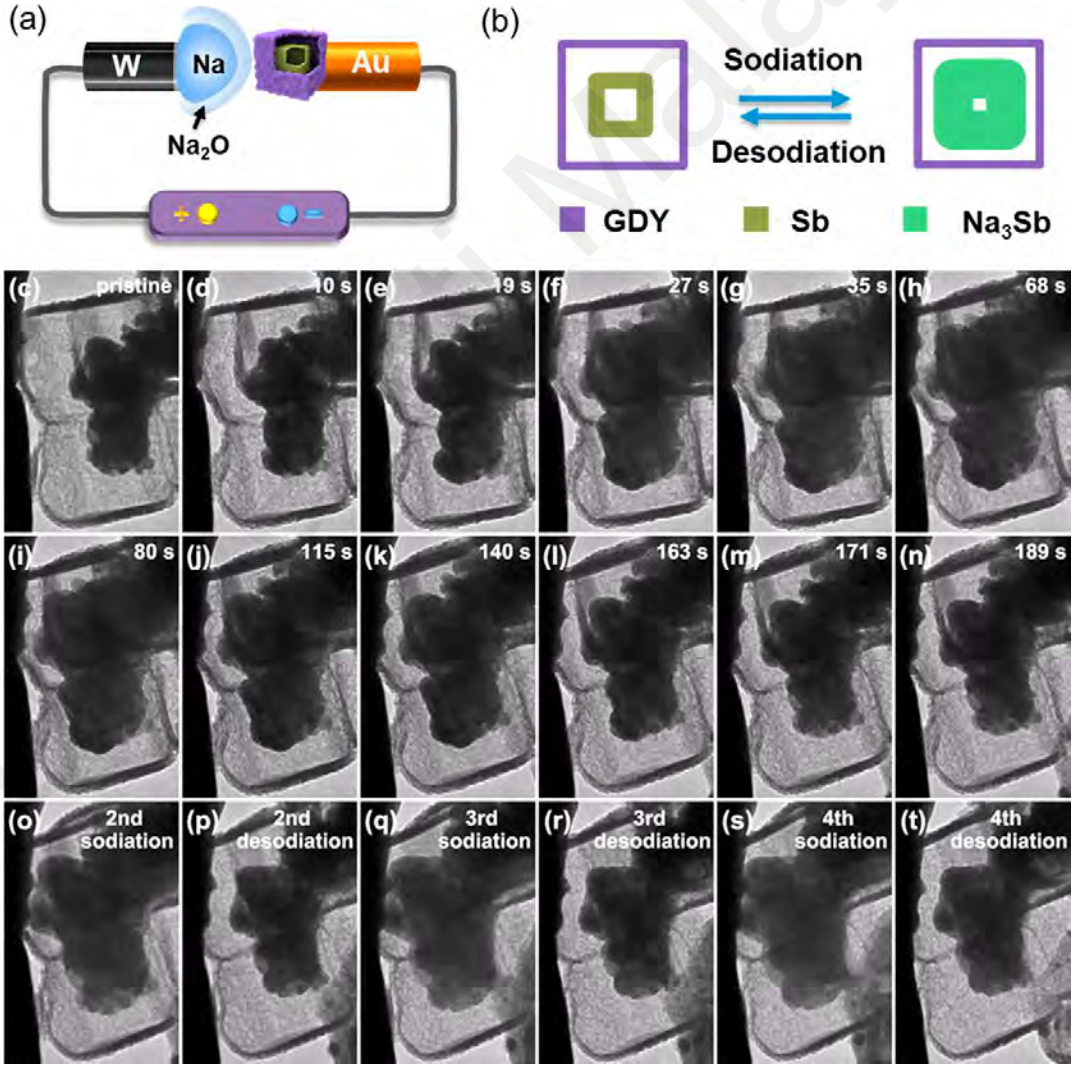

Figure 2.18: (a) Schematic illustration of the in-situ TEM device. (b) Schematic of morphological evolution of hollow yolk-shell Sb@Void@GDY NBs during sodiation/desodiation. (c-t) In-situ TEM images from a time-lapse video of the first four sodiation/desodiation cycles. (Yan Liu et al., 2023)

The alloying process of Sb can continuously induce interfacial side reactions and Na dendrite growth, leading to rapid capacity degradation, low Coulombic efficiency, and even internal short circuits. Interface engineering design is considered an effective strategy to improve the above shortcomings. Interfacial engineering can effectively reduce the energy band gap and Na^+ migration energy barrier during the interconversion of Sb and Na_3Sb phases. Based on this, Liu et al. synthesized porous hetero-interfacial MOFC-Sb using MOF-derived carbon as the carrier and buffer material, demonstrating excellent sodium storage capacity. (C. Liu et al., 2023) Moreover, based on a combined approach of interfacial chemistry and structural engineering, Li et al. proposed a flexible three-dimensional hollow porous carbon fiber framework embedded with Sb nanoparticles, exhibiting highly reversible gradient sodium storage properties. (Zhaopeng Li et al., 2024) Liu et al. successfully eliminated the substantial irreversible Na loss from Sb anodes by a chemical pretreatment strategy with sodium biphenyl. The pretreated Sb anode was able to trigger the selective decomposition of the electrolyte, which facilitated the formation of a NaF-rich inorganic SEI layer on the electrode surface. The inorganic-rich SEI layer mitigated the undesirable side reactions between the electrode/electrolyte and significantly enhanced the Sb anode's mechanical properties. (M. Liu et al., 2021)

Although various carbon composite strategies have been applied to alloy-type anodes, their inherent shortcomings, such as low conductivity and volume expansion, still need to be perfected by relevant research efforts targeting their intrinsic structure with internal design. Continued research and development in this field could lead to the

successful implementation of alloying-type anodes in commercial SIBs, contributing to the advancement of sustainable and high-performance energy storage solutions.

2.1.3.3 Phosphorus-Based Alloys

Phosphorus is a high-capacity alloying anode material with an extremely high theoretical specific capacity of 2596 mA h g^{-1}. The sodiation process forms Na_3P alloy: $P + 3Na \rightarrow Na_3P$. Phosphorus undergoes significant volume expansion (~490%) during cycling, resulting in electrode pulverization and rapid performance degradation. Additionally, phosphorus has poor electrical conductivity, limiting its electrochemical performance. As shown in Figure 2.19, Hu et al. formed a conductive backbone containing C-S-S groups by hybridizing P with a heat-treated functional conducting polyacrylonitrile polymer (P-SPAN). This functional conductive polymer is able to form P-S bonds between phosphorus and functional conductive matrix, thus accommodating the large volume strain during cycling. (Ye Hu et al., 2018) Liu et al. densely and uniformly deposited red phosphorus nanodots on reduced graphene oxide sheets to construct composites. The rGO network acts as an electron channel capable of minimizing the diffusion length of sodium ions and the volume expansion stress of phosphorus particles. (Yihang Liu et al., 2017) Similarly, Li et al. improved the sodium storage capacity of red P by confining nano-amorphous red P in a zeolite imidazolium salt framework-8 (ZIF-8)-derived N-doped microporous carbon matrix. The N-doped porous carbon with sub-1 nm micropores not only facilitates the enhancement of the rapid diffusion rate of the electrolyte into the electrode interior and the overall conductivity but also buffers the volumetric strain of red phosphorus during

electrochemical processes. (W. Li et al., 2017) Using electrostatic spinning, Liu et al. successfully encapsulated red phosphorus nanoparticles (approximately 97.7 nm) within porous N-doped carbon nanofibers. These fine amorphous phosphorus nanoparticles were evenly distributed within the porous N-doped carbon nanofibers, significantly enhancing electron and ion transfer. This uniform confinement also mitigated the crushing and fracture of the active material resulting from volume changes during extended cycling. (Yongchang Liu et al., 2017)

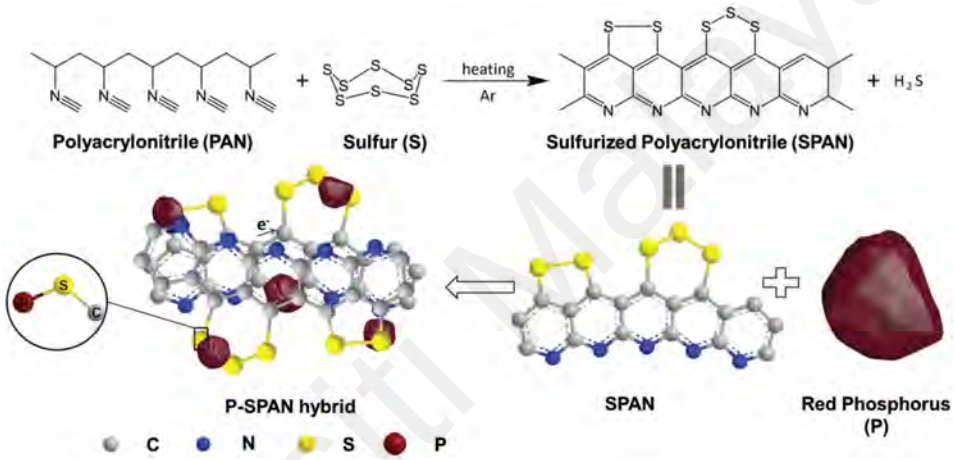

Figure 2.19: Schematic illustration of the preparation of the P-SPAN hybrid. (Ye Hu et al., 2018)

However, the low ICE and SEI instability of P/C composites limit their wide application. Song et al. compensated for the irreversible sodium loss in the S-doped P/C anode by precipitation. The pre-precipitated anode surface was able to generate a thin, uniform, and NaF-rich SEI layer during the natrization process, which in turn exhibited an ICE of up to 98.7% and stable cycling performance (Figure 2.20). (J. Song et al., 2023) While P anodes offer unmatched capacity, their sodiation and desodiation mechanisms remain unclear, limiting further optimization. Marbella et al. utilized a combination of experimental and theoretical methods to provide molecular-level insights into the desodiation pathways of black P anodes in SIBs. They identified the P

bonding in these materials by comparing structural models created through species exchange, ab initio random structure searching, and genetic algorithms. (Marbella et al., 2018)

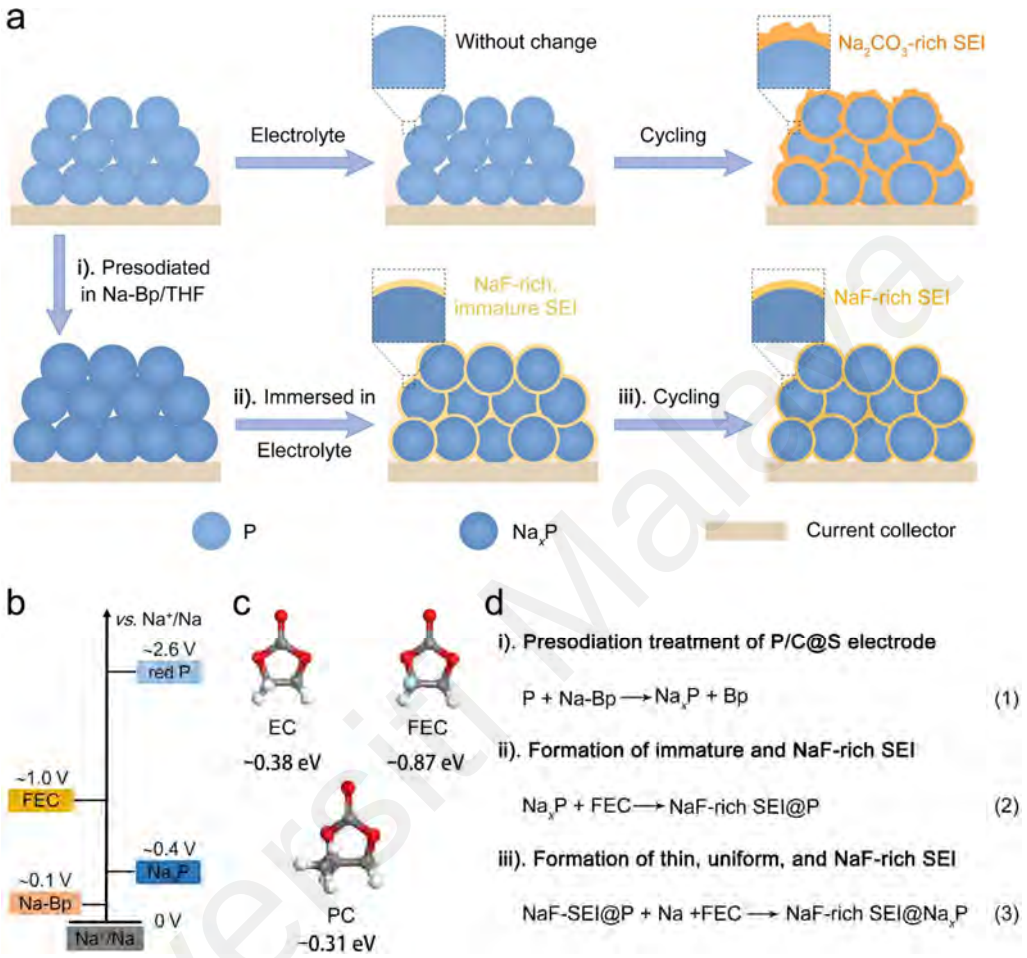

Figure 2.20: (a) Schematic illustration of presodiation of P/C@S electrode and the subsequent SEI formation process on P/C@S and pNa-P/C@S electrodes. (b) Comparison of redox potentials of Na-Bp, NaxP, FEC, and red P. (c) Molecular structure and LUMO energy level of EC, PC, and FEC. (d) Overall chemical reactions equations. (J. Song et al., 2023)

Alloying-type anode materials exhibit great potential in SIBs but face several challenges. Through nanostructuring, composite formation, and alloying with other elements, researchers continually optimize these materials' electrochemical performance and cycling stability. Tin-based, antimony-based, and phosphorus-based alloy anodes each have unique advantages and challenges. Future research will continue to focus on

material design and modification to enhance sodium-ion device performance and application prospects further.

2.1.4 Conversion-Type Anode

Conversion-type anodes operate by undergoing a complete phase transformation during the sodiation and desodiation processes. This involves the reduction of metal compounds to form metal nanoparticles dispersed in a sodium compound matrix. These materials typically exhibit high specific capacities but face challenges such as large volume changes and poor conductivity. The following sections review the specific types of conversion anodes: metal oxides (MOs), metal sulfides (MSs), and metal selenides (MSes). Figure 2.21 illustrates the conversion process of conversion-type anodes using MOs as an example.

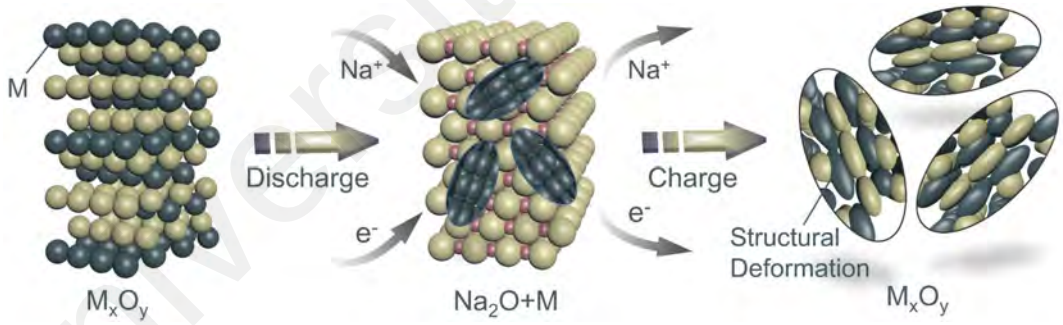

Figure 2.21: Schematic diagram of the conversion process of conversion-type anode with M_xO_y as an example.

2.1.4.1 Metal Oxides

MOs include iron oxide (Fe_2O_3), manganese oxide (MnO_2), and cobalt oxide (Co_3O_4), among others, which offer widespread availability and relatively low cost. During the sodiation (discharge) process, the initial MOs react with Na^+ and electrons to form a composite of metal nanoparticles (M) and sodium oxide (Na_2O). The reaction can be

summarized as $MO + 2Na^+ + 2e^- \rightarrow M + Na_2O$. Notably, this reaction is accompanied by significant volume changes and the formation of dispersed metal nanoparticles within a sodium compound matrix. During the desodiation (charge) process, the sodium compound decomposes back to the original metal oxide, releasing Na^+, which can be followed by the reaction of $M + Na_2O \rightarrow MO + 2Na^+ + 2e^-$. However, MOs often face significant challenges, such as substantial volume expansion, low electronic conductivity, and poor cycling stability. Yin et al. prepared α-Fe_2O_3/γ-Fe_2O_3/Fe/C nanocomposites with ultra-small particle size (25~80 nm) from $Fe(NO_3)_3$ and glucose. The introduction of carbon composites combined with the conversion reaction of Fe_2O_3 enabled the prepared SIBs to exhibit a high reversible capacity of more than 400 mA h g^{-1}. (Yin et al., 2020) Similarly, Shi et al. prepared amorphous Fe_2O_3 by in-situ preparation on three-dimensionally interconnected highly nitrogen-doped (10 at%) carbon nanofibers. The synergistic effect of nitrogen doping and amorphous state not only buffers the internal stress changes of Fe_2O_3 but also provides more electrochemically active sites for Na^+ storage, facilitating the rapid transfer of electrons and ions. (L. Shi et al., 2019) As shown in Figure 2.22a, Lin et al. prepared MnO_2/CNTs self-supported anode materials by a multistep carbon introduction strategy, in which CNTs were first grown in-situ on the surface of carbon cloth. Then, MnO_2 nanosheets were successfully loaded onto CNTs using the redox reaction between CNTs and $KMnO_4$.The secondary doping of CNTs can effectively enhance the material's overall electrical conductivity and full contact between electrodes/electrolytes. In addition, the strong interaction between CNTs and MnO_2 nanosheets effectively mitigated the stripping of MnO_2 nanosheets during the cycling process and promoted

effective Na^+ transfer. (Lin et al., 2024) As shown in Figure 2.22b, Zheng et al. generated manganese dioxide nanosheets on electrostatically spun polymer nanofibers through a combined strategy of in situ spraying and electrostatic spinning. Due to the excellent conductivity of the carbon nanofiber network combined with the one-dimensional/two-dimensional composite, the prepared electrodes exerted significantly improved electrochemical performance. (S. Zheng et al., 2022) Equally employing an electrostatic spinning strategy, Zhang et al. synthesized carbon-encapsulated tubular wire Co_3O_4/MnO_2 heterostructured nanofibers. Benefiting from the synergistic effect of the carbon-encapsulated outer tubular Co_3O_4 and inner wire MnO_2 heterostructures, the prepared composite electrodes exhibit a large internal buffer space and excellent electrical conductivity. (W. Zhang et al., 2018)

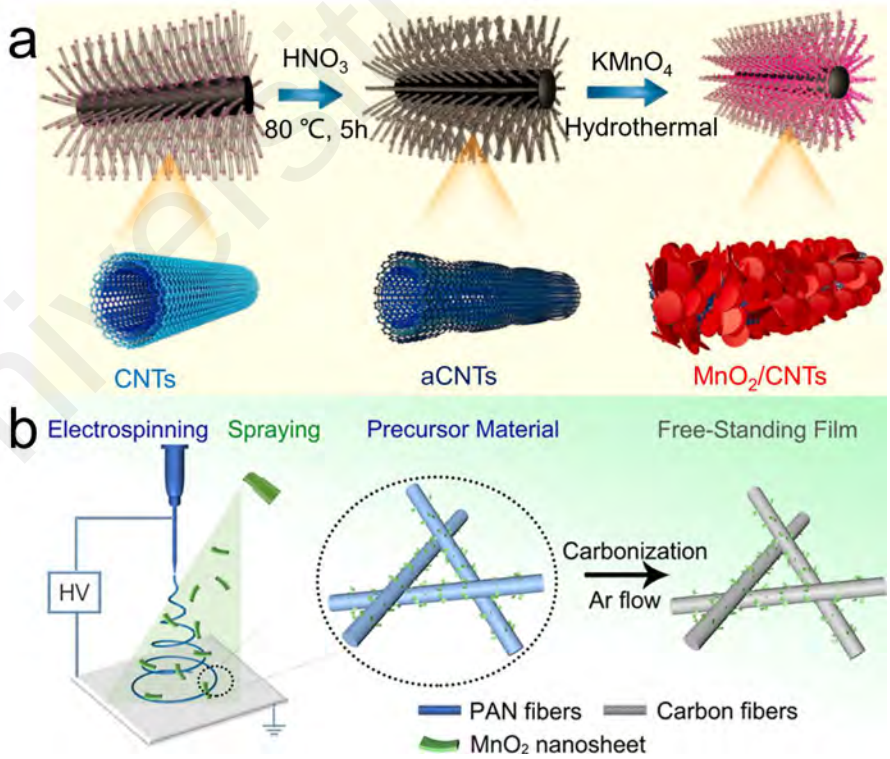

Figure 2.22: (a) Schematic illustration of MnO_2/CNTs material synthesis process. (Lin et al., 2024) (b) Schematic illustration of the in-situ assembly process for MnO_2 nanosheets on carbon nanofibers. MnO_2 were in-situ sprayed onto electrospun PAN nanofibers. The as-obtained composite film is carbonized under Ar flow. (S. Zheng et al., 2022)

2.1.4.2 Metal Sulfides

MSs provide better electronic conductivity compared to oxides, high theoretical capacities, and favorable reaction kinetics. Despite these advantages, they also experience volume changes, potential dissolution in electrolytes, and the formation of polysulfides, leading to the shuttle effect. FeS_2 has been widely investigated for use as an anode in SIBs by virtue of its low raw material cost, nontoxicity, and potentially high charge storage capacity. Walter et al. synthesized nanoscale FeS_2 by controlling the chemical reaction process, which exhibited significantly higher Na^+ storage capacity than bulk FeS_2. (Walter et al., 2015) However, FeS_2 still faces challenges such as structural collapse, active material exfoliation, and sulfur dissolution during complex point electrochemical processes. Chen et al. obtained FeS_2 electrodes with significantly improved cycling performance through a synergistic strategy of controlling the discharge cut-off voltage (0.5−3 V) combined with graphene coating. (K. Chen et al., 2017)

Layered MoS_2 has attracted wide attention as a conversion anode, but its inherent poor conductivity and slow Na^+ transport are the limiting factors for its application in SIBs. To improve the capacity output of MoS_2, Hu et al. synthesized MoS_2 nanoflower structures with extended (0 0 2) layer spacing. The extended layer spacing produced more active sites for Na^+ storage, leading to a significant initial capacity increase and improved ionic kinetics. (Z. Hu et al., 2014) Similarly, Su et al. prepared few-layer MoS_2 nanosheets using ultrasonic stripping. The ultra-thin thickness and the large layer spacing of the MoS_2 crystal structure (d(0 0 2)=6.38 Å) provided short diffusion paths,

which helped to realize efficient Na^+ transfer. (Su et al., 2015) As shown in Figure 2.23, Dai et al. reported a generalized strategy for a series of molecularly intercalated MoS_2, which enables precise control of the (0 0 2) interlayer distance (0.62−1.24 nm), as well as a wide range of adjustments in conductivity (1.3×10^{-4} to 3.5×10^{-2} S cm^{-1}). (Dai et al., 2021)

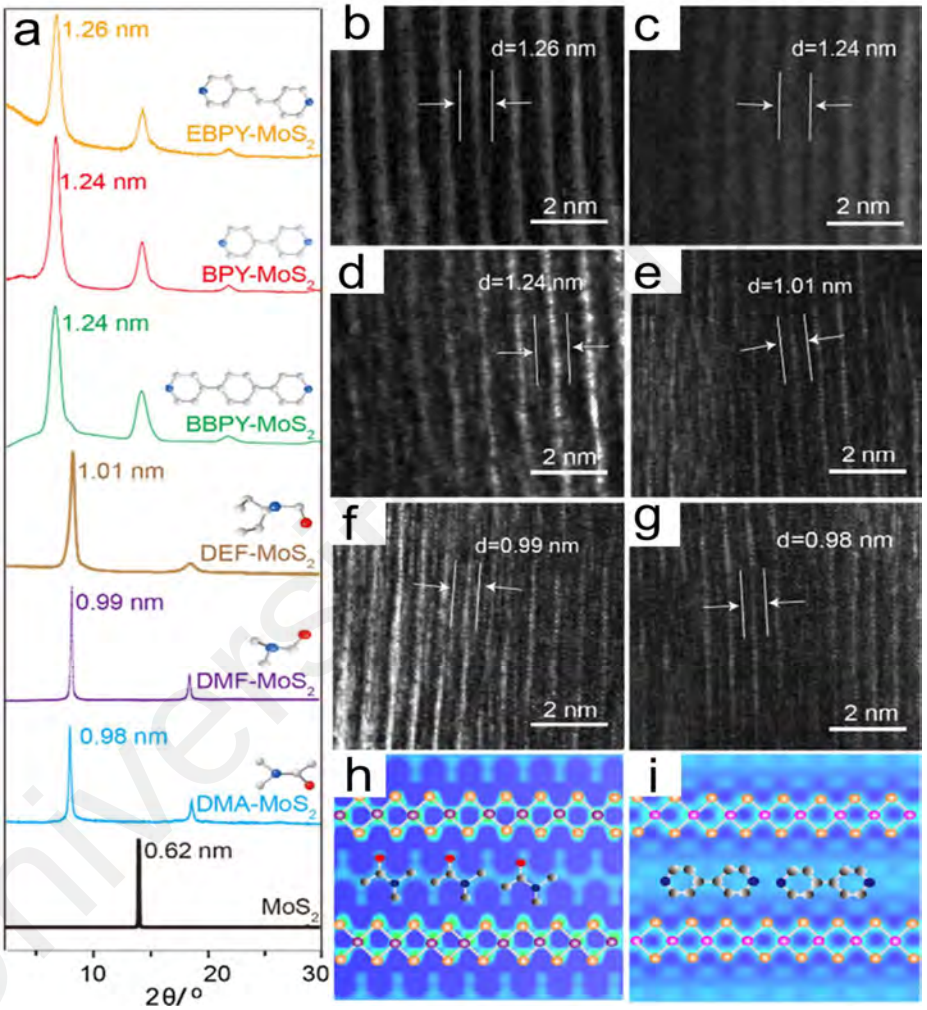

Figure 2.23: (a) PXRD patterns of MoS_2, DMA-MoS_2, DMF-MoS_2, DEF-MoS_2, BBPY-MoS_2, BPY-MoS_2, and EBPY-MoS_2 from bottom to top; (b-g) TEM image of EBPY-MoS_2, BPY-MoS_2, BBPY-MoS_2, DEF-MoS_2, DMF-MoS_2, and DMA-MoS_2; (h, i) electronic cloud distribution map showing the structure of hydrothermally synthesized DMA-MoS_2 and BPY-MoS_2. (Dai et al., 2021)

Carbon composite is another effective modification strategy for MS_2. As shown in Figure 2.24a, b, Zhang et al. prepared reduced graphene oxide aerogel-encapsulated MoS2 nanoflowers by a simple solvothermal method. Combined with the enlarged layer spacing and highly conductive carbon network, the prepared composite electrodes exhibit excellent electrochemical performance. (Xiangdan Zhang et al., 2020) Moreover, Han et al. prepared hierarchical porous MoS_2-C hollow rhombs by a self-templated solvothermal method (Figure 2.24c). The multilevel structural features enabled the prepared composite electrodes to exhibit ultra-long cycling stability at a high current density of 10 A g^{-1}. (L. Han et al., 2020)

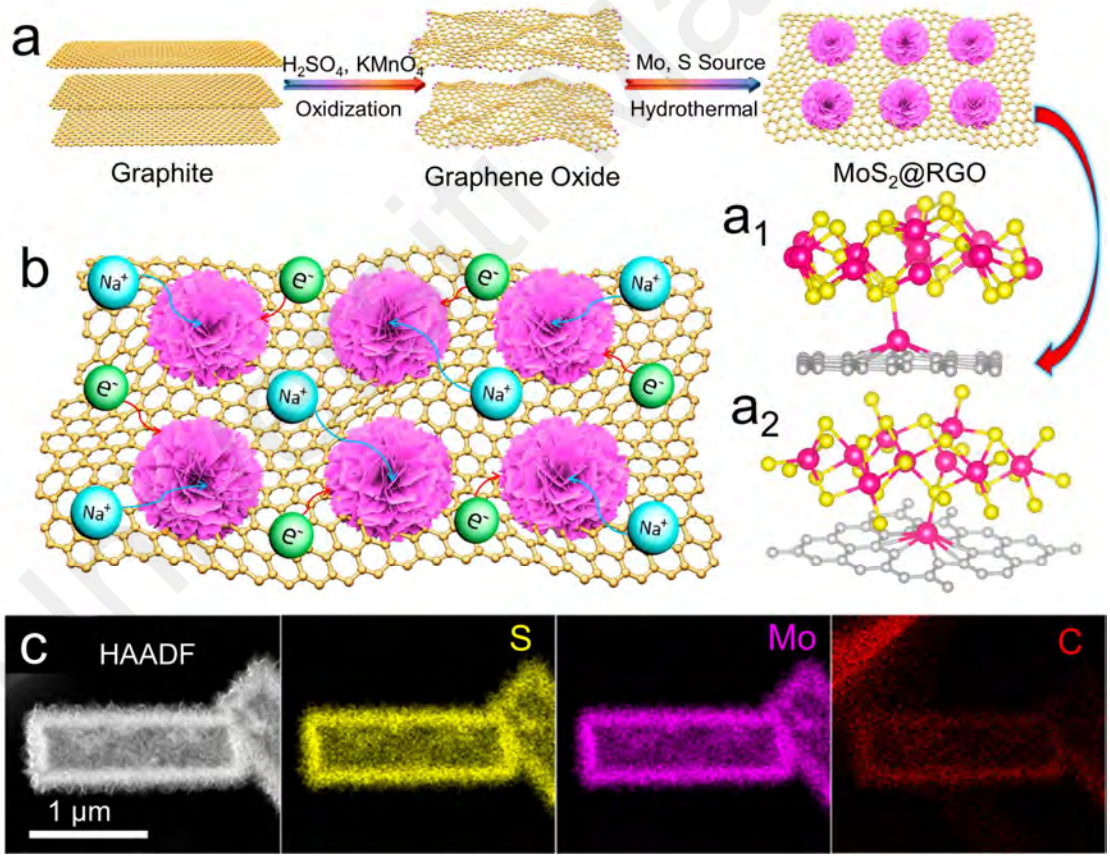

Figure 2.24: (a) Schematic illustration of the synthesis process of MoS_2@RGO and the DFT predicted stable configuration showing anchoring of MoS_2 on a vacancy site of graphene (pink for Mo atom, yellow for S atom and silver for C atom). (b) Schematic illustration showing transfer of Na^+ ions and electrons in the MoS_2@RGO electrode. (Xiangdan Zhang et al., 2020) (c) annular dark-field STEM image and elemental maps of the MoS_2-C hollow rhombs. (L. Han et al., 2020)

WS_2, another commonly transformed metal sulfide, is also one of the hot materials for research. However, its poor crystallinity and unstable crystal structure further limit its application in SIBs. To this end, Zhang et al. inserted metal ions into the interlayers of layered WS_2 via molten salt electrolysis, thus obtaining a less lamellar structure. Furthermore, their team revealed the effects of the molten salt system, the application of constant current, and the electrolysis time on the degree of WS_2 intrinsic exfoliation. (B.-L. Zhang et al., 2023) Moreover, Liu et al. prepared WS_2 nanosheets wrapped in carbon films and further introduced CNTs to construct tubular nanohybrid materials. The extended (0 0 2) layer spacing combined with the double carbon confinement structure enabled the WS_2 nanosheets to exhibit fast charge transport and excellent structural stability. (YangJie Liu et al., 2023) As shown in Figure 2.25, Xu et al. prepared vertically aligned WS_2 columnar platelet membranes as independent anodes directly on Al foils by a novel sputtering strategy, realizing an ultrathin (6 nm) carbon layer with controllable thickness, which improved the ion/electron transport efficiency and high stability of the electrode structure. (S. Xu et al., 2020)

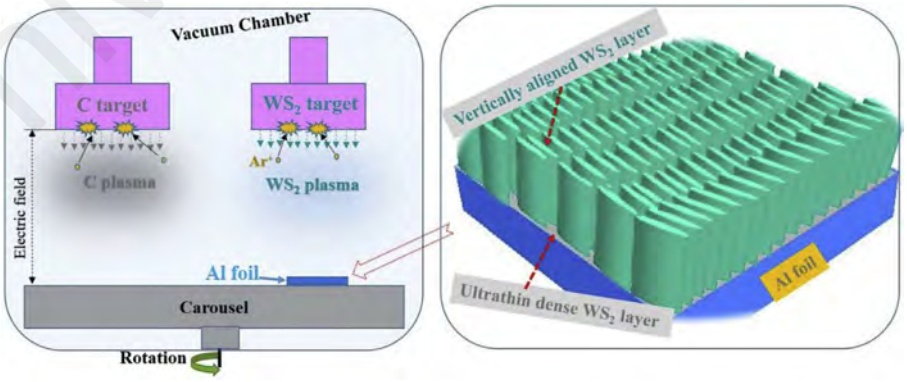

Figure 2.25: Schematic illustration of the direct deposition of WS_2 columnar platelet membranes on the Al foil current collector. (S. Xu et al., 2020)

2.1.4.2 Metal Selenides

Typically, similar to MSs, MSes possess a layered composition structure, where metal atoms are connected to two anions, forming a monolayer structural unit. (Z. Hao et al., 2022) The larger atomic radius of selenium compared to sulfur results in expanded lattice parameters, facilitating faster ion diffusion and better kinetics during sodiation/desodiation processes. Additionally, some MSes offer higher theoretical capacities and improved cycling stability due to their unique structural and electronic properties. Moreover, MSes have been extensively studied due to the narrower band gap and superior electrical conductivity compared to MSs. (M. Luo et al., 2020; Yuhan Wu et al., 2021) For instance, Wang et al. demonstrated that the introduction of selenides enhances the overall electrical conductivity and accelerates the ionic reaction kinetics by constructing heterostructures of MSs and MSes (Figure 2.26). (Tianshuai Wang et al., 2020) However, they also undergo significant volume changes during cycling, which can lead to mechanical degradation and electrode pulverization. Additionally, they still face certain limitations (the inescapable volumetric strain and conductivity degradation during charging and discharging processes), particularly in high-power applications. Several strategies can be employed to mitigate the above challenges associated with MSes. Nanostructuring materials at the nanoscale, such as creating nanoparticles, nanowires, or nanorods, can help accommodate the strain induced by sodiation/desodiation processes, thereby enhancing cycling stability. Li et al. prepared highly uniform $MoSe_2$ nanoparticles using a one-pot hydrothermal method and applied polyvinylpyrrolidone as a surfactant. The $MoSe_2$ nanoparticles exhibited better cycling stability and rate capability relative to the unmodified bulk $MoSe_2$. (N. Li et al., 2022)

Analogously, Zou et al. similarly prepared nanocrystalline WSe_2 by a one-pot hydrothermal method. Thanks to the highly ordered nanosheet structure and short ion/electron transport paths, the WSe_2 nanoparticles exhibit significantly better Na^+ storage properties than the microscale WSe_2. (Zou et al., 2024)

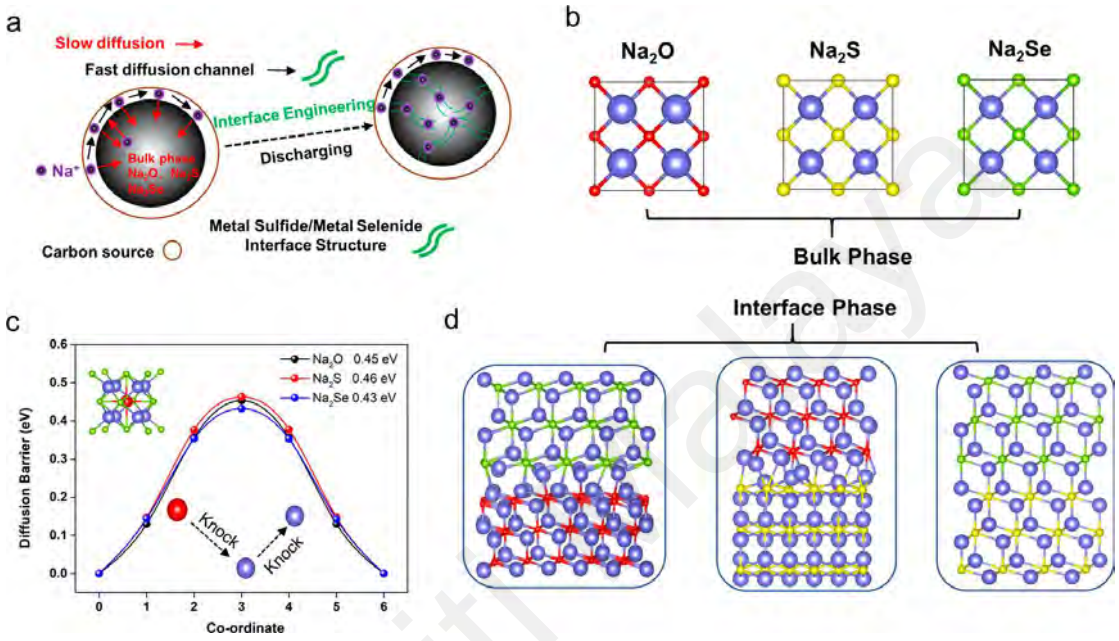

Figure 2.26: (a) The illustration for the interface engineering. (b) The atomic configurations of the bulk phase of Na_2O, Na_2S, and Na_2Se. (c) The diffusion energy barrier of Na atom in the bulk phases. (d) The optimized interface structures of Na_2O/Na_2Se, Na_2O/Na_2S, and Na_2S/Na_2Se. (Tianshuai Wang et al., 2020)

Forming composites with conductive matrices like carbon or graphene improves the mechanical integrity and conductivity of the electrode, buffering volume changes and providing continuous electronic pathways. Li et al. synthesized rGO and $MoSe_2$ composites by a one-step solvothermal method. On the one hand, the 3D structural design promotes rapid electrolyte penetration and provides sufficient buffer space for volumetric strain during electrochemical processes, resulting in excellent cycling performance at a high current density of 30 A g^{-1}. Further, as shown in Fig. 2.27a, in-situ XRD revealed that the prepared electrodes have a reversible conversion reaction

while exhibiting a clear initial insertion reaction. (Zhuanxia Li et al., 2024) Xu et al. synthesized rGO-coated $CoSe_2$-$MoSe_2$ composites ($CoSe_2$-$MoSe_2$/rGO) by in-situ hydrothermal selenization treatment. The unique hierarchical structure combined with the rGO capping resulted in significantly improved structural stability of the prepared electrodes. As shown in Figure 2.27b, in-situ XRD was further applied to probe the intermediate state process of MSes in the conversion reaction. The results show that the energy storage behavior of $CoSe_2$-$MoSe_2$/rGO is a combined mechanism of intercalation and transformation. Na_xCoSe_2 and $Mo_{15}Se_{19}$ as intermediate states can be significantly monitored in both mechanisms. (Yanan Xu et al., 2022) In addition, Lv et al. synthesized N-doped double carbon-coated $MoSe_2$ with multi-channel pathways by electrostatic spinning combined with selenization/carbonization process. Rational electronic modulation and structural design make the prepared composite electrodes have the 3D conductive network and abundant void space, which provide for electron transfer and buffer the volume expansion stress. (Chengkui Lv et al., 2022) Zhang et al. successfully constructed a hierarchical structure of vertically aligned WSe_2 nanosheets tightly anchored on micrometer-sized carbon spheres by combining molecular coupling and self-assembly strategies. The WSe_2 nanosheets combined with micrometer-sized carbon supports shorten the conduction path of Na^+ ions and provide an excellent conductive pathway for the composite. (G. Zhang et al., 2021)

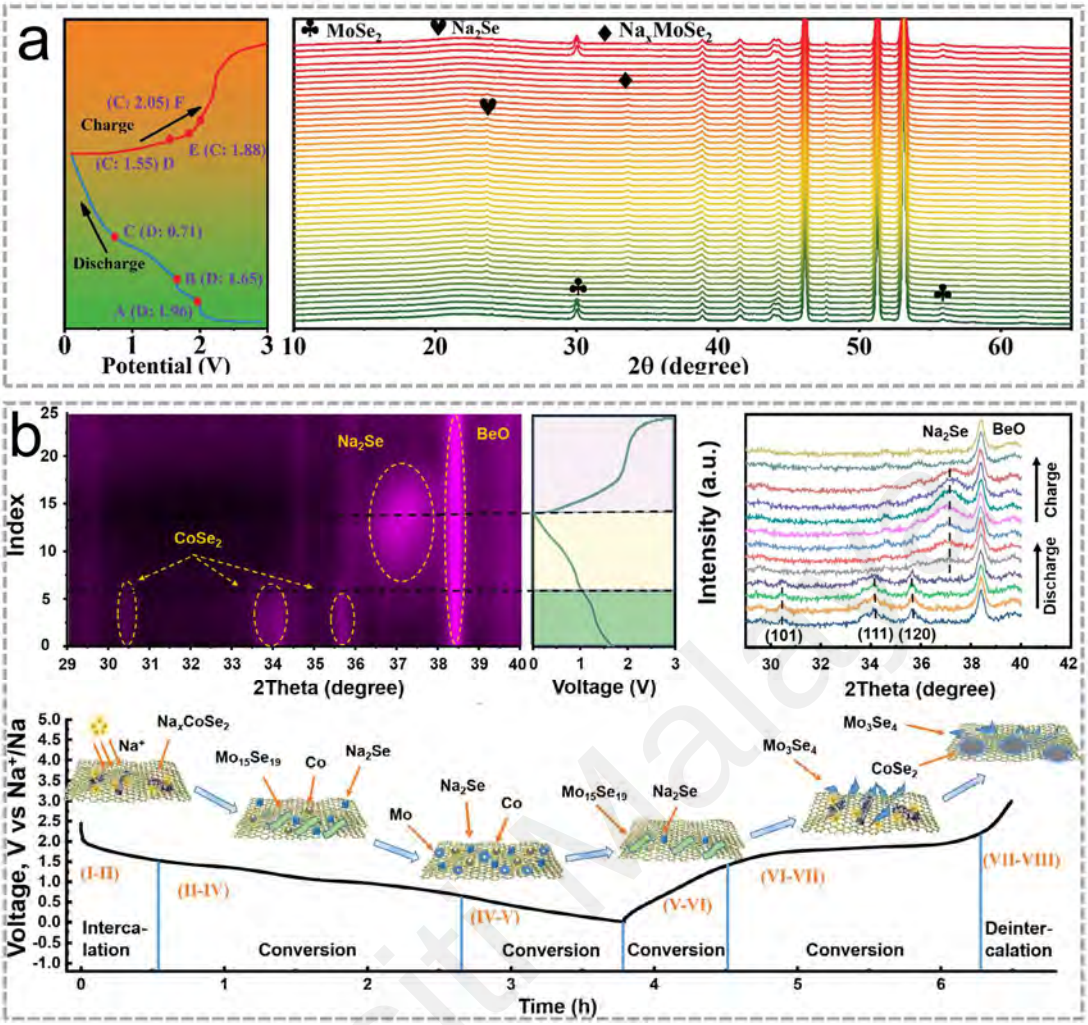

Figure 2.27: (a) Stacked in-situ XRD patterns of the $MoSe_2$ electrode during the initial discharge/charge cycle from the potential 0.01 to 3.0 V. (Zhuanxia Li et al., 2024) Reaction mechanism investigation of $CoSe_2$-$MoSe_2$/rGO tubes for SIBs: (b) In-situ XRD patterns in a contour plot for the first cycle at 0.2 A g^{-1} and the schematic illustration of the reaction mechanism at different stages. (Yanan Xu et al., 2022)

Applying protective coatings or buffer layers, such as metal oxides or polymers, manages volume expansion and protects the electrode from degradation by acting as a mechanical buffer and stabilizing the SEI. Kim et al. prepared WSe_2 nanosheets uniformly assembled on porous carbon cloth by impregnating carbon coating on the WO_3 surface. The carbon-coated structure effectively improved the conductivity of the composite electrode and slowed down the bulk strain of WSe_2 during the electrochemical process. (I. Kim et al., 2020) Additionally, developing advanced

electrolytes that form stable SEI layers enhances the compatibility and longevity of conversion-type anodes by minimizing side reactions and supporting stable cycling performance. As shown in Figure 2.28a, Yi et al. synthesized nitrogen-doped $MoSe_2$/graphene (N-$MoSe_2$/G) composites with unique biomorphic structures via a diatomaceous earth template design strategy, exhibiting abundant active sites, stable SEI structures, and fast pseudo-capacitance effects. (Yuyang Yi et al., 2020) Additionally, Guo et al. employed interfacial and electronic structural dual engineering to prepare $MoSe_2$ nanosheets with a dual-carbon coated sandwich structure (BH-$MoSe_2$@CNBs) in Figure 2.28b. On the one hand, the inner carbon shell acts as a supporting skeleton, inhibiting the accumulation of the lamellar $MoSe_2$ and buffering the bulk stress of the Na^+ embedding/de-embedding process. On the other hand, the presence of the outer carbon layer can adsorb polyselenide intermediates and form a stable SEI layer, which helps to maintain the cycling stability of the intermediate $MoSe_2$ electrode. (Guo et al., 2022) Although researchers have applied a series of strategies to optimize the above issues, including carbon coating, heteroatom doping, and voltage control, (Ou et al., 2017; Pan et al., 2018; Xia et al., 2019; Yuyang Yi et al., 2020) the critical issues such as the coating layer's thickness consistency, doping uniformity, and low energy density (caused by voltage regulation) still cannot be perfectly regulated.

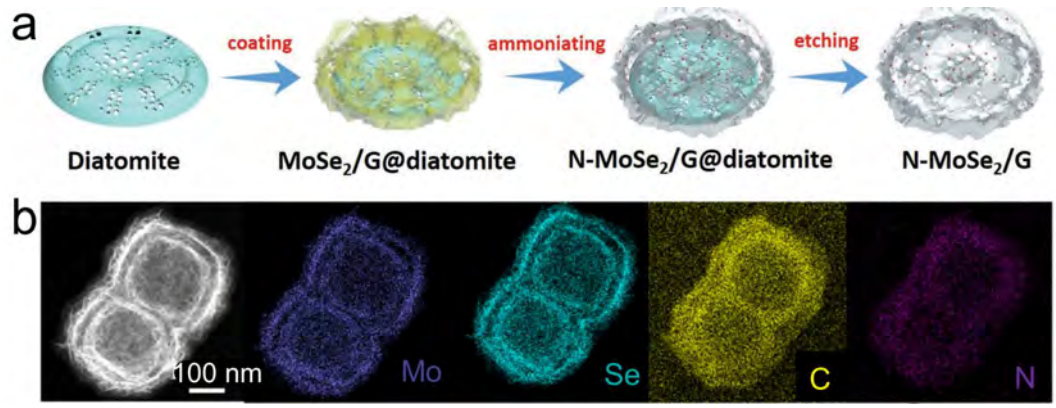

Figure 2.28: (a) Schematic illustration of the synthetic procedure of N-MoSe$_2$/G nanoarchitectures. (Yuyang Yi et al., 2020) (b) Corresponding elemental mapping images of BH-MoSe$_2$@CNBs. (Guo et al., 2022)

2.1.5 Summary

By comparing the advantages and disadvantages of different types of anode materials applied in SIBs, several key insights emerge: i) Intercalation-type anodes exhibit limited application potential in SIBs primarily due to the high insertion energy barriers associated with the large size of Na^+, resulting in significant drawbacks in specific capacity and high-power performance. ii) Adsorption-type anodes benefit from multiple active sites, which, despite some limitations in achieving high specific capacities, demonstrate superior rate performance due to their rapid ion transfer capabilities. iii) Alloy-type anodes offer the highest specific capacities compared to other types of electrodes, thanks to their extensive alloying processes; however, their development is hindered by significant volumetric expansion and the challenging dealloying process under high-power conditions. iv) Conversion-type anodes can achieve high specific capacity Na^+ storage through fast multi-electron transfer processes, and their rapid redox reactions provide the kinetic advantages needed to meet the demands of high-power devices. Collectively, conversion-type materials represent a promising class of anode materials for sodium-ion energy storage devices due to their high theoretical

capacities and diverse material options. MSes, in particular, offer advantages such as higher electronic conductivity and improved reaction kinetics compared to oxides and sulfides. However, challenges such as volume expansion, material cost, and SEI formation need to be addressed. Various strategies, including nanostructuring, composite formation, and electrolyte optimization, are being employed to enhance the performance of these materials. Continued research and innovation in this field could lead to the successful implementation of conversion-type anodes in commercial SIBs, contributing to the advancement of sustainable and high-performance energy storage solutions.

2.2 Microstructural Modification for Metal Selenides

Microstructural modification is a crucial strategy in enhancing the electrochemical performance of metal selenide anodes for SIBs and SICs. The microstructural modification involves tailoring the material at the microscopic level to improve properties such as capacity, cycling stability, rate performance, and overall durability. By modifying the microstructure, researchers aim to address inherent challenges associated with metal selenides, such as volume expansion, low electronic conductivity, and poor structural stability. Metal selenides undergo significant volume changes during the sodiation and desodiation processes. Microstructural modification for converted MSes can effectively enhance the electrochemical performance of electrodes in the material's intrinsic perspective. Firstly, microstructural modification can create structures that accommodate these volume changes without causing mechanical degradation or loss of electrical contact. Secondly, structurally engineered materials can

facilitate better electron transport pathways, reducing internal resistance and improving overall conductivity. Thirdly, microstructural designs can enhance the diffusion kinetics of Na^+, leading to faster and more efficient charge/discharge cycles. Fourthly, nanostructured materials offer a larger surface area for electrochemical reactions, enhancing capacity and rate performance. Fifthly, controlled microstructures help in maintaining the mechanical integrity of the electrode material, ensuring long-term stability and cycling performance. Compared to other modification strategies, such as simply chemical doping or composite formation, microstructural modification provides a more direct and often more effective means to tackle multiple performance-limiting factors simultaneously. It offers the flexibility to fine-tune the physical properties of the material at the nanoscale, leading to optimized performance. Therefore, microstructural modification plays a critical role in enhancing the performance of metal selenide anodes in SIBs. This section discusses various strategies, including micro-morphology design, heteroatom doping, defect engineering, and mixed-phase engineering.

2.2.1 Micro-Morphology Design

Micro-morphology design involves tailoring the physical structure of MSes at the micro and nanoscale to enhance their electrochemical properties. As shown in Figure 2.29, the micro-morphology design process includes creating zero-dimensional (0D) nanoparticles, one-dimensional (1D) nanowires, two-dimensional (2D) nanosheets, three-dimensional (3D) nanoflowers, and hierarchical structures. Each morphology offers unique benefits. Firstly, nanoparticles can reduce diffusion distances for ions and electrons, increasing reaction kinetics and capacity. Secondly, nanowires and nanorods

can provide direct pathways for electron transport and accommodate volume changes more effectively. Thirdly, nanosheets can offer a large surface area and short ion diffusion paths, enhancing capacity and rate performance. Fourthly, nanoflowers can increase active surface area and provide channels for electrolyte penetration, improving ion transport and reaction kinetics. Fifthly, the hierarchical structure design enables a flexible structural design that combines the advantages of other structures, thus demonstrating maximized electrochemical performance.

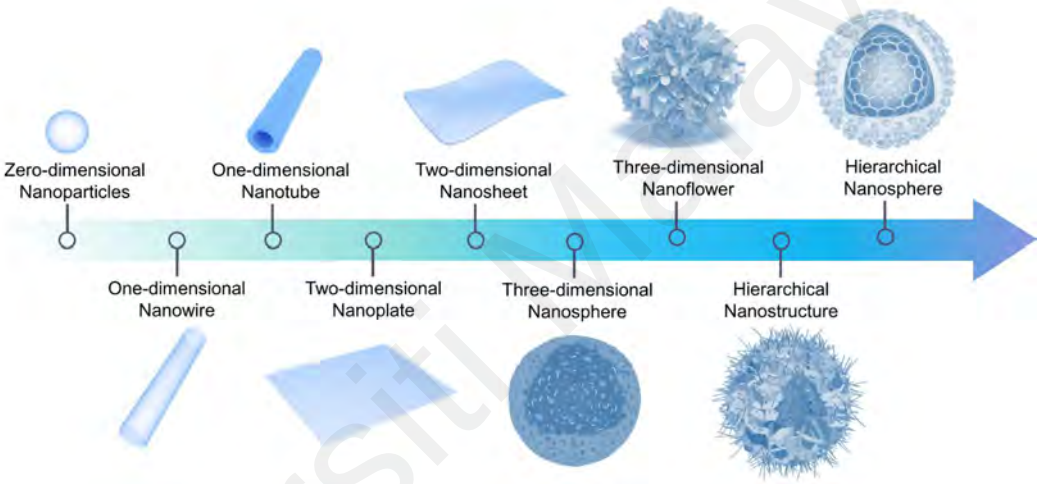

Figure 2.29: Schematic diagram of anode materials with different morphologies.

2.2.1.1 Zero-dimensional Structures

0D nanoparticles are characterized by their small size and high surface-to-volume ratio. These properties allow for a high number of active sites, which can significantly enhance electrochemical reactions. Nanoparticles can reduce the diffusion distance for ions and provide more interface area for charge transfer, increasing reaction kinetics and capacity. For example, highly dispersed $FeSe_2$ nanoparticles have shown excellent electrochemical performance due to their ability to maintain structural integrity and prevent aggregation during cycling, which contributes to their high capacity and long cycle life. (Tongxian Wang et al., 2020) Meanwhile, As shown in Figure 2.30a-c, Zhao

et al. prepared ultrasmall $FeSe_2$ nanoparticles (~5 nm) using a high-temperature solution method. The favorable nanosizing effect demonstrated significant Na^+ storage activity, exhibiting a large specific capacity (~500 mA h g^{-1}) close to the theoretical limit. (F. Zhao et al., 2017) Another example is $Ni_{0.6}Co_{0.4}Se_2$ nanoparticles in Figure 2.30d-e. The obtained $Ni_{0.6}Co_{0.4}Se_2$ nanoparticles demonstrate high rate capability and excellent cycle stability, which are attributed to their nanoscale dimensions and the synergistic effect between Co and Ni. (Yahui Wang et al., 2019) However, the high surface energy of nanoparticles can lead to accumulation during synthesis and cycling, which reduces the effective surface area and can lead to poor electrochemical performance. Additionally, nanoparticles often suffer from significant volume changes during charge/discharge cycles, leading to mechanical stress and potential structural degradation. Herein, Zhang et al. successfully in-situ encapsulated CoSe nanoparticles using nitrogen-doped CNTs. The encapsulated structure effectively suppressed the aggregation of CoSe nanoparticles, resulting in a sustained active effect and improved kinetics. (Z. Zhang et al., 2024)

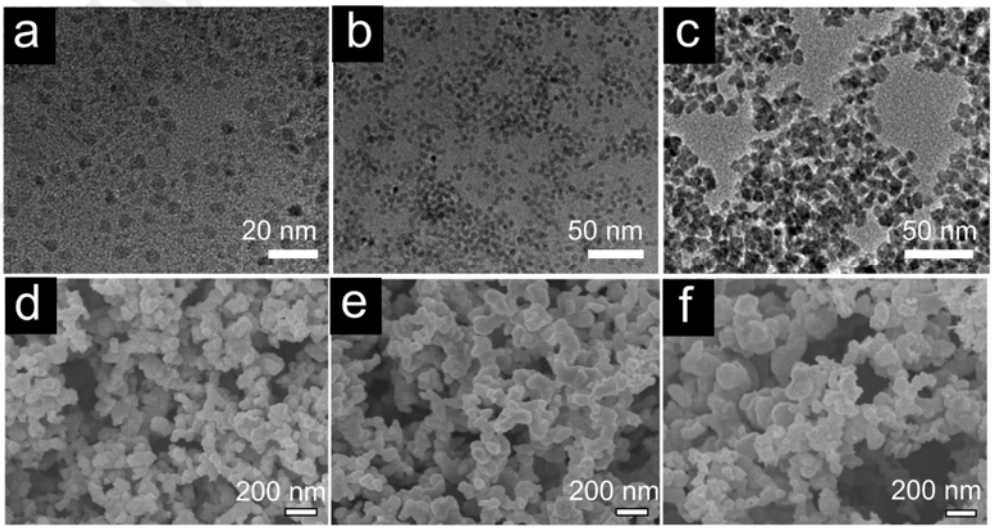

Figure 2.30: (a-c) TEM images of products prepared at 150 °C for (a) 5 min, (b) 10 min, and (c) 60 min. (F. Zhao et al., 2017) SEM images of (d) $Ni_{0.6}Co_{0.4}Se_2$, (e) $Ni_{0.8}Co_{0.2}Se_2$, (f) $NiSe_2$. (Yahui Wang et al., 2019)

2.2.1.2 One-dimensional Structures

1D nanostructures, such as nanowires, nanorods, and nanotubes, have demonstrated significant advantages in improving battery performance due to their unique morphology and size effects. The short diffusion paths and large surface areas of 1D nanostructures enhance electron and ion transport rates. In addition, nanowires have excellent mechanical flexibility and Young's modulus, which can accommodate volume expansion, inhibit mechanical degradation and extend cycling life. To synthesize 1D nanostructures, researchers have carried out many meticulous explorations through a variety of methods, including hydrothermal reactions, electrolytic deposition, calcination, electrostatic spinning, microemulsion techniques, template methods, and chemical vapor deposition. For instance, Chen et al. investigated the growth mechanism of SnSe nanorods and the effect of different metal complexes on their synthesized morphology (Figure 2.31a-c). Resultantly, compared with SnSe nanoparticles, SnSe nanorods exhibited a fast electron/ion transport path through the 1D nanostructure, which in turn displayed better rate performance and cycling stability. (Yaopeng Chen et al., 2021) Besides, as shown in Figure 2.31d, Aghdam et al. synthesized the α-MnSe nanorods with a length of 100 nm, a diameter of about 30 nm, and an enlarged layer spacing of 0.91 nm by a hydrothermal method. Afterward, they achieved higher pseudocapacitance performance and faster charge/discharge rate compared to α-MnO_2 by in situ electrochemical activation of α-MnSe nanorods. (Molaei Aghdam et al., 2023) Individual MSes nanorods are designed to inevitably suffer structural decomposition from the surface's rapid reaction during electrochemical processes. Accordingly, Li et al. prepared $FeSe_2$ nanorods with different oxide contents through a surface oxidation

strategy and revealed the sodium storage mechanism of surface oxides on $FeSe_2$ nanorods. During the electrochemical process, the surface oxides were transformed into a high-mechanical-strength protective shell, and the decomposition of the internal $FeSe_2$ was further suppressed based on the generated phase-transition resistance, which ensured the structural stability during the repeated Na^+ insertion/extraction process. (D. Li et al., 2018) Additionally, Jin et al. synthesized selenium-doped carbon nanotube/nickel selenide coaxial nanocables by combining chemical deposition and chemical vapor-phase reaction. The 1D nanostructure provides a large active substance/electrolyte contact area and facilitates rapid charge transfer. (Jin et al., 2021) Despite the above advantages, 1D nanostructures can still experience issues related to mechanical integrity. During repeated sodiation and desodiation cycles, nanowires and nanotubes may fracture or undergo structural collapse. Additionally, synthesizing uniform and defect-free 1D nanostructures can be challenging and often requires complex and costly fabrication techniques.

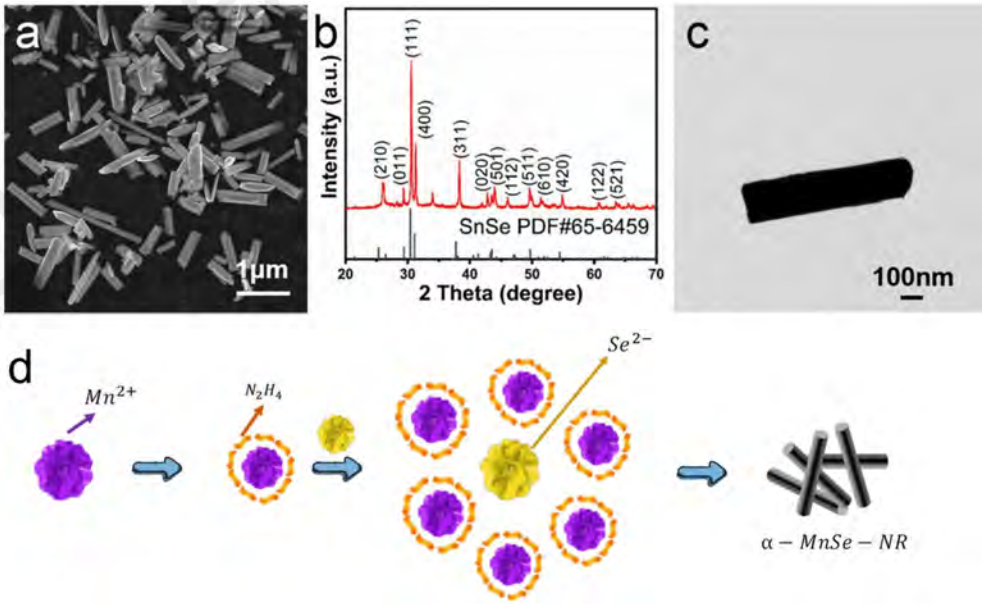

Figure 2.31: (a) SEM image and (b) XRD pattern of the SnSe nanorods. (c) TEM image (after ultrasonic dispersion) of the SnSe nanorods. (Yaopeng Chen et al., 2021) (d) Schematic of the *α*-MnSe-NR synthesis. (Molaei Aghdam et al., 2023)

2.2.1.3 Two-dimensional Structures

2D nanomaterials, such as nanosheets and nanobelts, are greatly interested in energy storage applications due to their high specific surface area and layered structures. These structures provide more active sites and larger electrolyte contact areas, enhancing the efficiency of electrochemical reactions. For example, Zhou et al. prepared layered $Co_{0.85}Se$ nanosheets based on a 2D directional attachment strategy via a solution method. Based on the 2D layered structure, the $Co_{0.85}Se$ nanosheets exhibited enhanced electrical conductivity and improved ion diffusion pathways, which in turn delivered superior electrochemical properties over $Co_{0.85}Se$ microspheres. (Jisheng Zhou et al., 2016) To explore the effects of different synthesis strategies on the nanosheets, Oh et al. synthesized V_2Se_9 ultrathin nanoribbons using the colloidal method, which yielded significantly higher specific surface areas than those of the solid reaction synthesized samples (Figure 2.32). It is worth mentioning that the selenium-enriched V_2Se_9 ultrathin nanoribbons have Se atoms exposed at all interfaces, exhibiting shorter ion diffusion distances and more electrochemically active sites. (Oh et al., 2023) However, the primary challenge with 2D structures is the potential for restacking or agglomeration during cycling, which can reduce the available surface area and hinder lithium-ion transport. Moreover, ensuring the mechanical flexibility and structural integrity of 2D materials over prolonged cycling can be difficult, which may lead to capacity fading and performance degradation. Although 2D nanosheet structures still have structural drawbacks, researchers have balanced their electrochemical performance exertion as electrodes through some additional modulation processes. For instance, Zhao et al. designed manganese modulation on cobalt selenide nanosheets with the aim of

highlighting the electrochemical activation of the active sites. The results indicated that the metal selenides could exhibit atomic disorder, electronic structure tuning, and conductivity optimization through the introduction of Mn modulation, thus effectively promoting the generation of active sites. (Xu Zhao, Li, et al., 2018) Similarly, Bhargav's team employed a top-down strategy to introduce Si nanoparticles into 2D-$MoSe_2$ to form a silicon-embedded layered nanosheet structure. The constructed bifunctional electrodes formed by trace amounts of Si inserted into the $MoSe_2$ matrix have enhanced high current density adaptability and strong physicochemical stability. (G. Kumar et al., 2024) Furthermore, Feng et al. obtained VSe_2 nanosheets by selenization with $VO(acac)_2$ as a precursor, followed by carbon nanoribbon aerogel polymerization and coating. As a result, the carbon nanoribbon aerogel with high surface area and high porosity exhibited enhanced electrical conductivity and structural protection for the VSe_2 nanosheet structure. (Y. Feng et al., 2022)

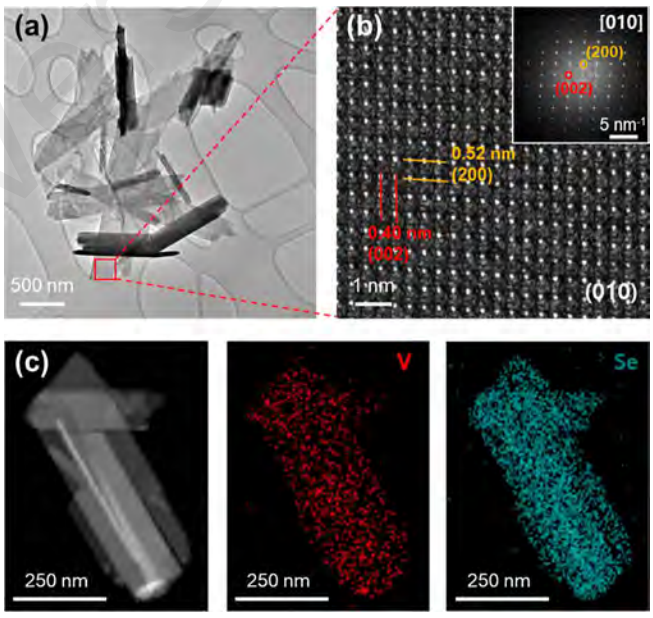

Figure 2.32: (a) TEM image of C-V_2Se_9, along with (b) HR-TEM image (inset: fast Fourier transform pattern). (c) STEM-EDS elemental mapping images of C-V_2Se_9. (Oh et al., 2023)

2.2.1.4 Three-dimensional Structures

3D structures, such as nanoflowers, nanospheres, and nanoporous structures, exhibit superior performance in practical applications due to their high structural stability and large specific surface area. 3D structures not only provide more active sites but also achieve better stress distribution through structural design, enhancing the material's cycle life. For instance, Jia et al. designed a Co-Fe bimetallic selenide with hollow nanosphere structure while introducing N-doped carbon (Figure 2.33a-d). In this unique 3D structure, the bimetallic selenide further improves the conductivity of the composite electrode. In addition, the N-doped carbon layer coating effectively inhibits the dissolution of electrochemical products and mitigates the spatial volume expansion of the 3D structure. When applied to K-Se batteries, the composite electrodes exhibit excellent slow charging/ultra-fast discharging capability and near 100% coulombic efficiency. (Jia et al., 2021) Xu et al. prepared WSe_2 with 3D ordered flower-like morphology by a one-step hydrothermal method and applied it to rechargeable magnesium-ion batteries, demonstrating excellent initial capacitance (90%) and rate capability. (J. Xu et al., 2021) Analogously, to explore the effect of morphology on the nanomaterial properties, Zhou et al. synthesized 2D nanosheets and 3D interconnected nanoflowers of WSe_2 using an advanced colloidal thermal injection strategy, respectively (Figure 2.33e). In this work, not only was the effectiveness of colloidal synthesis for precise control of morphology investigated but also WSe_2 with 3D nanoflower structure was demonstrated to have high capacity retention after 100 cycles. (P. Zhou et al., 2020) Although 3D structural design can be advantageous in terms of the structural mechanics of the material, achieving longer-term cycling stability still

requires significant challenges. As shown in Figure 2.33f, g, Du et al. prepared N-doped reduced graphene oxide/$Co_{0.85}Se$ nanoflowers (N-rGO/CS) by a two-step method to achieve synergistic structural design of highly conductive dielectrics and active materials. The prepared nanoflower composites have increased specific area and conductivity, which effectively promote highly active electron/ion transfer at the electrode mass transfer interface. The obtained composite electrodes have high active material loading (~8.83 mg cm^{-2}) and achieve a long cycle life of more than 6000 cycles (capacity retention of 85.8%). (M. Du et al., 2022) Moreover, Sun et al. first self-assembled Co^{2+} with glycerol molecules into nanospheres and constructed 3D ion diffusion channels by embedding $CoSe_2$ nanospheres in situ into the carbon matrix through a selenization process. The presence of a large number of pores in this 3D yolk-shell structure can effectively slow down the volume expansion and hinder the aggregation of $CoSe_2$. (X. Sun et al., 2021) Even further, it is worth mentioning that Moosavifard's team proposed the construction of binary metal-carbonate materials to realize the intelligent design of hollow structures on the nanoscale. Based on this, a simple self-templating method was used to prepare porous hollow copper-cobalt selenide nanospheres wrapped on reduced graphene oxide conductive networks, achieving bimetallic synergy at the atomic level and achieving 91.5% capacity retention after 6000 charge cycles. (Moosavifard et al., 2021)

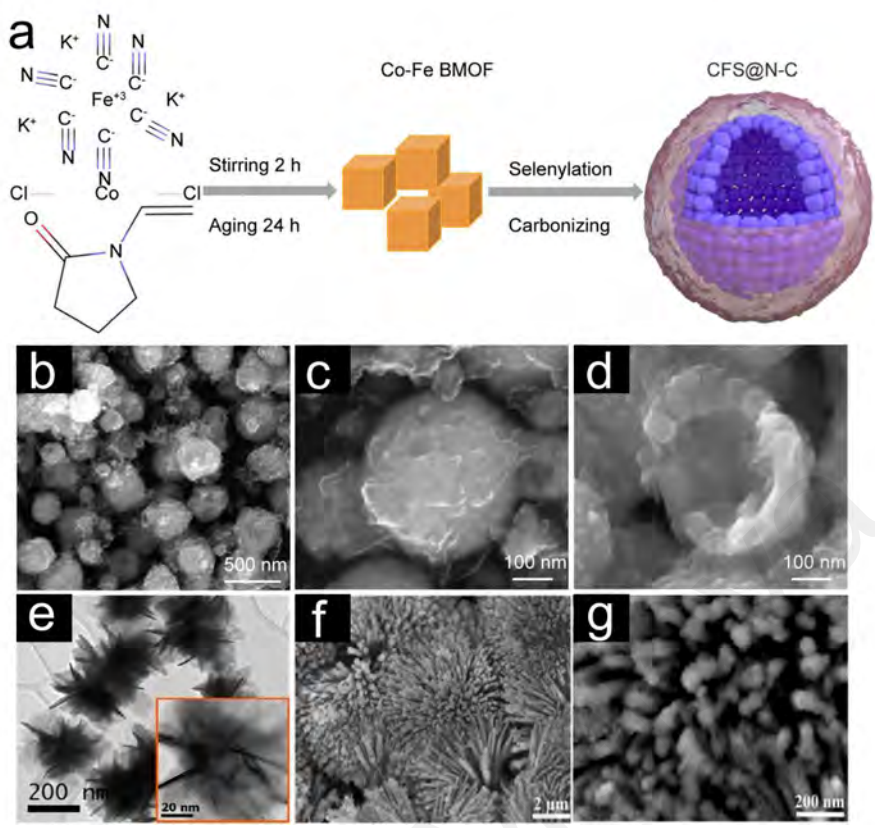

Figure 2.33: (a) Synthesis procedure schematic of CFS@N-C; (b) SEM image at low resolution; (c) SEM image of single intact spherical; (d) SEM image of incomplete spherical interior. (Jia et al., 2021) (e) Low-resolution TEM image of 3D WSe_2 nanoflowers. Insert: High-resolution TEM image. (P. Zhou et al., 2020) The SEM images of N-rGO/CS (f, g) at low and high magnification. (M. Du et al., 2022)

Overall, 3D structural design offers unique electrochemical advantages over other morphological design strategies. However, deficiencies in intrinsic conductivity and long-term cycling stability are still problems faced by current structure design. Therefore, additional strategies to enhance the conductivity while ensuring the structural design are necessary development strategies. Although the above summarized findings attempt to ensure excellent structural design while enhancing the overall electrical conductivity through multi-faceted design strategies, the synthesis process of 3D structures can be complex and costly to fabricate. Additionally, maintaining uniformity and consistency in the structural design can be challenging. There is also a risk of

incomplete electrolyte penetration into the inner regions of 3D structures, which can limit their electrochemical performance.

2.2.1.5 Hierarchical Structures

Hierarchical structures combine 1D, 2D, or 3D structures to form materials with multi-level architectures. This design leverages the advantages of different dimensional structures, achieving superior electrochemical performance. Hierarchical structures provide multi-scale pores and larger specific surface areas, enhancing ion and electron transport rates. Muska et al. synthesized $CoSe_2$ nanoparticles dispersed in WSe_2 nanosheets using a thermally injected colloidal process, constituting hierarchical nanostructured systems that exhibit enhanced electronic functionality. (Muska et al., 2021) Similarly, Jiang et al. prepared $MoSe_2@MoO_2$ with MoO_2 nanoparticles embedded on $MoSe_2$ nanosheets by hydrothermal method in Figure 2.34a. Investigations showed that well-dispersed MoO_2 nanoparticles prevented the re-stacking of $MoSe_2$ nanosheets, which enhanced the structural stability during electrochemical processes. (Qingqing Jiang et al., 2020) However, the complex construction process of hierarchical structures remains a great challenge. As shown in Figure 2.34b−d, Hu et al. applied a simple selenide recrystallization strategy to synthesize samples of Ni-Co selenides with graded nanoparticle/nanosheet structures. The specific hierarchical structure provided more electroactive sites for charge storage, and the optimized synergistic interaction between Ni and Co components further greatly tuned the charge storage performance. As a result, $Ni_{0.67}Co_{0.33}Se_2$ exhibited much higher Ni-Co selenides and Ni-Co oxides than other Ni-Co ratios and showed excellent cycling stability.

(Yuzhen Hu et al., 2019) However, hierarchical morphology still faces the problem of poor intrinsic conductivity. In previous investigations, smart elemental combinations and nanostructures are two effective strategies for improving intrinsic conductivity. Here, Ali et al. synthesized a graded porous binary transition metal selenide (Fe_2CoSe_4) nanomaterial with improved intrinsic conductivity. Under the synergistic effect of graded porous structure and improved intrinsic conductivity, the prepared Fe_2CoSe_4 exhibits excellent multiplicative properties and extended cycling stability. (Ali et al., 2018) Further, carbon coupling combined with hierarchical structural design is verified to enhance the overall structural performance and intrinsic conductivity through tight nanoparticle-carbon matrix contacts. Based on this, Gao et al. constructed hierarchical tubular hybrid nanostructures by encapsulating $CoSe_2$ nanoparticles into $MoSe_2$/C composite shells via a hydrothermal method combined with a gas-phase selenization strategy. The unique tubular structure realizes highly reversible Li^+/Na^+ pseudocapacitive storage, exhibiting high specific capacity, enhanced cycling stability, and excellent rate performance. (Gao et al., 2018)

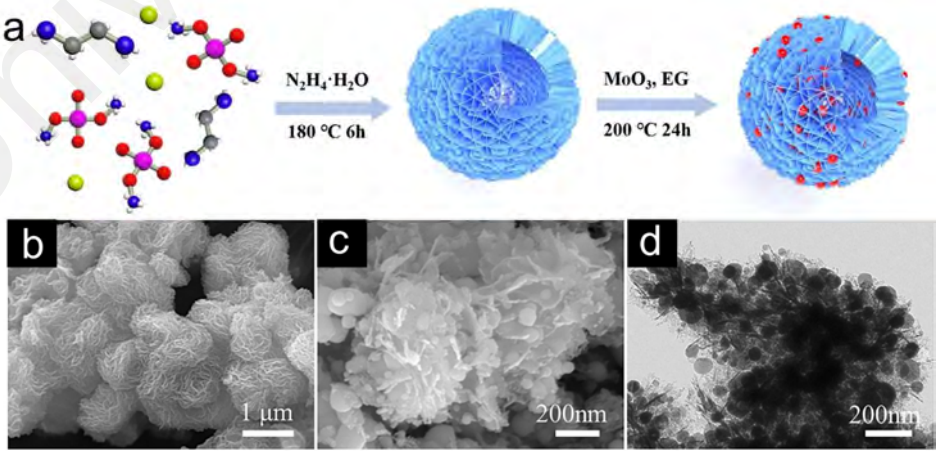

Figure 2.34: (a) Schematic illustration of the preparation process of M@M samples. (Qingqing Jiang et al., 2020) (b) SEM images of the Ni-Co hydroxide precursor. (b) SEM images of $Ni_{0.67}Co_{0.33}Se_2$. (c) TEM images of $Ni_{0.67}Co_{0.33}Se_2$. (Yuzhen Hu et al., 2019)

The hierarchical structural design enables the combination of multi-dimensional materials, which in turn can take advantage of different morphological structures in the same structural system. The hierarchical structure design can maximize the flexibility of the morphology design and thus meet the electrochemical performance of different MSes electrodes. However, the synthesis of hierarchical structures often involves multiple steps and can be time-consuming and expensive. Additionally, there is also the potential for mechanical instability if the hierarchical structure is not well-optimized, leading to performance degradation over time. Therefore, adopting a more efficient and concise hierarchical design strategy in future work is necessary to enable MSes anodes to stimulate greater electrochemical potential.

In summary, MSes anode materials hold great promise in the field of lithium-ion batteries due to their high specific capacity and excellent electrochemical properties. Significant optimization of material performance can be achieved through different microstructure designs, such as 0D, 1D, 2D, 3D, and hierarchical structures. Future research should continue to focus on the design of novel microstructures and the development of performance optimization strategies to further enhance the practical application performance of MSes anode materials.

2.2.2 Heteroatom Doping

MSes have emerged as promising candidates due to their high theoretical capacities and unique electrochemical properties. To further enhance their performance, heteroatom doping has been extensively explored as an effective strategy for modifying

the microstructure and improving the electrochemical characteristics of MSes anodes. Heteroatom doping involves the introduction of foreign atoms into the lattice structure of MSes. These dopants can alter the electronic structure, enhance conductivity, and improve the structural stability of the host material. Depending on their size and chemical compatibility with the host atoms, the doped atoms can occupy interstitial or substitutional sites within the crystal lattice. As for the mechanism of heteroatom doping, on the one hand, doping can alter the band structure of metal selenides, creating additional electronic states near the Fermi level, which enhances electrical conductivity. On the other hand, dopants can help mitigate the volume expansion and mechanical stress associated with the sodiation/desodiation process. Typically, the type of heteroatom doping can be categorized as in-situ doping and post-synthesis doping.

2.2.2.1 In-situ Doping

In-situ doping involves introducing dopant atoms during the synthesis of metal selenides. This method ensures uniform distribution of dopants within the crystal lattice. Solvothermal/hydrothermal synthesis is an efficient strategy for heteroatom in-situ doping. For instance, Fan et al. synthesized carbon layer-coated porous nickel-doped $CoSe_2$ (Ni-$CoSe_2$/C) nanorods by a hydrothermal method combined with a selenization strategy. The obtained Ni-$CoSe_2$/C electrodes were used as anode materials for SIBs, exhibiting ultra-high-rate performance and ultra-long cycle life. (S. Fan et al., 2020) Liu et al. prepared porous Fe-doped $NiSe_2$ nanosheets and used them as SIB anodes. The introduction of Fe creates abundant active sites and enhances electrical conductivity. Thanks to the abundant voids and short electron transport paths, the Fe-doped $NiSe_2$

nanosheets are able to adapt to the volume expansion stress caused by Na^+ insertion/deinsertion and exhibit fast charge transfer kinetics. (Jing Liu et al., 2023) Additionally, Deng et al. prepared Cu-doped $Co_{0.85}Se$ nanoparticles using ZIF-67 as a template by combining the room temperature co-precipitation method and in-situ polymerization (Figure 2.35a). Cu doping improves the material's electrical conductivity through modulation of electronic structure. (Deng et al., 2022) In addition, Tao et al. used a co-induced strategy to prepare Co-doped MoSe2 nanosheets and anchored them on reduced graphene oxide substrates (Figure 2.35b). Benefiting from the enlarged interlayer spacing due to Co doping, the prepared electrodes exhibited activated electronic conductivity and ionic diffusion kinetics, which in turn demonstrated enhanced K^+ reversible capacity and rate capability. (S. Tao et al., 2023)

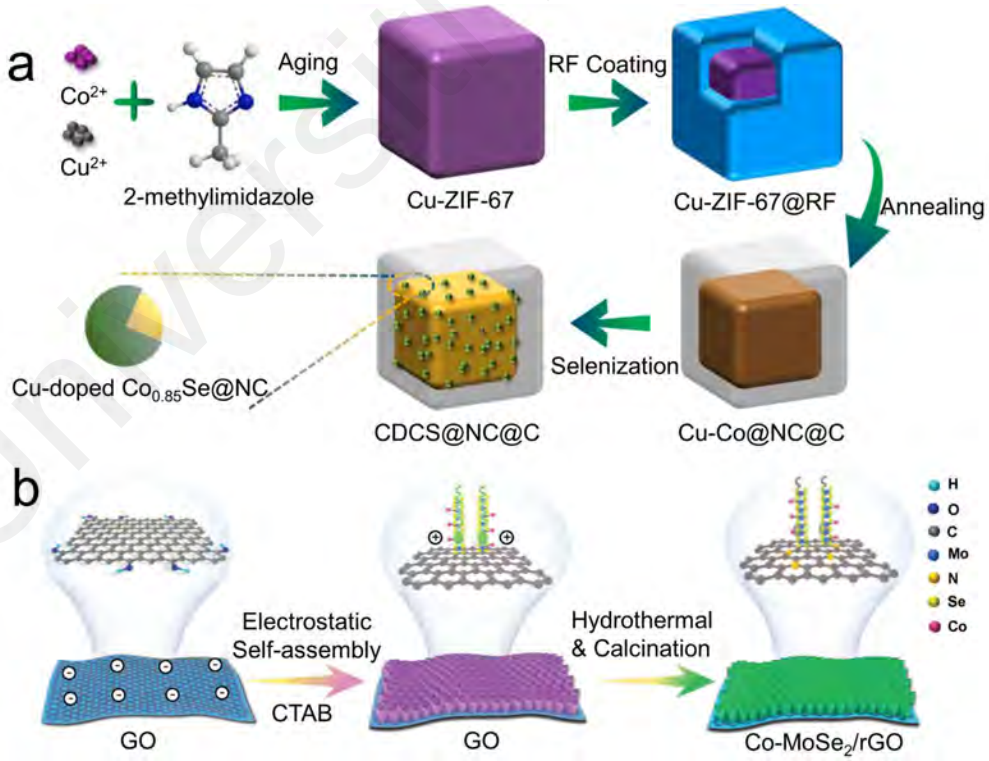

Figure 2.35: (a) Schematic diagram of fabrication route of CDCS@NC@C. (Deng et al., 2022) (b) Schematic illustration of the synthetic process of Co-$MoSe_2$/rGO. (S. Tao et al., 2023)

2.2.2.2 Post-synthesis Doping

Chemical vapor deposition (CVD) is another common strategy for introducing heteroatom doping. As shown in Figure 2.36a, Feng et al. first prepared hydrangea-like $Co_{0.85}Se$ with a microporous structure by a hydrothermal method. Then, they introduced S atoms into the crystal structure of $Co_{0.85}Se$ for doping using the chemical vapor-phase method. S-doped $Co_{0.85}Se$ possesses an enhanced electronic conductivity, which is able to effectively promote the conversion of polysulphides and induce and regulate the homogeneous deposition of insoluble Li_2S on its surface. (T. Feng et al., 2021) Similarly, Shi et al. co-doped the pristine anion-rich $Ni_{0.85}Se$ with Zn and S atoms (Figure 2.36b), which significantly mitigated the expanding effect of the electrode during long-cycle discharging/charging and thus exhibited superior electrochemical performance. (J. Shi et al., 2022) Notably, Li et al. prepared Te-doped 1T/2H-$MoSe_2$ nanosheets using a simple two-step reaction. The results indicated that Te doping had the effect of inducing a phase transition from stable 2H-$MoSe_2$ to 1T-$MoSe_2$, which could increase the conductivity and generate abundant active sites, facilitating the enhancement of the sodium storage capacity. (Zhiqi Li et al., 2024) Wang et al. synthesized W-doped $MoSe_2$ not only reduces the diffusion resistance of ions by increasing the layer spacing of $MoSe_2$ (0.73 nm), but also brings about the narrowest energy band structure (0.892 eV). (Wei Wang et al., 2024)

Figure 2.36: (a) Schematic illustration of the synthesis process for $Co_{0.85}SeS$. (T. Feng et al., 2021) (b) A traditional one-step sol-gel project for the synthesis of metal selenides is used (Plan A). (J. Shi et al., 2022)

The above results show that heteroatom doping can provide multiple advantages in the optimization of bulk phase structure. Firstly, doping metal selenides with heteroatoms can significantly improve their electrical conductivity. Secondly, dopants can help stabilize the structure of metal selenides during the sodiation/desodiation process, mitigating the effects of volume expansion and contraction. Thirdly, heteroatom doping can introduce additional active sites for Na^+ intercalation, thereby increasing the specific capacity and rate capability of metal selenide anodes. However, there are still some great challenges in the heteroatom doping process. Firstly, achieving a uniform distribution of dopants within the metal selenide lattice is challenging. Non-uniform doping can lead to localized stress and structural instability, affecting the overall performance of the anode. Secondly, scaling up doping techniques from

laboratory to industrial scale while maintaining consistency and quality is a significant challenge. Methods such as ion implantation and CVD are often costly and complex, limiting their large-scale application. Thirdly, ensuring the stability of dopants within the metal selenide lattice during cycling is crucial. Dopants that migrate or segregate during operation can degrade the performance of the anode material. To overcome the above challenges, future work on heteroatom doping can focus on the following directions: Firstly, developing advanced synthesis techniques that ensure uniform and stable doping at an industrial scale is essential. Techniques such as atomic layer deposition and molecular beam epitaxy could offer precise control over dopant incorporation. Secondly, exploring multi-doping strategies, where two or more types of dopants are introduced, can synergistically enhance the performance of metal selenide anodes. For example, co-doping with nitrogen and sulfur could combine the benefits of enhanced conductivity and increased active sites. Thirdly, conducting theoretical studies to understand the effects of different dopants on the electronic structure and electrochemical properties of metal selenides can guide the design of new doped materials. Density functional theory calculations can predict the most effective dopants and doping concentrations.

Overall, heteroatom doping is a powerful strategy for enhancing the performance of metal selenide anodes in SIBs. By modifying the electronic structure, creating defects, and improving structural stability, dopants can significantly improve the capacity, rate capability, and cycling stability of metal selenide anodes. Despite the challenges, advancements in synthesis techniques, multi-doping strategies, in-situ characterization,

and theoretical studies hold great promise for the future development of high-performance doped metal selenide anodes.

2.2.3 Defect Engineering

Defect engineering involves deliberately introducing or manipulating defects within the crystal lattice of metal selenides. These defects can significantly influence the electronic structure, ionic conductivity, and mechanical stability of the material. The types of defects commonly introduced include vacancies, interstitials, and grain boundaries.

2.2.3.1 Vacancies

Vacancies are missing atoms in the crystal lattice. Selenium vacancies in MSes can enhance Na^+ diffusion pathways and provide additional active sites for Na^+ intercalation, thereby increasing capacity and rate performance. Jiang et al. synthesized Se vacancy-rich VSe_2 nanosheets by simple solvothermal synthesis with the addition of hydrazine hydrate. The strong reducing power of hydrazine hydrate reduces part of V^{4+} to V^{3+}, resulting in the formation of abundant Se vacancies in VSe_2 nanosheets. The abundant Se vacancies in VSe_2 nanosheets bring about significant enhancement in the diffusion kinetics of ions and the number of electrochemically active sites. (Qiwang Jiang et al., 2020) As shown in Figure 2.37, Muhammad et al. employed a self-templating strategy to synthesize metallic cobalt-doped NiSe nanoparticles confined in 3D nitrogen-doped carbon nanohybrids (Co-NiSe/NMC-2). Electrochemical kinetic analyses and density functional theory calculations showed that cationic defect engineering was beneficial in

increasing the intrinsic conductivity of MSes. Notably, such cationic defect engineering not only reduces the overpotential but also accelerates the conversion reaction kinetics, ensuring excellent high-rate performance and longer durability. (Muhammad et al., 2024)

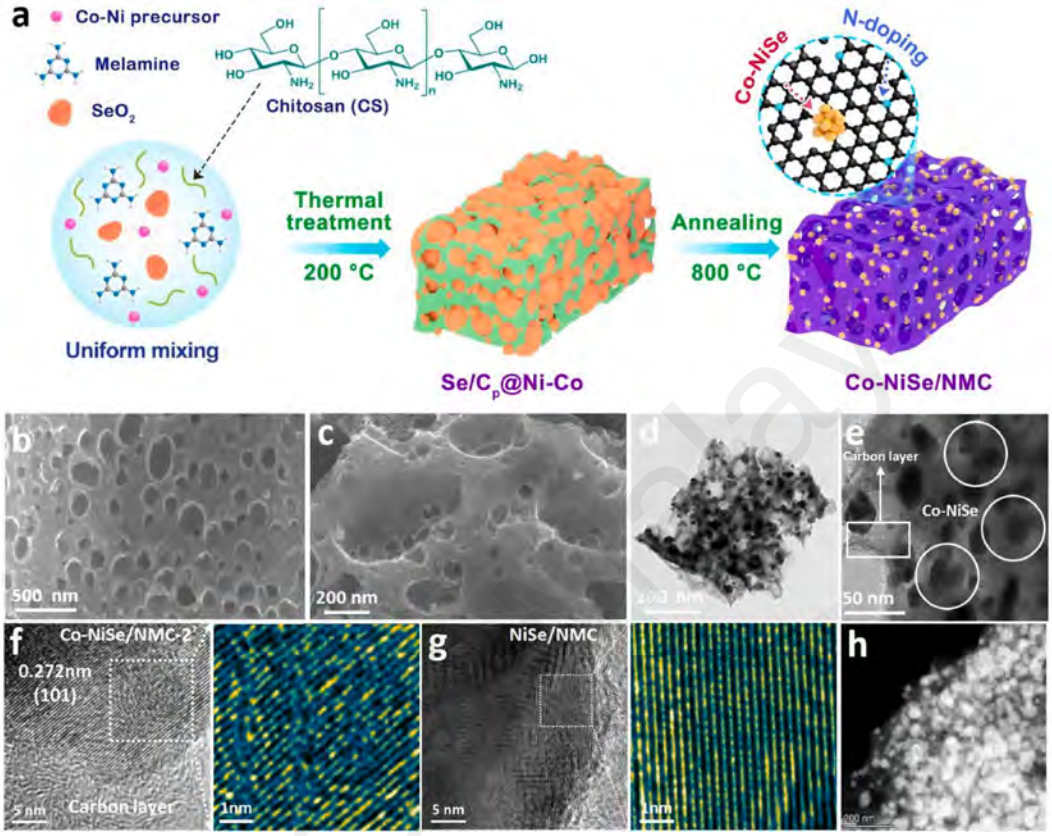

Figure 2.37: (a) Schematic illustration of the preparation process, (b, c) SEM images, (d, e) TEM images, (f) HRTEM image and related FFT-filtered atomic resolution images of the Co-NiSe/NMC-2, (g) HRTEM image and related FFT-filtered atomic resolution images of the NiSe/NMC, (h) EDX of the Co-NiSe/NMC-2. (Muhammad et al., 2024)

2.2.3.2 Interstitials

Interstitial defects occur when extra atoms occupy positions in the crystal lattice that are not normally occupied. These defects can improve the electronic conductivity and structural stability of the material. As shown in Figure 2.38a, Li et al. designed a vacancy-rich MoSSe grown vertically on reduced graphene oxide aerogel (rGO/MoSSe). Se atoms achieve interstitial anion occupancy in the MoS_2 lattice, generating abundant anionic vacancies and improving the intrinsic conductivity and ionophilic properties of

the composite electrode. (Hong Li et al., 2022) However, maintaining the stability of S vacancies and retaining their excellent activity is still a great challenge. Based on this, Zhu et al. stabilized and activated S vacancies by partially replacing S atoms in WS_2 nanosheets with Se atoms (Figure 2.38b, c). The more active sites brought by the vacancies not only promote the rapid adsorption of ions, but also further improve the conductivity of the electrode, which in turn significantly enhances the storage capacity and reaction kinetics of the active ions. (Q. Zhu et al., 2022) Additionally, Tian et al. successfully prepared MoSSe arrays with double anionic vacancies. The vacancy-rich MoSSe arrays significantly enhanced the adsorption of K^+ ions. As shown in Figure 2.38d, Density-functional theory calculations showed that the MoSSe interlayer had a more negative adsorption value (-1.74 eV), which was much higher than that of the vacancy-rich MoSSe (0.53 eV). (Z. Tian et al., 2020)

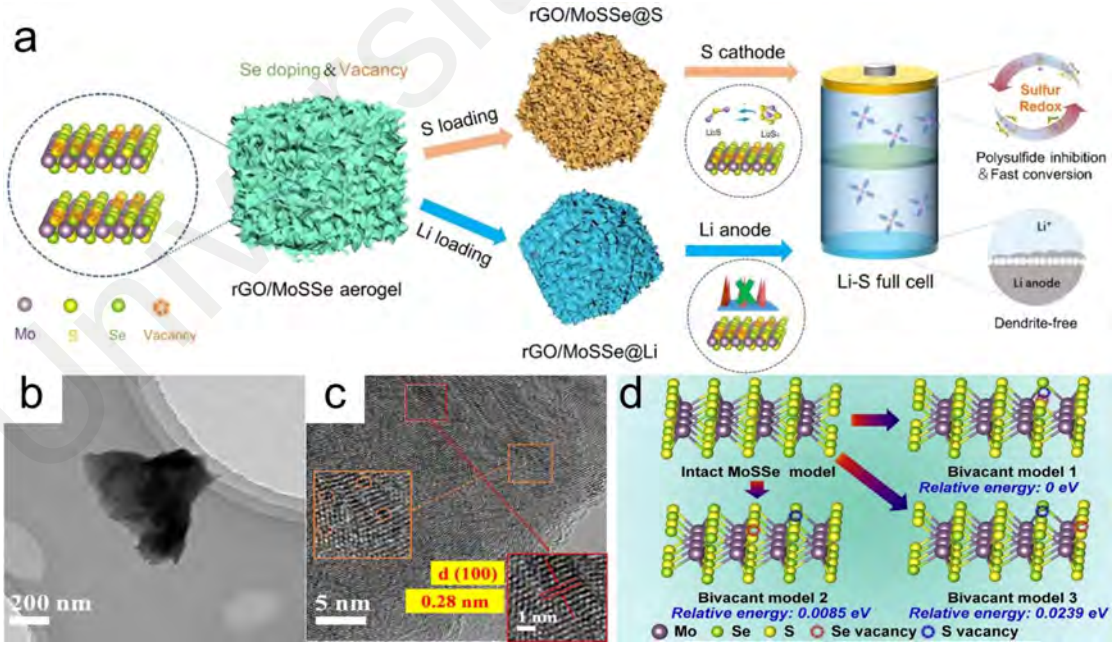

Figure 2.38: (a) Schematic of the sulfur and Li loading processes in a vacancy-rich rGO/MoSSe aerogel for the cathode and anode of Li-S batteries. (Hong Li et al., 2022) (b) TEM image and (c) HRTEM image of VS-WS_2-Se@NS. (Q. Zhu et al., 2022) (d) Bivacant models with corresponding relative energies after incorporating three different types of dual anionic vacancies. (Z. Tian et al., 2020)

2.2.3.3 Grain Boundaries

Grain boundaries are the interfaces between different crystalline grains in polycrystalline materials. These boundaries can serve as pathways for fast Li^+ diffusion and act as active sites for Na^+ storage. Engineering grain boundaries in MSes can significantly enhance their electrochemical performance. Wang et al. prepared trimetallic Co-Fe-$MoSe_2$@N-doped carbon composites with self-generated abundant phase boundaries by co-precipitation method and selenization process. As shown in the DFT results in Figure 2.39, the enriched boundaries brought about by multicomponent interventions provide sufficient active sites for electrochemical reactions for Na^+, which alleviates the Na^+ diffusion barrier and thus improves the charge/ion transfer efficiency. (Chao Wang et al., 2024)

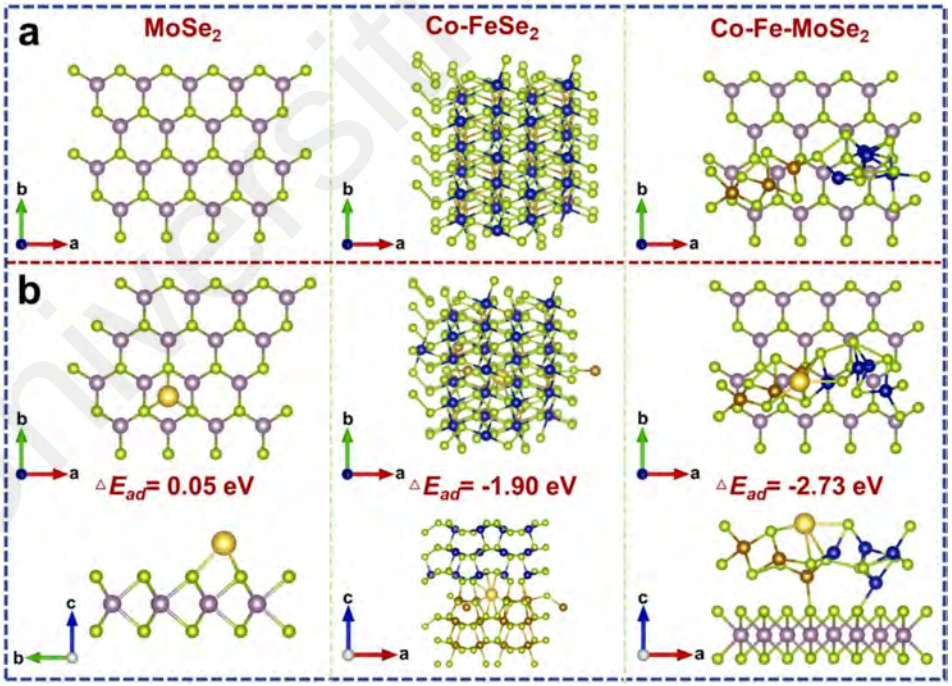

Figure 2.39: (a) The selected crystal structures of $MoSe_2$, Co-$FeSe_2$, and Co-$MoSe_2$ for DFT calculations. (b) Structural models of Na^+ adsorption sites for $MoSe_2$, Co-$FeSe_2$, and Co-Fe-$MoSe_2$ after optimization. (Chao Wang et al., 2024)

The above findings indicate that defect engineering has various positive effects on the electrochemical performance enhancement of MSes anodes. Firstly, defects such as vacancies and grain boundaries can provide additional pathways for Na^+ diffusion, reducing the diffusion distance and improving the rate capability of the anode material. Secondly, defects can create additional active sites for Na^+ intercalation, increasing the specific capacity of the material. Thirdly, interstitial defects and grain boundaries can enhance the electrical conductivity of MSes by providing additional pathways for electron transport. Fourthly, interstitial defects and grain boundaries can enhance the electrical conductivity of MSes by providing additional pathways for electron transport. Fifthly, defects can enhance the structural stability of MSes by relieving stress concentrations and preventing crack propagation.

Despite the various advantages of defect engineering in the structural modification of MSes, some current challenges deserve to be highlighted. Firstly, achieving precise control over the type and concentration of defects is challenging. Uncontrolled defect introduction can lead to structural instability and performance degradation. Secondly, scaling up defect engineering techniques for industrial applications while maintaining consistency and quality is a significant challenge. Techniques like ion implantation and laser irradiation are often expensive and difficult to implement on a large scale. Therefore, some key techniques should be further applied to optimize the design of defective works. Firstly, developing advanced synthesis techniques that allow for precise control over defect types and concentrations is essential. Secondly, employing in-situ characterization techniques to study the behavior of defects during

electrochemical cycling can provide insights into optimizing defect engineering strategies. Thirdly, conducting theoretical studies to understand the effects of different defects on the electronic structure and electrochemical properties of MSes can guide the design of new defect-engineered materials. Fifthly, exploring multi-defect strategies, where different types of defects are introduced simultaneously, can synergistically enhance the performance of MSes anodes.

2.2.4 Heterostructure Engineering

Heterostructure engineering is a sophisticated approach in materials science that involves deliberately integrating different phases within a single material to harness the synergistic effects between these phases. This method aims to enhance the overall performance of the material by leveraging the unique properties and interactions of the constituent phases. By carefully designing and combining different phases, it is possible to create materials with superior mechanical, electrical, thermal, and electrochemical properties compared to their single-phase counterparts. As shown in Figure 2.40, heterostructure engineering can be broadly categorized into analogous heterostructure engineering and dissimilar heterostructure engineering, each with its distinct strategies and advantages. Among them, the analogous heterostructures are utilized to construct heterogeneous interfaces using two similar crystal structures, so as to construct a built-in electric field to realize the rapid transfer of Na^+ within the bulk phase. Due to the adoption of two similar crystal structures, the analogous heterostructures are prone to form abundant heterogeneous interfaces and near-parallel large-angle heterogeneous effects during the construction process, which is conducive to forming a perpendicular

interlayer electric field force to increase the adsorption and storage capacity of Na^+, and thus increase the fast pseudocapacitance performance of the electrodes. According to our investigation, the analogous heterostructures can be further categorized into analogous cationic heterostructures and analogous anionic heterostructures. As shown in System 1 in Figure 2.40, the analogous cationic heterostructures is maintained by selecting two metal elements with similar metal properties and electronegativity while the anion remains the same (Se^{2-}). Similarly, as shown in System 2 of Figure 2.40, the analogous anionic heterostructures is achieved by selecting two nonmetallic elements of the same main group with similar chemical properties while the metal atoms remain unchanged. Since the same cation or anion is used in the similar heterogeneous structure, in this project we carried out the unification of the naming rules. The analogous cationic heterostructure is denoted as X_1X_2Y (X for metal ions and Y for anions) and the analogous anionic heterostructure is denoted as XY_1Y_2. In addition, as shown in System 3 of Figure 2.40, dissimilar heterostructures are mainly constructed by selecting two metal selenides with completely different crystal structures. Due to the great structural and chemical differences between the two crystals constituting dissimilar heterostructures, extra phase transitions and more perfect heterogeneous effects (interlayer heterogeneity) may be induced during their preparation. Due to the huge difference between the two crystals, the constructed heterostructure is more inclined to the homogeneous mixing of the two phases, so the dissimilar heterostructure is named X_1Y_1/X_2Y_2 composite in this project.

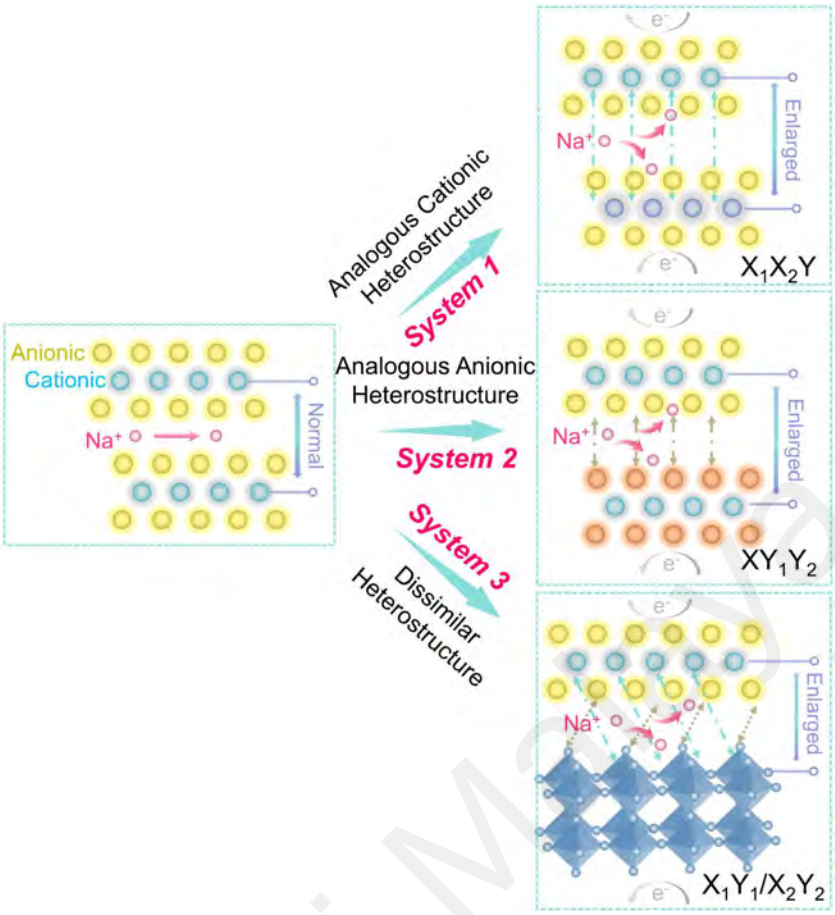

Figure 2.40: Nomenclature of different heterostructure designs.

2.2.4.1 Analogous Heterostructure Engineering

Constructing cationic heterostructures has recently been demonstrated to be an effective microstructure optimization strategy. (G. Chen et al., 2016; Park et al., 2021) The basic principle of heterogeneous structure involves the cross-distribution of different components within the bulk phase to change the original crystal structure, further creating a built-in electric field with an uneven electron distribution. The presence of the built-in electric field can improve the intrinsic material conductivity and accelerate the rapid ion transfer in the bulk phase. Analogous mixed-phase engineering involves combining chemically similar phases but differ in their crystal structures, valence states, or other intrinsic properties. This approach aims to optimize the microstructure and enhance the performance of the material by taking advantage of the

complementary properties of the analogous phases. The analogous phases are typically compatible in terms of chemical composition and lattice parameters, ensuring good interfacial stability and minimal phase separation during cycling. This can enhance the durability and longevity of the material under operational conditions. For example, $MoSe_2$ and WSe_2 are chemically and structurally similar but differ in the metal cations (Mo and W). This similarity allows for a seamless integration of the two phases, resulting in enhanced electrochemical properties. $MoSe_2$ and WSe_2 crystallize in similar layered structures, allowing easy integration and minimal lattice mismatch. This structural compatibility helps maintain the integrity of the material during cycling. Additionally, both Mo and W can exist in similar valence states, ensuring uniform redox activity across the heterostructure, which can enhance the overall electrochemical performance. Based on this, Patel et al. prepared $MoSe_2$@WSe_2 nanohybrid heterostructures using liquid stripping nanocrystals combined with a direct electrophoretic deposition strategy (Figure 2.41a). The edges of the nanocrystals after liquid stripping exhibited sufficient exposure to catalytically active sites. Meanwhile, a synergistic effect was generated on the analogous heterogeneous interface between $MoSe_2$ and WSe_2 nanocrystals. (Patel et al., 2022) However, the introduction of highly conductive carbon materials is considered to be an effective way to ensure the fast transport of electrons and ions in heterostructures. As shown in Figure 2.41b−e, graphene-loaded hollow WS_2/MoS_2@carbon microspheres were synthesized using the solvothermal method by Rao et al. Among them, the WS_2/MoS_2 heterostructure can provide a strong charge transport driving force by forming a built-in electric field. The introduction of the carbon layer and graphene not only provides a favorable electron/ion

transport medium in the material surface layer but also mitigates the huge volume strain of the electrode material during electrochemical processes, enhancing the fast electron/ion transfer kinetics. (Rao et al., 2022) Similarly, Zhao et al. first constructed composites with core-shell structures by building hierarchical MoS_2/WS_2 heterostructures, followed by coating with a double carbon layer. The analogous heterogeneous interfaces between MoS_2 and WS_2 modulate the interfacial energy barriers and electric field distributions, which promotes a faster ion transfer rate. The internal hard carbon core and external nitrogen-doped carbon shell can effectively ensure the structural stability of MoS_2/WS_2 and facilitate the acceleration of the fast electron transfer to the internal structure. (B. Zhao et al., 2024)

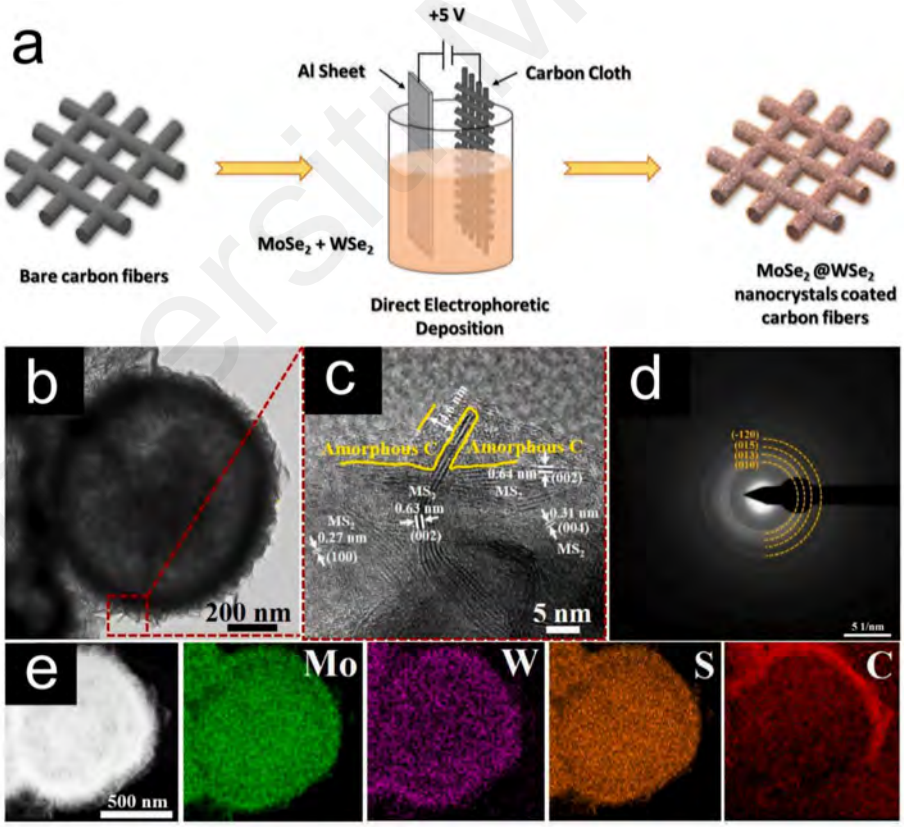

Figure 2.41: (a) Direct electrophoretic deposition of $MoSe_2$@WSe_2 thin film on carbon cloth substrate. (Patel et al., 2022) (b) TEM, (c) HRTEM, and (d) SAED images; (e) EDS mapping of Mo, W, S, and C elements in WS_2/MoS_2@carbon microspheres. (Rao et al., 2022)

Additionally, in analogous mixed-phase engineering, different crystal structures of the same material can be combined. For example, combining phases with different crystal symmetries (e.g., tetragonal, orthorhombic) can enhance mechanical properties and provide additional electronic and ionic transport pathways. As shown in Figure 2.42a-c, Wang et al. realized the phase transition of $MoSe_2$ from a 2H semiconductor phase to a 1T metallic phase by introducing W atoms into the $MoSe_2$ layered structure. This 2H/1T-$MoSe_2$ similar heterostructure exhibits excellent rate capability and long-term cycling stability during electrochemical processes. (K. Wang, Zhou, et al., 2023) Similarly, by introducing phytic acid, Chen et al. synthesized P-doped carbon-loaded 2H/3R heterophasic $MoSe_2$ nanosheets (Figure 2.42d). This analogous heterogeneous structure brings abundant defects and enlarged interlayer spacing, which facilitates electron/ion transfer and mass transfer. (L. Chen et al., 2020) Furthermore, exploring the transformation process between different phase structures is crucial for designing analogous heterostructures. Yue et al. successfully developed a strategy for electron irradiation-induced transformation of 2H-phase tungsten selenide (2H-WSe_2) into 1T-phase tungsten selenide (1T-WSe_2). This simple process offers great potential for the development of controlled phase transitions. (Yue et al., 2022)

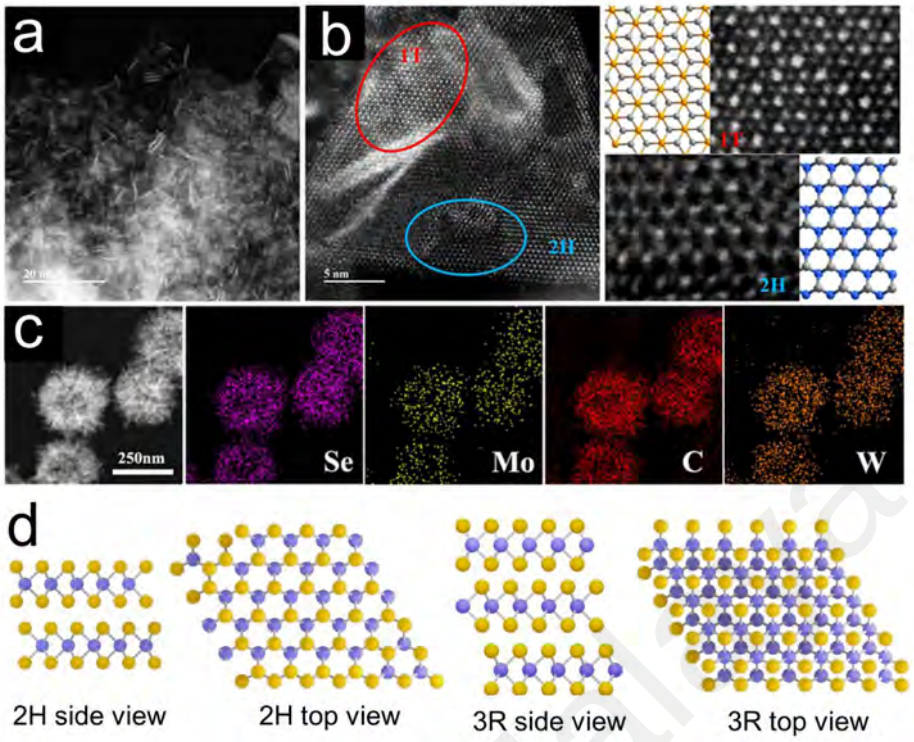

Figure 2.42: TEM (a) and STEM-HAADF (b) images of MWSe hierarchical hollow structure. (c) HRSTEM and element mapping images of the MWSe hierarchical hollow structure. (K. Wang, Zhou, et al., 2023) (d) typical crystalline structure of 2H-$MoSe_2$ and 3R-$MoSe_2$. (L. Chen et al., 2020)

By integrating phases with different valence states, it is possible to create materials with multiple redox-active sites. This can improve the electrochemical performance, such as capacity and rate capability, by providing a more significant number of active sites for Na^+ storage in SIBs. Wang et al. developed a hierarchical VS_2@VS_4 heterostructure by growing VS_4 nanorod arrays on VS_2 rose-type nanosheets, exhibiting excellent low-temperature electrochemical properties. (Yan Wang et al., 2022) Similarly, Agoro et al. prepared nanoscale heterogeneous mixed phases of FeS and FeS_2 using a ligand solvent-assisted method (Figure 2.43a). Then, they explored the morphology, stability, and structural properties of the prepared FeS/FeS_2, exhibiting considerable potential for applications. (Agoro et al., 2022) Moreover, as shown in Figure 2.43b, Feng et al. prepared $SnSe_2$/SnSe heterostructures for Li^+ storage using a high-

throughput wet-chemical method. The hierarchical nanoflower morphology of the $SnSe_2$/SnSe heterostructures effectively buffers the volume expansion during electrochemical processes. The built-in electric field of the structure exhibits strong metallic features, which are favorable for improving the fast charge transport ability and efficient ion storage. (W. Feng et al., 2023)

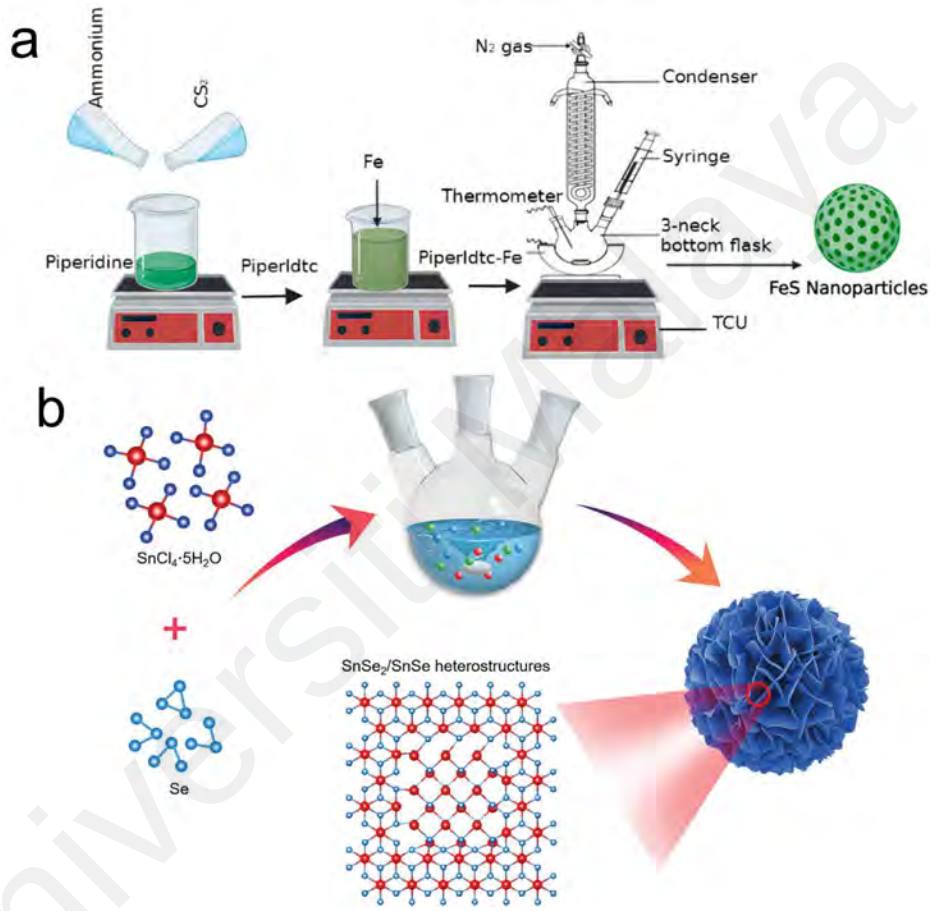

Figure 2.43: (a) Synthesis of iron sulfide nanoparticles as FeS#1, FeS#2 and FeS#3. (Agoro et al., 2022) (b) Schematic diagram of the wet chemical synthesis process. The $SnCl_4{\cdot}5H_2O$ and Se powders are the precursors, and the low boiling point is employed to promote the formation of $SnSe_2$/SnSe heterostructures with large specific surface areas. (W. Feng et al., 2023)

Analogous anionic heterostructures involve the combination of MSes with similar metal centers but potentially different anionic frameworks. An example would be the combination of MoS_2 and $MoSe_2$. Despite the different anions (S and Se), the similar structure and chemical properties of these compounds allow for coherent integration.

The anionic framework of S^{2-} in MoS_2 and Se^{2-} in $MoSe_2$ enables the creation of a stable heterostructure with minimal phase separation. The presence of different anionic species can provide multiple redox-active sites and pathways for ionic diffusion, improving the capacity and rate performance of the anode. Yang et al. prepared high-density vertically aligned $MoSe_2$ nanosheet array heterostructures on two-dimensional layered MoS_2 by a low-cost and high-yield solution processing strategy. The MoS_2-$MoSe_2$ heterostructures provide abundant active sites and open porous space, which promote efficient ion adsorption and transport. (J. Yang et al., 2017) Besides, Tang et al. prepared $SnSe_{0.5}S_{0.5}$/C nanocomposites by combining a polyol method with a hydrothermal/sintering process. The high pseudocapacitance contribution from the heterostructure of $SnSe_{0.5}S_{0.5}$/C promotes the charge transfer rate of the ions, which in turn exhibits excellent rate properties and cycling stability. (Q. Tang et al., 2017) as shown in Figure 2.44a, Tang et al. constructed a MoSSe anion heterostructure with an S: Se ratio of 1:1 by adjusting the introduction amount of Se atoms. DFT calculations show that the MoSSe anion heterostructure can further reduce the ion diffusion energy barriers and increase the adsorption energy of the ions, which can significantly increase the ion diffusion rate and avoid the rapid decrease of the voltage in the discharge process. (X. Yu et al., 2021) Similarly, Wang et al. synthesized porous $FeS_{0.5}Se_{0.5}$ nanorods by vulcanization and selenization processes using FeOOH nanorods as reaction templates (Figure 2.44b). The composite electrodes exhibited excellent sodium storage performance under the effect of dual anion-guided heterostructure. (Yifei Wang et al., 2023)

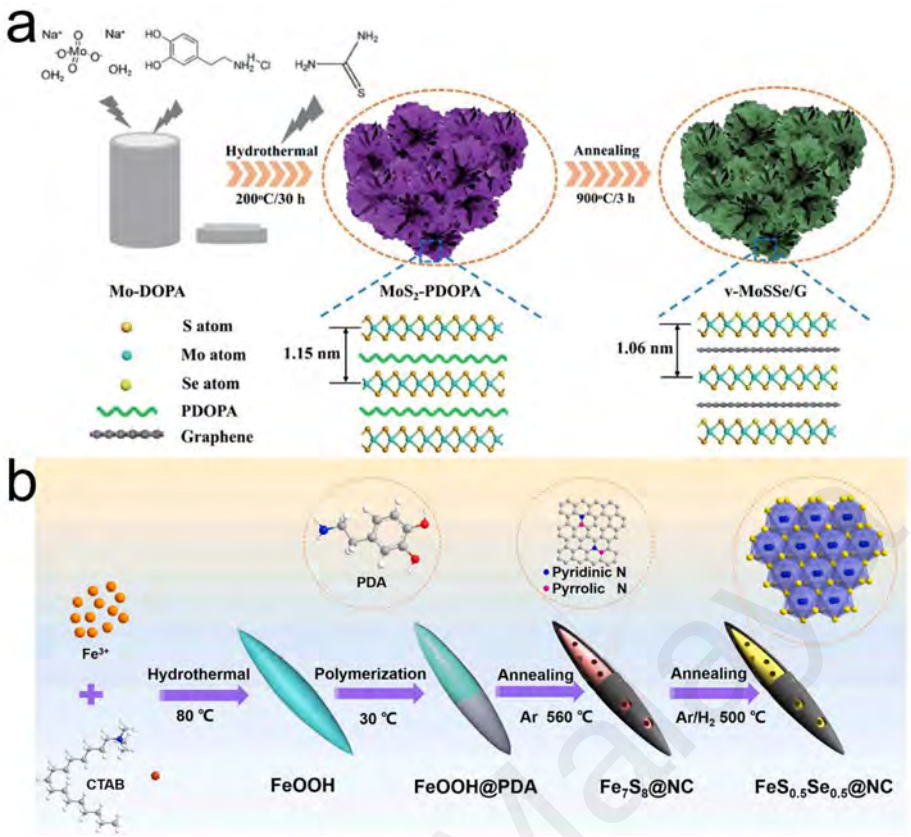

Figure 2.44: (a) Schematic for the synthesis v-MoSSe/G. (X. Yu et al., 2021) (b) Synthesis process of $FeS_{0.5}Se_{0.5}$@NC. (Yifei Wang et al., 2023)

2.2.4.2 Dissimilar Heterostructure Engineering

Dissimilar mixed-phase engineering involves the combination of MSes with distinctly different chemical compositions, crystal structures, or physical properties. This strategy aims to exploit the complementary advantages of each phase to overcome the limitations of the individual components and achieve a synergistic enhancement of the material's overall performance. Dissimilar mixed-phase engineering allows for the combination of materials with different functionalities, such as combining conductive phases with semiconductive phases. This can result in composites with unique properties that are not achievable with single-phase materials. Additionally, the interfaces between the dissimilar phases play a crucial role in determining the material's performance. Careful control of the interface structure and chemistry can lead to

improved charge transfer kinetics, enhanced mechanical bonding, and better stability against phase separation and degradation. Li et al. synthesized 3D nanoflower-like $Cu_{2-x}Se$-$MoSe_2$ heterojunction anodes by a simple co-precipitation method combined with a hydrothermal process. The 3D nano-heterostructures are able to increase the contact area with the electrolyte and buffer the volume change, which leads to excellent sodium storage performance and structural stability during cycling. (Shengkai Li et al., 2022) Using the same preparation strategy, a $FeSe_2$/$MoSe_2$ nanoflower with heterostructure was further synthesized. The prepared $FeSe_2$/$MoSe_2$ heterostructure exhibits abundant active sites and lattice interfaces. (Shengkai Li et al., 2023) Further, as shown in Figure 2.45a, Kang et al. prepared $MoSe_2$/$VSe_{1.6}$ bimetallic selenides by selenization using a ligand-bound precursor of $[Mo_7O_{24}]^{6-}$ and VO^{3-}. This hierarchical nanoflower can shorten the diffusion length of Na^+/K^+, increase the electronic conductivity, and buffer the volume change, thus promoting the Na^+/K^+ reaction kinetics and stabilizing the cycling performance. (Kang et al., 2024) To further reveal the mechanism of action of dissimilar heterostructures, Wang et al. synthesized $MoSe_2$/Cr_2Se_3 heterostructures uniformly embedded in N-doped hollow carbon nanorods (Figure 2.45b). The $MoSe_2$/Cr_2Se_3 heterostructures bring about spin-polarized states or local magnetic moments by inducing lattice mismatches at the interfaces, which leads to the spin-polarized surface capacitances. DFT calculations showed that the $MoSe_2$/Cr_2Se_3 heterostructures exhibit significant spin-polarized charge accumulation and narrower material band gaps at the $MoSe_2$/Cr_2Se_3 heterostructure interfaces. (X. Wang et al., 2024)

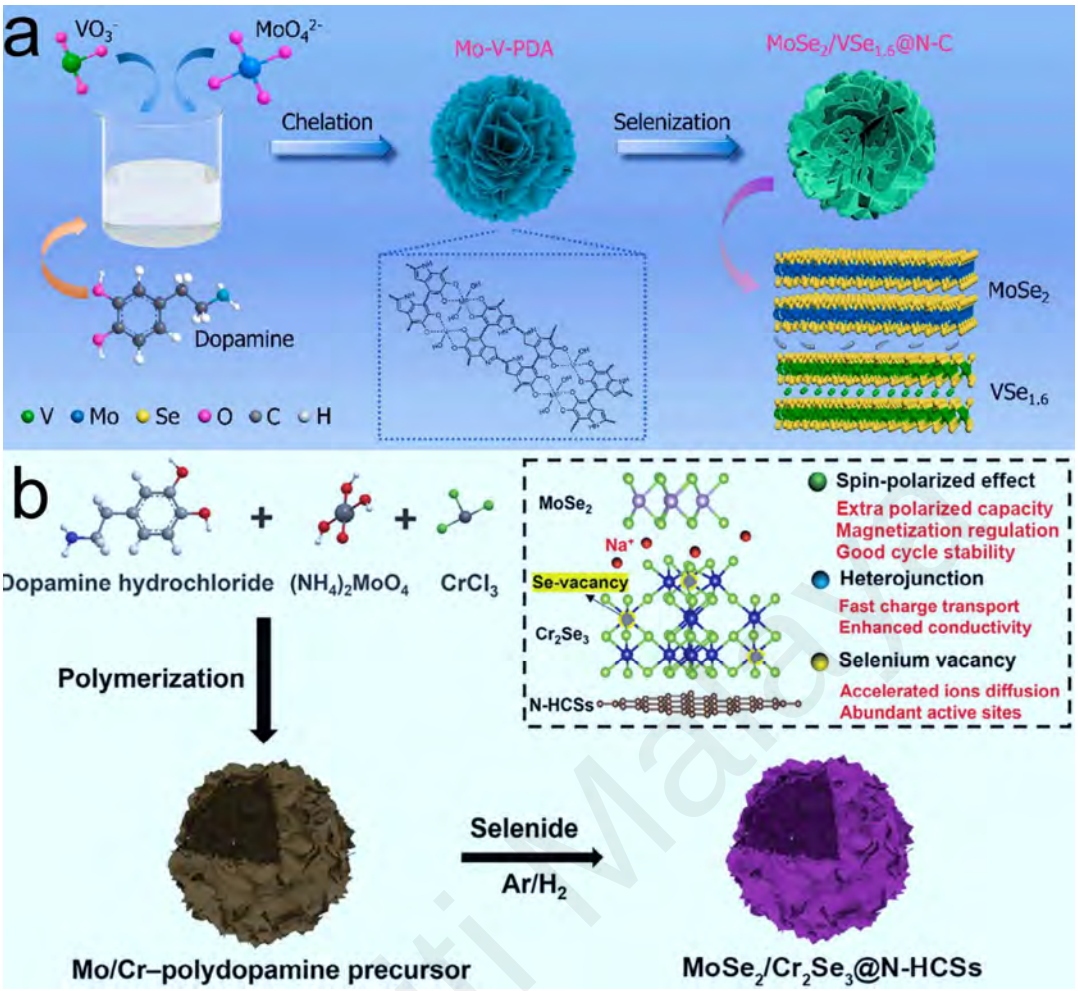

Figure 2.45: (a) Schematic illustration for the synthesis procedure of hierarchical $MoSe_2/VSe_{1.6}$@NC nanoflowers. (Kang et al., 2024) (b) Schematic representation depicting the synthesis process for the $MoSe_2/Cr_2Se_3$@N-HCSs. (X. Wang et al., 2024)

In summary, mixed-phase engineering represents a powerful strategy for the development of advanced materials with enhanced performance characteristics. Combining analogous or dissimilar phases makes it possible to create materials that address the limitations of single-phase systems and achieve superior mechanical, electrical, thermal, and electrochemical properties. This approach holds great potential for a wide range of applications, including energy storage, catalysis, and structural materials.

2.2.5 Carbon Composite Modification

In addition to microstructural modification, carbon introduction is typically considered to improve the electrical conductivity and surface ion adsorption capacity of materials. Accordingly, various carbon introduction strategies have been applied to modify the MSes electrode. (Chong et al., 2021; Ge et al., 2020; Jeong et al., 2018) This approach involves integrating carbon materials with metal selenides to improve their electronic conductivity, mechanical stability, and electrochemical performance. The primary strategies within this method include carbon loading, carbon encapsulation, and carbon homogenization composites. Each technique offers distinct advantages and addresses specific challenges associated with MSes anodes.

2.2.5.1 Carbon Loading

Carbon loading refers to introducing MSes into conductive carbon matrixes such as carbon cloth/nanosheet, graphene, or carbon nanotubes. This strategy aims to enhance the overall conductivity and structural integrity of the composite material. By embedding MSes in the carbon cloth matrix, the overall electronic conductivity of the composite is significantly improved. This enhancement in conductivity ensures efficient charge transfer within the electrode, which is crucial for high-rate performance in SIBs. For example, as shown in Figure 2.46a-c, Yang et al. successfully synthesized SnSe nanosheet arrays (SnSe NS) on carbon cloth using vacuum thermal evaporation and fabricated independent electrodes free of metal collector, binder, and conductive additives. Operando XRD and electrochemical kinetic tests demonstrated that the as-prepared SnSe NS electrodes have better reversibility and faster kinetic processes. (W.

Yang et al., 2023) In addition, Yu et al. prepared uniformly distributed MnSe nanoparticles on 3D carbon nanosheet substrates using a sol-gel combined with a selenization strategy. The prepared composite electrodes exhibited significant enhancement in specific surface area, number of active sites, and electrical conductivity, resulting in excellent electrochemical kinetics and bulk strain control. (L. Yu et al., 2021) Compared to carbon cloth/nanosheet, both graphene and carbon nanotubes can offer exceptionally high conductivity and surface area, facilitating rapid electron transport and providing numerous active sites for Na^+ adsorption and storage. In the case of graphene applications, Zhou et al. combined solvothermal and gas-phase selenization strategies to load hierarchical $NiCo_2Se_4$ nanopins/nanosheets onto N-doped 3D porous graphene skeletons. The exhibited high specific and rate capacities can be ascribed to the high electrical conductivity and pore structure brought by the 3D graphene skeleton, which provides fast ion and electron transport channels. (Chencheng Zhou et al., 2021) As shown in Figure 2.46d, Wu et al. synthesized hollow $Co_{0.85}Se$-Fe_7Se_8 nanocubes uniformly dispersed on reduced graphene oxide. The graphene-modified advanced hollow nanostructures combined with the cationic heterostructure design can provide effective buffered bulk stress and excellent electrical conductivity. (H. Wu et al., 2022) Carbon nanotubes are widely considered as a superior substrate for carbon loading due to their unique 1D pipeline-type diffusion channels. Liang et al. achieved the scale-up synthesis of N-doped carbon nanotubes loaded with $FeSe_2$ using a simple catalytic selenization of the natural hematite process. The interwoven carbon nanotube network significantly increased the contact area between the electrode and the electrolyte, and was able to effectively shorten the ion diffusion length while increasing the conductivity.

(Liang et al., 2021)

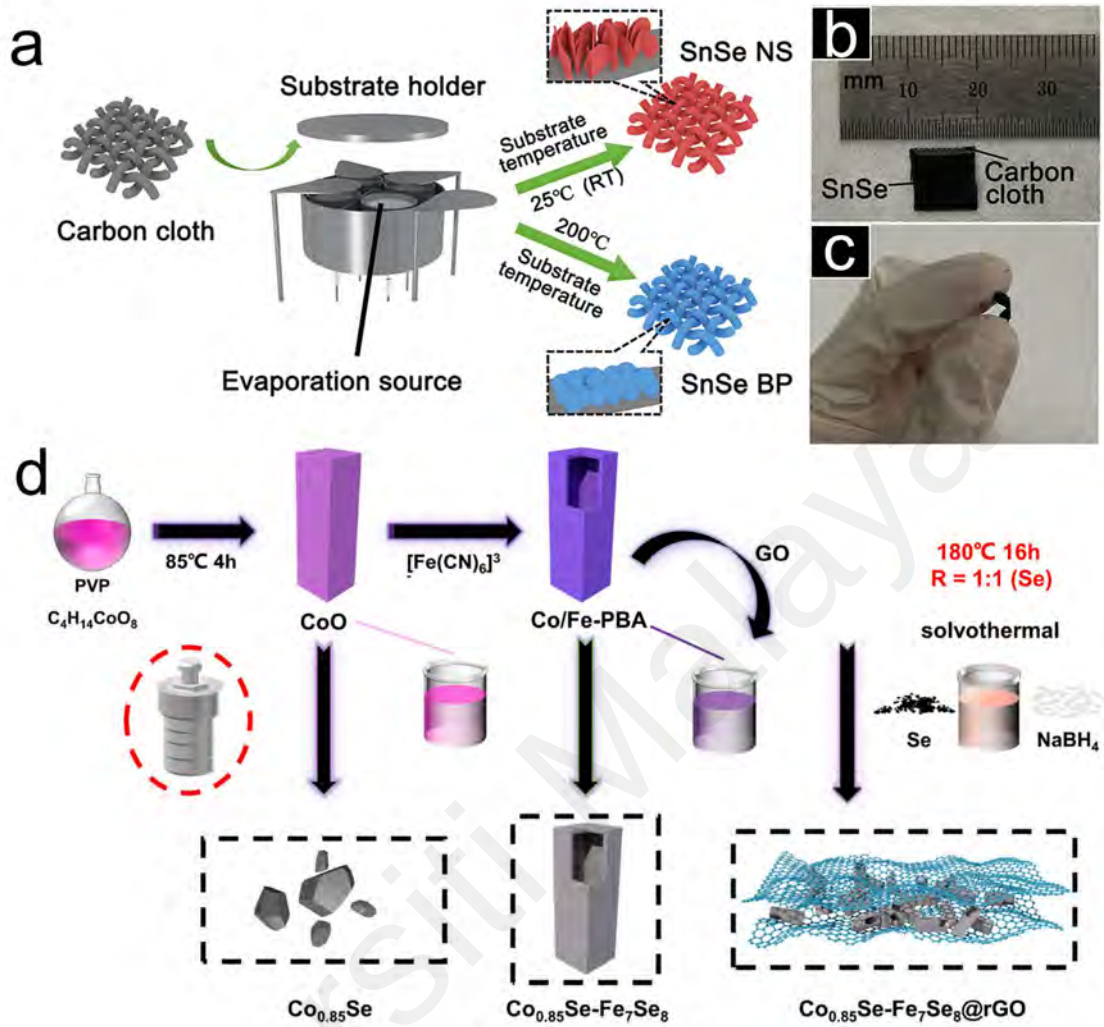

Figure 2.46: (a) Schematic illustration of the synthesis of SnSe NS and BP electrodes. (W. Yang et al., 2023) (b) The synthesis procedures of three kinds of selenides. (H. Wu et al., 2022)

The inclusion of carbon materials provides additional mechanical support to the metal selenide matrix. During the sodiation and desodiation processes, MSes undergo significant volume changes, leading to mechanical stress and potential pulverization. Carbon materials act as a buffer, mitigating these volume changes and enhancing the structural integrity of the composite. The elastic nature of carbon materials helps accommodate the volume changes of MSes, reducing stress and preventing the cracking and fragmentation of the electrode material. However, simple carbon loading strategies

do not guarantee interfacial exposure of MSes active materials and thus still have shortcomings in slowing down volume expansion and avoiding electrode pulverization. Additionally, carbon materials, especially in high concentrations, may aggregate, leading to uneven distribution and localized performance degradation. Therefore, more advanced carbon encapsulation and uniform distribution strategies need to be considered for comprehensive electrode protection and all-round conductivity optimization.

2.2.5.2 Carbon Encapsulation

Carbon encapsulation involves coating individual MSes particles with a thin layer of carbon. This technique provides several benefits, including protection from the electrolyte, enhanced cycling stability, and improved conductivity. Encapsulating MSes particles with a carbon layer prevents direct contact between the active material and the electrolyte. This barrier reduces undesirable side reactions, such as the formation of an unstable SEI, which can degrade the performance of the anode. A stable and uniform carbon coating helps in the formation of a more stable SEI layer, minimizing electrolyte decomposition and preserving the active material's integrity. As shown in Figure 2.47a, Yang et al. synthesized nitrogen-doped carbon-encapsulated Fe_7Se_8 nanorods with a core-shell structure via an in situ self-polymerization strategy. This carbon encapsulation strategy not only maintains the structural stability of the nanorods but also helps to form a thin and robust SEI layer. (S. Yang et al., 2023) Moreover, Sun et al. prepared mesoporous N-doped carbon-coated CoSe nanocrystals (CoSe-SC@NC) loaded on S-doped carbon nanosheets by combining carbon loading and carbon coating

(Figure 2.47b−e). In this structure, CoSe nanoparticles are uniformly distributed on carbon nanosheets, which helps to improve electronic conductivity and accelerate ion transfer. The presence of the mesoporous carbon coating slows down the volume expansion and helps to maintain the structural integrity. Notably, the mesoporous carbon-coated electrode has an ultrathin and robust SEI, exhibiting an ultra-high initial coulombic efficiency (92.4%). (Z. Sun et al., 2022)

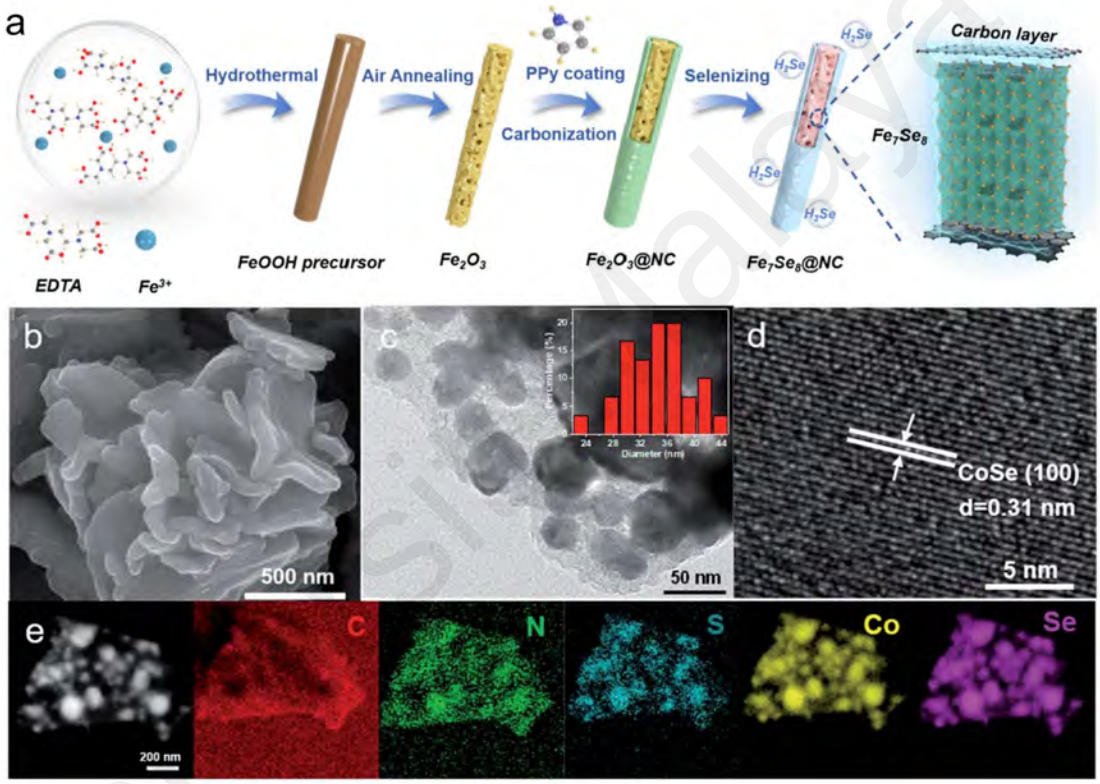

Figure 2.47: (a) Schematic illustration of the preparation of Fe_7Se_8@NC nanorods. (S. Yang et al., 2023) (b) SEM image. (c) TEM image. (d) HRTEM image. (e) Element mapping (C, N, S, Co, and Se). Inset (c) is the statistics for the size distribution of CoSe. (Z. Sun et al., 2022)

The carbon encapsulation layer helps maintain the structural integrity of metal selenide particles during cycling. This protective layer prevents the agglomeration of nanoparticles and mitigates the mechanical degradation caused by repeated sodiation/desodiation cycles. Encapsulation keeps individual metal selenide particles separated, preventing them from coalescing and maintaining their high surface area and

active sites for sodium storage. Zhou et al. uniformly encapsulated SnSe nanoparticles in carbon nanofibers by electrostatic spinning strategy. The results showed that this carbon encapsulation strategy not only helped to increase the Na^+/electron transport rate but also effectively prevented the agglomeration of SnSe nanoparticles. Meanwhile, the all-around carbon encapsulation is beneficial to buffer the large volume change of the electrode material during the sodiation/desodiation process, providing stable electrochemical performance. (X. Zhou et al., 2020) In addition, Wang et al. prepared dual-carbon bound $CoSe_2$/$FeSe_2$@NC@C nanocubes using isophthalaldehyde for coating and combining in-situ carbonization and selenization. The N-doped porous carbon coatings were able to effectively promote the rapid penetration of the electrolyte, which significantly reduced the agglomeration of the active materials during the charging and discharging process. (P. Wang et al., 2024)

A continuous carbon layer around the metal selenide particles ensures efficient electron transport pathways, which are essential for high-rate capability and overall electrochemical performance. The encapsulating carbon layer forms a conductive network that facilitates rapid electron movement, thereby improving the rate performance of the anode. However, controlling the thickness of the carbon coating is challenging. Too thick a coating can impede ion transport, while too thin a coating may not provide adequate protection. Moreover, the encapsulation process can be technically challenging and may require sophisticated equipment and processes to achieve uniform and defect-free coatings. Therefore, advanced carbon encapsulation processes or other advanced carbon introduction strategies should be developed to achieve homogeneous

carbon introduction without hindering the rapid transport of ions into the bulk phase.

2.2.5.3 Carbon Homogenization

Carbon homogenization composite involves uniformly distributing carbon materials throughout the metal selenide matrix. This technique ensures that carbon is evenly mixed with metal selenide, providing consistent electronic pathways and mechanical reinforcement. The homogeneous distribution of carbon materials within the MSes matrix ensures uniform electronic conductivity throughout the composite. This uniformity is critical for preventing localized areas of high resistance, which can negatively impact the overall electrochemical performance. Moreover, the even dispersion of carbon materials ensures that all parts of the electrode have similar conductivity, which enhances the efficiency of electron transport and minimizes energy losses. More importantly, uniformly distributed carbon materials provide mechanical reinforcement to the metal selenide matrix. This reinforcement helps buffer the volume changes associated with sodiation and desodiation, preventing electrode pulverization and maintaining structural integrity. The homogeneous dispersion of carbon materials helps evenly distribute mechanical stress throughout the electrode, reducing the risk of cracking and improving the cycling stability of the anode. Additionally, the combination of MSes with uniformly distributed carbon materials can result in synergistic effects that enhance the overall electrochemical performance of the composite. The synergistic interaction between carbon materials and metal selenides can improve sodium ion storage capacity and kinetics, leading to higher specific capacities and better rate performance. However, achieving a truly uniform distribution of carbon materials

within the metal selenide matrix can be challenging, often requiring advanced synthesis techniques and thorough mixing processes. In addition, maintaining the homogeneity of carbon distribution and avoiding particle aggregation during carbon introduction are still the key issues requiring attention. Furthermore, excessive incorporation of carbon can dilute the active material content, potentially reducing the overall capacity of the anode if not carefully controlled.

The preparation of metal compounds/carbon composites by further sintering using MOFs as precursors has been shown to be a homogeneous and effective method for carbon introduction. (Xingchen Xie et al., 2020; Zeng et al., 2019) In particular, based on the porous structure, flexible structural design, and homogeneous distribution of carbon, MOF-derived carbon composites can achieve good electrical conductivity while providing a solid structure and abundant adsorption sites for fast ion conduction. (Deepak P. Dubal et al., 2019; S. L. Zhang et al., 2019) More importantly, the MOF structure can introduce a second metal in the self-assembly process to build a unique three-dimensional structure and increase the synergy between the bimetals to achieve better electrochemical performance. (Songsong Li et al., 2021; Lou et al., 2018) As shown in Figure 2.48, Numerous studies have demonstrated that carbon homogeneous distribution from the interior to the exterior through the carbonized MOF derivatives can effectively ensure structural stability and fast electron transfer. (Huihua Li et al., 2022; B. Wang et al., 2022; Y. Yang et al., 2023) For example, Na et al. synthesized novel N-doped porous carbon nanofibers embedded with ultrafine ZnSe nanocrystals by sequencing ZIF-8 through electrostatic spinning and subsequent thermal treatment.

Among them, ZIF-8 was transformed into a hollow carbon framework during pyrolysis, resulting in the generation of abundant mesopores inside the nanofibers, which effectively relieved the mechanical stress of ZnSe during electrochemical processes and enhanced its electrical conductivity. (Na et al., 2021) Additionally, constructing bimetallic MOF structures has been presented as an effective strategy for mixing metals in a highly dispersed manner. Therefore, forming a bimetallic MOF design can enable the homogeneous distribution and is expected to build abundant heterostructures for efficient Na^+ transport. Han et al. synthesized $CoNiSe_2$/C nanocomposites with high specific surface area and abundant pore structure via a bimetallic MOF. The synergistic effect of bimetallic selenides derived from the MOF structure and the stabilized carbon network are able to promote the formation of secondary particles during the initial cycling process, which exhibit strong pseudocapacitive behavior. These properties not only promote rapid charge transfer, but also contribute to the formation of a stable solid-electrolyte interphase layer, which ultimately leads to excellent electrochemical performance. (Q. Han et al., 2024) Similarly, Li et al. synthesized $Co_{0.85}Se$ and ZnSe nanoparticles embedded in N-doped carbon matrix using ZIF-8/ZIF-67 as templates and further constructed in situ polymerized carbon layers (ZCS@NC@C). This dual-carbon introduction modulation strategy resulted in an enriched pore structure and prevented the agglomeration and decomposition of $Co_{0.85}Se$ and ZnSe particles during the sodiation/desodiation process. In addition, the carbon coating can form a protective layer to buffer the volumetric strain generated during the electrochemical process and further improve the electrical conductivity. Remarkably, the bimetallic MOF derivative strategy typically increases the Na^+ migration efficiency between layers by increasing

the layer spacing and creating an inhomogeneous built-in electric field.

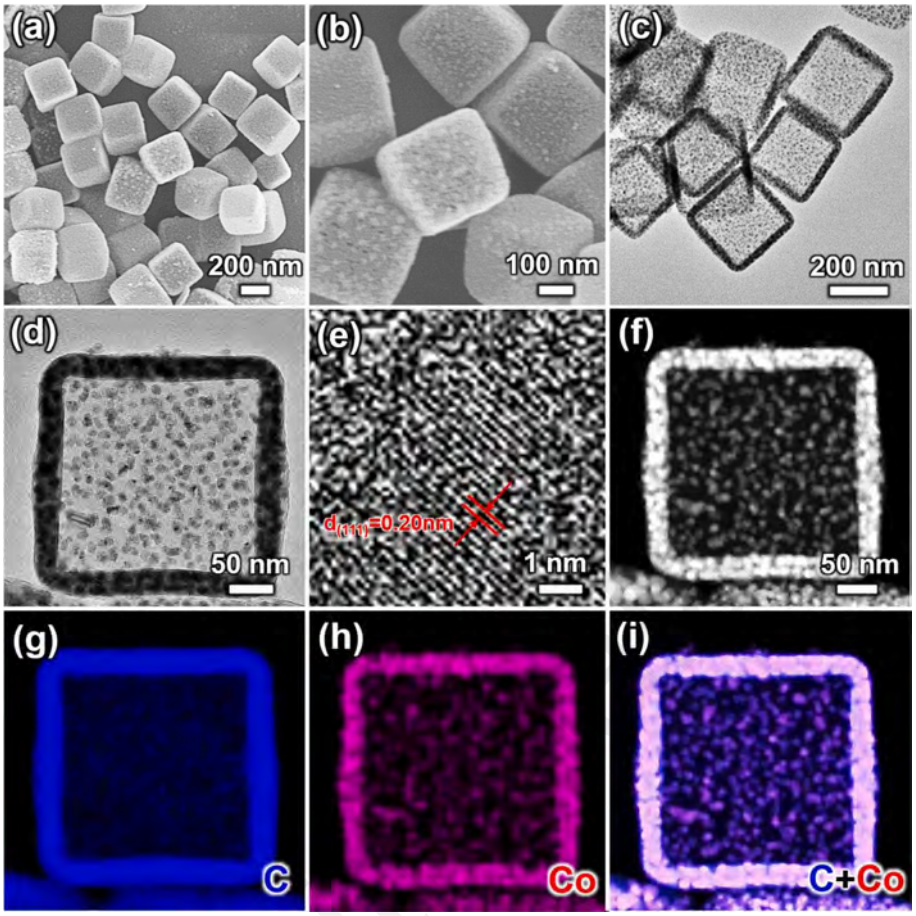

Figure 2.48: (a, b) FESEM, (c, d) TEM, (e) HRTEM, (f) HAADF-STEM images of Co/C HC. Elemental mapping images of (g) C, (h) Co and (i) overlay of an individual Co/C HC. (Y. Yang et al., 2023)

2.2.6 Electrolyte Optimization

Apart from the previous structural optimization, the evaluation and selection of the electrolyte is also a key factor affecting the battery's cycle stability and rate capability. Non-aqueous electrolytes commonly used in SIBs and SICs are mainly categorized as ester-based and ether-based. The schematic of the solvation behavior and the four pathways for ether-based electrolytes are shown in Figure 2.49. (Y. Li et al., 2022) Significantly, despite high salt solubility and voltage stability advantages, ester-based electrolytes tend to bring poor electrochemical performance when applied to the anodes. (Gong et al., 2023) Relatively, ether-based electrolytes tend to exhibit more stable

electrochemical properties. Targeting this phenomenon, He et al. suggested that ether-based electrolytes could reduce the occurrence of electrochemical polarization in hard carbon anode and thus generate a more stable SEI layer to ensure excellent rate performance. (Y. He et al., 2018) As for the selection of electrolytes for alloying anodes, researchers generally agree that ether-based electrolytes are favorable for the formation of a solid SEI layer to avoid the active material shedding during the alloying process. (Chenchen Wang et al., 2017; Xiaoshan Zhang et al., 2023) Although related studies have pointed out the advantages of ether-based electrolytes, the electrolyte variability for conversion-type materials still requires in-depth exploration.

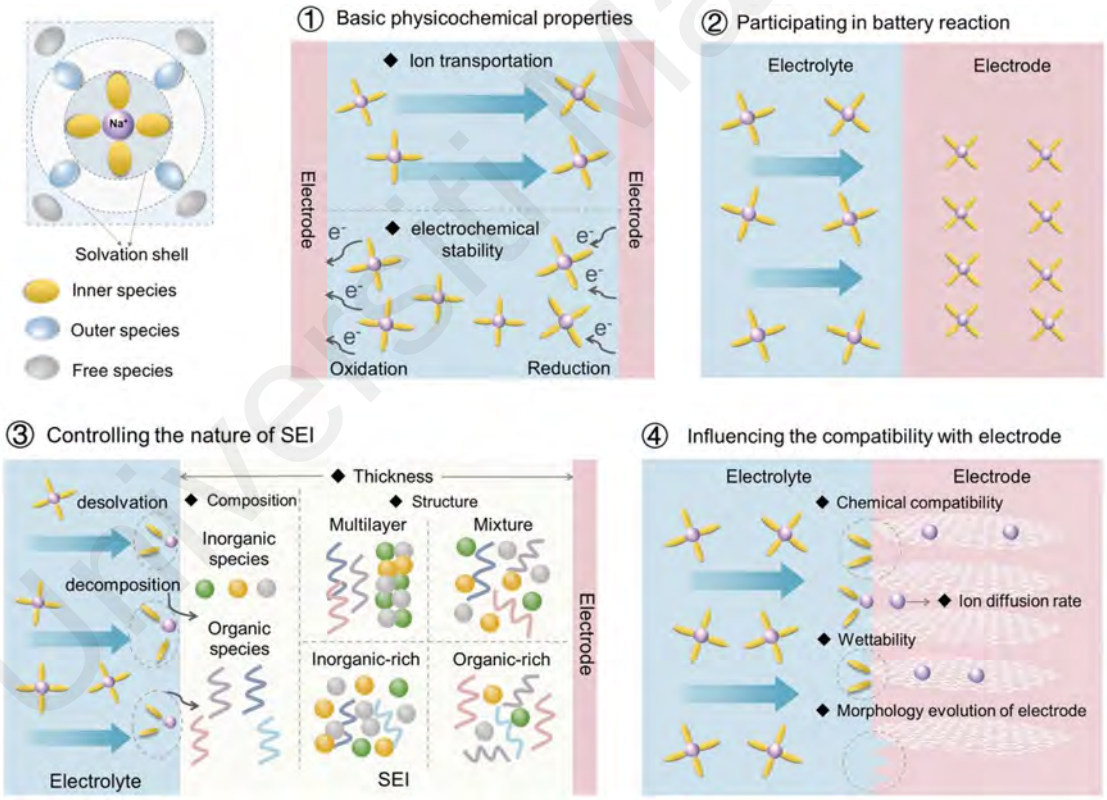

Figure 2.49: Schematic of the solvation behavior and the four pathways for ether-based electrolytes to influence the battery performance. (Y. Li et al., 2022)

2.2.7 Summary

In conclusion, carbon composite modification represents a powerful approach to

address the challenges associated with metal selenide anodes in SIBs. By employing strategies such as carbon loading, carbon encapsulation, and carbon homogenization composites, it is possible to significantly enhance the electronic conductivity, mechanical stability, and overall electrochemical performance of MSes anodes. These advancements are crucial for the development of high-performance SIBs, which hold great promise for large-scale energy storage applications. By addressing the challenges associated with electronic conductivity, mechanical stability, and electrochemical performance, these strategies can pave the way for the development of high-performance SIBs for large-scale energy storage applications.

CHAPTER 3: EXPERIMENTAL METHOD

3.1 Experimental Materials

Ammonium molybdate tetrahydrate ($(NH_4)_6Mo_7O_{24}$), Tungsten chloride (WCl_6), Molybdenum chloride ($MoCl_5$), Antimony trichloride ($SbCl_3$), L-serine, Trimesics acid, Triblock copolymer surfactant Pluronic F127, ribose, Thioacetamide (TAA), Trolamine, Ammonium vanadate (NH_4VO_3), Methanol (CH_4O), Pyrrole (C_4H_5N), Ammonium persulphate ($(NH_4)_2S_2O_8$), Fumaric acid, Iron (III) nitrate nonahydrate ($Fe(NO_3)_3 \cdot 9H_2O$), Sodium molybdate (Na_2MoO_4), Dimethylformamide (DMF), selenium powders (Se), and commercial activated carbon (AC) were purchased from Aladdin reagent. All reagents were used without further purification.

3.2 Material Synthesis and Preparation

3.2.1 Synthesis of MOF-Derived $MoWSe_2$/C Composites

3.2.1.1 Synthesis of Mo/W-MOF Precursor

First, 3.5 mmol of L-serine (0.371 g) was added to 20 mL of deionized water and stirred well to form Solution 1. After that, 7 mmol of trimesic acid (1.47 g) was dissolved into 40 mL of ethanol to form Solution 2. Solution 2 was then added to Solution 1 and stirred continuously for 20 min. Finally, 3.5 mmol $MoCl_5$ (0.956 g) and 3.5 mmol WCl_6 (1.388 g) were mixed well and then added to the above mixed solution with rapid stirring for 2 h. The solution was washed by centrifugation with ethanol for 3 times. Note that all the above processes are to be carried out in an ice-water mixing bath. Then, the Mo/W-MOF precursor was obtained.

3.2.1.2 Synthesis of $MoWSe_2$/C Composite

200 mg of the precursor and 8 mmol of selenium powder were ground thoroughly for 10 minutes to obtain a homogeneous mixture. After that, the obtained mixture was subjected to tableting. Subsequently, the resulting solid mixture was loaded into a magnetic boat and transferred to the center of a quartz tube furnace for calcination. The tube furnace was filled with high-purity argon gas for 20 min before heating to eliminate the oxygen inside the furnace. Afterward, the tube furnace was heated from room temperature to 650 °C at a heating rate of 5 °C min^{-1} under an argon atmosphere and held at 650 °C for 3 h. Finally, the tube furnace was naturally cooled to room temperature to obtain the target $MoWSe_2$/C composite.

3.2.2 Synthesis of MOF-Derived $MoWSe_2/WO_3$/C Composites

3.2.2.1 Synthesis of Core-Shell Mo/W-MOF Precursor

First, 0.5 mmol $(NH_4)_6Mo_7O_{24}$ (0.618 g) and 3.5 mmol WCl_6 (1.388 g) were dissolved into 20 mL of deionized water and stirred well to form solution 1. After that, 3.5 mmol L-serine (0.371 g) and 7 mmol trimesic acid (1.47 g) were dissolved into 40 mL of ethanol to form solution 2. Solution 2 was then added dropwise to Solution 1 with a syringe and stirred for 2 h. The solution was washed 3 times by centrifugation with ethanol to obtain core-shell Mo/W-MOF precursor.

3.2.2.2 Synthesis of $MoWSe_2/WO_3/C$ Composite

200 mg of the precursor and 8 mmol of selenium powder were ground for 10 min to obtain a homogeneous mixture. After that the obtained mixture was subjected to tableting. Subsequently, the resulting solid mixture was loaded into a magnetic boat and transferred to the center of a quartz tube furnace for calcination. The tube furnace was exhausted with high-purity argon gas for 20 min before heating to eliminate the oxygen inside the furnace. Afterward, the tube furnace was heated from room temperature to 600 °C at a heating rate of 5 °C min^{-1} under an argon atmosphere and held at 600 °C for 3 h. Finally, the tube furnace was naturally cooled to room temperature to obtain the final $MoWSe_2/WO_3/C$ composite.

3.2.3 Synthesis of Carbon Loading $WSSe_2/C$ Composites

3.2.3.1 Synthesis of WS_x/C Precursor

First, 0.015 mmol (F127), 0.24 mmol trolamine, and 40 mL of H_2O were mixed and stirred. Next, 1 g of ribose was added to form solution 1, after which 8 mmol of TAA was dissolved into 20 mL of methanol to form solution 2. Solution 2 was immediately added to solution 1, after which 2 mmol of WCl_6 was immediately added and stirred at room temperature for 2 h. The mixed solution was then transferred to an autoclave at 160 °C for 12 h. After completion of the reaction, it was centrifuged, washed, and dried to get the WS_x/C precursor.

3.2.3.2 Synthesis of $WSSe_2$/C Composite

200 mg of WS_x/C precursor and 70 mg of selenium powder were ground thoroughly for 10 minutes to obtain a homogeneous mixture. After that, the obtained mixture was subjected to tableting. Subsequently, the resulting solid mixture was loaded into a magnetic boat and transferred to the center of the microwave sintering furnace and tube furnace for calcination. The microwave sintering furnace was heated at a heating rate of 30 °C per minute to 500 °C and held for 30 min to obtain $WSSe_2$/C. As a comparison, a conventional tube sintering furnace was selected for the sintering process at a heating rate of 5 °C per minute to 500 °C and held for 2 h to obtain WSe_2/C. Note that the heating atmosphere used is an H_2/Ar mixture (10 vol% H_2).

3.2.4 Synthesis of Carbon-coated VSSe/C Composites

3.2.4.1 Synthesis of VS_4 Precursor

First, 0.5 g of Pluronic F127 and 3 mmol of NH_4VO_3 were dissolved into 30 mL of deionized water, followed by heating the mixture at 60 °C for 20 min until light yellow. After that, 30 mL of methanolic solution of thioacetamide (0.5 mol L^{-1}) was added to the above solution and stirred for 30 min at 60 °C on a magnetic stirrer. Then, the obtained solution was put into a 100 mL teflon-lined stainless autoclave and held in a drying oven at 160 °C for 12 h. After the reaction, the solution was washed 3−5 times with deionized water and alcohol alternately and then dried in a vacuum drying oven at 60 °C for 10 h to obtain VS_4 precursor.

3.2.4.2 Synthesis of VS_4/ppy

After dissolving 100 mg of VS_4 into 50 mL of deionized water, 100 μL of pyrrole was gradually added dropwise and stirred vigorously for 2 h. Subsequently, 100 mg of ammonium persulfate was added as initiator and stirred for 1 h. Finally, VS_4/ppy was obtained by filtration and vacuum drying.

3.2.4.3 Synthesis of VSSe/C Composites

The above obtained samples were mixed thoroughly with 88.2 mg of selenium powder, after which they were heated in a tube sintering furnace at a heating rate of 5 °C per minute to 450 °C and held for 2 h to obtain VSSe/C. Note that the heating atmosphere used is an H_2/Ar mixture (10 vol% H_2). As a comparison, samples with S/Se ratios of 1/3 and 3/1 were prepared according to the proportional replacement of S atoms in VS_4, respectively.

3.2.5 Synthesis of MOF-derived 1T/2H-$MoSe_2$/FeSe/C Composites

3.2.5.1 Synthesis of Fe/Mo-MOF Precursor

By dispersing 4 mmol of fumaric acid, 2 mmol of $Fe(NO_3)_3 \cdot 9H_2O$, and 2 mmol of Na_2MoO_4 sequentially in a conical flask containing 60 mL of DMF solution, a precursor solution was prepared by ultrasonication to ensure uniform dispersion. Subsequently, the prepared mixed solution was reacted at 110 °C for 30 min in a drying oven. Finally, the resulting mixture was cooled to room temperature, followed by centrifugation and alternating washing with DMF solution and methanol. The obtained orange powder after vacuum drying is referred to as Fe/Mo-MOF. As a comparison, Fe-MOF and Mo-

MOF monomers were synthesized using the same procedure as above, except that only the corresponding Fe and Mo salts were added.

3.2.5.2 Synthesis of 1T/2H-$MoSe_2$/FeSe/C Composites

First, 100 mg of Fe/Mo-MOF was weighed and then uniformly ground with 0.32 g (4 mmol) of selenium powder. Subsequently, the mixture was transferred into a crucible and placed at the center of a quartz tube furnace for calcination. Prior to heating, the furnace was purged with a hydrogen-argon mixture (10 vol% H_2) for 20 min to eliminate oxygen inside the furnace. Then, under a hydrogen-argon atmosphere, the tube furnace was heated from room temperature to 600 °C at a heating rate of 5°C min^{-1} and held at 600 °C for 2 h. Finally, the tube furnace was allowed to cool naturally to room temperature, resulting in the desired product named 1T/2H-$MoSe_2$/FeSe/C. Correspondingly, Fe-MOF and Mo-MOF were used as precursors to go through the above steps for selenization and carbonization processes to obtain $FeSe_2$/C and $MoSe_2$/C, respectively.

3.2.6 Synthesis of MOF-derived Sb_2Se_3/WSe_2/C Composites

3.2.6.1 Synthesis of Sb/W-Hybridization Precursor

First, 3.5 mmol of L-serine (0.371 g) was added to 20 mL of deionized water and stirred well to form Solution 1. After that, 7 mmol of trimesic acid (1.47 g) was dissolved into 40 mL of ethanol to form Solution 2. Solution 2 was then added to Solution 1 and stirred continuously for 20 min. Finally, 3.5 mmol $SbCl_3$ (0.798 g) and 3.5 mmol WCl_6 (1.388 g) were mixed well and then added to the above mixed solution

with rapid stirring for 2 h. The solution was washed by centrifugation with ethanol for 3 times. Contrastingly, only $SbCl_3$ and WCl_6 were added to the preparation process of the Sb-hybridization precursor and W-hybridization precursor, respectively, and other operational steps remained unchanged. Note that all the above processes are to be carried out in an ice-water mixing bath.

3.2.6.2 Synthesis of Sb/W Nano Fibers

1 g of the obtained Sb/W-hybridization precursor and 1 g selenium powder were dispersed in 10 g of DMF solution by ultrasonic treatment and stirred for 2 h, then 1.1 g of polyacrylonitrile (PAN) was added, and stirring was continued for 12 h to obtain the colloidal suspension. It was then loaded into a 20 mL syringe equipped with a 21-gage steel needle for electrospinning operation, and the collector used aluminum foil for spinning collection. The spinning load voltage was 18 kV, the scanning speed was 20 mm s^{-1}, the injection speed was 15 μL min^{-1}, the distance between the collector and stainless-steel needle was fixed at 12 cm, and the roller speed is 500 RPM. Subsequently, the as-spun nanofiber was vacuum-dried overnight at 80 °C.

3.2.6.3 Synthesis of $Sb_2Se_3/WSe_2/C$ Composites

The obtained nanofiber was loaded into a magnetic boat and transferred to the center of a quartz tube furnace for calcination. The tube furnace was exhausted with high-purity argon gas for 20 min before heating to eliminate the oxygen inside the furnace. Afterward, the tube furnace was heated from room temperature to 500 °C at a heating rate of 5 °C min^{-1} under an argon atmosphere and held at 500 °C for 3 h. Finally, the

tube furnace was naturally cooled to room temperature to obtain the target Sb_2Se_3/WSe_2/C-500. Sb_2Se_3/WSe_2/C-400 and Sb_2Se_3/WSe_2/C-600 samples were obtained by varying the calcination temperature to 400 °C and 600 °C, respectively.

3.3 Characterization Techniques

3.3.1 Physical Structural Characterization

3.3.1.1 Scanning Electron Microscopy (SEM)

SEM is an important test method for scanning the surface of a sample by means of a focused beam of electrons in order to obtain data on the sample's microscopic morphology. It can reveal the particle size and dimension of the sample.

The model of the equipment used in this project is Hitachi SU8010.

3.3.1.2 Transmission Electron Microscopy (TEM)

TEM is used to analyze the microstructure of a material by projecting an accelerated and aggregated electron beam onto a sample of very thin thickness, where the electrons collide with the atoms of the sample and change the direction of motion, thus generating three-dimensional angular scattering. The size of the scattering angle is related to the density and thickness of the sample so that different light and dark images can be formed, and the image will be displayed on the imaging device after magnification and focusing, which is used to analyze the microstructure of the material.

The model of the equipment used in this project is JEM-2010, and the manufacturer is JEOL of Japan.

3.3.1.3 Energy Dispersive Spectroscopy (EDS)

EDS is a widely used microanalytical technique for identifying and quantifying the distribution and content of each element in the local area of the sample. When integrated with an SEM or a TEM, EDS can produce elemental maps of samples.

The EDS test in this project is an important ancillary companion instrument that combines SEM and TEM.

3.3.1.4 X-ray Diffraction (XRD)

XRD analysis is a common research method for non-destructive qualitative and quantitative analysis of samples, which enables accurate measurement of crystal lattice constants and nanocrystal dimensions, as well as participation in the analysis of samples for crystallinity (crystalline and amorphous) and surface residual stresses.

The samples were analyzed using a Rigaku-type X-ray diffractometer manufactured by Rigaku Corporation, Japan. The experimental conditions were as follows: a Cu Kα radiation source was used, the wavelength of the emitted X-rays was 0.15418 nm, the applied voltage was 40 kV, the current was 100 mA, and the scanning angle was 10°−90°.

3.3.1.5 Raman Spectrometer

Raman spectroscopy is a non-destructive analytical technique that uses scattered light with a wavelength different from the incident light to examine a sample's chemical

structure, intermolecular interactions, and crystallinity through the interactions between chemical bonds within the material.

The Raman test used in this project was Raman spectroscopy (a Kr-Ar ion laser at 633 nm produced by Spectra-Physic Beamlok 2060-RS laser combining Symphony CCD-1LS detection system). system)

3.3.1.6 Resistivity Test

Resistivity testing is performed using the four-probe test technique. Therein, four probes in equally spaced configurations are staked on the surface of the semiconductor, and a constant current source supplies an appropriately small current (I) to the two outer probes. Then, the voltage (V) between the middle two probes is measured to derive the semiconductor's resistivity ultimately.

This project utilizes a fully automated four-probe test system (RTS-1389).

3.3.1.7 X-ray Photoelectron Spectroscopy (XPS)

XPS is a test technique that uses X-rays to irradiate the surface of a sample to excite the inner electrons and valence electrons of atoms to form photoelectrons. By measuring the number of photoelectrons with different energies and combining them with their kinetic energies, it is possible to determine the types of elements in materials as well as the chemical and electronic states of the elements contained therein.

The model of the equipment used in this project is XPS (PHI5600 Physical Electronics), manufactured by Perkin-Elmer, USA.

3.3.1.8 X-ray Fluorescence Spectrometer (XRF)

XRF was applied to measure the elemental contents in the samples. XRF is a method that uses primary X-ray photons or other microscopic ions to excite atoms in a material and produce fluorescence (secondary X-rays), which in turn analyzes the composition and chemical state of the material.

The model of the equipment used in this project is XRF (BRUKER M1MISTRAL).

3.3.1.9 Thermogravimetric Analysis (TGA)

TGA analysis investigates the thermal stability and composition of substances by measuring the relationship between the change in mass with temperature or time during a programmed warming process. TGA analysis is usually performed on high precision balances, which can detect small changes in mass, thus providing important information about reactions such as decomposition, oxidation, reduction, etc., of a material. Physical and chemical changes and thus mass changes occur in substances during heating in different atmospheres. By combining temperature and time parameters, thermogravimetric curves are derived to analyze the thermal stability and composition of the material.

TGA (Simultaneous Thermal Analyzer, 409 PC) was performed in this project at a heating rate of 10 °C min^{-1}. The temperature range used in TGA is 25 °C-1000 °C.

3.3.1.10 Brunauer-Emmett-Teller (BET)

BET can measure the surface area size per unit mass of the material, while the pore size and distribution in the material can be tested by nitrogen adsorption, which can help to reveal the energy storage mechanism. The size of a specific surface area can reflect the dispersion uniformity of nanoparticles to some extent.

The model chosen for this experiment is SSA-7000, and the manufacturer is Beijing Piande Electronic Technology Co.

3.3.1.11 Fourier Transform Infrared (FTIR) Spectroscopy

FTIR is an analytical method used to determine molecular structure and identify compounds by analyzing the relative vibrations between atoms within a molecule and molecular rotations through the use of a beam of infrared light with continuous wavelengths. When the vibration frequency of the infrared light matches the vibration frequency of a particular functional group, the molecule absorbs energy and transitions from its original ground vibrational state to a higher energy vibrational state.

The model of the equipment used in this project is FTIR-7600, whose spectral range is 7800~350 cm^{-1}. The acquisition time for each spectral line was 7 min, and the spectral resolution was 13 cm^{-1}.

3.3.1.12 Electron Paramagnetic Resonance (EPR)

EPR is a magnetic resonance technique originating from the magnetic moments of unpaired electrons, which can be used to qualitatively and quantitatively detect the unpaired electrons contained in atoms or molecules of matter and to explore the structural properties of their surroundings. For free radicals, the orbital magnetic moments play little or no role, and the vast majority (99% or more) of the total magnetic moment is contributed by the electron spin, so electron paramagnetic resonance is also known as "electron spin resonance".

The model of the equipment used in this project is EPR-Bruker A300. EPR was used in this project mainly to test the defective content of carbon.

3.3.2 Electrochemical Characterization

3.3.2.1 Sodium-ion Battery Assembly

For sodium ion half-cell, 80% active material, 10% conductive carbon (Super P), 10% polyvinylidene fluoride (PVDF) were homogeneously dispersed into N-Methyl pyrrolidone to make a slurry. The resulting slurry is then uniformly coated onto clean copper foil using a squeegee and dried under vacuum at 80 °C. The average mass loading of the active material on the electrodes was 1.3-1.5 mg cm^{-2}. A sodium sheet is the counter electrode, and glass fiber is the diaphragm to assemble a button-type 2032 half-cell. The electrolytes are 1.0 M $NaPF_6$ dissolved in ethylene glycol dimethyl ether (DME) and ethylene carbonate (EC)/dimethyl carbonate (DEC).

Assembly process: put the electrode sheet, battery shell, and other parts through the transition compartment of the glove box into the glove box, according to the negative shell, spring sheet, steel sheet, sodium, electrolyte, diaphragm, electrode sheet, electrolyte, positive shell in the order of the sequence of the stack, and then seal the battery with the sealing machine, that is, to get the usable coin cell.

3.3.2.2 Sodium-ion Capacitor assembly

For the assembly of SICs, commercial activated carbon is used as the cathode, and the obtained material is used as the anode. The preparation process and mixing ratio of the electrode sheets are similar to those of sodium ion half-cells. The difference is that the coating process is changed to control the mass loading of the cathode and anode separately. In this case, the relationship between the specific capacity (C) and mass (m) of the two electrodes follows the equation 3.1 (P. Cai et al., 2021):

$$\frac{m_+}{m_-} = (C_- \times \Delta E_-)/(C_+ \times \Delta E_+) \quad (3.1)$$

According to the calculation, the ratio of $\frac{m_+}{m_-}$ is about 3: 1. It should be noted that the electrode material needs to be pre-activated for 5 cycles in the SIBs before assembling the SICs. All of the above assembly processes are done in a glove box filled with high-purity argon gas (H_2O and O_2 < 0.1 ppm).

3.3.2.3 Galvanostatic Charge-Discharge (GCD)

GCD testing of the electrode material of interest is carried out using the Blue Power Test System. By maintaining a constant current, the target electrode materials are charged and discharged, and the potential and time parameters are recorded and plotted as images by taking points at fixed time intervals. The constant current charge/discharge system can be used to obtain the charge/discharge specific capacity, charge/discharge plateau, cycling performance, rate performance, and charge/discharge curve of the electrode material.

The model used in this experiment is CT2001A, with cutoff voltages of SIB (0.01−3 V) and SIC (0.01−3.8 V), and the manufacturer is Wuhan LAND Co.

3.3.2.4 Cyclic Voltammetry (CV)

CV method is a specific shaped pulse voltage load on the battery. It gets two branches of the current and voltage curves: the first half of the potential to the cathode direction scan, the experimental specimen in the electrode, is reduced and emits a reduction wave; the second half of the potential to the anode direction scan, the reduction product is oxidized, emitting oxidation wave. According to the shape of the curve, we can judge the occurrence position of the electrode reaction, the primary and secondary electrochemical reaction, and the platform of the first discharge.

The Princeton electrochemical workstation was used for CV testing in this thesis.

3.3.2.5 Differential Capacity Curve (dQ/dV)

The dQ/dV is used to analyze the relationship between voltage and charge of electrodes during charging and discharging. Through the differential relationship between voltage to charge during the battery charging and discharging process, the electrochemical reaction process and reaction rate of the electrode at different stages can be quickly analyzed.

The dQ/dV data in this project were analyzed using the LAND test system.

3.3.2.6 Electrochemical Impedance Spectroscopy (EIS)

The parameter of the diffusion process (D) can be further fitted by the relationship between $\omega^{-1/2}$ and Z', according to Equation (3.2) and Equation (3.3):

$$D = \frac{R^2T^2}{2A^2n^4F^4C^2\sigma_w^2} \tag{3.2}$$

$$Z' = R_e + R_{ct} + \sigma_w\omega^{-1/2} \tag{3.3}$$

3.3.2.7 Galvanostatic Intermittent Titration Technique (GITT)

GITT was employed to explore the kinetics of the Na^+ reaction, D_{Na^+} can be calculated by the Equation (3.4):

$$D_{Na^+} = \frac{4}{\pi\tau}\left(\frac{mV_m}{MS}\right)^2\left(\frac{\Delta E_s}{\Delta E_t}\right)^2\left(\tau'' \frac{l^2}{D_{Na^+}}\right) \tag{3.4}$$

Where m is the mass load, V_m is the molar volume, M is the molar mass, τ is the relaxation time, t is the current pulse duration, ΔE_s is the steady-state potential change caused by the current pulse during two adjacent relaxations and ΔE_t is the potential change during the constant-current pulse after eliminating the iR drop. l can be approximated as the thickness of the electrode.

3.3.2.8 Pseudocapacitance Behavior

The behavior of intercalation and pseudocapacitance of electrochemical processes was initially determined by the fitting relationship between peak current and scan rate in cathodic and anodic processes. According to Equation (3.5) and Equation (3.6):

$$i = av^b \tag{3.5}$$

$$\log i = b \log v + \log a \tag{3.6}$$

Where i is the peak current value at different scan rates, v is the scan rate in CV, and a and b are variable parameters. From that, b can be obtained by calculating the slope. When the value of b is close to 0.5, it indicates that the electrochemical process is mainly controlled by intercalation. When b is close to 1, the electrochemical process is primarily in the pseudocapacitive property.

$$i_v = k_1 v + k_2 v^{1/2} \tag{3.7}$$

Where $k_1 v$ and $k_2 v^{1/2}$ are the pseudocapacitance current contribution and the

intercalation current contribution, respectively.

3.3.2.9 Energy/Power Density Calculation

The specific capacitance (C, F g^{-1}), energy density (E, W h kg^{-1}), and power density (P, W kg^{-1}) of the SICs, based on the GCD tests, are calculated utilizing the equations (3.8), (3.9), and (3.10):

$$C = {It}/{\Delta V \times m} \tag{3.8}$$

$$E = {C(V_{max}^2 - V_{min}^2)}/{2 \times 3.6} \tag{3.9}$$

$$P = {E \times 3600}/{t} \tag{3.10}$$

Where I (A) is the discharge current, t (s) is the discharge time, V_{max} (V) and V_{min} (V) are the initial and final discharge potentials, ΔV (V) is the potential change, and m (g) is the total mass of active material in both the anodes and cathodes.

3.4 Density-Functional Theory (DFT) Calculations

The DFT calculations were performed using the Vienna ab-initio simulation package (VASP). The generalized gradient approximation of Perdew-Burke-Ernzerhof (GGA-PBE) is adopted to describe the exchange-correlation generalized function. The application of GGA-PBE also considers the effect of van der Waals forces. In this case, the k-grid point in the first Brillouin zone is 3×3×1. The plane wave truncation energy is 571.4 eV. In addition, a vacuum region of about 20 Å is constructed in the Z-axis direction to exclude the interaction between the two adjacent phases. Note that the

assembled model is wholly relaxed in terms of structure, the residual forces present in all directions for each atom do not exceed 0.03 eV, and the energy convergence conditions between the two ion steps vary within 1.0×10^{-5} eV.

CHAPTER 4: ANALOGOUS CATIONIC HETEROSTRUCTURE DESIGN

4.1 Introduction

As promising conversion materials, MSes are expected to be stimulated with faster reaction kinetics while exhibiting a significant specific capacity. Among various MSes, $MoSe_2$ and WSe_2 exhibit inherent physicochemical advantages and similar interlayer spacing (~0.65 nm), which are favorable for the insertion/deinsertion of bulky Na^+. However, some apparent deficiencies in electronic conductivity, fast response capability, and structural integrity further resulted in unstable rate performance and poor cycling stability. (F. Zheng et al., 2019) In the literature review section, a large number of research results show that microstructural modification of MSes can effectively overcome the above drawbacks. Based on that, several works about $MoSe_2$ and WSe_2 have elucidated the outstanding effect of constructing cationic heterostructures on electrochemical properties. For example, Li et al. verified the superior ability of heterostructures to enhance charge transport and promote reaction kinetics by constructing $FeSe_2/MoSe_2$ heterostructures. (Shengkai Li et al., 2023) Pei et al. achieved the effect of accelerated charge transfer and enhanced Na^+ adsorption capacity by preparing a $Co_{0.85}Se/WSe_2$ heterostructure phase with Se vacancies. (Pei et al., 2023) However, conventional strategies for constructing heterogeneous structures seldom fully consider the similarity of the crystal structures between two or more components.[3] According to the isomorphism theory, selecting elements with similar lattice parameters

[3] Most of the content in this chapter has been published in ACS Nano, 18, 10230–10242 and Journal of Energy Chemistry, 80, 291–301.

in constructing heterogeneous networks helps realize a wide range of mixing crystallization within the crystalline phases, thus achieving a result closer to the plane heterogeneity. (Langmuir, 1919) According to our investigation, $MoSe_2$ (JCPDS No. 29-0914) and WSe_2 (JCPDS No. 87-2418) belong to the same P63/mmc architecture of the hexagonal crystal system, which has a slight gap in crystallographic properties and has the potential to realize more advanced crystallographic heterogeneous bonding. Therefore, it is necessary to construct analogous cationic heterostructures of $MoSe_2$ and WSe_2 to further stimulate the potential capacity utilization and fast reaction kinetics.

In this chapter, we achieve homogeneous mixing of Mo, W, and C by constructing Mo/W bimetallic MOF (abbreviated as Mo/W-MOF) precursors in a one-step process. Notably, the Mo/W-MOF precursors with different morphologies are prepared by controlling the hydrolysis reaction during MOF preparation, respectively. Further, by modulating the calcination temperature of selenization/carbonization, we achieved the control of the degree of selenization of W, and obtained $MoWSe_2$/C and $MoWSe_2/WO_3$/C with different compositional heterogeneity, respectively.

4.2 MOF-Derived $MoWSe_2$/C Composites

We prepared Mo/W-MOF nanoparticles to achieve the uniform distribution of metal elements and the carbon introduction process by employing the hydrolysis property of perchlorides and "solvent-assisted" method. Subsequently, the sintered selenization was employed to construct high-level cationic heterostructures and carbonization processes. After microstructure optimization and electrolyte adaptive selection, the obtained $MoWSe_2$/C anode exhibited excellent capacity performance and cycling stability in

SIBs and SICs, respectively. Physical structure characterization tests and DFT calculations indicated that the fast ion transport capability was associated with the enlarged layer spacing and the built-in electric field formation produced by the abundant heterogeneous structure. Electrochemical tests performed on different electrolytes revealed the significant advantages of ether-based electrolytes in terms of rate capacity and cycling stability. Furthermore, the analytical results combining physical characterization and theoretical simulations indicated that a stable, porous, and inorganic-rich SEI layer was preferred to be formed in the ether-based electrolyte, thus avoiding active detachment and sodium dendrite generation.

4.2.1 Synthesis of $MoWSe_2$/C

The synthetic process of $MoWSe_2$/C is schematically illustrated in Figure 4.1. Firstly, the dual perchlorides ($MoCl_5$ and WCl_6) can leverage similar hydrolysis properties to ensure the homogeneous mixing of cations during the construction of bimetallic MOFs. Further, the modified ice-water bath can reduce the oxide evolution process by slowing the vigorous hydrolysis reaction, promoting Mo/W-MOF nucleation. Lastly, during the subsequent high-temperature annealing process, Mo/W-MOF completes the selenization responses to $MoSe_2$ and WSe_2, respectively. Meanwhile, the organic components in Mo/W-MOF are further carbonized to form a uniform amorphous carbon material. Consequently, $MoSe_2$, WSe_2, and C achieve a uniform distribution in the obtained $MWSe_2$/C composite.

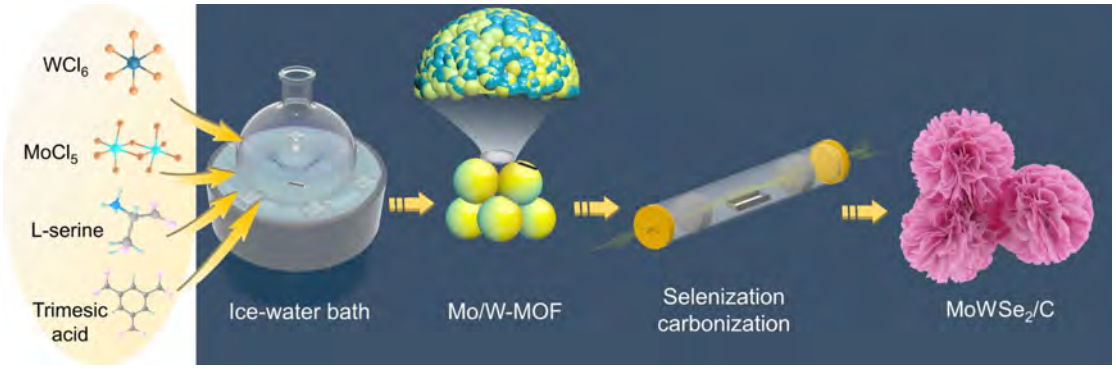

Figure 4.1: Schematic illustration of the synthetic process of the $MoWSe_2/C$.

4.2.2 Structural and Chemical Characterization of $MoWSe_2/C$

The primary morphologies of the synthesized samples are evaluated by SEM. As shown in Figure 4.2, the Mo/W-MOF precursor exhibits a distribution of spherical particles with regular particle size.

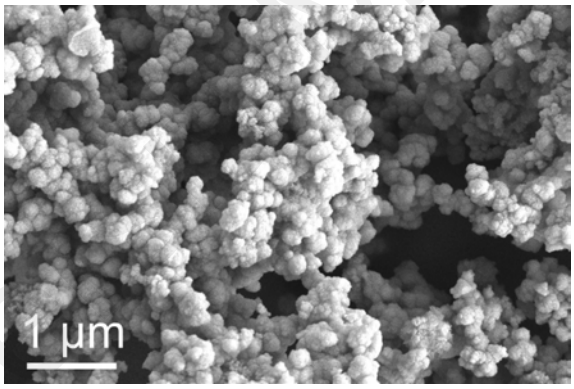

Figure 4.2: SEM images of Mo/W-MOF nanoparticles.

Moreover, the elemental mapping images indicate a uniform distribution of Mo, W, O, C, and N in the prepared Mo/W-MOF (**Figure 4.3**). The homogeneous distribution of the elements implies that the homogeneous mixing of Mo, W, and C was accomplished during the synthesis stage of the MOF precursor, providing for the subsequent generation of a rich heterogeneous interface.

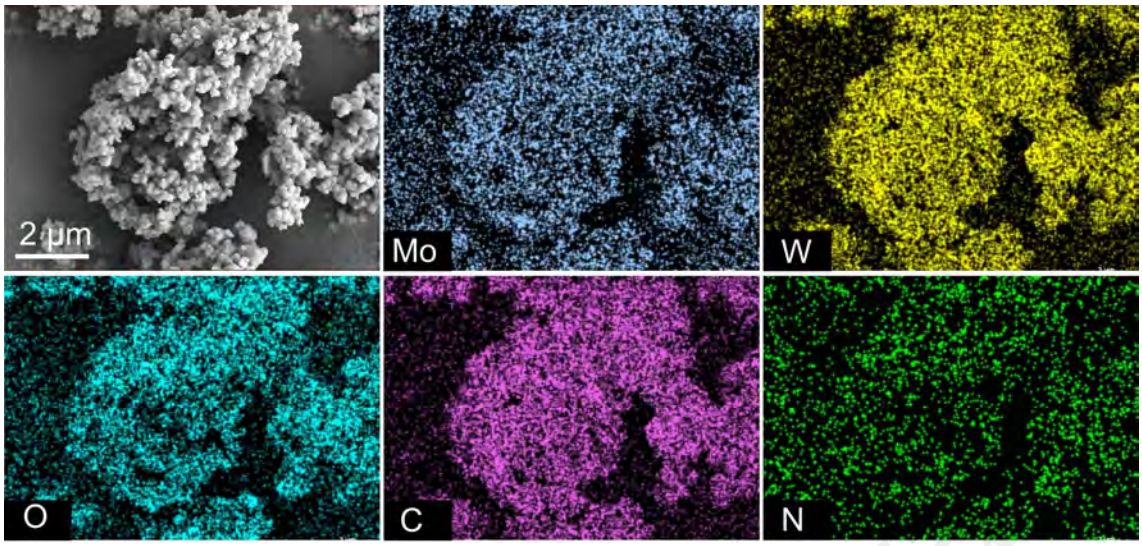

Figure 4.3: The elemental mapping images of the prepared Mo/W-MOF nanoparticles.

The SEM image of the final sample $MWSe_2/C$ in Figure 4.4a demonstrates the morphological transformation from spherical to assembly ultrathin cross-linked 2D nanosheets by the sintering process. Similarly, Figure 4.4b reveals the distribution of Mo, W, Se, and C elements in $MWSe_2/C$ through elemental mapping images.

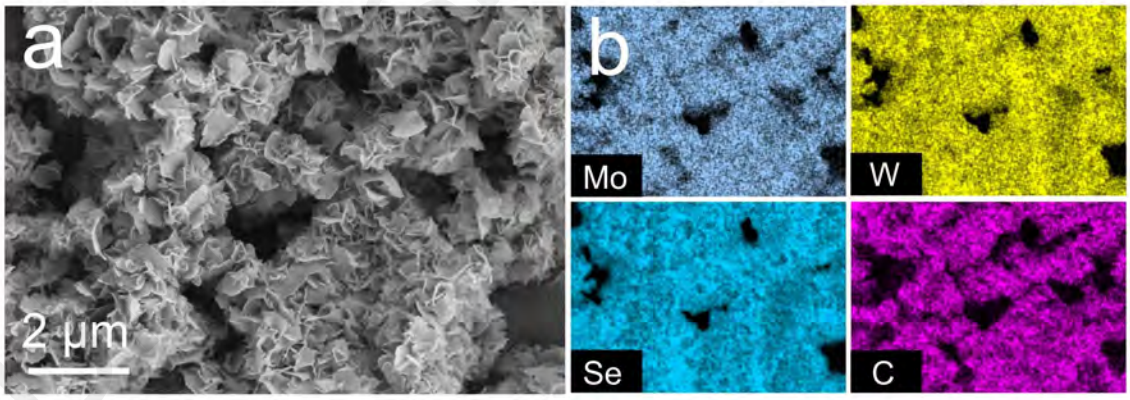

Figure 4.4: (a) SEM image and (b) the corresponding elemental mapping of $MoWSe_2/C$.

Moreover, EDS is employed to analyze the elemental content in the region of Figure 4.4. As shown in Figure 4.5, the moderate C content (about 35.8%) can ensure the overall specific capacity while providing buffer space for volume expansion. (B. Qin et al., 2023) The atomic percentages of N, O, Se, Mo, and W are 1.32%, 4.03%, 39.79%,

8.90%, and 10.16%, respectively. Among them, the number of atoms of Se is approximately two times the number of the combined number of atoms of Mo and W, suggesting the formation of diselenides. In addition, the comparable atomic numbers of Mo and W represent the final formation of $MoSe_2$ and WSe_2 consistent with the addition ratio. The small amount of N implies the introduction of a small number of N-doped elements brought in by the MOF formation process. The presence of O represents the unavoidable oxidization process on the surface of the sample.

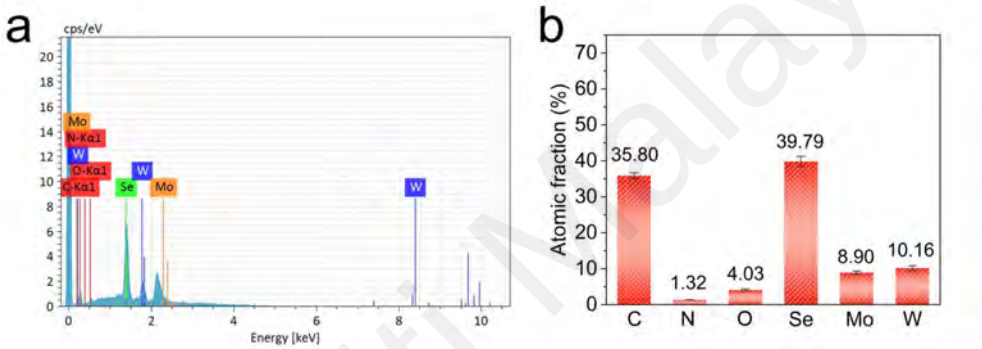

Figure 4.5: The elemental contents in $MoWSe_2$/C obtained by EDS.

High-resolution TEM (HRTEM) images present the refined crystal structure of the $MoWSe_2$/C phase (Figure 4.6). As shown in Figure 4.6a, the detected lattice spacing of 0.645 and 0.650 nm can be attributed to the (0 0 2) crystal planes of $MoSe_2$ and WSe_2. The (0 0 2) crystal planes of $MoSe_2$ and WSe_2 verify the successful synthesis of the composites. Besides, an enlarged interlayer spacing (0.677 nm) is further detected, which can be attributed to the (0 0 2) heterogeneous interface composed of $MoSe_2$ and WSe_2. Furthermore, the magnified images in regions 1 (Figure 4.6b) and 2 (Figure 4.6c) reveal the significant alternating distribution of the (1 0 0) crystal planes of $MoSe_2$ and WSe_2, with an angle of approximately 155°. This suggests an approximate plane heterostructure within the bulk phase, superior to traditional point and line

heterostructures. As further magnified in Figure 4.6d, the atomic arrangement of the (0 0 2) crystal planes illustrate the interfacial atom configuration. This suggests that the combination of $MoSe_2$ and WSe_2 can modify electron distribution, creating a built-in electric field and expanding the interlayer distance.

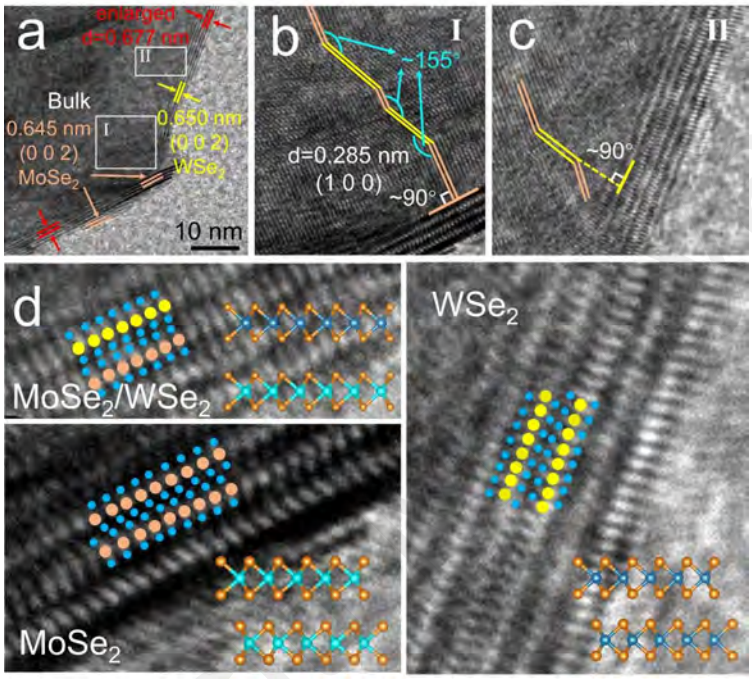

Figure 4.6: HRTEM diagrams of $MoWSe_2$/C.

XRD analysis is conducted to identify the physical structure visually. As shown in Figure 4.7, the Mo/W-MOF precursor exhibits a typical amorphous peak. The appearance of amorphous peaks represents the MOF structure with a typical low crystallinity organic-inorganic combined state. Meanwhile, all diffraction peaks of the final prepared $MoWSe_2$/C sample can be indexed to hexagonal $MoSe_2$ (JCPDS No. 29-0914) and WSe_2 (JCPDS No. 87-2418), respectively. The adequate correspondence of the XRD curves with the PDF cards implies a homogeneous synthesis of $MoWSe_2$. Furthermore, the presence of a distinct peak at around 26° represents the successful introduction of carbon, which is consistent with the elemental analysis.

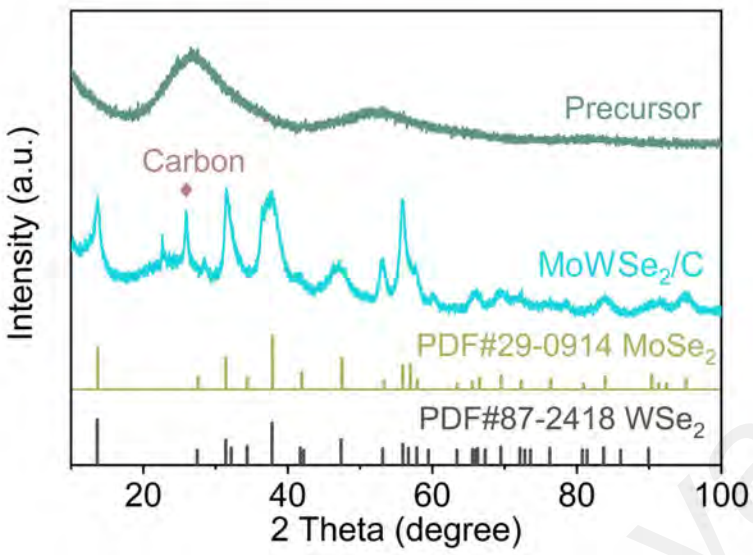

Figure 4.7: XRD patterns of the prepared Mo/W-MOF precursor and $MoWSe_2$/C.

In the Raman curves (Figure 4.8a), two characteristic peaks at 239.3 and 279.1 cm^{-1} can be attributed to the A_{1g} and E_{2g} vibrational modes in $MoSe_2$. (H. He et al., 2022; Xingchen Xie et al., 2023) Meanwhile, the E_{2g} characteristic peak of WSe_2 is observed at 252.3 cm^{-1}, representing the successful preparation of the $MoWSe_2$ composite. (Hussain et al., 2022; Q. Lv et al., 2023) Additionally, two peaks at 1389.92 and 1572.01 cm^{-1} imply the defects caused by sp3 hybridization of carbon atoms (D-band) and graphitization caused by sp2 hybridization (G-band), respectively (Figure 4.8b). The area ratio of the D-band and G-band is calculated (I_D/I_G=3.93), revealing the introduced carbon is dominated by defects.

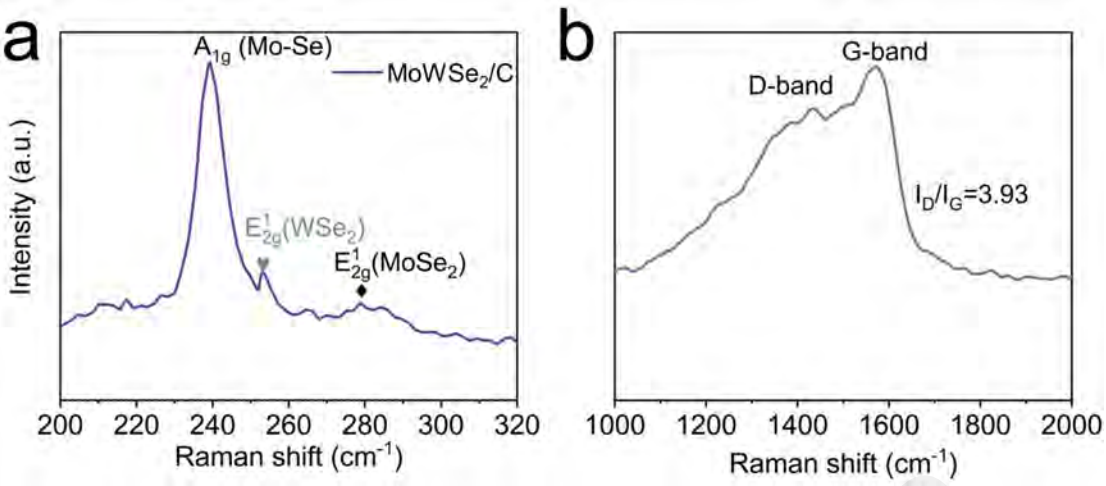

Figure 4.8: Raman spectra of the prepared $MoWSe_2/C$.

XPS is employed for surface chemical composition and electronic state analysis of the synthesized $MoWSe_2/C$ samples. From the high-resolution spectra of Mo 3d, two characteristic peaks located at 289.9 and 232.1 eV can be ascribed to Mo $3d_{5/2}$ and Mo $3d_{3/2}$ (Figure 4.9a). Notably, an obvious Mo-C peak is detected at 230.2 eV, representing the bond connection between $MoSe_2$ and carbon. (Chong et al., 2021; Xu Zhao, Cai, et al., 2018) In Figure 4.9b, the deconvolution peak of W 4f can be subdivided into two prominent peaks located at 32.4 and 34.6 eV, corresponding to W $4f_{7/2}$ and W $4f_{5/2}$, respectively. Moreover, two additional small peaks at high binding energies can be indexed to W' $4f_{7/2}$ and W' $4f_{5/2}$, triggered by the high valence state W^{6+} in the surface tungsten oxide. (P. Wang et al., 2022) A pair of characteristic peaks of Se $3d_{5/2}$ and Se $3d_{3/2}$ appear in the Se 3d spectrum (Figure 4.9c), which originated from M-Se (M=Mo and W). As shown in Figure 4.9d, the conventional C 1s orbital can be further split into C-C sp2, C-C sp3, and C-N/C-O bonds, indicating the presence of amorphous carbon in the composite material. The sp3 hybridization of carbon dominates, with one 2s and three 2p orbitals of the surface carbon atom mixing to form four orbitals of equal energy. The shape of these orbitals resembles the four vertices of a tetrahedron, favoring the

stability of the carbon structure. The detailed species of N elements in the prepared samples are further distinguished by high-resolution XPS spectra. As shown in Figure 4.9e, the split peaks located at 398.6, 399.8, and 400.7 eV can be attributed to pyridinic-N, pyrrolic-N, and graphitic-N, respectively. Among them, pyrrole nitrogen and pyridine nitrogen realize the modulation of the electronic structure of the active component by changing the local electron density of the carbon material and triggering the redistribution of electrons between the carrier and the active component. In addition, the introduction of graphitic nitrogen not only helps to improve the adsorption efficiency of the charcoal-loaded electrode, but also provides a stable anchoring site for the active component, thus improving the dispersion and stability of the active component on the charcoal carrier. In the prepared $MoWSe_2/C$ composites, graphitic nitrogen accounts for a larger proportion, which is favorable to enhance the pseudocapacitive performance of the electrode for fast adsorption.

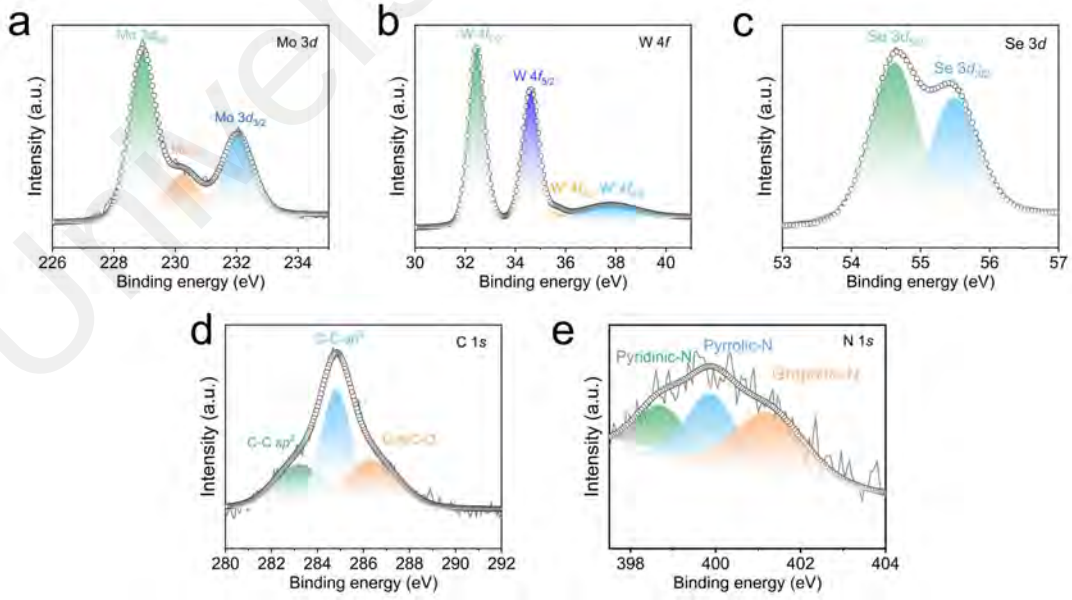

Figure 4.9: High-resolution Mo 3d (a), W 4f (b), Se 3d (c), C 1s (d), and N 1s XPS spectra of $MoWSe_2/C$.

4.2.3 Density Functional Theory Calculations

For a deeper understanding of the reaction mechanism of the heterostructures in the prepared $MoWSe_2$, DFT calculations are employed to analyze the electronic state and diffusive behavior. By selecting the (0 0 2) crystal plane as an example in Figure 4.10, the lattice distance of $MoSe_2$ and WSe_2 are 6.45 Å and 6.50 Å, respectively. The simulations indicate that the $MoWSe_2$ heterostructure has an enlarged lattice distance (6.77 Å) compared to the $MoSe_2$ and WSe_2 monomers, which is consistent with the previous TEM results.

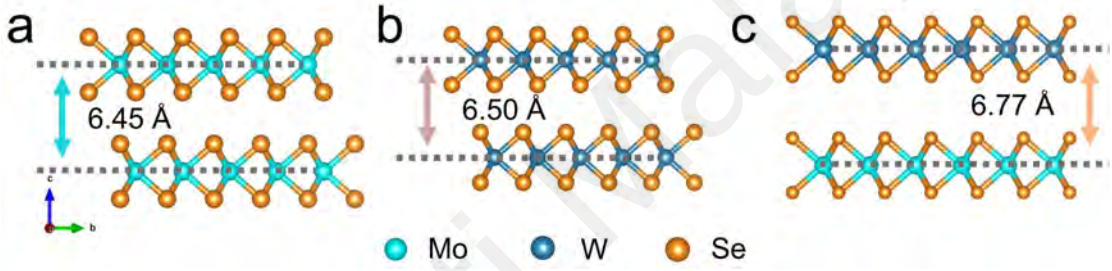

Figure 4.10: Schematic diagrams of the (0 0 2) lattice planes in $MoSe_2$, WSe_2, and $MoWSe_2$ heterostructure.

As shown in Figure 4.11a, the calculated band gap of the $MoWSe_2$ near the Fermi energy level is 1.303 eV. Contrastingly, the calculated band gap of $MoSe_2$ (Figure 4.11b) and WSe_2 (Figure 4.11c) are 1.507 and 1.628 eV, which are obviously larger than that of $MoWSe_2$. The smaller band gap represents the better metallic property of $MoWSe_2$ heterostructures.

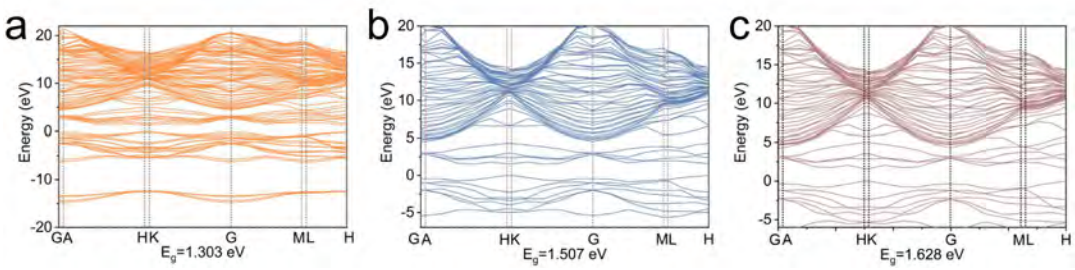

Figure 4.11: The calculated band gap for $MoWSe_2$ heterostructure (a), $MoSe_2$ (b), and WSe_2 (c).

Accordingly, density of states (DOS) calculations is performed for the synthesized three samples to study the electronic properties (Figure 4.12). From that, the broadened energy bands of $MoWSe_2$ heterostructures exhibit higher intensity and more delocalized electrons relative to $MoSe_2$ and WSe_2, especially near the Fermi energy level. Therefore, optimized metal properties can be achieved by the heterogeneous combination of $MoSe_2$ and WSe_2, thus promoting fast electron transport.

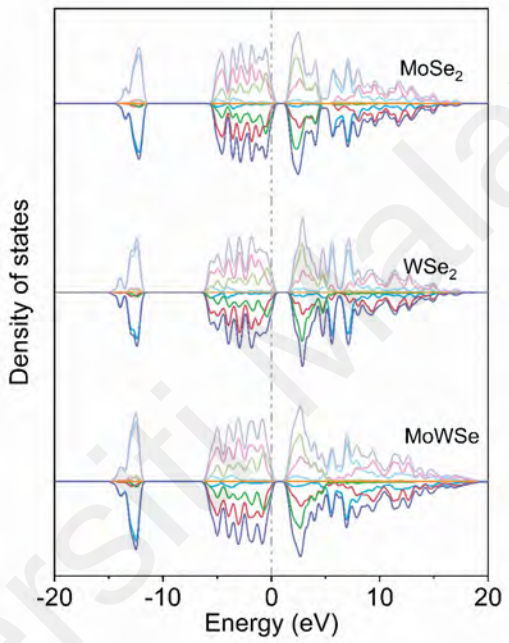

Figure 4.12: The density of states for $MoSe_2$, WSe_2, and $MoWSe_2$ heterostructure.

As shown in Figure 4.13, to evaluate the Na^+ storage kinetics, DFT calculations are applied to reveal the adsorption energies of Na^+ on the surfaces and interlayers of the $MoWSe_2$ heterostructure. The adsorption energies of Na^+ on the $MoSe_2$ side, WSe_2 side, and interlayer are -0.894, -1.063, and -0.025 eV, respectively, indicating that Na^+ prefers to adsorb to the surface. As a comparison, the Na^+ adsorption energies on the surfaces of $MoSe_2$ and WSe_2 monomers are calculated to be -0.88 and -0.84 eV, respectively (Figure 4.14). Consequently, since the adsorption value of Na^+ is more negative at the heterogeneous interface, the built-in electric field generated by the asymmetric

electronic structure in the $MoWSe_2$ heterostructure is favorable to the fast kinetics.

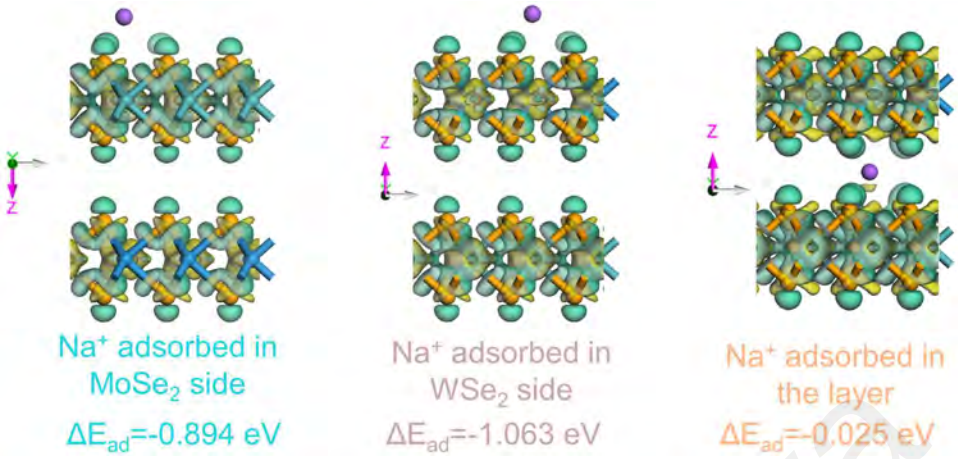

Figure 4.13: The adsorption energies of Na^+ on the surfaces and interlayers of the $MoWSe_2$ heterostructure.

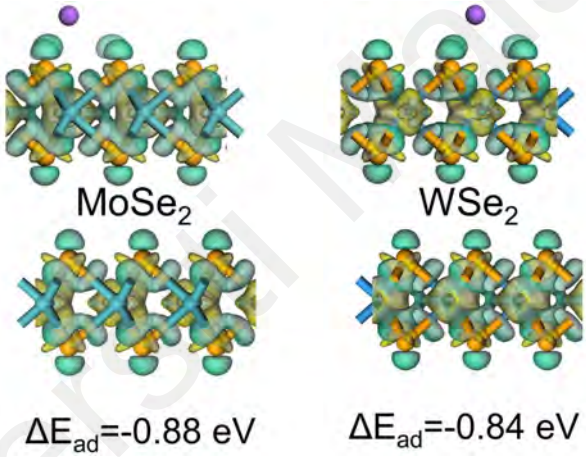

Figure 4.14: The Na^+ adsorption energies on the surfaces of $MoSe_2$ and WSe_2 monomers.

The charge differential density diagram in Figure 4.15 graphically reveals that the $MoWSe_2$ electrode possesses more unbalanced charge distribution than $MoSe_2$ and WSe_2 (yellow and green colors represent charge disappearance and accumulation, respectively), benefiting the transport of ions and electrons.

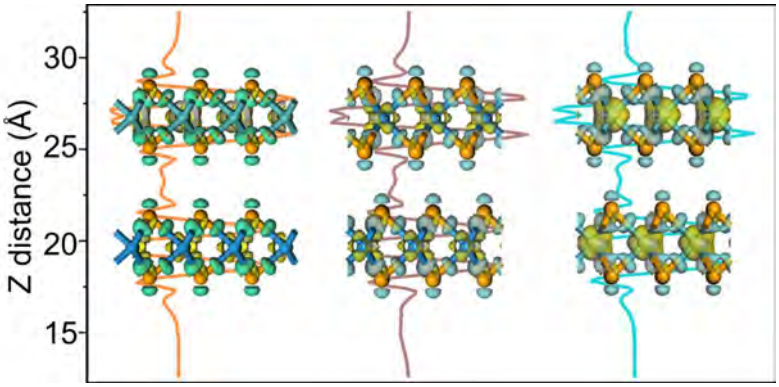

Figure 4.15: The planar-average charge density for $MoWSe_2$ heterostructure, WSe_2, and $MoSe_2$, respectively (from left to right).

Additionally, to profoundly investigate the Na^+ migration behavior at the heterogeneous interface, the ion migration paths and diffusion energy barriers are calculated for different diffusion states, respectively. As shown in Figure 4.16, the Na^+ diffusion energy barriers of the $MoWSe_2$ heterostructure on the $MoSe_2$ side, WSe_2 side, and the interlayer are 0.223, 0.177, and 0.765 eV, respectively, implying Na^+ prefer to transfer on the surface side other than the interlayer.

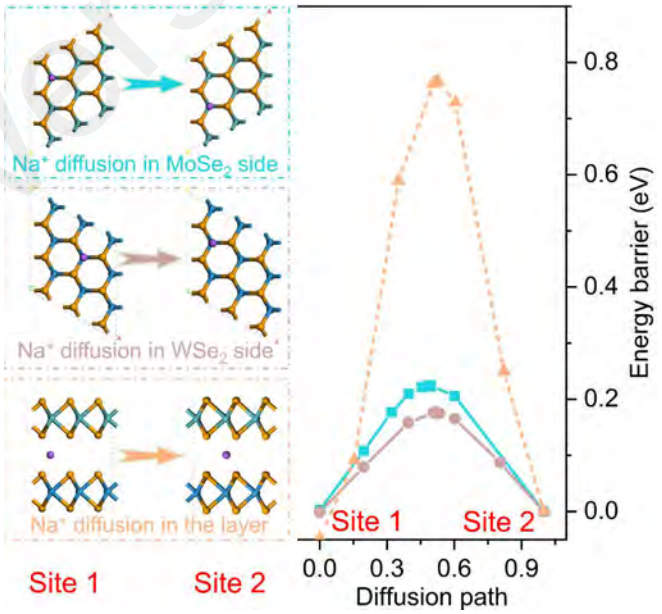

Figure 4.16: The schematic illustration for the Na^+ diffusion path and the corresponding diffusion energy barrier curves on the surfaces and interlayers of the $MoWSe_2$ heterostructure.

For a more detailed comparison, the surface Na^+ diffusion energy barriers of monomers $MoSe_2$ and WSe_2 are calculated separately. As shown in Figure 4.17, the surface Na^+ diffusion barriers of $MoSe_2$ and WSe_2 monomers are 0.251 and 0.221 eV, respectively, which are lower than $MoWSe_2$ heterostructure surface. The lower diffusion barrier of the $MoWSe_2$ heterostructure surface is beneficial for Na^+ diversion. Therefore, the created built-in electric field in the $MoWSe_2$ heterostructure can facilitate Na^+ surface adsorption and diffusion, which is favorable for achieving fast kinetics.

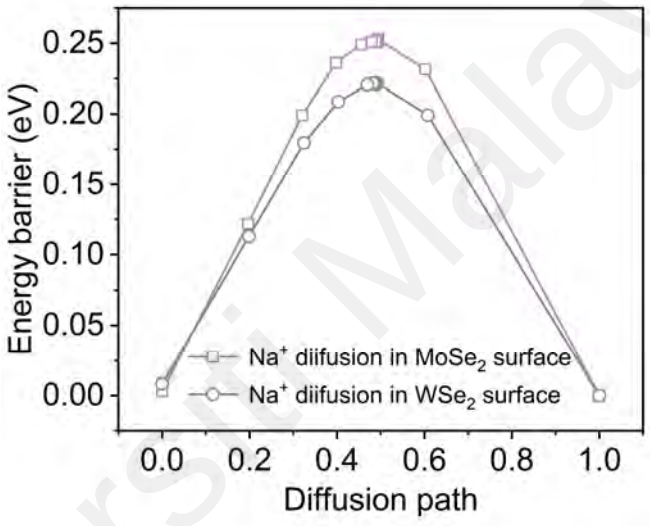

Figure 4.17: The calculations of surface diffusion paths for the $MoSe_2$ and WSe_2 monomers.

4.2.4 Electrochemical Properties of $MoWSe_2$/C Anode

The sodium storage capacities of the prepared electrodes in different electrolytes (DME and DMC/EC based) are evaluated by employing the assembled 2032 half-cell. Figure 4.18a reveals the electrochemical processes in DME-based electrolyte using CV for the initial three cycles of the $MWSe_2$/C electrode. During the initial cathodic scan, a distinct reduction peak appeared near 0.53 V, representing the conversion reaction occurrence and a stable SEI layer generation in the first discharge process. (J. S. Lee et al., 2023; S. Zhang et al., 2021) The scanning profiles of the 2nd and 3rd circles are

approximately the same, representing the excellent cyclic stability and reaction reversibility of the $MWSe_2$/C electrode. To more definitely distinguish the redox peaks of $MoSe_2$ and WSe_2 in the $MoWSe_2$/C electrode, the CV curves of $MoWSe_2$/C, $MoSe_2$/C, and WSe_2/C are compared in Figure 4.18b, respectively. By comparison, the redox peak located at 0.91/2.50 V corresponds to the reversible conversion process of WSe_2, while the peaks located at 1.44/1.64 V represents the reversible conversion of $MoSe_2$. The reversible reaction peaks located in the high-voltage region (purple rectangular area) represent Na^+ reversible insertion/de-insertion behavior. Notably, the redox peaks near 0 V represent the carbon-induced storage behavior in the $MWSe_2$/C electrode.

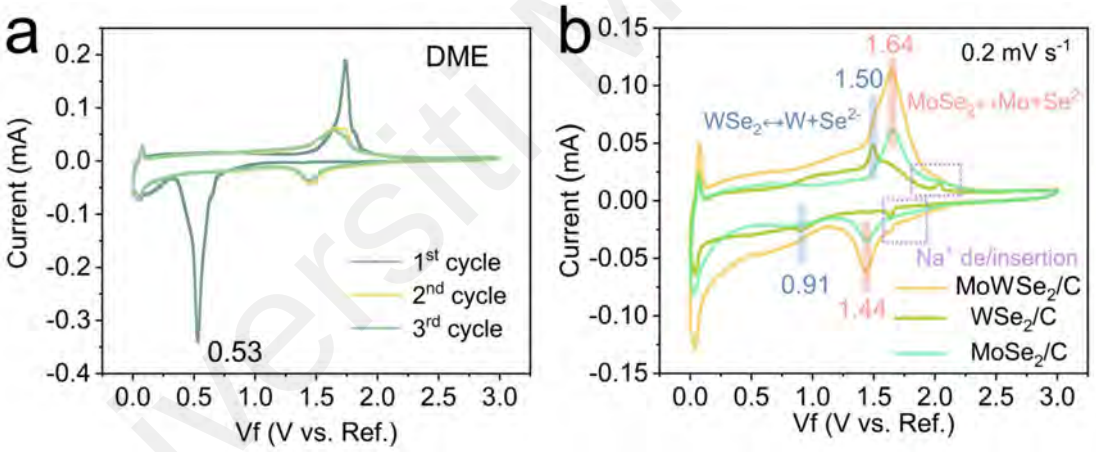

Figure 4.18: (a) CV curves from 0.01 to 3.0 V at the scan rate of 0.1 mV s^{-1} in DME electrolyte. (b) CV curves of $MoWSe_2$/C, $MoSe_2$/C, and WSe_2/C from 0.01 to 3.0 V at the scan rate of 0.2 mV s^{-1} in DME electrolyte.

As a comparison, Figure 4.19 shows the CV curves in the EC/DMC electrolyte system. In addition to the main peak located at 0.5 V in the first cathodic scan, an additional reaction peak appears at 0.66 V, suggesting a conventional Mo/W generation process. (J. S. Lee et al., 2023) Moreover, during the subsequent scans, an extra pair of redox peaks located at 1.92 V and 2.11 V appeared, corresponding to the reversible

conversion process of Se^{2-} to Se. (Niu et al., 2017) As we know, the small-sized Na_2Se_x generated during the Se^{2-}→Se process can cross the SEI layer and trigger a "shuttle effect", which will further aggravate the electrode material and SEI decomposition, thus leading to a rapid electrochemical degradation. (Huang et al., 2021) Notably, the CV curves in the DME electrolyte without monitoring the conversion reaction peaks of Se^{2-} and Se represent a stable cation conversion process, which is conducive to maintaining the structural stability of electrode and SEI layer.

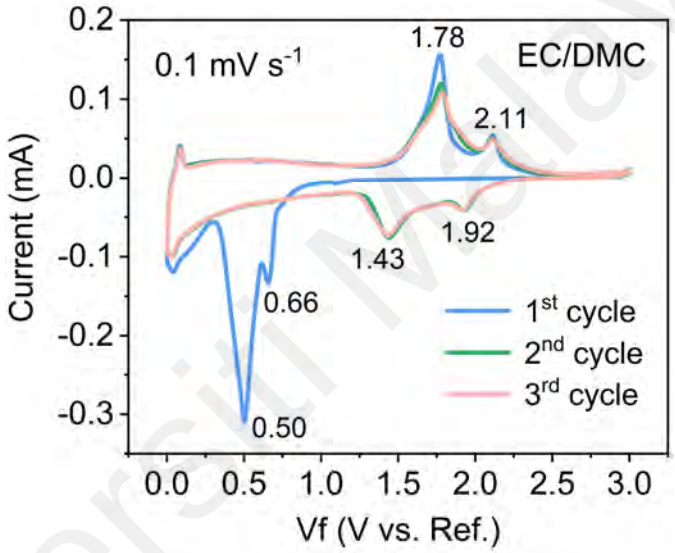

Figure 4.19: CV curves of $MoWSe_2$/C from 0.01 to 3.0 V at the scan rate of 0.1 mV s^{-1} in EC/DMC electrolyte.

The GCD curves of $MWSe_2$/C electrode in DME electrolyte have been presented in Figure 4.20a. From that, as the cycle proceeds (from 3rd to 200th), the charging and discharging capacity exhibits a decreasing and then increasing trend. At the same time, the corresponding charging and discharging platforms also change significantly. To detailly comprehend this change, the related dQ/dV profiles are further calculated (Figure 4.20b). At the 3rd cycle, the $MWSe_2$/C electrode exhibited two major redox peaks similar to the CV curve. As cycling to the 50th, the capacity decayed significantly

compared to the initial state, while the previous pair of major redox peaks began to split and became more obvious in the subsequent cycle. This phenomenon may be triggered by the exposure of more active surfaces under the current activation during the cycling process. Notably, a pair of small redox peaks located near 2.0 V is monitored during the 50th cycle and not observed during the subsequent cycles, which can be attributed to the reversible reaction of Se. The location of this pair of additional peaks is consistent with that in the EC/DMC electrolyte system, which may be one of the core factors contributing to the capacity decay.

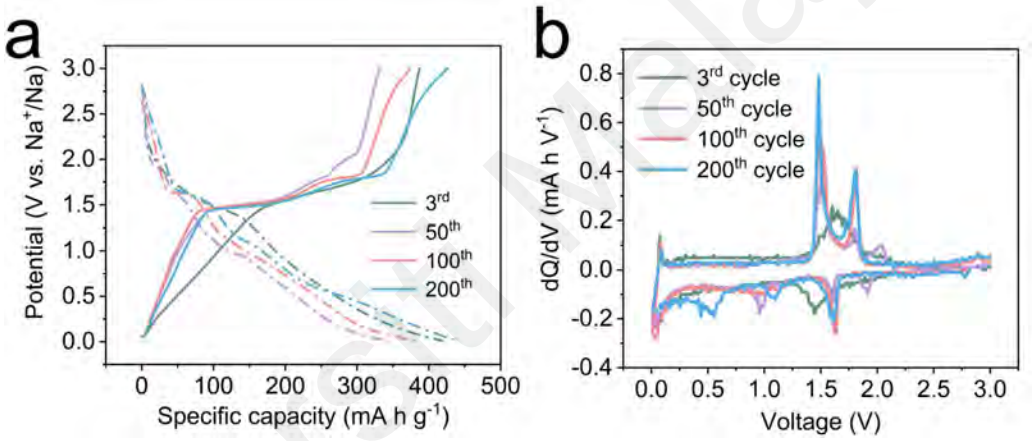

Figure 4.20: (a) Charge-discharge voltage profiles (3rd, 50th, 100th, and 200th), and (b) the corresponding differential capacity profiles of MoWSe$_2$/C electrode in DME.

Figure 4.21a exhibits the electrochemical performance of the MWSe$_2$/C electrode at a current density of 1 A g^{-1} in the DME and EC/DMC electrolyte systems, respectively. As a result, the MWSe$_2$/C electrode exhibits a significant activation during the initial process in the DME electrolyte system, while it shows a sharp capacity decay in the EC/DMC electrolyte. Consequently, MWSe$_2$/C electrode in DME electrolyte delivers a specific capacity of 439.9 mA h g^{-1} after 250 cycles. Figure 4.21b demonstrates the rate performance of the MWSe$_2$/C electrode in DME electrolyte. In particular, the activated MWSe$_2$/C electrode exhibits excellent rate performance at current densities of 1−6 A g^{-1}.

The long-term cycling ability of the $MWSe_2$/C electrode is evaluated under different electrolyte systems at a high current density of 10 A g^{-1} (Figure 4.21c). After 2000 cycles, the $MWSe_2$/C electrode exhibits a high-capacity retention of 347.3 mA h g^{-1} in the DME electrolyte, which is significantly higher than the EC/DMC system.

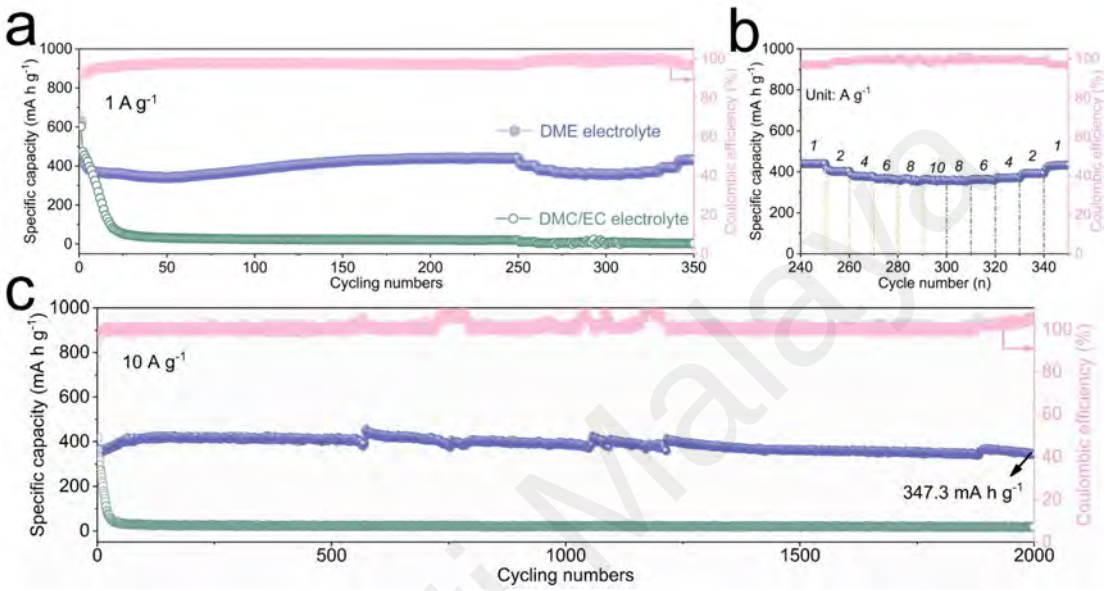

Figure 4.21: (a) Short cycling performance at 1 A g^{-1} and the cycled rate capability (b) of $MoWSe_2$/C electrode in DME and EC/DMC electrolytes. (c) Long cycling performance comparison in DME and EC/DMC electrolytes at the current density of 10 A g^{-1}.

To further reveal the heterogeneous behavior of $MoWSe_2$/C on the electrochemical performance, Figure 4.22 compares the short-cycling and rate capabilities of $MoSe_2$/C, WSe_2/C, and $MoSe_2$/C&WSe_2/C physical mixtures in DME, respectively. As can be seen, the $MWSe_2$/C electrode exhibits the best electrochemical performance among the above four samples, which implies that the $MoWSe_2$ heterostructure has a significant electrochemical enhancement.

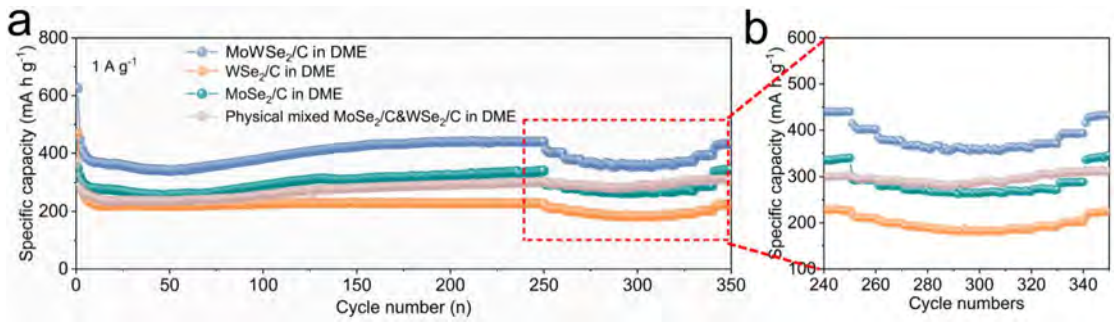

Figure 4.22: (a) Short cycling performance at 1 A g^{-1} and the cycled rate capability at 1, 2, 4, 6, 8, and 10 mA g^{-1} (b) of $MoSe_2$, WSe_2, $MoWSe_2$/C, and $MoSe_2$/C&WSe_2/C physical mixtures in DME electrolyte.

4.2.5 Sodium Storage Kinetics Investigation

CV curves with different scan rates from 0.1 to 5 mV s^{-1} are used to measure the kinetic properties of the $MoWSe_2$/C electrode in different electrolyte systems. Obviously, as the scan rate increases, the DME system exhibits a distinct central redox peak pair with a slight position shift, representing a slight polarization (Figure 4.23a). Differently, in the EC/DMC system of Figure 4.23b, the redox peaks exhibit an apparent shift as the scan rate increases, implying that a more significant polarization occurs. Furthermore, with the increased scanning rate, the CV curve in the EC/DMC system deviates significantly from the equilibrium current near 3.0 V. The overall curve tends toward a rectangular shape, indicating that the $MoWSe_2$/C electrode exhibits a greater electric double-layer storage mechanism at higher scan rates. This is consistent with the ultra-low capacity displayed by the $MoWSe_2$/C electrode in the EC/DMC system. Further, as in Figure 4.23c, the dominant behavior of the reaction kinetics is revealed by fitting the slope relationship (b value) between peak current and scan rate. By the calculation of Equation (3.5) and Equation (3.6), the b values of the cathodic and anodic in the DME system are 0.880 and 0.945, which are both close to 1, representing pseudocapacitance-dominated electrochemical processes. On the contrary, the b values

in the EC/DMC system are 0.434 and 0.304, representing the insertion behavior. Furthermore, the detailed proportions of the pseudocapacitance contributions in the two electrolyte systems are calculated by Equation (3.7), respectively (Figure 4.23d). Among them, the pseudocapacitance proportions of the $MoWSe_2$/C electrode in the DME system are 79.6%, 83.4%, 86.4%, 89.0%, 91.8%, and 96.6% from 0.1 to 5 mV s^{-1}, which are much higher than those of the EC/DMC system, implying a fast response with solid surface effect excitation.

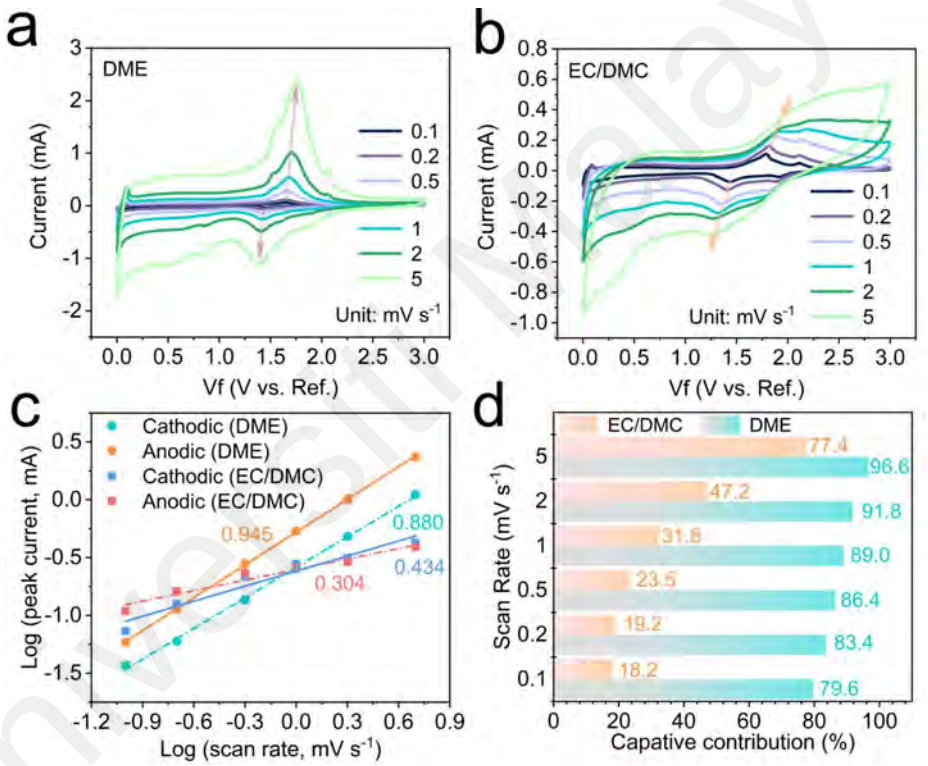

Figure 4.23: CV curves at different scan rates of $MoWSe_2$/C electrode in SIBs: (a) DME electrolyte and (b) EC/DMC electrolyte. (c) Linear diagrams of log (v) and log (i) corresponding to peak currents in different oxidation and reduction states of $MoWSe_2$/C electrode in DME and EC/DMC electrolytes. (d) Contribution ratio of the pseudocapacitance at different scan rates in DME and EC/DMC electrolytes.

EIS is further characterized to measure the kinetics processes of the $MoWSe_2$/C electrode in the DME system. From the Nyquist curves in Figure 4.24a, the semicircle diameters of the medium-high frequencies gradually decrease with cycling, implying

the smaller contact and charge transfer resistance of the electrodes. This is caused by the generation of more exposed heterogeneous interfaces during constant activation process. The line slope (D value) in the low-frequency region is related to the solid phase diffusion of Na^+ within the active material. The D value can be calculated by fitting the linear relationship between $\omega^{-1/2}$ and Z'. By the calculation of Equation (3.2) and Equation (3.3), the D value after cycling is much smaller than the initial state (Figure 4.24b), representing that the activation can contribute to achieving a rapid Na^+ transfer in the electrode interior.

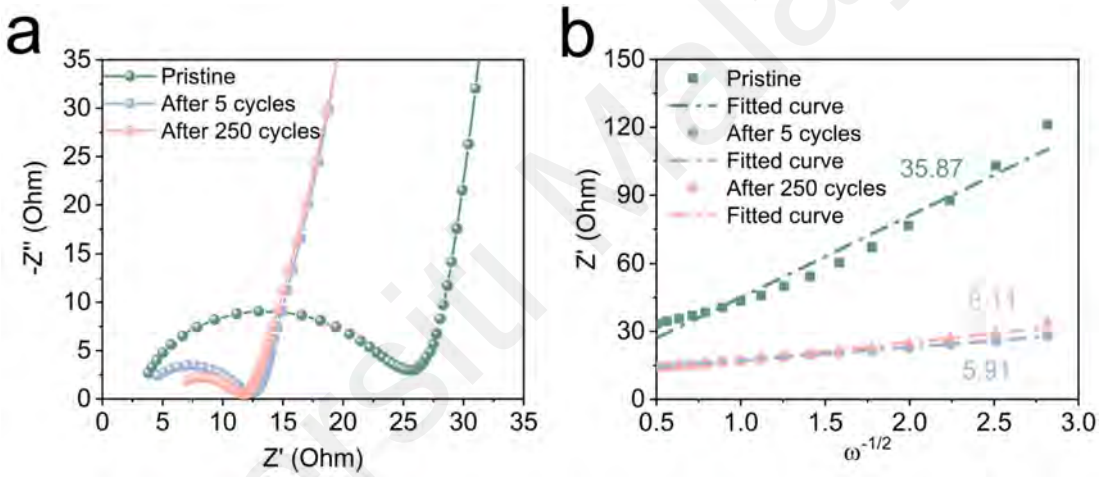

Figure 4.24: (a) Nyquist plots of $MoWSe_2$/C electrode at pristine, 5, and 250 cycles. (b) Relationship between Z' and $\omega^{-1/2}$.

The GITT is also applied to measure the interior Na^+ diffusion coefficients. As in Figure 4.25a, the relaxation processes of the $MoWSe_2$/C, $MoSe_2$/C, and WSe_2/C electrodes at a constant current can be calculated. A detailed graphical description of the parameters in a single pulse process is depicted in Figure 4.25b. By the calculation of Equation (3.4), the Na^+ diffusion coefficient ($\log D_{Na^+}$) in the $MoWSe_2$/C electrode is consistently above -12, significantly better than that of the $MoSe_2$/C and WSe_2/C electrodes. This suggests that the $MoWSe_2$/C heterostructure can effectively improve

the ion diffusion efficiency within the bulk phase.

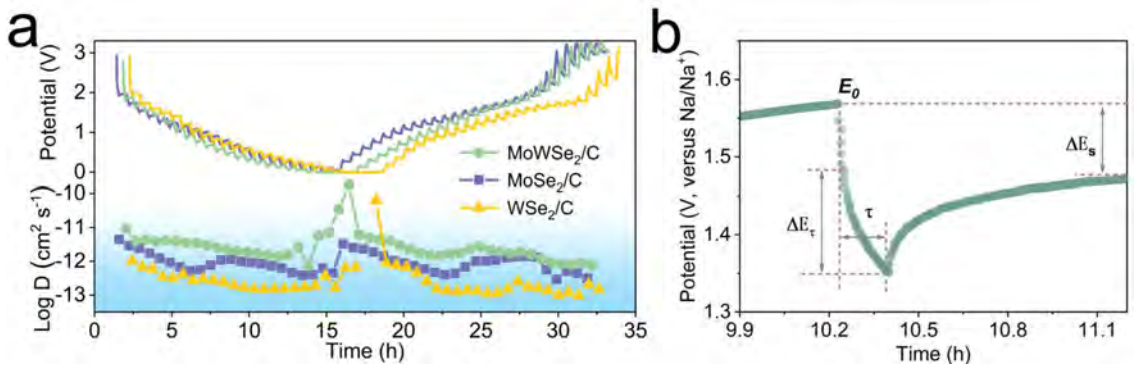

Figure 4.25: (a) GITT and Na^+ diffusion coefficients of $MoSe_2$, WSe_2, and $MoWSe_2$/C electrodes in DME electrolyte. (b) A detailed graphical description of the parameters in a single pulse process.

4.2.6 Electrolyte Selection and Matching

In previous electrochemistry, apart from the application of advanced structural designs, the electrolyte significantly affects sodium storage capacity. From the electrode SEM images in pristine, DME electrolytes (after 50 cycles), and EC/DMC electrolyte (after 50 cycles) in Figure 4.26, the pristine electrode displays a traditional assembly cross-linked nanosheets morphology and compact electrode interface (Figure 4.26a). With the cycling proceed, the $MoWSe_2$/C electrode reacts with ether-based molecules in the DME electrolyte and gradually evolves into a porous bulk structure with a stable SEI coating (Figure 4.26b). The passivated SEI layer can provide an adequate safeguard against the collapse of the electrode structure during the cycling process. Meanwhile, the evolved porous structure can alleviate the anodic residual stresses during the charging process, thus reducing the diffusion limitation and shortening the Na^+ diffusion distance. As can be seen from the SEM image of the electrode cross-section in the inset of Figure 4.26b, no significant exfoliation occurs in the DME electrolyte, corroborating the stability of the electrode process. Oppositely, The $MoWSe_2$/C electrode cycled in the

EC/DMC electrolyte continuously forms an unstable SEI layer and experiences inevitable volume changes, leading to the further fragmentation of large $MoWSe_2$/C particles into dispersed small-sized nanoparticles. The substantial physical and electrical isolation among dispersed small nanoparticles results in a sharp decrease in anode capacity and cycle life. Additionally, the obvious cracks exhibited in the inset of Figure 4.26c also verify the gradual detached behavior of the active material during repeated expansion/contraction processes.

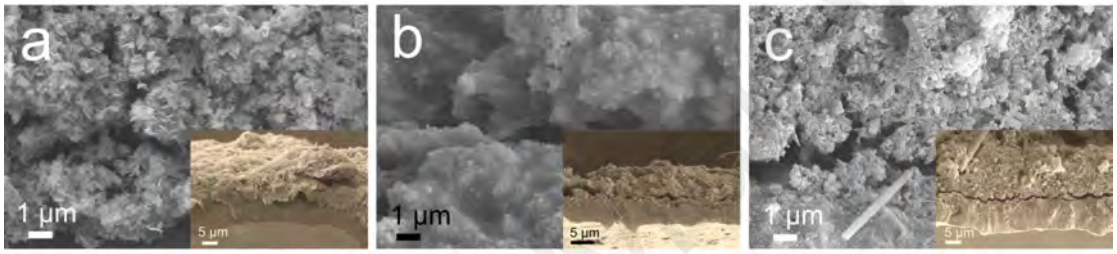

Figure 4.26: (a-c) The $MoWSe_2$/C electrode SEM images in the pristine, DME, and EC/DMC electrolytes (the insets are the corresponding cross-section of the electrodes).

Figure 4.27 employ EDS mapping to reveal the elemental distribution of the electrode cross sections in the initial state, DME, and EC/DMC electrolytes, respectively. Compared to the initial electrode (Figure 4.27a), the cross-section of the electrode in the DME electrolyte (Figure 4.27b) presents a homogeneous elemental distribution (Mo, W, Se, and C), implying that the activation process can activate more heterogeneous interfaces by promoting further mixing of elements. Furthermore, Na, P, F, and C are uniformly dispersed on the surface of the electrodes, revealing an anion-derived organic/inorganic SEI layer produced by oligomer reduction in ether-based solvents. (P. Song et al., 2023) The formed SEI layer can accommodate large deformations during charging/discharging under excellent mechanical elasticity. However, as shown in

Figure 4.27c, the $MoWSe_2$/C electrode in EC/DMC electrolyte exhibited sparse active substance loading after cycling, and lots of tiny needle-like dendrites appeared, which can be attributed to the inhomogeneous deposition and growth of Na dendrite during repeated insertion/deinsertion process. Na dendrite formation primarily results from surface irregularities and numerous protrusions caused by the repetitive expansion of the unstable SEI layer and continuous fragmentation of the active material. At these protrusions, there is an increasing accumulation of electronic charge distribution, consequently attracting more Na^+ ions to deposit. (Dong et al., 2021)

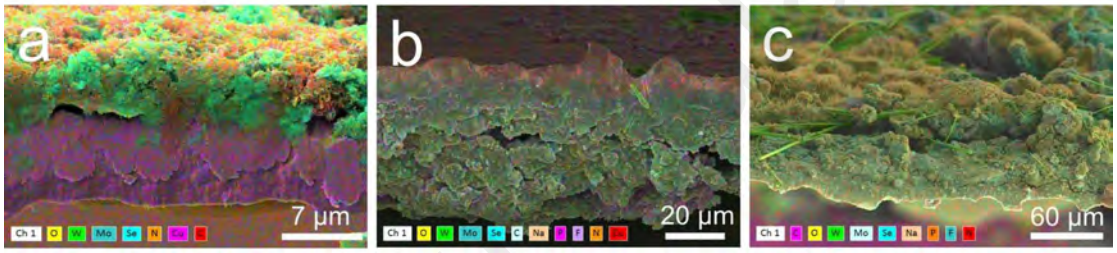

Figure 4.27: Elemental mapping images of the $MoWSe_2$/C electrodes' cross sections in the initial state (a), DME (b), and EC/DMC (c) electrolytes.

To more clearly compare the exfoliation of the active material in the two electrolytes, Figure 4.28a, b compares the physical photograph of the cycled separator on the electrode side. Apparently, little exfoliation occurred on the electrode side of the diaphragm in DME relative to the EC/DMC electrolyte, representing the excellent structural stability of the $MoWSe_2$/C electrode in DME. Additionally, the EDS mapping images of the electrode side separators are tested under different electrolyte systems (Figure 4.28c and Figure 4.28d). It can be seen that the separation of part of active material is monitored in the EC/DMC system, while it is not found in the DME system.

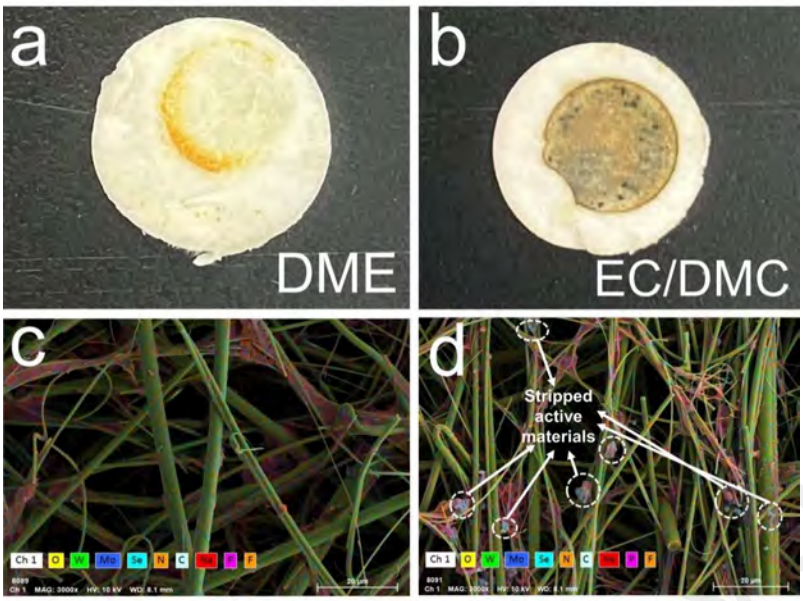

Figure 4.28: The physical photograph of the cycled separator on the electrode side: DME electrolyte (a) and EC/DMC electrolyte (b). The elemental mapping images of the electrode side separator in DME electrolyte (c) and EC/DMC electrolyte (d).

To further reveal the evolution of SEI on the electrode surface in the DME and EC/DMC electrolyte systems, XPS is performed on the electrode surface in the initial state and after 50 cycles, respectively. As shown in the C 1s high-resolution spectra in Figure 4.29a, both cycled electrode surfaces exhibit varying shifts toward lower binding energies, representing the generation of SEI structures. Differently, the offset of C 1s in the DME system is more prominent, representing more charge transfer during the SEI evolution process, favoring the form of a more stable SEI layer. (Hua et al., 2023) Besides, the deconvolution peak located at 289.4 eV can be attributed to the O-C=O organic carbonate, which mainly originates from the decomposition of DME, EC, and DMC. (X. Du et al., 2022) For the O 1s spectra in Figure 4.29b, C=O, C-O-C, RO-Na, and Na russet peaks were identified in both the DME and EC/DMC systems, corresponding to Na_2CO_3, RCH_2ONa, and ROCOONa on the surface of the $MoWSe_2$/C anode in the electrolyte, respectively. (C. Zhang et al., 2020) Distinctly, the positions of

the peaks after cycling all tend to shift towards higher binding energies relative to the initial state electrodes, representing an electron-receiving behavior during SEI formation, which corresponds to the results of C 1s. Notably, to the best of our knowledge, the RCH_2ONa content can promote rapid Na^+ transport, thus the highest RCH_2ONa content in the DME system is favorable for interfacial stability. (Chenchen Wang et al., 2017) Considering the crucial role of F-related products, the F 1s orbital is analyzed in detail, as shown in Figure 4.29c. Obviously, the characteristic peaks located at 684.4 and 687.6 eV monitored in the DME system are attributed to Na-F (NaF) and P-F (Na_xPF_y/Na_xPOF_y), respectively. (Cheng et al., 2023) However, in the EC/DMC system, the Na-F peak is almost undetectable due to localized electron accumulation and anion repulsion induced by the uneven and delaminated SEI layer formation. Furthermore, the relative study demonstrated that the uniformly distributed NaF and organic components can promote the generation of a stable electrode/electrolyte interface, thus accelerating the Na^+ rapid diffusion in the SEI layer. (Z. Tang et al., 2022) By comparing the high-resolution Se 3d spectra of $MoWSe_2$/C electrode in DME and EC/DMC (Figure 4.29d), peaks of Se $3d_{5/2}$ and Se $3d_{3/2}$ are monitored in the DME electrolyte, representing that Se^{2-} remains constant during the conversion process. Comparatively, the characteristic peaks about Se are not found in the EC/DMC electrolyte system, representing that Se^{2-} participates in the conversion reaction and generates small-sized polyselenides to undergo a shuttling effect, which further leads to a sharp capacity decay. (Lu et al., 2021) It can be seen that the DME electrolyte system facilitates the inhibition of the oxidation process of Se^{2-} and the formation of a stable SEI layer to prevent the shuttling of Na_2Se_x.

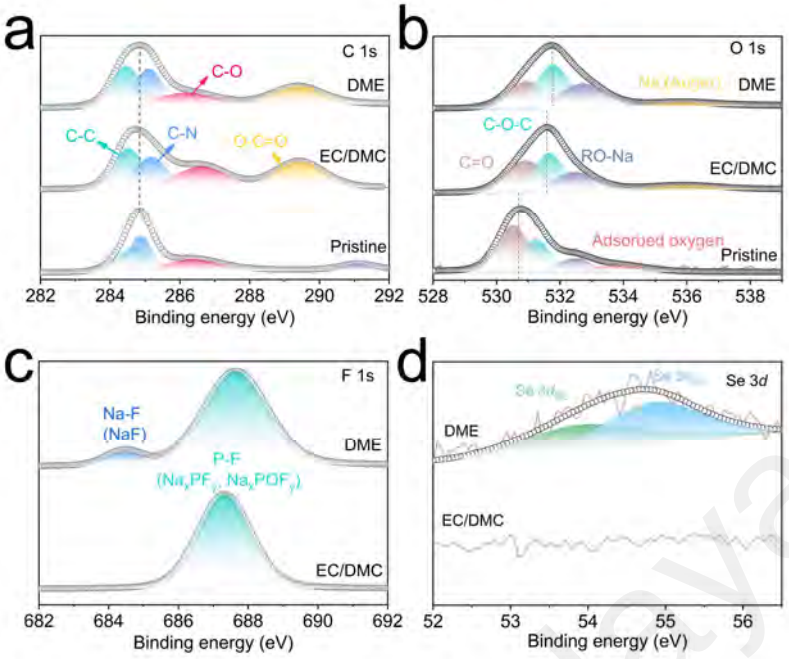

Figure 4.29: High-resolution C 1s (a), O 1s (b), F 1s (c), and Se 3d (d) XPS spectra of $MoWSe_2$/C electrode in the pristine, DME, and EC/DMC electrolytes.

To further evaluate the stability of the SEI layer formed in DME and EC/DMC electrolytes, the highest occupied molecular orbital (HOMO) and lowest unoccupied molecular orbital (LUMO) energy levels of the salts and solvents in the two electrolytes are calculated by employing the frontier molecular orbital theory. Typically, the HOMO energy level is associated with the electrolyte oxidation reaction occurring on the electrode surface, while the LUMO energy level corresponds to the reduction process. (G. Li et al., 2022) Therefore, the LUMO energy level is crucial for studying the SEI formation process. The LUMO and HOMO values for DMC, EC, DME, and $[PF_6]^-$ in the two electrolytes are calculated in Figure 4.30a, respectively. Among them, the LUMO value of DME solvent is 1.517 eV, significantly higher than that of EC (-0.313 eV) and DMC (-0.092 eV), indicating that the DME solvent has better reduction stability. The excellent reduction properties of DME help to prevent the shuttle effect triggered by the oxidative generation of Na_2Se_x from Se^{2-}, which in turn ensures the

structural stability of the $MoWSe_2$/C structure. This is consistent with previous CV (Figure 4.19) and XPS (Figure 4.29d) analyses. Contrastingly, the SEI layer composed of low reduction-stable EC/DMC electrolyte is more easily decomposed, which results in poor cycling stability. Besides, the LUMO energy level of $[PF_6]^-$ is 5.255 eV, which is much higher than that of other solvents, representing that $[PF_6]^-$ will start to decompose after various solvents decompose in constructing SEI. On the other hand, the effect of Na^+ solvation on the stability of solvent molecules should not be neglected. The LUMO energy levels of the Na^+-solvent and Na^+-$[PF_6]^-$ complexes are revealed in Figure 4.30b, respectively. The energy difference between the two energy levels (ΔE=HOMO-LUMO) can be applied to evaluate the electron transfer process from Na^+ to each solvent molecule. A greater ΔE indicates a reduced orbital similarity, thereby rendering the two components less prone to electron transfer during the binding process. (L. Zhou et al., 2020) As a result, the DME system has the largest ΔE, indicating that Na^+ is less likely to react with the solvent during solvation, which in turn prevents the electrolyte failure and ensures the stability of the system.

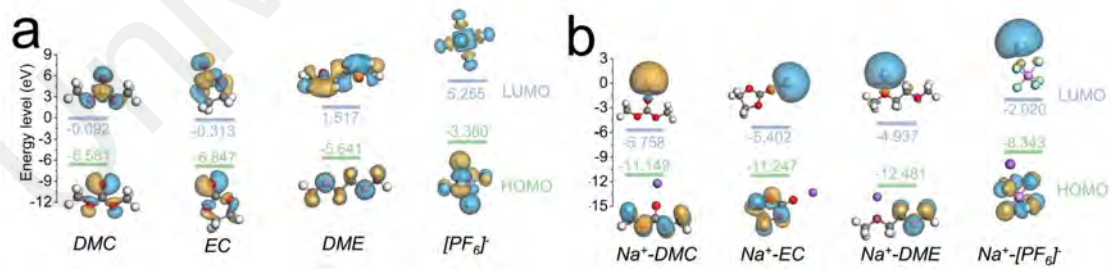

Figure 4.30: (a) The LUMO/HOMO energy level diagram of the solvent molecules and $[PF_6]^-$. (b) LUMO and HOMO of the Na^+-DMC, Na^+-EC, Na^+-DME, and Na^+-$[PF_6]^-$.

Figure 4.31 shows the electrostatic potential maps of solvated Na^+ in DME and EC/DMC electrolyte systems, respectively. The red part represents the negative potential due to the charge accumulation, while the blue represents the positive potential. The charge distribution around Na^+ in the DME system is significantly lighter than in EC/DMC, representing better solvation binding. Meanwhile, the vacant oxygen ions in the DME system have a higher electron density than EC/DMC, implying a stronger solvation capacity for Na^+. (Yanzhou Wu et al., 2023; Yan Zhao et al., 2023) Based on the previous analysis, we predicted a Na^+-solvent-$[PF_6]^-$ based interfacial model to reveal the SEI formation process in different electrolytes.

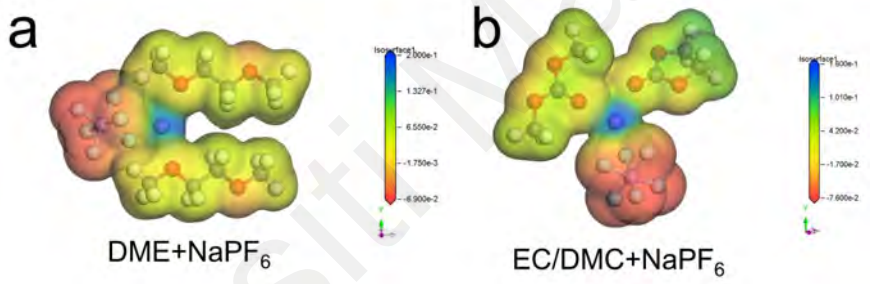

Figure 4.31: Electrostatic potential maps of Na^+ in DME and EC/DMC electrolyte systems.

As shown in Figure 4.32, as the discharge proceeds in the DME electrolyte, due to the high reduction stability (high LUMO value) of DME, Na^+ can accept free electrons from the electrode surface without reverse transfer to the solvent. This can facilitate the formation of an inorganic-rich SEI layer and avoid the continuous depletion of the electrolyte. Comparatively, within the EC/DMC system, the electron transfer induced by the lower LUMO energy level results in an additional electron acquisition by the EC and DMC solvents, leading to their decomposition and subsequent random deposition on the electrode surface. In this process, the continuously generated inhomogeneous and

organic-rich SEI layer can continually deteriorate the electrolyte. This further leads to a drastic capacity decay during cycling, consistent with the electrochemical performance.

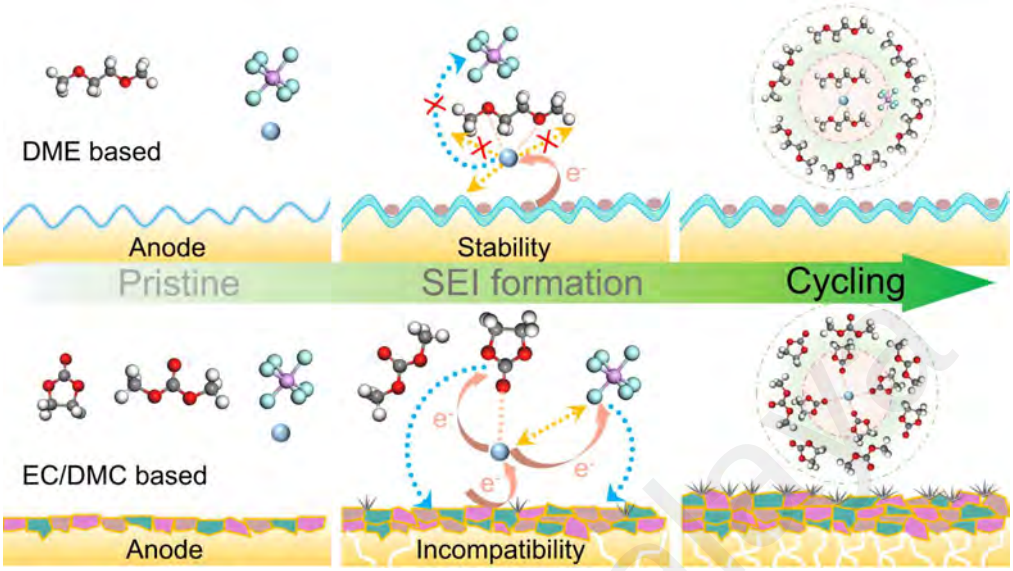

Figure 4.32: Schematic illustration of morphological evolution of the SEI formation process during cycling in DME and EC/DMC electrolytes.

4.2.7 Electrochemical Properties of $MoWSe_2$/C in SICs

To measure the property performance of the $MoWSe_2$/C electrode in SICs, commercial AC is used as the cathode for device assembly. Before that, the electrochemical performance of commercial AC is evaluated using sodium sheets as counter electrodes. The CV profiles of the AC electrode at different scan rates are measured from 2.5 to 4.2 V (Figure 4.33a). The CV curves at each scan rate exhibit a rectangular-like shape, verifying the dual-layer capacitor mechanism of AC. The GCD profiles of the AC electrode display a linear pattern at different current densities, again exhibiting the characteristics of a double-layer capacitor. In addition, the AC electrode delivers a reversible specific capacity of 59.8 mA h g^{-1} at a current density of 100 mA g^{-1} (Figure 4.33b). The long cycling performance of AC electrode is evaluated at 100 mA g^{-1}, and the result delivers a specific capacity of 40.8 mA h g^{-1} after 960 cycles

(Figure 4.33c).

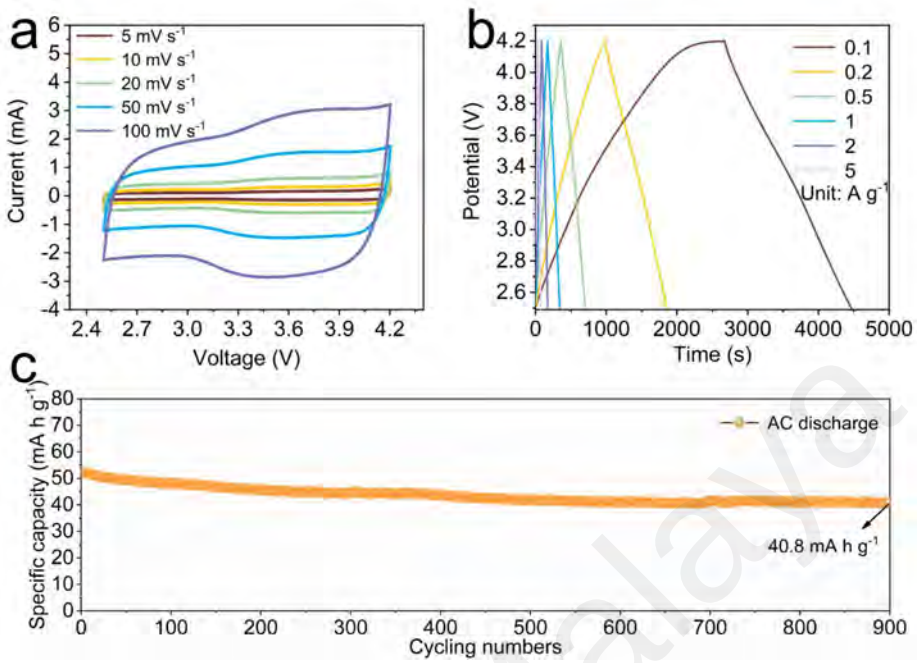

Figure 4.33: Electrochemical performance of AC: (a) CV curves at different scan rate, (b) GCD profiles at different rate, (c) long cycling performance at 100 mA g^{-1}.

To determine the maximum voltage limit for assembling SICs to perform better electrochemically, CV tests were performed at a scan rate of 10 mV s^{-1} over the voltage ranges of 0−3.6, 0−3.8, 0−4.0, and 0−4.2 V, respectively (Figure 4.34a). In general, a higher voltage limit represents a higher energy density that can be utilized by the device. From the results, when the voltage is higher than 3.8 V, there is a sharp peak at the upper voltage limit, which is brought about by the occurrence of a large polarization. (Ba et al., 2022) Therefore, 0−3.8 V is considered the best voltage range. Subsequently, as shown in Figure 4.34b, the electrode process is further reflected by the CV profiles at different scan rates from 0 to 3.8 V. As the scan rate increases, the CV profiles remain approximately constant, representing a stable electrochemical process. Additionally, the CV profiles exhibit rectangular-like shapes, and some redox peaks appeared, representing the combination of electrical double layer and pseudocapacitive storage

mechanisms. As shown in Figure 4.34c, the GCD curves tested at 0.2, 0.5, 1, and 2 A g^{-1} (corresponding to 380, 950, 1900, 3800 W kg^{-1}) exhibit the energy densities of 197.81, 188.81, 120.86, and 96.06 W h kg^{-1}, respectively. The long-term cycling capability of the assembled device was further measured at a current density of 3800 W kg^{-1} (Figure 4.34d). After up to 11,000 cycles, the obtained SIC still retained ~80% capacity retention, revealing the ultra-long cycling stability.

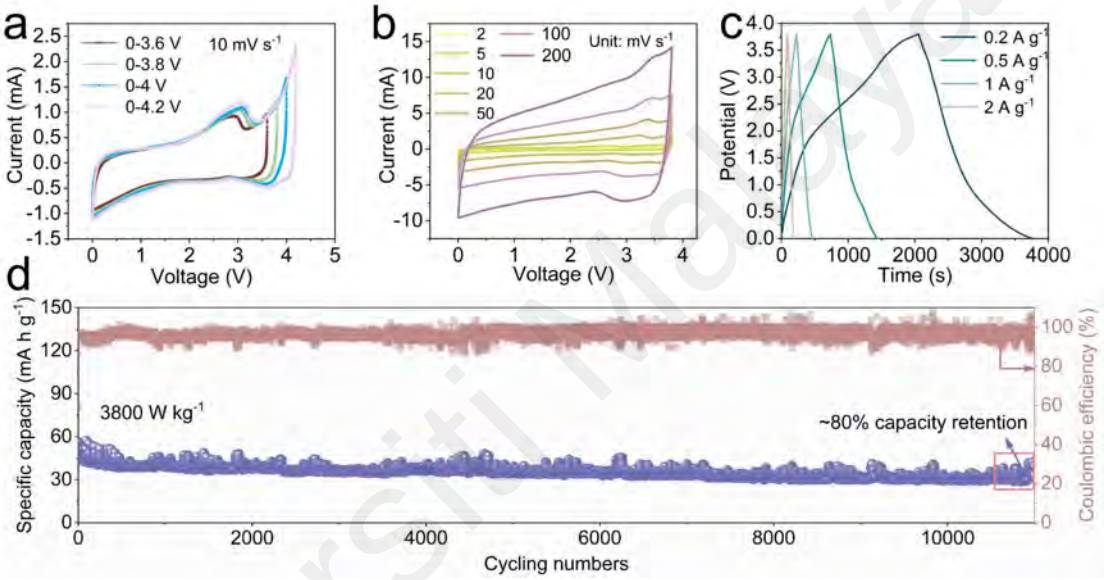

Figure 4.34: Electrochemical performance of $MoWSe_2$/C in SICs. (a) CV curves at different cut-off potentials. (b) CV curves at different scan rates, (c) GCD profiles of $MoWSe_2$/C//AC. (d) Cycling stability and coulombic efficiency of $MoWSe_2$/C//AC at 3800 W kg^{-1} for 11,000 cycles.

4.3 MOF-derived $MoWSe_2/WO_3$/C Composites

In this section, we construct the Mo/W-MOF with a core-shell structure, where the core and shell are W-MOF and Mo-MOF, respectively. Subsequently, the transformation of Mo/W-MOF precursors to $MoWSe_2/WO_3$/C is completed in the process of selenization and carbonization. Based on the selenization growth of Mo-MOF and the partial selenization of W-MOF, the structure changed from core-shell to core-shell petal like curled nanosheets. By DFT calculations, the obtained $MoWSe_2/WO_3$/C

heterostructure exhibit excellent electronic conduction and enlarged layer distance, facilitating the efficient Na^+ transfer.

4.3.1 Synthesis of $MoWSe_2/WO_3/C$

As shown in Figure 4.35, a solvent-assisted method combined with a conventional sintering strategy is used to obtain $MoWSe_2/WO_3/C$. First, ammonium molybdate is uniformly dispersed in deionized water, followed by adding WCl_6 under vigorous stirring. In this process, the combination of W^{6+} with oxygen in water triggers a strong hydrolysis reaction and releases large amounts of HCl. Subsequently, adding trimesic acid and L-serine mixed solution provides effective organic ligands. In this process, W^{6+} further binds O in trimesic acid and self-assembles into a spherical W-MOF structure in the presence of L-serine. Meanwhile, Mo ions and organic ligands are coordinated and form Mo-MOF shells on the acid-rich surface of W-MOF with L-serine vicinity. After that, a core-shell structure Mo/W-MOF composed of the external Mo-based MOF and the internal self-assembled W-based MOF was formed. Finally, the selenium powder and Mo/W-MOF are placed in the upstream and midstream positions of the tube for further sintering to achieve the simultaneous selenization and carbonization process. The internal W-MOF is transformed into WO_3/C, and a small amount of WSe_2 is formed on the surface. Meanwhile, the Mo-MOF shell evolved into $MoSe_2/C$ with petal-like curled nanosheets by selenization and carbonization.

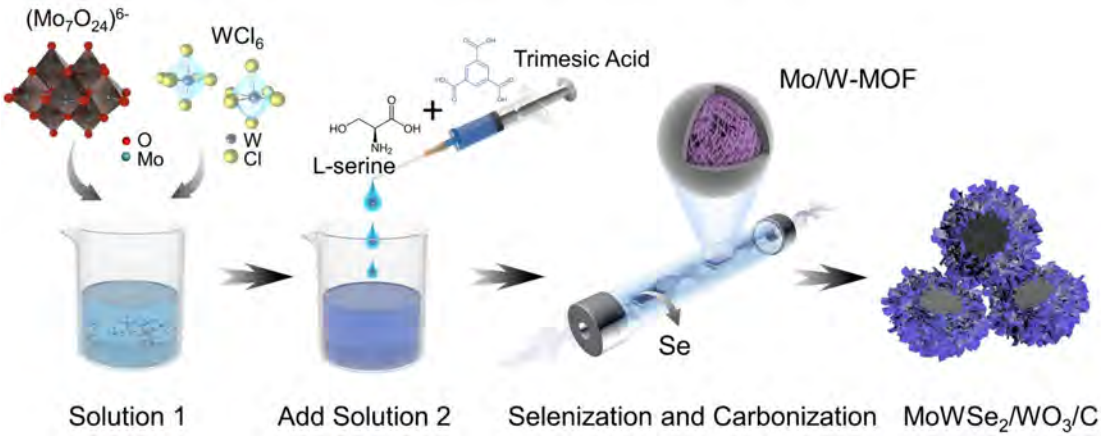

Figure 4.35: (a) Schematic illustration of the synthetic route for $MoWSe_2/WO_3/C$.

4.3.2 Structural and Chemical Characterization of $MoWSe_2/WO_3/C$

SEM revealed the microscopic morphology of Mo/W-MOF precursor. The SEM image in Figure 4.36a demonstrates the basics morphology of Mo/W-MOF at different scales, where the overall spherical morphology is distributed. The section results in Figure 4.36b shows the apparent core-shell structure, where the internal structure is the self-assembled Mo-based nanosheets and the external shell layer is a cross-linked structure formed by W and organic ligands.

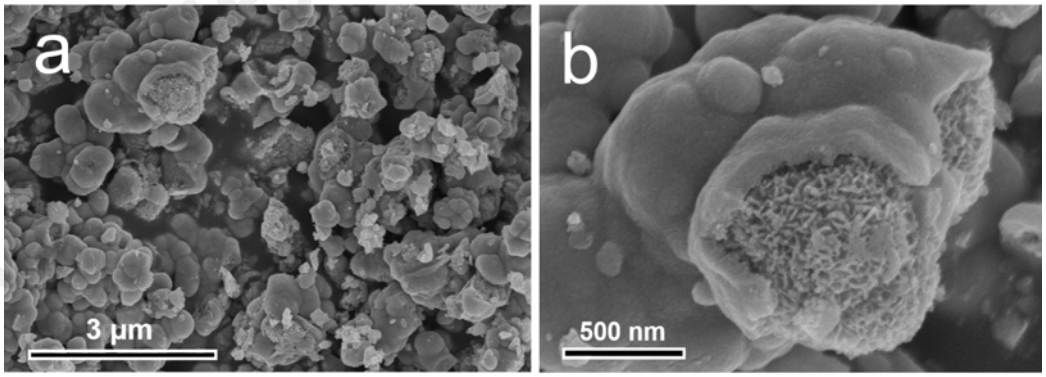

Figure 4.36: SEM images of Mo/W-MOF at different magnification.

The elemental mapping of the core-shell Mo/W-MOF precursor shown in Figure 4.37 indicates that the apparent Mo-MOF is concentrated in the outer shell (green), while W-MOF dominates the interior core (red). In addition, C, and N are uniformly distributed

in the spherical region, indicating the formation of MOF structures. It is worth noting that the presence of O is brought about by the unavoidable oxidation of the sample surface on the one hand, and by the incomplete selenization of WO_3 on the other hand.

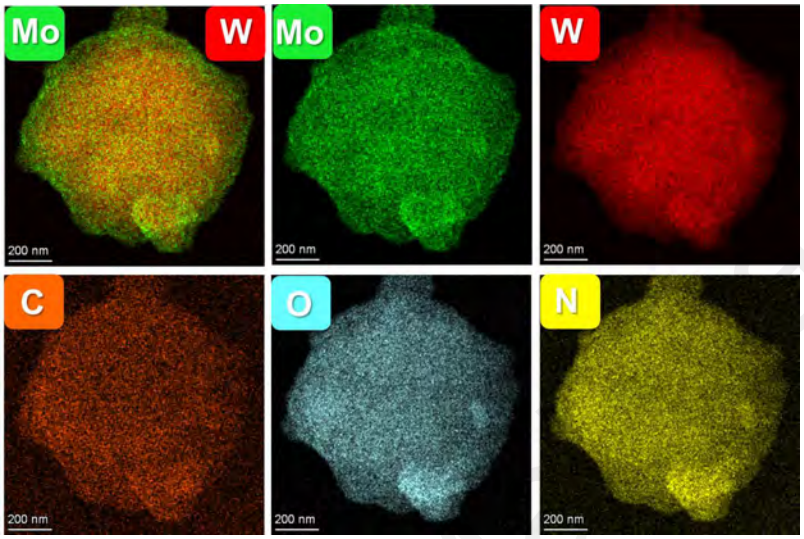

Figure 4.37: The elemental mapping images of Mo/W-MOF precursor.

SEM characterization of the final product $MoWSe_2/WO_3/C$ samples (Figure 4.38) reveals that the overall morphology developed from round core-shell structure to core-shell petal-like curled nanosheets after high-temperature annealing and selenization reaction. The surface of Mo-MOF shell is further extended outwardly with the selenization reaction, forming $MoSe_2/C$ petal-like curled nanosheets, surrounding the clusters of small particles in the center (WO_3/C). Remarkably, small upright flakes are observed in the transition region from the center to the peripheral petals, attributing to WSe_2 generated by partial selenization of WO_3. SEM images of the prepared $MoSe_2/C$ and WO_3/C monomers are also supplemented to reveal the formation process of $MoWSe_2/WO_3/C$.

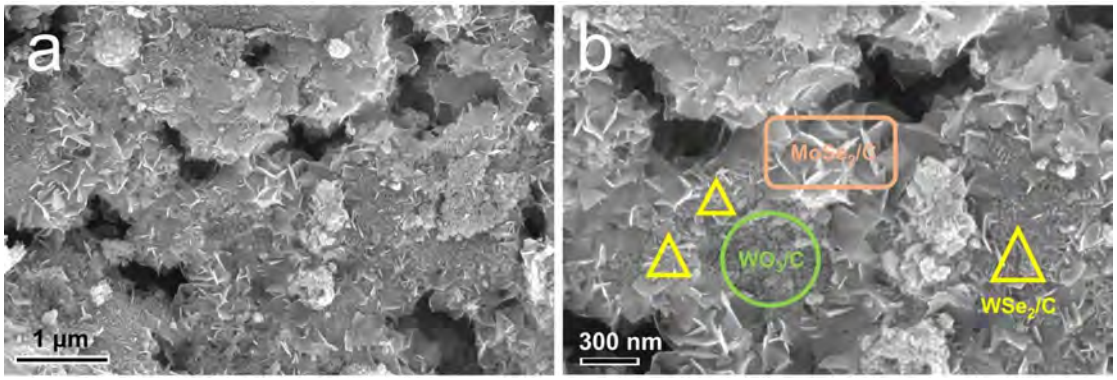

Figure 4.38: SEM images of $MoWSe_2/WO_3/C$ at different magnification.

From the elemental mapping of $MoWSe_2/WO_3/C$ in Figure 4.39, Mo and Se elements are highly uniformly distributed in the outer shell-nanosheet region, while W and O elements are also uniformly distributed in the central area surrounded by nanosheets. It indicates a complementary distribution of $MoSe_2$ and WO_3. Besides, the faint W and Se elements are detected around the WO_3/C, representing the formation of WSe_2 on the core surface.

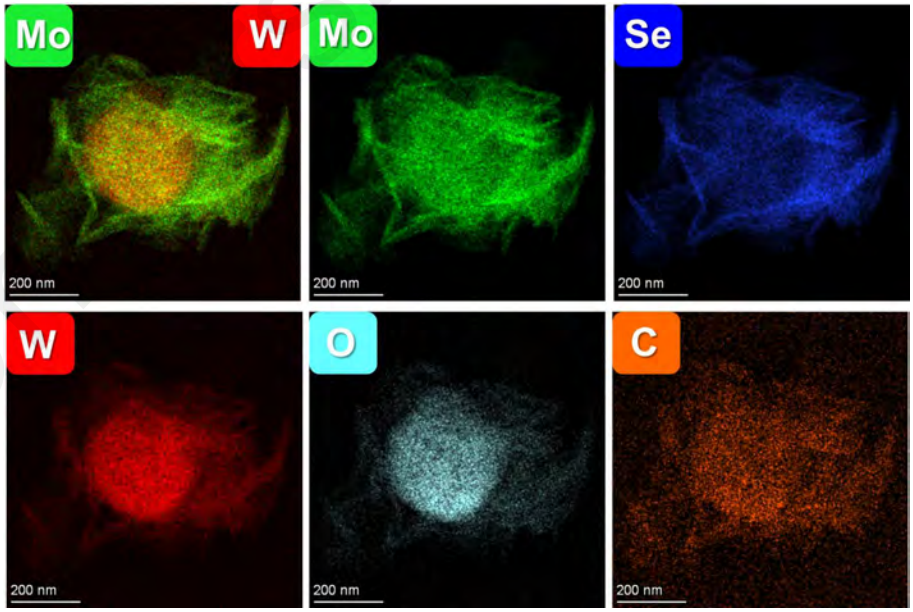

Figure 4.39: The elemental mapping of $MoWSe_2/WO_3/C$.

The atomic percentage information of $MoWSe_2/WO_3/C$ by the EDS is shown in Figure 4.40, where the atom ratios of C, N, O, Se, W, and Mo are about 28.46%, 0.73%,

35.38%, 14.19%, 14.77%, and 6.47%, respectively. O is less than three times that of W, representing a partial conversion of WO_3 to WSe_2.

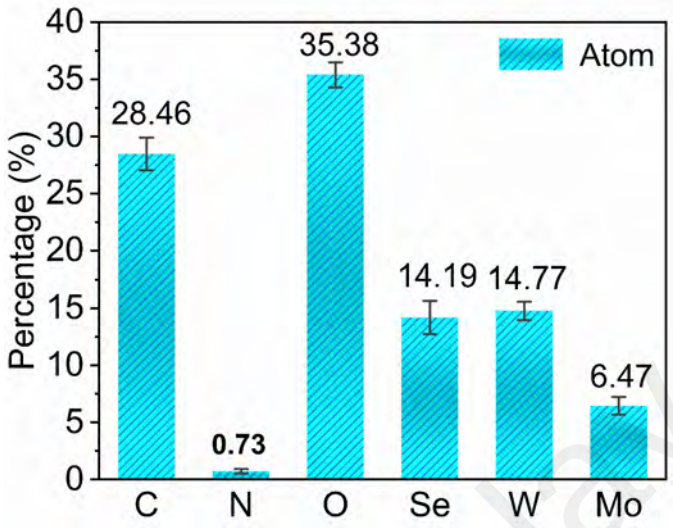

Figure 4.40: The element content analysis in atomic percentage of $MoWSe_2/WO_3/C$ by EDS.

In order to confirm the morphological composition and structural distribution of the $MoWSe_2/WO_3/C$ samples, SEM tests are performed on $MoSe_2/C$ and $WSe_2/WO_3/C$ monomers, respectively. Figure 4.41a reveals that $MoSe_2/C$ has a bent self-assembled bulk structure. In Figure 4.41b, the bulk small particle clusters in the center are $WSe_2/WO_3/C$, where the surface displays the partially selenized WSe_2 in a vertical small nanoflakes structure. This is consistent with the SEM analysis of $MoWSe_2/WO_3/C$.

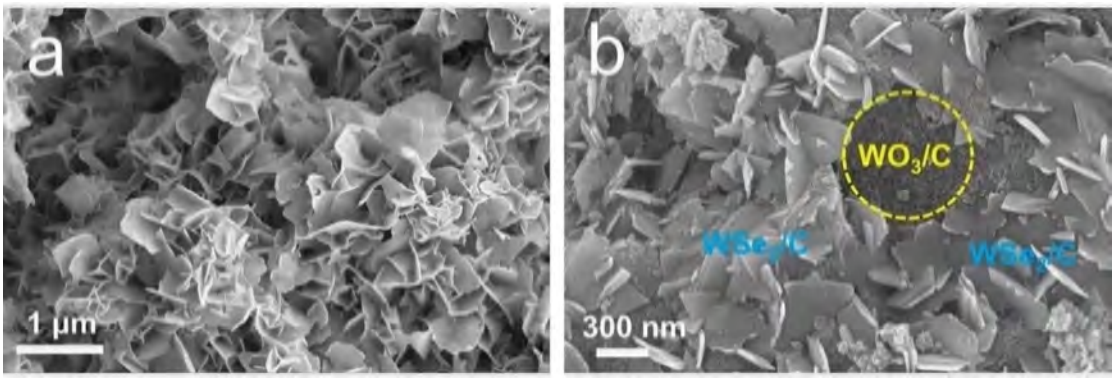

Figure 4.41: SEM images of $MoSe_2/C$ and $WSe_2/WO_3/C$ monomers.

For further comparison, the elemental mapping images of $MoSe_2$/C is carried out as shown in Figure 4.42. Obviously, C, N, O, Mo, and Se show a uniform distribution, revealing the successful synthesis of $MoSe_2$/C. Remarkably, the presence of a small amount of O is monitored in the mapping image, suggesting unavoidable oxidation of the material surface.

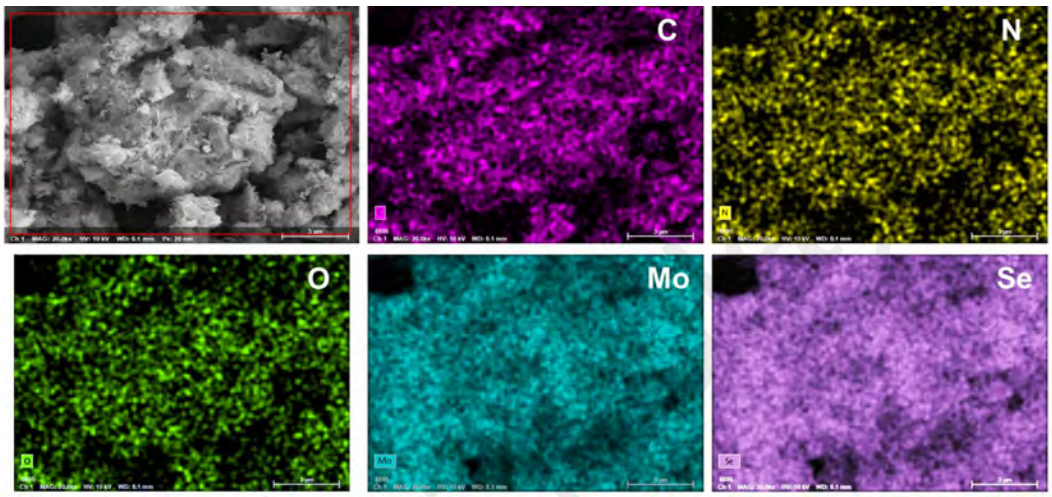

Figure 4.42: Elemental mapping of $MoSe_2$/C.

Furthermore, the EDS test is performed on the synthesized $MoSe_2$/C in Figure 4.43. Consequently, the atomic occupancies of C, N, O, Se, and Mo are 32.29%, 3.32%, 2.74%, 39.46%, and 22.10%, respectively. Se atomic occupancy is approximately two times that of Mo, representing the synthesis of active $MoSe_2$, which is consistent with the analytical results of elemental mapping. Additionally, a tiny amount of adsorbed oxygen indicates the complete conversion to $MoSe_2$.

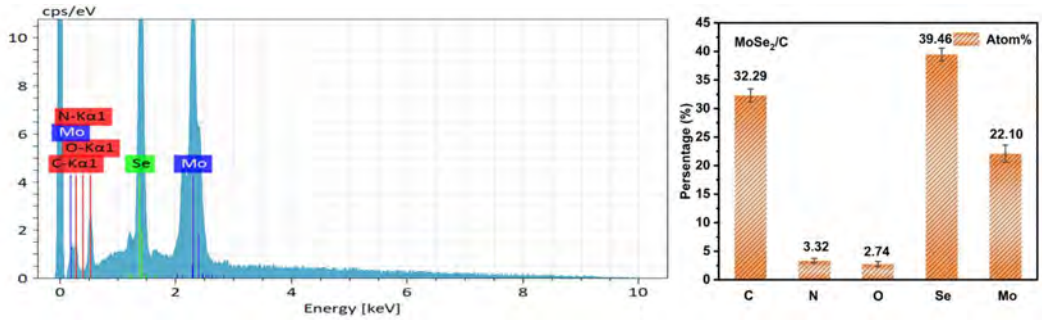

Figure 4.43. EDS element content analysis of $MoSe_2$/C.

Similarly, the elemental mapping diagram of $WSe_2/WO_3/C$ is further revealed in Figure 4.44. The simultaneous presence of Se and O indicates that the partial conversion of WO_3 to WSe_2 trend is accomplished at the setting calcination temperature. This also provides a plausible explanation for the simultaneous presence of WO_3 to WSe_2 multiphase structures in $MoWSe_2/WO_3/C$ composites.

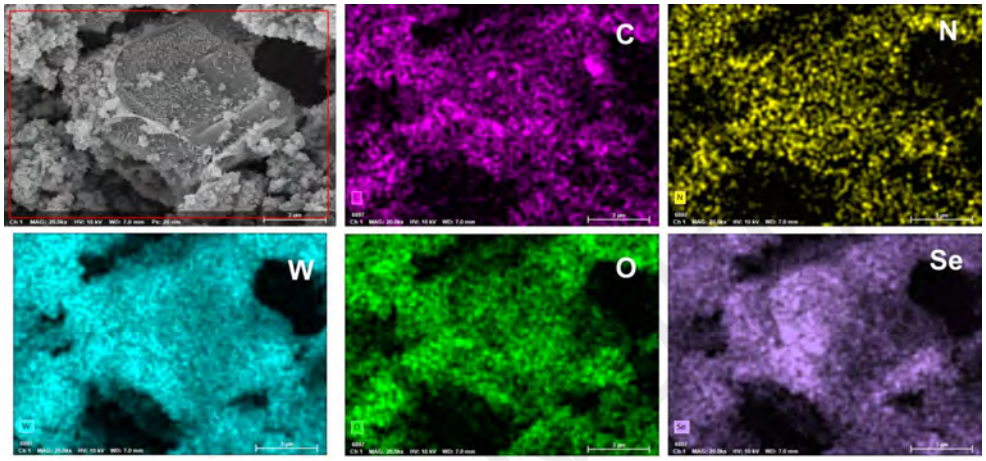

Figure 4.44: Elemental mapping of $WSe_2/WO_3/C$ sample.

The EDS elemental content of $WSe_2/WO_3/C$ is analyzed as shown in Figure 4.45. The atomic contents of C, N, O, Se, and W were 33.12%, 1.94%, 38.54%, 8.22%, and 18.17%, respectively. The content of carbon elements is around 30% in $MoWSe_2/WO_3/C$, $MoSe_2/C$, and $WSe_2/WO_3/C$, revealing the distributed content of carbon introduced by this MOF derivation strategy. In addition, Se of about 8.22% is observed in $WSe_2/WO_3/C$, which further verified that partial WSe_2 would be generated on the surface of WO_3 during the selenization process.

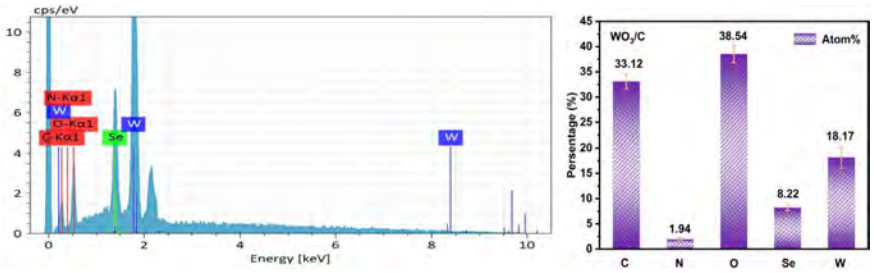

Figure 4.45: EDS element content analysis of $WSe_2/WO_3/C$.

The obtained $MoWSe_2/WO_3/C$ powders are verified using TEM characterization, as shown in Figure 4.46a. To further analyze the composition of $MoWSe_2/WO_3/C$, the HRTEM in Figure 4.46b reveals the lattice spacing of the surface are about 0.646 and 0.649 nm, which can be attributed to the (0 0 2) and (2 0 1) crystal planes of WSe_2 and $MoSe_2$, respectively. An enlarged interlayer distance of 0.677 nm is monitored at the junction of the two phases of $MoSe_2$ and WSe_2, representing the formation of the $MoWSe_2$ heterostructure. Furthermore, the lattice spacing of 0.268 nm is depicted in the internal bulk, which can be indexed to the (0 2 1) crystal plane of WO_3.

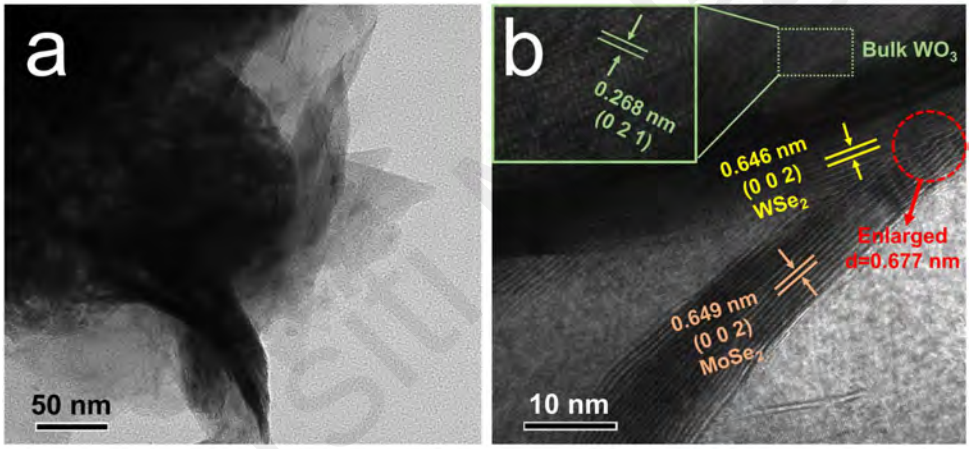

Figure 4.46: (a) TEM diagrams of $MoWSe_2/WO_3/C$. (b) HRTEM diagram of $MoWSe_2/WO_3/C$.

The XRD pattern in Figure 4.47 demonstrates a typical three-phase structure in the obtained $MoWSe_2/WO_3/C$. Several significant peaks located at 23.0°, 23.7°, 24.1°, and 34.0° can be indexed to the orthorhombic WO_3 (JCPDS No. 20-1324), while those at 13.6°, 31.5°, 37.8°, and 47.1° are attributed to $MoSe_2$ in hexagonal phase (JCPDS No. 29-0914). In addition, the reduction of surface WO_3 to the WSe_2 phase (JCPDS No. 38-1388) during selenization can be monitored. The favorable crystallinity and relativities verify the formation of the $MoWSe_2/WO_3$ heterostructure.

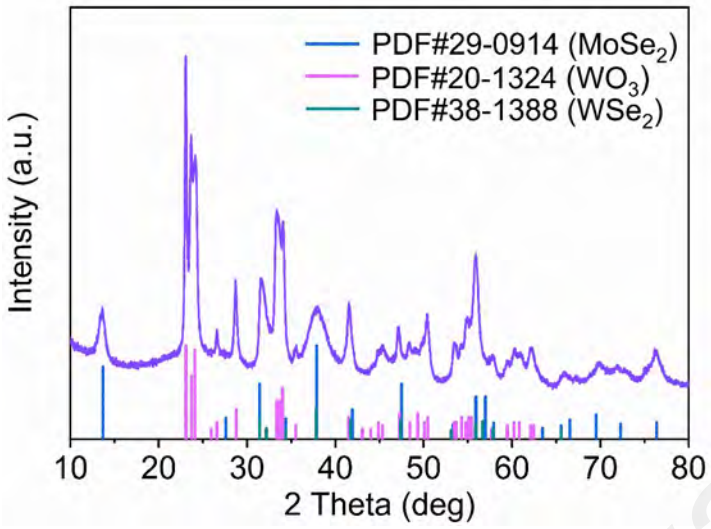

Figure 4.47: XRD pattern of $MoWSe_2/WO_3/C$.

However, there are strong overlapping between WSe_2 and $MoSe_2$ phases leading to further comparative tests on $WSe_2/WO_3/C$ and $MoSe_2/C$ monomers derived from W-MOF and Mo-MOF, respectively. The XRD pattern of $WSe_2/WO_3/C$ monomer is given in Figure 4.48 exhibiting that the WSe_2 phase is also generated at the selected temperatures (600 ℃). Meanwhile, WO_3 exists as a cubic phase (JCPDS No. 46–1096) after structural reorganization when sufficient Se is present, which is different from the orthorhombic WO_3 in Figure 4.47. The different crystal structures of WO_3 in $WSe_2/WO_3/C$ and $MoWSe_2/WO_3/C$ indicate that the presence of $MoSe_2$ can trigger changes in the electronic structure, which laterally demonstrates that the process of heterostructure formation can change the electron distribution.

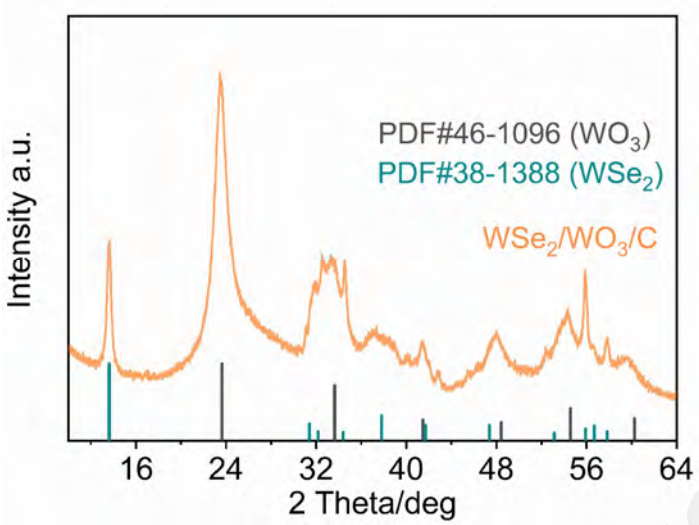

Figure 4.48: XRD pattern of $WSe_2/WO_3/C$.

In addition, XRD tests are performed on the $MoSe_2/C$ monomer to further determine its structural composition. As shown in Figure 4.49, the pure $MoSe_2$ phase is observed without the presence of MoO_2 indicating the complete conversion of $MoSe_2$ in the selenization process. The complete transformation of $MoSe_2$ can be attributed to its low formation energy and the low bond breaking energy of MoO_3.

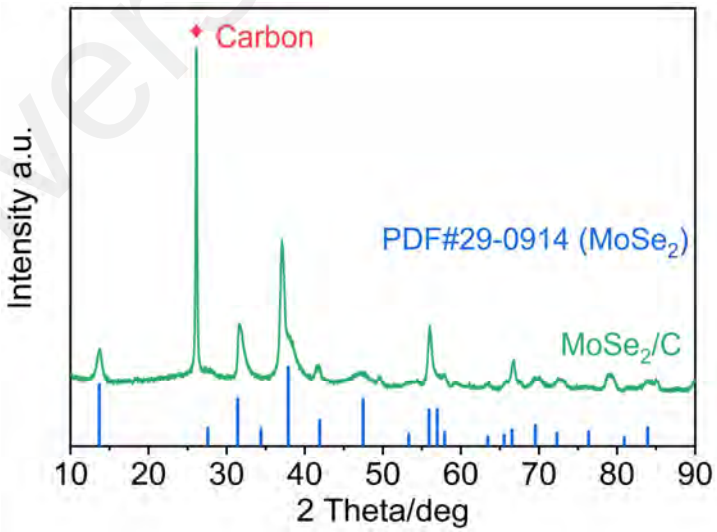

Figure 4.49: XRD pattern of $MoSe_2/C$.

The specific surface area and pore size distribution of the Mo/W-MOF and $MoWSe_2/WO_3/C$ samples are evaluated by the N_2 adsorption/desorption isotherms,

respectively. After high-temperature carbonization/selenization treatment, the W-MOF is further evolving into more primary small particles during sintering process and the expansive growth from Mo-MOF shell to $MoSe_2$ nanosheets. Therefore, the final product exhibits a higher specific surface area (about 22.8 m^2 g^{-1}) than the Mo/W-MOF precursor (Figure 4.50a). The larger specific surface area of $MoWSe_2/WO_3/C$ suggests that the morphological changes brought about by the calcination process help to provide more active sites to facilitate the rapid adsorption of Na^+. In addition, Figure 4.50b reveals the pore size distribution of the Mo/W-MOF precursor and $MoWSe_2/WO_3/C$. It can be seen that $MoWSe_2/WO_3/C$ exhibits more microporous distribution compared to the Mo/W-MOF precursor, which facilitates the rapid filling of Na^+ and thus enhances the fast ion reaction kinetics.

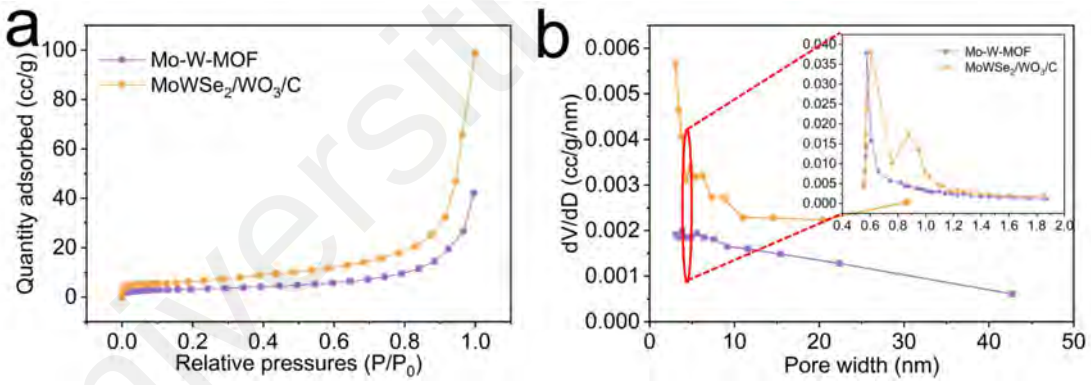

Figure 4.50: N_2 adsorption/desorption isotherm (a) and pore size distributions (b) of Mo/W-MOF and $MoWSe_2/WO_3/C$.

The Raman spectrogram in Figure 4.51a exhibit two firm peaks at 1369 and 1598 cm^{-1}, corresponding to defects caused by sp3 hybridization of carbon atoms (D-band) and graphitization caused by sp2 hybridization (G-band), respectively. The area ratio of the D-band and G-band is calculated (I_D/I_G=3.42), revealing the introduced carbon is dominated by defects. In addition, $MoWSe_2/WO_3/C$, $MoSe_2/C$, and WO_3/C samples are

further subjected to Raman tests in the low range (Figure 4.51b). In $MoSe_2$/C, two peaks are depicted at 235 and 279 cm^{-1} and can be attributed to the A_{1g} vibration and E_{2g} modes of $MoSe_2$. (Xingchen Xie et al., 2020) On the other hand, an E_{2g} mode belonging to WSe_2 is detected in WO_3/C, representing the presence of surface WSe_2. (Chiang et al., 2022) Two peaks located at 700 and 800 cm^{-1} are characterized by the γ(O-W-O) and ν(O-W-O) modes in WO_3. (Bao et al., 2017) All the above characteristic peaks that are observed in the $MoWSe_2/WO_3$/C sample show the formation of a heterogeneous composite structure, in agreement with XRD analysis.

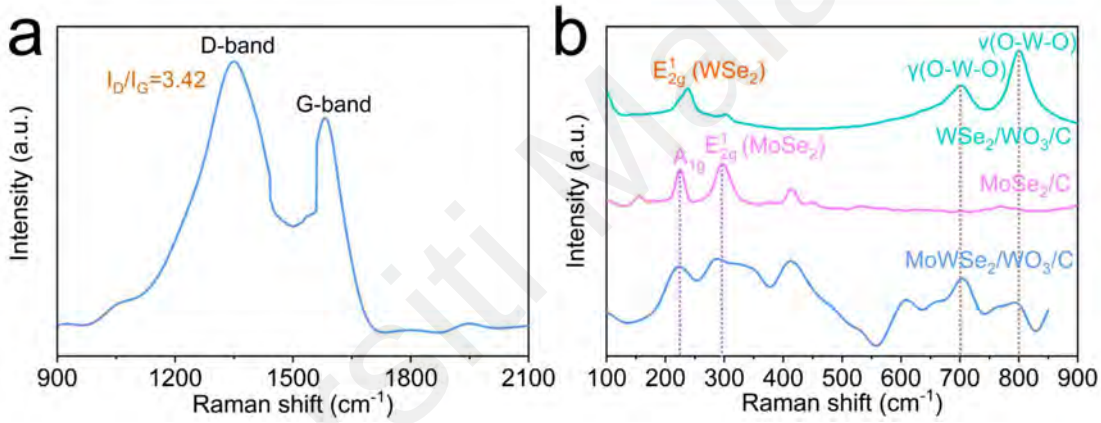

Figure 4.51: Raman spectrogram of $MoWSe_2/WO_3$/C.

XPS is performed to evaluate the valence and content of surface elements on $MoWSe_2/WO_3$/C, $MoSe_2$/C, and WO_3/C. From the high-resolution W 4f spectrum in Figure 4.52a, two significant peaks appear as W $4f_{7/2}$ and W $4f_{5/2}$ due to the spin-orbit coupling of the orbitals. The binding energies at 35.6 and 37.8 eV correspond to the W^{5+} state, while the other peaks at 36.2 and 38.3 eV belong to the W^{6+} state. (X. D. Liu et al., 2021) In contrast, W 4f in the WO_3/C monomer exhibits two additional orbital peaks at low binding energies, suggesting the formation of low valence WSe_2 under sufficient Se reduction. (Zhongchen Zhao et al., 2023) Notably, both samples have more substantial

W^{5+}, which further revealed the reduction of Se at the WO_3 surface. As shown in Figure 4.52b, the high-resolution spectra of Mo 3d in $MoWSe_2/WO_3/C$ and $MoSe_2$ demonstrate the characteristic peaks of Mo $3d_{5/2}$ and Mo $3d_{3/2}$ located at 229.0 and 232.1 eV, respectively. Note that a small peak around 230.1 eV can be attributed to the Mo-C bond, revealing the practical connection between $MoSe_2$ and C. (Chong et al., 2021; Xu Zhao, Cai, et al., 2018)

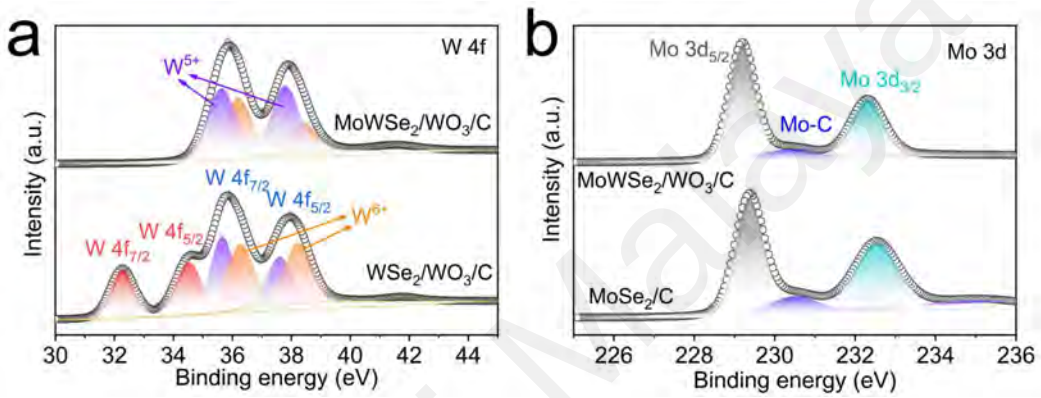

Figure 4.52: High-resolution XPS spectra of (a) W 4f, (b) Mo 3d.

Figure 4.53a displays the XPS spectrum of Se 3d, where the two major peaks located at 54.6 and 55.5 eV are attributed to Se $3d_{5/2}$ and Se $3d_{3/2}$, respectively. The broad peak at 54.0 eV is probably due to the electron-rich state of Se at the WSe_2 and WO_3 heterogeneous interface. (Niu et al., 2017) Regarding O 1s analysis (Figure 4.53b), the two prominent peaks at 530.7 and 531.9 eV correspond to lattice oxygen and adsorbed oxygen, respectively. (Yan Zhang et al., 2020)

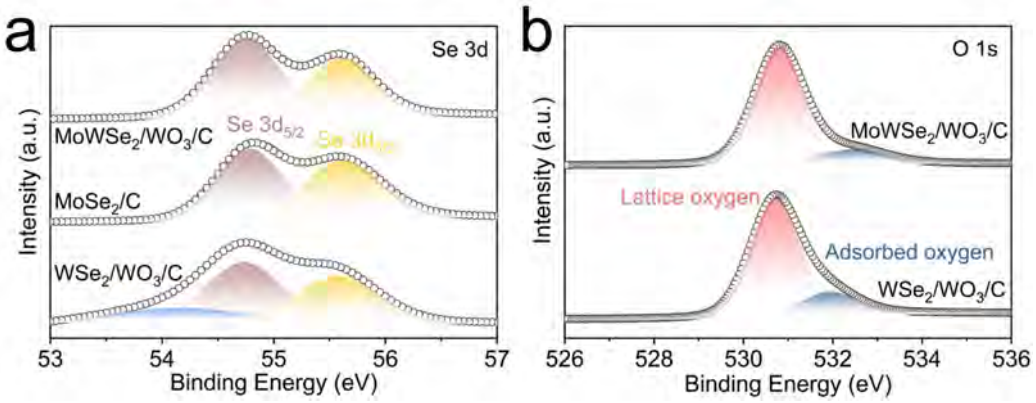

Figure 4.53: High-resolution XPS spectra of (a) Se 3d, (b) O 1s.

Figure 4.54a illustrates C-C, C-N, C-O, and C=O bonding states in C 1s, respectively. Moreover, the XPS surface elemental content analysis of three samples is shown in Figure 4.54b, where the atomic ratio of C is 30%−36%. In $MoWSe_2/WO_3/C$, the ratio of $MoSe_2$ to WO_3 is almost consistent with the EDS analysis. In addition, the contents of other elements in the three samples are consistent with the EDS analysis.

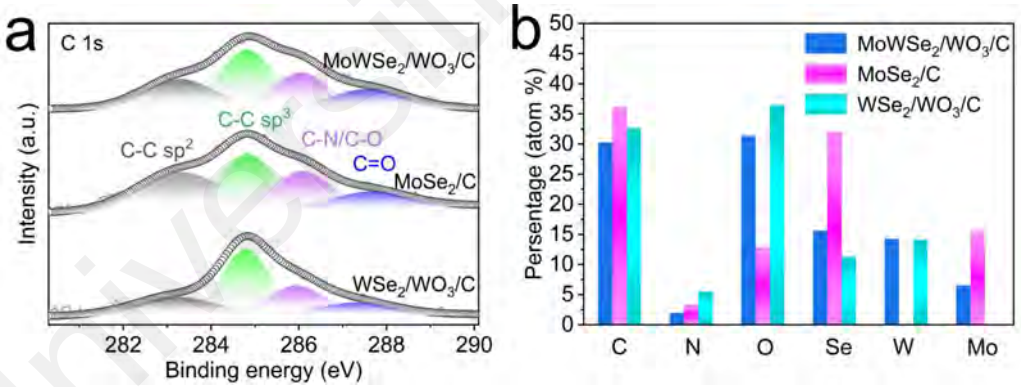

Figure 4.54: High-resolution XPS spectra of (a) C 1s, (b) The XPS surface elemental content analysis.

4.3.3 Density Functional Theory Calculations

To understand the interaction and ion diffusion between WO_3 and $MoSe_2$, DFT calculations are used to investigate them separately. Figure 4.55 displays the charge difference density models of WO_3 and $MoSe_2$. It can be seen that WO_3 and $MoSe_2$ possess a uniform electron cloud distribution.

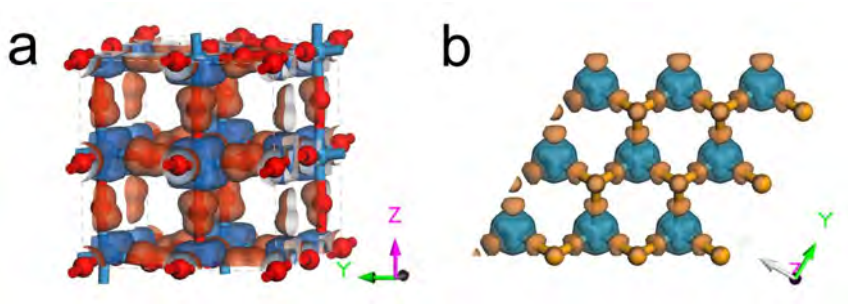

Figure 4.55: The charge difference density models on WO_3 (a) and $MoSe_2$ (b).

To further verify the heterogeneous connection between WO_3 and $MoSe_2$ via the transition WSe_2, a structural model as given in Figure 4.56 have been constructed.

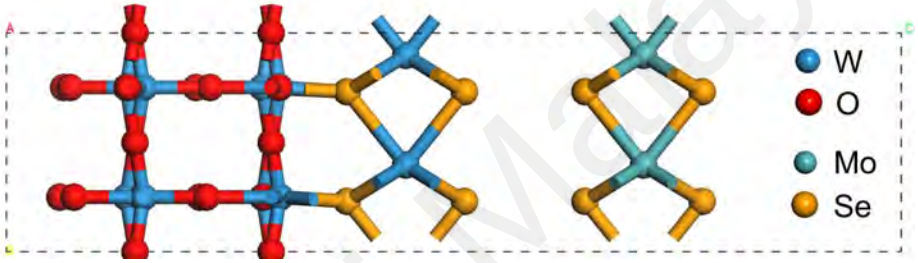

Figure 4.56: The established model of $MoWSe_2/WO_3/C$.

The DFT calculations indicate that the $MoWSe_2/WO_3$ heterostructure exhibits an enlarged (0 0 2) lattice spacing (6.772 Å) relative to $MoSe_2$ (6.462 Å) and WSe_2 (6.495 Å) (Figure 4.57), which can facilitate the rapid transfer of Na^+ between the layers.

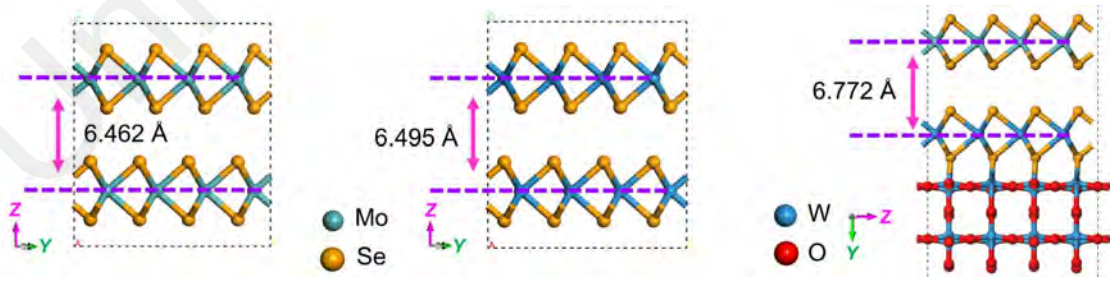

Figure 4.57: (a) The comparison of the (0 0 2) lattice spacing of $MoSe_2$, WSe_2, and $MoWSe_2/WO_3$.

Additionally, according to estimates, the band structure of $MoSe_2$ and WO_3 is shown in Figure 4.58. The indirect band gaps near the Fermi energy level are 1.497 eV ($MoSe_2$)

and 1.158 eV (WO_3), implying the semiconductor property of $MoSe_2$ and WO_3.

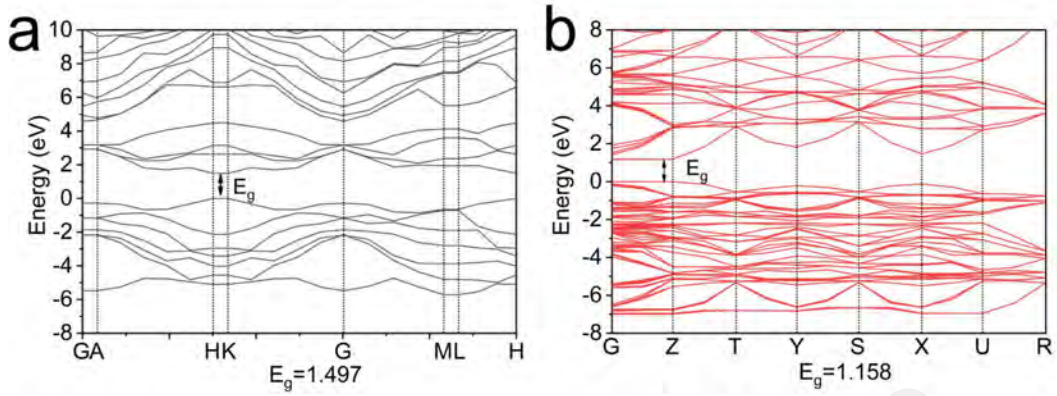

Figure 4.58: The calculated band gap of (a) $MoSe_2$ and (b) WO_3.

From the band structure of $MoWSe_2/WO_3/C$ in **Figure 4.59**, WO_3 with surface selenide state is heterogeneous through interlayer with $MoSe_2$. There is no obvious band gap near the Fermi energy level. The formed built-in electric field between the samples causes the energy band to slide to the Fermi energy level, exhibiting a metallic property.

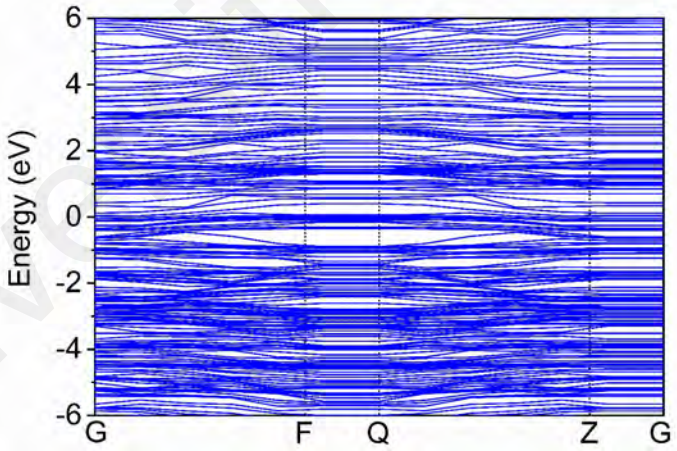

Figure 4.59: The calculated band gap of $MoWSe_2/WO_3$.

The DOS diagram in Figure 4.60 shows that $MoWSe_2/WO_3$ has the superposition of the peaks from $MoSe_2$ and WO_3 at the Fermi energy level, proving that $MoWSe_2/WO_3$ possesses metallic property.

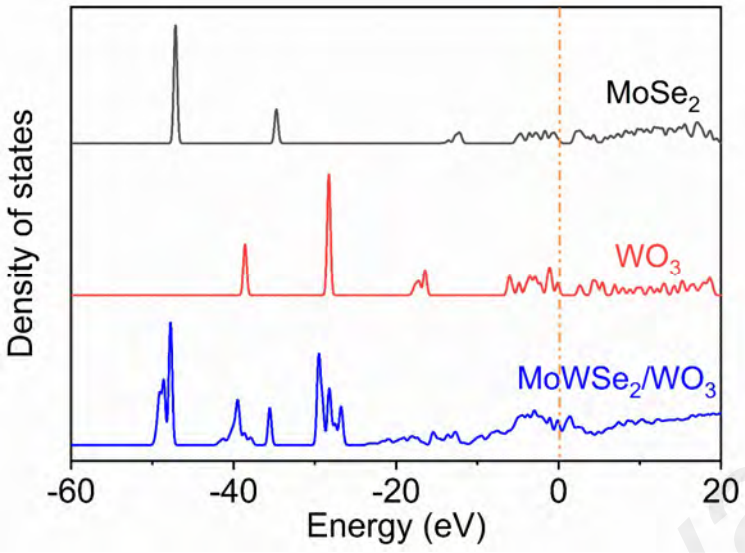

Figure 4.60: The density of states for $MoSe_2$, WSe_2, and $MoWSe_2/WO_3$.

Figure 4.61 exhibits the charge density difference of the $MoWSe_2/WO_3$ composite structure, where the yellow electron cloud presents charge depletion and the green region indicates electron accumulation. (Kokalj, 1999) The electron migration between the three phases is mainly occurred on the transition state WSe_2, with a significant charge accumulation space around the W atom. Furthermore, at the junction of WSe_2 and WO_3, a part of the charge is transferred from the Se atom to W (WO_3). On the interlayer side of $MoSe_2$ and WSe_2, Se atoms from WSe_2 transfer fewer electrons to W, allowing them to maintain a higher negative charge characteristic. However, Se atoms in $MoSe_2$ transfer more electrons to Mo atoms, further suggesting the formation of a built-in electric field between the layers as a result of the inhomogeneous charge distribution. That is beneficial to the transfer of Na^+ between layers.

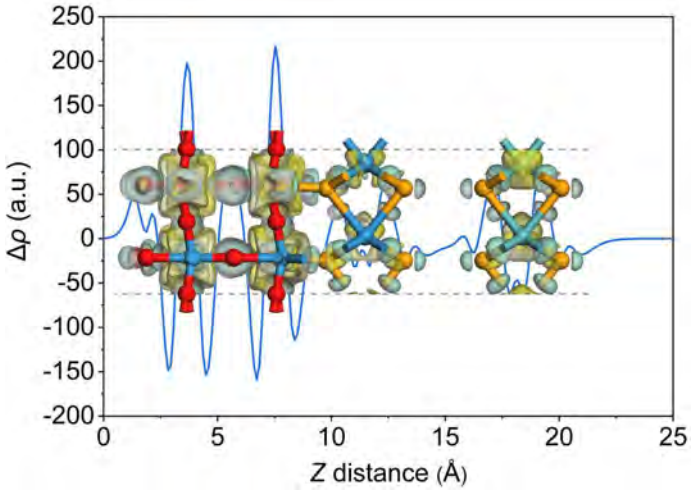

Figure 4.61: Charge density difference for $MoWSe_2/WO_3$.

The Na^+ diffusion potentials on the surface and inside $MoSe_2$ and WO_3 are investigated using the climbing image nudged elastic band (CI-NEB) method. Figure 62a displays the diffusion path of Na^+ on the $MoSe_2$ surface. According to Figure 62b, it can be concluded that the surface diffusion energy barrier of $MoSe_2$ is about 0.225 eV, contributing to the adsorptive diffusion of Na^+.

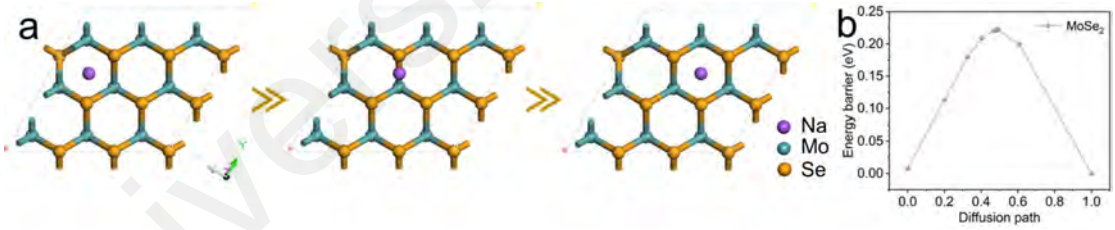

Figure 4.62: (a) The diffusion path of Na^+ on the $MoSe_2$ surface, and (b) the corresponding diffusion energy barrier.

Similarly, Figure 4.63a reveals the diffusion process of Na^+ in the internal cell of WO_3. Combined with Figure 4.63b, it can be concluded that the internal diffusion energy barrier is about 2.4 eV, and there is a specific diffusion resistance. Therefore, it is hard to realize Na^+ ultimately entered the WO_3 bulk phase for diffusion in the early stage (before activation).

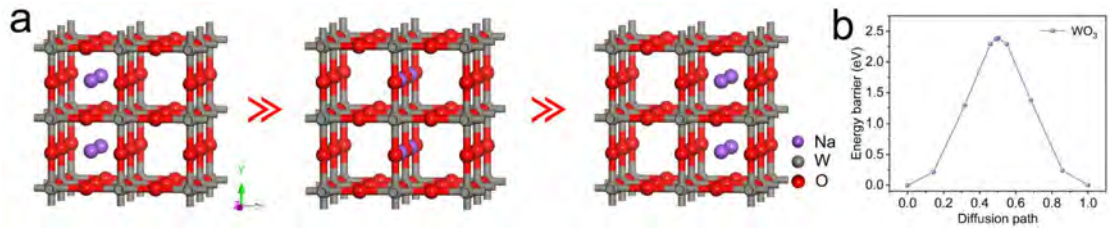

Figure 4.63: The diffusion path of Na^+ on the WO_3 internal cell, and (d) the corresponding diffusion energy barrier.

4.3.4 Electrochemical Properties of $MoWSe_2/WO_3/C$ in SIBs

The Na^+ storage performance of the $MoWSe_2/WO_3/C$ electrode is tested in a half-cell assembled with sodium metal as the counter electrode. The capacity performances of $MoWSe_2/WO_3/C$, $MoSe_2/C$, and $WSe_2/WO_3/C$ electrodes are measured in Figure 4.64. The $MoWSe_2/WO_3/C$ electrode presents a specific capacity of 406.1 mA h g^{-1} after 250 cycles at a current density of 2 A g^{-1}. In contrast, the $MoSe_2/C$ and $WSe_2/WO_3/C$ electrodes are slightly inferior, exhibiting specific capacities of 302.8 and 238.7 mA h g^{-1}, respectively.

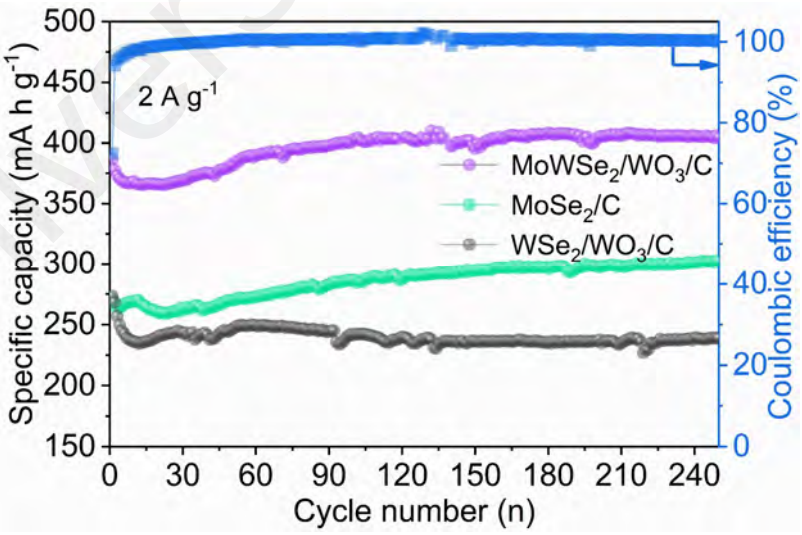

Figure 4.64: Short cycling performance of $MoSe_2/C$, $WSe_2/WO_3/C$, and $MoWSe_2/WO_3/C$ electrodes.

The rate ability of $MoWSe_2/WO_3/C$ at 1, 2, 4, 6, 8, and 10 A g^{-1} are also analyzed and can deliver the specific capacities of 453.9, 366.7, 336.5, 329.1, 326.3, and 322.9 mA h

g^{-1}, respectively (Figure 4.65). Immediately when the current density returns to 1 A g^{-1}, the specific capacity returns to 493.7 mA h g^{-1}, showing a good rate capability.

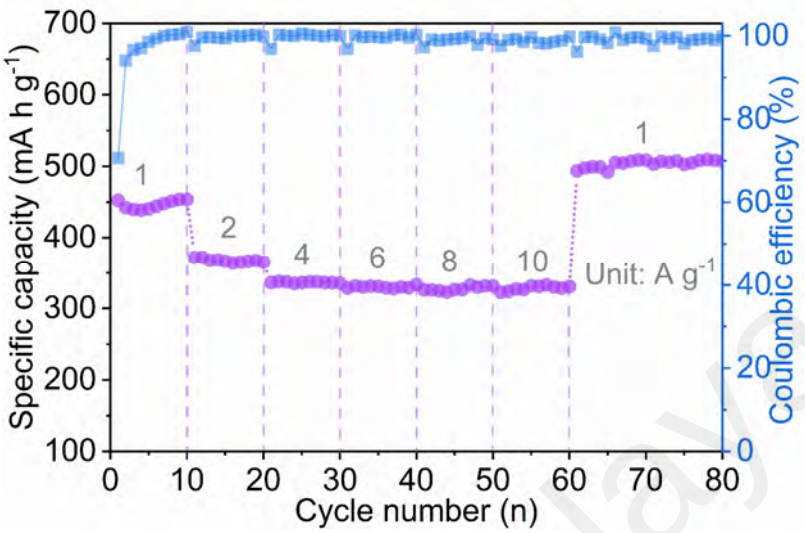

Figure 4.65: Rate capability of $MoWSe_2/WO_3$/C electrode.

The GCD curves of the $MoWSe_2/WO_3$/C electrode at different current densities are depicted in Figure 4.66a. From that, with the activating effect of high current, the $MoWSe_2/WO_3$/C electrodes exhibit additional charging and discharging plateaus. During the primary process, based on the adsorption effect of uniformly distributed amorphous carbon, Na^+ tends to transfer on the electrode surface and exhibits a storage process dominated by insertion reaction ($xNa^+ + xe^- + MoSe_2 \rightarrow Na_xMoSe_2 / xNa^+ + xe^- + WO_3 \rightarrow Na_xWO_3$), thus performing a lower capacity. (H. Liu et al., 2018) In contrast, under the activation effect of high current, the internal structure of each component is gradually exposed, and the role of the corresponding heterogeneous interface is further accentuated, thus can capture more ions on the surface. Consequently, the activated electrodes can exhibit a more significant conversion reaction ($Na_xMoSe_2 + (4-x)Na^+ + (4-x)e^- \rightarrow 2Na_2Se + Mo / Na_xWO_3 + (6-x)Na^+ + (6-x)e^- \rightarrow 3Na_2O + W$) and thus provide higher

capacity performance. (H. Zhang et al., 2018) Similarly, the above charge/discharge plateau changes from insertion reaction to conversion reaction during the activation process are also reflected in the GCD curves of different cycles at 2 A g^{-1} (Figure 4.66b).

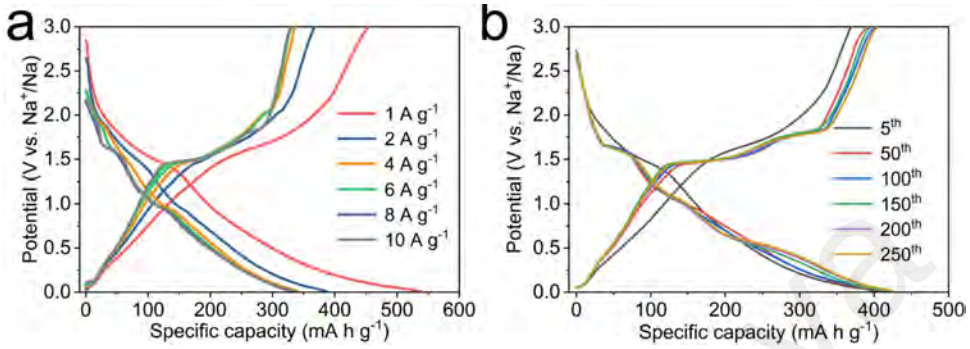

Figure 4.66: (a) GCD curves of $MoWSe_2/WO_3/C$ at different current densities. (b) different cycled GCD curves of $MoWSe_2/WO_3/C$ at 2 A g^{-1}.

As shown in Figure 4.67a, the specific capacity of 384.3 mA h g^{-1} is still stably maintained after 950 cycles at 10 A g^{-1}, indicating the fast charge/discharge capability and long cycling performance of $MoWSe_2/WO_3/C$ electrodes. Additionally, the SEM images of the after-cycling electrode in Figure 4.67b**, c** exhibit a completed flower-like morphology, indicating good structure stability of $MoWSe_2/WO_3/C$ electrode.

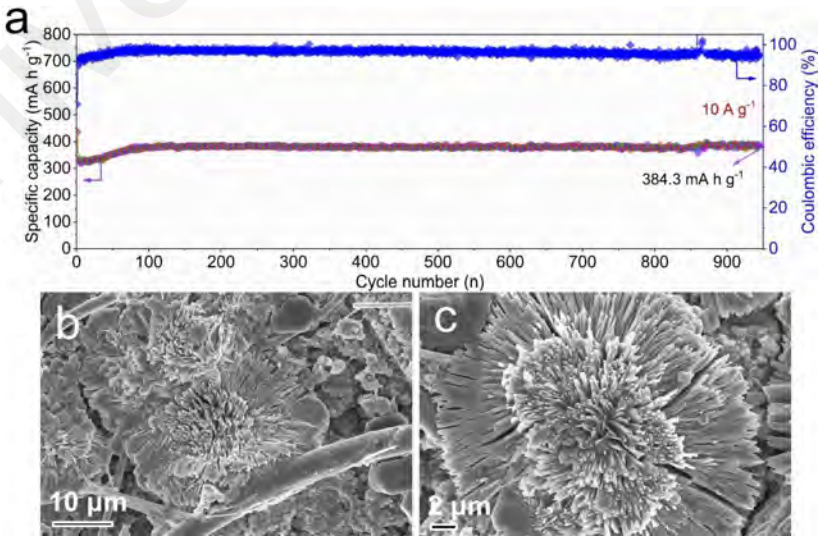

Figure 4.67: (a) Long cycling performance and Coulombic efficiency of $MoWSe_2/WO_3/C$ at the current density of 10 A g^{-1}. (b, c) SEM images of $MoWSe_2/WO_3/C$ electrode after 950 cycles at 10 A g^{-1}.

4.3.5 Electrochemical Reaction Process Investigation

To further study the activation process during the first 100 cycles, the dQ/dV profiles are obtained for the 3rd and 100th cycles. As shown in Figure 4.68, a pair of plateau peaks at 1.44/1.66 V can be measured in the third cycle, which corresponds to the cathodic/anodic peak pair of the CV curve. However, when cycling to the 100th cycle, the reduction peaks mainly appeared at 0.55, 1.08, and 1.62 V, while the oxidation peaks are located at 1.49 and 1.79 V. The charge/discharge plateau changes are based on different reaction types (insertion or conversion reactions).

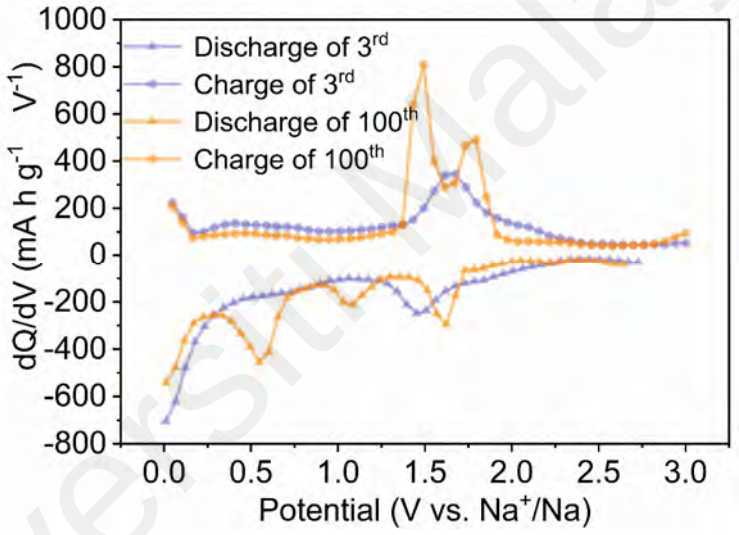

Figure 4.68 The dQ/dV profiles of $MoWSe_2/WO_3/C$ electrode after 3rd cycle and the 100th cycle.

To investigate the reaction source of the 100th cycle, the dQ/dV profiles of $MoWSe_2/WO_3/C$, $MoSe_2/C$, and WO_3/C are compared and analyzed, respectively. The dQ/dV profiles in discharge process exhibit three major reduction peaks, with only slight shift in locations and varies in peak intensities (Figure 4.69a). The same situation can be explored from the oxidation peaks in Figure 4.69b. In addition, some broad peaks at 2.06 V (the reduction peak), 0.46 V, and 2.27 V (the oxidation peaks) can only be detected in the WO_3/C and $MoWSe_2/WO_3/C$ samples, which can be attributed to the

reactions of WO_3. Generally, due to the similarity of the reactions, the reaction peaks of $MoWSe_2/WO_3/C$ react as a compromise and superposition of $MoSe_2/C$ and WO_3/C.

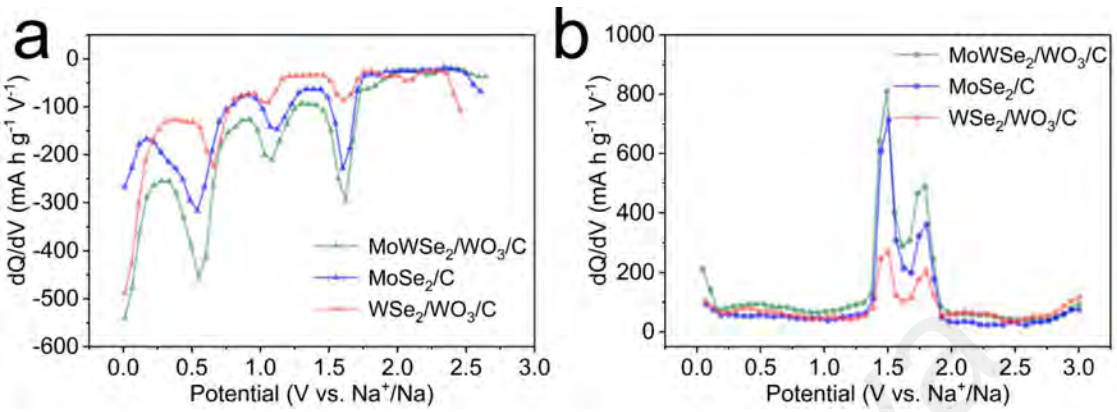

Figure 4.69: The dQ/dV profiles of $MoWSe_2/WO_3/C$, $MoSe_2/C$, and $WSe_2/WO_3/C$ electrode after 100th cycle.

CV is adopted to explore the Na^+ storage mechanism. As shown in Figure 4.70, a sharp reduction peak near 0.72 V is observed during the cathodic scan representing that Na^+ intercalated into the WO_3 and $MoSe_2$ lattices. Subsequently, a broad reduction peak near 0.49 V is also detected showing the formation of the SEI layer. (Niu et al., 2017) In addition, during the first anodic scan, several oxidation peaks with different intensity located near 0.36, 0.71, 1.75, and 2.62 V are depicted suggesting the gradual Na^+ deinsertion from WO_3 and $MoSe_2$. In the second scan, three pairs of cathodic/anodic peak at around 2.31/2.34 V, 1.44/1.66 V, and 1.54/1.51 V are observed. These peaks are stable and remain the same position in the following scans, revealing the excellent cyclic reversibility of the $MoWSe_2/WO_3/C$ electrode.

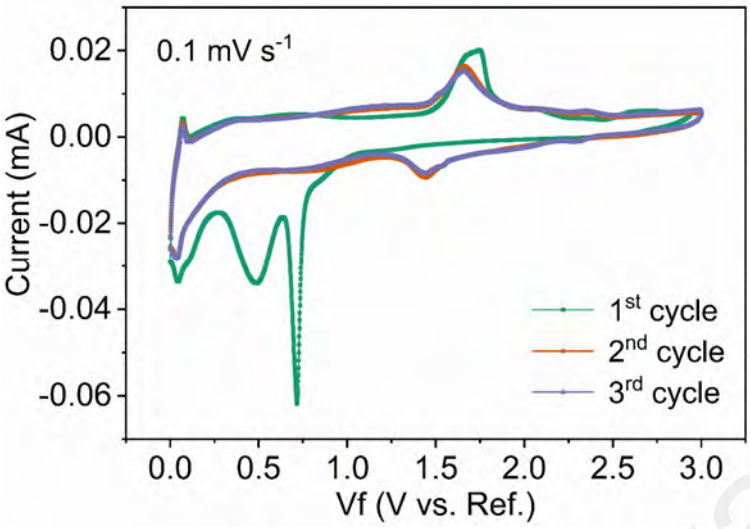

Figure 4.70: Cyclic voltammetry curves of $MoWSe_2/WO_3/C$ from 0.01 to 3.0 V at the scan rate of 0.1 mV s^{-1}.

To further understand the attribution of each reaction peak, the CV curves of $MoSe_2/C$ and WO_3/C are tested separately. As shown in Figure 4.71, all redox peaks of $MoSe_2/C$ and WO_3/C are well represented in $MoWSe_2/WO_3/C$ composites, demonstrating the mixing conversion process.

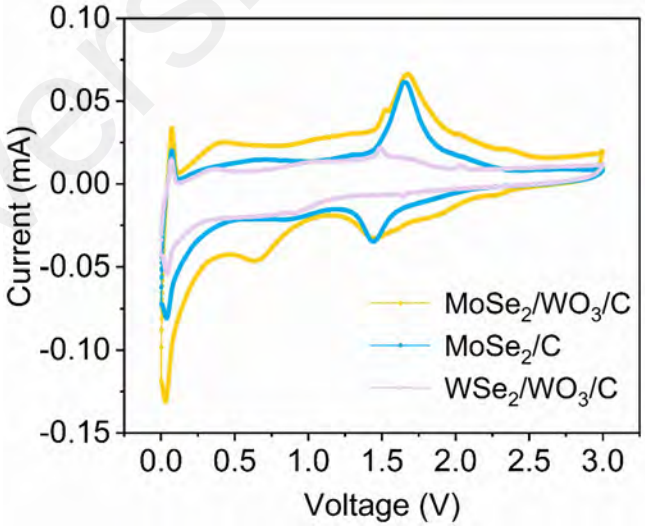

Figure 4.71: Cyclic voltammetry curves of $MoWSe_2/WO_3/C$, $MoSe_2/C$, and $WSe_2/WO_3/C$ from 0.01 to 3.0 V at the scan rate of 0.2 mV s^{-1}.

Figure 4.72 displays the ex-situ XRD results of the $MoWSe_2/WO_3/C$ electrode in the initial cycle at selected discharged and charged processes. According to the CV curves, the positions in the discharged process (0.6, 0.3, and 0 V) and charged process (0.2, 0.5, 1.8, and 3.0 V) are selected for testing. In the pristine electrode, a strong SeO_2 phase is monitored, which is not reflected in the prepared XRD patterns, probably due to oxidation during the preparation of the electrode sheet. The intensity trend of the SeO_2 peak and the appearance of the Se peak during the subsequent process reveal the extra reactions ($SeO_2 + 4Na^+ + 4e^- \rightarrow Se + 2Na_2O/Na_2Se + 2e^- \rightarrow Se + 2Na^+$). (Niu et al., 2017) When discharging to 0.6 V, the vital Mo_3Se_4 phase (JCPDS No. 24–0772) at 32.6° can be noticed, indicating the partial reduction of $MoSe_2$. The presence of the Mo_3Se_4 phase throughout the initial process implied that $MoSe_2$ is only partially converted, and the Na^+ insertion reaction still dominates the capacity contribution. The peak at 27.7° can be attributed to the Na_xWO_3 phase (JCPDS No. 46-0173/JCPDS No. 46-0174), and the peak intensity variation reveals the insertion/deinsertion of Na^+. Additionally, the small peak at 23.9° represents the presence of WO_{3-x} (JCPDS No. 53-0434), indicating the occurrence of the partial reduction reaction of W^{6+}. Moreover, a solid Na_2WO_4 phase is observed at 16.9° (JCPDS No. 12-0772), formed by the combination of Na_2O and WO_3. No W and Mo metal phases are detected during the charging and discharging process, which can be attributed to the resulting amorphous states and the incomplete reaction. (H. Wang et al., 2015) When discharging to 0 V, the Na_2Se phase at 26.8° can be observed.

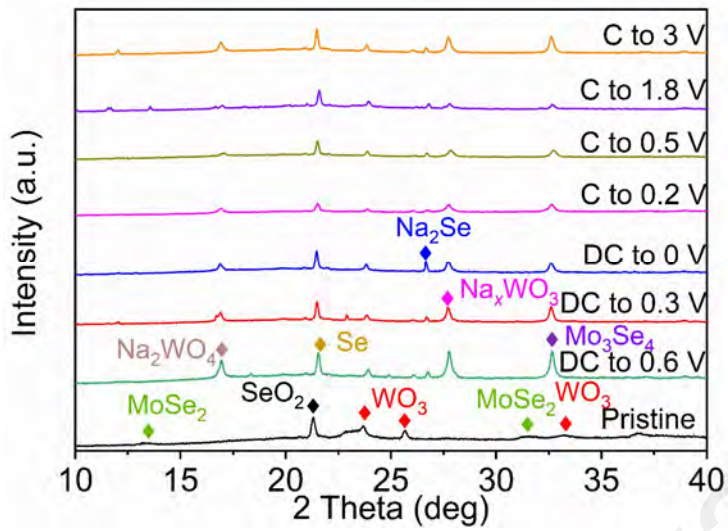

Figure 4.72: Ex-situ XRD patterns of $MoWSe_2/WO_3$/C electrode when discharge to 0.6, 0.3, 0 V, and charge to 0.2, 0.5, 1.8, 3 V in the initial cycle.

To further elucidate the sodiation/desodiation products of $MoWSe_2/WO_3$/C during the initial cycle, the fully discharged and charged electrodes are characterized by HRTEM. From Figure 4.73a, when discharged to 0 V, the measured crystal planes can be attributed to Na_2Se, Na_2WO_4, WO_{3-x}, Na_xWO_3, and Na_2O phases. In addition, the crystal planes of Mo_3Se_4, $MoSe_2$, WO_3, Se, and SeO_2 are found in the fully charged state (Figure 4.73b). It is in agreement with the ex-situ XRD analysis. In a word, the investigation of the initial charging and discharging process confirms that the reactions in the primary process are mainly dominated by the Na^+ insertion reactions (such as Na_xWO_3) in conjunction with the occurrence of partial conversion reactions (such as Mo_3Se_4 and WO_{3-x}). Concurrently, the changes of Se in different valence states during the reaction should also be noted.

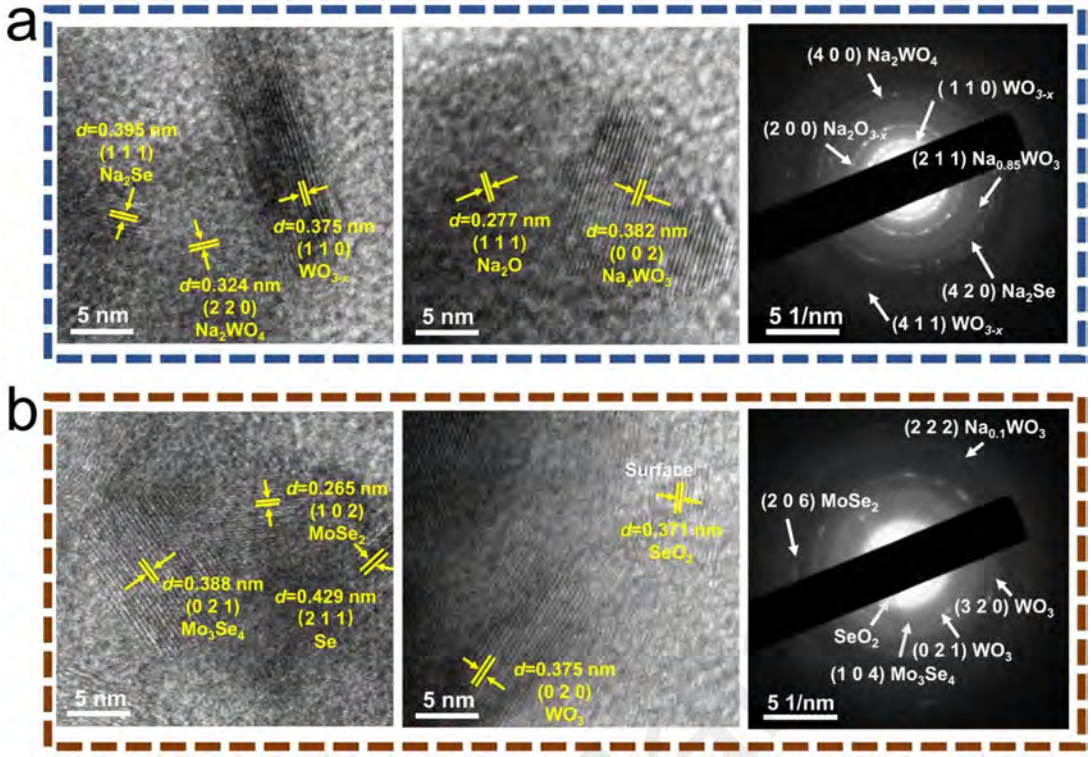

Figure 4.73: HRTEM diagram and SAED pattern of (a) fully discharged state and (b) fully charged state.

To further investigate the activation process of the $MoWSe_2/WO_3/C$ electrode during cycling, the electrode at discharge state (1.1, 0.6, and 0 V) and charge state (1.5 and 3 V) after 100 cycles are selected for ex-situ XRD analysis (Figure 4.74). Unlike the results of the initial process, when discharging to 1.1 V, the characteristic peaks of Na_2WO_4, WO_3, $MoSe_2$, and Na_xWO_3 are depicted at 16.9°, 23.1°, 27.6°, and 32.6°, respectively. As the discharge-charge proceeds, these peaks tend to disappear initially (discharging to 0 V) and then reappear at the end of charging to 3.0 V, indicating that complete conversion reactions have occurred in the main phases of $MoSe_2$ and WO_3. When discharged to 0.6 V, the intermediate phase of Mo_9Se_{11} appears at 12.7° and then become the most substantial peak with discharge to 0 V, after which it gradually decays with the charging process. In addition, when discharged to 0 V, the final discharge product of Na_2Se can be observed at 21.1°.

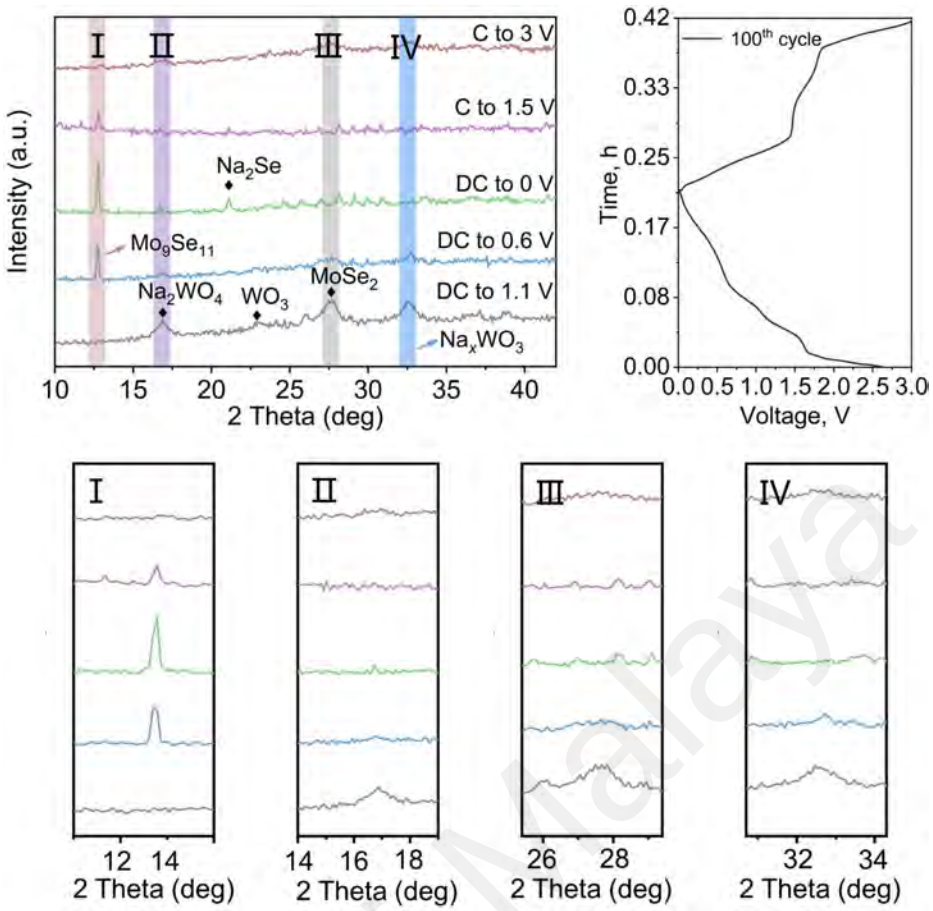

Figure 4.74: Ex-situ XRD patterns of $MoWSe_2/WO_3$/C electrode when discharge to 1.1, 0.6, 0 V, and charge to 1.5, 3 in the 100th cycle.

Figure 4.75 presents the XPS high-resolution spectra of Mo 3d and W 4f at the fully discharged and charged states. From Figure 4.75a, the Mo $3d_{3/2}$ peak is shifted toward the lower binding energy by about 0.15 eV at 0 V, indicating the reduction reaction of Mo ions during the discharge process. (Ge et al., 2020; J. K. Kim et al., 2020) When discharged to 0 V, the stronger W_0 $4f_{7/2}$ represents a deeper reductive valence state (Figure 4.75b). Moreover, the changes ratio of W^{5+} to W^{6+} in the fully discharged and charged states are equally implied the redox process of W. It is consistent with the redox reactions analyzed by the ex-situ XRD results.

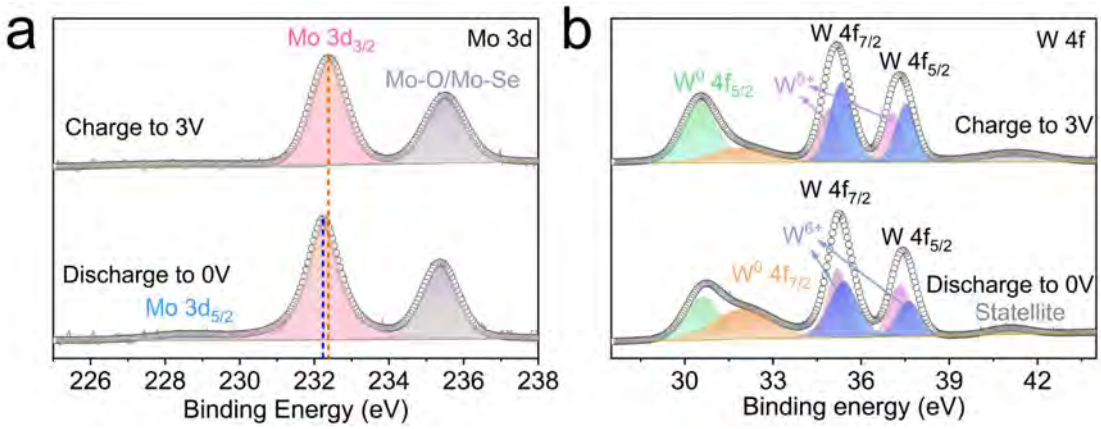

Figure 4.75: High-resolution XPS spectra of (a) Mo 3d and (b) W 4f at fully discharge/charge state after 100 cycles.

4.3.6 Sodium Storage Kinetics Investigation

To evaluate the electrochemical reaction kinetics of the $MoWSe_2/WO_3/C$ electrode, EIS is employed to analyze the impedance changes in the initial state and after 3 cycles. As shown in Figure 4.76a, the semicircle in the high-medium frequency region reflects the charge transfer resistance (R_{ct}), while the solid-state ion diffusion is measured by the slope in the low-frequency region. From the Nyquist plots, it can be obtained that the diameter of the semicircle located in the high-medium frequencies is significantly smaller than the initial state after three cycles, demonstrating the faster Na^+ transfer kinetics after cycling. That may be caused by the formation of the SEI layer and the activation of the prepared electrodes. To further compare the Na^+ diffusion coefficients before and after cycling, Figure 4.76b is fitted with the relationship between $\omega^{-1/2}$ and Z'.

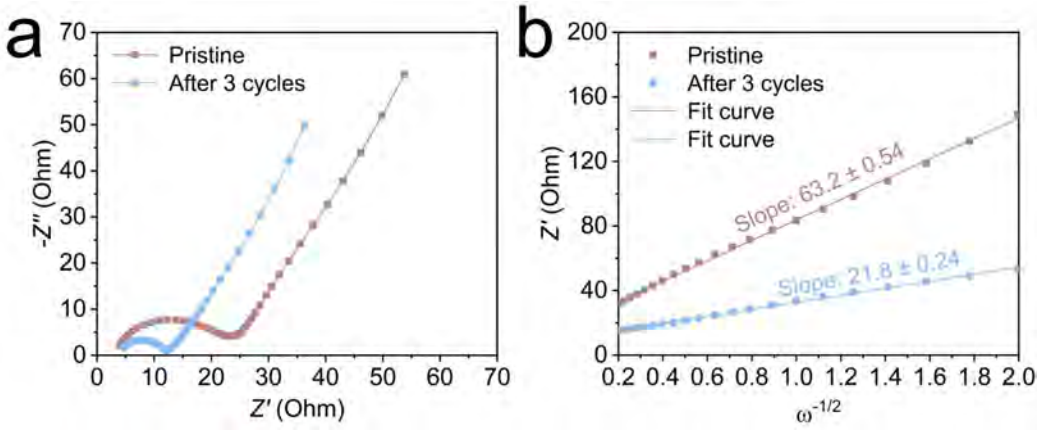

Figure 4.76: (a) Nyquist plots of $MoWSe_2/WO_3/C$ before and after 3 cycles. (b) Relationship between Z' and $\omega^{-1/2}$.

The GITT is adopted to characterize the sodium ion diffusion coefficient (D_{Na^+}) in the voltage range of 0−3 V (Figure 4.77a). As a more definitive elaboration, Figure 4.77b displays a graphical illustration of the single relaxation process.

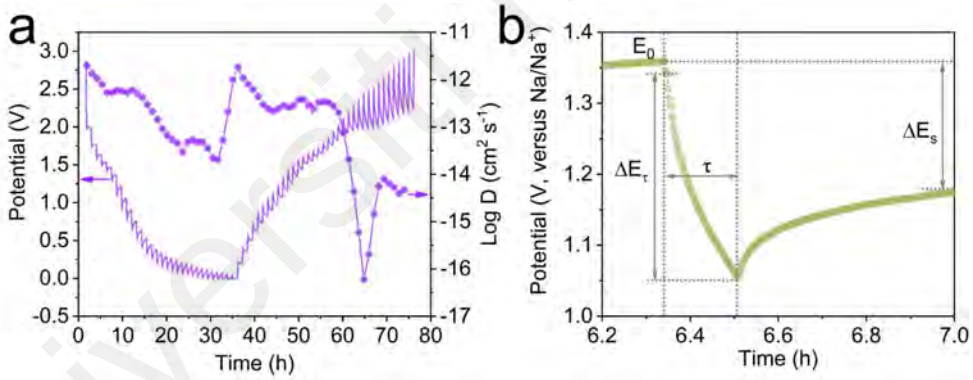

Figure 4.77: (a) GITT and Na^+ diffusion coefficients of $MoWSe_2/WO_3/C$ electrode. (b) Graphical illustration of the single relaxation process in GITT.

As shown in Figure 4.78, sodium ion diffusion coefficient profiles of $MoWSe_2/WO_3/C$, $MoSe_2/C$, and WO_3/C during the discharge and charging processes are compared, respectively. Throughout the process, the $MoWSe_2/WO_3/C$ electrode exhibits the higher D_{Na^+} values than the other two compared electrodes. The excellent rate performance and fast charge/discharge capability of $MoWSe_2/WO_3/C$ electrodes are profoundly related to the contribution of fast reaction kinetics and surface

pseudocapacitance.

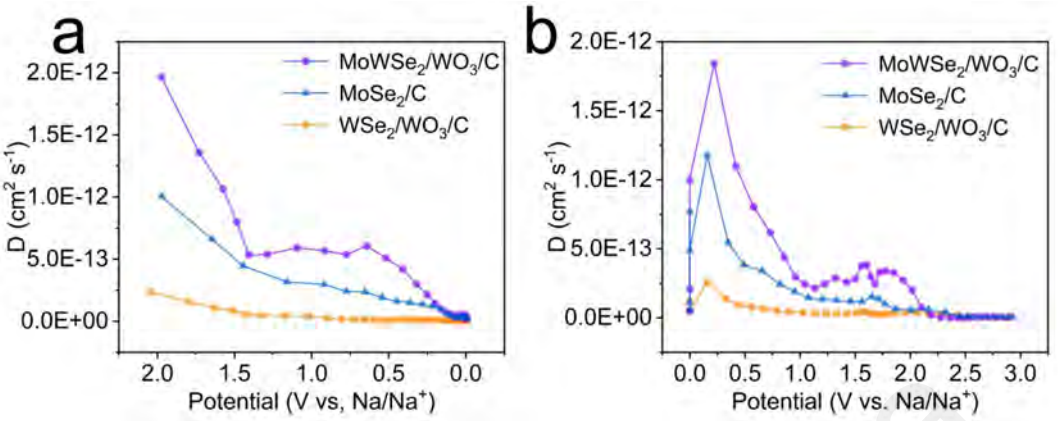

Figure 4.78: The comparison of the $MoWSe_2/WO_3/C$, $MoSe_2/C$, and $WSe_2/WO_3/C$ electrodes during (a) sodiation and (b) desodiation process.

In Figure 4.79a, the CV curves obtained at different scan rates are used to further measure the electrochemical reaction kinetics of the $MoWSe_2/WO_3/C$ electrode. The relationship between the fitted peak currents and scan rates for the cathodic and anodic processes are exhibited in Figure 4.79b, respectively. The obtained *b* values corresponding to the cathodic and anodic peaks are 0.903 and 0.912, respectively, which are all close to 1, revealing that the pseudocapacitive behavior is the leading cause of the fast reaction kinetics. The capacitive contributions at different scan rates are shown in Figure 4.79c. The capacitive contributions were calculated to be 76.4%, 81.3%, 84.4%, 87.2%, 90.8%, and 96.3% at scan rates of 0.1, 0.2, 0.5, 1, 2, and 5 mV s^{-1}, respectively. The shaded percentages of the CV curves in Figure 4.79d demonstrate the pseudocapacitive contribution at the scan rate of 5 mV s^{-1}.

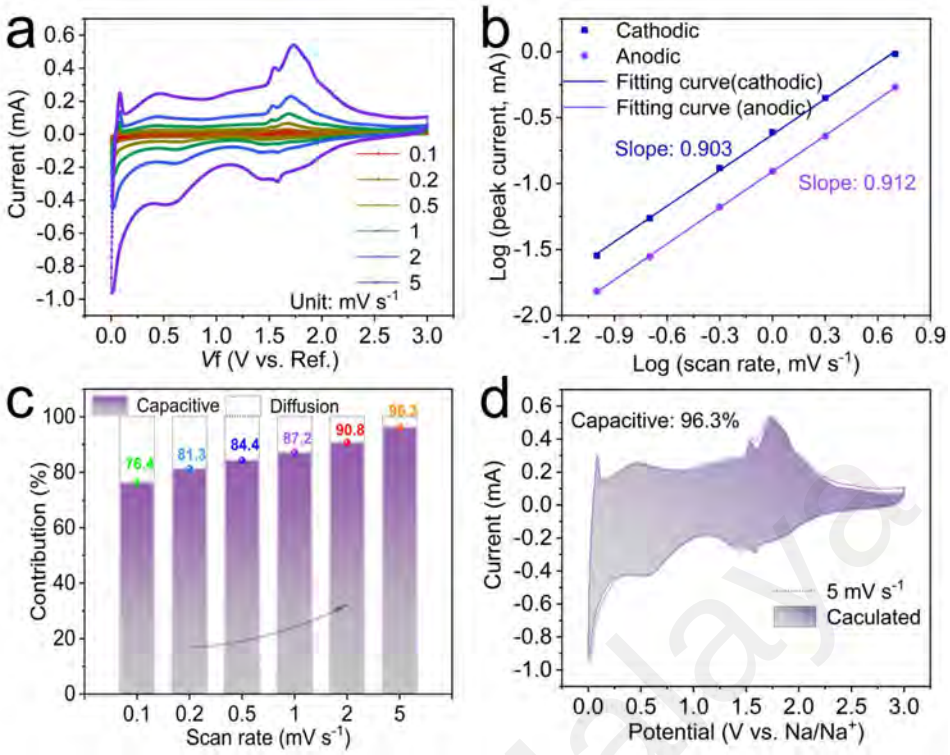

Figure 4.79: (a) CV curves at different scan rates of $MoWSe_2/WO_3/C$ electrode in SIBs. (b) Linear diagrams of log(v) and log(i) corresponding to peak currents in different oxidation and reduction states of $MoWSe_2/WO_3/C$. (c) Contribution ratio of the capacitive and diffusion-controlled charge versus the scan rate. (d) The capacitive contribution of $MoWSe_2/WO_3/C$ electrode at a scan rate of 5 mV s^{-1}.

4.3.7 Electrochemical Properties of $MoWSe_2/WO_3/C$ in SICs

To confirm a reasonable charge/discharge region for the SICs, CV tests are performed in the voltage ranges of 0−3.6, 0−3.8, 0−4.0, and 0−4.2 V, respectively (Figure 4.80a). A significant sharp angle is produced in the high voltage zone when the voltage is higher than 3.8 V, representing the occurrence of a large polarization phenomenon. Therefore, 0−3.8 V is selected as the voltage interval for the SICs. Moreover, the CV curves of SICs are evaluated at different scan rates (from 2 to 100 mV s^{-1}) in the range of 0−3.8 V (Figure 4.80b). According to the results, the CV curves present a quasi-rectangular with minor deformation, and even can maintain at a large scan rate of 100 mV s^{-1}, verifying that the assembled SICs is a hybrid mechanism with the coexistence of Faraday and

non-Faraday reactions.

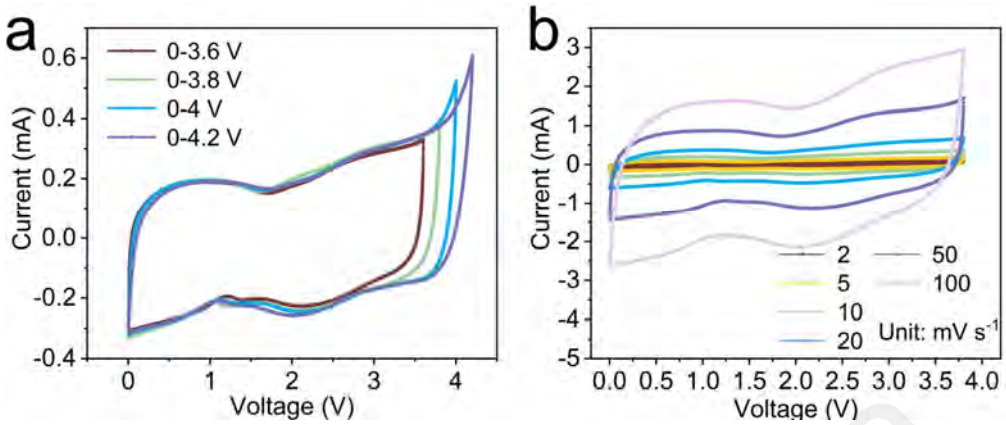

Figure 4.80: (a) CV curves at different cut-off potentials. (b) CV curves of $MoWSe_2/WO_3/C//AC$ SICs.

In addition, the hybrid mechanism is also corroborated by the slightly distorted triangular GCD curves at different current densities (Figure 4.81a). The rate performance of the SICs in Figure 4.81b performs only a slight degradation with the current density gradually increasing from 0.1 A g^{-1} to 2 A g^{-1}, displaying the excellent rate performance.

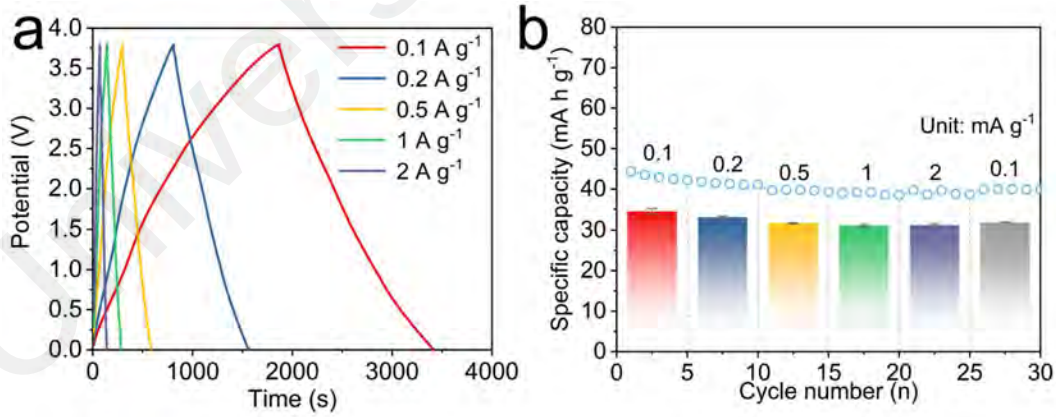

Figure 4.81: (a) GCD profiles, and (b) rate performance of $MoWSe_2/WO_3/C//AC$ SICs.

Additionally, the long-cycle capability of the assembled SICs is evaluated at a current density of 2 A g^{-1} (Figure 4.82). The specific capacity of 42.1 mA h g^{-1} is performed after 4000 cycles (97% capacity retention), suggesting the long life-span ability. Note

that the jump in capacity occurred several times during cycling, which is related to the electrolyte composition and the unstable interface of electrode and electrolyte.

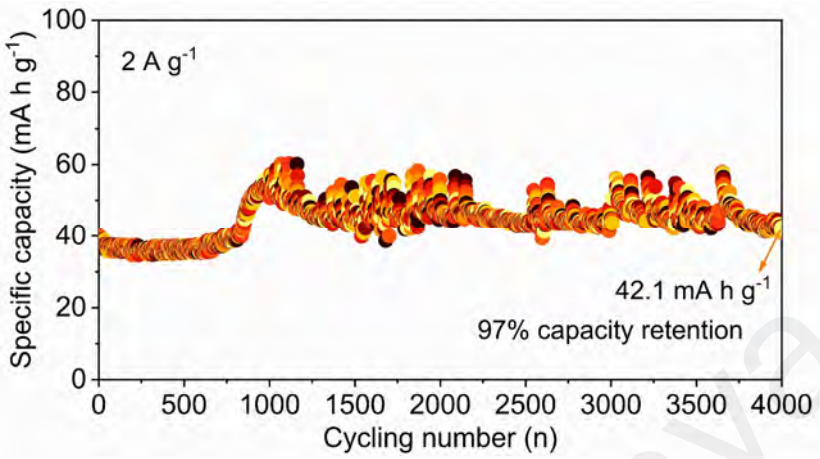

Figure 4.82: Cycling stability of $MoWSe_2/WO_3/C//AC$ SICs at 2 A g^{-1} for 4000 cycles.

4.4 Summary

The realization of sodium-ion devices with high-power density and long-cycle capability is challenging due to the difficulties of carrier diffusion and electrode fragmentation in transition MSes anodes. In this chapter, we have prepared selenides of Mo and W by a bimetallic MOF derivatization strategy to construct analogous cationic heterostructures, achieving microstructural modification and homogeneous introduction of carbon. It is worth mentioning that Mo/W-MOF precursors with nanoparticle and core-shell structures are obtained by controlling the hydrolysis process of MOF synthesis, respectively. Further, partial selenization of W is achieved by changing the selenization/carbonization temperature, which adds the heterogeneous effect of WO_3 to the original $MoSe_2$ and WSe_2 heterostructures, resulting in a further enhancement of the electrochemical behavior. The specific conclusions are as follows:

1. Mo/W-MOF nanoparticles is constructed by a one-step method through rational selection, after which $MoWSe_2/C$ heterostructures with large angles is synthesized

by a facile selenization/carbonization strategy. Through physical characterization and theoretical calculations, the synthesized $MoWSe_2$/C electrode delivers obvious structural advantages and excellent electrochemical performance in ethylene glycol dimethyl ether electrolyte. Furthermore, the electrochemical vehicle mechanism of ions in electrolyte is systematically revealed through comparative analyses. Resultantly, ether-based electrolytes advantageously construct stable solid electrolyte interfaces and avoid electrolyte decomposition. Based on the above benefits, the Na half-cell assembled with $MoWSe_2$/C electrodes demonstrated excellent rate capability and a high specific capacity of 347.3 mA h g^{-1} even after cycling 2000 cycles at 10 A g^{-1}. Meanwhile, the constructed SIC maintains ~80% capacity retention after 11,000 ultra-long cycles at a high-power density of 3800 W kg^{-1}. The findings can broaden the mechanistic understanding of conversion anodes in different electrolytes and provide a reference for the structure design of anodes with high capacity, fast kinetics, and long-cycle stability.

2. The Mo/W-MOF with core-shell structure is first formed by a facile strategy, followed by a selenization and carbonization strategy to finally prepare multileveled $MoWSe_2/WO_3$/C anode materials with core-shell petal like curled nanosheet structure. Between the petal ($MoSe_2$)-core (WO_3) structure, the formation of WSe_2 flakes by partial selenization on the surface of WO_3 serves as a heterogeneous connection between $MoSe_2$ and WO_3. The enlarged layer distance (0.677 nm) between $MoSe_2$ and WSe_2 can facilitate the rapid transfer of Na^+ and electrons. The DFT calculations verify that the $MoWSe_2/WO_3$/C heterostructure performs excellent metallic properties. Ex-situ XRD, XPS, and TEM confirm the activation process

from the initial insertion reaction to the later conversion reaction. Resultantly, when employed as the anode of SIBs, a remarkable capacity of 384.3 mA h g^{-1} after 950 cycles at 10 A g^{-1} is performed. Furthermore, the SICs assembled with commercial activated carbon (AC) as the cathode exhibits a remarkable energy density of 81.86 W h kg^{-1} (at 190 W kg^{-1}) and 72.83 W h kg^{-1} (at 3800 W kg^{-1}). The unique structural design and the reaction investigation of the electrode process can provide a reference for the development of transition metal chalcogenides anodes.

CHAPTER 5: ANALOGOUS ANIONIC HETEROSTRUCTURE DESIGN

5.1 Introduction

The larger Na^+ (1.02 Å) places harsher demands on the electrode material, especially for fast storage behavior at high power densities.[4] Conversion-based materials can stimulate fast reaction kinetics through a rapid conversion process. Based on the research in the previous chapters, layered MSes can be expected to exhibit better cycling stability at high power density by the layered two-dimensional structure connected with van der Waals forces. However, most layered MSes are semiconductor materials with a large bandgap, resulting in only a small number of electrons being able to jump across the bandgap from the valence band to the conduction band, leading to their limited electrical conductivity during rapid response. In addition, the connection through interlayer Van der Waals forces in layered TMCs restricts the movement of electrons in the direction perpendicular to the layers, which further reduces their ability to transport electrons rapidly at high power densities. The limited electrical conductivity and structural instability during rapid response still cannot ensure stable performance at high power densities. (Shinde et al., 2023) Therefore, some effective modification strategies are needed to improve the fast reaction kinetics. As we know, enhancing the pseudocapacitive reactivity can accelerate Na^+ transfer by boosting the fast redox reaction and ion adsorption on the surface thus ensuring the structural stability. (Peng et al., 2023; Zhenyun Zhao et al., 2023) From the studies in the previous chapters, the

[4] Most of the content in this chapter has been published in Journal of Power Sources, 614, 234991 and Chemical Engineering Journal, 464, 142764.

internal structure design between different MSes was realized by the strategy of constructing bimetallic MOFs. The basic idea lies in the construction of large-angle cationic heterostructures, which can effectively expand the layer spacing and form a built-in electric field to promote rapid Na^+ transport. However, for the internal structural design, beyond the conventional anionic heterogeneous structure design, the ion doping and anionic heterostructure design can also achieve the effect of widening the layer spacing. The difference is that ion doping can only widen the layer spacing in terms of physical layers and cannot create a built-in electric field. For example, Zhao et al. prepared K^+ pre-embedded single-phase WSe_2 (K_xWSe_2) anodes exhibiting fast K^+ reaction kinetics and excellent rate capability. (Zhongchen Zhao et al., 2023) However, since the pre-embedded guest ions are involved in electrochemical migration, the repeated insertion/de-insertion process inevitably produces guest ion loss, which in turn results in the narrowing of the WSe_2 lattice spacing. This is not conducive to maintaining long-term cycling capability. Consequently, alkali metal ion introduction only obtains short-term rapid ion diffusion by a physical expansion of the layer spacing. More durable solutions still require the construction of built-in electric fields within the bulk phase. Recently, the built-in electric field constructed via cationic heterostructures has been extensively studied. Notably, only limited studies have constructed built-in electric fields by introducing different anions. S and Se, as non-metallic atoms of the same main group, when combined with the same metal atom (Mo, W or V) to construct compounds, the resulting $MoS_2/MoSe_2$, WS_2/WSe_2 or VS_2/VSe_2 exhibit highly similar crystal structures. Therefore, it is necessary to apply the similar anionic properties of S and Se to construct anionic heterostructures to promote rapid Na^+ transfer by realizing

abundant built-in electric fields. Related research work has been fully explored for Mo-based anionic heterostructures. For example, Cai et al. prepared MoSSe with large interlayers and abundant anionic vacancies effectively lowering the diffusion energy barriers of guest ions. (M. Cai et al., 2022) Similarly, Yuan et al. synthesized dual anion-intervened MoS_xSe_{2-x}. The anionic defects triggered by S^{2-} and Se^{2-} significantly improved the adsorption and transport efficiency of the guest ions. (Z. Yuan et al., 2023) Moreover, Liu et al. developed an idea of carbon-coated $MoS_{1.5}Te_{0.5}$ nanocables for anionic heterogeneous design and validated the associated sodium ion storage process. (Yangjie Liu et al., 2022) However, S/Se analogous anionic heterostructures targeting the W and V groups have not been fully developed. Therefore, it is necessary to investigate the effect of double anion introduction in W-based compounds (WS_2 and WSe_2) and V-based compounds (VS_2 and VSe_2).

The current mainstream anionic heterostructure construction strategy focuses on anionic partial substitution targeting metal disulfides and diselenides as precursors. However, there are large reaction barriers to the realization of this strategy due to the overly stable dihalide structure. Typically, the conventional heterogeneous process for stable valence state of sulfur genus elements (O^{2-}, S^{2-}, Se^{2-} and Te^{2-}) must first suffer the bond-breaking process with metal ions, which requires a large consumption of reaction energy and has greater randomness. Therefore, it is necessary to develop the anionic heterogeneous projects with uniformity of heterogeneous interface distribution by convenient preparation processes. In this chapter, we pioneered the construction of analogous anionic heterostructures by employing W and V polysulfides as precursors

for partial Se atom substitution for S atoms. Unstable metal polysulfides can easily achieve partial substitution of S atoms, creating conditions for large-scale production. In particular, related work has revealed that W and V-based polysulfides with different chemical states can achieve efficient Na^+ storage. (Z. Qin et al., 2022; Xiao Zhang et al., 2020; Yingying Zhao et al., 2021) Notably, unlike the conventional S-M-S bonded construction, the S atom exhibits various valence states in polysulfides, e.g., S is present as $[S_2]^{2-}$ in VS_4, which significantly reduces the reaction energy barriers in some substitution processes. However, the uneven distribution of the interlayer electric field in the bond-breaking process accelerated further decomposition of the structure. (Park et al., 2021; Z. Wang et al., 2021) Therefore, the rational structure and interlayer electric field design based on WS_x and VS_4 electrodes are favorable to realizing the stable capacity output during the electrochemical process.

5.2 Carbon Sphere-Introduced $WSSe_2$/C Composites

High-capacity MSes exhibit intrinsically low conductivity and ion transport efficiency when applied to sodium-ion energy storage devices. Here, carbon-encapsulated WS_x precursors are synthesized using high chloride hydrolysis properties combined with a hydrothermal process. Afterwards, $WSSe_2$/C anodes with dual anion effect are prepared by rapidly replacing some S atoms in WS_x with Se atoms employing a microwave sintering process. The obtained $WSSe_2$/C electrode exhibits a significantly enlarged crystal spacing by constructing built-in electric fields, which ensures rapid and stable Na^+ transport. The carbon-encapsulated strategy aims to improve electrical conductivity while providing a buffer medium for volume expansion during

electrochemical phase transitions. Additionally, by exploring the effects of different carbon introductions on the electrochemical properties, it is determined that 1 g ribose encapsulated $WSSe_2$ ($WSSe_2$/C-1) provides the best intervening effect.

5.2.1 Synthesis of WS_xSe_{2-x}/C

The preparation process of $WSSe_2$/C is shown schematically in Figure 5.1. First, WCl_6 is rapidly hydrolyzed to form a uniformly distributed mixed solution. Adding F127 as a surfactant ensures agglomeration in the rapid hydrolysis of WCl_6, which in turn forms a uniformly distributed mixed solution. Afterwards, the addition of ribose provides carbon source for the complex reaction process. Notably, the addition of triethanolamine in the first step is able to form coordination compounds with W ions, and also binds to the hydroxyl group in the ribose through hydrogen bonding, which can promote further complexation of the ribose with W ions. Moreover, TAA is able to provide the sufficient S source and combine with W ions to form WS_x. The initial carbonization process of WS_x and carbon spheres is formed under hydrothermal action. Finally, the evolution from WS_x/C to $WSSe_2$/C is achieved by a selenization/carbonization process (microwave sintering). Based on the rapid heating ability and efficient reaction process of microwave sintering, the synthesis of $WSSe_2$/C using a relatively short calcination time is able to obtain a partial substitution of Se atoms for S atoms.

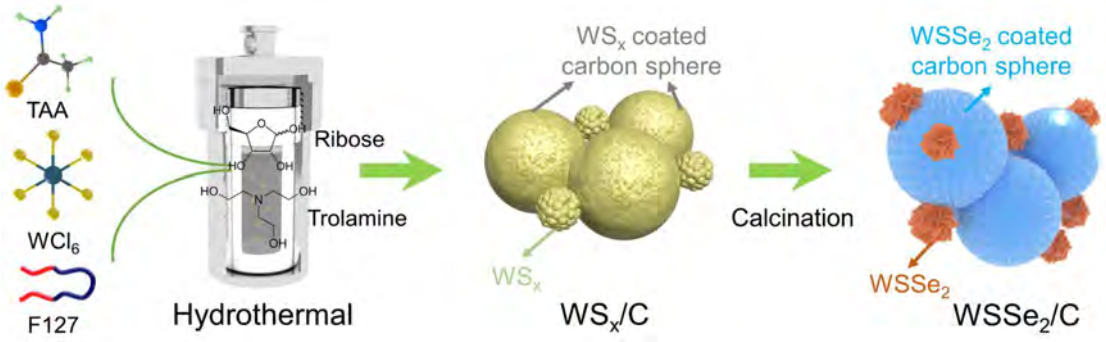

Figure 5.1: Schematic illustration of the synthetic process of the $WSSe_2$/C.

5.2.2 Structural and Chemical Characterization of WS_xSe_{2-x}/C

As the SEM images in Figure 5.2, the formed WS_x precursors with different ribose additions are uniformly distributed on the surface of the carbon spheres, forming connections and mediating interactions. By comparing these SEM images, it is found that the sample with 1 g additions exhibits a significant mediating effect, which avoids the large aggregation of WS_x on the surface while ensuring the distribution amount.

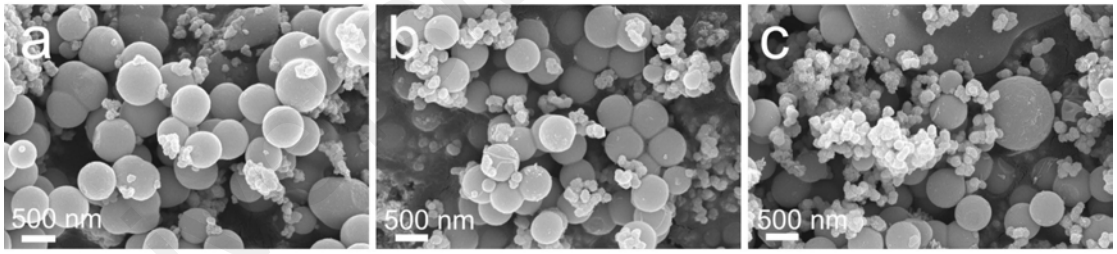

Figure 5.2: SEM images of 0.5 g (a), 1 g (b), and 1.5 g (c) ribose introduced WS_x/C precursors.

From the elemental mapping images in Figure 5.3, W, S, and C elements present uniform distribution, representing the formation of WS_x/C.

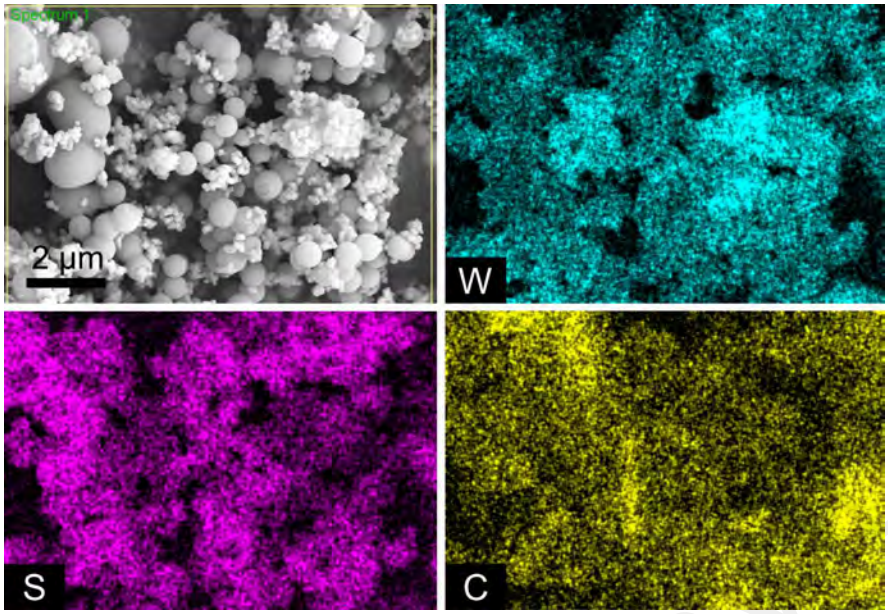

Figure 5.3: Elemental mapping images of WS_x/C.

The SEM image of $WSSe_2$/C-1 in Figure 5.4a reveals that the spherical WS_x evolves into a self-assembled sheet-like $WSSe_2$ and achieves a uniform interstitial distribution. Additionally, by comparing the SEM images of WSe_2/C-1 under the normal sintered sample in Figure 5.4b, the $WSSe_2$/C-1 under microwave sintering exhibit uniform size distribution and connectivity effects.

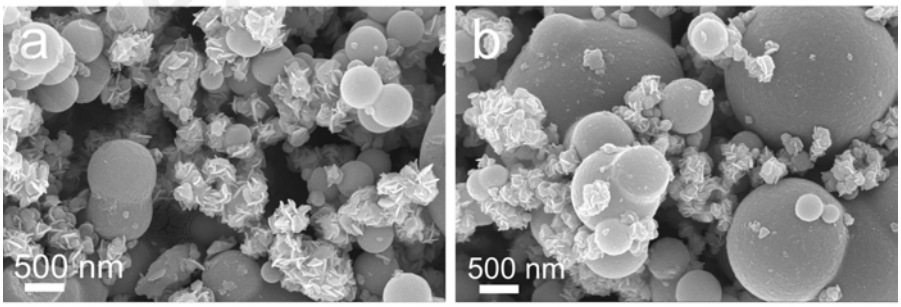

Figure 5.4: SEM images of $WSSe_2$/C-1 under microwave sintering (a) and WSe_2/C-1 under normal tube furnace (b).

The microscopic spherical region of $WSSe_2$/C-1 is selected for TEM testing (Figure 5.5a). There is a second phase distribution on the spherical surface, which can be attributed to $WSSe_2$. As shown in Figure 5.5b, high-resolution TEM is further utilized to

measure the lattice information of $WSSe_2$/C-1. Apparently, crystal spacing of 0.81 and 0.27 nm (compare to normal 0.65 and 0.26 nm in WSe_2) are observed, which can be attributed to the enlarged (0 0 2) and (1 0 2) crystal planes brought about by the anionic heterogeneity (S and Se). The enlarged interlayer distance can be attributed to the built-in electric field formed by the occupation of Se atoms by S atoms in WSe_2, which facilitates the rapid Na^+ transfer. (J. Wang, Cui, et al., 2023)

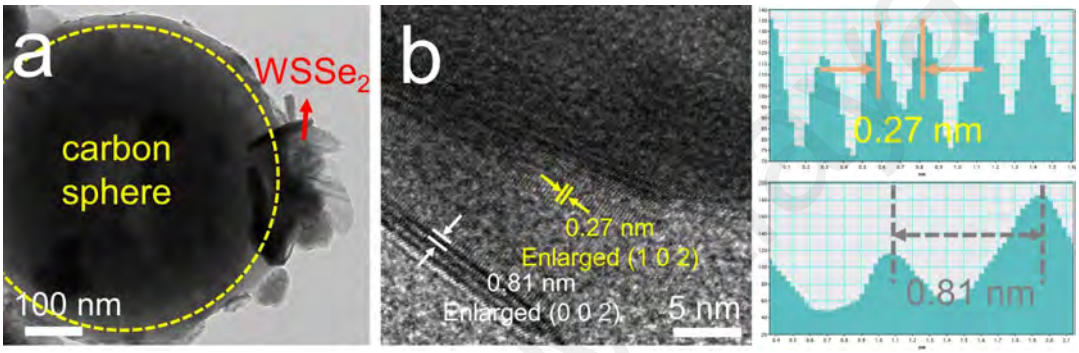

Figure 5.5: TEM (a), and HRTEM (b) images of $WSSe_2$/C-1 under microwave sintering.

The elemental mapping images of $WSSe_2$/C-1 in Figure 5.6 reveal spherical regions with uniform elemental distributions of C, W, S, Se, and N.

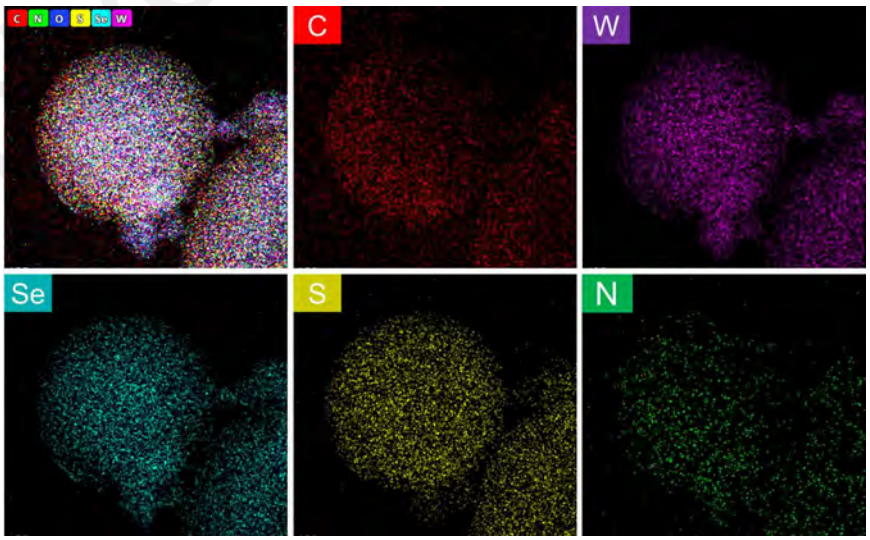

Figure 5.6: Elemental mapping of $WSSe_2$/C-1 under microwave sintering.

The EDS is employed to analyze the contents of elements in the prepared samples. As shown in Figure 5.7, the atomic contents of W, S, and C in the WS_x/C-1 precursor are approximately 5.9%, 18.6%, and 62.1%. Among them, the content of S atoms is about three times that of W, suggesting that WS_x may exist in the form of amorphous WS_3.

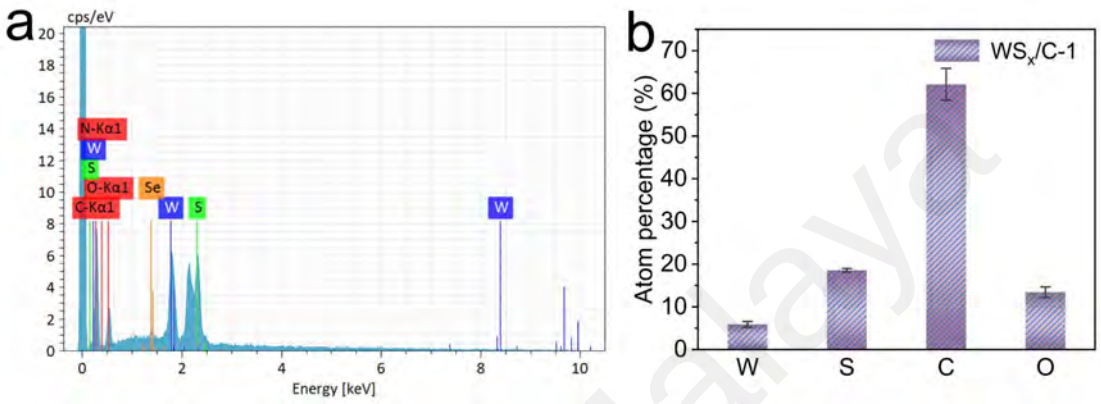

Figure 5.7: The elemental contents of WS_x/C-1 by EDS analysis.

Furthermore, the EDS results for WSe_2/C-1 exhibit atomic contents of W, Se, S, and C of about 11.9%, 18.3%, 15.8%, and 49.7%, realizing partial substitution of S by Se atoms (Figure 5.8). Notably, the carbon content in WSe_2/C-1 is reduced relative to the WS_x/C-1 precursor, revealing the heat loss of organic carbon during sintering carbonization.

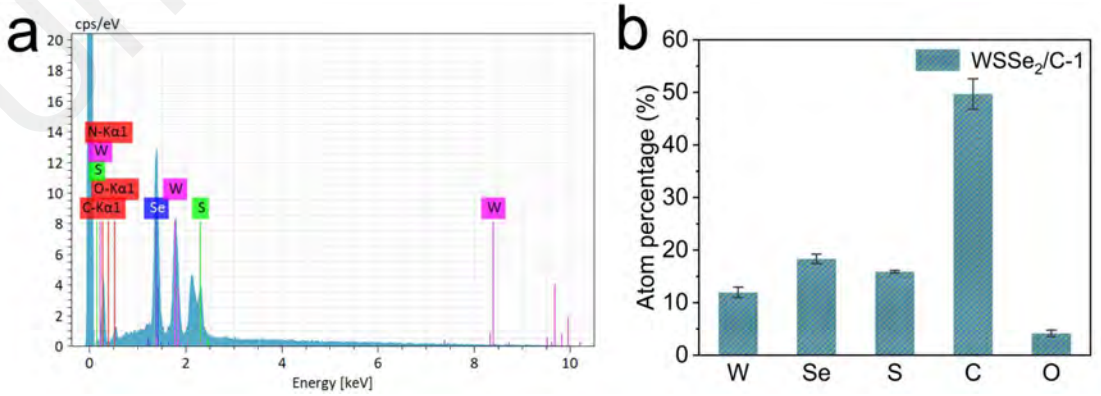

Figure 5.8: The elemental contents of WSe_2/C-1 by EDS analysis.

Moreover, the EDS results for WSe_2/C-1 exhibit atomic contents of W, Se, S, and C of about 14.6%, 26.5%, 2.2%, and 51.3%. The Se atoms in WSe_2/C-1 are about twice as abundant as W, suggesting the formation of WSe_2 (Figure 5.9).

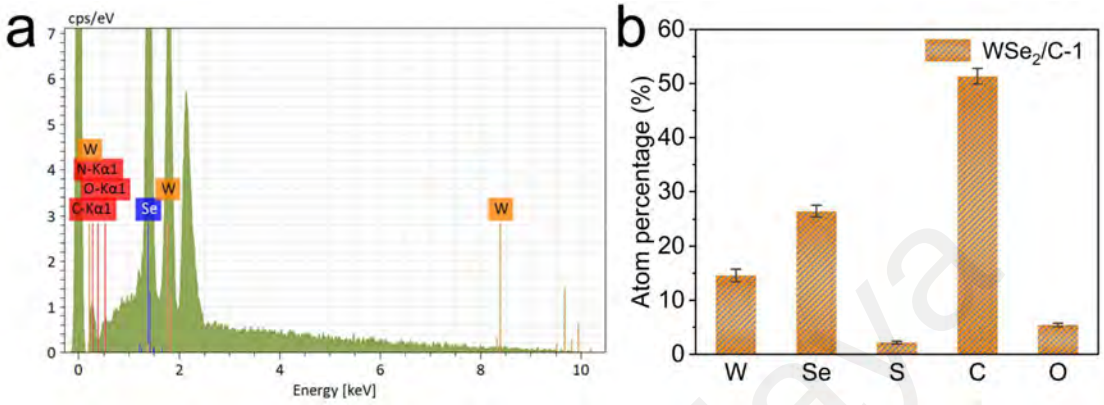

Figure 5.9: The elemental contents of WSe_2/C-1 by EDS analysis.

Additionally, the carbon content in the prepared $WSSe_2$/C-1 is accurately analyzed by TG curves. As shown in Figure 5.10, the weight loss of $WSSe_2$/C-1 and $WSSe_2$ are 41.4% and 31.7%, respectively. Based on the transformation of $WSSe_2$/C-1 after the TG test as shown below:

$$WSSe_2 + O_2 \rightarrow WO_3 + SO_2/SeO_2 \uparrow \quad (5.1)$$

$$C + O_2 \rightarrow CO_2 \uparrow \quad (5.2)$$

The carbon content in $WSSe_2$/C-1 is calculated by Equation (5.3) and Equation (5.4):

$$41.4\%m = 31.7\%m \cdot (1 - c) + m \cdot c \quad (5.3)$$

$$c = 14.2\% \quad (5.4)$$

Where m represents the total mass of $WSSe_2$/C-1, c is the percentage composition of carbon in the $WSSe_2$/C-1. By calculating the weight loss of $WSSe_2$/C-1 and $WSSe_2$, the mass fraction of carbon in $WSSe_2$/C-1 is derived to be 14.2%, which is similar to the atomic fraction analysis of EDS.

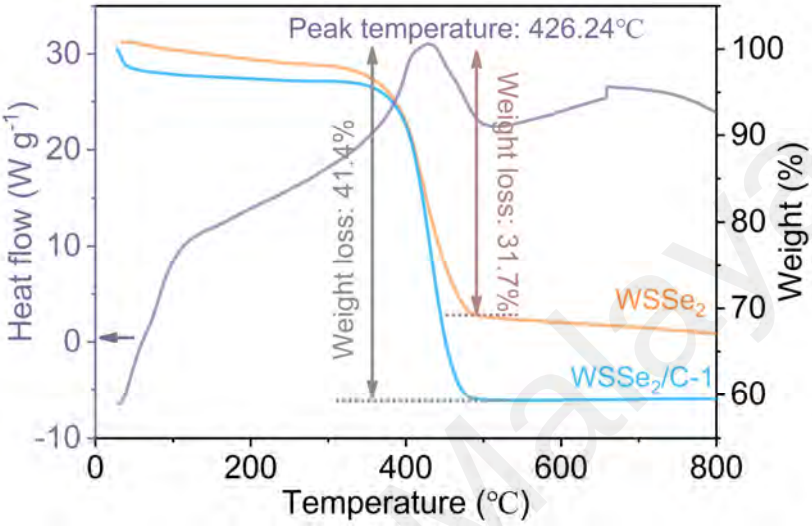

Figure 5.10: The TG-DSC curves of $WSSe_2$/C-1 and $WSSe_2$.

XRD is employed to characterize the crystallographic structure of the prepared samples. As shown in Figure 5.11, the diffraction profiles in normal and microwave calcination environments, respectively, can be indexed to the WSe_2 phase (JCPDS No. 71-0600). Compared to the normal-calcined WSe_2/C-1 sample, the characteristic peaks of microwave-calcined $WSSe_2$/C-1 exhibit a significant shifting tendency towards small angles, representing the enlarged lattice spacing from the partial replacement of S by Se. This is consistent with the HRTEM analysis.

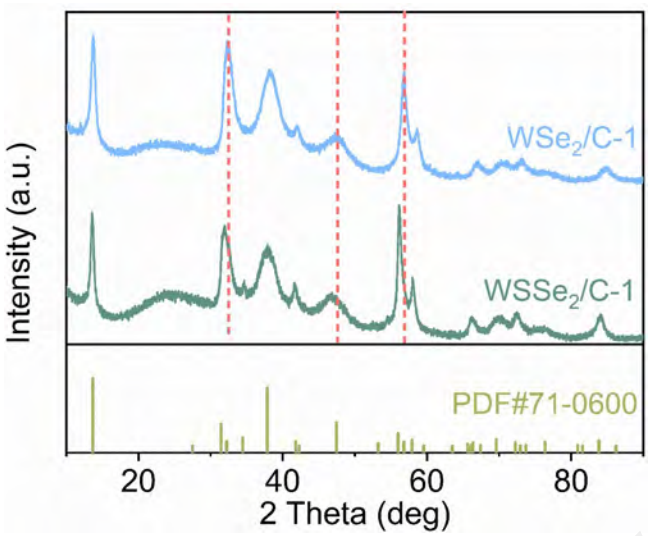

Figure 5.11: XRD patterns of $WSSe_2$/C-1 and WSe_2/C-1.

Raman curve is employed to measure the degree of graphitization of the prepared $WSSe_2$/C-1 samples. Two peaks at 1390 cm^{-1} and 1573 cm^{-1} imply the defects caused by sp3 hybridization of carbon atoms (D-band) and graphitization caused by sp2 hybridization (G-band), respectively. After fitting, the value of I_D/I_G is about 6.35, which represents that the carbon in the composite is dominated by defects (Figure 5.12).

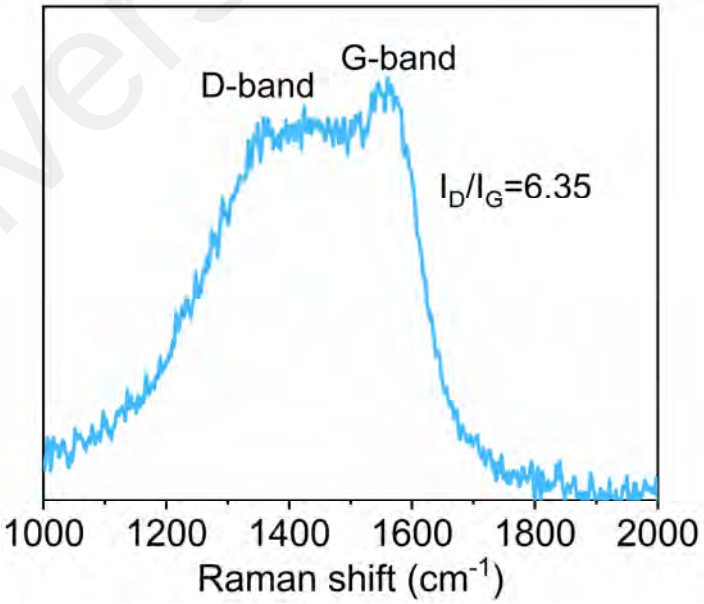

Figure 5.12: The Raman curve of $WSSe_2$/C-1.

Resistivity tests are performed using the three-probe method for $WSSe_2$, $WSSe_2$/C-1,

and WSe_2/C-1, respectively. Resultantly, $WSSe_2$/C-1 exhibits the lowest resistivity, which is favorable for fast electron conduction (Figure 5.13). The lower resistivity of $WSSe_2$ than WSe_2/C-1 indicates that the synergistic effect of anionic partial substitution and doping is favorable for the conductivity.

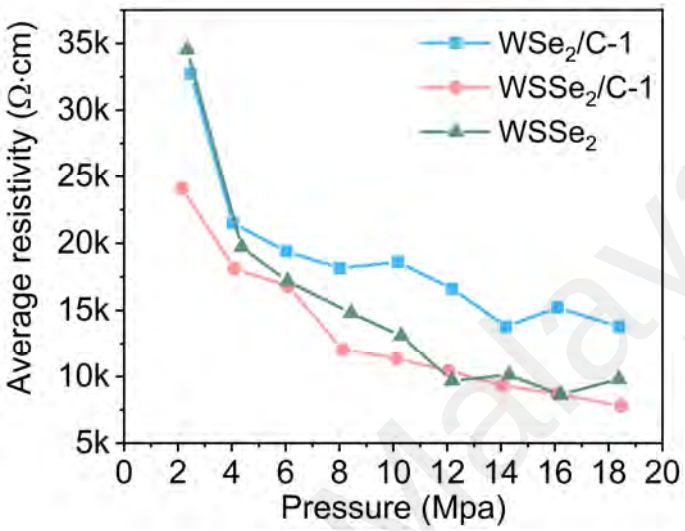

Figure 5.13: Resistivity tests of $WSSe_2$, $WSSe_2$/C-1, and WSe_2/C-1.

The chemical bonding information and surface elemental valence states of the $WSSe_2$ samples are further revealed by XPS. The two deconvolution peaks located at 31.93 and 34.07 eV in the high-resolution spectrum of W 4f in Figure 5.14a can be attributed to W $4f_{7/2}$ and W $4f_{5/2}$. Additionally, the presence of W' $4f_{7/2}$ (35.56 eV) and W' $4f_{5/2}$ (37.67 eV) in the high energy range implies high valence W^{6+}, which can be attributed to valence occupation and surface oxidation brought about by the incomplete release of S during the rapid sintering process. (Lei et al., 2023; P. Wang et al., 2022) High-resolution spectra of Se 3d exhibit two splitting peaks located at 54.47 and 55.06 eV, revealing the presence of W-Se bonds (Figure 5.14b). (P. Wang et al., 2022; P. Zhou et al., 2020) Further, according to the high-resolution spectrum of S 2p in Figure 5.14c, the C-S-C/-C=S- and -SO_x- bonds are monitored at 165.14 and 166.82 eV, respectively,

implying that a stable chemical bonding linkage exists between S and C in the complex. (Shaohui Li et al., 2020) The strong peak of S 2p appears to demonstrate the formation of $WSSe_2$. The C 1s spectra of Figure 5.14d validate the evolution of ribose-derived carbon. Among them, the splitting peaks located at 284.41 and 285.12 eV can be attributed to the sp2 and sp3 hybridization of the C-C bond. (F. Yuan et al., 2023) Moreover, additional C-O and C=O are detected at 286.22 and 288.52 eV, representing the inorganic evolution of the ribose molecule. (T. Liu et al., 2019)

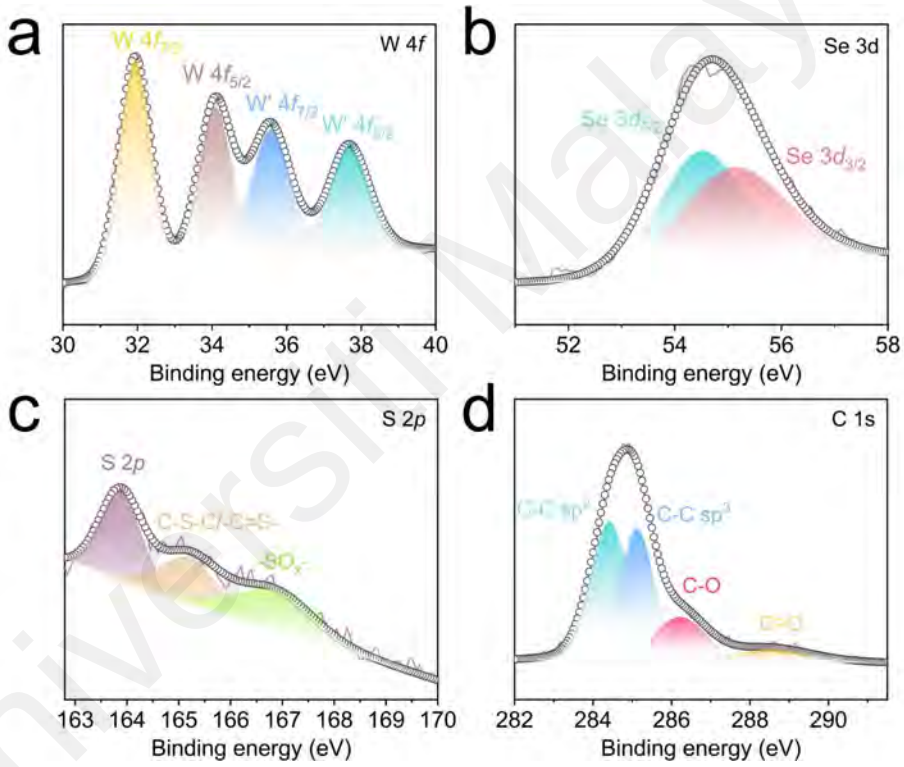

Figure 5.14: High-resolution XPS spectra of W 4f (a), Se 3d (b), S 2p (c), and C 1s (d).

To accurately measure the elemental composition in the obtained $WSSe_2$/C, XRF is further applied. As shown in Figure 5.15, the atomic percentages of normalized W, S, and Se in $WSSe_2$/C are 25.46%, 34.53%, and 40.01%, respectively. The total molar content of S and Se atoms is about three times that of W atoms, representing the completion of partial substitution of Se atoms in the precursor WS_3 to form the $WSSe_2$

heterostructure. As a comparison, the elemental contents of W, Se, and S in WSe_2/C-1 are 31.39%, 65.91%, and 2.70%, respectively. The Se atoms are about twice as abundant as the W atoms, indicating the formation of WSe_2 during complete selenization process. The above XRF results are basically consistent with the analysis of the EDS results.

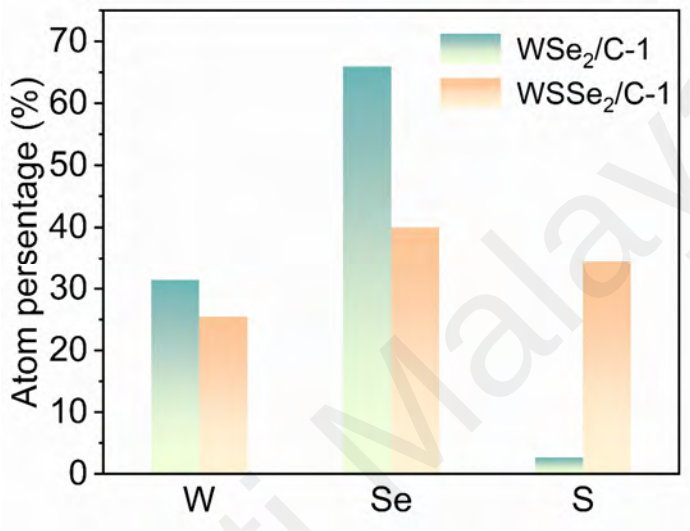

Figure 5.15: XRF results of $WSSe_2$/C-1 and WSe_2/C-1.

5.2.3 DFT Calculations of $WSSe_2$ Anionic Heterostructure

DFT calculations are employed to reveal the anionic synergistic effects of the prepared $WSSe_2$. As shown in Figure 5.16, modeling and interlayer distance calculations are performed for WSe_2, partially anion-substituted WSe_2, and S-doped & anion-substituted $WSSe_2$ by selecting the (0 0 2) crystal plane, respectively. By calculation, the interlayer distance of the pristine WSe_2 is 6.495 Å, which increases to 7.421 Å after partial S substitution of Se, and the final interlayer distance is finally enlarged to 8.094 Å by further interlayer doping of S atoms. The enlarged layer spacing provides a fast channel for the bulk Na^+ transfer at high power densities.

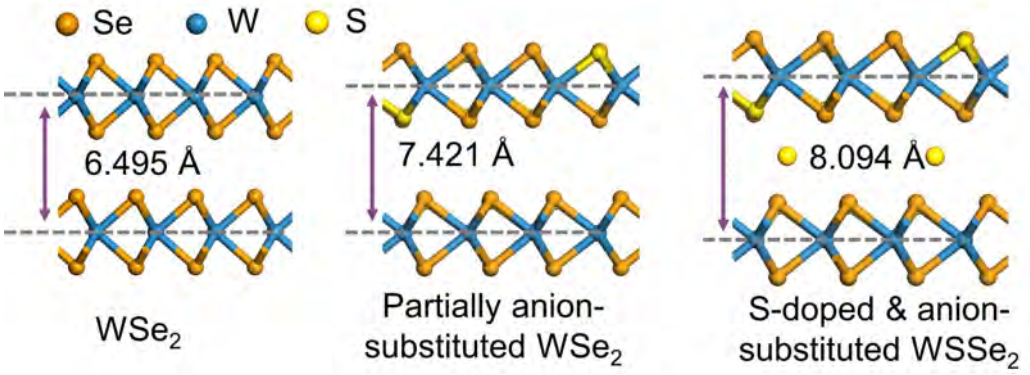

Figure 5.16: Modeling and interlayer distance calculations of WSe_2, partially anion-substituted WSe_2, and S-doped & anion-substituted $WSSe_2$.

Moreover, Figure 5.17 calculates the band gaps of WSe_2 and $WSSe_2$ as 1.628 and 0.206 eV, respectively. The smaller band gaps near the Fermi energy level imply that $WSSe_2$ has stronger metallic properties, which are favorable for the fast electron transfer. This is consistent with the results of the conductivity analysis in Figure 5.13.

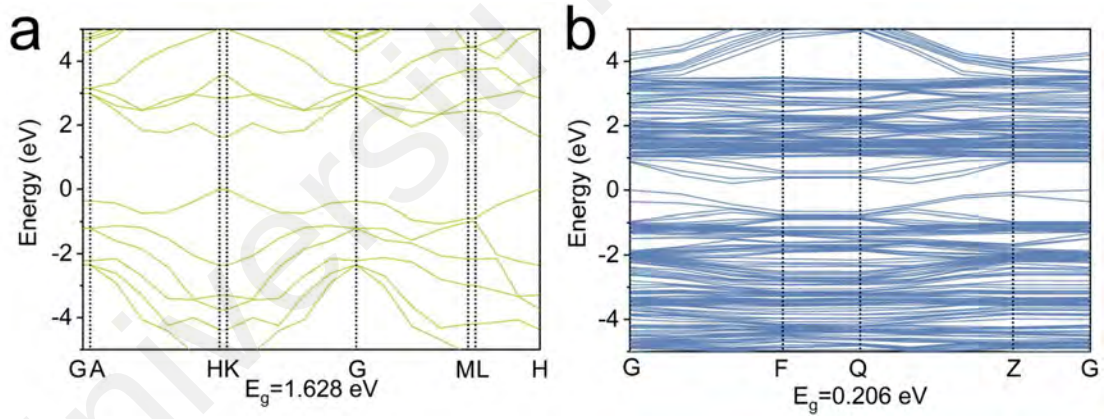

Figure 5.17: The band gaps of WSe_2 and $WSSe_2$.

Additionally, to evaluate the effect of the built-in electric field resulting from partial anion substitution, differential charge density calculations are performed in Figure 5.18. The blue electron cloud represents charge accumulation, while the yellow one represents charge disappearance. The appearance of uneven charge distribution near the S atom represents the formation of a built-in electric field in the interlayer. Unlike the uniform electric field distribution, the formation of the built-in electric field facilitates

the rapid ions transfer between the layers.

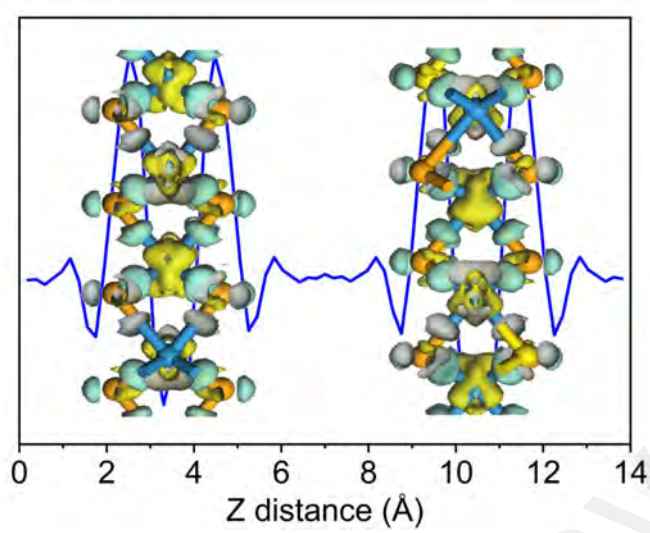

Figure 5.18: The differential charge density calculation of $WSSe_2$.

5.2.4 Electrochemical Properties of $WSSe_2$/C in SIBs

The Na^+ storage capacity of the $WSSe_2$/C electrode is investigated by assembling the Na half-cells. Figure 5.19 compares the short-term cycling performance of WSe_2/C-1 and $WSSe_2$/C-1 electrodes at a current density of 1 A g^{-1}, respectively. As can be seen, the $WSSe_2$/C-1 electrode exerts a specific capacity of 715.3 mA h g^{-1} after 200 cycles, which is significantly higher than that of the WSe_2/C electrode. The higher specific capacity of the $WSSe_2$/C-1 electrode can be attributed to the built-in electric field formed by the synergistic effect of anions and the enlarged layer spacing, which facilitates the activation of electrochemical reactions in the bulk phase, and thus promotes the full occurrence of the reactions and the fast pseudocapacitance capability. According to the previous study, the gradually increasing electrochemical performance during cycling may be related to the continuously exposed electrochemically active interface. The exposed bulk-phase structure can not only shorten the transport path between the electrode and the electrolyte, but also facilitate the activation of abundant

active sites, leading to the fast pseudocapacitive reaction process.

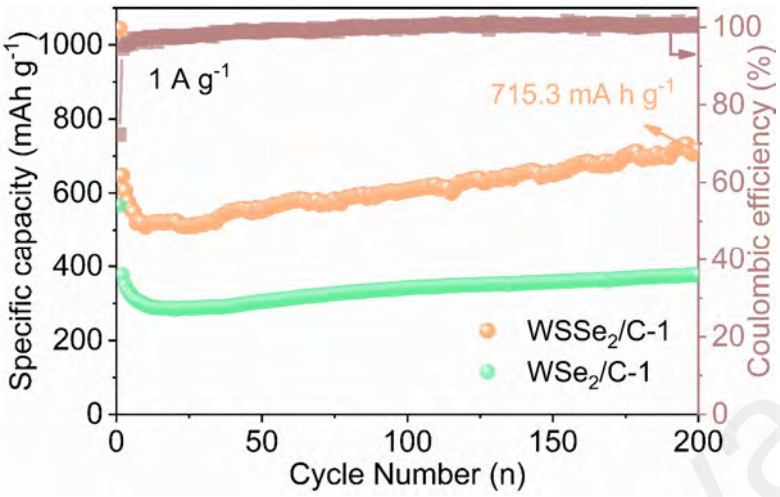

Figure 5.19: Short cycling performance at 1 A g^{-1} of $WSSe_2$/C-1 and WSe_2/C-1 electrodes.

Motivated by the consideration that $WSSe_2$/C-1 electrode exhibits a significant activation process during cycling, the electrodes after 200 cycles in Figure 5.20 are used to evaluate the rate capability. The $WSSe_2$/C-1 electrode exhibited specific capacities of 706.1, 525.1, 434.4, 406.5, 359.6, and 346.4 mA h g^{-1} at current densities of 1, 2, 4, 6, 8, and 10 A g^{-1}, respectively. When the current density gradually recovers from 10 A g^{-1} to 1 A g^{-1}, a gradual recovery of the specific capacity is also achieved, suggesting excellent rate performance.

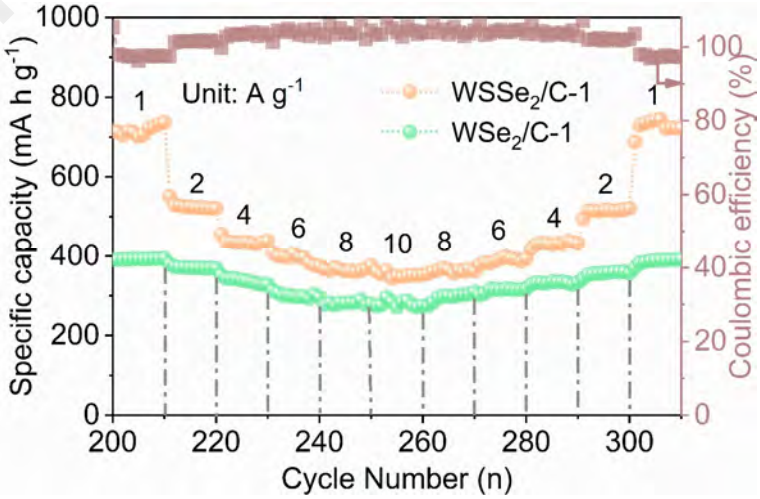

Figure 5.20: The cycled rate capability of $WSSe_2$/C-1 and WSe_2/C-1 electrodes.

Subsequently, as shown in Figure 5.21a and b, the charge/discharge curves at different current densities of $WSSe_2$/C-1 and WSe_2/C-1 do not undergo significant plateau shift with increasing current density, indicating that the constructed composite structure has significant high-current adaptability.

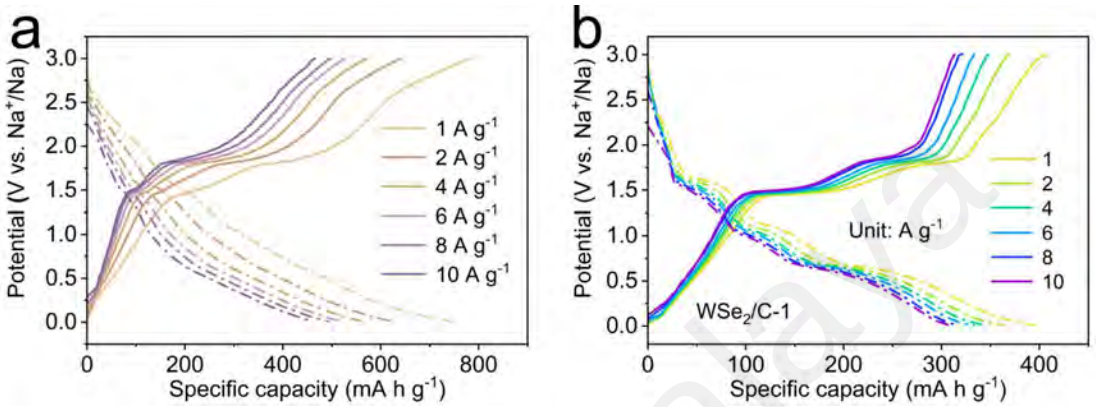

Figure 5.21: Charge-discharge voltage profiles of $WSSe_2$/C-1 and WSe_2/C-1 at different current densities.

Additionally, to explore the activation process of the $WSSe_2$/C-1 electrode in detail, the dynamic dQ/dV for the initial 50 cycles are further summarized in Figure 5.22a (discharge process) and Figure 5.22b (charging process). From Figure 5.22a, as the discharge reaches about 10 cycles, a distinct peak starts to appear near 0.62 V, representing the conversion process of doped S to S^{2-}. (S. Chen et al., 2023; Ma et al., 2023) Notably, no corresponding charging reaction peak was monitored in Figure 5.22b, implying an irreversible process of S^{2-}. Moreover, two obvious reaction peaks (1.03 and 1.63 V) appear in Figure 5.22a as the cycle proceeds, representing the conversion process of $W^{4+} \rightarrow W$. Correspondingly, the reaction peak (1.46 and 1.82 V) of $W \rightarrow W^{4+}$ appears in Figure 5.22b, indicating the good reversible conversion ability of the $WSSe_2$/C-1 electrode in the electrochemical process.

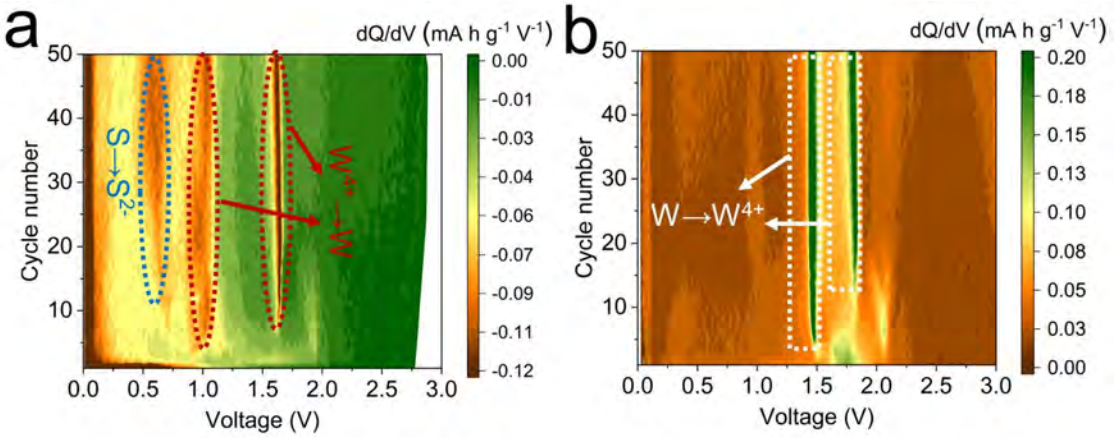

Figure 5.22: The dQ/dV cruves evolution of the $WSSe_2$/C-1 electrode for the first 50 cycles: (a) discharge process and (b) charge process.

Figure 5.23 further evaluates the long-term cycling performance of the $WSSe_2$/C-1 electrode at a high current density of 10 A g^{-1}, which can maintain a specific capacity of 378.9 mA h g^{-1} after 1000 cycles.

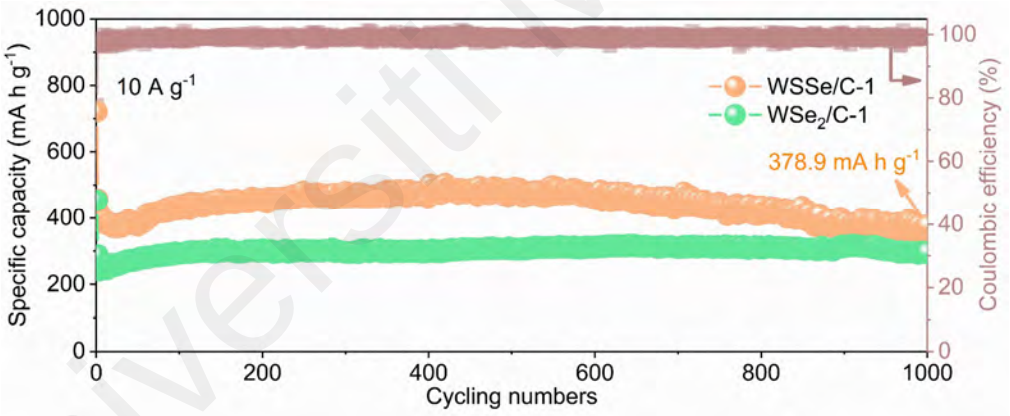

Figure 5.23: Long cycling performance comparison at the current density of 10 A g^{-1}.

In addition, we further explored the effects of different ribose addition ratios (0.5, 1, and 1.5 g) on the electrochemical performance of $WSSe_2$/C. As shown in Figure 5.24, the $WSSe_2$/C-1 electrode exhibits the best electrochemical performance. From that, the appropriate ribose addition helps to regulate the distribution between $WSSe_2$ and carbon matrix, thus promoting the electrochemical capability. Notably, compared to $WSSe_2$/C-0.5 and $WSSe_2$/C-1.5, the high pseudocapacitance capacity of $WSSe_2$/C-1 originates

from the homogeneous distribution between the active material and carbon. The less carbon amount reduces the overall electronic conductivity, which in turn weakens the fast reactivity and the degree of response of the W phase transition process. Moreover, the excessive carbon content can lead to localized carbon accumulation, which reduces the exposure of the fast reaction active site while causing a decrease in the overall specific capacity. Therefore, under reasonable anionic interactions, the $WSSe_2$/C-1 electrode exhibits an additional excellent pseudocapacitance slope capacity in addition to the plateau capacity, which facilitates the rapid adsorption and transfer of Na^+.

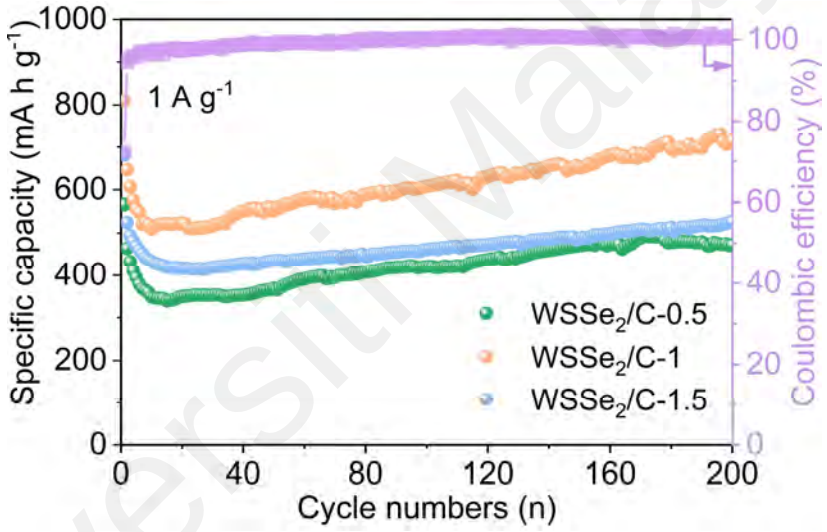

Figure 5.24: Comparison of the short-term cycling performance of $WSSe_2$/C-0.5, $WSSe_2$/C-1, and $WSSe_2$/C-1.5 at 1 A g^{-1}.

Additionally, Figure 5.25 compares the charging/discharging curves of the prepared electrodes during the initial process. Among them, the WSe_2/C-1 electrode exhibits an obvious charging/discharging plateau (discharging: 0.57 V; charging: 1.71 V). Unlike the WSe_2/C-1 electrode, the $WSSe_2$/C-1 electrode exhibits a ramp capacity with strong pseudocapacitance capability while providing a plateau capacity, which is conducive to achieving a higher specific capacity.

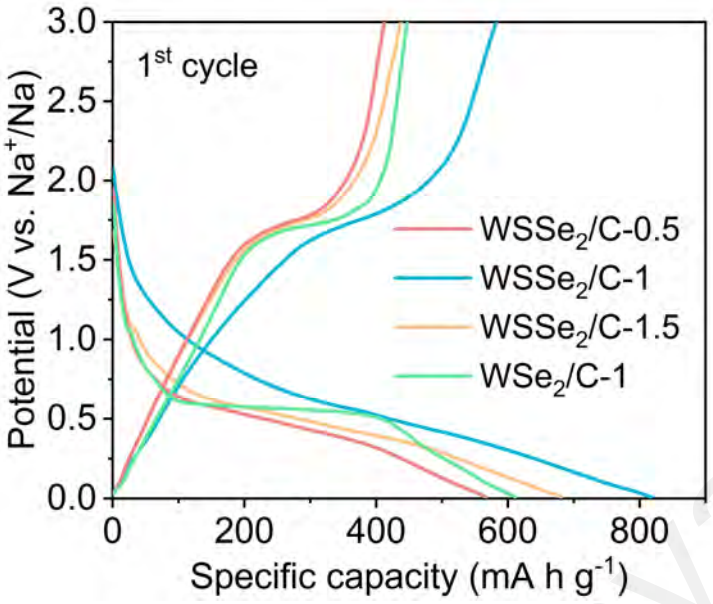

Figure 5.25: The initial charging/discharging curves of the prepared electrodes.

To further clarify the effect of carbon introduction on the electrochemical performance, Figure 5.26 compares the short-cycling performance of $WSSe_2$/C-1 and $WSSe_2$ electrodes at 1 A g^{-1}, respectively. The results show that $WSSe_2$/C-1 exhibits a significant electrochemical advantage compared to $WSSe_2$ without carbon composite.

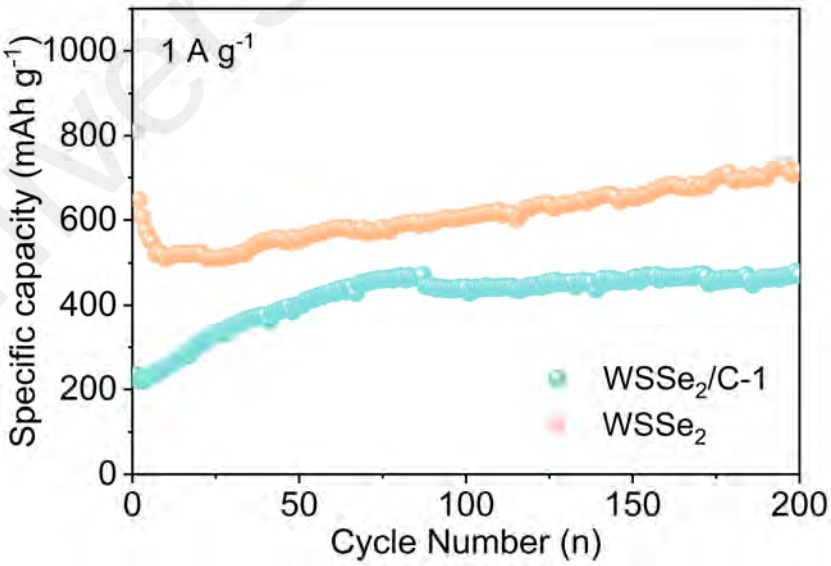

Figure 5.26: The short-cycling performance of $WSSe_2$/C-1 and $WSSe_2$ electrodes at 1 A g^{-1}.

In addition, the electrochemical properties of the $WSSe_2$/C-1 and WS_x/C-1 precursors are compared in Figure 5.27. WS_x/C-1 exhibits poor specific capacity play and sharp capacity decay due to low ionic and electronic conduction brought about by incomplete hydrothermal carbonation and shuttling effects triggered by the conversion of S to polysulfide.

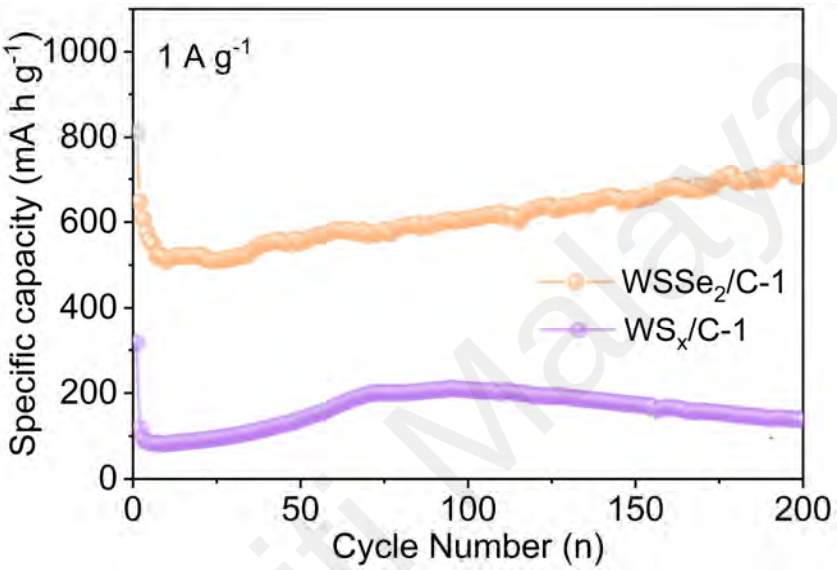

Figure 5.27: The electrochemical properties of the $WSSe_2$/C-1 and WS_x/C-1 precursors.

5.2.5 Sodium Storage Kinetics Investigation

The CV curves in Figure 5.28 explore the electrochemical processes for the initial three cycles at 0.1 mV s^{-1}. During the initial cathodic scan, a series of peaks appear near 0.5 V, representing the formation of the SEI and the $WSSe_2$ conversion process. In the subsequent anodic scan, the oxidation peak located around 1.78 V indicates a reversible conversion from W to $WSSe_2$. The CV curves from the second and third circles exhibit a pair of redox peaks located around 1.46 and 1.66 V, symbolizing the excellent reversible conversion capability of $WSSe_2$.

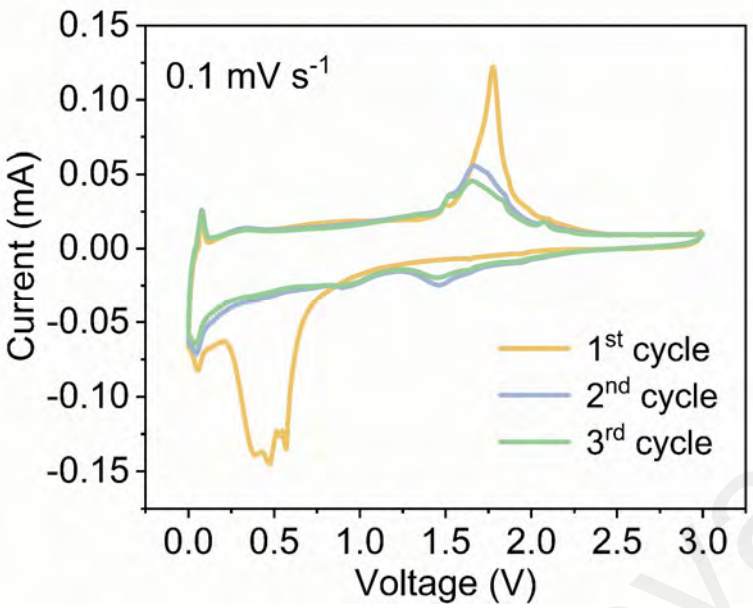

Figure 5.28: CV curves of $WSSe_2$/C-1 electrode from 0.01 to 3.0 V at the scan rate of 0.1 mV s^{-1}.

The CV curves at different scan rates are applied to evaluate the pseudocapacitance capability of the $WSSe_2$/C-1 electrode (Figure 5.29a). The shape of the CV curves remains essentially unchanged as the scan rate increases, verifying the stable reaction behavior of the $WSSe_2$. In Figure 5.29b, to explore the dominant behavior of the electrochemical process, the main anodic (Peak 1) and cathodic (Peak 2) peaks are selected to obtain *b*-values by fitting the peak currents and scanning rates, respectively. The fitted *b*-values for the cathodic and anodic peaks are 0.945 and 0948, respectively, which are both close to 1, representing pseudocapacitance-dominated diffusion behavior. Additionally, Figure 5.29c calculated the pseudocapacitance contributions of 60.8%, 67.3%, 72.4%, 76.4%, 81.9%, and 92.0% at 0.1, 0.2, 0.5, 1, 2, and 5 mV s^{-1}, respectively, demonstrating that large scan rates contribute to the excitation of fast pseudocapacitance storage behavior. The shaded percentages of the CV curves in Figure 5.29d demonstrate the pseudocapacitance contribution at the scan rate of 5 mV s^{-1}.

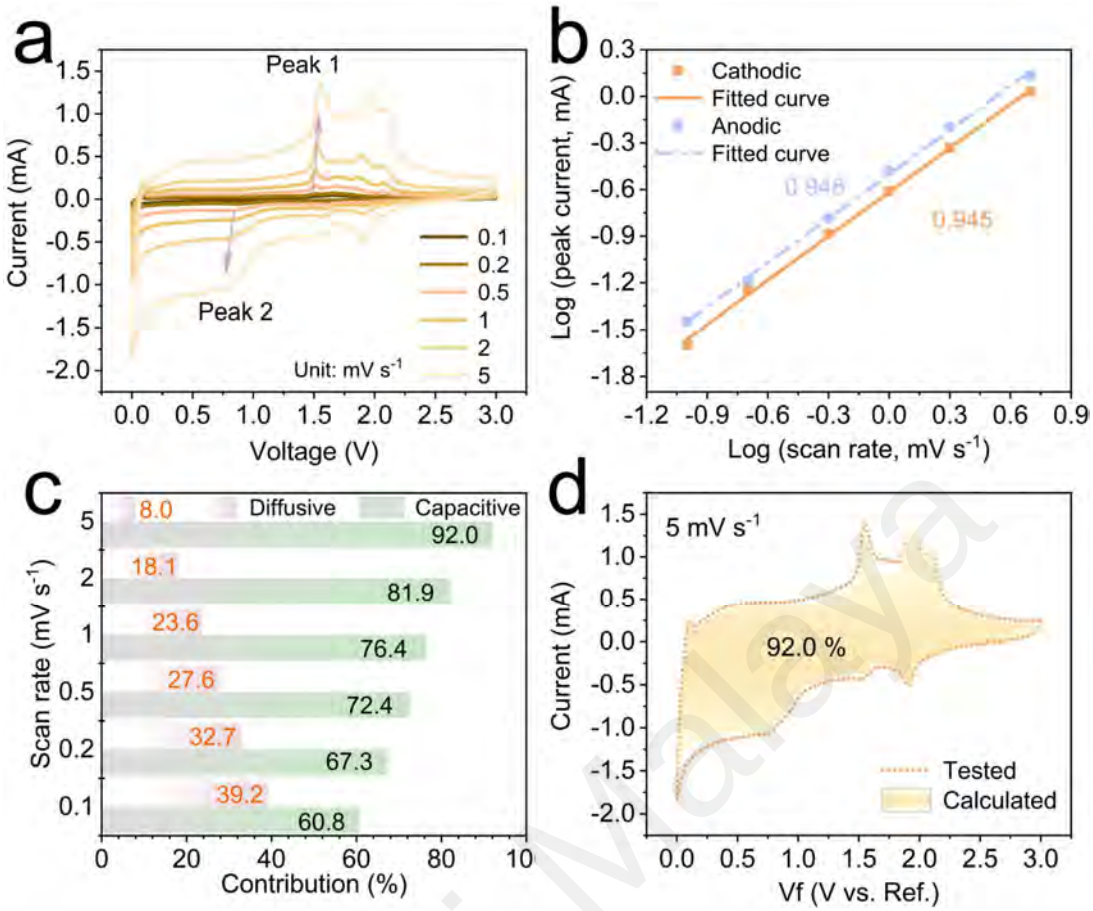

Figure 5.29: (a) CV curves at different scan rates of $WSSe_2$/C-1 electrode in SIBs. (b) Linear diagrams of log (v) and log (i) corresponding to peak currents in different oxidation and reduction states of $WSSe_2$/C-1 electrode. (c) The pseudocapacitance contribution ratios of $WSSe_2$/C-1 electrode at different scan rates. (d) The pseudocapacitance contribution of $WSSe_2$/C-1 electrode at a scan rate of 5 mV s^{-1}.

EIS is exploited to characterize the electrode reaction kinetics of $WSSe_2$/C-1. Figure 5.30a analyzes the Nyquist curves of the electrodes in the initial state and after 5 cycles. In this case, the semicircle diameters of the middle-high frequencies become progressively smaller as the cycle progresses, representing lower contact and charge transfer resistance. Figure 5.30b analyzes the Na^+ diffusion behavior (D) by fitting the slopes of $\omega^{-1/2}$ and Z' in the low-frequency region. As can be seen, the D value in the pristine and after 5 cycles are 180.22 and 39.14, respectively. The lower D value after 5 cycles implies that the abundant anionic heterogeneous interface brought about by the

activation process contributes to the ion's diffusion in the electrode interior.

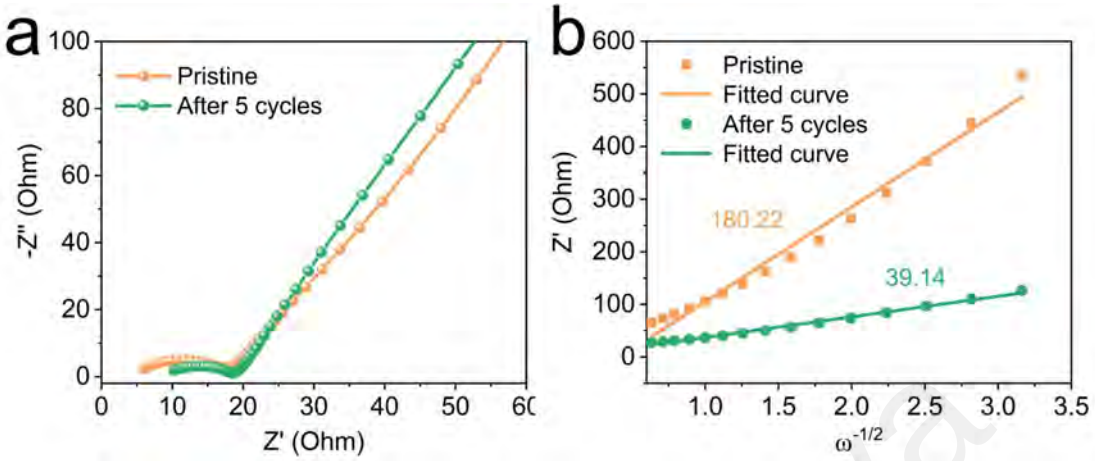

Figure 5.30: (a) Nyquist plots of $WSSe_2$/C-1 electrode at pristine and 5th cycle. (b) Relationship between Z' and $\omega^{-1/2}$.

To further compare the difference in EIS between electrodes $WSSe_2$/C-1 and WSe_2/C-1, the Nyquist curve of WSe_2/C-1 electrode is tested in Figure 5.31. Consequently, the semicircle of the mid-high frequency region of the WSe_2/C-1 electrode after 5 cycles is significantly smaller than that of the initial state, indicating that the activation effect of the current leads to the decrease of the contact and charge transfer resistance. In addition, the D values of the WSe_2/C-1 electrode are 91.74 and 34.33 in the initial state and after 5 turns of cycling, respectively, again indicating that the activation effect of the electrode leads to an increase in the diffusion rate.

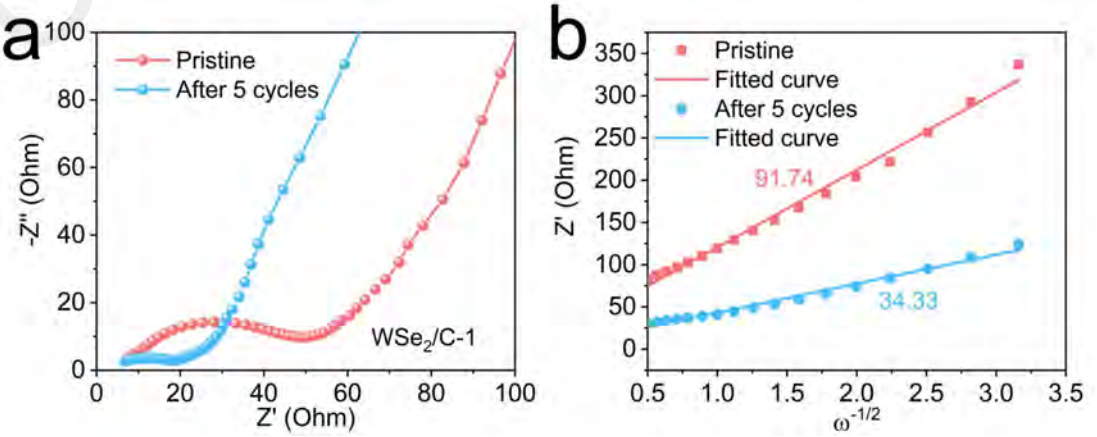

Figure 5.31: The Nyquist curve of WSe_2/C-1 electrode.

Moreover, the detailed EIS fitting results for $WSSe_2$/C-1 and WSe_2/C-1 are presented in Table 5.1. As shown in Table 5.1, the pristine sum value of (R_f+R_{ct}) composed of the SEI film resistance (R_f) and the charge transfer resistance (R_{ct}). The R_f+R_{ct} value from 11.396 Ω decreases to 8.274 Ω after 5 cycles, which is associated with the activation process as a result of the increased infiltration of electrolyte into the electrode material. Contrastingly, the R_f+R_{ct} values of both $WSSe_2$/C-1 electrodes are smaller than WSe_2/C-1, indicating that they have less resistance to electron transfer. Therefore, benefiting from the anion synergism, the $WSSe_2$/C-1 electrode exhibits a lower impedance performance and a faster ion diffusion rate.

Table 5.1: Fitting results of EIS for $WSSe_2$/C-1 and WSe_2/C-1 electrode in SIBs with the proposed equivalent circuit.

Electrodes	Cycle number	R_s (Ω)	R_f+R_{ct} (Ω)
$WSSe_2$/C-1	Pristine	5.546	11.396
	After 5 cycles	10.250	8.274
WSe_2/C-1	Pristine	8.878	40.353
	After 5 cycles	7.623	11.318

The GITT is utilized to accurately measure the diffusion coefficient of Na^+. As shown in Figure 5.32, the Na^+ diffusion efficiency ($\log D_{Na^+}$) in the $WSSe_2$/C-1 electrode is between -13.6~-11, which is higher than WSe_2/C-1 electrode, displaying a stable and fast ion diffusion process.

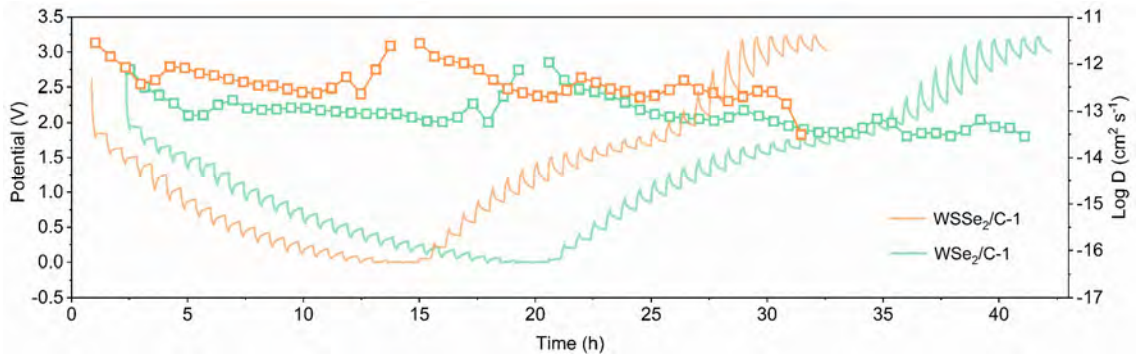

Figure 5.32: GITT and Na^+ diffusion coefficients of $WSSe_2$/C-1 and WSe_2/C-1 electrodes.

5.2.6 Electrochemical Properties of $WSSe_2$/C-1 in SICs

A comprehensive electrochemical performance evaluation of the $WSSe_2$/C-1 electrode is performed by assembling SICs using commercial activated carbon as the cathode. The suitable voltage range is selected by testing the CV curves in different voltage ranges at a scan rate of 10 mV s^{-1}. When the cut-off voltage is higher than 3.8 V, an additional oxidation peak appears near the cut-off voltage, representing the occurrence of polarization (Figure 5.33a). Therefore, it can be determined that 0−3.8 V is the appropriate voltage range. Subsequently, the CV curves of the assembled SICs are measured at different scan rates, respectively (Figure 5.33b). The results indicate that the CV curve shape does not change significantly (rectangle-like shape) with the increase of scan rate, indicating that the assembled SICs are suitable for high power densities.

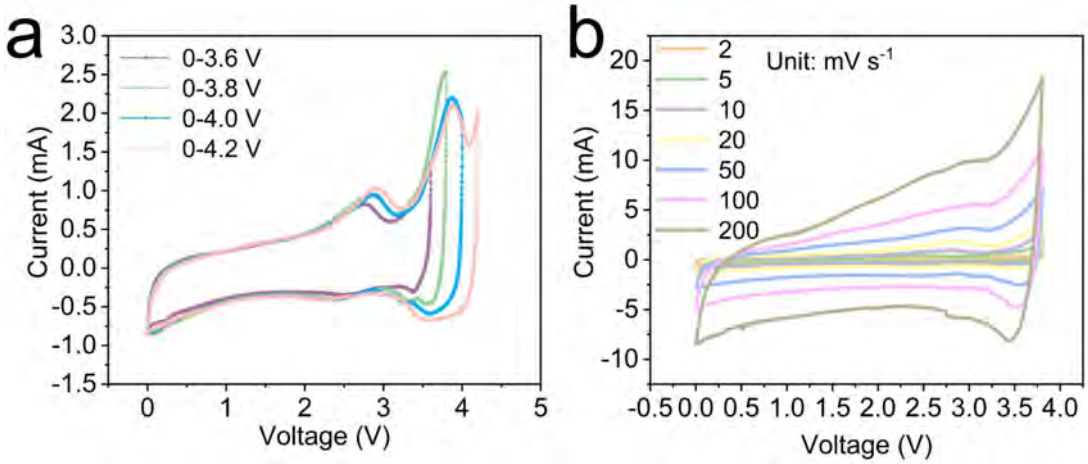

Figure 5.33: (a) CV curves at different cutoff potentials. (b) CV curves at different scan rates.

In Figure 5.34a, rate performance tests are presented at current densities of 0.2, 0.5, 1, and 2 mA g^{-1}, respectively. Resultantly, the assembled SICs can exhibit energy densities of 107.14, 91.57, 84.97, and 82.33 W h kg^{-1} at power densities of 380, 950, 1900, and 3800 W kg^{-1}, respectively. The GCD curves at different current densities exhibit a triangle-like shape, representing a mixed mechanism of pseudocapacitance and double electric layer (Figure 5.34b).

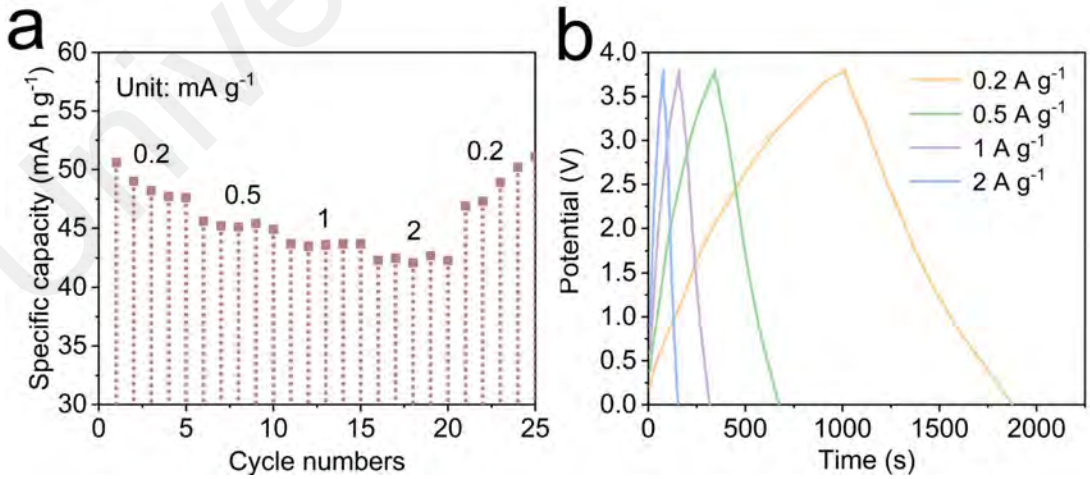

Figure 5.34: (a) Rate performance of $WSSe_2$/C-1//AC. (b) GCD profiles of $WSSe_2$/C-1//AC at different current densities.

The long-term cycling test is performed at a high-power density of 3800 W kg^{-1}. The results indicate a capacity retention of 86.5% can still be obtained even after 13000 cycles (Figure 5.35).

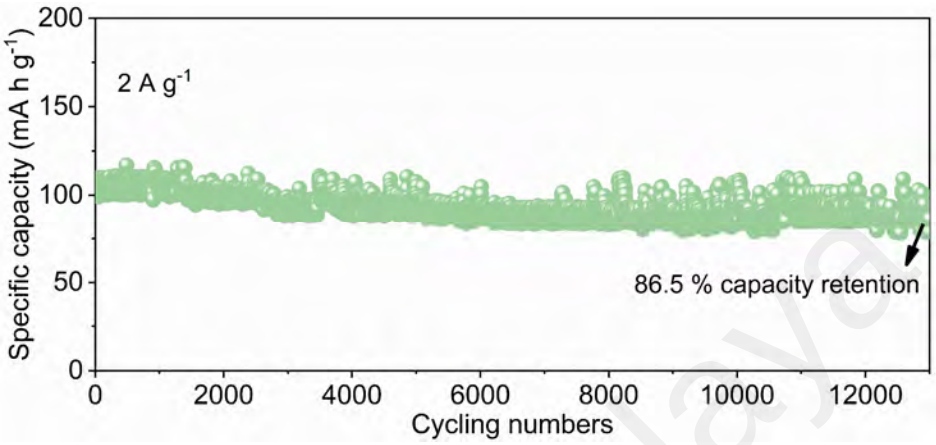

Figure 5.35: Cycling stability and coulombic efficiency of $WSSe_2$/C-1//AC at 3800 W kg^{-1} for 13000 cycles.

5.3 Carbon-Coated VSSe/C Composites

To reorganize the original VS_4 at the structural design level, a simple anionic heterogenization strategy is applied to design a uniformly distributed $V_{1.11}S_2/V_{1.13}Se_2$ heterogeneous interface with the pyrrole-derived carbon surface coating. Unlike the conventional way of constructing heterostructures using disulfides, this work adopts the high-capacity VS_4 as a precursor. Benefiting from the weaker V-S_2^{2-} bond, the alternating $V_{1.11}S_2$ and $V_{1.13}Se_2$ heterogeneous structure is in-situ formed during the later selenization process. Specifically, a stable V-based disulfide/selenide heterogeneous interface is constructed to form the regular built-in electric field and extended interlayer distance to ensure fast and stable sodium ion transfer. At the same time, multi-defective carbon coating layers are further formed during the heterogeneous process, which can enhance the rapid ion adsorption and the electrical conductivity of the overall structure. DFT calculations indicate that the expanded interlayer distance in the VSSe

heterogeneous interface could facilitate the rapid transfer of Na^+. In addition, the presence of the built-in electric field enhances the adsorption capacity and overall electrical conductivity of the reaction products, which consequently delivers stronger structural properties. Moreover, by theoretical calculations, our work further clarified the diffusion energy barriers of Na^+ in $V_{1.11}S_2$ and $V_{1.13}Se_2$ phases and the migration tendency of the discharge products (Na_2S and Na_2Se) between the above two phases had been predicted by charge distribution. The ex-situ XRD and XPS show that the initial charging and discharging processes contained only cation conversion reactions, and no valence transitions of anions are detected, demonstrating the stability of the constructed structures.

5.3.1 Synthesis of VSSe/C

The stepwise reorganization of VS_4 into VSSe/C is shown schematically in **Figure 5.36**. First, VS_4 is synthesized by the conventional solvothermal method. (Yanrong Wang et al., 2018) Then, the induced pyrrole monomer polymerization is employed to achieve a homogeneous polymeric coating on the surface of VS_4. To complete the anionic heterogeneization process, the selenium powder is mixed with the above products in proportion and subjected to an anionic substitution at 450 °C in H_2/Ar (10% H_2) gas mixture. Meanwhile, the polypyrrole on the surface completes the transformation to defective carbon. Remarkably, the heterogeneous process of VS_4 can be ascribed to the breakage of the V-S_2^{2-} bond at high temperatures. Half of the S_2^{2-} loses electrons during the bond-breaking process and transfers to the remaining S_2^{2-} to form a stable layered $V_{1.13}S_2$. After that, the reduced Se^{2-} further occupies the broken-

bond vacancies to form a layered $V_{1.11}Se_2$.

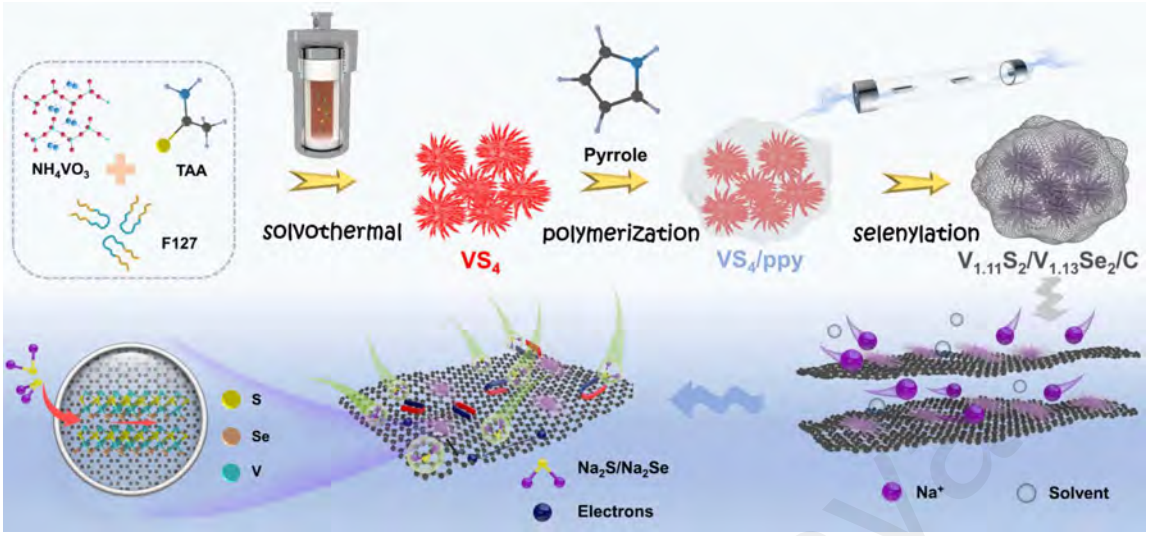

Figure 5.36: Schematic illustration of the synthetic route for VSSe/C.

5.3.2 Structural and Chemical Characterization of VSSe/C

As the SEM images shown in Figure 5.37, the prepared VS_4 delivers sea urchin-like morphology.

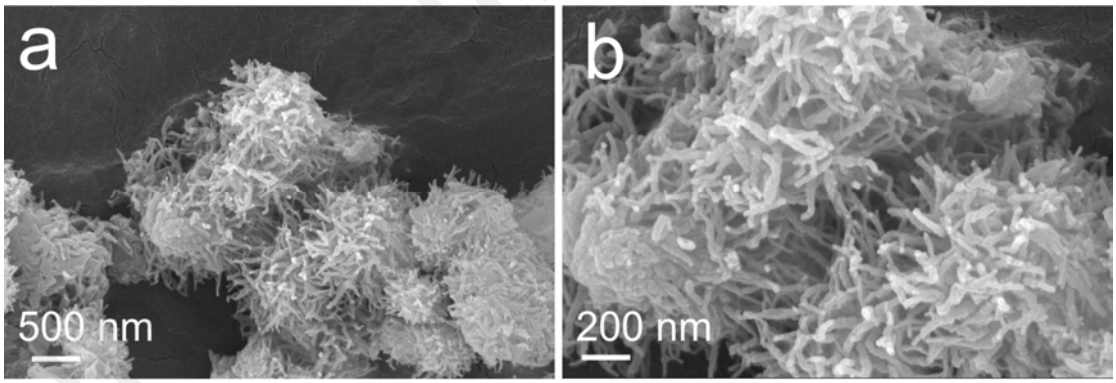

Figure 5.37: SEM images of VS_4.

The SEM image in Figure 5.38a exhibits the microscopic morphology of the resulting VSSe/C. It can be seen that the original sea urchin-like morphology is further subdivided into short rods after the heterogeneous/carbonation process. This is beneficial to increasing the effective solid-liquid contact and thus can improve ion transport efficiency. According to the TEM image in Figure 5.38b, clear amorphous

defective carbon coatings (5−11 nm) are observed on the bulk VSSe/C surface. The carbon coating can stabilize the overall structure and enhance the electronic conductivity to accommodate the rapid surface ion transfer.

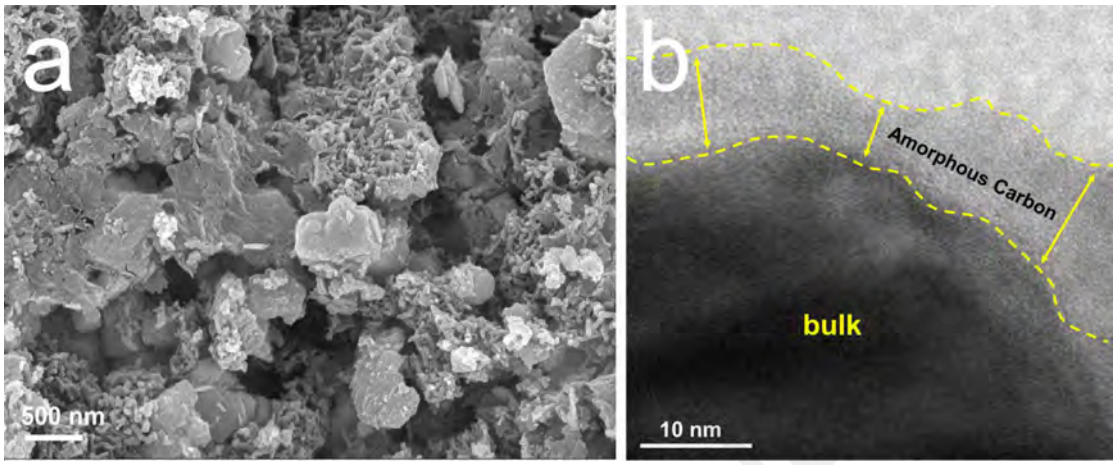

Figure 5.38: SEM image (b) and TEM diagrams (c) of VSSe/C.

The HRTEM results in Figure 5.39a further validate the existence of $V_{1.11}S_2$ and $V_{1.13}Se_2$. Besides, an expanded interlayer distance (0.593 nm) is formed between the regions of $V_{1.11}S_2$ and $V_{1.13}Se_2$ phase, representing the formation of a heterogeneous interface. From the selected area electron diffraction (SAED) patterns in Figure 5.39b, the well-defined diffraction rings can be attributed to $V_{1.11}S_2$ and $V_{1.13}Se_2$, further confirming the polycrystallinity features of the obtained VSSe/C sample.

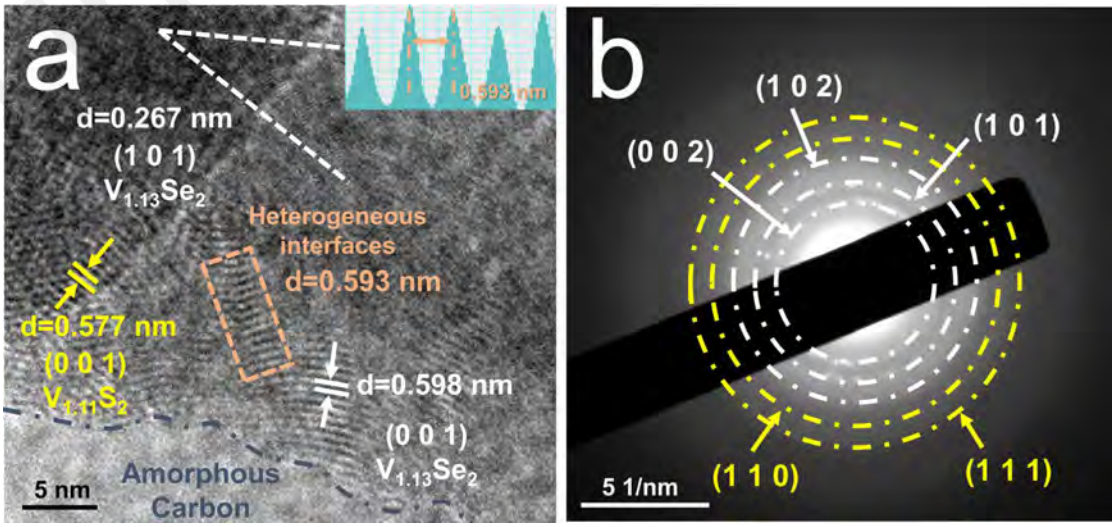

Figure 5.39. HRTEM diagram (a) and SAED pattern (b) of VSSe/C.

The TEM mapping images in Figure 5.40 demonstrate the uniform elemental distribution of VSSe/C, revealing the successful phase convention and carbon coating. Additionally, the mapping image of N element demonstrates the uniform distribution of nitrogen in the amorphous carbon layer.

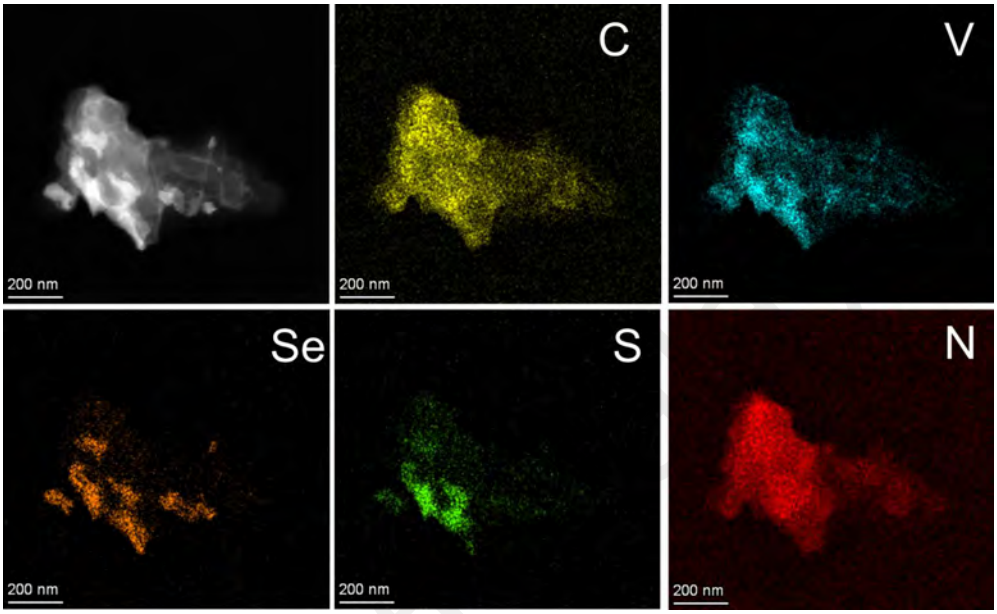

Figure 5.40: Elemental mapping of VSSe/C.

The prepared VSSe/C is analyzed by EDS for the elemental species and content of the microregion composition. The content of carbon atoms in the selected region is about 37.81%, and the ratio of Se and S atom content is about 1.5/1 (Figure 5.41). It can be further predicted that the contained $V_{1.13}Se_2$ is about 1.5 times of $V_{1.11}S_2$.

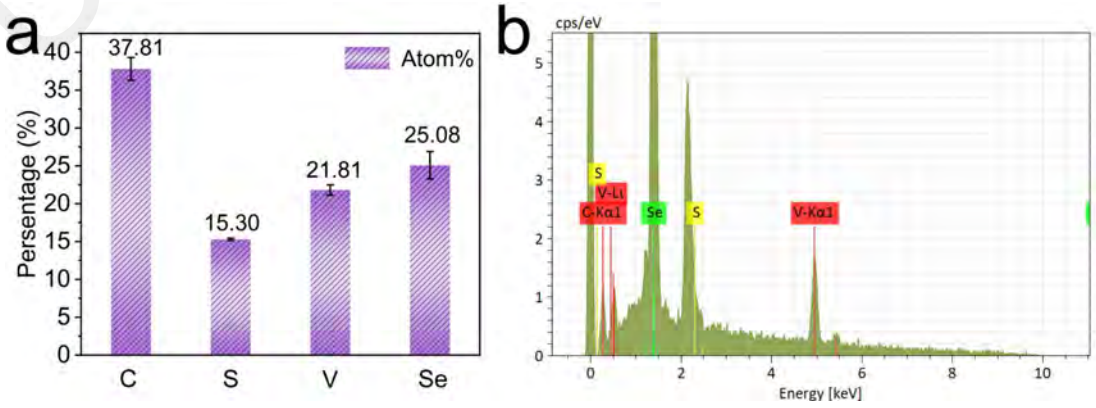

Figure 5.41: EDS elemental content analysis of VSSe/C.

XRD analysis is adopted to measure the physical phase structure of the resulting sample. As shown in Figure 5.42a, the VS_4 synthesized in the initial step can be indexed to JCPDS No. 21-1434, representing the successful preparation of pure phase VS_4. Besides, the XRD diffraction pattern of VSSe/C is consisted of $V_{1.11}S_2$ (JCPDS No. 33-1445) and $V_{1.13}Se_2$ (JCPDS No. 32-1415). Among them, the paired splitting peaks can be directly observed in (0 0 1), (1 0 1), (1 0 2), and (1 1 0), which are attributed to the above two phases. Notably, $V_{1.11}S_2$ and $V_{1.13}Se_2$ have extra cations that are not equivalently coordinated with respect to VS_2 and VSe_2 in the conventional chemical state, exhibiting a more typical vacant state of the anions (S and Se). The crystal structure model of VSSe/C is schematically described in Figure 5.42b. According to the side view, $V_{1.11}S_2$ and $V_{1.13}Se_2$ exhibit a laminar alternating arrangement, where Se and S atoms form a laminar anionic heterogeneous interface.

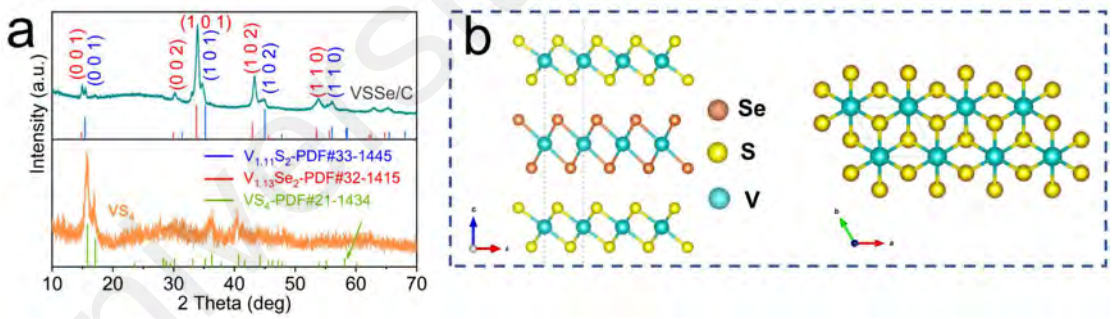

Figure 5.42: XRD patterns (a) and the corresponding crystal structure model (b).

The chemical structure of the sample is further analyzed by Raman spectroscopy. As shown in Figure 5.43, the presence of characteristic peaks located around 200 and 300 cm^{-1} in the initial VS_4 can be attributed to V-S bond stretching peak, and the apparent peak located near 350 cm^{-1} is caused by breathing the V_2S_4-cage. (B. Liu et al., 2022; Z. Qin et al., 2022) After the anionic heterogeneous interaction, due to the internal electric field structure change, the two characteristic peaks located at 280.7 and 333.8 cm^{-1} can

be assumed to be a division from the VS_4 peak, corresponding to in-plane V-S and V-Se E_{1g} models. (Ci et al., 2020; Junhua Zhou et al., 2017) Similarly, the peaks at 431.2 and 471.9 cm^{-1} are attributed to A_{1g} vibration of $V_{1.11}S_2$ and $V_{1.13}Se_2$, respectively. Meanwhile, the two prominent peaks in VSSe/C appear at 1330.9 and 1602.1 cm^{-1}, corresponding to defective carbon (D-band) and graphitized carbon (G-band), respectively. (F. Yuan, Li, et al., 2022) The integrated area ratio (I_D/I_G) of the D and G peaks is 2.42, indicating that the amorphous carbon layer on the surface is dominated by defects, which is favorable for achieving rapid ion adsorption.

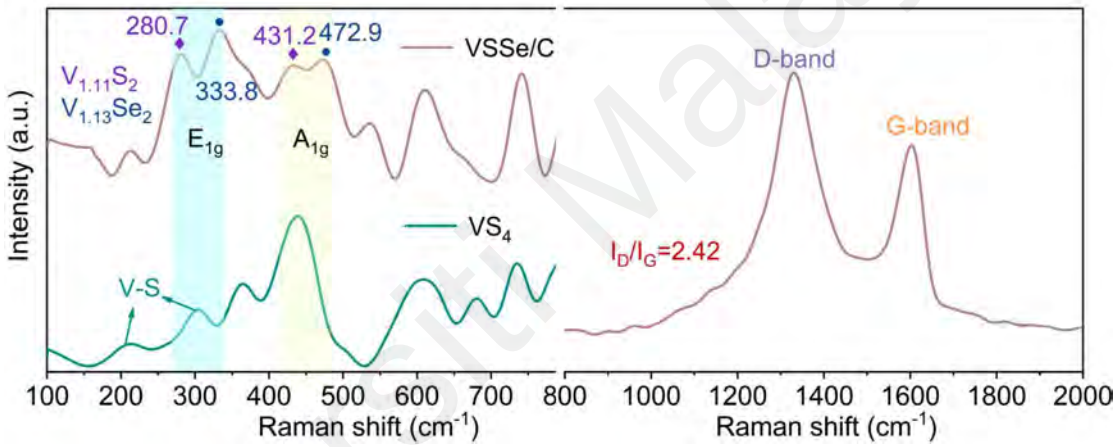

Figure 5.43: Raman spectra of VSSe/C.

From the TG curves in **Figure 5.44**, the thermal weight loss of VSSe/C sample at 360 °C is about 70.9% and then does not change with temperature improving, indicating the generation of stable V_2O_5 products. Contrastingly, the VSSe sample without carbon coating exhibits the weight loss of 53.8% at 360 °C. Based on the transformation of VSSe after the TG test as shown below:

$$V_{1.11}S_2/V_{1.13}Se_2 + O_2 \rightarrow V_2O_5 + SO_2/SeO_2 \uparrow \quad (5.1)$$

$$C + O_2 \rightarrow CO_2 \uparrow \quad (5.2)$$

The difference in heat loss between the above two samples can be attributed to the volatilization of carbon during the heating process. Therefore, the specific carbon content in VSSe/C can be calculated by Equation (6.3) and Equation (6.4).

$$70.9\%m = 53.8\%m \cdot (1 - c) + m \cdot c \quad (5.3)$$

$$c = 37.0\% \quad (5.4)$$

Where m represents the total mass of VSSe/C, c is the percentage composition of carbon in the VSSe/C. The carbon content in VSSe/C is calculated to be about 37.0% by comparing the TG curve of pure VSSe.

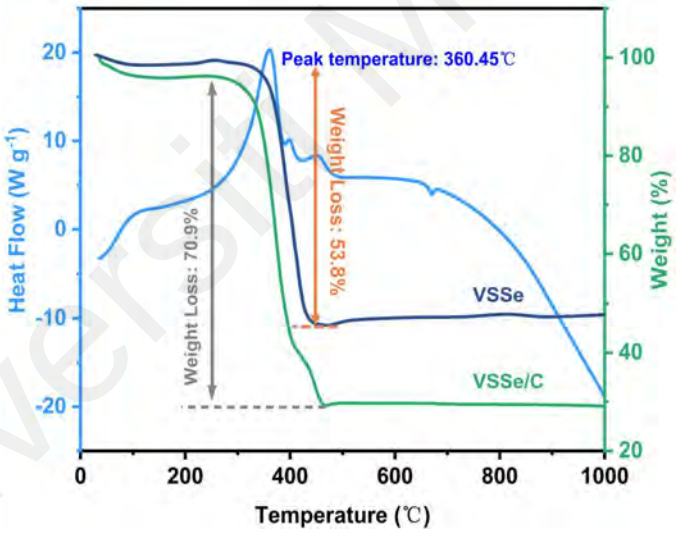

Figure 5.44: TG curves of VSSe/C and VSSe.

The surface elemental composition and chemical states of both samples are evaluated by XPS. From the high-resolution spectra of V 2p orbitals in Figure 5.45a, both the two samples could be further fitted with four orbital peaks of $2p_{3/2}$ and $2p_{1/2}$ in different valence states (V^{3+} and V^{4+}). Unusually, the initial VS_4 exhibits two additional characteristic peaks located at 514.1 eV and 521.7 eV, which can be attributed to the

unique V-[S_2] $2p_{3/2}$ and V-[S_2] $2p_{1/2}$ orbital peaks of the polysulfide. (L. Cao et al., 2021) In addition, all the characteristic peaks of VSSe/C are shifted toward lower energies, implying that the introduction of Se to form a V-Se bond can modify the redox state of the V atom. (W. Yao et al., 2021) Note that the relatively increased proportion of V^{3+} in VSSe/C suggests that a partial S vacancy is created during the break-up process of VS_4. The binding energy of S 2p also exhibits a down-shift trend, indicating that the conversion occurs from $[S_2]^{2-}$ to S^{2-} (Figure 5.45b). (Sunita Dey et al., 2020) Furthermore, the C-S-C/-C=S- peak at 165.2 eV indicates that a heterocyclic configuration is formed between the outer S atoms and the carbon layer, which is beneficial to the overall structural stability and the rapid transfer of adsorbed ions from the surface to the interior. (Shaohui Li et al., 2020) Another peak at 167.6 eV is attributed to -SO_x-, caused by the inevitable oxidation of surface sulfur atoms. Besides, the SeO_2 peak located at 59.0 eV is similarly due to the oxidation in the surface of the sample (Figure 5.45c). Two main peaks located at 53.5 and 55.5 eV can be assigned to Se $3d_{5/2}$ and Se $3d_{3/2}$, respectively. As for the C 1s in Figure 5.45d, the four peaks at 284.3, 285.0, 286.0, and 287.8 eV correspond to C-C sp^2, C-C sp^3, C-S/C-N, and C=O, respectively. (Yuyu Wang et al., 2022) Based on the generally positive effect of nitrogen in pyrrole-derived carbon, the N 1s orbitals are analyzed in Figure 5.45e. Among them, pyridine nitrogen and pyrrole nitrogen are favorable to produce more active sites and improve the adsorption of Na^+, while the presence of graphite nitrogen is friendly to the improvement of the electrical conductivity. Additionally, the elemental content analysis of XPS indicates that the percentage of carbon atoms in VSSe/C is about 40.36%, and the ratio of S to Se is in general agreement with the EDS analysis (Figure 5.45f).

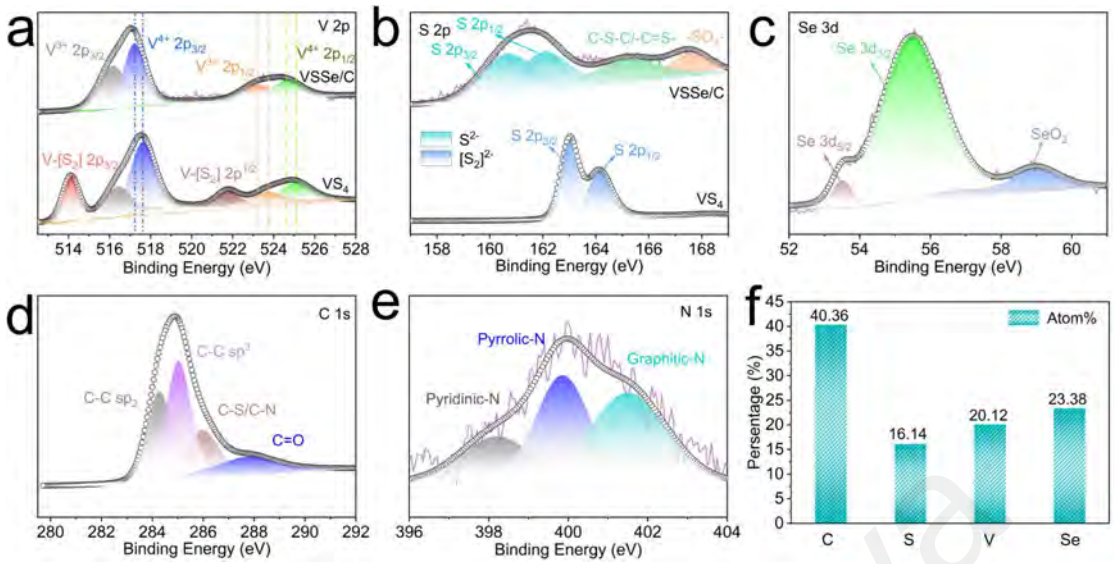

Figure 5.45: High-resolution V 2p (a), S 2p (b), Se 3d (c), C 1s (d), and N 1s (e) XPS spectra of VSSe/C. (f) XPS elemental analysis of VSSe/C composites.

5.3.3 DFT Calculations for VSSe

The characterization of the heterogeneous structure of VSSe is simulated using DFT. Taking the (0 0 1) crystal plane as an example, Figure 5.46 displays the lattice spacing changes of VS_4 and VSSe heterostructure before and after sodium insertions. Compared to the lattice spacing of VS_4 (5.755 Å), the heterogeneously designed VSSe structure provides an expanded distance of 5.926 Å for a larger volume of Na^+ insertion. Then, the lattice spacing becomes 6.582 Å after the Na^+ embedding in the VSSe structure.

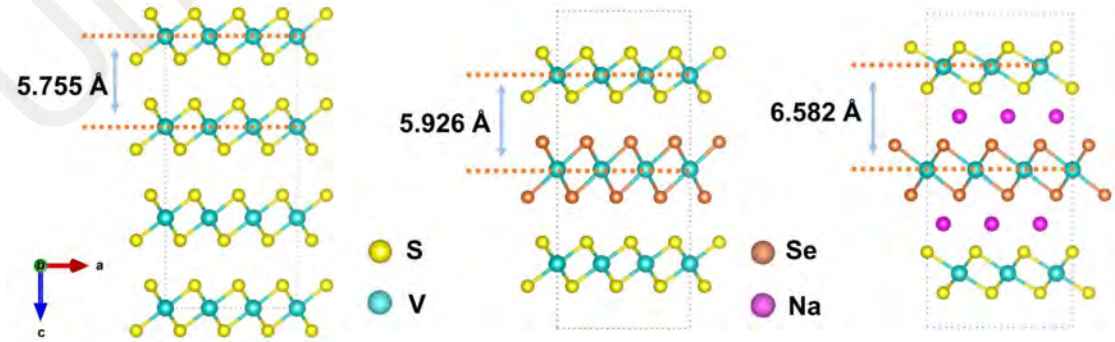

Figure 5.46: Schematic diagrams of the changed (0 0 1) lattice planes from VS_2 to VSSe, and Na^+ embedding state.

Furthermore, the band structures of VSSe heterostructures are calculated. As shown in Figure 5.47, the VSSe structure designed with the anionic heterostructure has no band gap at the Fermi energy level (0 eV) and exhibits metallic properties with better conductivity.

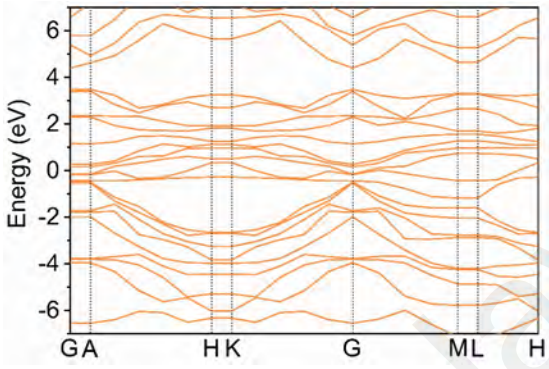

Figure 5.47: The calculated bandgap structures for VSSe.

Additionally, the charge difference density and the average charge distribution of the layered VSSe heterogeneous structure are calculated in Figure 5.48. In this case, the green electron cloud represents charge accumulation, while the yellow electron cloud means charge disappearance. The interior of both $V_{1.11}S_2$ and $V_{1.13}Se_2$ crystal structures show the disappearance of electrons near V and their accumulation near S and Se atoms. In particular, electrons accumulate on both sides in the heterogeneous layer composed of S and Se atoms, which is favorable for the adsorption of Na^+.

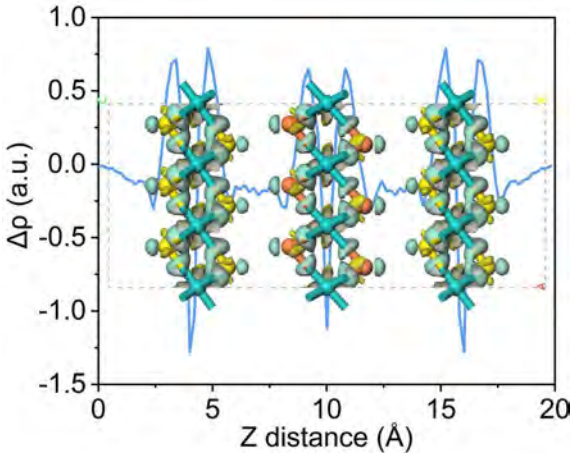

Figure 5.48: The planar-average charge density for VSSe.

From the DOS analysis of the VS_4 and VSSe structures in Figure 5.49, the VSSe heterostructure exhibits a significant superposition peak near the Fermi energy level but disappears in VS_4. This represents the built-in electric field generated by the asymmetric electronic structure in the heterostructure could facilitate electron conduction and thus exhibits metallic properties, which is consistent with the band gap analysis.

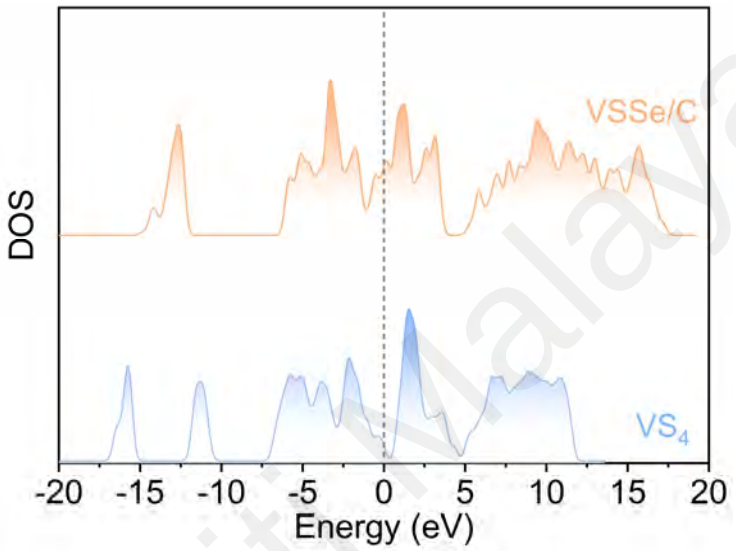

Figure 5.49: The density of states for VS_4 and VSSe.

As shown in Figure 5.50, the phase change reaction process is further investigated by simulating the Gibbs free energy change from the initial state to the fully discharged state. The detailed calculation process can be referred to Equation (6.5) and Equation (6.6). (Yangjie Liu et al., 2022) Considering the reaction from $V_{Z_1}S_x$ and $V_{Z_2}Se_y$ to Na_2S, Na_2Se, and V according to the following Equation (6.5):

$$V_{Z_1}S_x + V_{Z_2}Se_y + 2(x+y)Na \rightarrow (Z_1 + Z_2)V + xNa_2S + yNa_2Se \qquad (5.5)$$

ΔG can be approximated by the total energies from DFT calculations neglecting the entropic contributions (0 K), according to Equation (6.6):

$$\frac{xE_{(Na_2S)} + yE_{(Na_2Se)} + (Z_1 + Z_2)E_{(V)} - E_{(V_{Z_1}S_x)} - E_{(V_{Z_2}Se_y)} - 2(x+y)E_{(Na)}}{2(x+y)} \quad (5.6)$$

Where $E_{(Na_2S)}$, $E_{(Na_2Se)}$, $E_{(V_{Z_1}S_x)}$, and $E_{(V_{Z_2}Se_y)}$ are the DFT total energies at the optimized state, $E_{(Na)}$ and $E_{(V)}$ is the energy per atom in the respective metal phase. The overall free energy exhibits a decreasing trend with electrode reactions. The anionic heterogeneous VSSe with a more negative tendency represents lower free energy, favoring the fast kinetics of sodium ions in the electrode process, which is consistent with the experimental results.

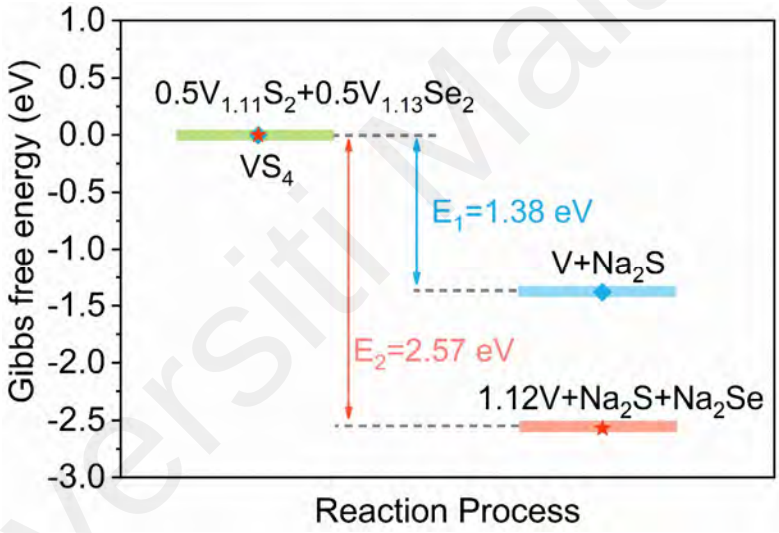

Figure 5.50: Free energy diagrams for the conversion reaction of VS_4 and VSSe.

To further investigate the mechanism of the adsorption of electrochemical products (Na_2S and Na_2Se) by heterogeneous interfacial layers, the charge distribution is analyzed by adopting the charge difference density. As shown in Figure 5.51, Na_2S tends to adsorb toward the Se atomic layer side in the presence of an asymmetric electric field. Conversely, Na_2Se tends to shift toward the S-atom side. This anisotropic adsorption can effectively avoid the electron repulsion effect caused by the homogeneous anion adsorption, which can enhance the stability of the adsorption

structure and the balanced charge distribution of the overall structure. This is consistent with the stability exhibited by the electrochemical results.

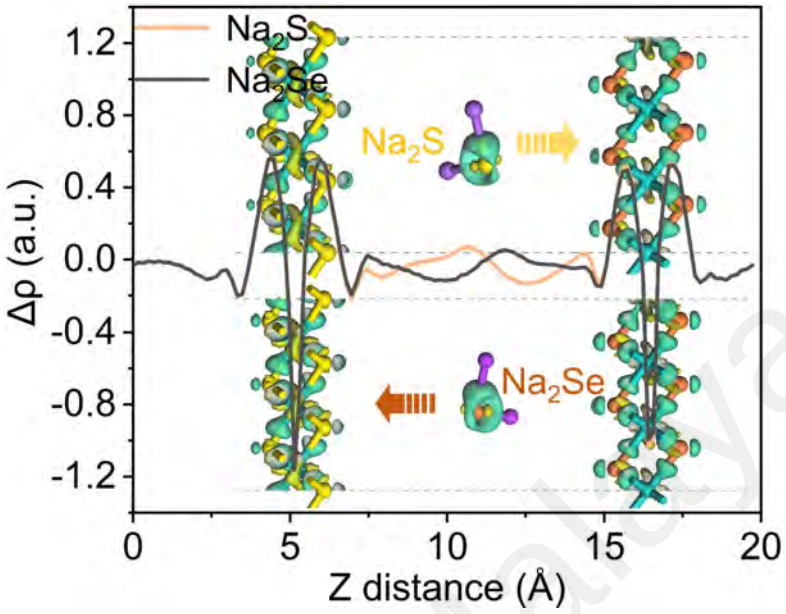

Figure 5.51: The planar-average charge density of intercalated Na_2S and Na_2Se in the (0 0 1) lattice plane.

Furthermore, to deeply investigate the migration behavior of Na^+ on the surface of the structure (non-interlayer), the ion migration paths and the diffusion energy barriers at different diffusion states are calculated, respectively. Figure 5.52a exhibit the migration paths of Na^+ in $V_{1.11}S_2$ and $V_{1.13}Se_2$, respectively. Accordingly, as the calculated diffusion energy barrier in Figure 5.52b, the diffusion of Na^+ from position 1 to position 2 and then to position 3 in $V_{1.11}S_2$ requires the consumption of 0.31 eV and 0.28 eV, respectively. Meanwhile, the diffusion energy barriers of Na^+ in $V_{1.13}Se_2$ are 0.17 eV and 0.21 eV in the two stages, which is easier to achieve the diffusion of Na^+ relative to $V_{1.11}S_2$.

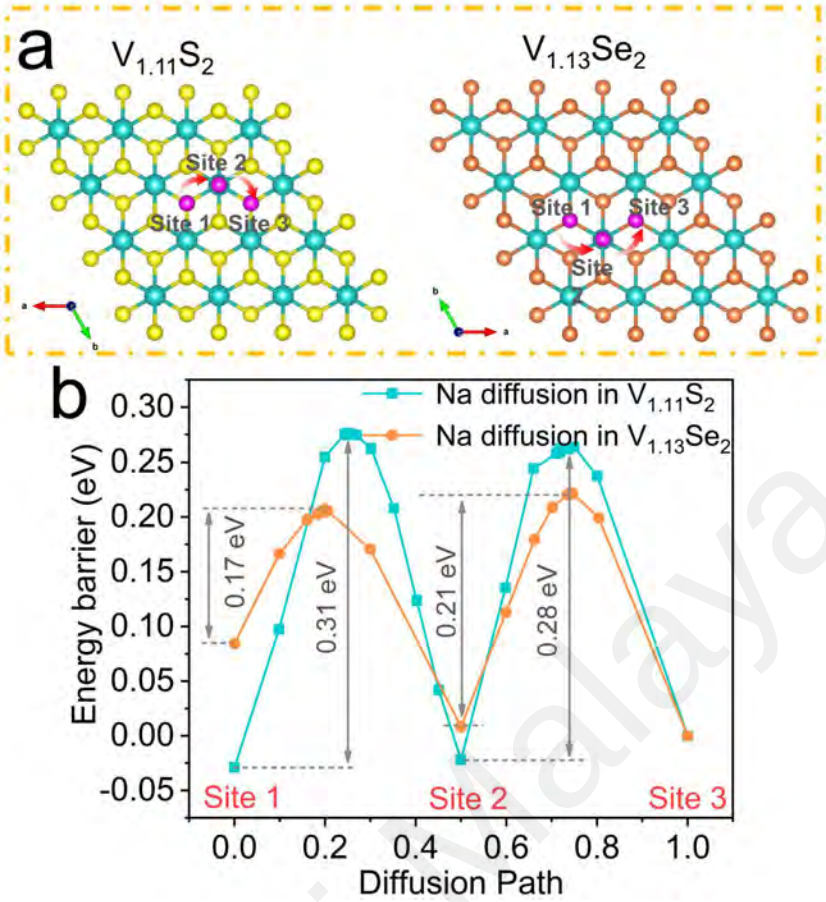

Figure 5.52: The schematic illustration for the diffusion path of a Na atom in the $V_{1.11}S_2$ and $V_{1.13}Se_2$ (a), and the corresponding diffusion energy barrier curves (b).

5.3.4 Electrochemical Properties of VSSe/C in SIBs

In view of the previous structural analysis, the VSSe/C electrode is assembled to explore its electrochemical performance in a sodium ion half-cell. As shown in Figure 5.53a, the initial electrochemical process is explored using cyclic voltammetry at a scan rate of 0.1 mV s^{-1}. During the initial cathodic scan, three broad reduction peaks are located near 1.75, 1.29, and 0.82 V, representing the initial insertion of Na^+ and its participation in the conversion process. Meanwhile, the corresponding oxidation peaks at 2.08, 1.84, and 1.51 V appear in the anodic process, indicating the initial reversible desodiation process. Additionally, a sharp peak near 0.36 V occurs in the first cathodic process and disappears in the subsequent scans, representing the formation of a SEI

layer. The appearance of three major pairs of redox peaks with well-overlapping properties in the subsequent cycles indicates excellent cycle reversibility of the VSSe/C electrode. As a comparison, the CV curves of the pure VS_4 electrode are equally measured (Figure 5.53b). The results exhibit different degrees of peak intensity changes and position migration during the first three scans. The extremely poor recombination of redox peak positions implies its drastic structural changes during repeated charging and discharging.

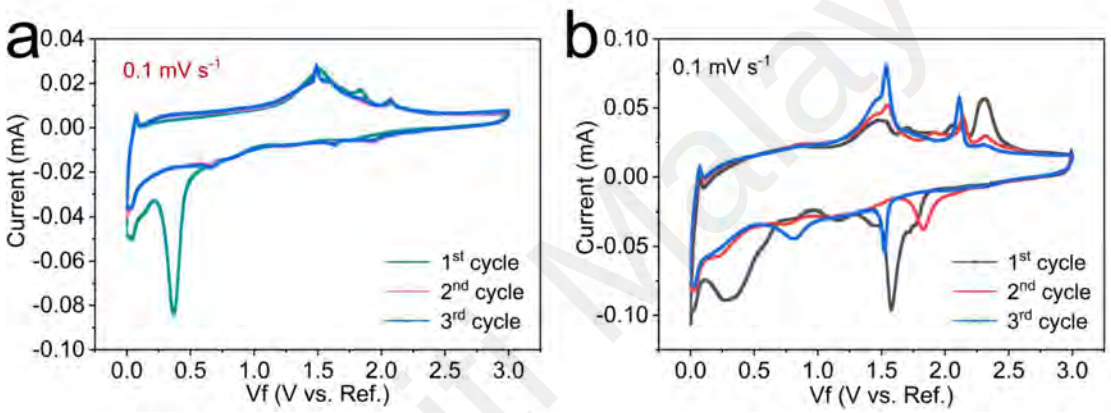

Figure 5.53: CV curves from 0.01 to 3.0 V at the scan rate of 0.1 mV s^{-1} for VSSe/C (a) and VS_4 (b) electrodes.

The short-term cycling capabilities of VSSe/C and VS_4 electrodes are compared at a current density of 2 A g^{-1} (Figure 5.54). The results illustrate that the VSSe/C electrode with an anionic heterostructure exhibits a pre-continuous activation process and exerts a specific capacity of 784.9 mA h g^{-1} after 500 cycles. However, pure VS_4 electrodes exhibit fluctuating cycling trends due to structural instabilities triggered by complex reactions.

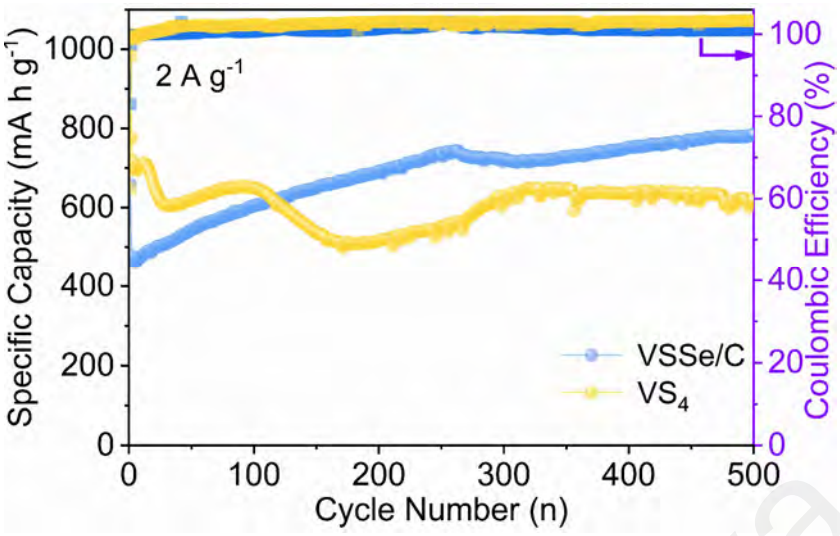

Figure 5.54: Short cycling performance at 2 A g^{-1} of VSSe/C and VS_4 electrodes.

Moreover, Figure 5.55 compares the effect of different addition ratios of selenium powder (measured by theoretical substitution of the number of S atoms in VS_4) on the cycling performance. By comparison, the selenium powder with half of the sulfur atoms substituted in VS_4 has the best cycling performance, representing the ability to achieve better structural stability. Notably, all three different ratios of VSSe samples exhibit a decay of the specific capacity in the initial cycles, and then a gradual increase in the specific capacity. The decay process can be attributed to the formation of SEI layer and the Na^+ insertion in the apparent VSSe. (R. Fan et al., 2022) As the cycle proceeds, the Na^+ in the electrolyte further penetrates into the interior of the VSSe electrode and excites the conversion reaction, thereby exposing more boundary sites and heterogeneous interfaces, thus exhibiting a progressive increase in specific capacity. (Yuhao Yi et al., 2022)

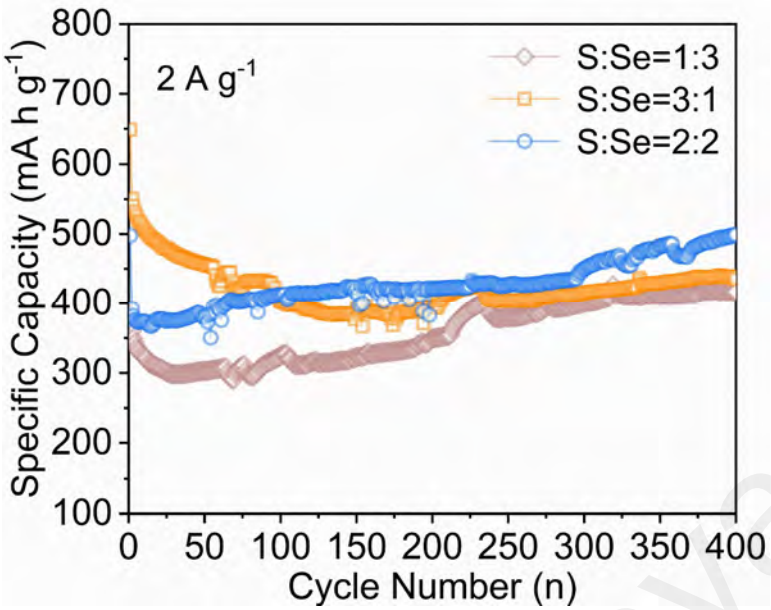

Figure 5.55: Cycling performance of VSSe electrodes at different selenium powder ratios.

To corroborate the above process, the charging/discharging plateaus before and after activation are analyzed for pure VSSe after 3, 250, and 400 cycles by charge-discharge and dQ/dV profiles (Figure 5.56). The results show that the position of the main redox peak is essentially unchanged before and after activation, representing that no additional redox reaction occurrs in pure VSSe. Notably, the main charging reaction occurs at higher voltages in the pre-activation dQ/dV curves, implying a greater resistance to Na^+ deinsertion (requiring higher voltage drive) due to the lack of exposed boundary sites and electrolyte penetration depth before activation, while the main reaction after activation occurs at lower voltage regions and remains essentially the same at 250^{th} and 400^{th} cycles.

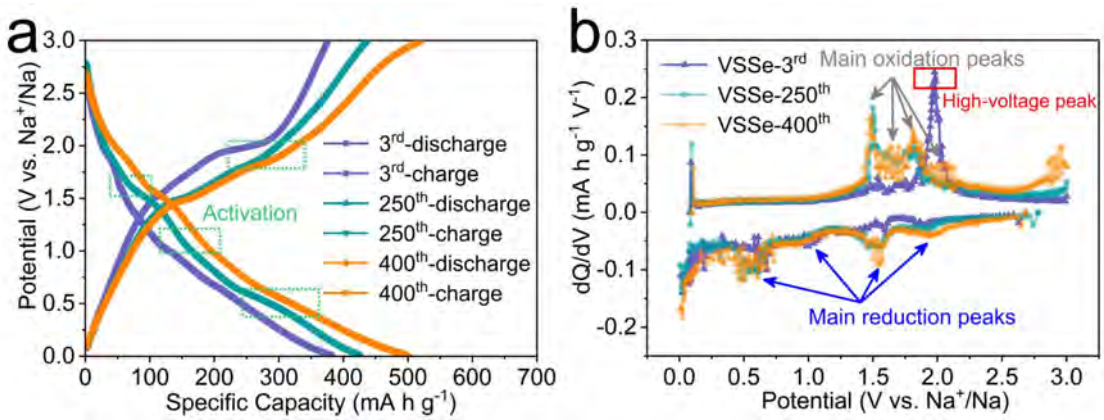

Figure 5.56: (a) Charge-discharge voltage profiles (3rd, 250th, and 400th cycles), and (b) the corresponding differential capacity (dQ/dV) profiles of pure VSSe electrode.

The rate capacity of the two electrodes is evaluated at current densities of 1, 2, 4, 6, 8, and 10 A g^{-1} (Figure 5.57a). As the activation proceeds, the VSSe/C electrode exhibits a stronger rate performance than the VS_4 electrode, especially when the current density recovered from 10 A g^{-1} to 1 A g^{-1}, with a specific capacity of 626.1 mA h g^{-1} regained. The charge-discharge profiles of the VSSe/C electrode at different rates are performed in Figure 5.57b.

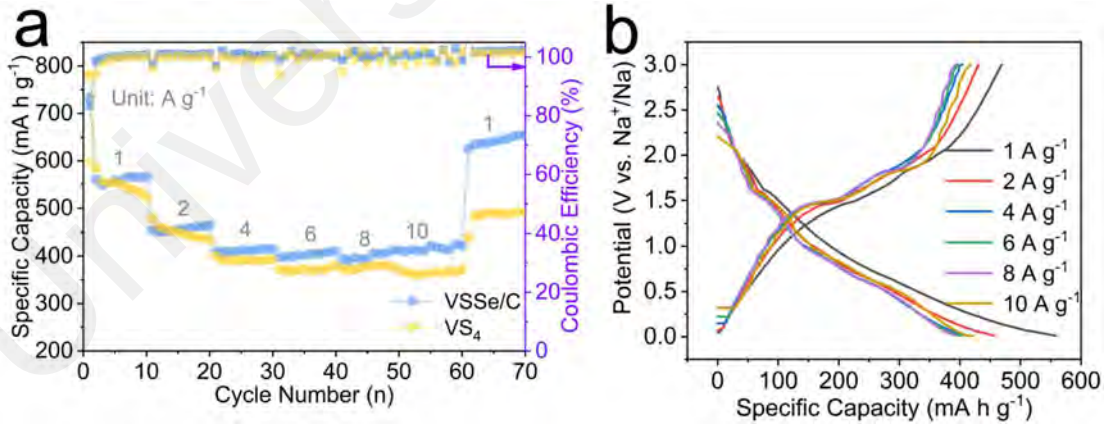

Figure 5.57: The rate performance (a) and charge-discharge profiles (b) of VSSe/C electrode at different rates.

Additionally, the electrochemical performance of VSSe is tested to distinguish the effect of carbon coating and built-in electric field on the electrochemical performance. As shown in Figure 5.58, the VSSe electrode exhibited a more stable electrochemical

performance (415.8 mA h g^{-1} at 2 A g^{-1}) and excellent rate ability after 1000 cycles under the built-in electric field formed by the heterogeneous structure.

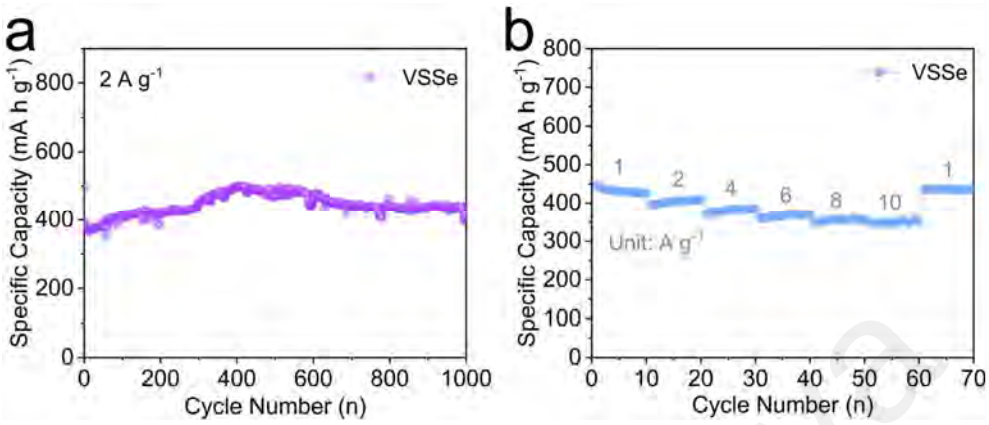

Figure 5.58: Cycling and rate performance of pure VSSe electrode.

Subsequently, to systematically investigate the activation process occurring at the VSSe/C and VS_4 electrodes, the charge/discharge curves and dQ/dV analysis before (3^{rd}) and after (250^{th}) activation are selected for further investigation (Figure 5.59). From Figure 5.59b, the peak voltage at which each electrode reaction occurs corresponds exactly to the charge/discharge voltage plateau in Figure 5.59a. It is remarkable that the positions of the VSSe/C electrodes hardly change before and after activation, and the activated electrodes exhibit a significant increase in the intensity of the reaction peaks compared to that before activation. This means that no new reaction occurred during the activation process, verifying the stability of the constructed heterogeneous structure and the physical activation process caused by charging and discharging (SEI layer formation, electrolyte infiltration, and exposure of more boundary sites). This is consistent with the aforementioned activation process of pure VSSe. In contrast, the VS_4 electrode performs different degrees of peak shifts and the appearance of new reaction peaks located at 1.9 V (discharge process) and 0.9 V (charging process), demonstrating the significant structural changes and the occurrence of unstable side reactions during the activation

process.

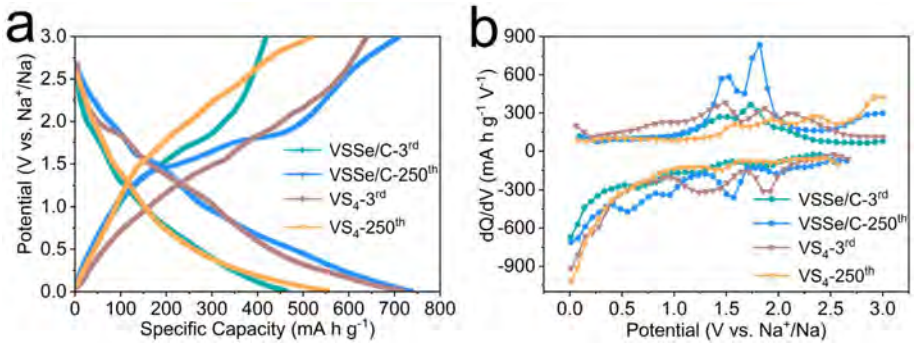

Figure 5.59: (a) charge-discharge voltage profiles (3rd and 250th), and (b) the corresponding differential capacity (dQ/dV) profiles of VSSe/C and VS_4 electrodes.

The long-term cycling capability of the VSSe/C and VS_4 electrodes is tested using a high current density of 10 A g^{-1}. As shown in Figure 5.60, the VSSe/C electrode maintains a specific capacity of 553.2 mA h g^{-1} after 1000 cycles, demonstrating superior cycling capability. However, due to structural disintegration, the VS_4 electrode exhibits significant capacity decay at 300 cycles.

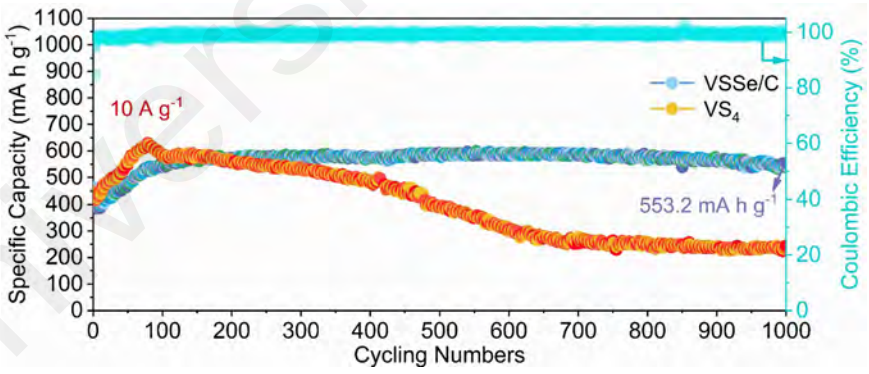

Figure 5.60: Long cycling performance and coulombic efficiency of VSSe/C and VS_4 electrodes at the current density of 10 A g^{-1}.

The SEM images of the VSSe/C electrode after cycling still exhibit the nanorod cluster structure, which represents excellent structural stability (Figure 5.61). In a word, the outstanding electrochemical performance during charging and discharging can be attributed to the different band gap microstructures generated by the formation of built-

in electric fields at the anion heterogeneous interfaces, which consequently trigger strong adsorption effects on reaction products and excellent electron and ion transport efficiency.

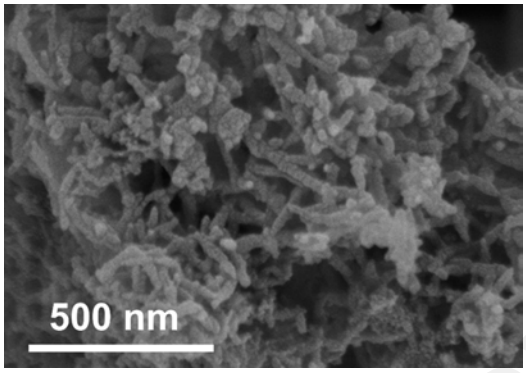

Figure 5.61: SEM images of the VSSe/C electrode after 500 cycles.

5.3.5 Electrochemical Process Study of VSSe/C Electrode

To clarify the physical phase changes in the initial process, ex-situ XRD and XPS are applied to characterize the VSSe/C electrode at different voltage states. The different discharged and charged states are selected for measurement according to the location where the reaction occurs in the CV curve, as displayed in Figure 5.62a. During the entire discharge/charge process, the characteristic peaks located at 29.4° and 30.9° present a tendency to disappear and then reappear, which can be indexed to the intermediate $NaVSe_2$ and Na-V phases formed during the stepwise insertion/deinsertion of Na^+. With the discharge to 0 V, the peaks at 27.2° and 28.3° can be attributed to the Na_2S phase produced during fully discharging. Similarly, the Na_2Se characteristic peak is detected in the discharge-ending state. Besides, the distinct peaks of V_3O_4 and V_2O_3 are observed at 17.9° and 33.1°, respectively, while no direct V peaks are identified, resulting from the high oxidation of V monomers in air. Notably, no additional valence peaks about S other than S^{2-} are found throughout the process, further verifying the

absence of low-valent polysulfides triggering shuttle effects. Meanwhile, the characteristic peaks of the related discharge reaction products (Na_2S, Na_2Se, and V_xO_y) in Figure 5.62b show a tendency to appear and then disappear during the process of fully discharging to fully charging, and reach the strongest when discharging to 0 V, further revealing the reaction process of the VSSe/C electrode ($V_{1.11}S_2 + 4Na^+ + 4e^- \rightarrow 2Na_2S + 1.11V/V_{1.13}Se_2 + 4Na^+ + 4e^- \rightarrow 2Na_2Se + 1.13V$).

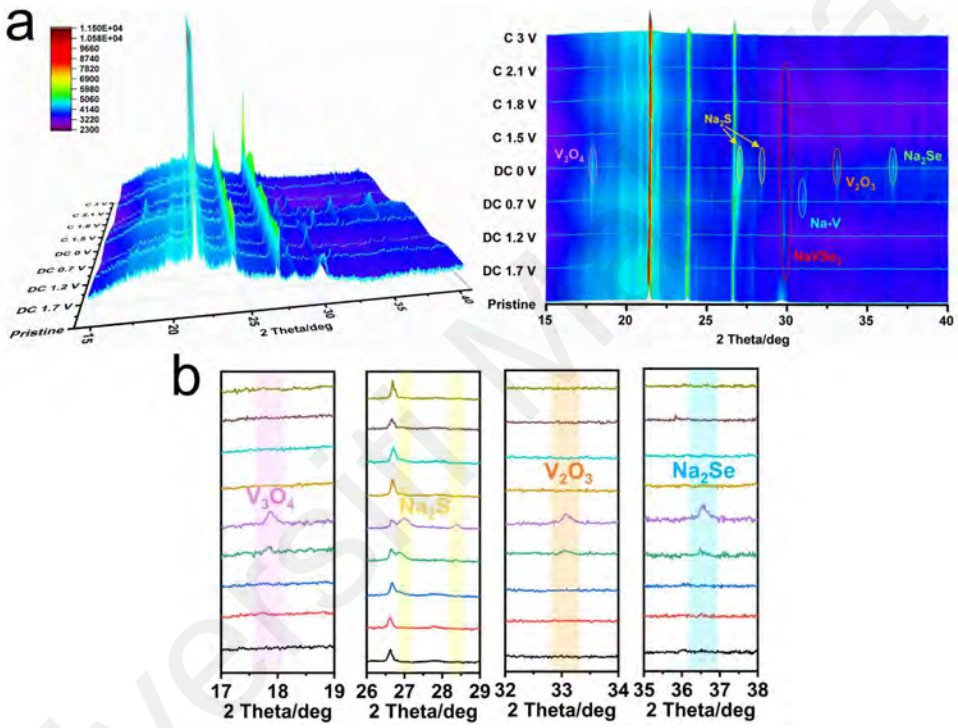

Figure 5.62: Ex-situ XRD of VSSe/C electrodes at different discharge-charge states in the initial process.

The ex-situ XPS is applied to explore the initial process by selecting fully discharge and charge states. As shown in the high-resolution spectrum of V 2p in Figure 5.63a, the overall peak shifts about 0.4 eV toward the lower binding energy when fully discharged to 0 V, representing the reduction of the V oxidation state. Afterward, when fully charged to 3 V, the peak position reverts to the initial post, suggesting excellent cycle reversibility. The S 2p orbital peak in Figure 5.63b exhibits a similar trend. The peak

attributed to V-S bond formation is significantly weakened when discharging to 0 V. Correspondingly, the increased unsaturated -C=S- peak further indicates that the V with a high oxidation state gets electrons during the discharge leading to the breakage of the V-S bond, while the vacant S further forms an unstable bond state with C. Moreover, when recharged to 3 V, the V-S 2p orbital peak reverted, in agreement with the results for V 2p. By evaluating the orbital peaks of the different reaction states in more detail, as shown in Figure 5.63c, the V^{3+} exhibits an increasing and decreasing trend during the whole process of discharging and charging. In contrast, the V^{4+} offers the opposite tendency. This further implies the entire process of V reduction followed by oxidation. Additionally, the V-S 2p orbital peaks occupy a dominant position in the initial and charge cutoff states. Conversely, at the fully discharged state, it is dominated by unsaturated -C=S- bonds, clearly indicating the bond-breaking and reorganization process of V-S bonds.

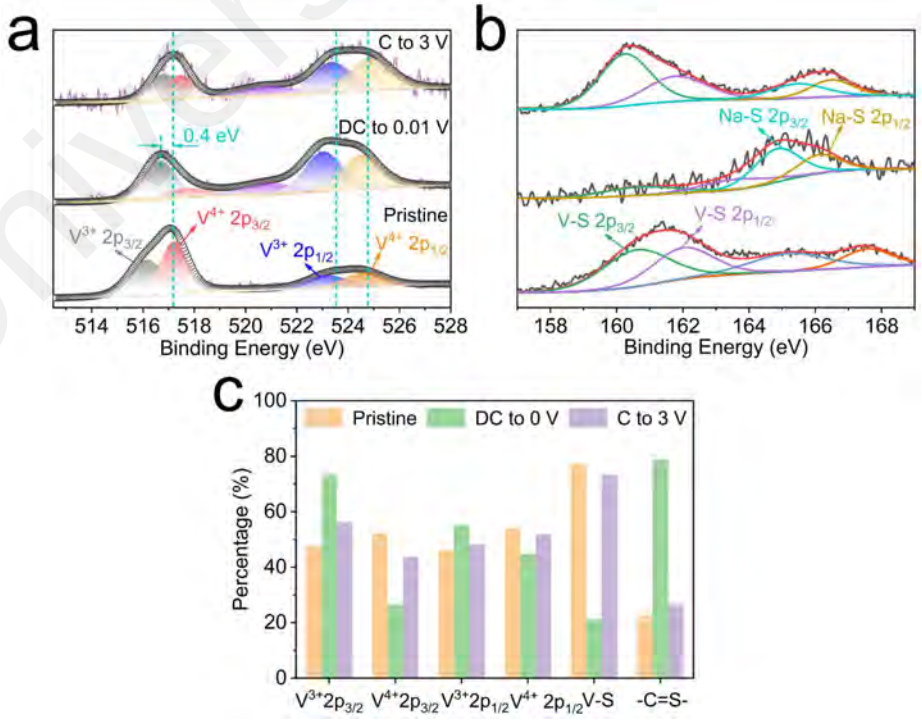

Figure 5.63: High-resolution V 2p (a), S 2p (b), and the corresponding valence distribution (c).

5.3.6 Sodium Storage Kinetics Investigation

EIS is applied to measure the kinetics of the electrode process. In the Nyquist curve in Figure 5.64a, the semicircle diameter in the high-medium frequency region after 5 cycles becomes smaller compared to the initial state, implying a smaller contact and charge transfer resistance. As shown in Table 5.2, the pristine sum value of (R_f+R_{ct}) of 47.254 Ω composed of the SEI film resistance (R_f) and the charge transfer resistance (R_{ct}) decreases to 10.744 Ω after 5 cycles, which is associated with the activation process as a result of the increased infiltration of electrolyte into the electrode material. (F. Yuan, Zhang, et al., 2022) Moreover, the line slope in the low-frequency region is related to the solid phase diffusion of Na^+ within the active material. The parameter of the diffusion process (D) can be further fitted by the relationship between $\omega^{-1/2}$ and Z' (Figure 5.64b). The smaller D value (78.32) after 5 cycles represents a faster Na^+ diffusion efficiency produced as the activation proceeds.

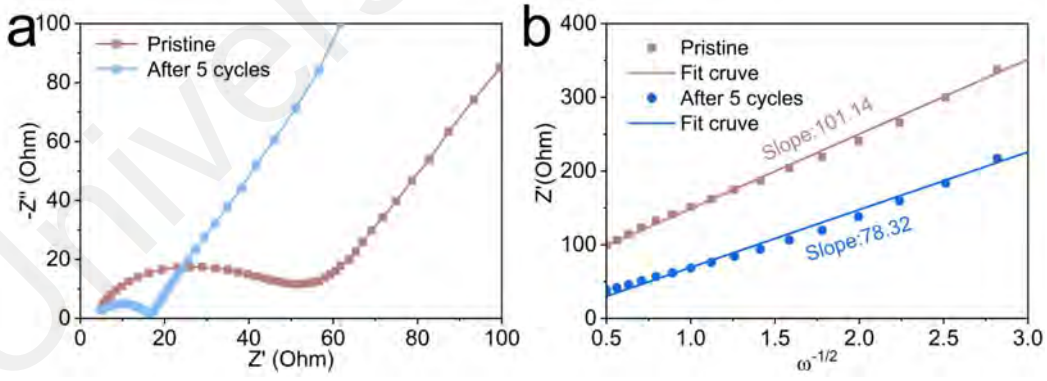

Figure 5.64: (a) Nyquist plots of VSSe/C before and after 5 cycles. (b) Relationship between Z' and $\omega^{-1/2}$.

Table 5.2: Fitting results of EIS for VSSe/C electrode in SIBs with the proposed equivalent circuit.

Cycle number	R_s (Ω)	R_f+R_{ct} (Ω)
Pristine	5.102	47.254
After 5 cycles	5.194	10.744

As in Figure 5.65a, the control of surface pseudocapacitance and internal diffusion on the overall electrochemical process is further investigated by measuring the CV curves at different scan rates. The sloping curve in Figure 5.65b is obtained by fitting the relationship between peak current and scan rate. The slopes of 0.88 and 0.98 for the cathodic and anodic processes imply that the overall electrochemical process prefers to be controlled by a pseudocapacitive process with fast response capability. The variation of the pseudocapacitance control percentages at different scan rates are shown in Figure 5.65c, revealing that the pseudocapacitance effect dominates the entire electrochemical process as the scan rate increases. The pseudocapacitance distribution at 5 mV s^{-1} demonstrates a control ratio of up to 88.7%, implying a fast response at high power density by a strong surface effect excitation (Figure 5.65d).

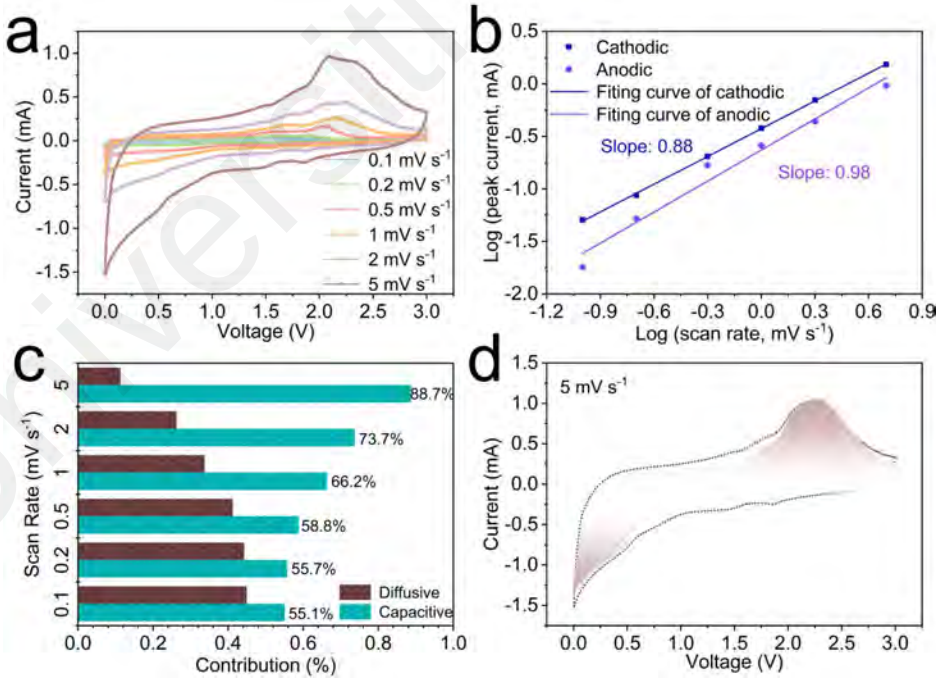

Figure 5.65: (a) CV curves at different scan rates of VSSe/C electrode in SIBs. (b) Linear diagrams of log (v) and log (i) corresponding to peak currents in different oxidation and reduction states of VSSe/C. (c) Contribution ratio of the capacitive and diffusion-controlled at different scan rates. (d) The capacitive contribution of VSSe/C electrode at a scan rate of 5 mV s^{-1}.

The GITT is performed to investigate the diffusion coefficient of Na^+ within the active material. Figure 5.66 illustrates the prepared VSSe/C and VS_4 electrodes with constant current relaxation. The diffusion coefficient (D_{Na^+}) of the VSSe/C electrode remains between 10^{-11} and 10^{-13}, which is significantly higher than that of the VS_4 electrode. This further verifies that the built-in electric field generated through the anion heterogeneous interaction can effectively enhance the diffusion efficiency of sodium ions in the bulk phase.

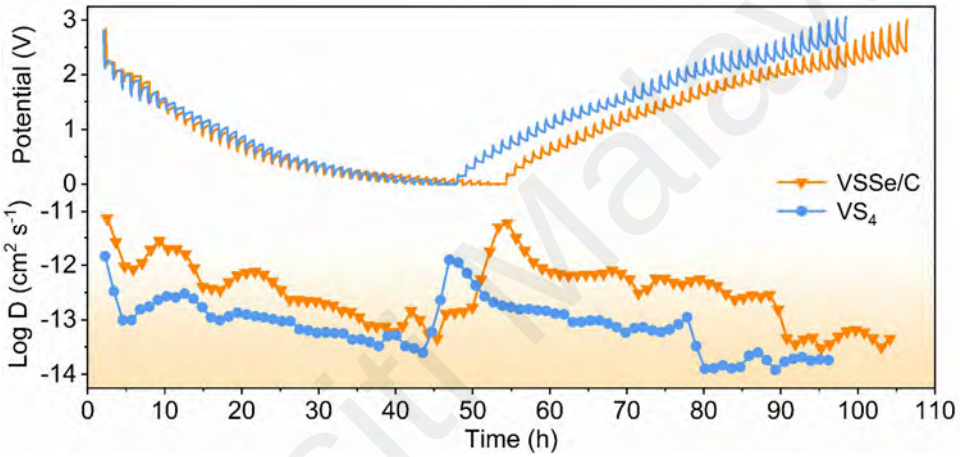

Figure 5.66: GITT and Na^+ diffusion coefficients of VSSe/C electrode.

5.3.7 Electrochemical Properties of VSSe/C in SICs

To further measure the electrochemical performance of VSSe/C electrodes, AC is used as the cathode assembled into SICs for evaluation. The CV curves are measured at 10 mV s^{-1} for cutoff voltages of 3.6, 3.8, 4.0, and 4.2 V, respectively (Figure 5.67a). From there, when the voltage is higher than 3.8 V, there is a sharp peak angle near 4.0 V and 4.2 V, which may be triggered by the decomposition and polarization of the electrolyte. (Ba et al., 2022) This defines that a cutoff voltage of 3.8 V is appropriate for the assembled device. Consequently, the CV curves are tested in the voltage range of 0−3.8 V for different scan rates, respectively (Figure 5.67b). The results indicate that the

general shape of the CV curves exhibits a hybrid mechanism combining double layer (quasi-rectangular shape) and pseudocapacitance (reaction peak shape).

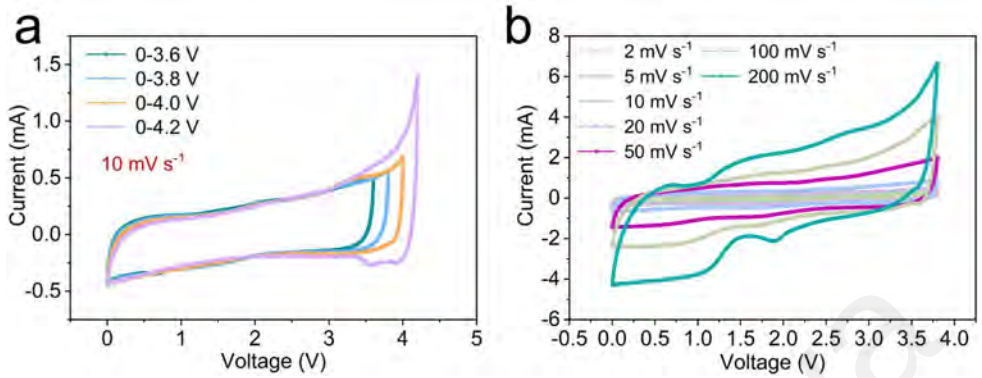

Figure 5.67: CV curves at different cutoff potentials (a) and CV curves at different scan rates (b) of VSSe/C//AC SICs.

As shown in Figure 5.68a, the rate performance of the assembled SICs devices is measured at current densities of 0.2, 0.5, 1, and 2 A g^{-1}, respectively. Notably, capacity recovery is gradually achieved after a current density shift from 2 A g^{-1} to 0.2 A g^{-1}. The GCD curves at different currents in Figure 5.68b displayed a triangle-like shape. This is consistent with the CV curves, confirming that the assembled device has a hybrid mechanism.

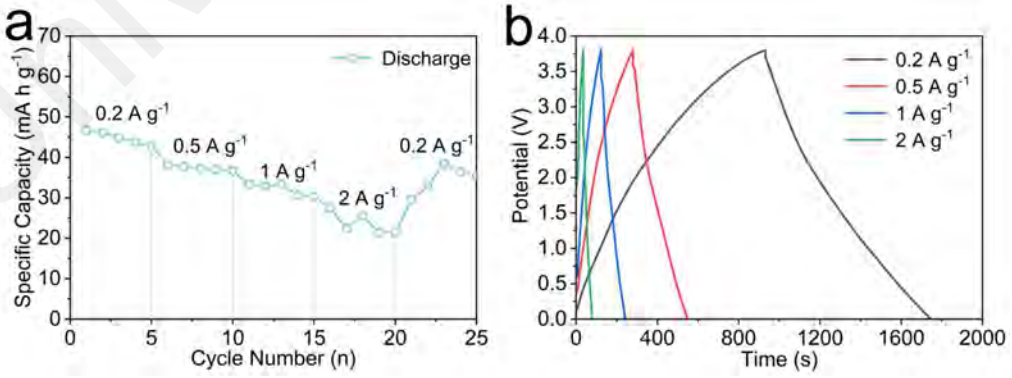

Figure 5.68: (a) Rate performance, and (b) GCD profiles of VSSe/C//AC SICs.

To confirm the cycling capability of the assembled hybrid SICs, long-term cycling tests are performed at a current density of 2 A g^{-1} (3800 W kg^{-1}). The results indicate

that a specific capacity of 28.93 mA h g^{-1} (50.7 W h kg^{-1}) can still be developed even after 2000 cycles, with a corresponding capacity retention rate of 96.6% (Figure 5.69).

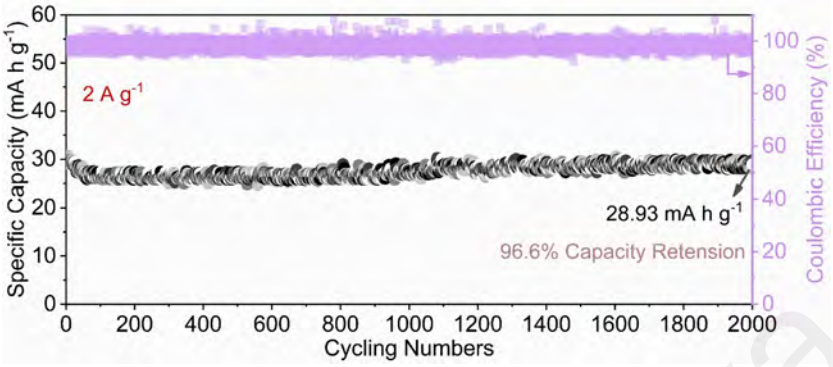

Figure 5.69: Cycling stability and coulombic efficiency of VSSe/C//AC SICs at 2 A g^{-1} for 2000 cycles.

To further understand the resistive behavior of electrode materials, the EIS tests before and after cycling for SICs have been presented in Figure 5.70. Compare to the initial state, the semicircle diameter in the high-medium frequency region exhibits a decreasing trend (after 5 cycles) followed by an increasing trend (after 100 cycles). The smaller R_f+R_{ct} value of the 5th cycle is triggered by the gradual infiltration of the electrolyte into the electrode material (Table 5.3). Continually, the larger resistance after 100 cycles is associated with the passivation of the electrode by the electrolyte. Additionally, the smallest line slope of 5th cycle in the low-frequency region represents the smallest solid phase diffusion of Na^+ within the active material.

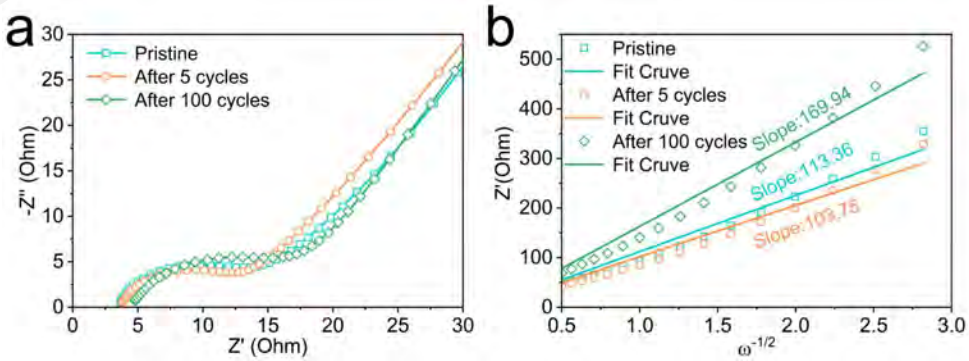

Figure 5.70: (a) Nyquist plots of VSSe/C//AC SICs before and after cycling. (b) Relationship between Z' and $\omega^{-1/2}$.

Table 5.3: Fitting results of EIS for VSSe/C//AC in SICs with the proposed equivalent circuit.

Cycle number	R_s (Ω)	R_f+R_{ct} (Ω)
Pristine	3.685	9.538
After 5 cycles	3.748	7.465
After 100 cycles	4.792	10.449

5.4 Summary

In this chapter, we realized the analogous anionic heterostructure design of VSSe and $WSSe_2$ by partial S-atom substitution by Se atoms via VS_4 and WS_x as precursors, respectively. In addition, carbon introduction strategies other than the previously mentioned MOF-derived carbon strategies, including conducting polymer-derived carbon coating and organic monosaccharide-derived carbon composite, were also validated. Benefiting from the analogous anionic heterostructure and carbon encapsulation strategy, the prepared $WSSe_2$/C and VSSe/C exhibit excellent Na^+ storage performance. The specific conclusions are as follows:

1. The carbon homogeneously encapsulated WS_x precursor is prepared by a one-pot method combined with hydrolysis of perchlorides. This is followed by carbonization and selenization in a fast microwave sintering process and resulted in $WSSe_2$/C. The S atoms in WS_x are partially replaced by Se atoms during the sintering process to realize the S and Se double anion introduction effect. Additionally, ribose-derived C is fully carbonized during sintering to improve the overall electrical conductivity. Under the action of the built-in electric field, the $WSSe_2$ exhibited the enlarged layer spacing, which facilitated Na^+ rapid transfer within the bulk phase. Furthermore, the

appropriate distribution of $WSSe_2$ nanosheets on the surface could promote rapid Na^+ adsorption on the surface and transfer to the interior. Consequently, in the assembled Na half-cell, the $WSSe_2$/C-1 anode displays a high specific capacity of 715.3 mA h g^{-1} after 200 cycles of activation at 1 A g^{-1}. Further, the assembled SIC exhibits a high-capacity retention of 86.5% after 13,000 cycles at a high-power density of 3,800 W kg^{-1}.

2. The analogous anionic heterogeneous modification engineering of the VS_4 system is achieved by employing one-step strategy. The prepared layered VSSe/C exhibits expanded layer distance (5.926 Å) and improved metallicity properties. Furthermore, the constructed built-in electric field achieves lower free energy and effective adsorption of reaction products. Resultantly, when applied to the SIBs anode, a high specific capacity of 784.9 mA h g^{-1} is achieved with 500 cycles at a current density of 2 A g^{-1}. Impressively, a high-capacity retention of 553.2 mA h g^{-1} is performed after 1000 cycles at 10 A g^{-1}, which is significantly better than the unmodified VS_4 electrode. Additionally, the assembled sodium ion capacitor exhibits excellent energy densities of 89.1 W h kg^{-1} at 380 W kg^{-1} and an ultra-high-capacity retention rate of 96.6% over 2000 cycles at a high-power density of 3800 W kg^{-1}. Ex-situ XRD and XPS results reveal a stable disulfide/selenide conversion process, and no intermediate polysulfide formation.

CHAPTER 6: DISSIMILAR HETEROSTRUCTURE DESIGN

6.1 Introduction

With the increased depth of understanding of nanoscale materials, the design of heterogeneous structures for MSes can achieve more significant potential in the field of energy storage by each heterogeneous interface design, excellent structural stability, and synergy between heterogeneous ions. (Ke et al., 2022; D. Yu et al., 2021; Yingying Zhang et al., 2021) In the previous two chapters, we have discussed analogous cationic heterostructures (Chapter 4) and analogous anionic heterostructures (Chapter 5), respectively. However, dissimilar heterostructure design by two MSes with completely different crystal structures is likewise considered as an effective microstructure modification strategy. In particular, a deeper heterocomposite effect is expected to be stimulated by virtue of the large electronegativity difference between the different metals during the dissimilar heterostructure design process. He et al. engineered NiCoP heterostructures for fast electron/ion transport by adopting an in-situ heterogeneous strategy and revealed the mechanism of electronic structure regulation. (S. He et al., 2021) Additionally, Cao et al. constructed VS_4/SnS heterostructure to inhibit the diffusion of polysulfide intermediates and thus achieve excellent potassium ion storage (L. Cao et al., 2021).[5]

[5] Most of the content in this chapter has been published in ACS Materials Letters, 6(1), 222–232.1 and Advanced Functional Materials, 34(28), 2400261.

$MoSe_2$, as a typical low-cost layered transition metal selenide, has a large interlayer spacing of 0.65 nm in the c-axis direction to facilitate Na^+ insertion and de-insertion. (Ge et al., 2020) $MoSe_2$ can exist in two different phases based on the d-band charge localization of Mo atoms: the stable semiconductor 2H phase and the less stable metallic 1T phase. (H. He et al., 2022) The 2H phase, although stable, exhibits low electrical conductivity, limiting its suitability for high-power applications. In contrast, the 1T phase offers high charge transfer capability due to its metallic properties. Consequently, research efforts have been focused on exploring the transition process from the 2H to the 1T phase to improve the electrochemical kinetics of $MoSe_2$. Liu et al. has successfully induced the phase transition from the 2H to the 1T phase through an electron injection strategy, enabling stable sodium-ion storage at high power densities. (F. Liu et al., 2022) Similarly, He et al. employed plasma induction to modify the electronic structure of $MoSe_2$, effectively reducing the energy barrier for the 2H-to-1T phase transition. (H. He et al., 2022) However, despite the superior metallic electronic conductivity and favorable Na^+ diffusion characteristics exhibited by the 1T-$MoSe_2$ phase, its inherent thermodynamic instability remains a key challenge that hinders its practical implementation. To overcome this limitation, a partial phase transformation approach has been proposed to achieve a hybrid 2H/1T phase with improved stability under both steady-state and non-steady-state conditions. Wang et al. has successfully achieved a controlled phase transition from the 2H to the 1T phase through in-situ embedding of Li^+. This process has resulted to the formation of a mixed 2H/1T phase with enhanced adsorption of conversion products (e.g., polysulfides) and improved reaction kinetics in the Li-S battery system. (Yunke Wang, Zhao, et al., 2023) While

many reported phases transition methods often involved multi-step or complex processes with stochastic transformable positions, there is a need to develop a concise and efficient scheme to induce the phase transition, particularly crucial for large-scale production purposes.

Iron-based selenides (Fe_xSe_y) have garnered considerable research interest as viable candidates for low-cost transformative materials in SIBs. (L. Wang & Zhang, 2023; Shige Wang et al., 2022; J. Yuan et al., 2022; Zhai et al., 2022) Among these materials, $FeSe_2$ has been extensively studied due to its facile synthesis and the high theoretical specific capacity triggered by the high-valence iron ions. In contrast, hexagonal FeSe (H-FeSe), characterized by its open body structure and superior ionic conductivity, remains a relatively unexplored material. (K. Wu et al., 2019) H-FeSe exhibits a Fermi surface composed of six elliptical electron pockets, giving rise to metallic properties and facilitating the construction of heterogeneous structures by coupling with other selenide components that possess varying band gaps. (Y. Cao et al., 2021; Coldea et al., 2018; Kreisel et al., 2020) For example, Hu et al. has effectively enhanced the sustained reduction of polysulfides by constructing FeSe-MnSe structures endowed with abundant heterogeneous interfaces. (S. Hu et al., 2022) Moreover, Liu et al. demonstrated an enhanced electrical conductivity and Na^+ diffusion efficiency in Fe_3Se_4/FeSe heterostructures. (Jiawei Liu et al., 2021) Collectively, the incorporation of FeSe and the formation of heterogeneous structural systems, which encompass cations with varying band gaps, have proven to be successful strategies for accommodating fast reaction kinetics of Na^+ within the interior of the material. Therefore, in the first part of this

chapter we designed a mixed phase of $MoSe_2$ with FeSe, which has a large difference in electronegativity, hoping to produce a 1H/2T mixed-phase of $MoSe_2$ along with the excitation of dissimilar cationic heterostructures, thus facilitating the efficient storage of Na^+.

Apart from the traditional conversional MSes previously mentioned, some alloy-based selenides can stimulate both conversion-alloying reactions, which facilitates further capacity enhancement. (Chong et al., 2023; Shijian Wang et al., 2020) Sb_2Se_3, an MSe, undergoes a conversion-alloying reaction as an anode for SIBs. (Zihao Yang et al., 2022) Typically, the Sb_2Se_3 electrode exhibits predominantly Na^+ embedding during the pre-discharge stage. Then, the electron transfer triggers the conversion reaction to produce Sb metal and Se^{2+}. Notably, The Sb metal can further alloy with Na^+ to generate Na_xSb. This multi-step reaction process enables the Sb_2Se_3 anode to exhibit a higher capacity output than conventional conversion-based materials. However, the alloying process tends to deliver a more severe volume expansion than the conversion process. (Zihao Yang et al., 2022) Moreover, the intermediate phases formed during the charge-discharge processes tend to migrate freely, reducing ion and electron transfer efficiency. (S. Wu et al., 2023) Therefore, Sb_2Se_3 electrode requires modification strategies to preserve material structural stability and facilitate rapid ion transport. Introducing additional phases to construct heterostructures has been a hot research direction. For example, Li et al. applied electrodeposition to grow rice-spike-like SbBi-Bi_2Se_3-Sb_2Se_3 (SbBi-Se) on a copper plate, forming abundant heterostructure interfaces with uniformly distributed SbBi, Bi_2Se_3, and Sb_2Se_3. (Xinyan Li et al., 2023) However,

the introduction of another volume-expanded bismuth alloy to build a non-homogeneous structure suffers from the problem of active material shedding during long-term cycling. By investigation, we found that combining alloy-type chalcogenides with stable transition metal disulfides/diselenides could achieve high power density with extended cycling capability. Zhu et al. demonstrated that the $MoS_2@Sb_2S_3$ heterostructure could accelerate the ion and electron transfer and deliver rich active sites, facilitating electrolyte penetration and improving interfacial reaction kinetics. (M. Zhu et al., 2023) Moreover, Li et al. prepared $SnSe_2/NiSe_2$ structures with heterogeneous interfaces and Se vacancies, enhancing Na^+ adsorption energy while effectively improving the Na^+ transfer efficiency. (Huan Li et al., 2023) WSe_2, as a conversion material, delivered stable long-term cyclability and fast reaction kinetics in the Chapter 4. (J. Wang, Shao, et al., 2023) Therefore, in the second part of this chapter, Sb_2Se_3 with WSe_2 are combined to construct heterostructures, which is expected to achieve excellent capacity output at high power density.

6.2 MOF-Derived 1T/2H-$MoSe_2$/FeSe/C Composites

Herein, we report the synthesis of Mo-Fe bimetallic MOF structures via a solvent-assisted construction method. Subsequently, 1T/2H-$MoSe_2$/FeSe/C composites are prepared through a carbonization/selenization process. The derived MOF derivatives exhibit a homogeneous distribution of metal ions within the amorphous carbon matrix, facilitating rapid adsorption/desorption of Na^+ on the carbon surface and providing a structural foundation for further Na^+ migration into the interior of the active material. Moreover, the introduction of Fe induces a phase structure transition in $MoSe_2$ from a

single stable 2H phase to a mixed 1T/2H phase structure, with the 1T phase present at the edges and the 2H phase in the interior. This modification alters the electronic structure distribution and enhances the metallic properties at the edge, facilitating the efficient transfer of electrons/ions from the amorphous carbon to the bulk 2H-$MoSe_2$ phase. The $MoSe_2$/FeSe heterostructure, formed by cation coupling, exhibits a rich heterogeneous interface that generates a strong built-in electric field with metallic characteristics, ensuring fast reaction kinetics of electrons/ions within the electrode. DFT calculations confirm the superior metallic properties of the $MoSe_2$/FeSe heterogeneous interface compared to $MoSe_2$ and FeSe.

6.2.1 Synthesis of 1T/2H-$MoSe_2$/FeSe/C

Figure 6.1 illustrates a simple two-step synthesis schematic of 1T/2H-$MoSe_2$/FeSe/C. First, porous Mo/Fe-MOF precursors are synthesized by the liquid-phase method under the complexation of antisuccinic acid. Subsequently, the selenium powder and Mo/Fe-MOF are thoroughly mixed, followed by selenization and carbonization under H_2/Ar (10 vol% H_2) gas mixture to finally obtain $MoSe_2$/FeSe/C composites with cationic heterostructures. Remarkably, the generation of FeSe in $MoSe_2$/FeSe/C is attributed to the charge redistribution and phase-heterogeneous protonation caused by the different coordination environment during the formation of bimetallic Mo/Fe-MOF compared with $FeSe_2$/C monomer synthesized by Fe-MOF. (Jablonka et al., 2021) In addition, during the selenization process, there is an electron transfer between Mo and Fe due to the cationic coupling effect, which consequently forms the $MoSe_2$/FeSe/C heterostructure.

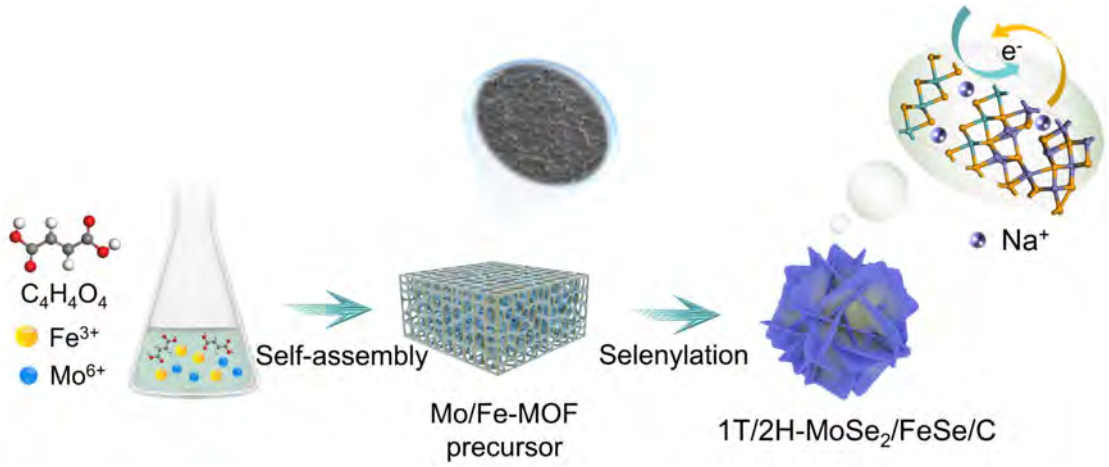

Figure 6.1: Schematic illustration of the synthetic route for 1T/2H-$MoSe_2$/FeSe/C.

6.2.2 Structural and Chemical Characterization of 1T/2H-$MoSe_2$/FeSe/C

Figure 6.2 shows the SEM images of 1T/2H-$MoSe_2$/FeSe/C, from which the morphology changes from a bulk porous Mo/Fe-MOF precursor (Figure 6.2a) to an ordered self-assembled lamellar shape after the selenization/carbonization process. The self-assembled lamellar can deliver more stable mechanical properties and anti-shock characteristics.

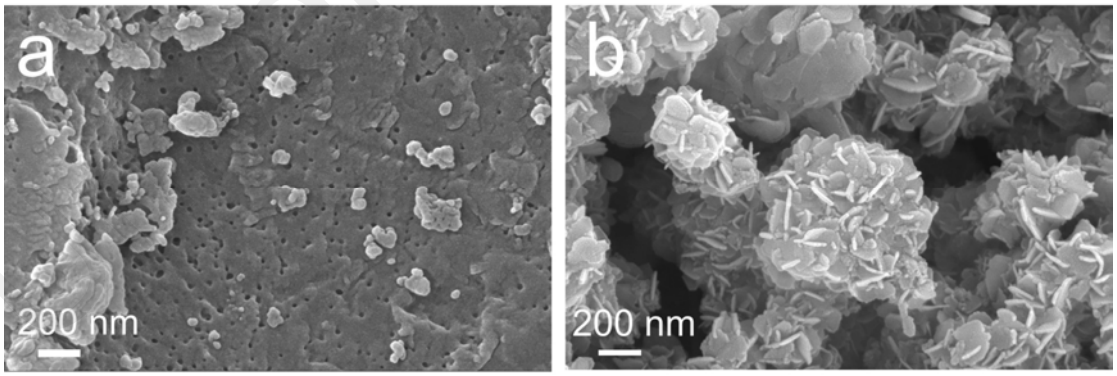

Figure 6.2: SEM images of Mo/Fe-MOF precursor (a) and 1T/2H-$MoSe_2$/FeSe/C (b).

Furthermore, HRTEM is used to evaluate the crystal structure and interface of 1T/2H-$MoSe_2$/FeSe/C (Figure 6.3). Among them, the lattice spacing of 0.263 nm in Figure 6.3a can be attributed to the (1 0 2) crystal plane of 2H-$MoSe_2$. Notably, an octahedral lattice

structure (octahedral coordination) appears around the main 2H phase, corresponding to the 1T phase of $MoSe_2$. The formation of 1T-$MoSe_2$ can be attributed to the edge phase transition effect induced by Fe atoms during the selenization process. (H. He et al., 2022; Yingshuang Xu et al., 2022) According to our knowledge, $MoSe_2$ in the edge 1T phase has better metallic properties and local electron density compared to the 2H phase, which can contribute to improving the electron transfer between phase boundaries. (Ge et al., 2020; Yunke Wang, Zhao, et al., 2023) Furthermore, the lattice spacings of 0.337 and 0.276 nm in Figure 6.3b are attributed to the (0 0 4) and (1 0 1) crystal planes of $MoSe_2$ and FeSe, respectively. The angle of the heterogeneous interface between the two phases is nearly parallel (28.2°), representing that the constructed $MoSe_2$/FeSe heterostructure system not only possesses the conventional point and line heterogeneity, but also achieves deeper contact at the crystalline plane level. This is conducive to the enhanced built-in electric field effect. (Shan et al., 2021)

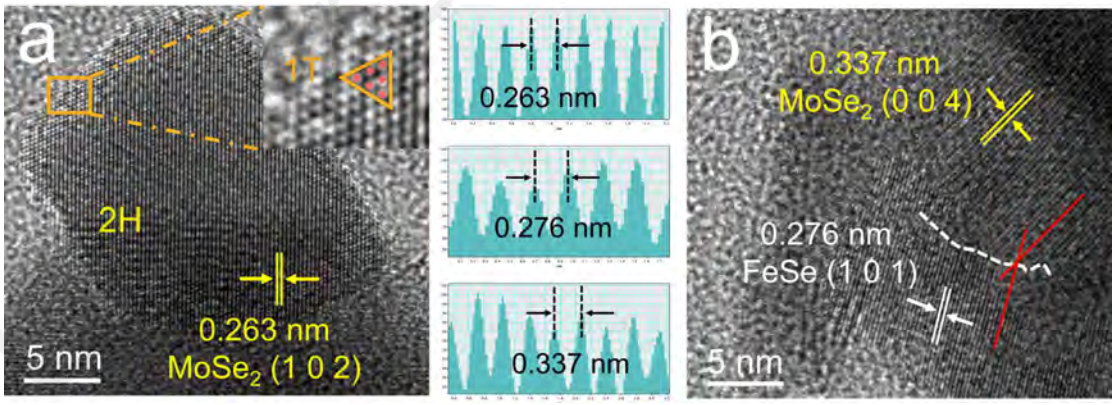

Figure 6.3: HRTEM diagrams of 1T/2H-$MoSe_2$/FeSe/C.

As shown in Figure 6.4, the elemental distribution of the self-assembled lamellar $MoSe_2$/FeSe/C is revealed by TEM mapping, in which Fe, Mo, Se, and C all exhibit a uniform distribution. Furthermore, the C element exhibits a significant high brightness, indicating that the homogeneous carbon layer constructed with MOF self-sacrificial

bodies has a strong protective and buffering effect on the internal non-homogeneous structure.

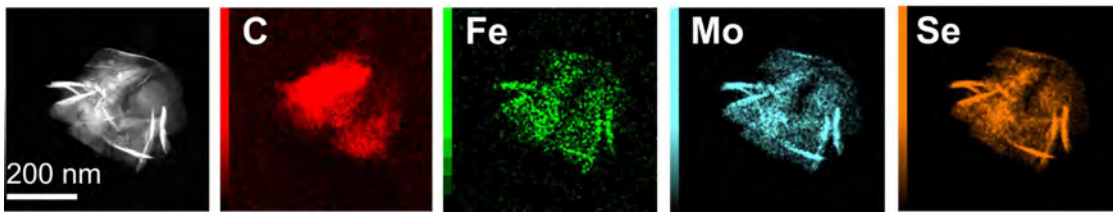

Figure 6.4: Elemental mapping of 1T/2H-$MoSe_2$/FeSe/C.

The XRD results in Figure 6.5a demonstrate the physical phase information of $MoSe_2$/FeSe/C. The peaks located at 31.4°, 37.9°, 34.4°, and 47.5° can be indexed to the (1 0 0), (1 0 3), (1 0 2), and (1 0 5) crystal planes of $MoSe_2$ (JCPDS No. 29-0914). Simultaneously, the peaks located at 32.4°, 42.2°, and 50.5° correspond to the (1 0 1), (1 0 2), and (1 1 0) crystal planes of the FeSe phase (JCPDS No. 75-0608), respectively. As a comparison, the XRD results of the Fe-MOF monomer samples after selenization exhibit a typical $FeSe_2$ phase with high cationic valence (JCPDS No.82-0269), which laterally confirms the electron transfer during the selenization between Mo and Fe (Figure 6.5b).

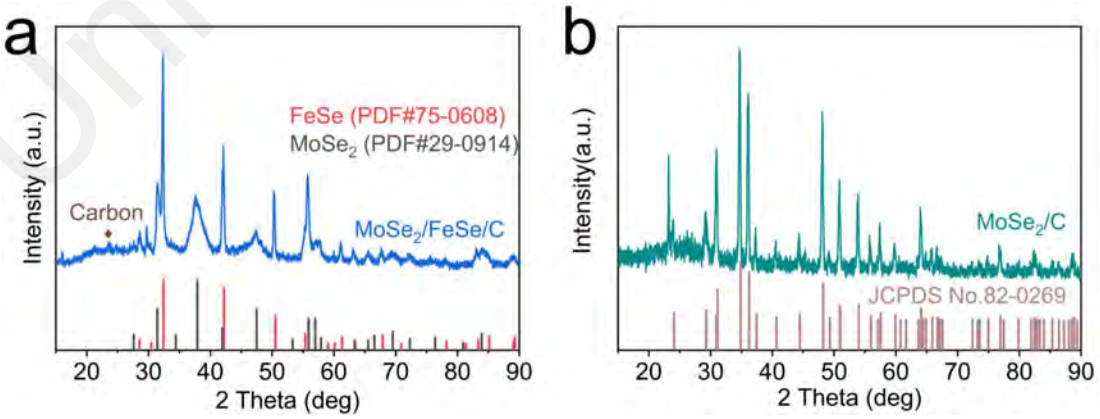

Figure 6.5: XRD patterns of 1T/2H-$MoSe_2$/FeSe/C (a) and Fe-MOF monomer-derived $FeSe_2$ (b).

The TG curves in air atmosphere exhibit a slight mass loss at the initial stage, which can be ascribed to the evaporation of surface adsorbates and water (Figure 6.6a). When the temperature reaches about 350 ℃, a significant mass loss can be observed (~55.47%), indicating that the oxidative decomposition of $MoSe_2$, FeSe, and C occurs simultaneously during the process. Raman spectroscopy is employed to further confirm the selenization results (1T/2H-$MoSe_2$/FeSe/C). As shown in Figure 6.6b, the characteristic peaks appearing at 215.1, 278.8, and 388.2 cm^{-1} imply Se-Se vibrations and stretching vibrations or a combination of them in the resulting product. (J. Cao et al., 2021; L. Liu et al., 2021; Y. Tian et al., 2021) Meanwhile, the inset shows two peaks located at 1347 cm^{-1} and 1563 cm^{-1}, representing defective carbon (D-band) and graphitic carbon (G-band), respectively (F. Yuan, Zhang, et al., 2022). The fitted results by peak intensity derived an I_D/I_G value of 1.685, implying that the prepared composites have a large number of defects, which is favorable for the rapid adsorption of Na^+.

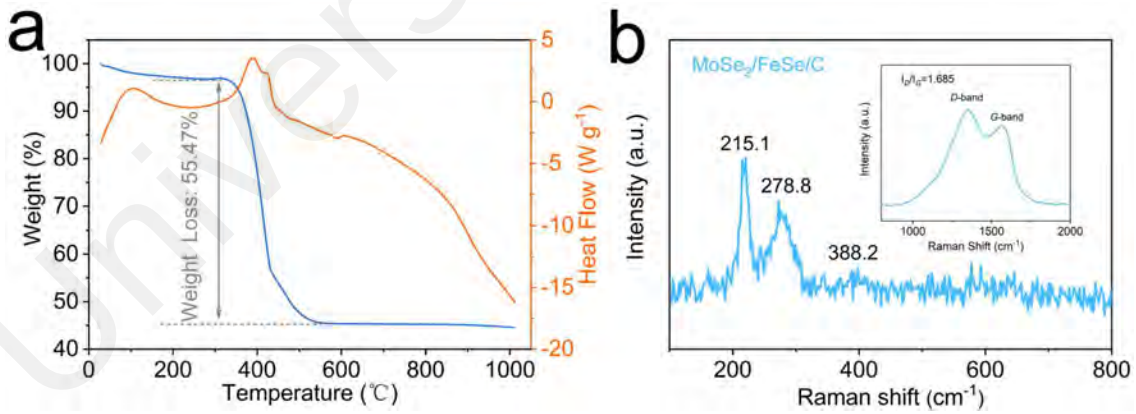

Figure 6.6: (a) TG curves of 1T/2H-$MoSe_2$/FeSe/C in air atmosphere. (b) Raman spectra of 1T/2H-$MoSe_2$/FeSe/C.

XPS is applied to analyze the composition and surface chemical state of the resulting samples. From the high-resolution spectra of the Mo 3d orbitals in Figure 6.7a, $MoSe_2$/FeSe/C sample exhibits two additional orbital peaks located at 232.99 and

235.98 eV relative to pure $MoSe_2$/C, which can be referred to Mo $3d_{5/2}$ and Mo $3d_{3/2}$. The appearance of the Mo 3d peak in the high binding energy direction represents a decrease in the electron density around Mo, suggesting a surface charge transfer between Mo and Fe. Moreover, the Mo-C orbital peak located at 230.11 eV appears in both samples, representing the interfacial homogeneous bonding during the self-sacrificial carbonization of MOF precursor. (J. Tao et al., 2022) Figure 6.7b displays the Fe 2p orbital peaks of $MoSe_2$/FeSe/C and FeSe/C. By comparison, both samples exhibit Fe $2p_{3/2}$ and Fe $2p_{1/2}$ characteristic peaks with different valence states. In contrast, the Fe 2p orbital of $MoSe_2$/FeSe/C delivers two extra orbital peaks located at 707.68 and 720.33 eV, which can be attributed to the shift of Fe $2p_{3/2}$ and Fe $2p_{1/2}$, respectively. The energy level splitting toward the lower binding energy indicates that the low oxidation state Fe^{2+} generated by the cationic crystal field effect and electron interaction between Fe and Mo in $MoSe_2$/FeSe/C. This confirms the electron transfer phenomenon between $MoSe_2$ and FeSe, which is consistent with the presentation of the Mo 3d orbital peak. Additionally, the C 1s orbital can be further assigned to three orbital peaks (Figure 6.7c).The peak located at 282.59 eV is caused by Mo-C/Fe-C, revealing the connection information between the active $MoSe_2$/FeSe and amorphous carbon, responding to the Mo-C peak existing in the Mo 3d orbital. (J. Tao et al., 2022) Moreover, the two peaks located at 284.77 and 285.52 eV are produced by C-C and C-O bonds, respectively. (Q. Li et al., 2022) For lower range of binding energy as shown in Figure 6.7d, the Se 3d orbitals can be further divided into Se $3d_{5/2}$ (located at 54.47 eV) and Se $3d_{3/2}$ (located at 55.35 eV).

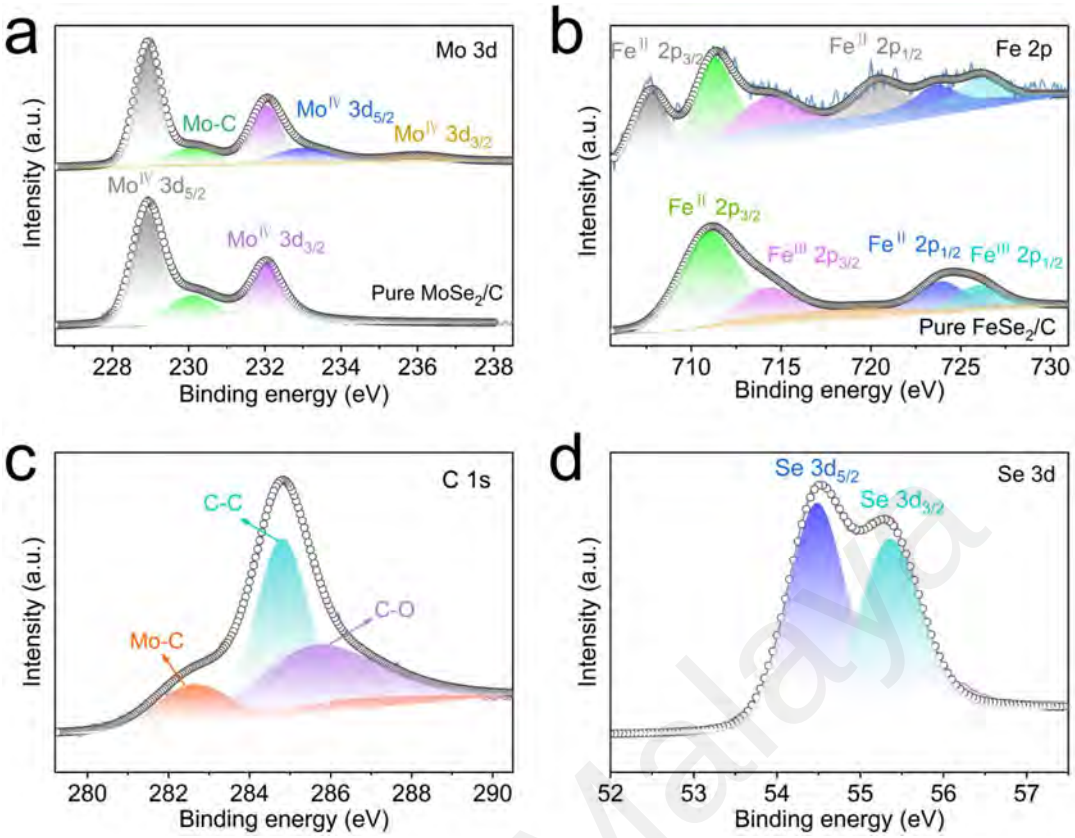

Figure 6.7: High-resolution Mo 3d (a) and Fe 2p (b) XPS spectra of 1T/2H-$MoSe_2$/FeSe/C, $MoSe_2$/C, and $FeSe_2$/C. C 1s High-resolution XPS spectra of C 1s (c) and Se 3d (d) of 1T/2H-$MoSe_2$/FeSe/C.

Additionally, to further reveal the microstructural evolution during the synthesis, the BET surface area and the corresponding pore distribution of Mo/Fe-MOF precursors and $MoSe_2$/FeSe/C are measured separately (Figure 6.8a). From that, $MoSe_2$/FeSe/C exhibits a smaller specific surface area and pore size distribution compared to the Mo/Fe-MOF precursor, verifying the transformation process of the porous precursor to a more stable self-assembled lamellar structure during the selenization process. Moreover, the pore size distribution in Figure 6.8b reveals that the Mo/Fe-MOF precursor is dominated by mesopores with diameters of 2−20 nm.

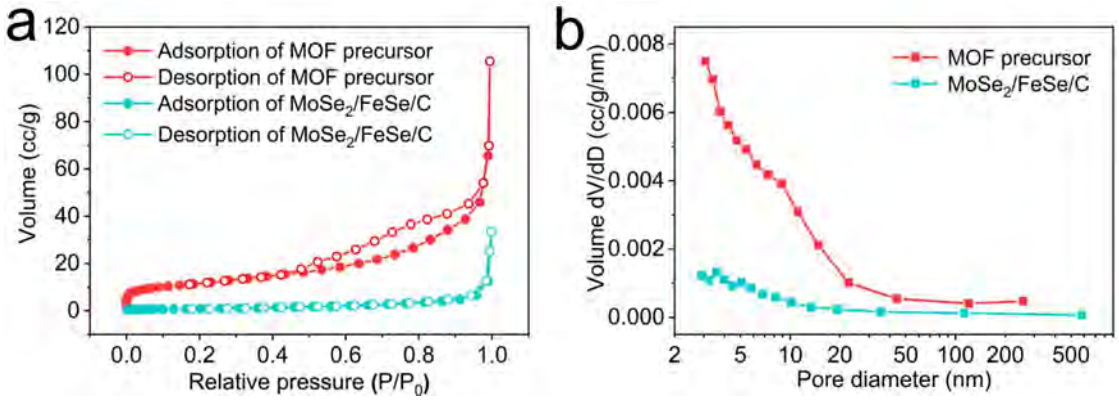

Figure 6.8: N_2 adsorption-desorption isotherms (a) and pore size distribution plots (b) of Mo/Fe-MOF and 1T/2H-$MoSe_2$/FeSe/C.

6.2.3 Density Functional Theory Calculations

The heterogeneous structural properties of $MoSe_2$/FeSe are investigated by DFT calculations. Figure 6.9 illustrates the model of the constructed composite, in which the $MoSe_2$ and FeSe are connected by Se atoms.

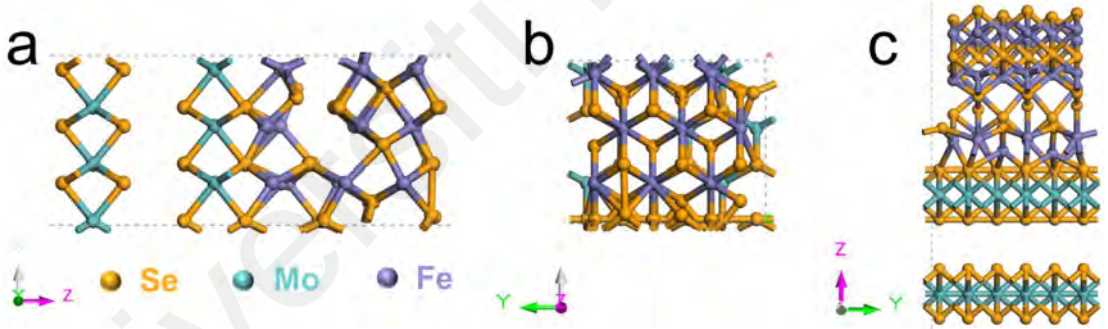

Figure 6.9: (a) The model of the constructed $MoSe_2$/FeSe composite on different views: (a) left view, (b) top view, and (c) vertical view.

The band structure of $MoSe_2$/FeSe has been calculated in Figure 6.10a. Apparently, no significant energy band gap appears near the Fermi energy level (0 eV), implying a strong metallic property. Conversely, the band structure of FeSe in Figure 6.10b display significant energy band gap near the Fermi energy level (E_g=0.014 eV), implying the semiconducting property. Similarly, $MoSe_2$ exhibit the E_g value of -1.402 eV, representing the obvious semiconducting property (Figure 6.10c), respectively. From

that, $MoSe_2$/FeSe benefits from the superconducting properties of FeSe and exhibits metallic properties in combination with the built-in electric field formed at the heterogeneous interface.

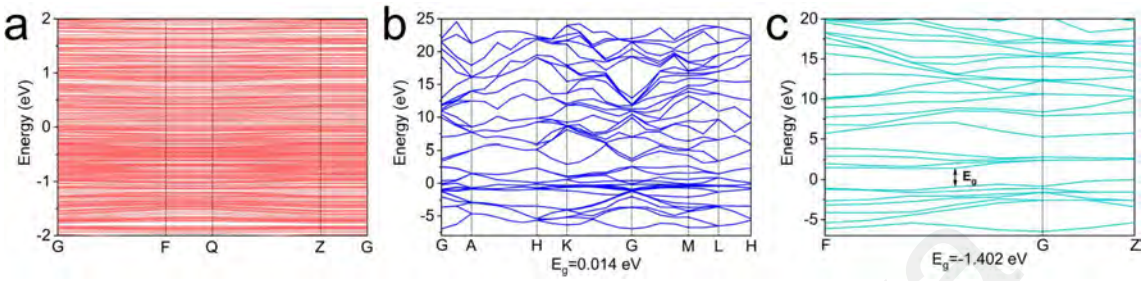

Figure 6.10: The calculated bandgap structures for $MoSe_2$/FeSe (a), FeSe (b), and $MoSe_2$ (c).

Futhermore, DOS analysis is performed for $MoSe_2$/FeSe, $MoSe_2$, and FeSe structures, respectively (Figure 6.11). The results exhibit that $MoSe_2$ has no superposition peaks near the Fermi energy level, while FeSe and $MoSe_2$/FeSe show different degrees of superposition peaks. The superposition intensity of $MoSe_2$/FeSe is greater than that of FeSe, indicating that $MoSe_2$/FeSe has a stronger metallic capability. This is consistent with the energy band structure analysis.

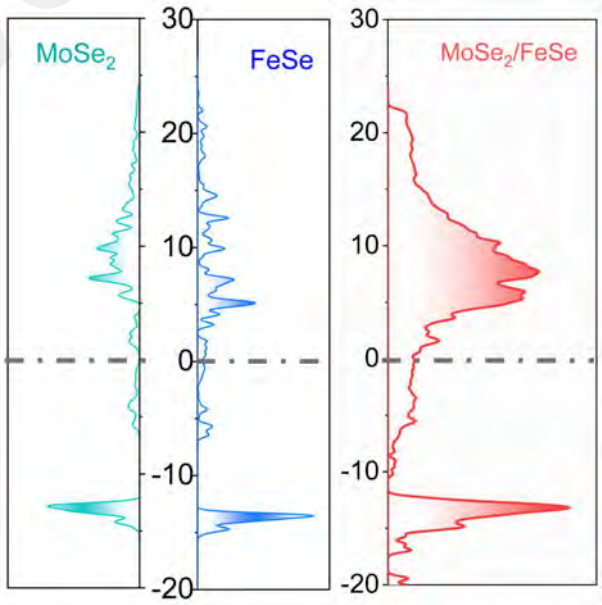

Figure 6.11: The density of states for $MoSe_2$, FeSe, and $MoSe_2$/FeSe.

To visually describe the charge distribution pattern of the built-in electric field in the heterogeneous structure, the charge differential density of the $MoSe_2$/FeSe structure is calculated in Figure 6.12a. Wherein, the yellow electron cloud represents charge disappearance and the green electron cloud represents charge accumulation. From that, unlike the charge distribution of the regular $MoSe_2$ layer below, the $MoSe_2$ layer at the border with FeSe (at a distance of about 10 in the Z-axis direction) exhibits a stronger charge accumulation, suggesting the formation of a built-in electric field between the $MoSe_2$ layers. Additionally, the Se atoms located at the junction of $MoSe_2$ and FeSe exhibit a clear charge transfer trend (from Se to Fe), revealing that the interfacial Fe has a more distinct charge-rich state, which is favorable for the rapid conduction of electrons at the heterogeneous interface. To compare the charge distribution differences in more detail, the charge distributions of $MoSe_2$ and FeSe are calculated separately (Figure 6.12b and Figure 6.12c).

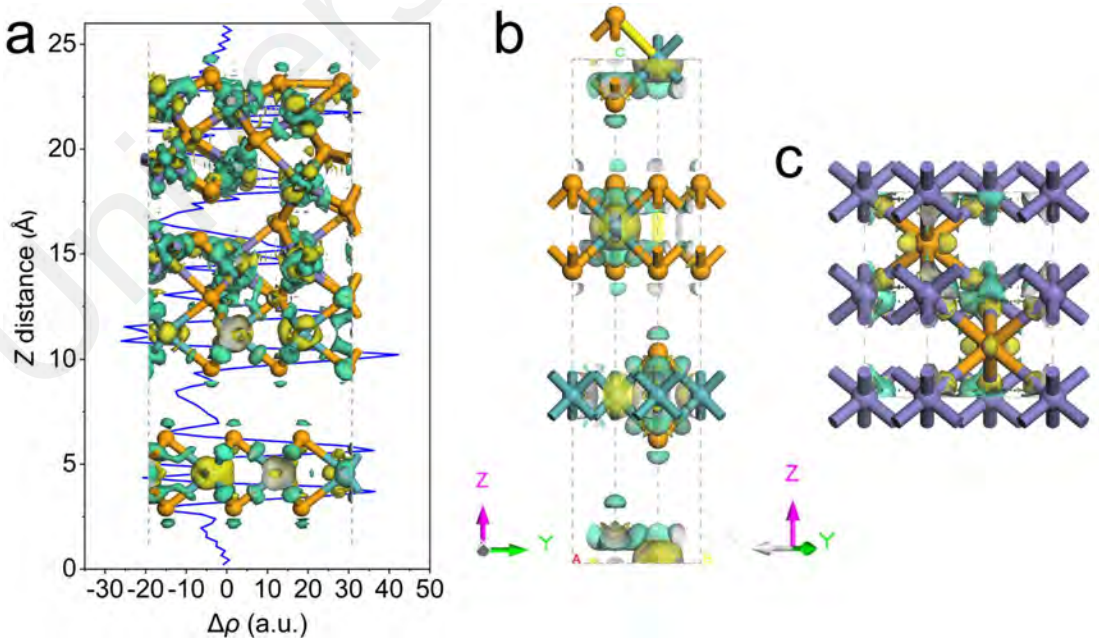

Figure 6.12: The planar-average charge density of $MoSe_2$/FeSe heterostructure (a), $MoSe_2$ (b), and FeSe (c).

Additionally, the adsorption capacities of 1T-type and 2H-type $MoSe_2$ for Na^+ are explored using DFT calculations. The calculated adsorption energies of 1T-$MoSe_2$ and 2H-$MoSe_2$ are -4.36 eV and -3.84 eV, respectively, as shown in Figure 6.13. The more negative adsorption energy of the 1T-$MoSe_2$ phase represents a stronger adsorption capacity for Na^+.

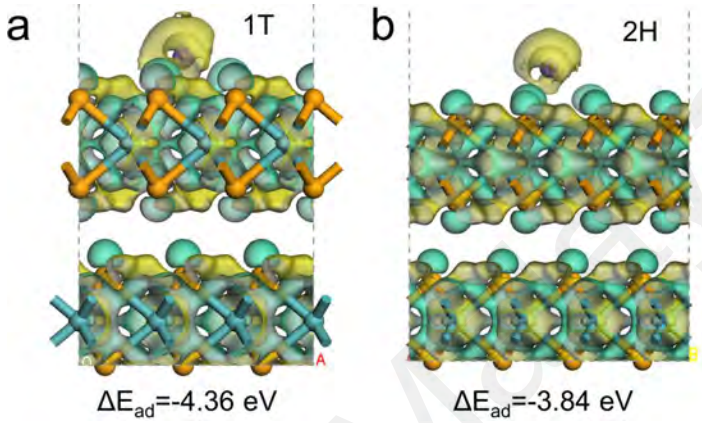

Figure 6.13: The adsorption energies of Na^+ on the surfaces of 1T-$MoSe_2$ (a) and 2H-$MoSe_2$ (b).

6.2.4 Electrochemical Properties of 1T/2H-$MoSe_2$/FeSe/C in SIBs

To evaluate the electrochemical performance and reaction kinetics of 1T/2H-$MoSe_2$/FeSe/C employs as electrode in SIBs, half-cells are assembled using sodium metal as counter electrode. Figure 6.14a records the cycling performance of the three materials employed as electrodes (1T/2H-$MoSe_2$/FeSe/C, $MoSe_2$/C, and FeSe/C) at 2 A g^{-1}, respectively. By comparison, 1T/2H-$MoSe_2$/FeSe/C exhibits a discharge specific capacity of 597.2 mA h g^{-1} after 1000 cycles, which is significantly higher than that of the $MoSe_2$/C (333.5 mA h g^{-1}) and $FeSe_2$/C (465.5 mA h g^{-1}) electrodes. Notably, the specific capacities of all three materials show a trend of decreasing and then increasing during the initial 200 cycles, which is related to the activation of the electrodes during the initial process. The activation process has been explored in detail in our previous

work. (J. Wang, Shao, et al., 2023) Accordingly, the GCD profiles at different cycles in Figure 6.14b indicates that the charging and discharging plateau driven by the conversion reaction gradually became obvious as the cycling proceeded, especially compared to the 3rd cycle. The initial activation process verifies that more heterogeneous interfaces and boundary sites are exposed under the activation effect of electrochemistry.

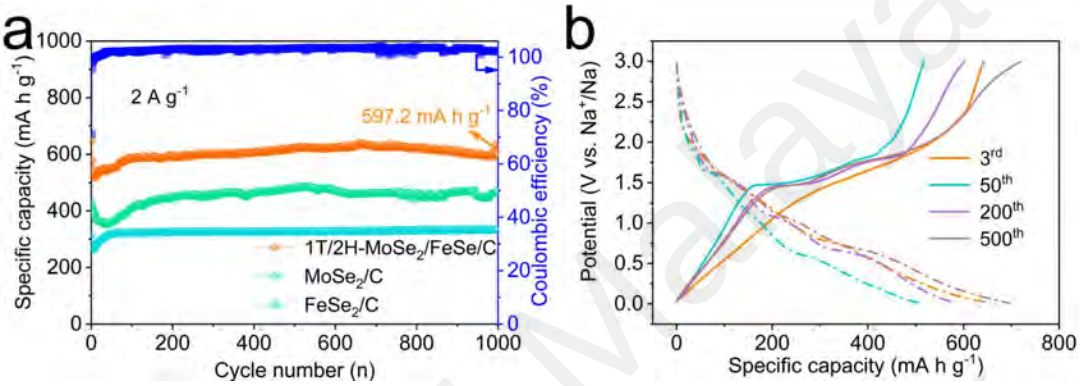

Figure 6.14: Electrochemical performance for SIBs. (a) Short cycling performance at 2 A g^{-1} of the as-prepared three materials. (b) GCD profiles (3rd, 50th, 200th, and 500th) of 1T/2H-$MoSe_2$/FeSe/C electrode.

To further verify this activation process, we plotted the dQ/dV for the first 100 cycles (Figure 6.15). As can be seen, the two main conversion reactions (conversion 1 and 2) are gradually activated as the cycle proceeds, corroborating the activation process of the electrodes.

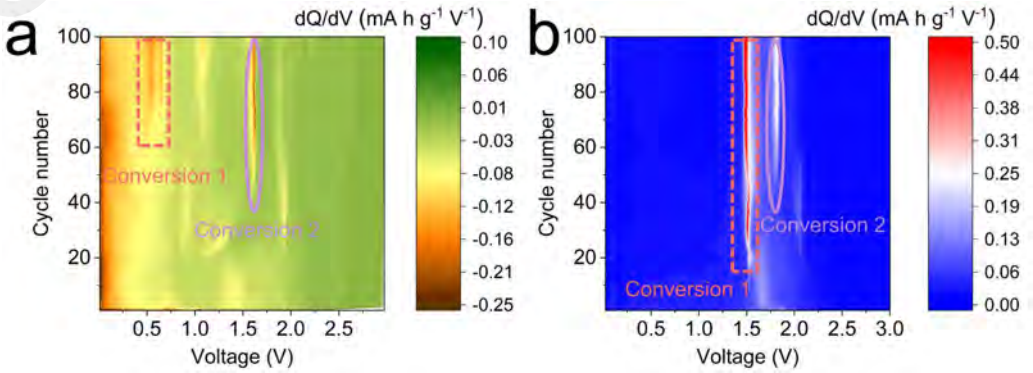

Figure 6.15: dQ/dV cruves of the 1T/2H-$MoSe_2$/FeSe/C electrode for the first 100 cycles: (a) discharge process and (b) charge process.

The ICE is one of the key factors to measure the electrode quality. Generally, conductivity shortcomings lead to overall poor ICE performance in conversion materials. The GCD curves and initial ICE of three prepared samples were measured separately as shown in Figure 6.16a. Therein, the initial ICEs of the three electrodes 1T/2H-$MoSe_2$/FeSe/C, $MoSe_2$/C, and $FeSe_2$/C are 77.57%, 72.46%, and 75.13%, respectively. All ICEs were higher than 70%, illustrating that uniformly dispersed amorphous carbon can promote reversible transfer of ions and electrons. $MoSe_2$/FeSe/C electrode exhibited the highest ICE suggesting that the dual action of heterogeneous structure and carbon can effectively promote reversible de-embedding of Na^+ from the interior to the exterior. Figure 6.16b further compares the GCD profiles of the three materials, illustrating that the voltage plateau of 1T/2H-$MoSe_2$/FeSe/C is a combination of $MoSe_2$/C and FeSe/C. Meanwhile, the 1T/2H-$MoSe_2$/FeSe/C electrode displays the smallest polarization caused by the heterogeneous structure.

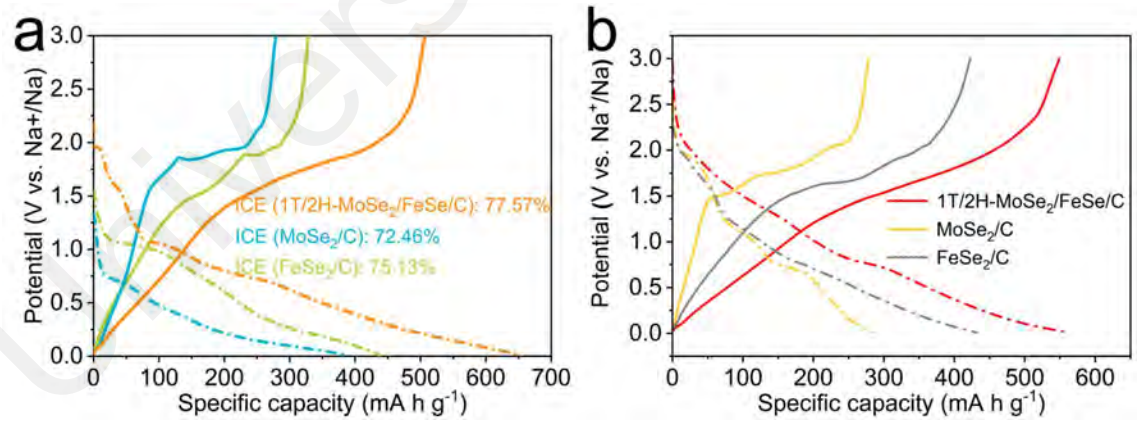

Figure 6.16: (a) The first cycled GCD curves of the 1T/2H-$MoSe_2$/FeSe/C, $MoSe_2$/C, and $FeSe_2$/C electrodes and the corresponding ICEs. GCD profiles (3rd, 50th, 200th, and 500th) of 1T/2H-$MoSe_2$/FeSe/C electrode.

Additionally, the rate capability of 1T/2H-$MoSe_2$/FeSe/C electrode is tested at the current densities of 1, 2, 4, 6, 8, and 10 A g^{-1}, delivering 578.0, 531.3, 487.4, 459.3, 439.6, and 427.1 mA h g^{-1} respectively (Figure 6.17a). When the current density returns

to 1 A g^{-1}, it is still possible to recover a specific capacity of 504.1 mA h g^{-1}. In contrast, with the built-in electric field and boundary effect formed by the heterogeneous structure, the 1T/2H-$MoSe_2$/FeSe/C electrode achieves higher rate capacity with faster ion transport while ensuring the most stable rate capability. To further measure the performance of the 1T/2H-$MoSe_2$/FeSe/C electrode at high-power density, as shown in Figure 6.17b, the specific capacity of 336.5 mA h g^{-1} can be remained after 3000 cycles at 10 A g^{-1}, demonstrating the excellent cycling capability.

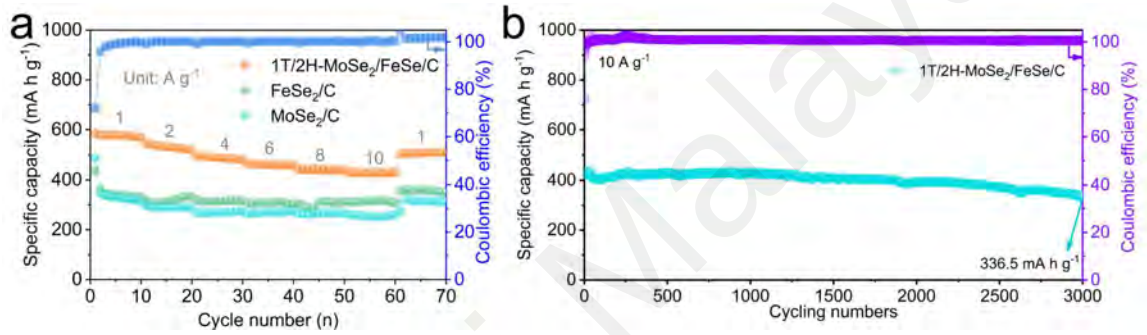

Figure 6.17: (a) Rate capabilities between the as-prepared three materials. (b) Long cycling performance and coulombic efficiency of 1T/2H-$MoSe_2$/FeSe/C electrode at the current density of 10 A g^{-1}.

For a deeper insight into the mechanism behind the high electrochemical performance, two transport mechanisms are depicted in Figure 6.18 to visualize the transport of Na^+ from the surface to the interior of the bulk phase. On the one hand, the Na^+ adsorbed by the defect-rich amorphous carbon is rapidly conducted into the interior of the 2H-$MoSe_2$ phase via the 1T phase on the $MoSe_2$ surface, enabling rapid ion mediation. On the other hand, the inhomogeneous electric field distribution can promote the rapid transfer of Na^+ within the bulk phases of $MoSe_2$ and FeSe under the effect of the built-in electric field formed by the heterogeneous structure. Collectively, the 1T/2H-$MoSe_2$/FeSe/C electrode can achieve stable and efficient Na^+ storage at high power density.

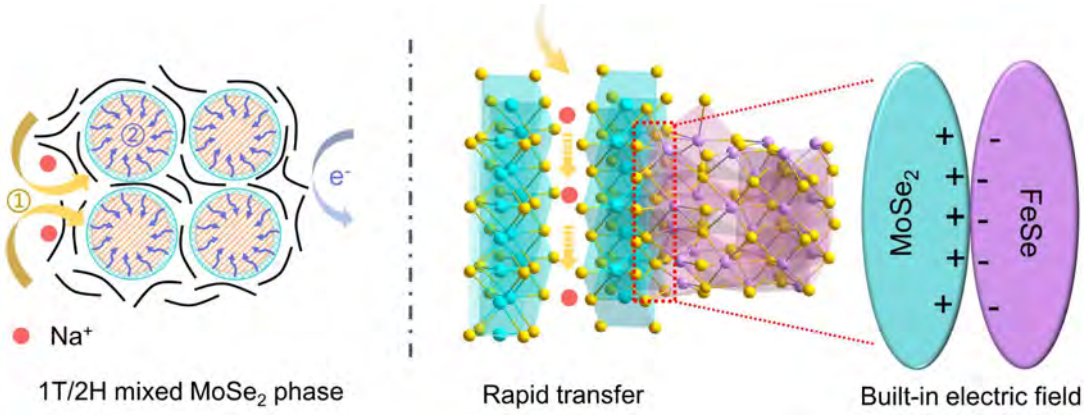

Figure 6.18: Schematic illustration of Na^+ transport mechanisms in 1T/2H-$MoSe_2$/FeSe/C electrode.

6.2.5 Sodium Storage Kinetics Investigation

CV is applied to study the electrochemical processes of the 1T/2H-$MoSe_2$/FeSe/C electrodes. As the CV curves at 0.1 mV s^{-1} in Figure 6.19a, the reduction peaks located at 1.08 V appear during the first cathodic scan, signifying the migration of sodium ions into the FeSe and $MoSe_2$ phases to form Na_xFeSe and Na_xMoSe_2 respectively (Guo et al., 2022; Chunxiao Lv et al., 2019). Meanwhile, the peak at 0.84 V implies the occurrence of conversion reactions ($MoSe_2$→Mo; FeSe→Fe). The broad reduction peak at 0.54 V presents the formation of irreversible SEI (Jiawei Liu et al., 2021). Subsequently, two main peaks located at 1.51 V and 1.76 V appeared during the first anodic scan, representing the reverse conversion reaction and the Na^+ desorption process from the interlayer, respectively. Note that a pair of small redox peaks appearing near 0 V can be attributed to the role of amorphous carbon in the composite. Extraordinarily, the second and third CV scan curves almost overlap, predicting favorable reversibility of the later redox reactions. Apart from the CV curves of the first circle, a pair of major conversion peaks (0.79/1.51 V) dominates in the second and third circles. The peaks representing Na^+ insertion/deinsertion in the interlayer become

weaker and shift toward higher voltages accordingly, suggesting that the conversion-type mechanism dominates the reaction process at the $MoSe_2$/FeSe/C electrode in the early stage. To reveal the reaction behavior during the early charge/discharge process in detail, as shown in Figure 6.19b, CV tests are performed for $MoSe_2$/C and $FeSe_2$/C, respectively. By comparison, the reaction peak of 1T/2H-$MoSe_2$/FeSe/C is almost the combined result of $MoSe_2$/C and $FeSe_2$/C, indicating that the main reaction in the heterogeneous structure is consistent. Only a slight shift in the peak position exists, representing a smaller polarization of the electrode process in 1T/2H-$MoSe_2$/FeSe/C.

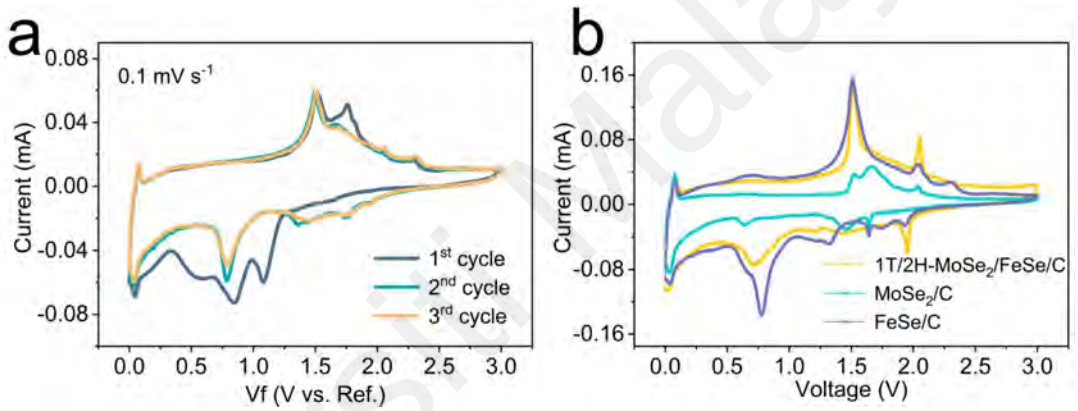

Figure 6.19: (a) CV curves from 0.01 to 3.0 V at the scan rate of 0.1 mV s^{-1} for 1T/2H-$MoSe_2$/FeSe/C electrode in SIBs. (b) The CV curves comparison of the as-prepared three materials at the scan rate of 0.2 mV s^{-1}.

The pseudocapacitance characteristics of the 1T/2H-$MoSe_2$/FeSe/C electrode are investigated by the CV curves at different scan rates (Figure 6.20a). The slope relationship between the fitted peak current and the scan rate can be initially used to determine the behavior type (insertion behavior dominant or pseudocapacitive behavior dominant) in the electrode process. As shown in Figure 6.20b, the b-values fitted for the cathodic and anodic processes are 0.99 and 0.95, respectively, both close to 1, representing that the whole electrode process is dominated by the pseudocapacitive behavior. The strong pseudocapacitive behavior can be attributed to the synergistic

effect of two modes of action: surface redox pseudocapacitance and intercalation pseudocapacitance. In particular, the surface pseudocapacitance is due to the strong ion adsorption effect brought about by the uniformly distributed amorphous carbon, which significantly shortens the ion diffusion distance. On the other hand, the fast intercalation pseudocapacitance is generated by the fast ion conduction channel or interlayer diffusion produced by the abundant built-in electric fields created by the bulk heterostructure. Besides, the pseudocapacitance contribution ratio of the electrodes increases correspondingly with the increase of the scan rate, revealing the stronger pseudocapacitance ability at high currents (Figure 6.20c). The pseudocapacitance control area with a scan rate of 5 mV s^{-1} accounted for up to 96.2% (Figure 6.20d), revealing the fast electrochemical behavior triggered by high surface behavior.

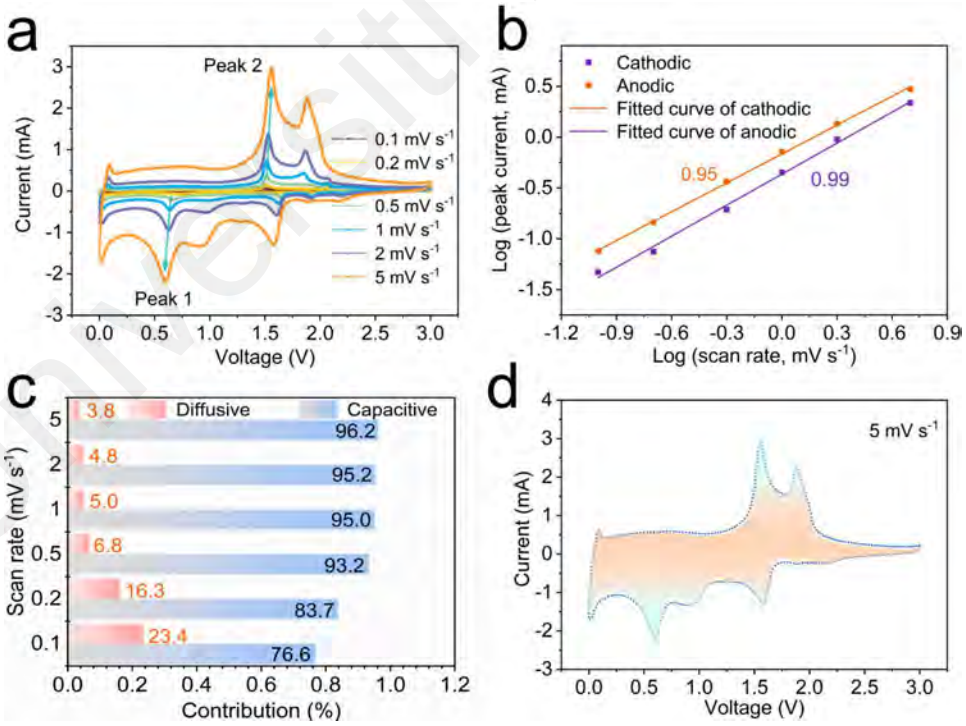

Figure 6.20: (a) CV curves at different scan rates of 1T/2H-$MoSe_2$/FeSe/C electrode in SIBs. (b) Linear diagrams of log (v) and log (i) corresponding to peak currents in different oxidation and reduction states of 1T/2H-$MoSe_2$/FeSe/C. (c) Contribution ratio of the capacitive and diffusion-controlled at different scan rates. (d) The capacitive contribution of 1T/2H-$MoSe_2$/FeSe/C electrode at a scan rate of 5 mV s^{-1}.

As shown in Figure 6.21, GITT is employed to evaluate the ion transport in 1T/2H-$MoSe_2$/FeSe/C, $MoSe_2$/C, and $FeSe_2$/C materials, respectively. During the whole electrode charging and discharging process, all three prepared materials exhibited a gradual decrease in the ionic diffusion efficiency (*D* value). Remarkably, the Log *D* of the 1T/2H-$MoSe_2$/FeSe/C electrode is between 10^{-13} and 10^{-11} over the whole process, which is the highest value among the three materials, verifying that the built-in electric field generated by the heterogeneous structure can facilitate the rapid diffusion of Na^+ within the bulk phase.

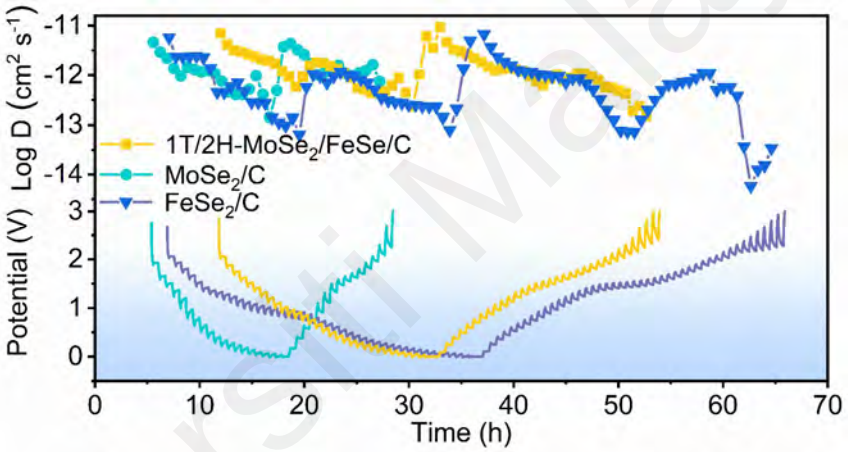

Figure 6.21: GITT and Na^+ diffusion coefficients of the as-prepared three materials.

EIS is employed to evaluate the kinetic behavior of the 1T/2H-$MoSe_2$/FeSe/C electrode. The Nyquist curves in Figure 6.22a reveal the resistance of the 1T/2H-$MoSe_2$/FeSe/C electrode in the initial state and after 50 cycles, respectively. From that, the semicircle diameter in the mid-high frequency region becomes smaller (relative to the initial state) after 50 cycles, representing lower contact and charge transfer resistance, which may be due to the progressive exposure of heterogeneous interfaces during the activation process. Furthermore, the sloping lines in the low frequency region can be utilized to indicate the Na^+ migration process in solid phase. The parameter of

the diffusion process (D) can be further fitted by the relationship between $\omega^{-1/2}$ and Z' (Figure 6.22b). The fitting results of the slope line indicate that the slope in the low frequency region after 50 cycles is 12.8, which is much lower than the slope value of the initial state (165.8), implying that the activation process can significantly enhance the Na^+ migration efficiency.

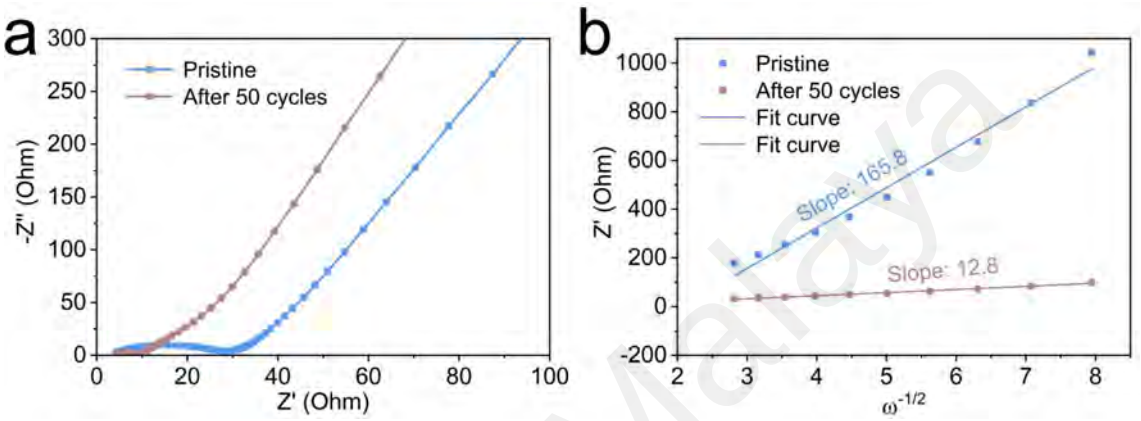

Figure 6.22: Nyquist plots of 1T/2H-$MoSe_2$/FeSe/C before and after 50 cycles (a), and the relationship between Z' and $\omega^{-1/2}$ (b).

6.2.6 Electrochemical Properties of 1T/2H-$MoSe_2$/FeSe/C in SICs

1T/2H-$MoSe_2$/FeSe/C electrode with fast charging and discharging capability is required to be capable of matching the demands of high-power devices. For this purpose, we assembled a hybrid SICs device with high power advantages using commercial AC as the cathode and 1T/2H-$MoSe_2$/FeSe/C as the anode. Figure 6.23 exhibits a physical photograph of six LEDs continuously lit for 120 s by the assembled hybrid SICs.

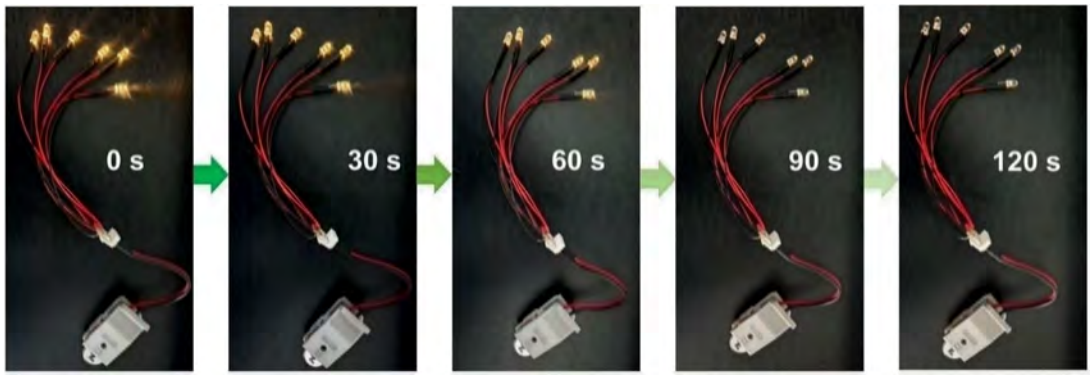

Figure 6.23: The physical photos of the assembled SIC lighting up six LEDs.

To determine a reasonable voltage range for the assembled SICs, CV tests are performed in the voltage ranges of 0−3.6, 0−3.8, 0−4, and 0−4.2 V, respectively. As shown in Figure 6.24a, the test results indicate that when the test voltage is higher than 3.8 V, a sharp peak triggered by a larger polarization appears near the upper voltage limit, demonstrating that 0−3.8 V is a reasonable voltage range. The CV curves of the assembled SICs tested at different scan rates over the voltage range of 0−3.8 V are presented in Figure 6.24b. It can be seen that the CV shapes remain consistent at different scan rates and no shape distortion caused by excessive scan rates is observed. Moreover, the CV profiles exhibit a combination of rectangular-like and redox peaks, representing the combination of bilayer and pseudocapacitive storage mechanisms.

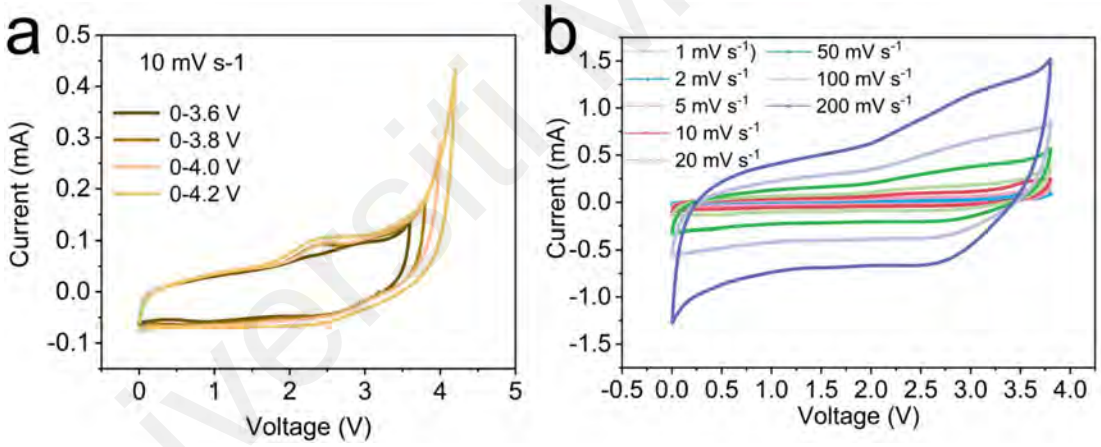

Figure 6.24: CV curves of the assembled SIC at different cutoff potentials (a) and different scan rates (b).

The rate capability of the assembled SICs is tested at current densities of 0.2, 0.5, 1, and 2 A g^{-1}, respectively. As shown in Figure 6.25a, the results exhibit a stable and excellent rate performance even though the current changed from 2 A g^{-1} to 0.2 A g^{-1}. Additionally, the GCD curves at different current densities display the triangle-like shape, signifying a hybrid storage mechanism for the assembled SICs (Figure 6.25b). Furthermore, the long-term cycling capability of the assembled SICs is shown in Figure

6.25c. From that, the specific capacity of 34.25 mA h g^{-1} is maintained with excellent cycling performance even after 8000 cycles at 2 A g^{-1}.

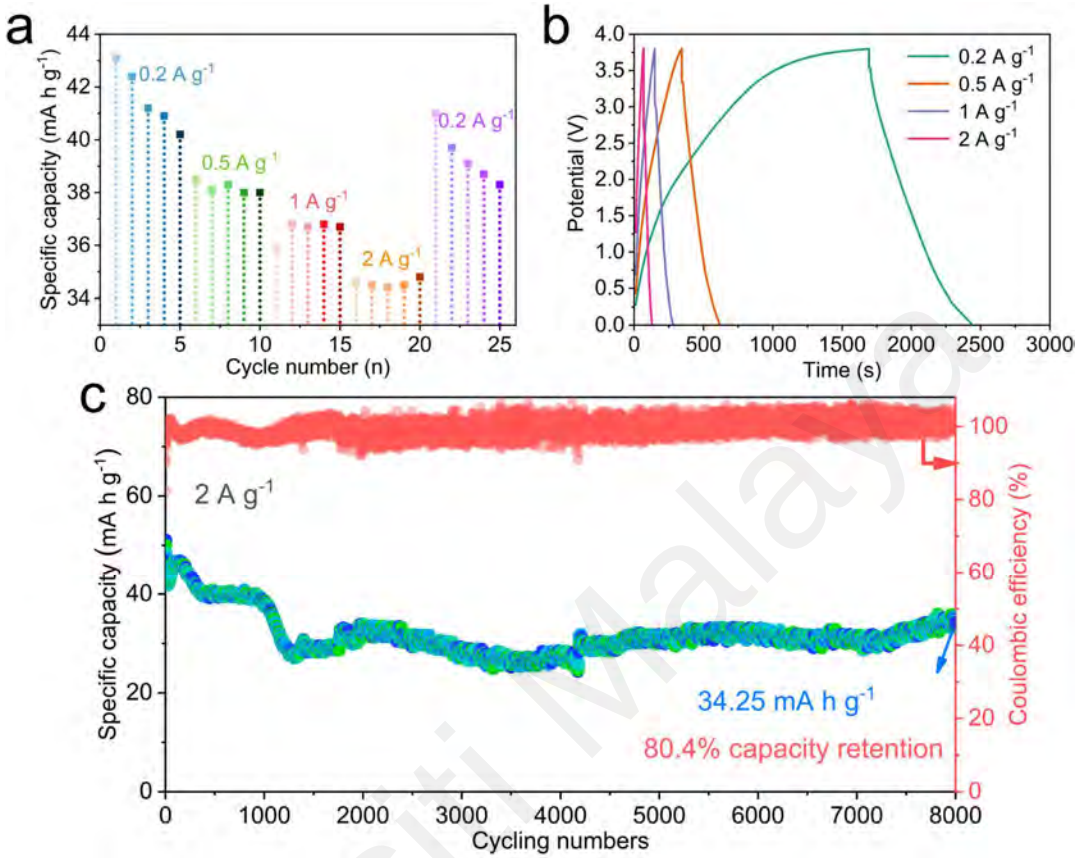

Figure 6.25: (a) Rate performance, and (b) GCD profiles of the assembled SIC. (c) Cycling stability and coulombic efficiency of the assembled SIC at 2 A g^{-1} for 8000 cycles.

6.3 MOF-derived Interlayered Sb_2Se_3-WSe_2/C Composites

In this section, we synthesized Sb/W bimetallic MOF precursors to obtain homogeneous metal distribution and carbon introduction by exploiting the hydrolysis of perchlorides. Subsequently, electrostatic spinning technology was applied to achieve the fiber encapsulation. Finally, the low-temperature selenization/carbonization process was employed to fabricate Sb_2Se_3/WSe_2/C heterostructure. The amorphous carbon distribution from interior to exterior was achieved after a dual carbon introduction strategy (MOF construction and electrostatic spinning), facilitating efficient electron

conduction and rapid Na^+ adsorption. Moreover, the interlayer built-in electric field formed by Sb_2Se_3/WSe_2 heterostructure promoted the rapid Na^+ transfer within the bulk phase, thus improving the slow reaction kinetics of the alloying process. Benefiting from the above advantages, the prepared Sb_2Se_3/WSe_2/C-500 electrode can exhibit excellent electrochemical properties.

6.3.1 Synthesis of Sb_2Se_3/WSe_2/C

The preparation process is shown schematically in Figure 6.26. Firstly, the Sb/W-hybridization structure is synthesized by a one-step method. Notably, the synthesis process utilizes the hydrolysis of perchlorides to achieve a uniform distribution and self-assembly process. Subsequently, the uniform encapsulation of Sb/W-hybridization precursor is successfully achieved by introducing a conductive polymer and performing electrostatic spinning.

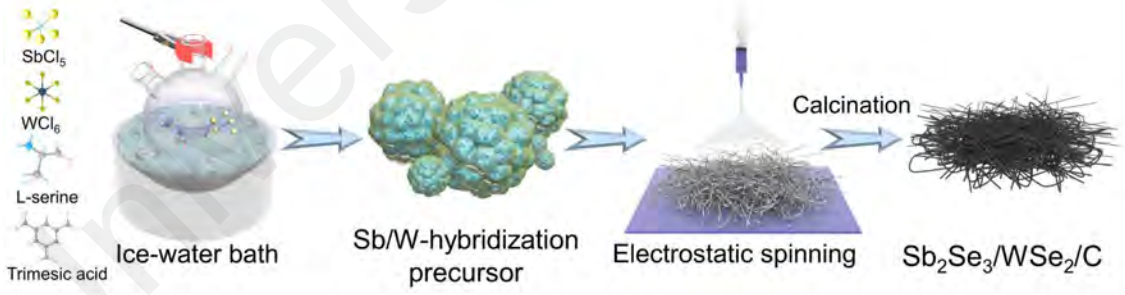

Figure 6.26: Schematic illustration of the synthetic process of the Sb_2Se_3/WSe_2/C.

6.3.2 Structural and Chemical Characterization of Sb_2Se_3-WSe_2/C

The SEM image of the Sb/W-hybridization precursor in Figure 6.27a demonstrates the cluster morphology assembled by microparticles. The SEM-mapping images verify the uniformly distributed Sb, W, O, and C elements in the prepared Sb/W-hybridization precursor (Figure 6.27b).

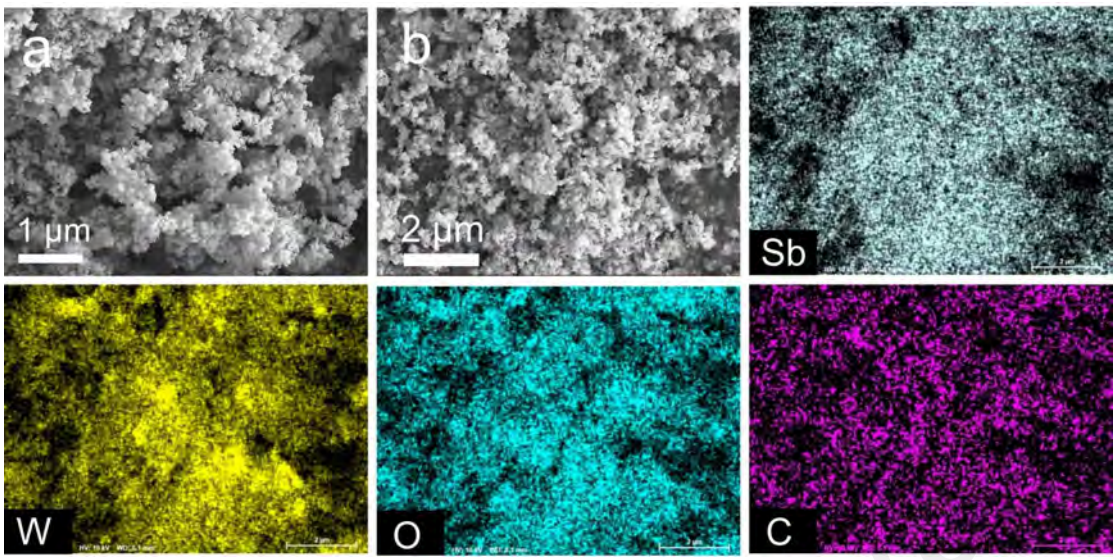

Figure 6.27: The SEM image of Sb/W-hybridization precursor (a) and the corresponding elemental mapping (b).

As shown in Figure 6.28a, b, the products present crossed fibers with about 500 to 600 nm diameters after electrostatic spinning. Finally, the obtained nanofibers are subjected to carbonization and selenization at different temperatures (400 °C, 500 °C, and 600 °C), resulting in dual-carbon introduced Sb_2Se_3 and WSe_2 heterostructure ($Sb_2Se_3/WSe_2/C$). The SEM image of the final obtained $Sb_2Se_3/WSe_2/C$-500 sample demonstrates a diameter of less than 500 nm (Figure 6.28c), implying a volume shrinkage triggered by the carbonization of the organic components in the nanofibers.

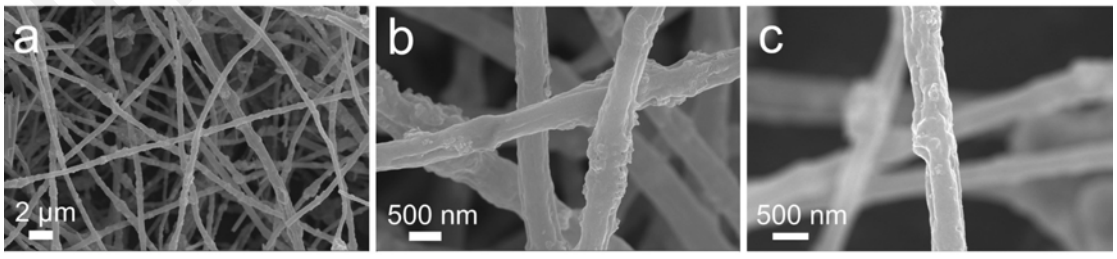

Figure 6.28: SEM images of the electrostatic spinning products before sintering (a, b) and the final obtained $Sb_2Se_3/WSe_2/C$-500 (c).

From the TEM image of $Sb_2Se_3/WSe_2/C$-500 in Figure 6.29a, the Sb_2Se_3 and WSe_2 particles are dispersed in the carbon nanofibers for effective encapsulation. The crystal

structure of Sb_2Se_3/WSe_2/C-500 is investigated using HRTEM. As shown in Figure 6.29b, the crystal spacing of 0.29 nm and 0.65 nm are monitored, which can be attributed to (2 2 1) of Sb_2Se_3 and (0 0 2) of WSe_2, respectively. Notably, the 1.24 nm crystal spacing is found during the measurements. Figure 6.29c zooms in on the selected region to explore the composition more precisely. The results reveal the enlarged (0 0 2) crystal plane of WSe_2 with a single (2 2 1) crystal plane of Sb_2Se_3 embedded between the two atomic layers. That fully demonstrated the formation of an interlayer heterostructure between Sb_2Se_3 and WSe_2. In the magnified HRTEM of Figure 6.29b incomplete lattice fringes (red regions are Se atomic vacancies) can be monitored, suggesting the loss of Se atoms during selenization. The presence of selenium vacancies is favorable for the rapid surface adsorption of Na^+, thereby promoting the reaction kinetics at high power density. (Sha et al., 2023)

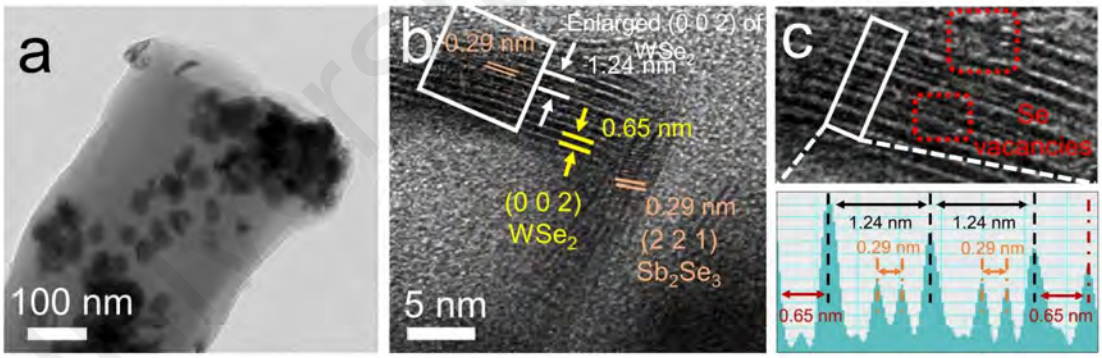

Figure 6.29: (a) TEM image of Sb_2Se_3/WSe_2/C-500. (b) HRTEM diagram and (c) enlarged image in the white area of S Sb_2Se_3/WSe_2/C-500.

Subsequently, elemental mapping performed on Sb_2Se_3/WSe_2/C-500 indicate that the constructed Sb_2Se_3/WSe_2 heterostructure, C, and N are distributed within the nanofibers (Figure 6.30). Additionally, the distribution of N in carbon fibers is consistent with C, while it is not monitored in the profiles of Sb and W, suggesting that N is uniformly doped into C, which can promote the rapid ion adsorption. (L. F. Chen et al., 2017; Yang

Xu et al., 2018)

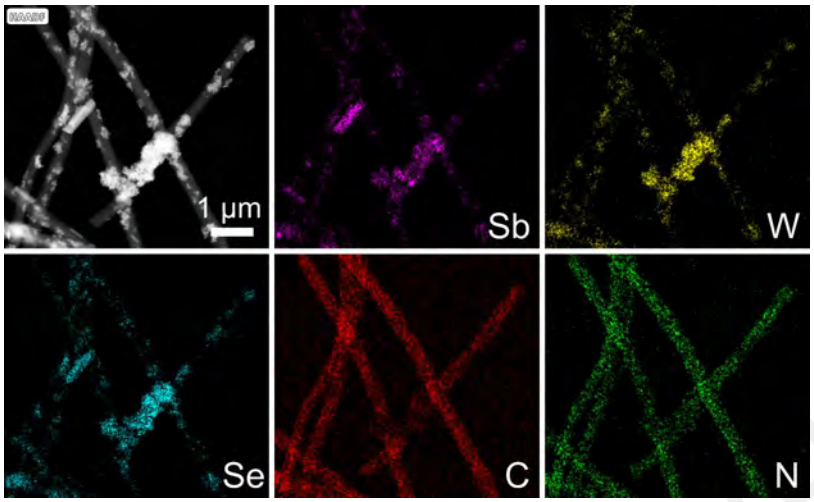

Figure 6.30: Elemental mapping of Sb_2Se_3/WSe_2/C-500.

As shown in Figure 6.31, the elemental content in the Sb_2Se_3/WSe_2/C-500 sample is further evaluated by EDS. In particular, the higher carbon content (67.63%) ensures excellent structural stability of the electrode during cycling at high power densities. Additionally, the contents of Sb and W are 5.70% and 6.29%, respectively, verifying the homogeneous introductions of the two metallic elements. Notably, the measured Se content of 14.69% is smaller than the theoretical content corresponding to Sb and W, representing the unavoidable generation of Se vacancies during selenization, which is consistent with the HRTEM results.

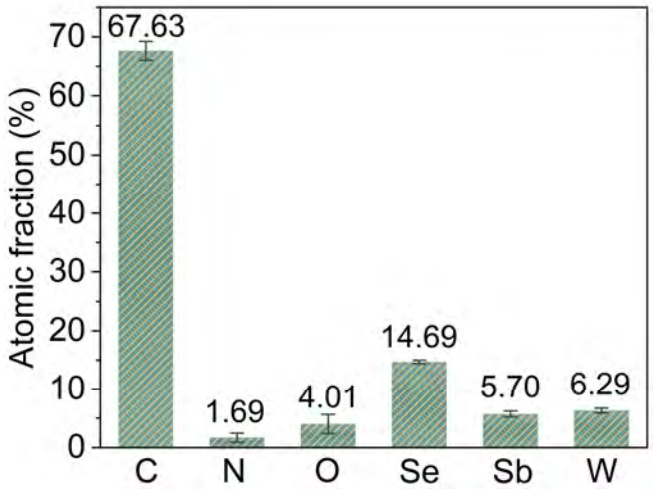

Figure 6.31: The elemental content in the Sb_2Se_3/WSe_2/C-500 evaluated by EDS.

XRD is applied to reveal the detailed crystal structure of the synthesized Sb/W-hybridization precursor and $Sb_2Se_3/WSe_2/C$ samples. From Figure 6.32a, all the characteristic peaks can be indexed to JCPDS No. 15-0861 and JCPDS No. 87-2418, implying the formation of mixed phases Sb_2Se_3 and WSe_2 with favorable crystal characteristics. To further compare the phase transition of $Sb_2Se_3/WSe_2/C$ during sintering, the XRD patterns for different sintering temperatures are investigated. When the sintering temperature is 400 °C, the XRD of $Sb_2Se_3/WSe_2/C$-400 exhibits the corresponding Sb_2O_3 (JCPDS No. 71-0383), Se (JCPDS No. 01-0848), and WO_3 (JCPDS No. 85-2459) phases, revealing the residual Se powder and unconverted Sb and W oxides at insufficient sintering temperature (Figure 6.32b). Besides, $Sb_2Se_3/WSe_2/C$-600 obtained at 600 °C exhibits the same Sb_2Se_3 and WSe_2 phases as $Sb_2Se_3/WSe_2/C$-500 (Figure 6.32c). Differently, the high-temperature sintering process resulted in partial decomposition of Sb, which in turn exhibited a strong WSe_2 phase.

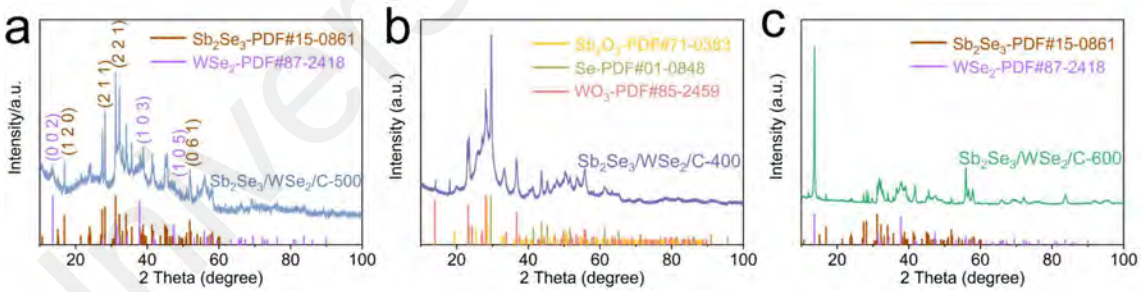

Figure 6.32. XRD patterns of $Sb_2Se_3/WSe_2/C$-500 (a), $Sb_2Se_3/WSe_2/C$-400 (b), and $Sb_2Se_3/WSe_2/C$-600 (c).

The nitrogen adsorption–desorption isotherm curve of the sintered $Sb_2Se_3/WSe_2/C$-500 show a higher specific surface area and pore size distribution (Figure 6.33). This indicates that the pyrolytic shrinkage of organic carbon creates more defects, which can enhance the pseudocapacitive ability of the material.

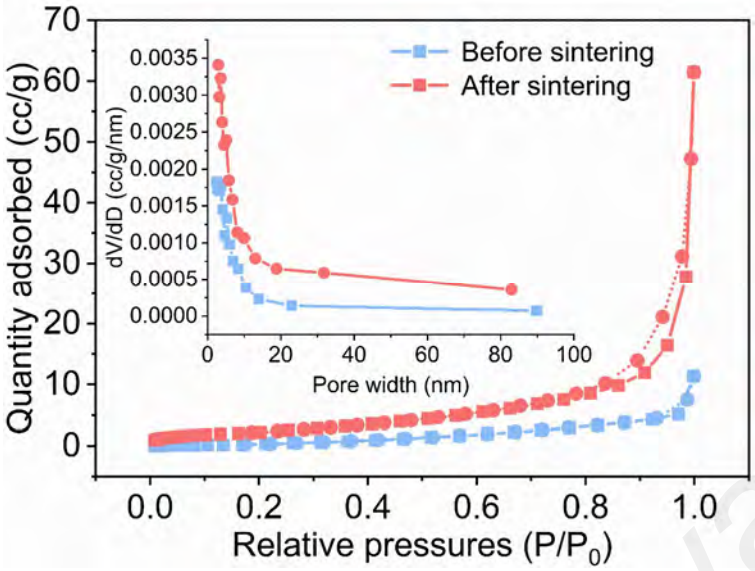

Figure 6.33: N_2 adsorption/desorption isotherm and pore size distributions of electrostatic spinning products before and after sintering.

To investigate the effect of different sintering temperatures on $Sb_2Se_3/WSe_2/C$ in more detail, Raman spectra of three samples are tested in Figure 6.34. All samples exhibit D-bands and G-bands at 1343 and 1581 cm^{-1} representing the defective and graphitized structures, respectively. (S. Wu et al., 2024) Furthermore, the D peaks can be further deconvoluted for D1 (exposed edge defects), D2 (polyene or ionic impurity), and D3 (amorphous carbon) located at 1358, 1240, and 1491 cm^{-1}, respectively. (Quan et al., 2023; F. Yuan, Shi, et al., 2022) The I_{D1}/I_G intensity ratio can be calculated to further assess the relationship between edge defect content and capacity contribution. Among the I_{D1}/I_G values of the obtained samples under different temperatures, $Sb_2Se_3/WSe_2/C$-500 has the largest value, representing more exposed edge defect sites to promote rapid surface adsorption of Na^+.

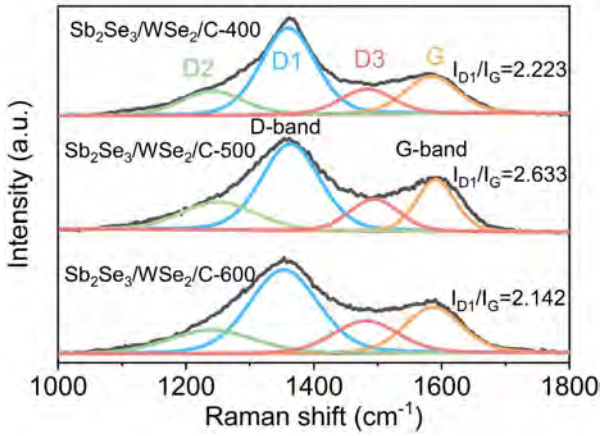

Figure 6.34: Raman spectra of Sb_2Se_3/WSe_2/C-400, Sb_2Se_3/WSe_2/C-500, and Sb_2Se_3/WSe_2/C-600.

FTIR spectroscopy is employed to study the carbon evolution process at different temperatures. As shown in Figure 6.35, the peaks located at 1400, 1630, and 2360 cm^{-1} can be assigned to the C=C, C=O, and C≡C stretching vibrations with π-π* and n-π* transitions, respectively. (Qu et al., 2022; Tripathi et al., 2022) Notably, the above peaks exhibit a slight blueshift with increasing temperature, suggesting that the strength of the unsaturated conjugated structure decreases at higher temperatures, leading to stronger electron-withdrawal capacity of the exposed heteroatoms. (Y. Q. Zheng et al., 2017) Therefore, calcination at an intermediate temperature (500 °C) facilitates forming a moderate organic-inorganic hybrid structure to expose more defect sites.

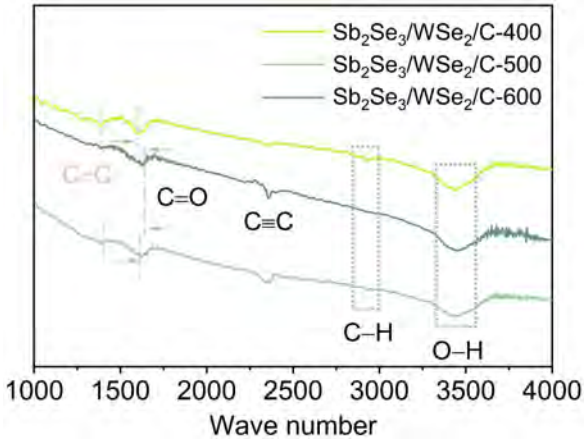

Figure 6.35: FTIR spectra of Sb_2Se_3/WSe_2/C-400, Sb_2Se_3/WSe_2/C-500, and Sb_2Se_3/WSe_2/C-600.

Further, EPR is utilized to investigate the defects of Sb_2Se_3/WSe_2/C-400/500/600 (Figure 6.36). All three samples exhibit Lorentz lines of different intensities centered at g=2.0022, indicating the formation of unpaired electrons on the π-conjugated carbon atoms. Furthermore, Sb_2Se_3/WSe_2/C-500 exhibits the smallest linewidth (3.517), indicating the presence of more unpaired electrons from edge defects. This is consistent with the Raman test results.

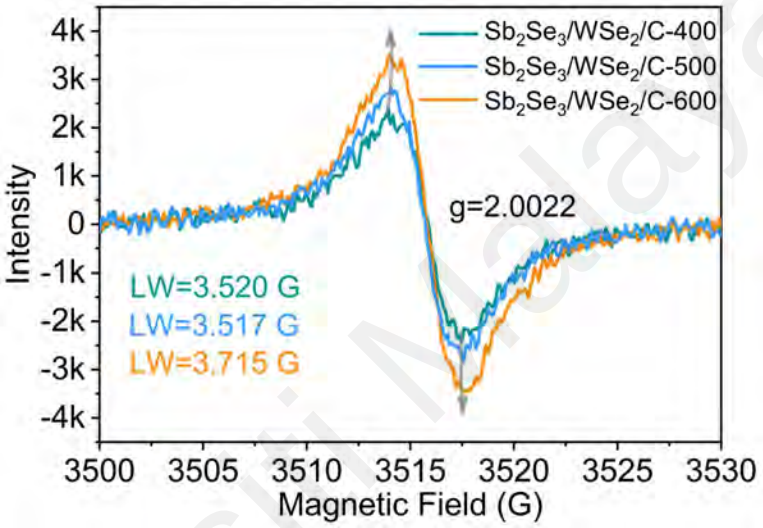

Figure 6.36: EPR spectra of Sb_2Se_3/WSe_2/C-400, Sb_2Se_3/WSe_2/C-500, and Sb_2Se_3/WSe_2/C-600.

To better evaluate the elemental composition and chemical state information of the synthesized Sb_2Se_3/WSe_2/C-500, XPS is further applied. From the high-resolution Sb 3d/O 1s spectrum in Figure 6.37a, two distinct spin-splitting peaks can be observed at the high and low binding energies, representing Sb $3d_{3/2}$ and Sb $3d_{5/2}$, respectively. (G. Xu et al., 2022) Additionally, the Sb-O (-C) peak is monitored at 531.9 eV, resulting from the pairing of Sb and oxygen-deficient electrons produced by the unsaturated conjugated structure during calcination. (Q. Luo et al., 2022) In the W 4f spectrum of Sb_2Se_3/WSe_2/C-500 (Figure 6.37b), two pairs of peaks of W $4f_{7/2}$ and W $4f_{5/2}$ further split into W-Se and W-O bonds, suggesting the unavoidable surface oxidation of W. (G.

Zhang et al., 2021; S. Zhang et al., 2021) According to the HRTEM results, the SbWSe heterostructures probably introduce valence changes in Se element. Therefore, the Se 3d high-resolution spectra of $Sb_2Se_3/WSe_2/C$, Sb_2Se_3/C, and WSe_2/C are compared, respectively. By comparison, both Se $3d_{5/2}$ and Se $3d_{3/2}$ split in Sb_2Se_3/WSe_2 exhibit a shifting trend toward lower binding energies, representing the increased electron density around Se, thus exhibiting more negative valence states (Figure 6.37c). (Hua et al., 2023) The valence difference introduced by the heterogeneous structure proves the formation of an inhomogeneous built-in electric field, which is favorable to promote the rapid Na^+ transport. Additionally, we further analyzed the XPS high-resolution spectra of C (Figure 6.37d). The results show that carbon and nitrogen elements are successfully introduced into the $Sb_2Se_3/WSe_2/C$-500 composites after selenization process.

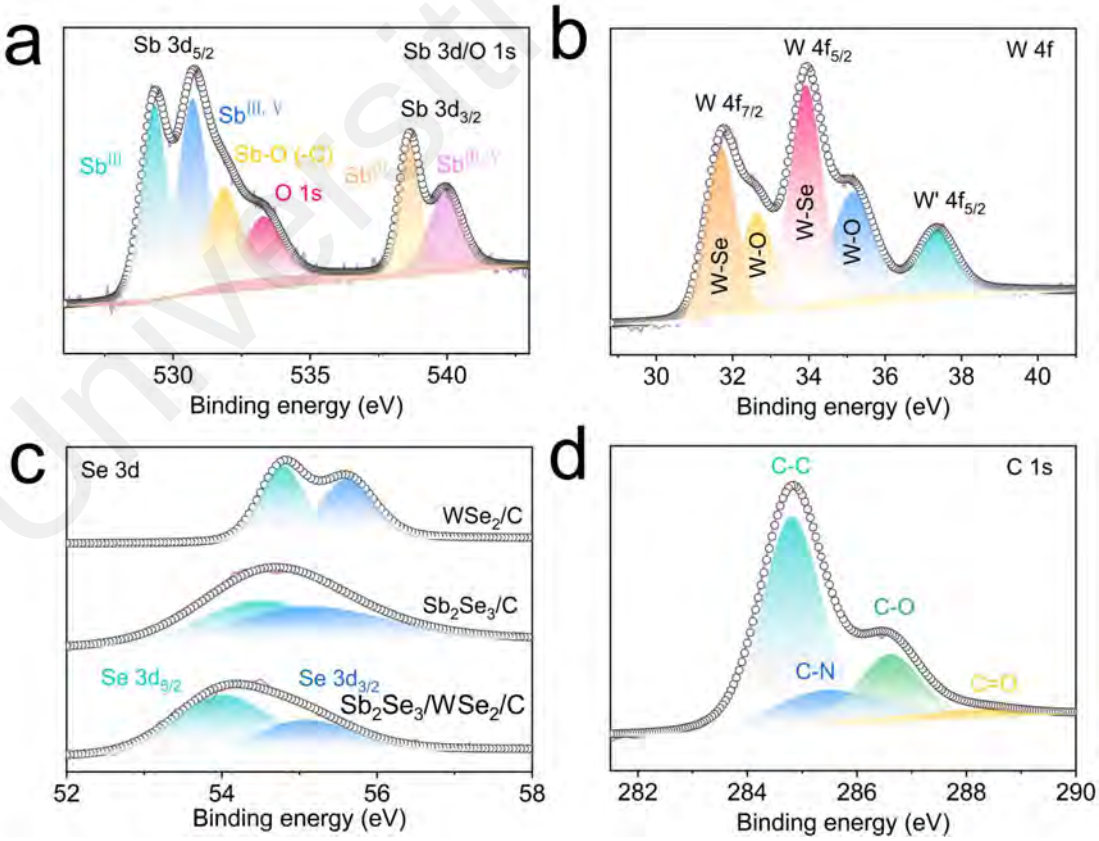

Figure 6.37: High-resolution XPS spectra Sb 3d/O 1s (a), W 4f (b), Se 3d (c), and C 1s (d).

6.3.3 Electrochemical Properties of Sb_2Se_3/WSe_2/C in SIBs

The Na^+ storage behaviors of the Sb_2Se_3/WSe_2/C-400/500/600 electrodes are evaluated by employing sodium metal as a counter electrode in an assembled 2032 coin-type half-cell. Firstly, as shown in Figure 6.38, the electrochemical processes in the initial three cycles are revealed by measuring the CV curves at 0.1 mV s^{-1}. During the first cathodic scan, all three samples exhibit a distinct broad peak near 0.5 V, representing the occurrence of the conversion reaction and the formation of the SEI. All three electrodes display overlapping curve profiles during subsequent scans (2^{nd} and 3^{rd}), representing excellent reversibility. However, by further comparison, the Sb_2Se_3/WSe_2/C-400 and Sb_2Se_3/WSe_2/C-500 electrodes deliver highly similar CV curves and three pairs of redox peaks located at 0.44/0.69 V, 0.93/1.50 V, and 1.63/2.04 V. Wherein, the redox peak located at 0.44/0.69 V can be attributed to the reversible alloying/dealloying process of Sb and Na_xSb. (Z. Liu et al., 2016) The two additional pairs of redox peaks located at 0.93/1.50 V and 1.63/2.04 V can be indexed to the reversible conversion from Sb_2Se_3 to Sb and Na_2Se. (Ihsan-Ul-Haq et al., 2021) As for the Sb_2Se_3/WSe_2/C-600 electrode, only one main pair of redox peaks located at 1.44/1.66 V appeares, representing only the reversible redox reaction from WSe_2 to W and Na_2Se. (Pei et al., 2023; S. Zhang et al., 2021)

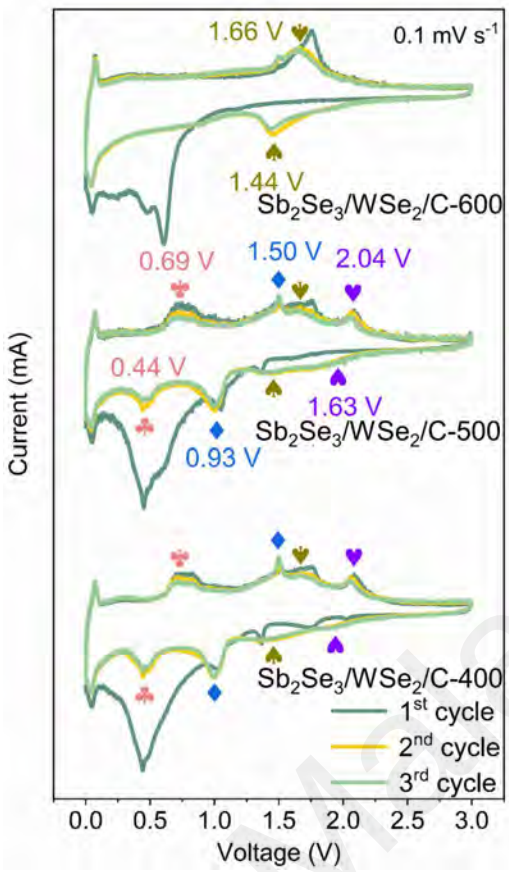

Figure 6.38: Electrochemical performance of Sb_2Se_3/WSe_2/C in SIBs: CV curves of Sb_2Se_3/WSe_2/C-400, Sb_2Se_3/WSe_2/C-500, and Sb_2Se_3/WSe_2/C-600 electrodes from 0.01 to 3.0 V at the scan rate of 0.1 mV s^{-1}.

Additionally, as shown in Figure 6.39, the short-cycling tests of the three electrodes at a current density of 2 A g^{-1} indicate that the Sb_2Se_3/WSe_2/C-500 electrode present the highest capacity output (553.7 mA h g^{-1} after 250 cycles). Notably, all three electrodes show different degrees of activation during the cycling process.

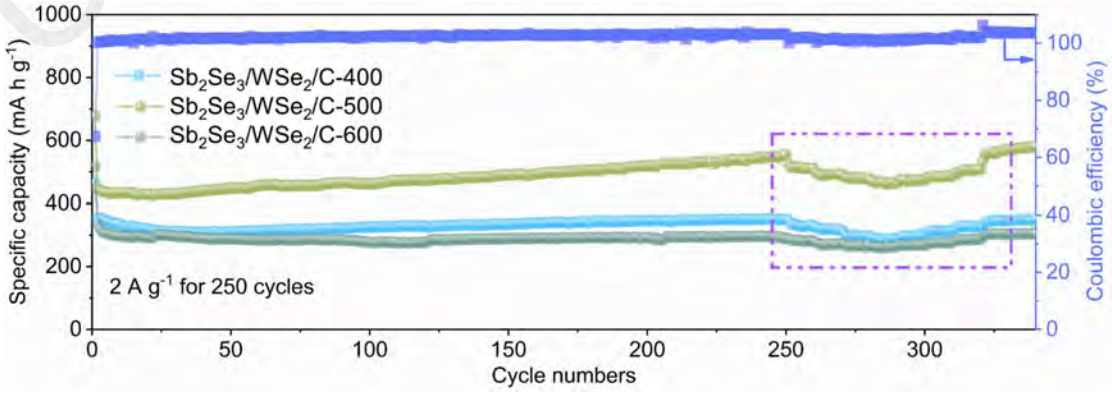

Figure 6.39: Short cycling performance of Sb_2Se_3/WSe_2/C-400, Sb_2Se_3/WSe_2/C-500, and Sb_2Se_3/WSe_2/C-600 electrodes at 2 A g^{-1} and the cycled rate capability.

To more accurately evaluate the rate capabilities of the prepared electrodes, we directly subjected the short-cycled electrodes to rate testing. After being tested at different current densities (2, 4, 6, 8, and 10 A g^{-1}), the Sb_2Se_3/WSe_2/C-500 electrode exhibits a significant specific capacity advantage while ensuring a stable rate capability at high current densities (Figure 6.40a). Further, the GCD curves of SbWSe/C/NF-500 electrode at different current densities show that the charge/discharge plateau remains unchanged with the increase of current density, and almost no apparent polarization occurs (Figure 6.40b).

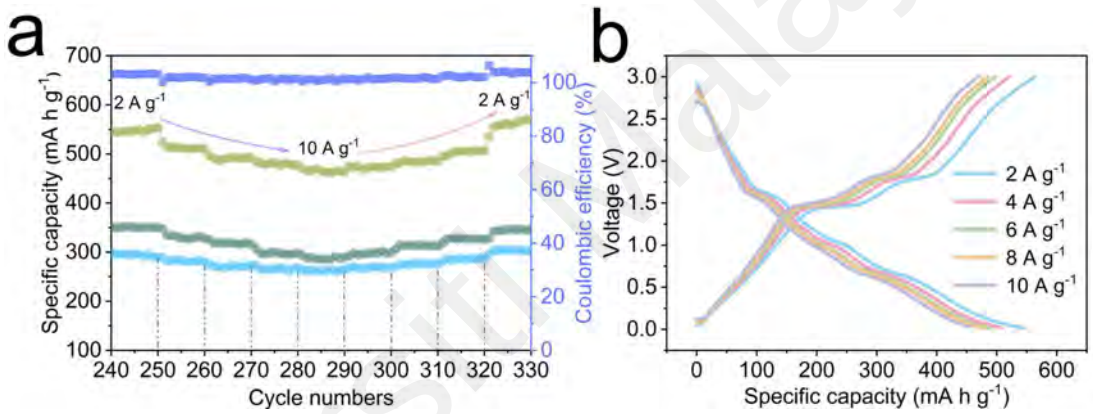

Figure 6.40: The cycled rate capability (a) of Sb_2Se_3/WSe_2/C-400, Sb_2Se_3/WSe_2/C-500, and Sb_2Se_3/WSe_2/C-600 electrodes. (b) Charge-discharge profiles of Sb_2Se_3/WSe_2/C-500 under different current densities.

To detect the long-term cycling ability of the prepared electrodes, the rapid charge/discharge tests are performed at a high current density of 10 A g^{-1}. The Sb_2Se_3/WSe_2/C-500 electrode remains a high-capacity retention of 344.56 mA h g^{-1} even after 4300 cycles, revealing its excellent cycling ability (Figure 6.41).

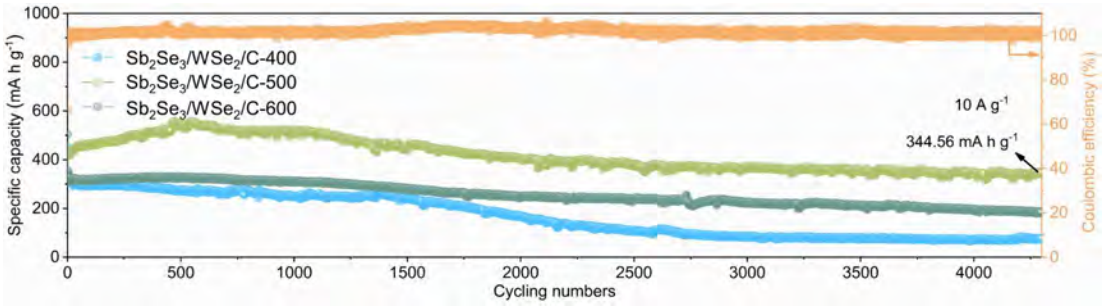

Figure 6.41: Long cycling performance comparison of Sb_2Se_3/WSe_2/C-400, Sb_2Se_3/WSe_2/C-500, and Sb_2Se_3/WSe_2/C-600 electrodes at the current density of 10 A g^{-1}.

Although the Sb_2Se_3/WSe_2/C-500 electrode exhibits excellent cycling stability, the stabilizing effect of the second carbon introduction (electrostatic spinning) on the electrode structure needs to be further verified. The physical photographs of the Sb_2Se_3/WSe_2/C-500 and Sb_2Se_3/WSe_2/MOF-C electrode side separators after 250 cycles (Figure 6.42a, d) illustrate that electrostatic spinning is effective in avoiding the detachment of the active material during the cycling process. Moreover, the TEM images of the above two electrodes after 250 cycles indicates that the Sb_2Se_3/WSe_2/C-500 electrode still has a stable morphology after undergoing cycling (Figure 6.42b, c), whereas the Sb_2Se_3/WSe_2/C electrode displays obvious dispersion (Figure 6.42e, f).

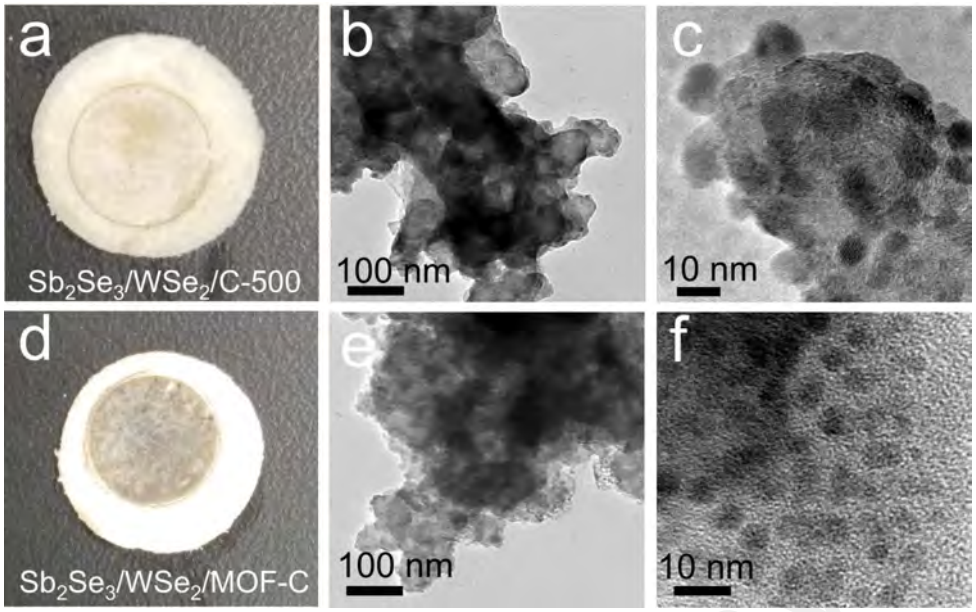

Figure 6.42: The physical photographs of the Sb_2Se_3/WSe_2/C-500 and Sb_2Se_3/WSe_2/MOF-C electrode side separators (a, d) after 250 cycles. The TEM images of the electrodes after 250 cycles: Sb_2Se_3/WSe_2/C-500 (b, c), Sb_2Se_3/WSe_2/MOF-C (e, f).

6.3.4 Density Functional Theory Calculations

DFT calculations are applied to investigate the mechanism of Sb_2Se_3/WSe_2/C heterogeneous structures in detail. The calculation models of the Sb_2Se_3/WSe_2/C, Sb_2Se_3/C, and WSe_2/C structures are shown in Figure 6.43.

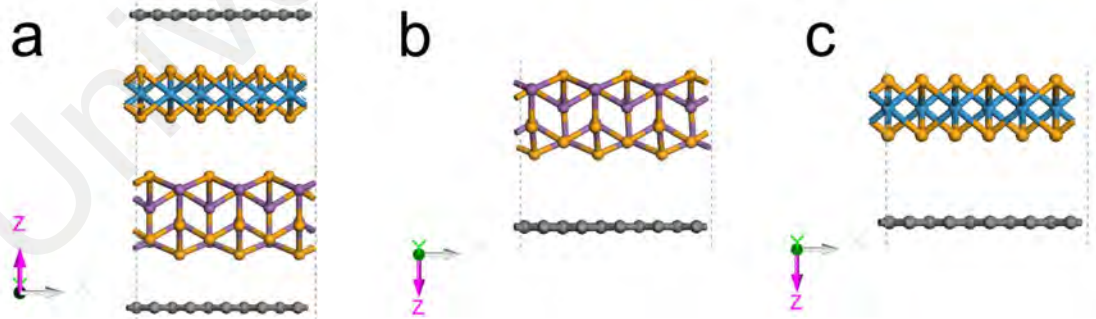

Figure 6.43: The calculation models regarding the Sb_2Se_3/WSe_2/C, Sb_2Se_3/C, and WSe_2/C structures.

The band structure calculation in Figure 6.44a reveals that Sb_2Se_3/WSe_2/C has no band gap (E_g) near the Fermi energy level. This suggests that the constructed heterostructure is strongly metallic, facilitating fast electron conduction. Contrastingly,

Sb_2Se_3/C and WSe_2/C exhibit weaker metallic properties with energy band gaps of 0.773 and 0.032 eV, respectively (Figure 6.44b, c).

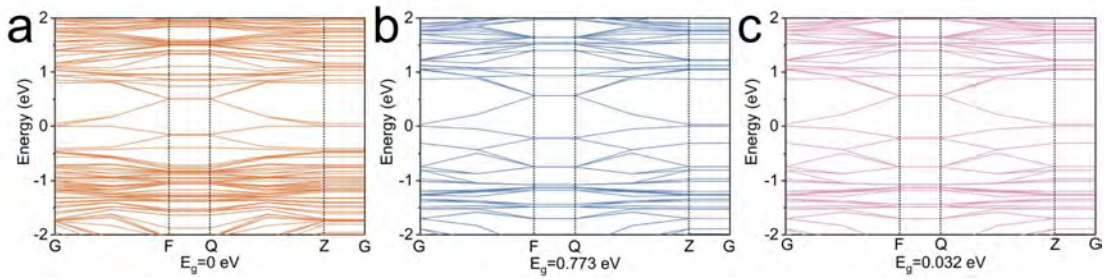

Figure 6.44: The calculated band gap for Sb_2Se_3/WSe_2/C heterostructure (a), Sb_2Se_3/C (b) and WSe_2/C (c).

Furthermore, DOS calculations of the prepared three samples reveal that Sb_2Se_3/WSe_2/C exhibits the most significant superposition peaks near the Fermi energy level, representing its high electronic conductivity, which is consistent with the band gap analysis (Figure 6.45).

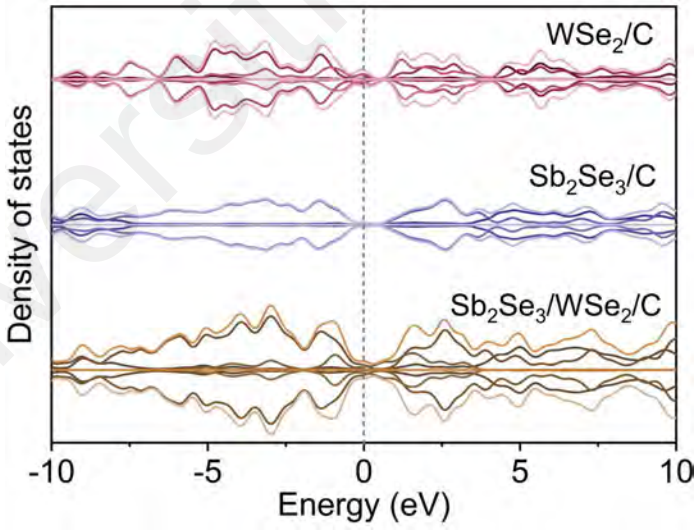

Figure 6.45: The density of states for Sb_2Se_3/WSe_2/C, Sb_2Se_3/C, and WSe_2/C.

The charge differential densities are used to evaluate the charge distribution of the Sb_2Se_3/WSe_2/C heterostructure (Figure 6.46a). From that, the green electron cloud represents charge accumulation, while the yellow electron cloud means charge disappearance. By comparing the charge distributions of Sb_2Se_3/C and WSe_2/C (Figure

6.46b, c), the $Sb_2Se_3/WSe_2/C$ heterostructure exhibits a significantly inhomogeneous charge distribution between the Sb_2Se_3 and WSe_2 phases. This represents the formation of a built-in electric field, which is conducive to promoting rapid interlayer Na^+ transport.

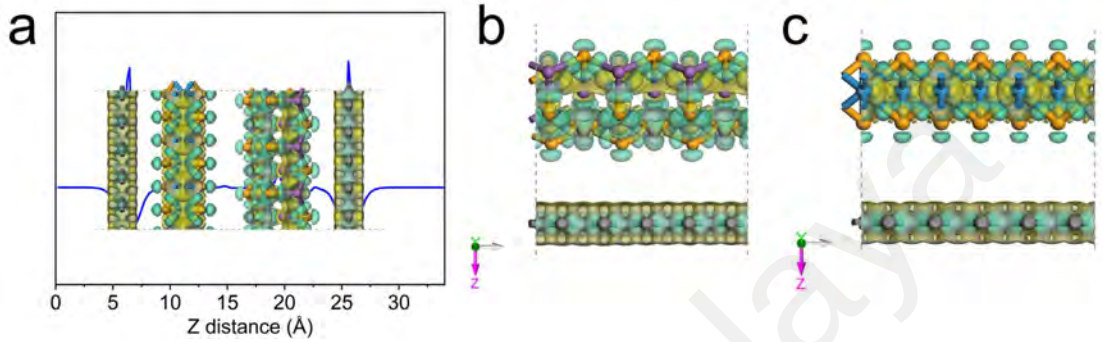

Figure 6.46: The charge distribution of the $Sb_2Se_3/WSe_2/C$ heterostructure (a), Sb_2Se_3/C (b), and WSe_2/C (c).

Further, Figure 6.47a explores the migration path of Na^+ at the $Sb_2Se_3/WSe_2/C$ heterogeneous interface. Accordingly, as shown in Figure 6.47b, the calculated Na^+ diffusion energy barrier in the $Sb_2Se_3/WSe_2/C$ heterostructure is 0.416 eV, which is much lower than Sb_2Se_3/C (0.615 eV) and WSe_2/C (1.197 eV).

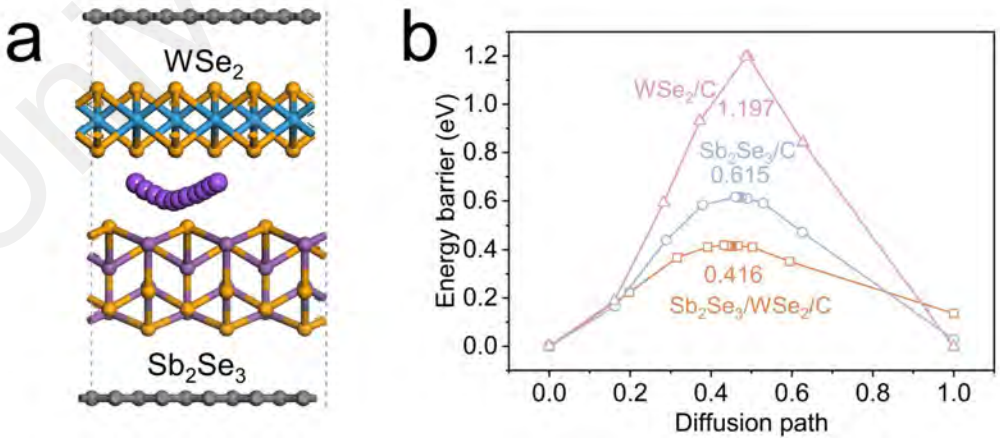

Figure 6.47: (a) The Na^+ migration path at the $Sb_2Se_3/WSe_2/C$ heterogeneous interface. (b) The Na^+ diffusion energy barrier curves in $Sb_2Se_3/WSe_2/C$, Sb_2Se_3/C, and WSe_2/C.

Figure 6.48 summarily demonstrates the electron and Na^+ transfer behaviors of

Sb_2Se_3/WSe_2 heterostructures with dual-carbon composites. On the one hand, the defect-rich amorphous carbon coating layer with excellent electrical conductivity can provide sufficient active sites to accept desolated Na^+. On the other hand, the built-in electric field provided by the constructed Sb_2Se_3/WSe_2 heterostructures can further promote the rapid Na^+ transfer in the interior of the active materials for the fast conversion and alloying process.

Figure 6.48: The schematic illustration of electron and Na^+ transfer behaviors in SbWSe heterostructures with dual-carbon composites.

6.3.5 Electrochemical Process Study of $Sb_2Se_3/WSe_2/C$ Electrode

The dual-carbon introduction strategy provides the strong capacity performance to the $Sb_2Se_3/WSe_2/C$ heterostructures. However, further evaluation of the electrochemical differences between $Sb_2Se_3/WSe_2/C$, its monomers (Sb_2Se_3/C and WSe_2/C), and the physical mixed $Sb_2Se_3/C\&WSe_2/C$ before electrostatic spinning is still needed to highlight the heterogeneous structure effect. From Figure 6.49a, $Sb_2Se_3/WSe_2/C$ electrode exhibits the specific capacity of 388.5 mA h g^{-1} after 250 cycles at 1 A g^{-1}, significantly better than Sb_2Se_3/C, WSe_2/C, and $Sb_2Se_3/C\&WSe_2/C$. Further, as the 5th GCD curves comparison in Figure 6.49b, SbWSe/C is demonstrated to possess a series of charging and discharging platforms in combination with Sb_2Se_3/C and WSe_2/C.

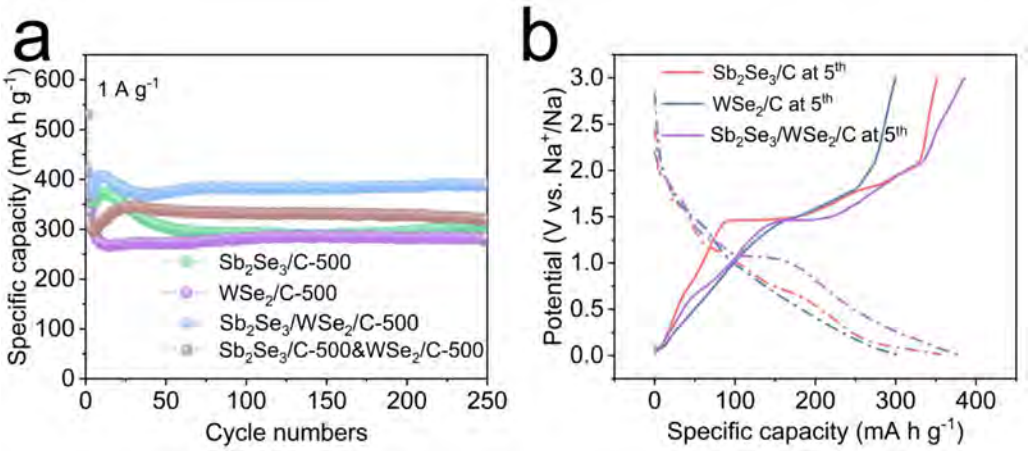

Figure 6.49: (a) Short cycling performance comparison of $Sb_2Se_3/WSe_2/C$, Sb_2Se_3/C, WSe_2/C, and the physical mixed $Sb_2Se_3/C\&WSe_2/C$ electrodes at 1 A g^{-1}. (b) GCD curves comparison of $Sb_2Se_3/WSe_2/C$, Sb_2Se_3/C, and WSe_2/C electrodes at 5th cycle.

To explore the charge/discharge response plateau of $Sb_2Se_3/WSe_2/C$ in more detail, the dQ/dV curves of $Sb_2Se_3/WSe_2/C$, WSe_2/C, and Sb_2Se_3/C for the initial three cycles are further plotted (Figure 6.50). By comparison, the blue peaks in Figure 6.50a are attributed to the reactions of Sb_2Se_3, representing the phase conversion and Na alloying process. Correspondingly, the red peak position implies the conversion reaction of WSe_2.

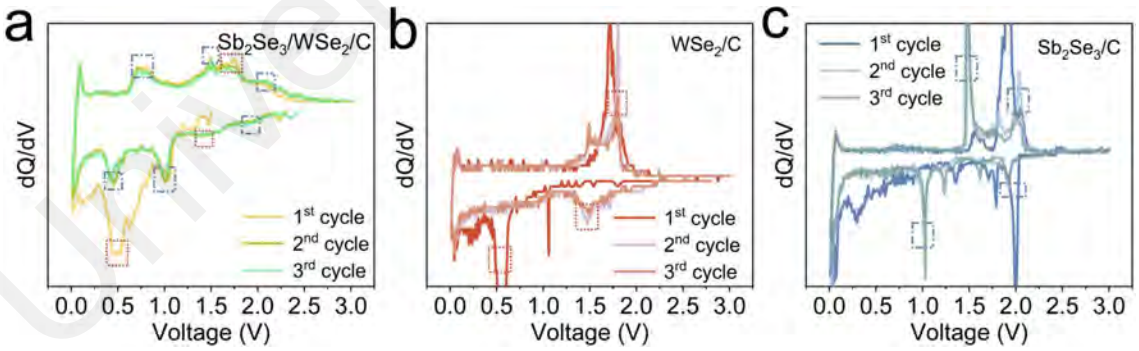

Figure 6.50: The dQ/dV profiles of $Sb_2Se_3/WSe_2/C$ (a), WSe_2/C (b), and Sb_2Se_3/C (c) electrodes (The first three cycles).

Supplementarily, Figure 6.51a and b present the initial three cycles of CV curves for WSe_2/C and Sb_2Se_3/C at 0.1 mV s^{-1}, respectively, which are consistent with the dQ/dV results. The dQ/dV curves of $Sb_2Se_3/WSe_2/C$ show the same redox reaction peaks as the

CV curves for Sb_2Se_3/WSe_2/C-500, indicating that the electrostatic spinning has no effect to the original reaction of Sb_2Se_3/WSe_2/C.

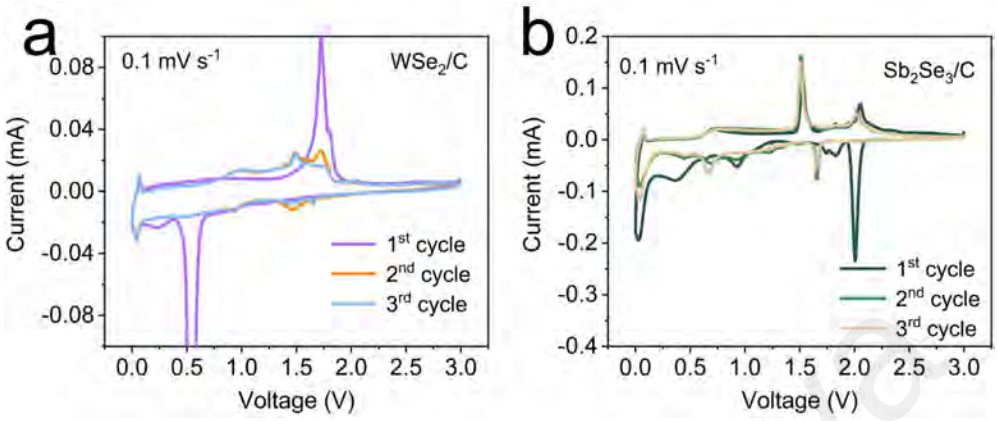

Figure 6.51: The initial three cycles of CV curves for WSe_2/C (a) and Sb_2Se_3/C (b) at 0.1 mV s^{-1}.

Subsequently, the GCD curves before and after cycling the Sb_2Se_3/WSe_2/C electrode in Figure 6.52 reveal the voltage platform changes as charging and discharging proceed, suggesting a similar activation process to Sb_2Se_3/WSe_2/C.

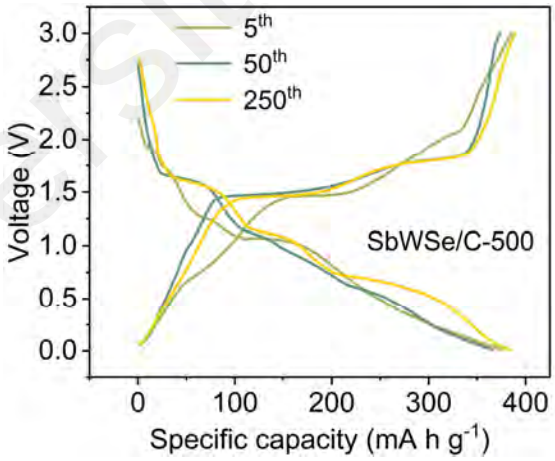

Figure 6.52: GCD curves (5th, 50th, and 250th) of Sb_2Se_3/WSe_2/C electrode.

To evaluate the evolution of each redox peak during the activation process more systematically, the dQ/dV curves of the three electrodes for the initial 20 cycles are investigated separately. Figure 6.53a-c exhibit the discharged dQ/dV curves of Sb_2Se_3/WSe_2/C, WSe_2/C, and Sb_2Se_3/C, respectively. Contrastingly, the evolution of the

different peak positions in Figure 6.53a covers the $Sb_2Se_3 + 6e^- \rightarrow 2Sb + 3Se^{2-}$, $WSe_2 + 4e^- \rightarrow W + 2Se^{2-}$, and $xNa^+ + Sb \rightarrow Na_xSb$ reactions. The corresponding reaction processes can also be found in WSe_2/C (Figure 6.53b) and Sb_2Se_3/C (Figure 6.53c) electrodes. The heterostructure introduces an inhomogeneous charge distribution, which lowers the Na_xSb alloying potential of SbWSe/C compared to Sb_2Se_3/C. In addition, the reaction in pre-cycled Sb_2Se_3/WSe_2/C electrode is mainly dominated by the conversion reaction of WSe_2 until the 10th cycle. After that the conversion reaction of Sb_2Se_3 gradually dominates.

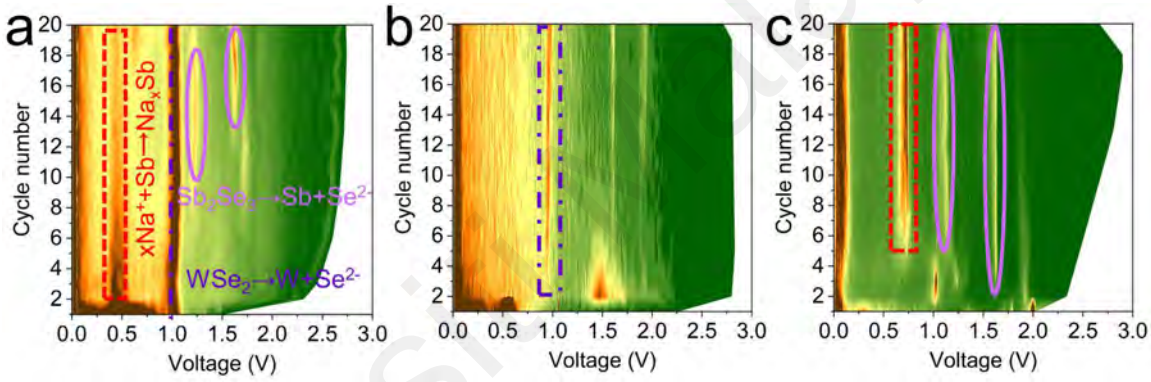

Figure 6.53: The dQ/dV cruves evolution of the Sb_2Se_3/WSe_2/C (a), WSe_2/C (b), and Sb_2Se_3/C (c) electrodes for the first 20 cycles: discharge process.

Correspondingly, Figure 6.54a-c reveals the charging dQ/dV curve evolution trend of Sb_2Se_3/WSe_2/C, WSe_2/C, and Sb_2Se_3/C electrodes, respectively. The evolutionary behavior in charging process at each stage is consistent with the discharge process, implying that the electrode has an excellent reversible conversion capability. Distinctively, the corresponding dealloying reaction peaks of Na_xSb are not found in the charging process of the Sb_2Se_3/C electrode, representing the poor dealloying ability, which further explains its poor electrochemical capability. The Sb_2Se_3/C electrode present an obvious Na_xSb dealloying peak during the charging process, which results

from the decreased dealloying barrier due to the built-in electric field in the heterostructure. The lower alloying potential and more obvious dealloying process in $Sb_2Se_3/WSe_2/C$ heterostructure can reduce the dead Na phenomenon and the electrolyte failure, ensuring a longer-term cycling capability.

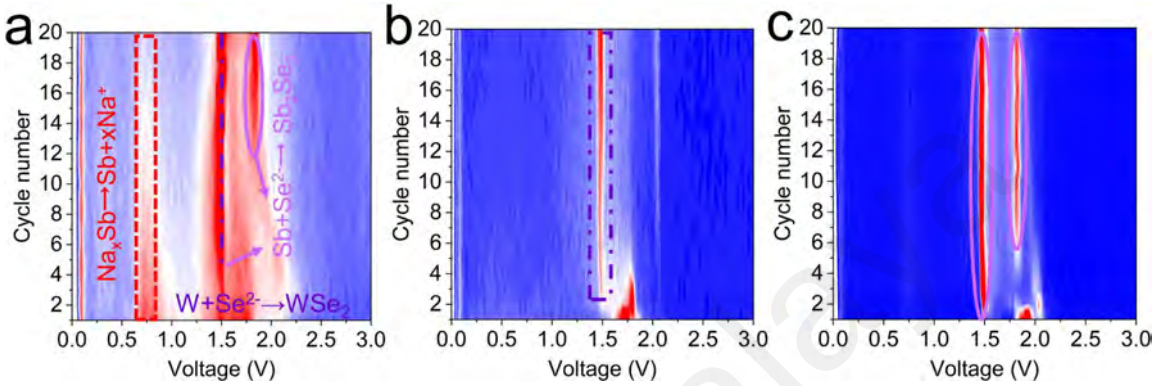

Figure 6.54: The dQ/dV cruves evolution of the $Sb_2Se_3/WSe_2/C$ (a), WSe_2/C (b), and Sb_2Se_3/C (c) electrodes for the first 20 cycles: charge process.

To further verify the difference between the dealloying evolution process of $Sb_2Se_3/WSe_2/C$ and Sb_2Se_3/C electrodes, HRTEM tests are performed for the electrodes after 5 cycles. As shown in Figure 6.55, the electrodes are selected for characterization in fully discharged, charged to 1 V, and fully charged states, respectively. As can be seen, the lattice spacing of 0.416 nm is monitored in both $Sb_2Se_3/WSe_2/C$ and Sb_2Se_3/C electrodes at the fully discharged state, which can be attributed to the (1 0 1) crystal plane of Na_xSb. Principally, the Sb dealloying process occurs at the charging potential of 0−1 V. Therefore, when charged to 1 V, the metallic Sb phase with a distinct lattice can be found in the Sb_2Se_3/C electrode, representing the successful dealloying process. In contrast, no crystalline Sb is observed at the Sb_2Se_3/C electrode, and an amorphous region appeared, which can be attributed to amorphous Sb or Na_xSb. When charged to 3 V, complete Sb_2Se_3 and WSe_2 phases are monitored in the $Sb_2Se_3/WSe_2/C$ electrode,

representing the reversible conversion reaction process. Additionally, some Sb_2Se_3 is still observed in the Sb_2Se_3/C electrode, suggesting that the same partially reversible conversion reaction exists.

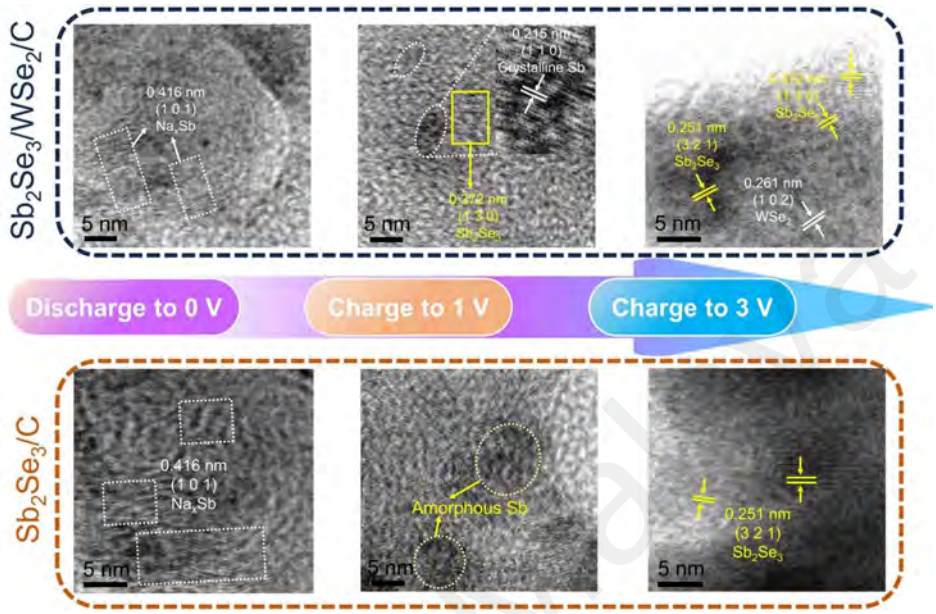

Figure 6.55: HRTEM diagrams of Sb_2Se_3/WSe_2/C and Sb_2Se_3/C electrodes at 5th cycle in different potential states (discharge to 0 V, charge to 1 V, and charge to 3 V).

6.3.6 Sodium Storage Kinetics Investigation

CV curves at different scan rates (0.5, 1, 2, and 5 mV s^{-1}) are employed to characterize the pseudocapacitance of the Sb_2Se_3/WSe_2/C-400/500/600 electrode. As shown in Figure 6.56a-c, six distinct evolutionary peaks (Peak 1−6) can be significantly observed with increasing scan rate.

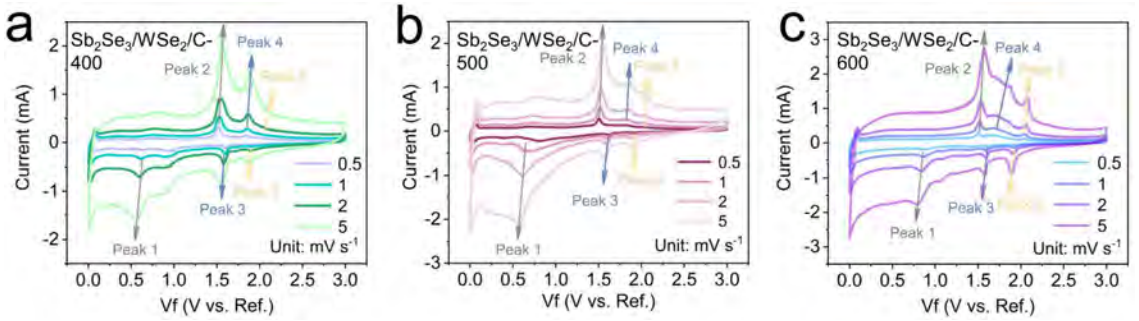

Figure 6.56. CV curves at different scan rates of Sb_2Se_3/WSe_2/C-400 (a), Sb_2Se_3/WSe_2/C-500 (b), and Sb_2Se_3/WSe_2/C-600 (c) electrodes in SIBs.

The electrochemical behavior (insertion behavior dominant or pseudocapacitive behavior dominant) during the electrode process is revealed by fitting the slope relationship between the individual peak currents and the scan rates. Fitting the individual peaks of Peak 1−6 (Figure 6.57a-c) reveals that all b values are close to 1, representing a significant pseudocapacitive behavior of the prepared $Sb_2Se_3/WSe_2/C$ electrodes. With more detailed comparisons, the $Sb_2Se_3/WSe_2/C$-500 electrode slope plot in Figure 6.57b exhibits a value closer to 1, revealing a stronger pseudocapacitance capability. The pseudocapacitive behavior has a dual mechanism: redox pseudocapacitance on the surface and intercalation pseudocapacitance in the bulk. The defect-rich amorphous carbon facilitates strong ion adsorption on the surface, reducing ion diffusion distances. The abundant inherent electric fields enable fast ion conduction pathways or interlayer diffusion in the bulk Sb_2Se_3/WSe_2 heterostructure.

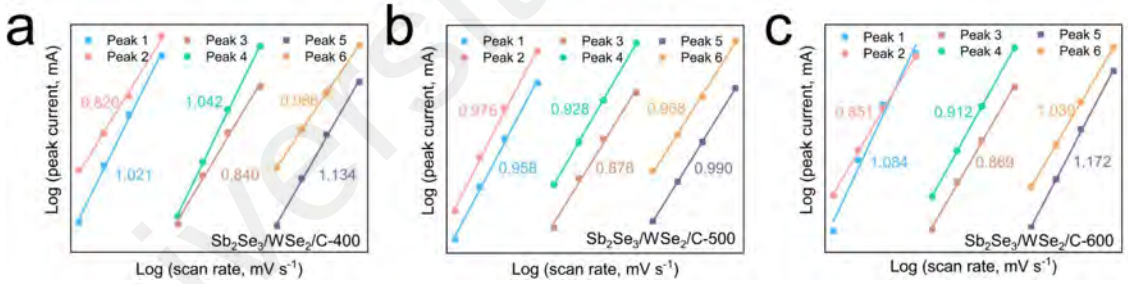

Figure 6.57: Linear diagrams of log (v) and log (i) corresponding to peak currents in different oxidation and reduction states of $Sb_2Se_3/WSe_2/C$-400 (a), $Sb_2Se_3/WSe_2/C$-500 (b), and $Sb_2Se_3/WSe_2/C$-600 (c) electrodes.

Additionally, the pseudocapacitance contributions of the three electrodes at different scan rates are calculated in Figure 6.58. Clearly, the $Sb_2Se_3/WSe_2/C$-500 electrode performed the most excellent among the three electrodes with the pseudocapacitance contributions of 79.4%, 82.1%, 86.2%, and 95.5% at 0.5, 1, 2, and 5 mV s^{-1} scan rates, respectively.

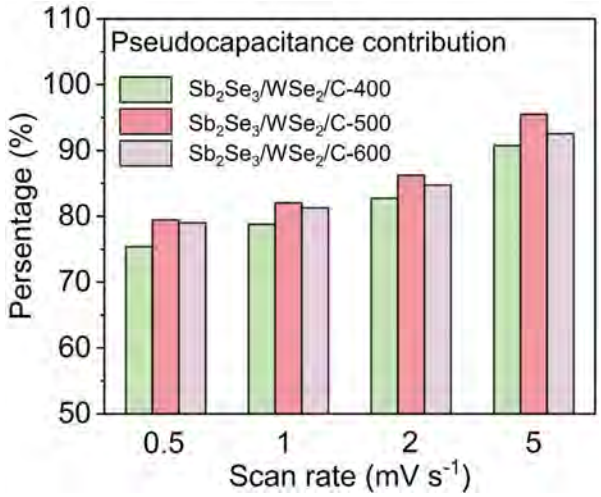

Figure 6.58: The capacitive contribution ratios of Sb_2Se_3/WSe_2/C-400, Sb_2Se_3/WSe_2/C-500, and Sb_2Se_3/WSe_2/C-600 electrodes at different scan rates.

The kinetic processes of the Sb_2Se_3/WSe_2/C-500 electrode are measured by employing EIS. As shown in the Nyquist curves of Figure 6.59a, the electrode after 5 cycles exhibits smaller semicircular diameters in the medium-high frequencies compared to the initial state, representing a smaller contact and charge-transfer resistance. Moreover, the solid-phase diffusion process of Na^+ in the active material is further evaluated by fitting the linear slope (D value) in the low-frequency region. Resultantly, the electrodes exhibited low D values after cycling, implying that the activation process could substantially promote the Na^+ diffusion within the electrodes (Figure 6.59b).

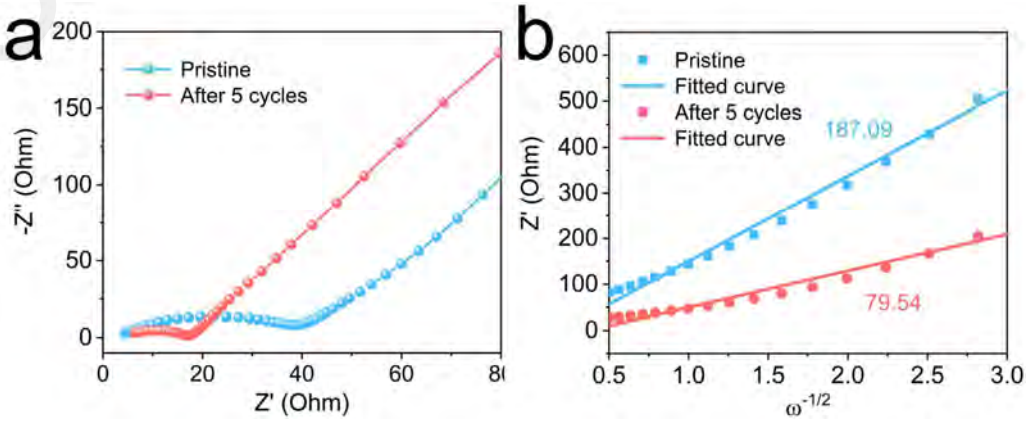

Figure 6.59: (a) Nyquist plots of Sb_2Se_3/WSe_2/C-500 electrode at pristine and 5th cycle. (b) Relationship between Z' and $\omega^{-1/2}$.

GITT is applied to further evaluate the Na^+ diffusion coefficients of the prepared $Sb_2Se_3/WSe_2/C$ heterostructures. Obviously, the $Sb_2Se_3/WSe_2/C$ electrode exhibits the highest $\log D_{Na^+}$ (10^{-13} and 10^{-10}) over the whole process (Figure 6.60), verifying that the built-in electric field generated by the heterogeneous structure can facilitate the rapid diffusion of Na^+ within the bulk phase.

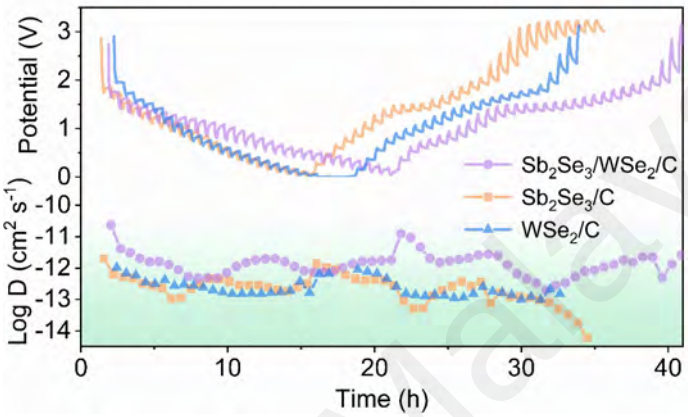

Figure 6.60: GITT and Na^+ diffusion coefficients of $Sb_2Se_3/WSe_2/C$, Sb_2Se_3/C, and WSe_2/C electrodes.

6.3.7 Electrochemical Properties of $Sb_2Se_3/WSe_2/C$ in SICs

For fully exploring the potential of $Sb_2Se_3/WSe_2/C$-500 electrodes in high-power output applications, hybrid SICs are assembled using AC as the cathode. Notably, both the corresponding cathode and anode need to be preactivated before assembling the SICs. The pretreatment voltage can be referred to the CV curve in Figure 6.61.

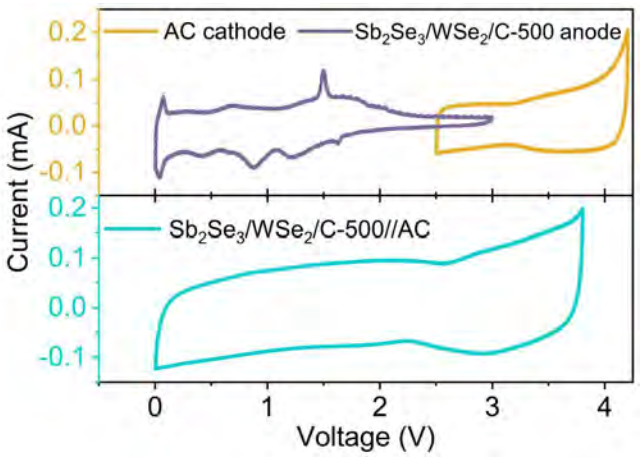

Figure 6.61: The cathode, anode, and overall CV profiles of the assembled SICs.

A reasonable voltage range is critical to the performance of SICs. CV tests in the voltage of 0−4 V, and 0−4.2 V show a sharp peak at high potentials when the voltage is higher than 3.8 V, which is due to the polarization (Figure 6.62a). In this case, 0−3.8 V is considered a reasonable operating voltage range. The CV curves of the assembled SICs tested at different scan rates over the voltage range of 0−3.8 V are presented in Figure 6.62b. The CV curves are no shape distortion with increasing scan rates, revealing the good reaction stability at large scan rates. In addition, the CV curves exhibit a rectangle-like shape, representing a storage mechanism that combines electrical double-layer and pseudocapacitance.

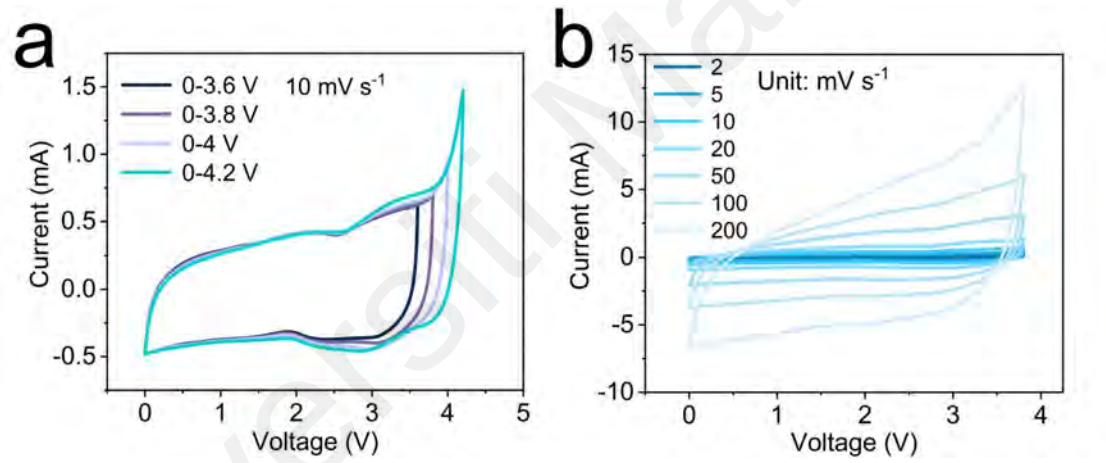

Figure 6.62: CV curves at different cutoff potentials (a) and different scan rates (b).

Rate capability tests in Figure 6.63a exhibit capacity outputs of 60.8, 56.3, 53.4, and 50.6 mA h g^{-1} (energy densities: 120.49, 108.99, 102.13, and 96.06 W h kg^{-1}) at current densities of 0.2, 0.5, 1, and 2 mA g^{-1} (power densities: 380, 950, 1900, 3800 W kg^{-1}), respectively. When the current density reverts from 2 back to 0.2 mA g^{-1}, the capacity is largely able to recover, implying excellent rate capability. Moreover, the GCD curves at different current densities exhibit a triangle-like shape, implying a hybrid storage mechanism, which is consistent with the CV analysis (Figure 5.63b).

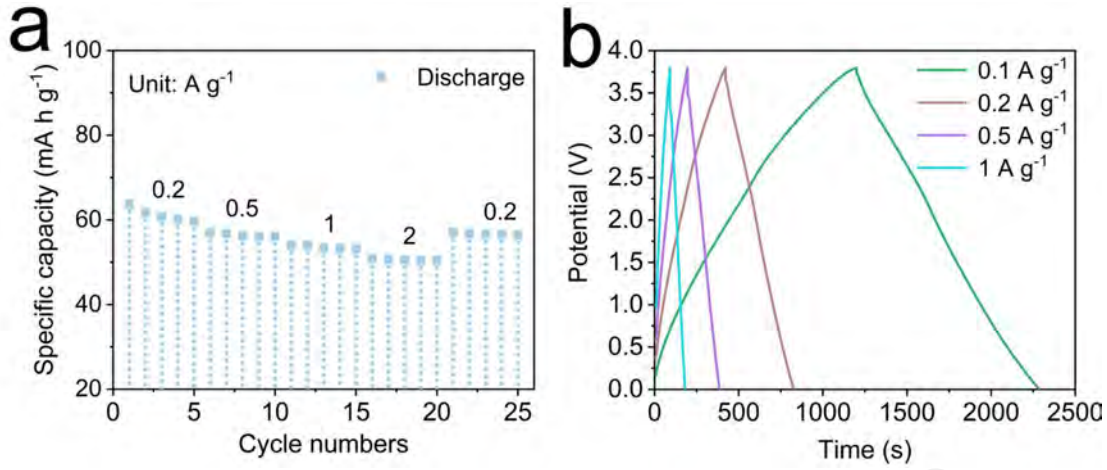

Figure 6.63: (a) Rate performance of Sb_2Se_3/WSe_2/C-500//AC. (b) GCD profiles of Sb_2Se_3/WSe_2/C-500//AC SIC at different current densities.

The long-cycling performance of the assembled SIC is tested at a power density of 3800 W kg^{-1}. As shown in Figure 6.64, a capacity retention of 80.83% is retained after 8000 cycles.

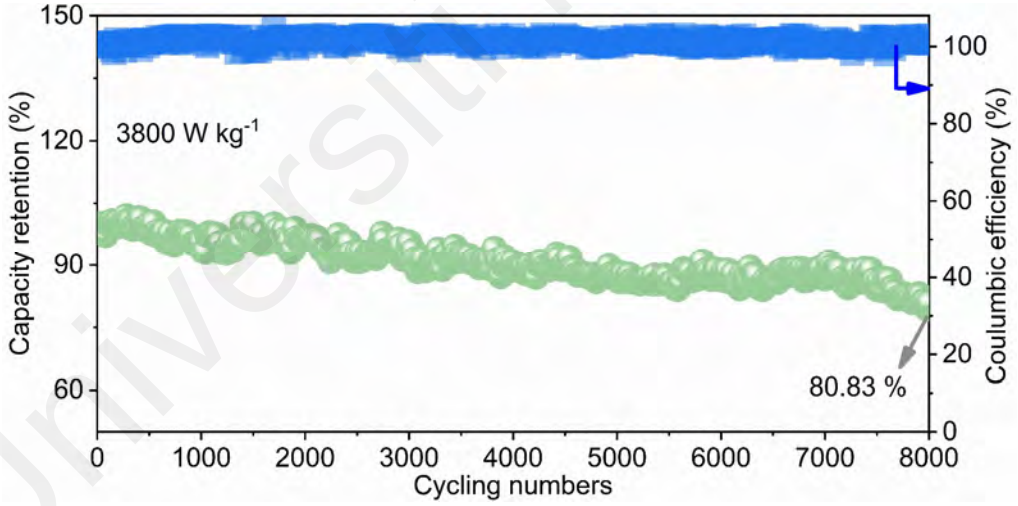

Figure 6.64: Cycling stability and coulombic efficiency of Sb_2Se_3/WSe_2/C-500//AC at 3800 W kg^{-1} for 8000 cycles.

6.4 Summary

A rational structural design for MSes can effectively promote the rapid transfer of Na^+ on the surface and bulk phase. In this chapter, we constructed Fe/Mo bimetallic MOF and Sb/W bimetallic MOF precursors with carbonization/selenization strategies to

obtain two composite structures ($MoSe_2$/FeSe/C and Sb_2Se_3/WSe_2/C), respectively. Notably, in addition to the constructed cationic heterostructures in the above two structures, the mixed-phase structure design was further carried out. Among them, the 1T/2H mixed-phase $MoSe_2$ was constructed in $MoSe_2$/FeSe/C, while the interlattice perfectly parallel heterogeneous mixed-phase design of Sb_2Se_3 and WSe_2 phases was realized in the Sb_2Se_3/WSe_2/C composite. The dissimilar heterostructure combined with the deep phase structure design facilitate the high-capacity Na^+ storage and fast transfer of Na^+ within the bulk phase. The specific conclusions are as follows:

1. Presently, a cation-coupled $MoSe_2$/FeSe/C heterostructure is developed by a facile two-step reaction and applied to sodium ion battery/capacitor (SIBs/SICs). Wherein, a unique edge mixed phase (1T/2H-$MoSe_2$) is generated under Fe induction. Additionally, the MOF-derived carbon guarantees structural stability and provides support for the rapid adsorption and transport of Na^+ on the surface and bulk. Significantly, DFT calculations verify that the constructed $MoSe_2$/FeSe heterogeneous interface has a strong metallic property, which can facilitate the rapid transfer of electrons and ions within the bulk phase. Resultantly, the prepared $MoSe_2$/FeSe/C can deliver a high specific capacity of 597.2 mA h g^{-1} (after 1000 cycles) at a current density of 2 A g^{-1} when applied as the anode of SIBs. Impressively, 3000 cycles can be stabilized even at a high current density of 10 A g^{-1}. When applied to SICs anodes, a capacity retention of 80.4% can be achieved at 2 A g^{-1} after 8000 cycles. The strategy of combining cation-coupled induced phase transitions with heterostructure design can serve as a reference for exploring the potential of TMSe in high-power energy storage devices.

2. Sb/W-hybridization precursor is synthesized by one-step reaction, followed by electrostatic spinning strategy to achieve a localized domain-limiting effect. Finally, the carbon mediated $Sb_2Se_3/WSe_2/C$ heterostructure are obtained after carbonization/selenization process. Physical characterization and theoretical calculations reveal that the $Sb_2Se_3/WSe_2/C$-500 has a heterogeneous structure and abundant edge carbon defects, facilitating rapid Na^+ transfer from exterior to interior. Furthermore, compared with the Sb_2Se_3/C monomer, the $Sb_2Se_3/WSe_2/C$ heterostructure shows a significant dealloying reaction at high current densities, enhancing capacity utilization. Resultantly, the Na half-cell with $Sb_2Se_3/WSe_2/C$-500 electrode demonstrates excellent rate capability and a high specific capacity of 553.7 mA h g^{-1} after 250 cycles at 2 A g^{-1}. Meanwhile, the assembled SIC exhibits 80.83% capacity retention after 8000 cycles at 3800 W kg^{-1}. The structure design strategy of dissimilar heterostructures with dual-carbon introduction provides a reference for developing high-power anodes.

CHAPTER 7: CONCLUSION AND SUGGESTIONS FOR FURTHER WORK

7.1 Conclusion

Overall, the thesis employs the microstructural integration of bimetallic selenides to construct analogous cationic heterostructures, analogous anionic heterostructures, and dissimilar heterostructures, respectively. A series of characterizations, supported by theoretical calculations, clearly reveal the structural superiority of these heterostructures compared to unmodified monometallic selenides. Firstly, analogous cationic heterostructures ($MoWSe_2$/C and $MoWSe_2/WO_3$/C) based on Mo and W bimetallic MOF, Se and MOF-derived carbon were synthesized. Secondly, analogous anionic heterostructures ($WSSe_2$/C and VSSe/C) were synthesized based on WS_3 and VS_4 polysulfides, Se, monosaccharide-derived and polymer-derived (PPy and PAN) carbon. Thirdly, dissimilar cationic heterostructures (abbreviated as $MoSe_2$/FeSe/C and Sb_2Se_3/WSe_2/C) were prepared based on Mo and Fe bimetallic MOF, Sb and W bimetallic MOF, Se, and MOF-derived carbon. Fourthly, the physical and structural properties (morphology, crystal structure, thermal stability and surface chemical state) of the synthesized composites were characterized using advanced analytical techniques and DFT simulations. Fifthly, the electrochemical performance (CV, GCD, dQ/dV, pseudocapacitance behavior, energy and power density) of the synthesized composites were investigated as anodes in SIBs and SICs. The specific findings are as follows:

1. The $MoWSe_2$/C electrode prepared with a MOF template achieves both

compositional optimizations through a uniform elemental distribution (Mo, W, and C) and microstructural optimization by creating rich large-angle $MoWSe_2$ heterostructures within the bulk phase. Benefitting from the built-in electric field formed by the heterostructures, the stronger metallic properties promote fast carrier transport. Additionally, the analysis of the $MoWSe_2$/C electrode in both ester-based and ether-based electrolytes indicated that: i) by virtue of the high LUMO energy level, DME electrolyte can avoid the electrolyte failure caused by the acceptance of free electrons; ii) DME electrolyte is more prone to form a stable and porous SEI layer to promote the rapid transfer of Na^+; iii) DME electrolyte can effectively avoid the electrode structure fragmentation and Na dendritic growth. By combining the advanced structural design with the optimized choice of electrolyte, the prepared $MoWSe_2$/C electrode exhibits excellent power density and cycling stability in sodium ion devices. When applied to SIBs, the $MoWSe_2$/C electrode achieves 94% capacity retention after 2000 cycles at a current density of 10 A g^{-1}. In assembled SICs, the $MoWSe_2$/C electrode similarly undergoes more than 11,000 cycles (capacity retention: ~80%) at a power density of 3800 W kg^{-1}. These promising results are intended to encourage development strategies that combine electrode structural optimization and electrolyte optimization, which is expected to produce richer research results in the era of fast energy storage.

2. The $MoWSe_2/WO_3$/C composite exhibited a high specific capacity of 384.3 mA h g^{-1} at 10 A g^{-1} in SIBs. The assembled SICs delivered excellent energy densities (81.86 and 72.83 Wh kg^{-1}) at the power densities of 190 and 3800 W kg^{-1}. In addition, the excellent electrochemical performance can be attributed to the

following aspects: i) the rational three-dimensional petal-core structure design provided structural stability in a large scale range; ii) the MOF structure determines the uniform carbon distribution of the composite products, which improved the overall electron conduction performance; iii) the pseudocapacitive surface behavior due to the large specific surface area derived from MOF promoted the rapid adsorption of Na^+; iv) the heterogeneous interface between $MoSe_2$, WSe_2 and WO_3 provide an enlarged layer spacing for Na^+ transport; v) the metallic property of $MoWSe_2/WO_3/C$ enhanced the electron conduction efficiency. The electrochemical behaviors of the initial and after activation were probed by ex-situ XRD, TEM, and XPS, revealing different reaction states during the cycling process. The unique heterostructure design and the reaction investigation of the electrode reactions can provide a reference for developing MSes anodes.

3. A simple method is presented to fabricate carbon-encapsulated $WSSe_2$ nanostructured hybrids. From that, 1 g ribose as the optimal addition amount in the preparation of $WSSe_2/C$ electrodes were identified. Benefiting from the built-in electric field generated by the double anions (S^{2-} and Se^{2-}) and the carbon encapsulation strategy, the enlarged interlayer space and synergistic internal/external ion-transport structure of the $WSSe_2/C$-1 electrodes provide excellent specific capacity and rate performance as well as a long-cycle life for Na^+ storage. The $WSSe_2/C$-1 electrode exhibits a high specific capacity of 715.3 mA h g^{-1} after 200 cycles at the current density of 1 A g^{-1} in SIBs, which is substantially ahead of the unmodified WSe_2/C-1 electrode. Similarly, the assembled SIC maintained over 13,000 ultra-long cycles at a high-power density of 3,800 W kg^{-1},

demonstrating its reliability and practicability. This work presents a promising strategy of carbon encapsulation combined with anionic construction of built-in electric fields for tungsten-based materials, which could apply to large-scale and high-power-density sodium-ion devices for energy storage systems.

4. Targeting the structural design of transition metal polysulfides, representative VS_4 samples were selected and a simple one-step strategy of anionic heterogenization with surface carbon coating was implemented. The obtained VSSe/C samples successfully achieved an extended S-Se interlayer distance. The built-in unbalanced electric field in the heterogeneous structure produced low free energy and efficient ion adsorption. Under the dual effect of anionic heterostructure and carbon coating, the resulting VSSe/C structure achieved efficient electron conduction and enhanced pseudocapacitance contribution. Resonantly, a high specific capacity of 553.2 mA h g^{-1} after 1000 cycles at 10 A g^{-1} was successfully achieved in the SIBs, which was much higher than the unmodified VS_4 electrode. Similarly, in SICs, 96.6% energy density retention is maintained even after 2000 cycles at a power density of 3800 W kg^{-1}. This work provides a perspective on anionic heterogeneous structure engineering for transition metal polysulfides toward the effective design of electrodes to boost advanced batteries.
5. The $MoSe_2$/FeSe/C heterostructure was designed by constructing a bimetallic MOF. In the preparation process, a hybrid phase of 1T/2H-$MoSe_2$ with an edge effect is formed, induced by cation. DFT calculations indicated that the abundant $MoSe_2$/FeSe heterogeneous interface has strong metallic properties, which can provide support for the fast electron and ion transport within the bulk phase.

Moreover, the highly conductive 1T-$MoSe_2$ at the edges becomes a key link for charge exchange between the internal 2H-$MoSe_2$ and amorphous carbon. Meanwhile, the stable internal 2H-$MoSe_2$ contributes to the improvement of the overall structural stability. Resonantly, the $MoSe_2$/FeSe/C electrode achieves a high reversible specific capacity of 597.2 mA h g^{-1} at a current density of 2 A g^{-1}, which is substantially higher than that of $MoSe_2$/C and FeSe/C monomers. A capacity retention (336.5 mA h g^{-1}) was still achieved after 3000 cycles at a high current density of 10 A g^{-1}. In the assembled SICs, the capacity retention of 80.4% was still achieved after 8000 cycles at a current density of 2 A g^{-1}, demonstrating excellent cycling performance. This work provides perspectives on the design of highly conductive anode materials through cations-coupled structural design and induced phase transitions.

6. Sb_2Se_3/WSe_2/C heterostructures, featuring alloying/conversion mechanisms, are prepared using a hybridization strategy. Additionally, the dual-carbon Sb_2Se_3/WSe_2/C samples are obtained through an electrospinning technique. By exploring different carbonization temperatures combined with physical characterization, the obtained Sb_2Se_3/WSe_2/C-500 exhibits abundant edge defect sites, which are favorable for the rapid adsorption of Na^+. Remarkably, the obtained Sb_2Se_3/WSe_2/C-500 electrode displays an obvious dealloying reaction different from the Sb_2Se_3/C electrode during the charging process, which is conducive to significantly improving the capacity exertion. With the dual-carbon introduction and bulk phase heterostructure, the obtained Sb_2Se_3/WSe_2/C-500 electrode is able to exert a specific capacity of 344.56 mA h g^{-1} in SIBs after 4300 cycles (at a high

current density of 10 A g^{-1}), demonstrating superior structural stability and excellent power capability. In the assembled SICs, the Sb_2Se_3/WSe_2/C-500 electrode similarly undergoes more than 8000 cycles (capacity retention: ~80.83 %) at a high-power density of 3800 W kg^{-1}. These promising results are expected to provide a reference for the structural design of high-power alloy/conversion-based anode materials.

Consequently, through different heterostructure design strategies we found that analogous anionic heterostructures can exert higher specific capacity at high current densities, but have poor cycling stability (around 1000 cycles). Comparatively, the dissimilar heterostructure design provides a more stable cycle life (higher than 3,000 cycles), but with a lower specific capacity. Finally, the analogous cationic heterostructure design can provide moderate specific capacity and long cycling ability.

7.2 Suggestions for Further Work

In this thesis, from the perspective of microstructural modification of electrodes, the built-in electric field is constructed mainly through heterostructure design, which in turn promotes high-capacity Na^+ storage and fast transport within the bulk phase. This thesis discusses constructing three types of heterostructures: analogous cationic heterostructures, analogous anionic heterostructures, and dissimilar heterostructures. However, due to the diversity of MSes, the heterostructure construction process for different species still needs to be explored in greater depth. It should be noted that whichever heterostructure is constructed, the degree of dispersion between multiple phases should be ensured as much as possible, which in turn creates a sufficiently rich heterogeneous interface. In addition, three or more synthesis schemes for high-entropy

heterostructures can be considered in future work. Specific recommendations are set out below.

First, for the construction of analogous cationic heterostructures, future work should start from MSes with similar crystal structures to achieve as much controllability of the heterogeneous angle between the two phases during the synthesis process. Second, for analogous anionic heterostructures, future work should shorten the preparation process and accomplish controlled S-atom substitution during the synthesis of polysulfides whenever possible. Third, for the construction of dissimilar heterostructures, only heterogeneous combinations of MSes with large differences in crystal structures are discussed in this thesis. However, combinations of different types of sulfides and selenides or even oxides should also be further explored in future work. Finally, researchers should pay attention to the additional effects brought by heterostructures (similar to those discussed in Chapter 6) and fully reveal their triggering processes in future developments.

Meanwhile, the promotion of carbon introduction on electrode conductivity and fast reaction kinetics is verified by MOF-derived carbon homogeneous distribution, carbon loading, and carbon encapsulation strategies. In future work, researchers should carry out multifaceted carbon modification strategies (e.g., dual-carbon introduction, as mentioned in this thesis) while ensuring the homogeneity of carbon distribution. It is worth mentioning that through the diversity of MOF derivatization strategies, the effect of MOF precursors with different morphologies on the electrochemical properties of the

final products should be additionally explored in future work under the premise of guaranteeing a suitable degree of carbon introduction.

The above strategies are well recognized as the broad strategies that can effectively enhance the electrochemical performance of MSes anodes. However, there are still many challenges that need to be improved in the process of carbon composite. Therefore, the necessary directions for improvement need to be noted. Firstly, developing more efficient and scalable synthesis techniques for carbon composite materials will be crucial. This includes improving methods for achieving uniform carbon distribution and optimizing the thickness of carbon coatings. Secondly, future research should focus on designing synergistic composites that combine the advantages of carbon loading, encapsulation, and homogenization. This could involve multi-step fabrication processes to create hierarchical structures with enhanced electrochemical performance. Thirdly, the development of environmentally friendly and cost-effective synthesis methods will be essential for the large-scale application of carbon-modified metal selenide anodes in commercial SIBs. Fourthly, investigating the compatibility of these carbon-modified anodes with advanced electrolytes will be important to ensure stable SEI formation and long-term cycling stability.

REFERENCES

Agoro, M. A., & Meyer, E. L. (2022). FeS/FeS_2 nanoscale structures synthesized in one step from Fe (ll) dithiocarbamate complexes as a single source precursor. *Frontiers in Chemistry*, *10*, 1035594.

Ali, Z., Asif, M., Huang, X., Tang, T., & Hou, Y. (2018). Hierarchically porous Fe_2CoSe_4 binary-metal selenide for extraordinary rate performance and durable anode of sodium-ion batteries. *Advanced Materials*, *30*(36), 1802745.

Ba, D., Gui, Q., Liu, W., Wang, Z., Li, Y., & Liu, J. (2022). Robust cathode-ether electrolyte interphase on interfacial redox assembled fluorophosphate enabling high-rate and ultrastable sodium ion full cells. *Nano Energy*, *94*, 106918.

Bao, K., Mao, W., Liu, G., Ye, L., Xie, H., Ji, S., Wang, D., Chen, C., & Li, Y. (2017). Preparation and electrochemical characterization of ultrathin WO_{3-x}/C nanosheets as anode materials in lithium ion batteries. *Nano Research*, *10*(6), 1903–1911.

Cai, C., Chen, Y., Hu, P., Zhu, T., Li, X., Yu, Q., Zhou, L., Yang, X., & Mai, L. (2022). Regulating the interlayer spacings of hard carbon nanofibers enables enhanced pore filling sodium storage. *Small*, *18*(6), 2105303.

Cai, M., Zhang, H., Zhang, Y., Xiao, B., Wang, L., Li, M., Wu, Y., Sa, B., Liao, H., Zhang, L., Chen, S., Peng, D. L., Wang, M. S., & Zhang, Q. (2022). Boosting the potassium-ion storage performance enabled by engineering of hierarchical MoSSe nanosheets modified with carbon on porous carbon sphere. *Science Bulletin*, *67*(9), 933–945.

Cai, P., Zou, K., Deng, X., Wang, B., Zheng, M., Li, L., Hou, H., Zou, G., & Ji, X. (2021). Comprehensive understanding of sodium-ion capacitors: definition, mechanisms, configurations, materials, key technologies, and future developments. *Advanced Energy Materials*, *11*(16), 2003804.

Cao, J., Wang, L., Li, D., Yuan, Z., Xu, H., Li, J., Chen, R., Shulga, V., Shen, G., & Han, W. (2021). $Ti_3C_2T_x$ MXene conductive layers supported bio-derived $Fe_{x-1}Se_x$/MXene/carbonaceous nanoribbons for high-performance half/full sodium-ion and potassium-ion batteries. *Advanced Materials*, *33*(34), 2101535.

Cao, L., Luo, B., Xu, B., Zhang, J., Wang, C., Xiao, Z., Li, S., Li, Y., Zhang, B., Zou, G., Hou, H., Ou, X., & Ji, X. (2021). Stabilizing intermediate phases via efficient entrapment effects of layered VS_4/SnS@C heterostructure for ultralong lifespan potassium-ion batteries. *Advanced Functional Materials*, *31*(36), 2103802.

Cao, Y., Huang, S., Peng, Z., Yao, F., Li, X., Liu, Y., Huang, H., & Wu, M. (2021).

Phase control of ultrafine FeSe nanocrystals in a N-doped carbon matrix for highly efficient and stable oxygen reduction reaction. *Journal of Materials Chemistry A*, *9*(6), 3464–3471.

Chandel, S., Wang, C., Singh, S. P., Wang, N., & Rai, A. K. (2022). Significant enhancement in the electrochemical performances of a nanostructured sodium titanate anode by molybdenum doping for applications as sodium-ion batteries. *ACS Applied Nano Materials*, *5*(12), 18591–18602.

Chen, G., Yan, L., Luo, H., & Guo, S. (2016). Nanoscale engineering of heterostructured anode materials for boosting lithium-ion storage. *Advanced Materials*, *28*(35), 7580–7602.

Chen, K., Zhang, W., Xue, L., Chen, W., Xiang, X., Wan, M., & Huang, Y. (2017). Mechanism of capacity fade in sodium storage and the strategies of improvement for FeS_2 anode. *ACS Applied Materials & Interfaces*, *9*(2), 1536–1541.

Chen, L. F., Lu, Y., Yu, L., & Lou, X. W. (2017). Designed formation of hollow particle-based nitrogen-doped carbon nanofibers for high-performance supercapacitors. *Energy and Environmental Science*, *10*(8), 1777–1783.

Chen, L., Feng, H., Zhang, R., Wang, S., Zhang, X., Wei, Z., Zhu, Y., Gu, M., & Zhao, C. (2020). Phase-controlled synthesis of 2H/3R-$MoSe_2$ nanosheets on P-doped carbon for synergistic hydrogen evolution. *ACS Applied Nano Materials*, *3*(7), 6516–6523.

Chen, S., Liang, L., Li, Y., Wang, D., Lu, J., Zhan, X., Hou, Y., Zhang, Q., & Lu, J. (2023). Brain capillary-inspired self-assembled covalent organic framework membrane for sodium–sulfur battery separator. *Advanced Energy Materials*, *13*(11), 2204334.

Chen, Yaopeng, Yang, Q., Wu, P., Xu, T., Wang, J., & Li, Y. (2021). Metal-complex-assisted synthesis of SnSe nanorods for lithium-ion-battery anodes. *ACS Applied Nano Materials*, *4*(12), 13010–13017.

Chen, Yuncai, Woo, H. J., Rizwan, M., Yahya, R. B., Cui, D., Luo, D., Chen, L., Arof, A. K. M., & Wang, F. (2019). Nanoscale morphology control of Na-rich prussian blue cathode materials for sodium ion batteries with good thermal stability. *ACS Applied Energy Materials*, *2*(12), 8570–8579.

Chen, Z., Wang, T., Zhang, M., & Cao, G. (2017). A phase-separation route to synthesize porous CNTs with excellent stability for Na^+ storage. *Small*, *13*(22), 1604045.

Cheng, Q., Deng, Q., Zhong, W., Tan, T., Liu, X., Chen, C., Hu, J., Lin, Z., Huang, K., & Yang, C. (2023). Criticality of solid electrolyte interphase in achieving high

performance of sodium-ion batteries. *Chemical Engineering Journal*, *457*, 141097.

Chiang, C.-H., Yang, Y.-C., Lin, J.-W., Lin, Y.-C., Chen, P.-T., Dong, C.-L., Lin, H.-M., Chan, K. M., Kao, Y.-T., & Suenaga, K. (2022). Bifunctional monolayer WSe_2/graphene self-stitching heterojunction microreactors for efficient overall water splitting in neutral medium. *ACS Nano*, *16*(11), 18274–18283.

Chong, S., Wei, X., Wu, Y., Sun, L., Shu, C., Lu, Q., Hu, Y., Cao, G., & Huang, W. (2021). Expanded $MoSe_2$ nanosheets vertically bonded on reduced graphene oxide for sodium and potassium-ion storage. *ACS Applied Materials and Interfaces*, *13*(11), 13158–13169.

Chong, S., Yuan, L., Zhou, Q., Wang, Y., Qiao, S., Li, T., Ma, M., Yuan, B., & Liu, Z. (2023). Bismuth telluride nanoplates hierarchically confined by graphene and N-doped C as conversion-alloying anode materials for potassium-ion batteries. *Small*, *19*(46), 2303985.

Ci, H., Cai, J., Ma, H., Shi, Z., Cui, G., Wang, M., Jin, J., Wei, N., Lu, C., Zhao, W., Sun, J., & Liu, Z. (2020). Defective VSe_2-graphene heterostructures enabling in situ electrocatalyst evolution for lithium-sulfur batteries. *ACS Nano*, *14*(9), 11929–11938.

Coldea, A. I., & Watson, M. D. (2018). The key ingredients of the electronic structure of FeSe. *Annual Review of Condensed Matter Physics*, *9*, 125–146.

Daali, A., Zhou, X., Zhao, C., Hwang, I., Yang, Z., Liu, Y., Amine, R., Sun, C.-J., Otieno, W., & Xu, G.-L. (2023). In situ microscopy and spectroscopy characterization of microsized Sn anode for sodium-ion batteries. *Nano Energy*, *115*, 108753.

Dai, H., Tang, M., Huang, J., & Wang, Z. (2021). A series of molecule-intercalated MoS_2 as anode materials for sodium ion batteries. *ACS Applied Materials & Interfaces*, *13*(9), 10870–10877.

Deng, R., Li, Q., Wang, P., Zheng, Q., Huo, Y., Xie, F., & Lin, D. (2022). Metal-organic framework derived core-shell structured Cu-doped $Co_{0.85}Se$@NC@C microcubes as advanced anodes for sodium-ion batteries. *Electrochimica Acta*, *432*, 141157.

Dey, Sonjoy, & Singh, G. (2023). Differentiating cyclability and kinetics of Na^+ ions in surface-functionalized and nanostructured graphite using electrochemical impedance spectroscopy. *Batteries*, *9*(11).

Dey, Sunita, Lee, J., Britto, S., Stratford, J. M., Keyzer, E. N., Dunstan, M. T., Cibin, G., Cassidy, S. J., Elgaml, M., & Grey, C. P. (2020). Exploring cation-anion redox processes in one-dimensional linear chain vanadium tetrasulfide rechargeable

magnesium ion cathodes. *Journal of the American Chemical Society*, *142*(46), 19588–19601.

Dong, R., Zheng, L., Bai, Y., Ni, Q., Li, Y., Wu, F., Ren, H., & Wu, C. (2021). Elucidating the mechanism of fast Na storage kinetics in ether electrolytes for hard carbon anodes. *Advanced Materials*, *33*(36), 2008810.

Du, M., Wang, Z., Yang, C., Deng, Y., Wang, T., Zhong, W., Yin, W., Jiao, Z., Xia, W., & Jiang, B. (2022). N-doped reduced graphene oxide/$Co_{0.85}Se$ microflowers with high mass loading as battery-type materials for quasi-solid-state hybrid supercapacitors. *Journal of Alloys and Compounds*, *890*, 161801.

Du, X., Gao, Y., Hou, Z., Guo, X., Zhu, Y., & Zhang, B. (2022). Stabilizing microsized Sn anodes for Na-ion batteries with extended ether electrolyte chemistry. *ACS Applied Energy Materials*, *5*(2), 2252–2259.

Dubal, D. P., Ayyad, O., Ruiz, V., & Gómez-Romero, P. (2015). Hybrid energy storage: The merging of battery and supercapacitor chemistries. *Chemical Society Reviews*, *44*(7), 1777–1790.

Dubal, Deepak P., Jayaramulu, K., Sunil, J., Kment, Š., Gomez-Romero, P., Narayana, C., Zbořil, R., & Fischer, R. A. (2019). Metal–organic framework (MOF) derived electrodes with robust and fast lithium storage for Li-ion hybrid capacitors. *Advanced Functional Materials*, *29*(19), 1900532.

Fan, R., Zhao, C., Ma, J., Lei, S., Liang, G., He, T., Zhu, G., & Cai, Y. (2022). Boosting reaction kinetics and improving long cycle life in lamellar VS_2/MoS_2 heterojunctions for superior sodium storage performance. *Journal of Materials Chemistry A*, *10*(2), 939–949.

Fan, S., Li, G., Cai, F., & Yang, G. (2020). Synthesis of porous Ni-doped $CoSe_2$/C nanospheres towards high-rate and long-term sodium-ion half/full batteries. *Chemistry–A European Journal*, *26*(39), 8579–8587.

Fan, X., Kong, X., Zhang, P., & Wang, J. (2024). Research progress on hard carbon materials in advanced sodium-ion batteries. *Energy Storage Materials*, *69*, 103386.

Feng, T., Zhao, T., Zhu, S., Zhang, N., Wei, Z., Wang, K., Li, L., Wu, F., & Chen, R. (2021). Anion-doped cobalt selenide with porous architecture for high-rate and flexible lithium–sulfur batteries. *Small Methods*, *5*(9), 2100649.

Feng, W., Wen, X., Wang, Y., Song, L., Li, X., Du, R., Yang, J., Li, H., He, J., & Shi, J. (2023). Interfacial coupling $SnSe_2$/SnSe heterostructures as long cyclic anodes of lithium-ion battery. *Advanced Science*, *10*(2), 2204671.

Feng, Y., Wu, K., Xu, C., Wu, S., Guo, Z., He, M., Xu, X., & Xue, M. (2022).

Cellulose/lignin-based carbon nanobelt aerogels coating on VSe_2 nanosheets as anode for high performance potassium-ion batteries. *Journal of Power Sources*, *548*, 232033.

Gao, J., Li, Y., Shi, L., Li, J., & Zhang, G. (2018). Rational design of hierarchical nanotubes through encapsulating $CoSe_2$ nanoparticles into $MoSe_2$/C composite shells with enhanced lithium and sodium storage performance. *ACS Applied Materials and Interfaces*, *10*(24), 20635–20642.

Ge, P., Zhang, L., Yang, Y., Sun, W., Hu, Y., & Ji, X. (2020). Advanced $MoSe_2$/carbon electrodes in Li/Na-ions batteries. *Advanced Materials Interfaces*, *7*(2), 1901651.

Ghani, U., Iqbal, N., Aboalhassan, A. A., Liu, B., Aftab, T., Zada, I., Ullah, F., Gu, J., Li, Y., & Zhu, S. (2022). One-step sonochemical fabrication of biomass-derived porous hard carbons; towards tuned-surface anodes of sodium-ion batteries. *Journal of Colloid and Interface Science*, *611*, 578–587.

Gong, Y., Li, Y., Li, Y., Liu, M., Bai, Y., & Wu, C. (2023). Metal selenides anode materials for sodium ion batteries: synthesis, modification, and application. *Small*, *19*(4), 2206194.

Guo, J., Yang, J., Guan, J., Chen, X., Zhu, Y., Fu, H., Liu, Q., Wei, B., & Geng, H. (2022). Interface and electronic structure dual-engineering on $MoSe_2$ with multi-ion/electron transportation channels for boosted sodium-ion half/full batteries. *Chemical Engineering Journal*, *450*, 138007.

Han, L., Wu, S., Hu, Z., Chen, M., Ding, J., Wang, S., Zhang, Y., Guo, D., Zhang, L., & Cao, S. (2020). Hierarchically porous MoS_2–carbon hollow rhomboids for superior performance of the anode of sodium-ion batteries. *ACS Applied Materials & Interfaces*, *12*(9), 10402–10409.

Han, Q., Zhang, W., Zhu, L., Liu, M., Xia, C., Xie, L., Qiu, X., Xiao, Y., Yi, L., & Cao, X. (2024). MOF-derived bimetallic selenide $CoNiSe_2$ nanododecahedrons encapsulated in porous carbon matrix as advanced anodes for lithium-ion batteries. *ACS Applied Materials & Interfaces*, *16*(5), 6033–6047.

Hao, J., Xu, L., Bai, J., Wang, X., Guo, Q., Wang, Y., Yang, Y., & Zhao, J. (2021). Porous structure O-rich carbon nanotubes as anode material for sodium-ion batteries. *Ionics*, *27*(2), 667–675.

Hao, Z., Shi, X., Yang, Z., Li, L., & Chou, S. L. (2022). Developing high-performance metal selenides for sodium-ion batteries. *Advanced Functional Materials*, *32*(51), 2208093.

He, H., Zhang, H., Huang, D., Kuang, W., Li, X., Hao, J., Guo, Z., & Zhang, C. (2022). Harnessing plasma-assisted doping engineering to stabilize metallic phase $MoSe_2$

for fast and durable sodium-ion storage. *Advanced Materials*, *34*(15), 2200397.

He, S., Guo, F., Yang, Q., Mi, H., Li, J., Yang, N., & Qiu, J. (2021). Design and fabrication of hierarchical NiCoP–MOF heterostructure with enhanced pseudocapacitive properties. *Small*, *17*(21), 2100353.

He, Y., Bai, P., Gao, S., & Xu, Y. (2018). Marriage of an ether-based electrolyte with hard carbon anodes creates superior sodium-ion batteries with high mass loading. *ACS Applied Materials & Interfaces*, *10*(48), 41380–41388.

Hu, S., Wang, T., Lu, B., Wu, D., Wang, H., Liu, X., & Zhang, J. (2022). Ionic-liquid-assisted synthesis of FeSe–MnSe heterointerfaces with abundant Se vacancies embedded in N,B Co-doped hollow carbon microspheres for accelerating the sulfur reduction reaction. *Advanced Materials*, *34*(41), 2204147.

Hu, X., Sun, X., Yoo, S. J., Evanko, B., Fan, F., Cai, S., Zheng, C., Hu, W., & Stucky, G. D. (2019). Nitrogen-rich hierarchically porous carbon as a high-rate anode material with ultra-stable cyclability and high capacity for capacitive sodium-ion batteries. *Nano Energy*, *56*, 828–839.

Hu, Ye, Li, B., Jiao, X., Zhang, C., Dai, X., & Song, J. (2018). Stable cycling of phosphorus anode for sodium-ion batteries through chemical bonding with sulfurized polyacrylonitrile. *Advanced Functional Materials*, *28*(23), 1801010.

Hu, Yuzhen, Huang, C., Jiang, S., Qin, Y., & Chen, H. C. (2019). Hierarchical nickel-cobalt selenide nanoparticles/nanosheets as advanced electroactive battery materials for hybrid supercapacitors. *Journal of Colloid and Interface Science*, *558*, 291–300.

Hu, Z., Wang, L., Zhang, K., Wang, J., Cheng, F., Tao, Z., & Chen, J. (2014). MoS_2 nanoflowers with expanded interlayers as high-performance anodes for sodium-ion batteries. *Angewandte Chemie International Edition*, *53*(47), 12794–12798.

Hua, W., Shang, T., Li, H., Sun, Y., Guo, Y., Xia, J., Geng, C., Hu, Z., Peng, L., Han, Z., Zhang, C., Lv, W., & Wan, Y. (2023). Optimizing the p charge of S in p-block metal sulfides for sulfur reduction electrocatalysis. *Nature Catalysis*, *6*(2), 174–184.

Huang, X. L., Zhou, C., He, W., Sun, S., Chueh, Y.-L., Wang, Z. M., Liu, H. K., & Dou, S. X. (2021). An emerging energy storage system: advanced Na–Se batteries. *ACS Nano*, *15*(4), 5876–5903.

Hussain, S., Vikraman, D., Mehran, M. T., Hussain, M., Nazir, G., Patil, S. A., Kim, H. S., & Jung, J. (2022). Ultrasonically derived WSe_2 nanostructure embedded MXene hybrid composites for supercapacitors and hydrogen evolution reactions. *Renewable Energy*, *185*, 585–597.

Hwang, J.-Y., Myung, S.-T., & Sun, Y.-K. (2017). Sodium-ion batteries: present and future. *Chemical Society Reviews*, *46*(12), 3529–3614.

Ihsan-Ul-Haq, M., Huang, H., Wu, J., Mubarak, N., Susca, A., Luo, Z., Huang, B., & Kim, J. K. (2021). Unveiling solid electrolyte interface morphology and electrochemical kinetics of amorphous Sb_2Se_3/CNT composite anodes for ultrafast sodium storage. *Carbon*, *171*, 119–129.

Jablonka, K. M., Ongari, D., Moosavi, S. M., & Smit, B. (2021). Using collective knowledge to assign oxidation states of metal cations in metal–organic frameworks. *Nature Chemistry*, *13*(8), 771–777.

Jeong, S. Y., Park, S. K., Kang, Y. C., & Cho, J. S. (2018). One-dimensional nanostructure comprising $MoSe_2$ nanosheets and carbon with uniformly defined nanovoids as an anode for high-performance sodium-ion batteries. *Chemical Engineering Journal*, *351*(April), 559–568.

Jia, X.-X., Yu, X.-Z., & Lu, B.-A. (2021). $Fe_{0.8}CoSe_2$ nanosphere coated by N-doped carbon for ultra-high rate potassium selenium battery. *Rare Metals*, *40*(9), 2455–2463.

Jiang, Qingqing, Hu, S., Wang, L., Huang, Z., Yang, H. J., Han, X., Li, Y., Lv, C., He, Y. S., Zhou, T., & Hu, J. (2020). Boosting potassium storage in nanosheet assembled $MoSe_2$ hollow sphere through surface decoration of MoO_2 nanoparticles. *Applied Surface Science*, *505*, 144573.

Jiang, Qiwang, Wang, J., Jiang, Y., Li, L., Cao, X., & Cao, M. (2020). Selenium vacancy-rich and carbon-free VSe_2 nanosheets for high-performance lithium storage. *Nanoscale*, *12*(16), 8858–8866.

Jin, F., Li, M., Xie, L., & Jiang, J. (2021). Selenium-doped carbon nanotubes/nickel selenide coaxial nanocables for energy storage. *Journal of Power Sources*, *514*, 230587.

Kang, W., Mou, Z., Hu, X., Fan, X., & Sun, D. (2024). Dual engineering of hetero-interfaces and architecture in $MoSe_2/VSe_{1.6}$@NC nanoflower for fast and stable sodium/potassium storage. *Journal of Colloid and Interface Science*, *666*, 1–11.

Ke, C., Shao, R., Zhang, Y., Sun, Z., Qi, S., Zhang, H., Li, M., Chen, Z., Wang, Y., Sa, B., Lin, H., Liu, H., Wang, M. S., Chen, S., & Zhang, Q. (2022). Synergistic engineering of heterointerface and architecture in new-type ZnS/Sn heterostructures in situ encapsulated in nitrogen-doped carbon toward high-efficient lithium-ion storage. *Advanced Functional Materials*, *32*(38), 2205635.

Kim, C., Kim, I., Kim, H., Sadan, M. K., Yeo, H., Cho, G., Ahn, J., Ahn, J., & Ahn, H.

(2018). A self-healing Sn anode with an ultra-long cycle life for sodium-ion batteries. *Journal of Materials Chemistry A*, *6*(45), 22809–22818.

Kim, C., Lee, K.-Y., Kim, I., Park, J., Cho, G., Kim, K.-W., Ahn, J.-H., & Ahn, H.-J. (2016). Long-term cycling stability of porous Sn anode for sodium-ion batteries. *Journal of Power Sources*, *317*, 153–158.

Kim, I., Park, S.-W., & Kim, D.-W. (2020). Carbon-coated tungsten diselenide nanosheets uniformly assembled on porous carbon cloth as flexible binder-free anodes for sodium-ion batteries with improved electrochemical performance. *Journal of Alloys and Compounds*, *827*, 154348.

Kim, J. K., Lim, K. E., Hwang, W. J., Kang, Y. C., & Park, S. K. (2020). Hierarchical tubular-structured $MoSe_2$ nanosheets/N-doped carbon nanocomposite with enhanced sodium storage properties. *ChemSusChem*, *13*(6), 1546–1555.

Kim, Y. B., Seo, H. Y., Kim, K., Cho, J. S., Kang, Y. C., & Park, G. D. (2024). Synthesis of iron sulfide nanocrystals encapsulated in highly porous carbon-coated CNT microsphere as anode materials for sodium-ion batteries. *Small*, *20*(7), 2305686.

Kokalj, A. (1999). XCrySDen-a new program for displaying crystalline structures and electron densities. *Journal of Molecular Graphics and Modelling*, *17*(3–4), 176–179.

Kreisel, A., Hirschfeld, P. J., & Andersen, B. M. (2020). On the remarkable superconductivity of fese and its close cousins. *Symmetry*, *12*(9), 1–72.

Kumar, G., Francis, M. K., Bhargav, P. B., & Ahmed, N. (2024). Silicon infused molybedenum di-selinide ($MoSe_2$) nanosheets for enhanced hydrogen evolution reaction (HER) and lithium-ion battery (LIB) applications. *International Journal of Hydrogen Energy*, *51*, 1448–1461.

Kumar, U., Goonetilleke, D., Gaikwad, V., Pramudita, J. C., Joshi, R. K., Sharma, N., & Sahajwalla, V. (2019). Activated carbon from E-waste plastics as a promising anode for sodium-ion batteries. *ACS Sustainable Chemistry and Engineering*, *7*(12), 10310–10322.

Kundu, D., Talaie, E., Duffort, V., & Nazar, L. F. (2015). The emerging chemistry of sodium ion batteries for electrochemical energy storage. *Angewandte Chemie International Edition*, *54*(11), 3431–3448.

Langmuir, I. (1919). ISOMORPHISM, ISOSTERISM AND COVALENCE. *Journal of the American Chemical Society*, *41*(10), 1543–1559.

Lee, J. S., Park, J. S., Baek, K. W., Saroha, R., Yang, S. H., Kang, Y. C., & Cho, J. S.

(2023). Coral-like porous microspheres comprising polydopamine-derived N-doped C-coated $MoSe_2$ nanosheets composited with graphitic carbon as anodes for high-rate sodium- and potassium-ion batteries. *Chemical Engineering Journal*, *456*, 141118.

Lee, Y., Lim, H., Kim, S.-O., Kim, H.-S., Kim, K. J., Lee, K.-Y., & Choi, W. (2018). Thermal stability of Sn anode material with non-aqueous electrolytes in sodium-ion batteries. *Journal of Materials Chemistry A*, *6*(41), 20383–20392.

Lei, H., Wang, H., Cheng, B., Zhang, F., Liu, X., Wang, G., & Wang, B. (2023). Anion-vacancy modified WSSe nanosheets on 3D cross-networked porous carbon skeleton for non-aqueous sodium-based dual-ion storage. *Small*, *19*(10), 2206340.

Li, D., Zhou, J., Chen, X., & Song, H. (2018). Achieving ultrafast and stable Na-ion storage in $FeSe_2$ nanorods/graphene anodes by controlling the surface oxide. *ACS Applied Materials & Interfaces*, *10*(26), 22841–22850.

Li, G., Wang, J., Chu, J., Li, M., Hu, Z., Wang, F., Han, Y., Cai, T., & Song, Z. (2022). Ultrafast and ultrastable Na-ion storage in zero-strain sodium perylenetetracarboxylate anode enabled by ether electrolyte. *Energy Storage Materials*, *47*, 1–12.

Li, Haomiao, Wang, K., Zhou, M., Li, W., Tao, H., Wang, R., Cheng, S., & Jiang, K. (2019). Facile tailoring of multidimensional nanostructured Sb for sodium storage applications. *ACS Nano*, *13*(8), 9533–9540.

Li, Hong, Gao, R., Chen, B., Zhou, C., Shao, F., Wei, H., Han, Z., Hu, N., & Zhou, G. (2022). Vacancy-rich MoSSe with sulfiphilicity–lithiophilicity dual function for kinetics-enhanced and dendrite-free Li-S batteries. *Nano Letters*, *22*(12), 4999–5008.

Li, Huan, He, Y., Wang, Q., Gu, S., Wang, L., Yu, J., Zhou, G., & Xu, L. (2023). $SnSe_2$/$NiSe_2$@N-doped carbon yolk-shell heterostructure construction and selenium vacancies engineering for ultrastable sodium-ion storage. *Advanced Energy Materials*, *13*(47), 2302901.

Li, Huihua, Zhang, H., Wu, F., Zarrabeitia, M., Geiger, D., Kaiser, U., Varzi, A., & Passerini, S. (2022). Sodiophilic current collectors based on MOF-derived nanocomposites for anode-less Na-metal batteries. *Advanced Energy Materials*, *12*(43), 2202293.

Li, N., Zhou, Q., Lin, J., Lu, Y., Hou, Z., & Qian, Y. (2022). One-pot synthesis of uniform $MoSe_2$ nanoparticles as high performance anode materials for lithium/sodium ion batteries. *Journal of Alloys and Compounds*, *922*, 166306.

Li, Q., Zhao, X., Zhang, Z., Xun, X., Zhao, B., Xu, L., Kang, Z., Liao, Q., & Zhang, Y.

(2022). Architecture design and interface engineering of self-assembly VS_4/rGO heterostructures for ultrathin absorbent. *Nano-Micro Letters*, *14*, 67.

Li, Q., Zhu, Y., Zhao, P., Yuan, C., Chen, M., & Wang, C. (2018). Commercial activated carbon as a novel precursor of the amorphous carbon for high-performance sodium-ion batteries anode. *Carbon*, *129*, 85–94.

Li, Shaohui, Chen, J., Xiong, J., Gong, X., Ciou, J., & Lee, P. S. (2020). Encapsulation of MnS nanocrystals into N, S-Co-doped carbon as anode material for full cell sodium-ion capacitors. *Nano-Micro Letters*, *12*, 34.

Li, Shengkai, Zhang, H., Cao, Y., Zhang, S., Liu, Z., Yang, C., Wang, Y., & Wan, B. (2023). Self-assembled nanoflower-like $FeSe_2$/$MoSe_2$ heterojunction anode with enhanced kinetics for superior-performance Na-ion half/full batteries. *Nanoscale*, *15*(12), 5655–5664.

Li, Shengkai, Zhang, S., Zhang, H., Liu, Z., Yang, C., Wang, Y., Wan, B., & Wen, D. (2022). Constructing three-dimensional (3D) nanoflower-like $Cu_{2-x}Se$-$MoSe_2$ heterojunction as an excellent long-life and high-rate anode for half/full Na-ion batteries. *Electrochimica Acta*, *432*, 141181.

Li, Songsong, Gao, Y., Li, N., Ge, L., Bu, X., & Feng, P. (2021). Transition metal-based bimetallic MOFs and MOF-derived catalysts for electrochemical oxygen evolution reaction. *Energy and Environmental Science*, *14*(4), 1897–1927.

Li, W., Hu, S., Luo, X., Li, Z., Sun, X., Li, M., Liu, F., & Yu, Y. (2017). Confined amorphous red phosphorus in MOF-derived N-doped microporous carbon as a superior anode for sodium-ion battery. *Advanced Materials*, *29*(16), 1605820.

Li, Xianwei, Wu, Z., Ma, X., Xin, L., Yu, X., & Liu, Y. (2023). MOF-derived crystalline carbon with graphite-like crystal: A high initial coulombic efficiency, low potential and large capacity anode for Na-ion batteries. *Carbon*, *208*, 10–21.

Li, Xinyan, Xiao, S., Guo, D., Jiang, J., Niu, X., Wu, R., Pan, T., & Song Chen, J. (2023). Homogeneously distributed heterostructured interfaces in rice panicle-like SbBi-Bi_2Se_3-Sb_2Se_3 nanowalls for robust sodium storage. *Chemical Engineering Journal*, *452*(P3), 139363.

Li, Y., Wu, F., Li, Y., Liu, M., Feng, X., Bai, Y., & Wu, C. (2022). Ether-based electrolytes for sodium ion batteries. *Chemical Society Reviews*, *51*(11), 4484–4536.

Li, Zhaopeng, Qin, H., Tian, W., Miao, L., Cao, K., Si, Y., Li, H., Wang, Q., & Jiao, L. (2024). 3D Sb-based composite framework with gradient sodiophilicity for ultrastable sodium metal anodes. *Advanced Functional Materials*, *34*(5), 2301554.

Li, Zhiqi, Yan, J., Li, Q., Xu, A., Sun, J., Wang, Y., Zhang, X., Sun, X., Jiang, F., & Zhou, Y. (2024). Te doped 1T/2H-$MoSe_2$ nanosheets with rich defects as advanced anode materials for high-rate sodium ion half/full batteries. *Inorganic Chemistry Frontiers*, *11*(7), 2017–2028.

Li, Zhuanxia, Yu, L., Tao, X., Li, Y., Zhang, L., He, X., Chen, Y., Xiong, S., Hu, W., & Li, J. (2024). Honeycomb-structured $MoSe_2$/rGO Composites as high-performance anode materials for sodium-ion batteries. *Small*, *20*(6), 2304124.

Liang, T., Wang, H., Wang, R., He, B., Gong, Y., & Yan, C. (2021). Nitrogen-doped carbon nanotube-buffered $FeSe_2$ anodes for fast-charging and high-capacity lithium storage. *Electrochimica Acta*, *389*, 138686.

Lin, R., Xiao, M., Xu, Y., Zeng, L., Zhu, F., Zhang, Y., & Meng, Y. (2024). MnO_2 nanoflakes anchored on carbon nanotubes as self-standing anode for sodium ion batteries. *Journal of Energy Storage*, *92*, 112291.

Liu, B., Wang, L., Zhu, Y., Peng, H., Du, C., Yang, X., Zhao, Q., Hou, J., & Cao, C. (2022). Ammonium-modified synthesis of vanadium sulfide nanosheet assemblies toward high sodium storage. *ACS Nano*, *16*(8), 12900–12909.

Liu, C., Fu, X., Liao, S., Zou, G., & Yang, H. (2023). Interface engineering enables high-performance Sb anode for sodium storage. *Nanomaterials*, *13*(2), 254.

Liu, F., Zou, Y., Tang, X., Mao, L., Du, D., Wang, H., Zhang, M., Wang, Z., Yao, N., Zhao, W., Bai, M., Zhao, T., Liu, Y., & Ma, Y. (2022). Phase engineering and alkali cation stabilization for 1T molybdenum dichalcogenides monolayers. *Advanced Functional Materials*, *32*(36), 2204601.

Liu, H., Guo, H., Liu, B., Liang, M., Lv, Z., Adair, K. R., & Sun, X. (2018). Few-layer $MoSe_2$ nanosheets with expanded (002) planes confined in hollow carbon nanospheres for ultrahigh-performance Na-ion batteries. *Advanced Functional Materials*, *28*(19), 1707480.

Liu, Jiawei, Xiao, S., Li, X., Li, Z., Li, X., Zhang, W., Xiang, Y., Niu, X., & Chen, J. S. (2021). Interface engineering of Fe_3Se_4/FeSe heterostructure encapsulated in electrospun carbon nanofibers for fast and robust sodium storage. *Chemical Engineering Journal*, *417*, 129279.

Liu, Jing, Xie, J., Dong, H., Wei, H., Sun, C., Yang, J., & Geng, H. (2023). Iron doping of $NiSe_2$ nanosheets to accelerate reaction kinetics in sodium-ion half/full batteries. *Science China Materials*, *66*(1), 69–78.

Liu, L., Xu, J., Sun, J., He, S., Wang, K., Chen, Y., Dou, S., Du, Z., Du, H., Ai, W., & Huang, W. (2021). A stable and ultrafast K ion storage anode based on phase-engineered $MoSe_2$. *Chemical Communications*, *57*(32), 3885–3888.

Liu, M., Yang, Z., Shen, Y., Guo, S., Zhang, J., Ai, X., Yang, H., & Qian, J. (2021). Chemically presodiated Sb with a fluoride-rich interphase as a cycle-stable anode for high-energy sodium ion batteries. *Journal of Materials Chemistry A*, *9*(9), 5639–5647.

Liu, S., Feng, J., Bian, X., Liu, J., & Xu, H. (2016). The morphology-controlled synthesis of a nanoporous-antimony anode for high-performance sodium-ion batteries. *Energy & Environmental Science*, *9*(4), 1229–1236.

Liu, T., Zhang, L., Cheng, B., & Yu, J. (2019). Hollow carbon spheres and their hybrid nanomaterials in electrochemical energy storage. *Advanced Energy Materials*, *9*(17), 1803900.

Liu, W., Chen, X., Zhang, C., Xu, H., Sun, X., Zheng, Y., Yu, Y., Li, S., Huang, Y., & Li, J. (2019). Gassing in Sn-anode sodium-ion batteries and its remedy by metallurgically prealloying Na. *ACS Applied Materials & Interfaces*, *11*(26), 23207–23212.

Liu, X. D., Yang, Q., Yuan, L., Qi, D., Wei, X., Zhou, X., Chen, S., Cao, L., Zeng, Y., Jia, J., & Wang, C. (2021). Oxygen vacancy-rich WO_3 heterophase structure: A trade-off between surface-limited pseudocapacitance and intercalation-limited behaviour. *Chemical Engineering Journal*, *425*(August), 131431.

Liu, X., Si, Y., Li, K., Xu, Y., Zhao, Z., Li, C., Fu, Y., & Li, D. (2021). Exploring sodium storage mechanism of topological insulator Bi_2Te_3 nanosheets encapsulated in conductive polymer. *Energy Storage Materials*, *41*, 255–263.

Liu, Yan, Qing, Y., Zhou, B., Wang, L., Pu, B., Zhou, X., Wang, Y., Zhang, M., Bai, J., & Tang, Q. (2023). Yolk–shell Sb@void@graphdiyne nanoboxes for high-rate and long cycle life sodium-ion batteries. *ACS Nano*, *17*(3), 2431–2439.

Liu, Yangjie, Hu, X., Li, J., Zhong, G., Yuan, J., Zhan, H., Tang, Y., & Wen, Z. (2022). Carbon-coated $MoS_{1.5}Te_{0.5}$ nanocables for efficient sodium-ion storage in non-aqueous dual-ion batteries. *Nature Communications*, *13*, 663.

Liu, YangJie, Li, J., Liu, B., Chen, Y., Wu, Y., Hu, X., Zhong, G., Yuan, J., Chen, J., & Zhan, H. (2023). Confined WS_2 nanosheets tubular nanohybrid as high-kinetic and durable anode for sodium-based dual ion batteries. *ChemSusChem*, *16*(4), e202201200.

Liu, Yayuan, Zhu, Y., & Cui, Y. (2019). Challenges and opportunities towards fast-charging battery materials. *Nature Energy*, *4*(7), 540–550.

Liu, Yihang, Zhang, A., Shen, C., Liu, Q., Cao, X., Ma, Y., Chen, L., Lau, C., Chen, T.-C., & Wei, F. (2017). Red phosphorus nanodots on reduced graphene oxide as a

flexible and ultra-fast anode for sodium-ion batteries. *ACS Nano*, *11*(6), 5530–5537.

Liu, Yongchang, Zhang, N., Jiao, L., Tao, Z., & Chen, J. (2015). Ultrasmall Sn nanoparticles embedded in carbon as high-performance anode for sodium-ion batteries. *Advanced Functional Materials*, *25*(2), 214–220.

Liu, Yongchang, Zhang, N., Liu, X., Chen, C., Fan, L.-Z., & Jiao, L. (2017). Red phosphorus nanoparticles embedded in porous N-doped carbon nanofibers as high-performance anode for sodium-ion batteries. *Energy Storage Materials*, *9*, 170–178.

Liu, Z., Yu, X.-Y., Lou, X. W. D., & Paik, U. (2016). Sb@C coaxial nanotubes as a superior long-life and high-rate anode for sodium ion batteries. *Energy & Environmental Science*, *9*(7), 2314–2318.

Lou, X., Ning, Y., Li, C., Hu, X., Shen, M., & Hu, B. (2018). Bimetallic zeolite imidazolate framework for enhanced lithium storage boosted by the redox participation of nitrogen atoms. *Science China Materials*, *61*(8), 1040–1048.

Lu, C., Li, A., Li, G., Yan, Y., Zhang, M., Yang, Q., Zhou, W., & Guo, L. (2021). S-decorated porous Ti_3C_2 MXene combined with in situ forming Cu_2Se as effective shuttling interrupter in Na–Se batteries. *Advanced Materials*, *33*(33), 2008414.

Luo, M., Yu, H., Hu, F., Liu, T., Cheng, X., Zheng, R., Bai, Y., Shui, M., & Shu, J. (2020). Metal selenides for high performance sodium ion batteries. *Chemical Engineering Journal*, *380*, 122557.

Luo, Q., Wen, J., Liu, G., Ye, Z., Wang, Q., Liu, L., & Yang, X. (2022). Sb_2Se_3/Sb embedded in carbon nanofibers as flexible and twistable anode for potassium-ion batteries. *Journal of Power Sources*, *545*, 231917.

Lv, Chengkui, Lin, C., Dong, H., Wei, H., Yang, J., & Geng, H. (2022). Electronic modulation and structure engineered $MoSe_2$ with multichannel paths as an advanced anode for sodium-ion half/full batteries. *Science China Materials*, *65*(11), 2997–3006.

Lv, Chunxiao, Liu, H., Li, D., Chen, S., Zhang, H., She, X., Guo, X., & Yang, D. (2019). Ultrafine FeSe nanoparticles embedded into 3D carbon nanofiber aerogels with FeSe/Carbon interface for efficient and long-life sodium storage. *Carbon*, *143*, 106–115.

Lv, Q., Tan, J., Wang, Z., Gu, P., Liu, H., Yu, L., Wei, Y., Gan, L., Liu, B., Li, J., Kang, F., Cheng, H. M., Xiong, Q., & Lv, R. (2023). Ultrafast charge transfer in mixed-dimensional WO_{3-x} nanowire/WSe_2 heterostructures for attomolar-level molecular

sensing. *Nature Communications*, *14*, 2717.

Ma, C., Wang, X., Lan, J., Zhang, J., Song, K., Chen, J., Ge, J., & Chen, W. (2023). Dynamic multistage coupling of FeS_2/S enables ultrahigh reversible Na–S batteries. *Advanced Functional Materials*, *33*(5), 2211821.

Mace, A., Montalvo, M., Lu, Y., Wujcik, E. K., & Jeon, J. W. (2020). Three-dimensional porous graphene anodes for sodium-ion batteries. *Functional Materials Letters*, *13*(1), 1951009.

Marbella, L. E., Evans, M. L., Groh, M. F., Nelson, J., Griffith, K. J., Morris, A. J., & Grey, C. P. (2018). Sodiation and desodiation via helical phosphorus intermediates in high-capacity anodes for sodium-ion batteries. *Journal of the American Chemical Society*, *140*(25), 7994–8004.

Molaei Aghdam, A., Habibzadeh, S., Javanbakht, M., Ershadi, M., & Ganjali, M. R. (2023). High interspace-layer manganese selenide nanorods as a high-performance cathode for aqueous zinc-ion batteries. *ACS Applied Energy Materials*, *6*(6), 3225–3235.

Moosavifard, S. E., Mohammadi, A., Darzi, M. E., Kariman, A., Abdi, M. M., & Karimi, G. (2021). A facile strategy to synthesis graphene-wrapped nanoporous copper-cobalt-selenide hollow spheres as an efficient electrode for hybrid supercapacitors. *Chemical Engineering Journal*, *415*, 128662.

Muhammad, M. A., Pan, D., Liu, Y., Chen, J., Yuan, J., Wu, Y., Haruna, B., Makin, A. M., Abdel-Aziz, A., & Wen, Z. (2024). N-doped 3D carbon encapsulating nickel selenide nanoarchitecture with cation defect engineering: An ultrafast and long-life anode for sodium-ion batteries. *Journal of Colloid and Interface Science*, *670*, 191–203.

Muska, M., Yang, J., Sun, Y., Wang, J., Wang, Y., & Yang, Q. (2021). CoSe2 Nanoparticles Dispersed in WSe 2 Nanosheets for E ffi cient Electrocatalysis and Supercapacitance Applications. *ACS Applied Nano Materials*, *4*(6), 5796–5807.

Na, J. H., Kang, Y. C., & Park, S.-K. (2021). Electrospun MOF-based ZnSe nanocrystals confined in N-doped mesoporous carbon fibers as anode materials for potassium ion batteries with long-term cycling stability. *Chemical Engineering Journal*, *425*, 131651.

Nayak, P. K., Yang, L., Brehm, W., & Adelhelm, P. (2018). From lithium-ion to sodium-ion batteries: advantages, challenges, and surprises. *Angewandte Chemie - International Edition*, *57*(1), 102–120.

Niu, F., Yang, J., Wang, N., Zhang, D., Fan, W., Yang, J., & Qian, Y. (2017). $MoSe_2$-covered N,P-doped carbon nanosheets as a long-life and high-rate anode material

for sodium-ion batteries. *Advanced Functional Materials*, *27*(23), 1700522.

O'Heir, J. (2017). Building better batteries. *Mechanical Engineering*, *139*(1), 10–11.

Oh, S., Woo, C., Ahn, J., Kim, T. Y., Dong, X., Kim, Y., Choi, K. H., Chae, S., Zhang, X., & Bang, H.-S. (2023). Colloidal synthesis of ultrathin and Se-rich V_2Se_9 nanobelts as high-performance anode materials for Li-ion batteries. *ACS Applied Materials & Interfaces*, *15*(48), 55745–55752.

Ou, X., Liang, X., Zheng, F., Wu, P., Pan, Q., Xiong, X., Yang, C., & Liu, M. (2017). In situ X-ray diffraction investigation of $CoSe_2$ anode for Na-ion storage: Effect of cut-off voltage on cycling stability. *Electrochimica Acta*, *258*, 1387–1396.

Pan, Y., Cheng, X., Gong, L., Shi, L., Zhou, T., Deng, Y., & Zhang, H. (2018). Double-morphology CoS_2 anchored on N-doped multichannel carbon nanofibers as high-performance anode materials for Na-ion batteries. *ACS Applied Materials & Interfaces*, *10*(37), 31441–31451.

Park, G. D., Park, J. S., Kim, J. K., & Kang, Y. C. (2021). Recent advances in heterostructured anode materials with multiple anions for advanced alkali-ion batteries. *Advanced Energy Materials*, *11*(27), 2003058.

Patel, A. B., Vaghasiya, J. V, Chauhan, P., Sumesh, C. K., Patel, V., Soni, S. S., Patel, K. D., Garg, P., Solanki, G. K., & Pathak, V. M. (2022). Synergistic 2D $MoSe_2$@ WSe_2 nanohybrid heterostructure toward superior hydrogen evolution and flexible supercapacitor. *Nanoscale*, *14*(17), 6636–6647.

Pei, Y. R., Zhou, H. Y., Zhao, M., Li, J. C., Ge, X., Zhang, W., Yang, C. C., & Jiang, Q. (2023). High-efficiency sodium storage of $Co_{0.85}Se/WSe_2$ encapsulated in N-doped carbon polyhedron via vacancy and heterojunction engineering. *Carbon Energy*, *6*(1), e374.

Peng, B., Xu, S., Lv, Z., Zhang, S., Gao, Y., Lin, T., & Huang, F. (2023). Toward extremely fast charging through boosting intercalative redox pseudocapacitance: A $SbCrSe_3$ anode for large and fast sodium storage. *Advanced Energy Materials*, *13*(2), 2203187.

Perveen, T., Siddiq, M., Shahzad, N., Ihsan, R., Ahmad, A., & Shahzad, M. I. (2020). Prospects in anode materials for sodium ion batteries-A review. *Renewable and Sustainable Energy Reviews*, *119*, 109549.

Qin, B., Wang, M., Wu, S., Li, Y., Liu, C., Zhang, Y., & Fan, H. (2023). Carbon dots confined nanosheets assembled $NiCo_2S_4$@CDs cross-stacked architecture for enhanced sodium ion storage. *Chinese Chemical Letters*, *35*(7), 108921.

Qin, Z., Hu, Y., Lv, C., Yao, S., & Chen, G. (2022). Low-temperature solid-state

synthesis of interlayer engineered VS_4 for high-capacity and ultrafast sodium-ion storage. *Chemical Engineering Journal*, *433*(P3), 133765.

Qu, Z., Zhang, X., Huang, R., Wu, S., Chen, R., Wu, F., & Li, L. (2022). Ultrastable bioderived organic anode induced by synergistic coupling of binder/carbon-network for advanced potassium-ion storage. *Nano Letters*, *22*(10), 4115–4123.

Quan, Z., Wang, F., Wang, Y., Liu, Z., Zhang, C., Qi, F., Zhang, M., Ye, C., Tan, J., & Liu, J. (2023). Robust micro-sized and defect-rich carbon–carbon composites as advanced anodes for potassium-ion batteries. *Small*, *2305841*, 2305841.

Rao, Y., Wang, J., Liang, P., Zheng, H., Wu, M., Chen, J., Shi, F., Yan, K., Liu, J., & Bian, K. (2022). Heterostructured WS_2/MoS_2@ carbon hollow microspheres anchored on graphene for high-performance Li/Na storage. *Chemical Engineering Journal*, *443*, 136080.

Sarkar, A., Manohar, C. V, & Mitra, S. (2020). A simple approach to minimize the first cycle irreversible loss of sodium titanate anode towards the development of sodium-ion battery. *Nano Energy*, *70*, 104520.

Sha, D., You, Y., Hu, R., Cao, X., Wei, Y., Zhang, H., Pan, L., & Sun, Z. (2023). Comprehensively understanding the role of anion vacancies on K-ion storage: a case study of Se-vacancy-engineered VSe_2. *Advanced Materials*, *35*(15), 2211311.

Shan, H., Qin, J., Ding, Y., Sari, H. M. K., Song, X., Liu, W., Hao, Y., Wang, J., Xie, C., Zhang, J., & Li, X. (2021). Controllable heterojunctions with a semicoherent phase boundary boosting the potassium storage of $CoSe_2/FeSe_2$. *Advanced Materials*, *33*(37), 2102471.

Sheng Huang, Peng Huang, Lei Wang, Junbo Han, Yu Chen, H. Z. (2024). Halogenated-methylammonium based three dimensional halide perovskites. *Advanced Materials*, *31*(42), 1903830.

Shi, J., Liu, Y., Su, M., Gao, F., & Lu, Q. (2022). Harnessing the volume expansion of metal selenide anode by composition engineering to achieve ultrastable sodium storage. *Journal of Power Sources*, *540*, 231636.

Shi, L., Li, Y., Zeng, F., Ran, S., Dong, C., Leu, S.-Y., Boles, S. T., & Lam, K. H. (2019). In situ growth of amorphous Fe_2O_3 on 3D interconnected nitrogen-doped carbon nanofibers as high-performance anode materials for sodium-ion batteries. *Chemical Engineering Journal*, *356*, 107–116.

Shinde, P. A., Chodankar, N. R., Kim, H. J., Abdelkareem, M. A., Ghaferi, A. Al, Han, Y. K., Olabi, A. G., & Ariga, K. (2023). Ultrastable 1T-2H WS_2 heterostructures by nanoarchitectonics of phosphorus-triggered phase transition for hybrid supercapacitors. *ACS Energy Letters*, *8*(10), 4474–4487.

Song, J., Wu, M., Fang, K., Tian, T., Wang, R., & Tang, H. (2023). NaF-rich interphase and high initial coulombic efficiency of red phosphorus anode for sodium-ion batteries by chemical presodiation. *Journal of Colloid and Interface Science*, *630*, 443–452.

Song, P., Yang, J., Wang, C., Wang, T., Gao, H., Wang, G., & Li, J. (2023). Interface engineering of Fe_7S_8/FeS_2 heterostructure in situ encapsulated into nitrogen-doped carbon nanotubes for high power sodium-ion batteries. *Nano-Micro Letters*, *15*, 118.

Su, D., Dou, S., & Wang, G. (2015). Ultrathin MoS_2 nanosheets as anode materials for sodium-ion batteries with superior performance. *Advanced Energy Materials*, *5*(6), 1401205.

Sun, X., Zeng, S., Man, R., Wang, L., Zhang, B., Tian, F., Qian, Y., & Xu, L. (2021). Yolk–shell structured $CoSe_2$/C nanospheres as multifunctional anode materials for both full/half sodium-ion and full/half potassium-ion batteries. *Nanoscale*, *13*(23), 10385–10392.

Sun, Y., Liu, N., & Cui, Y. (2016). Promises and challenges of nanomaterials for lithium-based rechargeable batteries. *Nature Energy*, *1*(7), 16071.

Sun, Z., Gu, Z., Shi, W., Sun, Z., Gan, S., Xu, L., Liang, H., Ma, Y., Qu, D., & Zhong, L. (2022). Mesoporous N-doped carbon-coated CoSe nanocrystals encapsulated in S-doped carbon nanosheets as advanced anode with ultrathin solid electrolyte interphase for high-performance sodium-ion half/full batteries. *Journal of Materials Chemistry A*, *10*(4), 2113–2121.

Tang, Q., Cui, Y., Wu, J., Qu, D., Baker, A. P., Ma, Y., Song, X., & Liu, Y. (2017). Nano Energy performance anode for lithium-ion and sodium-ion batteries. *Nano Energy*, *41*, 377–386.

Tang, Z., Wang, H., Wu, P., Zhou, S., Huang, Y., Zhang, R., Sun, D., Tang, Y., & Wang, H. (2022). Electrode–electrolyte interfacial chemistry modulation for ultra-high rate sodium-ion batteries. *Angewandte Chemie*, *61*(18), e202200475.

Tao, J., Yan, Z., Wang, D., Zhong, W., Yang, Y., Li, J., Lin, Y., & Huang, Z. (2022). Rational designing of $MoSe_2$ nanosheets in carbon framework for high-performance potassium-ion batteries. *Chemical Engineering Journal*, *448*, 137658.

Tao, S., Zhang, X., Gao, Z., Chen, T., Min, H., Yang, H., Chen, H., Shen, X., Wang, J., & Yang, H. (2023). Dynamic electronic and ionic transport actuated by cobalt-doped $MoSe_2$/rGO for superior potassium-ion batteries. *Small*, *19*(48), 2304200.

Tian, Y., Lu, J., Tang, H., Wang, X., Zhang, L., Hu, P., Zhou, L., Wang, Y., Guo, Y., Khatoon, R., Zhang, Q., He, Q., He, Y., Qiu, M., Hou, Y., & Ye, Z. (2021). An ultra-stable anode material for high/low-temperature workable super-fast charging sodium-ion batteries. *Chemical Engineering Journal*, *422*, 130054.

Tian, Y. R., Yi, Z. L., Su, F. Y., Xie, L. J., Zhang, X. F., Li, X. F., Cheng, J. Y., Chen, J. P., & Chen, C. M. (2024). Regulating the pore structure of activated carbon by pitch for high-performance sodium-ion storage. *ACS Applied Materials and Interfaces*, *16*(14), 17553–17562.

Tian, Z., Chui, N., Lian, R., Yang, Q., Wang, W., Yang, C., Rao, D., Huang, J., Zhang, Y., & Lai, F. (2020). Dual anionic vacancies on carbon nanofiber threaded MoSSe arrays: A free-standing anode for high-performance potassium-ion storage. *Energy Storage Materials*, *27*, 591–598.

Tripathi, B., Pandit, S., Sharma, A., Chauhan, S., Mathuriya, A. S., Dikshit, P. K., Gupta, P. K., Singh, R. C., Sahni, M., Pant, K., & Singh, S. (2022). Modification of graphite sheet anode with iron (II, III) oxide-carbon dots for enhancing the performance of microbial fuel cell. *Catalysts*, *12*(9), 1040.

Vaalma, C., Buchholz, D., Weil, M., & Passerini, S. (2018). A cost and resource analysis of sodium-ion batteries. *Nature Reviews Materials*, *3*(4), 18013.

Walter, M., Zünd, T., & Kovalenko, M. V. (2015). Pyrite (FeS_2) nanocrystals as inexpensive high-performance lithium-ion cathode and sodium-ion anode materials. *Nanoscale*, *7*(20), 9158–9163.

Wang, B., Gu, L., Yuan, F., Zhang, D., Sun, H., Wang, J., Wang, Q., Wang, H., & Li, Z. (2022). Edge-enrich N-doped graphitic carbon: Boosting rate capability and cyclability for potassium ion battery. *Chemical Engineering Journal*, *432*, 134321.

Wang, B., Li, J., Ye, M., Zhang, Y., Tang, Y., Hu, X., He, J., & Li, C. C. (2022). Dual-redox sites guarantee high-capacity sodium storage in two-dimension conjugated metal–organic frameworks. *Advanced Functional Materials*, *32*(22), 2112072.

Wang, B., Zhang, Z., Yuan, F., Zhang, D., Wang, Q., Li, W., Li, Z., Wu, Y. A., & Wang, W. (2022). An insight into the initial Coulombic efficiency of carbon-based anode materials for potassium-ion batteries. *Chemical Engineering Journal*, *428*, 131093.

Wang, Chao, Wan, J., Li, J., Zhang, L., Wang, R., Liu, Y., Ma, Y., Qin, Q., Qian, M., & Li, H. (2024). Enhancing sodium storage through tri-phase heterointerfaces in Co–Fe–$MoSe_2$@N-doped carbon nanocubes with self-generated rich phase boundaries. *Journal of Alloys and Compounds*, *987*, 174177.

Wang, Chenchen, Wang, L., Li, F., Cheng, F., & Chen, J. (2017). Bulk Bismuth as a High-Capacity and Ultralong Cycle-Life Anode for Sodium-Ion Batteries by Coupling with Glyme-Based Electrolytes. *Advanced Materials*, *29*(35), 1702212.

Wang, H., Lan, X., Jiang, D., Zhang, Y., Zhong, H., Zhang, Z., & Jiang, Y. (2015). Sodium storage and transport properties in pyrolysis synthesized $MoSe_2$ nanoplates for high performance sodium-ion batteries. *Journal of Power Sources*, *283*, 187–194.

Wang, J., Cui, J., Li, Z., Zhang, D., Sun, H., Wang, H., Wang, Q., Woo, H. J., Ramesh, S., & Wang, B. (2023). Polysulfide-derived anion heterogeneous interfaces engineering to facilitate high-efficiency sodium ion storage. *Chemical Engineering Journal*, *464*, 142764.

Wang, J., Shao, Y., Yuan, F., Sun, H., Zhang, D., Li, Z., Ramesh, S., Woo, H. J., & Wang, B. (2023). Hierarchically designed $MoWSe_2/WO_3/C$ anode for fast and efficient Na^+ storage. *Journal of Energy Chemistry*, *80*, 291–301.

Wang, K., Zhou, Y., Cheng, L., Li, D., Hu, Z., Chen, S., Wu, C., Song, L., & Ge, B. (2023). Engineering phase transition from 2H to 1T in $MoSe_2$ by W cluster doping toward lithium-ion battery. *Inorganic Chemistry*, *62*(51), 21257–21264.

Wang, L., & Zhang, L. (2023). Layered hollow $FeSe_2$ based on salt template as anode for sodium-ion batteries with advanced electrochemical performance. *Journal of Electroanalytical Chemistry*, *937*, 117432.

Wang, P., Liao, X., Xie, M., Zheng, Q., Chen, Y., Lam, K.-H., Zhang, H., & Lin, D. (2024). Heterogeneous engineering and carbon confinement strategy to synergistically boost the sodium storage performance of transition metal selenides. *Journal of Colloid and Interface Science*, *665*, 355–364.

Wang, P., Sun, F., Xiong, S., Zhang, Z., Duan, B., Zhang, C., Feng, J., & Xi, B. (2022). WSe2 Flakelets on N-Doped Graphene for Accelerating Polysulfide Redox and Regulating Li Plating. *Angewandte Chemie International Edition*, *61*(7), e202116048.

Wang, Shige, Cui, T., Shao, L., Yang, S., Yu, L., Guan, J., Shi, X., Cai, J., & Sun, Z. (2022). In-situ fabrication of active interfaces towards FeSe as advanced performance anode for sodium-ion batteries. *Journal of Colloid and Interface Science*, *627*, 922–930.

Wang, Shijian, Xiong, P., Guo, X., Zhang, J., Gao, X., Zhang, F., Tang, X., Notten, P. H. L., & Wang, G. (2020). A stable conversion and alloying anode for potassium-ion batteries: A combined strategy of encapsulation and confinement. *Advanced Functional Materials*, *30*(27), 2001588.

Wang, Tianshuai, Legut, D., Fan, Y., Qin, J., Li, X., & Zhang, Q. (2020). Building fast diffusion channel by constructing metal sulfide/metal selenide heterostructures for high-performance sodium ion batteries anode. *Nano Letters*, *20*(8), 6199–6205.

Wang, Tongxian, Guo, W., Wang, G., Wang, H., Bai, J., & Wang, B. (2020). Highly dispersed $FeSe_2$ nanoparticles in porous carbon nanofibers as advanced anodes for sodium and potassium ion batteries. *Journal of Alloys and Compounds*, *834*, 155265.

Wang, Wei, Chen, J. Y., Ouyang, J., Yin, H., Li, A. J., Chen, L., Huang, J. L., Zhu, Y. C., Li, G. Y., & Hou, Z. H. (2024). Spray pyrolysis-derived W-doped $MoSe_2$/rGO paper-like microspheres: optimization of microstructure and mesostructure for enhanced lithium storage. *Rare Metals*, *43*(7), 3019–3031.

Wang, Weixu, Wang, Y., Jiang, Z., Deng, B., & Jiang, Z.-J. (2023). Seed-mediated formation of multiphase zero-valent Sb nanoparticles as alloying-type anodes for sodium-ion batteries with high capacity and ultra-long durability. *Journal of Materials Chemistry A*, *11*(40), 21561–21568.

Wang, X., Zhang, X., Chen, Y., Dong, J., & Zhao, J. (2024). Optimizing electron spin-polarized states of $MoSe_2/Cr_2Se_3$ heterojunction-embedded carbon nanospheres for superior sodium/potassium-ion battery performances. *Small*, 2312130.

Wang, Yahui, Liu, R., Sun, S., & Wu, X. (2019). Facile synthesis of nickel-cobalt selenide nanoparticles as battery-type electrode for all-solid-state asymmetric supercapacitors. *Journal of Colloid and Interface Science*, *549*, 16–21.

Wang, Yan, Shen, Z., Lin, X., Ding, Q., Huang, X., Han, T., Zhang, H., & Liu, J. (2022). Rational engineering of VS_4 nanorod array on rose-shaped VS_2 nanosheets for high-performance aluminium-ion batteries. *Chemical Communications*, *58*(83), 11677–11680.

Wang, Yanrong, Liu, Z., Wang, C., Yi, X., Chen, R., Ma, L., Hu, Y., Zhu, G., Chen, T., Tie, Z., Ma, J., Liu, J., & Jin, Z. (2018). Highly branched VS_4 nanodendrites with 1D atomic-chain structure as a promising cathode material for long-cycling magnesium batteries. *Advanced Materials*, *30*(32), 1802563.

Wang, Yifei, Liu, Y., Li, Q., Li, Z., Xu, A., Dong, C., Sun, J., Zhang, X., Sun, X., & Yang, J. (2023). New dual-anions $FeS_{0.5}Se_{0.5}$@NC porous nanorods as advanced electrode materials for wide-temperature sodium-ion half/full batteries. *Applied Surface Science*, *620*, 156836.

Wang, Yunke, Zhao, Y., Liu, K., Wang, S., Li, N., Shao, G., Wang, F., & Zhang, P. (2023). Li intercalation in an $MoSe_2$ electrocatalyst: In situ observation and modulation of its precisely controllable phase engineering for a high-performance

flexible Li-S battery. *Carbon Energy*, *5*(2), e255.

Wang, Yuyu, Kang, W., Pu, X., Liang, Y., Xu, B., Lu, X., Sun, D., & Cao, Y. (2022). Template-directed synthesis of $Co_2P/MoSe_2$ in a N-doped carbon hollow structure for efficient and stable sodium/potassium ion storage. *Nano Energy*, *93*, 106897.

Wang, Z., Li, X., Guo, W., & Fu, Y. (2021). Anion intercalation of VS_4 triggers atomic sulfur transfer to organic disulfide in rechargeable lithium battery. *Advanced Functional Materials*, *31*(16), 2009875.

Wen, Y., He, K., Zhu, Y., Han, F., Xu, Y., Matsuda, I., Ishii, Y., Cumings, J., & Wang, C. (2014). Expanded graphite as superior anode for sodium-ion batteries. *Nature Communications*, *5*, 4033.

Wu, H., Yuan, R., Li, M., Liu, L., Liu, Y., Song, Q., Ai, W., Du, H., Du, Z., & Wang, K. (2022). $Co_{0.85}Se–Fe_7Se_8$ nanocuboids embedded in reduced graphene oxides as cycle-stable anodes for sodium-ion batteries. *Carbon*, *198*, 171–178.

Wu, K., Chen, F., Ma, Z., Guo, B., Lyu, Y., Wang, P., Yang, H., Li, Q., Wang, H., & Nie, A. (2019). In situ TEM and half cell investigation of sodium storage in hexagonal FeSe nanoparticles. *Chemical Communications*, *55*(39), 5611–5614.

Wu, S., Peng, H., Huang, L., Liu, Y., Wu, Y., Liu, L., Ai, W., & Sun, Z. (2023). P-doped hard carbon microspheres for sodium-ion battery anodes with superior rate and cyclic performance. *Inorganic Chemistry Frontiers*, *10*(20), 5908–5916.

Wu, S., Peng, H., Xu, J., Huang, L., Liu, Y., Xu, X., Wu, Y., & Sun, Z. (2024). Nitrogen/phosphorus co-doped ultramicropores hard carbon spheres for rapid sodium storage. *Carbon*, *218*, 118756.

Wu, Yanzhou, Hu, Q., Liang, H., Wang, A., Xu, H., Wang, L., & He, X. (2023). Electrostatic Potential as Solvent Descriptor to Enable Rational Electrolyte Design for Lithium Batteries. *Advanced Energy Materials*, *13*(22), 2300259.

Wu, Yuhan, Zhang, C., Zhao, H., & Lei, Y. (2021). Recent advances in ferromagnetic metal sulfides and selenides as anodes for sodium- and potassium-ion batteries. *Journal of Materials Chemistry A*, *9*(15), 9506–9534.

Xia, J., Jiang, K., Xie, J., Guo, S., Liu, L., Zhang, Y., Nie, S., Yuan, Y., Yan, H., & Wang, X. (2019). Tin disulfide embedded in N-, S-doped carbon nanofibers as anode material for sodium-ion batteries. *Chemical Engineering Journal*, *359*, 1244–1251.

Xie, M., Li, C., Ren, S., Ma, Y., Chen, X., Fan, X., Han, Y., Shi, Z., & Feng, S. (2022). Ultrafine Sb nanoparticles in situ confined in covalent organic frameworks for high-performance sodium-ion battery anodes. *Journal of Materials Chemistry A*,

10(28), 15089–15100.

Xie, Xingchen, Huang, K., Wu, X., Wu, N., Xu, Y., Zhang, S., & Zhang, C. (2020). Binding hierarchical $MoSe_2$ on MOF-derived N-doped carbon dodecahedron for fast and durable sodium-ion storage. *Carbon*, *169*, 1–8.

Xie, Xingchen, Wang, N., Sun, B., Zhong, L., He, L., Komarneni, S., & Hu, W. (2023). $MoSe_2$ hollow nanospheres with expanded selenide interlayers for high-performance aqueous zinc-ion batteries. *Journal of Colloid and Interface Science*, *650*, 456–465.

Xie, Xiuqiang, Kretschmer, K., Zhang, J., Sun, B., Su, D., & Wang, G. (2015). Sn@ CNT nanopillars grown perpendicularly on carbon paper: a novel free-standing anode for sodium ion batteries. *Nano Energy*, *13*, 208–217.

Xu, F., Qu, C., Lu, Q., Meng, J., Zhang, X., Xu, X., Qiu, Y., Ding, B., Yang, J., & Cao, F. (2022). Atomic Sn–enabled high-utilization, large-capacity, and long-life Na anode. *Science Advances*, *8*(19), eabm7489.

Xu, G., Ma, L., Gu, C., Jie, Z., Cui, X., Zhang, C., & Liu, L. (2022). Solvothermal preparation and electrochemical characteristics of Sb_2Se_3@C nanorods in quasi-solid-state batteries. *Acta Materialia*, *240*, 118310.

Xu, J., Wei, Z., Zhang, S., Wang, X., Wang, Y., He, M., & Huang, K. (2021). Hierarchical WSe_2 nanoflower as a cathode material for rechargeable Mg-ion batteries. *Journal of Colloid and Interface Science*, *588*, 378–383.

Xu, S., Gao, X., Hua, Y., Neville, A., Wang, Y., & Zhang, K. (2020). Rapid deposition of WS_2 platelet thin films as additive-free anode for sodium ion batteries with superior volumetric capacity. *Energy Storage Materials*, *26*, 534–542.

Xu, Yanan, Liu, X., Su, H., Jiang, S., Zhang, J., & Li, D. (2022). Hierarchical bimetallic selenides $CoSe_2$–$MoSe_2$/rGO for sodium/potassium-ion batteries anode: Insights into the intercalation and conversion mechanism. *Energy and Environmental Materials*, *5*(2), 627–636.

Xu, Yang, Zhang, C., Zhou, M., Fu, Q., Zhao, C., Wu, M., & Lei, Y. (2018). Highly nitrogen doped carbon nanofibers with superior rate capability and cyclability for potassium ion batteries. *Nature Communications*, *9*, 1720.

Xu, Yingshuang, Fo, Y., Lv, H., Cui, X., Liu, G., Zhou, X., & Jiang, L. (2022). Anderson-type polyoxometalate-assisted synthesis of defect-rich doped 1T/2H-$MoSe_2$ nanosheets for efficient seawater splitting and Mg/seawater batteries. *ACS Applied Materials & Interfaces*, *14*(8), 10246–10256.

Yan, J., Chen, X. L., Cui, Y., Yang, G. Z., Zheng, Z. L., Bin, D. S., & Li, D. (2022).

Engineering microstructure of a robust polymer anode by moderate pyrolysis for high-performance sodium storage. *ACS Applied Materials and Interfaces*, *14*(44), 49641–49649.

Yang, H., Yin, J., Yang, J., Tang, S., Zhang, W., & Yang, G. (2024). From macro to micro: Biomass-derived advanced carbon microtube assembly for sodium-ion batteries. *Nano Energy*, *125*, 109591.

Yang, J., Zhu, J., Xu, J., Zhang, C., & Liu, T. (2017). $MoSe_2$ nanosheet array with layered MoS_2 heterostructures for superior hydrogen evolution and lithium storage performance. *ACS Applied Materials and Interfaces*, *9*(51), 44550–44559.

Yang, S., Jiang, J., He, W., Wu, L., Xu, Y., Ding, B., Dou, H., & Zhang, X. (2023). Nitrogen-doped carbon encapsulating Fe_7Se_8 anode with core-shell structure enables high-performance sodium-ion capacitors. *Journal of Colloid and Interface Science*, *630*, 144–154.

Yang, W., Chen, Y., Yin, X., Lai, X., Wang, J., & Jian, J. (2023). SnSe nanosheet array on carbon cloth as a high-capacity anode for sodium-ion batteries. *ACS Applied Materials & Interfaces*, *15*(36), 42811–42822.

Yang, Y., Ma, Y., Wang, X., Gao, Z., Yu, J., & Liu, T. (2023). In-situ evolution of CoS/C hollow nanocubes from metal-organic frameworks for sodium-ion hybrid capacitors. *Chemical Engineering Journal*, *455*, 140610.

Yang, Zhenguo, Zhang, J., Kintner-meyer, M. C. W., Lu, X., Choi, D., & Lemmon, J. P. (2011). Electrochemical energy storage for green grid: Status and challenges. *ECS Meeting Abstracts*, 3577–3613.

Yang, Zihao, Li, W., Zhang, G., Wang, J., Zuo, J., Xu, Q., Shan, H., He, X., Lv, M., Hu, J., Huang, W., Zhang, J., & Li, X. (2022). Constructing Sb–O–C bond to improve the alloying reaction reversibility of free-standing Sb_2Se_3 nanorods for potassium-ion batteries. *Nano Energy*, *93*, 106764.

Yao, T., Wang, H., Qin, Y., Shi, J.-W., & Cheng, Y. (2023). Enhancing pseudocapacitive behavior of MOF-derived TiO_{2-x}@Carbon nanocubes via Mo-doping for high-performance sodium-ion capacitors. *Composites Part B: Engineering*, *253*, 110557.

Yao, W., Zheng, W., Xu, J., Tian, C., Han, K., Sun, W., & Xiao, S. (2021). ZnS-SnS@NC heterostructure as robust lithiophilicity and sulfiphilicity mediator toward high-Rate and long-life lithium-sulfur batteries. *ACS Nano*, *15*(4), 7114–7130.

Yi, Yuhao, Du, X., Zhao, Z., Liu, Y., Guan, H., Liu, X., Pei, X., Zhang, S., & Li, D. (2022). Coupling of metallic VSe_2 and conductive polypyrrole for boosted sodium-

ion storage by reinforced conductivity within and outside. *ACS Nano*, *16*(5), 7772–7782.

Yi, Yuyang, Sun, Z., Li, C., Tian, Z., Lu, C., Shao, Y., Li, J., Sun, J., & Liu, Z. (2020). Designing 3D biomorphic nitrogen-doped $MoSe_2$/graphene composites toward high-performance potassium-ion capacitors. *Advanced Functional Materials*, *30*(4), 1903878.

Yin, L., Pan, Y., Li, M., Zhao, Y., & Luo, S. (2020). Facile and scalable synthesis of α-Fe_2O_3/γ-Fe_2O_3/Fe/C nanocomposite as advanced anode materials for lithium/sodium ion batteries. *Nanotechnology*, *31*(15), 155402.

Yu, D., Wei, Z., Zhang, X., Zeng, Y., Wang, C., Chen, G., Shen, Z. X., & Du, F. (2021). Boosting Zn^{2+} and NH_4^+ storage in aqueous media via in-situ electrochemical induced VS_2/VO_x heterostructures. *Advanced Functional Materials*, *31*(11), 2008743.

Yu, L., Zhang, L., Kang, J., & Kim, K. H. (2021). Facile synthesis of manganese selenide anchored in three-dimensional carbon nanosheet matrix with enhanced lithium storage properties. *Chemical Engineering Journal*, *423*, 130243.

Yu, X., Zhao, G., Wu, C., Huang, H., Liu, C., Shen, X., Wang, M., Bai, X., & Zhang, N. (2021). Constructing anion vacancy-rich MoSSe/G van der Waals heterostructures for high-performance Mg–Li hybrid-ion batteries. *Journal of Materials Chemistry A*, *9*(40), 23276–23285.

Yuan, F., Li, Y., Wang, Y., Li, Z., Wang, Q., Sun, H., Zhang, D., Wang, W., & Wang, B. (2023). Cobalt nanoparticles synergize with oxygen-containing functional groups to realize fast and stable potassium storage for carbon anode. *Advanced Functional Materials*, *33*(46), 2304753.

Yuan, F., Li, Z., Zhang, D., Wang, Q., Wang, H., Sun, H., Yu, Q., Wang, W., & Wang, B. (2022). Fundamental understanding and research progress on the interfacial behaviors for potassium-ion battery anode. *Advanced Science*, *9*(20), 2200683.

Yuan, F., Shi, C., Li, Q., Wang, J., Zhang, D., Wang, Q., Wang, H., Li, Z., Wang, W., & Wang, B. (2022). Unraveling the effect of intrinsic carbon defects on potassium storage performance. *Advanced Functional Materials*, *32*(48), 2208966.

Yuan, F., Zhang, D., Li, Z., Sun, H., Yu, Q., Wang, Q., Zhang, J., Wu, Y., Xi, K., & Wang, B. (2022). Unraveling the intercorrelation between micro/mesopores and K migration behavior in hard carbon. *Small*, *18*(12), 2107113.

Yuan, J., Gan, Y., Xu, X., Mu, M., He, H., Li, X., Zhang, X., & Liu, J. (2022). Construction of Fe_7Se_8@Carbon nanotubes with enhanced sodium/potassium storage. *Journal of Colloid and Interface Science*, *626*, 355–363.

Yuan, Z., Zheng, J., Chen, X., Xiao, F., Yang, X., Luo, L., Xiong, P., Lai, W., Lin, C., Qin, F., Peng, W., Chen, Z., Qian, Q., Chen, Q., & Zeng, L. (2023). In situ encapsulation of MoS_xSe_{2-x} nanocrystals with the synergistic function of anion doping and physical confinement with chemical bonding for high-performance sodium/potassium-ion batteries with wide temperature workability. *ACS Sustainable Chemistry and Engineering*, *11*(35), 13050–13061.

Yue, X., Yang, J., Li, W., Jing, Y., Dong, L., Zhang, Y., & Li, X. (2022). Electron irradiation induces the conversion from 2H-WSe_2 to 1T-WSe_2 and promotes the performance of electrocatalytic hydrogen evolution. *ACS Sustainable Chemistry & Engineering*, *10*(7), 2420–2428.

Zeng, L., Fang, Y., Xu, L., Zheng, C., Yang, M. Q., He, J., Xue, H., Qian, Q., Wei, M., & Chen, Q. (2019). Rational design of few-layer $MoSe_2$ confined within ZnSe-C hollow porous spheres for high-performance lithium-ion and sodium-ion batteries. *Nanoscale*, *11*(14), 6766–6775.

Zhai, L., Yu, J. M., Yu, J. P., Xiong, W. W., & Zhang, Q. (2022). Thermodynamic transformation of crystalline organic hybrid iron selenide to Fe_xSe_y@CN microrods for sodium ion storage. *ACS Applied Materials and Interfaces*, *14*(44), 49854–49864.

Zhang, B.-L., Chen, X., Zhao, H.-J., Xie, H.-W., & Yin, H.-Y. (2023). Electrochemically exfoliated WS_2 in molten salt for sodium-ion battery anode. *Rare Metals*, *42*(4), 1227–1237.

Zhang, C., Wang, F., Han, F., Wu, H., Zhang, F., Zhang, G., & Liu, J. (2020). Improved electrochemical performance of sodium/potassium-ion batteries in ether-based electrolyte: Cases study of MoS_2@C and Fe_7S_8@C anodes. *Advanced Materials Interfaces*, *7*(13), 2000486.

Zhang, G., Ou, X., Yang, J., & Tang, Y. (2021). Molecular coupling and self-assembly strategy toward WSe_2/carbon micro–nano hierarchical structure for elevated sodium-ion storage. *Small Methods*, *5*(8), 2100374.

Zhang, H., Hasa, I., & Passerini, S. (2018). Beyond insertion for Na-ion batteries: Nanostructured alloying and conversion anode materials. *Advanced Energy Materials*, *8*(17), 1702582.

Zhang, M., Li, Y., Wu, F., Bai, Y., & Wu, C. (2021). Boost sodium-ion batteries to commercialization: Strategies to enhance initial Coulombic efficiency of hard carbon anode. *Nano Energy*, *82*, 105738.

Zhang, N., Chen, X., Xu, J., He, P., & Ding, X. (2023). Hexagonal Sb nanocrystals as high-capacity and long-cycle anode materials for sodium-ion batteries. *ACS*

Applied Materials & Interfaces, *15*(22), 26728–26736.

Zhang, S. L., Guan, B. Y., & Lou, X. W. (David). (2019). Co–Fe alloy/N-doped carbon hollow spheres derived from dual metal–organic frameworks for enhanced electrocatalytic oxygen reduction. *Small*, *15*(13), 1805324.

Zhang, S., Sun, L., Yu, L., Zhai, G., Li, L., Liu, X., & Wang, H. (2021). Core–shell $CoSe_2/WSe_2$ heterostructures@carbon in porous carbon nanosheets as advanced anode for sodium ion batteries. *Small*, *17*(49), 2103005.

Zhang, W., Yue, Z., Miao, W., Liu, S., Fu, C., Li, L., Zhang, Z., & Wang, H. (2018). Carbon-encapsulated tube-wire Co_3O_4/MnO_2 heterostructure nanofibers as anode material for sodium-ion batteries. *Particle & Particle Systems Characterization*, *35*(9), 1800138.

Zhang, Xiangdan, Liu, K., Zhang, S., Miao, F., Xiao, W., Shen, Y., Zhang, P., Wang, Z., & Shao, G. (2020). Enabling remarkable cycling performance of high-loading MoS_2@ Graphene anode for sodium ion batteries with tunable cut-off voltage. *Journal of Power Sources*, *458*, 228040.

Zhang, Xiao, He, Q., Xu, X., Xiong, T., Xiao, Z., Meng, J., Wang, X., Wu, L., Chen, J., & Mai, L. (2020). Insights into the storage mechanism of layered VS_2 cathode in alkali metal-ion batteries. *Advanced Energy Materials*, *10*(22), 1904118.

Zhang, Xiaoshan, Qiu, X., Lin, J., Lin, Z., Sun, S., Yin, J., Alshareef, H. N., & Zhang, W. (2023). Structure and interface engineering of ultrahigh-rate 3D bismuth anodes for sodium-ion batteries. *Small*, *19*(35), 2302071.

Zhang, Yan, Deng, S., Shen, Y., Liu, B., Pan, G., Liu, Q., Wang, X., Wang, Y., Xia, X., & Tu, J. (2020). Construction of 1T-$MoSe_2$/TiC@C branch–core arrays as advanced anodes for enhanced sodium ion storage. *ChemSusChem*, *13*(6), 1575–1581.

Zhang, Yingying, Chen, P., Wang, Q., Wang, Q., Zhu, K., Ye, K., Wang, G., Cao, D., Yan, J., & Zhang, Q. (2021). High-capacity and kinetically accelerated lithium storage in MoO_3 enabled by oxygen vacancies and heterostructure. *Advanced Energy Materials*, *11*(31), 2101712.

Zhang, Z., Xu, Y., He, C., Zhou, J., Wu, X., & Yang, Z. (2024). In situ encapsulation of cobalt selenide nanoparticles in N-doped carbon nanotubes with a full sulfiphilic surface as a catalytic interlayer for lithium–sulfur batteries. *Energy & Fuels*, *38*(10), 9072–9079.

Zhao, B., Suo, G., Mu, R., Lin, C., Li, J., Hou, X., Ye, X., Yang, Y., & Zhang, L. (2024). Constructing hierarchical MoS_2/WS_2 heterostructures in dual carbon layer for enhanced sodium ions batteries performance. *Journal of Colloid and Interface*

Science, *668*, 565–574.

Zhao, F., Shen, S., Cheng, L., Ma, L., Zhou, J., Ye, H., Han, N., Wu, T., Li, Y., & Lu, J. (2017). Improved sodium-ion storage performance of ultrasmall iron selenide nanoparticles. *Nano Letters*, *17*(7), 4137–4142.

Zhao, J., Zhou, M., Chen, J., Tao, L., Zhang, Q., Li, Z., Zhong, S., Fu, H., Wang, H., & Wu, L. (2021). Phthalocyanine-based covalent organic frameworks as novel anode materials for high-performance lithium-ion/sodium-ion batteries. *Chemical Engineering Journal*, *425*, 131630.

Zhao, Xiaoying, Liu, N., Mu, C., Qin, B., & Wang, L. (2024). Pb nanospheres encapsulated in metal–organic frameworks-derived porous carbon as anode for high-performance sodium-ion batteries. *Journal of Colloid and Interface Science*, *669*, 647–656.

Zhao, Xu, Cai, W., Yang, Y., Song, X., Neale, Z., Wang, H. E., Sui, J., & Cao, G. (2018). $MoSe_2$ nanosheets perpendicularly grown on graphene with Mo–C bonding for sodium-ion capacitors. *Nano Energy*, *47*, 224–234.

Zhao, Xu, Li, X., Yan, Y., Xing, Y., Lu, S., Zhao, L., Zhou, S., Peng, Z., & Zeng, J. (2018). Electrical and structural engineering of cobalt selenide nanosheets by Mn modulation for efficient oxygen evolution. *Applied Catalysis B: Environmental*, *236*, 569–575.

Zhao, Yan, Zhou, T., Mensi, M., Choi, J. W., & Coskun, A. (2023). Electrolyte engineering via ether solvent fluorination for developing stable non-aqueous lithium metal batteries. *Nature Communications*, *14*, 299.

Zhao, Yingying, Yang, D., He, T., Li, J., Wei, L., Wang, D., Wang, Y., Wang, X., Chen, G., & Wei, Y. (2021). Vacancy engineering in VS_2 nanosheets for ultrafast pseudocapacitive sodium ion storage. *Chemical Engineering Journal*, *421*, 129715.

Zhao, Zhenyun, Wu, Y., Hu, R., Lu, J., Chen, D., Li, T., Guo, Y., Zhang, L., Chen, H., & Ye, Z. (2023). Intercalation pseudocapacitance in 2D $VS_2/Ti_3C_2T_x$ MXene hybrids for all-climate and long-cycle sodium-ion batteries. *Advanced Functional Materials*, *33*(50), 2307794.

Zhao, Zhongchen, Xu, T., & Yu, X. (2023). Unlock the potassium storage behavior of single-phased tungsten selenide nanorods via large cation insertion. *Advanced Materials*, *35*(5), 2208096.

Zheng, C., Yao, Q., Li, R., Ji, D., Wang, C., Bai, Z., Wang, N., Dou, S., Liu, H., & Yang, J. (2024). Construction of robust solid-electrolyte interphase via electrode additive for high-performance Sn-based anodes of sodium-ion batteries. *Energy Storage Materials*, *67*, 103334.

Zheng, F., Zhong, W., Deng, Q., Pan, Q., Ou, X., Liu, Y., Xiong, X., Yang, C., Chen, Y., & Liu, M. (2019). Three-dimensional (3D) flower-like $MoSe_2$/N-doped carbon composite as a long-life and high-rate anode material for sodium-ion batteries. *Chemical Engineering Journal*, *357*, 226–236.

Zheng, S., Li, D., Li, W., Chen, J., Rao, X., Wang, N., Qi, J., Wang, B., Luo, S., & Zhao, Y. (2022). MnO_2 nanosheets on a carbon nanofiber freestanding film by electrospinning and in situ spraying for lithium and sodium storage. *ACS Applied Energy Materials*, *5*(3), 3587–3594.

Zheng, Y. Q., Yao, Z. F., Lei, T., Dou, J. H., Yang, C. Y., Zou, L., Meng, X., Ma, W., Wang, J. Y., & Pei, J. (2017). Unraveling the solution-state supramolecular structures of donor–acceptor polymers and their influence on solid-state morphology and charge-transport properties. *Advanced Materials*, *29*(42), 1701072.

Zhou, Chencheng, Zhang, P., Liu, J., Zhou, J., Wang, W., Li, K., Wu, J., Lei, Y., & Chen, L. (2021). Hierarchical $NiCo_2Se_4$ nanoneedles/nanosheets with N-doped 3D porous graphene architecture as free-standing anode for superior sodium ion batteries. *Journal of Colloid and Interface Science*, *587*, 260–270.

Zhou, Chunli, Wang, D., Li, A., Pan, E., Liu, H., Chen, X., Jia, M., & Song, H. (2020). Three-dimensional porous carbon doped with N, O and P heteroatoms as high-performance anode materials for sodium ion batteries. *Chemical Engineering Journal*, *380*, 122457.

Zhou, Jisheng, Wang, Y., Zhang, J., Chen, T., Song, H., & Yang, H. Y. (2016). Two dimensional layered $Co_{0.85}Se$ nanosheets as a high-capacity anode for lithium-ion batteries. *Nanoscale*, *8*(32), 14992–15000.

Zhou, Junhua, Wang, L., Yang, M., Wu, J., Chen, F., Huang, W., Han, N., Ye, H., Zhao, F., Li, Y., & Li, Y. (2017). Hierarchical VS_2 nanosheet assemblies: A universal host material for the reversible storage of alkali metal ions. *Advanced Materials*, *29*(35), 1702061.

Zhou, L., Cao, Z., Zhang, J., Sun, Q., Wu, Y., Wahyudi, W., Hwang, J. Y., Wang, L., Cavallo, L., Sun, Y. K., Alshareef, H. N., & Ming, J. (2020). Engineering sodium-ion solvation structure to stabilize sodium anodes: Universal strategy for fast-charging and safer sodium-ion batteries. *Nano Letters*, *20*(5), 3247–3254.

Zhou, P., Collins, G., Hens, Z., Ryan, K. M., Geaney, H., & Singh, S. (2020). Colloidal WSe_2 nanocrystals as anodes for lithium-ion batteries. *Nanoscale*, *12*(43), 22307–22316.

Zhou, X., Ding, S., He, H., Huang, Z., Cai, M., Cai, Y., & Zhang, M. (2020). Encapsulated SnSe in carbon nanofibers as anode of sodium ion batteries with

improved properties. *Ionics*, *26*(8), 3937–3946.

Zhu, H., Li, Z., Xu, F., Qin, Z., Sun, R., Wang, C., Lu, S., Zhang, Y., & Fan, H. (2022). Ni_3Se_4@$CoSe_2$ hetero-nanocrystals encapsulated into CNT-porous carbon interpenetrating frameworks for high-performance sodium ion battery. *Journal of Colloid and Interface Science*, *611*, 718–725.

Zhu, L.-M., Ding, G.-C., Han, Q., Miao, Y.-X., Li, X., Yang, X.-L., Chen, L., Wang, G.-K., Xie, L.-L., & Cao, X.-Y. (2022). Enhancing electrochemical performances of small quinone toward lithium and sodium energy storage. *Rare Metals*, *41*, 425–437.

Zhu, M., Li, J., Yang, X., Li, X., Wang, L., & Lü, W. (2023). 3D reduced graphene oxide wrapped MoS_2@Sb_2S_3 heterostructures for high performance sodium-ion batteries. *Applied Surface Science*, *624*, 157106.

Zhu, Q., Li, W., Wu, J., Tian, N., Li, Y., Yang, J., & Liu, B. (2022). Filling selenium into sulfur vacancies in ultrathin tungsten sulfide nanosheets for superior potassium storage. *ACS Applied Materials & Interfaces*, *14*(46), 51994–52006.

Zou, H.-Y., Fang, L., Yu, G., & Wang, D. (2024). Nanocrystalline WSe_2 excels at high-performance anode for Na storage via a facile one-pot hydrothermal method. *Tungsten*, *6*(1), 248–258.

Zuo, W., Li, R., Zhou, C., Li, Y., Xia, J., & Liu, J. (2017). Battery-supercapacitor hybrid devices: Recent progress and future prospects. *Advanced Science*, *4*(7), 1600539.